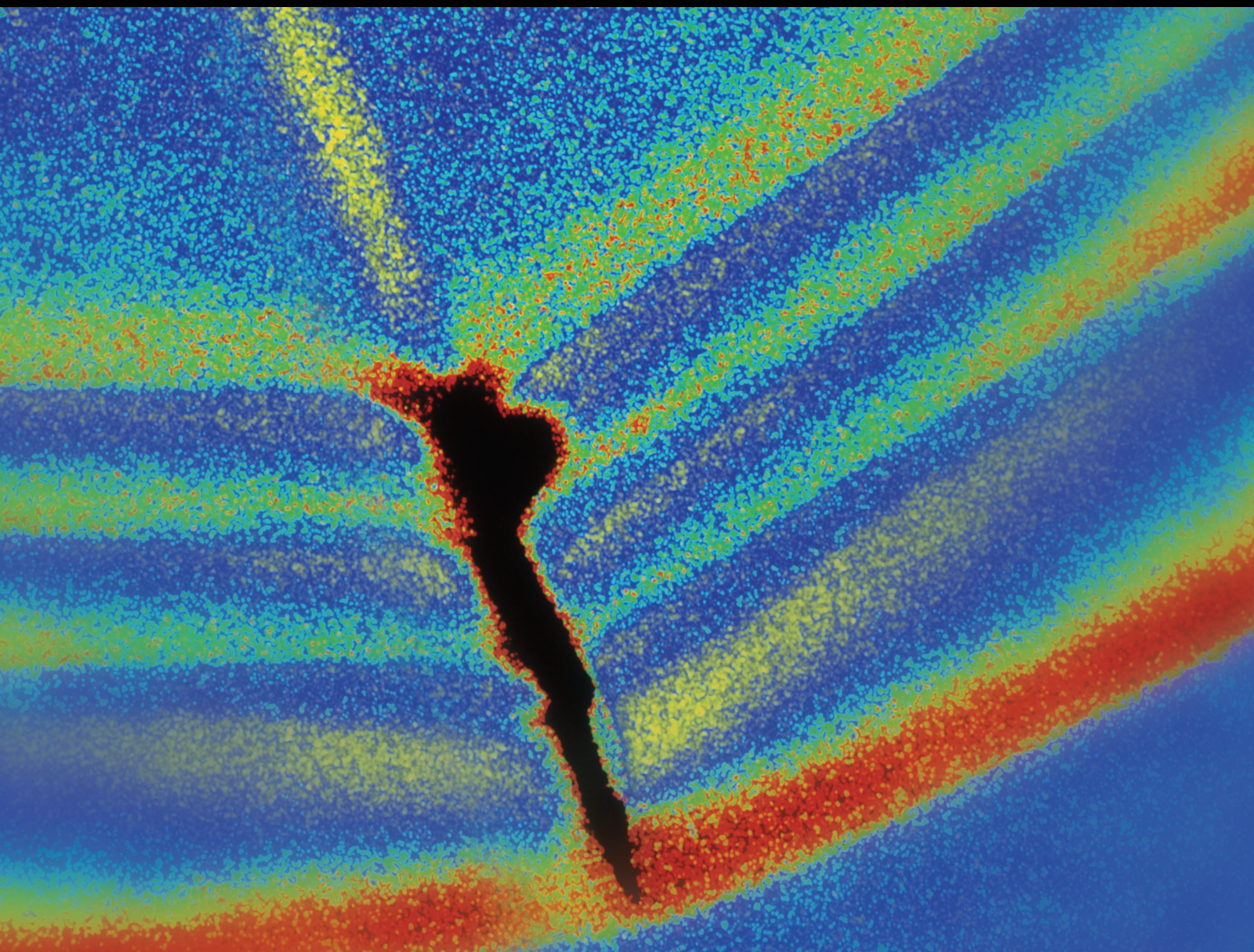


# Responses and Protection of Structures against Multiple Dynamic Hazards

Lead Guest Editor: Shao-Bo Kang

Guest Editors: Bing Zhang, Feng Fu, Honghao Li, Jingxuan Wang, and Shan Gao





---

# **Responses and Protection of Structures against Multiple Dynamic Hazards**

Shock and Vibration

---

## **Responses and Protection of Structures against Multiple Dynamic Hazards**

Lead Guest Editor: Shao-Bo Kang

Guest Editors: Bing Zhang, Feng Fu, Honghao Li,  
Jingxuan Wang, and Shan Gao



---

Copyright © 2023 Hindawi Limited. All rights reserved.

This is a special issue published in “Shock and Vibration.” All articles are open access articles distributed under the Creative Commons Attribution License, which permits unrestricted use, distribution, and reproduction in any medium, provided the original work is properly cited.

# Chief Editor

Huu-Tai Thai , Australia


## Associate Editors

Ivo Calìo , Italy  
Nawawi Chouw , New Zealand  
Longjun Dong , China  
Farzad Ebrahimi , Iran  
Mickaël Lallart , France  
Vadim V. Silberschmidt , United Kingdom  
Mario Terzo , Italy  
Angelo Marcelo Tusset , Brazil

## Academic Editors

Omid A. Yamini , Iran  
Maher Abdelghani, Tunisia  
Haim Abramovich , Israel  
Desmond Adair , Kazakhstan  
Manuel Aenlle Lopez , Spain  
Brij N. Agrawal, USA  
Ehsan Ahmadi, United Kingdom  
Felix Albu , Romania  
Marco Alfano, Italy  
Sara Amoroso, Italy  
Huaming An, China  
P. Antonaci , Italy  
José V. Araújo dos Santos , Portugal  
Lutz Auersch , Germany  
Matteo Aureli , USA  
Azwan I. Azmi , Malaysia  
Antonio Batista , Brazil  
Mattia Battarra, Italy  
Marco Belloli, Italy  
Francisco Beltran-Carbajal , Mexico  
Denis Benasciutti, Italy  
Marta Berardengo , Italy  
Sébastien Besset, France  
Giosuè Boscato , Italy  
Fabio Botta , Italy  
Giuseppe Brandonisio , Italy  
Francesco Bucchi , Italy  
Rafał Burdzik , Poland  
Salvatore Caddemi , Italy  
Wahyu Caesarendra , Brunei Darussalam  
Baoping Cai, China  
Sandro Carbonari , Italy  
Cristina Castejón , Spain

Nicola Caterino , Italy  
Gabriele Cazzulani , Italy  
Athanasios Chasalevris , Greece  
Guoda Chen , China  
Xavier Chimentin , France  
Simone Cinquemani , Italy  
Marco Civera , Italy  
Marco Cocconcelli , Italy  
Alvaro Cunha , Portugal  
Giorgio Dalpiaz , Italy  
Thanh-Phong Dao , Vietnam  
Arka Jyoti Das , India  
Raj Das, Australia  
Silvio L.T. De Souza , Brazil  
Xiaowei Deng , Hong Kong  
Dario Di Maio , The Netherlands  
Raffaella Di Sante , Italy  
Luigi Di Sarno, Italy  
Enrique Lopez Droguett , Chile  
Mădălina Dumitriu, Romania  
Sami El-Borgi , Qatar  
Mohammad Elahinia , USA  
Said Elias , Iceland  
Selçuk Erkaya , Turkey  
Gaoliang Fang , Canada  
Fiorenzo A. Fazzolari , United Kingdom  
Luis A. Felipe-Sese , Spain  
Matteo Filippi , Italy  
Piotr Fołga , Poland  
Paola Forte , Italy  
Francesco Franco , Italy  
Juan C. G. Prada , Spain  
Roman Gabl , United Kingdom  
Pedro Galvín , Spain  
Jinqiang Gan , China  
Cong Gao , China  
Arturo García García-Perez, Mexico  
Rozaimi Ghazali , Malaysia  
Marco Gherlone , Italy  
Anindya Ghoshal , USA  
Gilbert R. Gillich , Romania  
Antonio Giuffrida , Italy  
Annalisa Greco , Italy  
Jiajie Guo, China

Amal Hajjaj , United Kingdom  
Mohammad A. Hariri-Ardebili , USA  
Seyed M. Hashemi , Canada  
Xue-qiu He, China  
Agustin Herrera-May , Mexico  
M.I. Herreros , Spain  
Duc-Duy Ho , Vietnam  
Hamid Hosano , Japan  
Jin Huang , China  
Ahmed Ibrahim , USA  
Bernard W. Ikuu, Kenya  
Xingxing Jiang , China  
Jiang Jin , China  
Xiaohang Jin, China  
MOUSTAFA KASSEM , Malaysia  
Shao-Bo Kang , China  
Yuri S. Karinski , Israel  
Andrzej Katunin , Poland  
Manoj Khandelwal, Australia  
Denise-Penelope Kontoni , Greece  
Mohammadreza Koopialipour, Iran  
Georges Kouroussis , Belgium  
Genadijus Kulvietis, Lithuania  
Pradeep Kundu , USA  
Luca Landi , Italy  
Moon G. Lee , Republic of Korea  
Trupti Ranjan Lenka , India  
Arcanjo Lenzi, Brazil  
Marco Lepidi , Italy  
Jinhua Li , China  
Shuang Li , China  
Zhixiong Li , China  
Xihui Liang , Canada  
Tzu-Kang Lin , Taiwan  
Jinxin Liu , China  
Ruonan Liu, China  
Xiuquan Liu, China  
Siliang Lu, China  
Yixiang Lu , China  
R. Luo , China  
Tianshou Ma , China  
Nuno M. Maia , Portugal  
Abdollah Malekjafarian , Ireland  
Stefano Manzoni , Italy

Stefano Marchesiello , Italy  
Francesco S. Marulo, Italy  
Traian Mazilu , Romania  
Vittorio Memmolo , Italy  
Jean-Mathieu Mencik , France  
Laurent Mevel , France  
Letícia Fleck Fadel Miguel , Brazil  
FuRen Ming , China  
Fabio Minghini , Italy  
Marco Miniaci , USA  
Mahdi Mohammadpour , United Kingdom  
Rui Moreira , Portugal  
Emiliano Mucchi , Italy  
Peter Múčka , Slovakia  
Fehmi Najar, Tunisia  
M. Z. Naser, USA  
Amr A. Nassr, Egypt  
Sundararajan Natarajan , India  
Toshiaki Natsuki, Japan  
Miguel Neves , Portugal  
Sy Dzung Nguyen , Republic of Korea  
Trung Nguyen-Thoi , Vietnam  
Gianni Niccolini, Italy  
Rodrigo Nicoletti , Brazil  
Bin Niu , China  
Leilei Niu, China  
Yan Niu , China  
Lucio Olivares, Italy  
Erkan Oterkus, United Kingdom  
Roberto Palma , Spain  
Junhong Park , Republic of Korea  
Francesco Pellicano , Italy  
Paolo Pennacchi , Italy  
Giuseppe Petrone , Italy  
Evgeny Petrov, United Kingdom  
Franck Poisson , France  
Luca Pugi , Italy  
Yi Qin , China  
Virginio Quaglini , Italy  
Mohammad Rafiee , Canada  
Carlo Rainieri , Italy  
Vasudevan Rajamohan , India  
Ricardo A. Ramirez-Mendoza , Mexico  
José J. Rangel-Magdaleno , Mexico

Didier Rémond , France  
Dario Richiedi , Italy  
Fabio Rizzo, Italy  
Carlo Rosso , Italy  
Riccardo Rubini , Italy  
Salvatore Russo , Italy  
Giuseppe Ruta , Italy  
Edoardo Sabbioni , Italy  
Pouyan Roodgar Saffari , Iran  
Filippo Santucci de Magistris , Italy  
Fabrizio Scozzese , Italy  
Abdullah Seçgin, Turkey  
Roger Serra , France  
S. Mahdi Seyed-Kolbadi, Iran  
Yujie Shen, China  
Bao-Jun Shi , China  
Chengzhi Shi , USA  
Gerardo Silva-Navarro , Mexico  
Marcos Silveira , Brazil  
Kumar V. Singh , USA  
Jean-Jacques Sinou , France  
Isabelle Sochet , France  
Alba Sofi , Italy  
Jussi Sopanen , Finland  
Stefano Sorace , Italy  
Andrea Spaggiari , Italy  
Lei Su , China  
Shuaishuai Sun , Australia  
Fidelis Tawiah Suorineni , Kazakhstan  
Cecilia Surace , Italy  
Tomasz Szolc, Poland  
Iacopo Tamellini , Italy  
Zhuhua Tan, China  
Gang Tang , China  
Chao Tao, China  
Tianyou Tao, China  
Marco Tarabini , Italy  
Hamid Toopchi-Nezhad , Iran  
Carlo Trigona, Italy  
Federica Tubino , Italy  
Nerio Tullini , Italy  
Nicolò Vaiana , Italy  
Marcello Vanali , Italy  
Christian Vanhille , Spain

Dr. Govind Vashishtha, Poland  
F. Viadero, Spain  
M. Ahmer Wadee , United Kingdom  
C. M. Wang , Australia  
Gaoxin Wang , China  
Huiqi Wang , China  
Pengfei Wang , China  
Weiqiang Wang, Australia  
Xian-Bo Wang, China  
YuRen Wang , China  
Wai-on Wong , Hong Kong  
Yuanping XU , China  
Biao Xiang, China  
Qilong Xue , China  
Xin Xue , China  
Diansen Yang , China  
Jie Yang , Australia  
Chang-Ping Yi , Sweden  
Nicolo Zampieri , Italy  
Chao-Ping Zang , China  
Enrico Zappino , Italy  
Guo-Qing Zhang , China  
Shaojian Zhang , China  
Yongfang Zhang , China  
Yaobing Zhao , China  
Zhipeng Zhao, Japan  
Changjie Zheng , China  
Chuanbo Zhou , China  
Hongwei Zhou, China  
Hongyuan Zhou , China  
Jiaxi Zhou , China  
Yunlai Zhou, China  
Radoslaw Zimroz , Poland

# Contents

## **Seismic Behaviour of Multistorey Steel Framed Tall Buildings Using Intentionally Eccentric Braces**

Nima Gholizadeh and Feng Fu 




Research Article (20 pages), Article ID 7288450, Volume 2023 (2023)

## **Seismic Performance of Concrete-Filled Square Steel Tubular Column-Steel Beam Sleeve Joint**

Xiangong Huang, Man Xu , Nan Guo , Senwen Deng, and Le Huang

Research Article (18 pages), Article ID 3639936, Volume 2022 (2022)

## **Dynamic Characterization of a Reinforcement Rammed Wall for the Earthen Ruins**

Bei Liu , Yucheng Shi , Kun Liu , Tao Li, and Shaopeng Wang






Research Article (6 pages), Article ID 3439431, Volume 2022 (2022)

## **Probability Distribution and Determination of Blast Loading during Structural Blast Resistant Study**

Taochun Yang , Yaozhi Luo , Guangqing Hu , and Yi Jiang 





Research Article (19 pages), Article ID 7367288, Volume 2022 (2022)

## **Inversion for Constitutive Model Parameters of Bird in Case of Bird Striking**

Peng Yu , Siliu Yu , Sheng He , Xinheng Huang , and Weijing Yun 

Research Article (10 pages), Article ID 2456777, Volume 2022 (2022)

## **Shaking Table Test of a New Type Insulation Decorative Block Wall under Out-of-Plane Loading**

Jian Wu , Yuan Yuan Lv , Shuai Shuai Yin , and Qi Wang 

Research Article (15 pages), Article ID 7423912, Volume 2022 (2022)

## **Investigation of Dynamic Responses and Vibration Serviceability of Temporary Grandstands by a 3 DOF Interaction Model due to Swaying Motion**

Jian Yuan, Suhui Yu, Cong Liu , Chengqiang Gao, Wei Wang, Lin He, and Feng Fan

Research Article (32 pages), Article ID 6217148, Volume 2022 (2022)

## **Experimental Research on Damping Effect of Double-Layer Tuned Mass Damper for High-Rise Structure**

Botan Shen, Jin Wang , Weibing Xu , Yanjiang Chen, Weiming Yan, Jianhui Huang, and Zhenyun Tang





Research Article (22 pages), Article ID 7523127, Volume 2021 (2021)

## **Modeling Research and Test Verification of the Seismic Response of a Multistage Series Liquid Tank**

Xiaoguang Yao , Lijun Meng , Peng Chu , and Liang Yao 

Research Article (13 pages), Article ID 9695139, Volume 2021 (2021)

## **Overlapping Decentralized Control Strategies of Building Structures' Vibration with Time Delay Based on $H_\infty$ Control Algorithms under Seismic Excitation**

Xiaofang Kang , Jian Wu, Yewei Zhang, Guoliang Liu, Suhui Zhang, Xueting Tao , Guanghui Xia , Dawei Man , and Qinghu Xu

Research Article (12 pages), Article ID 9115938, Volume 2021 (2021)




**Dynamic Response and Parametric Studies of Elliptical Blast-Resistant Door with the Combined Structure for Large Vacuum Explosion Containers**

Saiwei Cheng , Xiaojie Li , Yang Wang , Yuxin Wang , and Honghao Yan   
Research Article (14 pages), Article ID 3591512, Volume 2021 (2021)


**A Case Study on the Deformation of Metro Foundation Pit in Silt Stratum in North China**

Yonggang Zhang , Yonghong Wang, and Yuanyuan Zhao   
Research Article (11 pages), Article ID 7454596, Volume 2021 (2021)


**Elaborate Modeling and Fragility Assessment of a Multiframe PC Box-Girder Bridge with Intermediate Hinges in California**

Tong Wu, Zhan Li, and Shengchun Liu   
Research Article (18 pages), Article ID 6046209, Volume 2021 (2021)


**The research into the propagation law of the shock wave of a gas explosion inside a building**

Shu-Chao Lin, You-Chun Xu, Pei-Dong Yang, Shan Gao , Yi-Jun Zhou, and Jin Xu  
Research Article (16 pages), Article ID 4939014, Volume 2021 (2021)



**Seismic Behavior Experimental Study on the Joint of Circular Tubed Steel-Reinforced Concrete Columns**

Yan Dai , Shaofeng Nie, Tianhua Zhou, Chengfeng Xue, and Jingrong Peng  
Research Article (15 pages), Article ID 6602309, Volume 2021 (2021)



**Restoring Force Model Research on Joint of Circular Tubed Steel-Reinforced Concrete Column**

Yan Dai , Shaofeng Nie, Tianhua Zhou, Yichun Xu, and Jingrong Peng  
Research Article (11 pages), Article ID 9021167, Volume 2021 (2021)

**Analysis for Shear Behavior of SRC Deep Beams Based on Tests, Digital Image Correlation Technique, and Finite Elemental Simulation**

Buqing Chen , Jun Wu , Changjun Liu, Yanhua Liu, Wenmei Zhou, and Yunfeng Xiao  
Research Article (13 pages), Article ID 5964480, Volume 2021 (2021)

**Seismic Performance of CFST Frame-Steel Plate Shear Walls Connected to Beams Only**

Qin Rong, Zhonghui Zhao, Lanhui Guo, Xiaomeng Hou , Li Lin , and Hongtao Bi  
Research Article (13 pages), Article ID 5850073, Volume 2021 (2021)

**Simulation of Delamination Evolution of Slab Ballastless Track under Vertical Impact**

Yu Liu , Qianqi Xu , Xiaodan Sun , Guotao Yang , and Guotang Zhao   
Research Article (13 pages), Article ID 4022875, Volume 2021 (2021)

## Research Article

# Seismic Behaviour of Multistorey Steel Framed Tall Buildings Using Intentionally Eccentric Braces

Nima Gholizadeh and Feng Fu 

*Department of Engineering, School of Science and Technology, City, University of London, EC1V 0HB, London, UK*

Correspondence should be addressed to Feng Fu; [feng.fu.1@city.ac.uk](mailto:feng.fu.1@city.ac.uk)

Received 12 October 2021; Revised 1 March 2022; Accepted 2 May 2023; Published 21 June 2023

Academic Editor: Ehsan Ahmadi

Copyright © 2023 Nima Gholizadeh and Feng Fu. This is an open access article distributed under the Creative Commons Attribution License, which permits unrestricted use, distribution, and reproduction in any medium, provided the original work is properly cited.

Braces with intentional eccentricity (BIE) are recently proposed to improve the seismic behaviour of conventional buckling braces (CBBs) by inserting intentional eccentricity along the brace length. Due to this eccentricity and the resultant bending moment, the BIE bends uniformly from small storey drifts and moves smoothly into the postbuckling behaviour under compression and sustains trilinear behaviour under tension. This behaviour delays the appearance of midlength local buckling which causes unstable energy dissipation. BIEs have a desirable postyielding stiffness which results in stable energy dissipation during cyclic loading and are capable of dissipating energy during low-intensity earthquakes. The seismic behaviour of structures with BIEs for use in buildings has not yet been investigated, specifically in tall buildings. Therefore, this study concentrates on investigating the seismic behaviour of tall buildings equipped with BIEs that uses a 3-dimensional (3D) finite element model in ETABS. In the first step, a 20-storey structure is designed using both eccentric brace frame (EBF) and BIE system and their seismic performance under the TABAS earthquake record is compared. In the second step, the seismic performance of a 25-storey irregular structure is assessed to evaluate the efficiency of the BIE system in irregular structures. Results show the desirable performance and energy dissipation capacity of the BIE system but it also shows large out-of-plane deformation in some cases.

## 1. Introduction

Bracing systems are widely used as lateral resisting systems in various types of low-rise and tall buildings. Bracing is an efficient and economical method to provide stiffness and strength against lateral loads. Its efficiency is mainly because of the fact that the diagonal members work primarily in the axial stress, so that minimum member sizes are required in the structural systems. Concentric bracing and eccentric bracing are the two major categories of bracing.

The typical concentrically braced frames (CBFs) can only take axial loading in the braces. In a concentric bracing system, all of the members (beams, columns, and bracing) are oriented in a manner that all of them meet at a common point [1]. One of the main disadvantages of CBFs is their unreliable behaviour under cyclic loading. On the other hand, the energy dissipation mechanism is not quite efficient in concentrically braced frames [2–4]. As another

disadvantage of CBFs, many experimental studies have revealed that because of the rapid increase in concentrated plastic strain, fracture follows the local buckling of concentric braces.

In eccentric bracings (EBFs), both axial loading members and bending members (the horizontal members) are involved in the lateral load-carrying mechanism. In eccentric bracing, the braces are placed with an offset from the columns. Eccentric bracing can provide the advantages of concentric bracing, while it has a significant ductility. On the other hand, in the context of architectural considerations, EBFs may provide larger openings in braced spans. However, the required detailing in EBFs is much more complicated than the concentric bracing [5].

The postyielding stiffness is one of the behavioural parameters that affect the structural response besides the strength, stiffness, and ductility. The high postyielding stiffness of structures results in a larger amount of energy

being absorbed during seismic excitation [6] and also less seismic demand in terms of strength and residual displacement [7]. The load-displacement relationship of structural systems with high postyielding stiffness may be characterized by trilinear behaviour which better satisfies the multilevel seismic design criteria [8]. In addition, larger postyielding stiffness results in a reduction in residual displacement demand of structures and help to prevent the soft-storey mechanism [9]. While conventional bracings provide limited postyielding stiffness, it, however, enhances the aforementioned weaknesses of CBFs which may be considered a motivation for developing new steel bracing systems.

Recently a new design of bracings has been introduced to improve the seismic performance of braced structures by controlling important structural characteristics, such as the initial stiffness, yield strength, the drift at which the system starts to dissipate energy, the postyielding stiffness, the local buckling concentration, the total dissipated energy, and the drift at which fracture occurs. In this newly introduced bracing named as braces with intentional eccentricity (BIE), an intentional eccentricity is inserted along the brace length which controls the brace deformation.

The first outstanding research work on BIEs was carried out by Skalomenos et al. [10]. They proposed a prototype design of conventional buckling braces by introducing an initial eccentricity along the brace length which results in an improved seismic performance. In their experimental work, five half-scaled BIE specimens were tested under a cyclic lateral load protocol for drift angles ranging from 0.10 to 4.0%. Also, they tested a conventional brace specimen with identical dimensions and zero eccentricity under the same loading pattern to conduct a comparative study. Their results showed the capability of the proposed steel brace in enhancing some of the negative traits of conventional steel brace. They concluded that their proposed bracing system may be considered as a viable alternative for steel bracings.

Skalomenos et al. [10] developed an online hybrid test environment to assess the seismic performance of the gusset plate connections of steel braces. In this regard, they incorporated substructuring techniques and finite element methods. Skalomenos et al. [11] presented an experimental investigation on the material properties of induction heat (IH) treated with steel elements used in BIEs. They used IH treatment and applied it to one-half of the cross-section to enhance the strength of that part, while the remaining part had the conventional properties of steel. Their tests showed that the treated brace exhibits a high postyielding tensile stiffness (equal to 20% of the initial stiffness). Also, the specimen was capable of dissipating energy during cyclic loading up to 2.0% storey drift because of the considerable delay in local buckling.

González Ureña et al. [12] used a procedure based on the direct displacement-based design (DDBD) method for the seismic design of 2D frames with BIEs. By using this method, they designed buildings with 4, 8, and 12 storeys. BIEs were assumed to be of HSS sections with target drift ratios of 1.5% and 2.5%. They also designed the same buildings with special CBFs to provide a comparative study. Their results showed that the design procedure they employed was suitable for the design of BIEs. They assessed the seismic performance of the structures and concluded that BIEs may provide an economically efficient alternative to conventional CBFs.

While the abovementioned experimental and analytical research works have been carried out on the cyclic behaviour of this type of braces on the element level, the global behaviour of structures equipped with these bracings has not yet been assessed, especially for tall buildings. Therefore, this research aims at investigating the seismic behaviour of tall steel structures equipped with BIEs under earthquake records and comparing its energy dissipation capacity with the EBF system. The 3-dimensional (3D) finite element models in ETABS will be used to provide a detailed understanding of the structural responses.

Response-history analyses are performed using ETABS to assess the seismic performance of the structure. The storey drifts, base shear, and dissipated energy are assessed using the responses under the TABAS earthquake record. The cyclic behaviour of BIEs is also assessed.

## 2. Braces with Intentional Eccentricity (BIE)

In braces with intentional eccentricity (BIE), as shown in Figure 1, an intentional eccentricity  $e$  is introduced along the brace length which affects the deformation of the brace. With this eccentricity, BIEs undergo overall bending with a small storey drift. Figure 2 shows the deformed shape of a BIE. The moment generated by the eccentrically applied axial force results in more uniformly distributed stresses and strains along the brace length. This delays the local buckling concentration resulting in extended ductile behaviour of the brace element.

The cyclic behaviour of BIEs is the main aspect of these bracing systems which affects the global behaviour of the structure under seismic loadings. Since ETABS will be used to analyse the structure and acquire the structural responses under earthquake records, a proper model of the BIE should be developed in ETABS. This model should be verified by the results from previous studies to attain a proper estimate of the BIE's cyclic behaviour and backbone curve.

The first step in modelling the BIE system in structures is developing a model of the brace at the element level. A beam element with fiber hinges is used here to model the flexural behaviour and an axial hinge is used to model the axial behaviour of the element. These hinges are modelled in parallel and placed at the middle and two ends of the

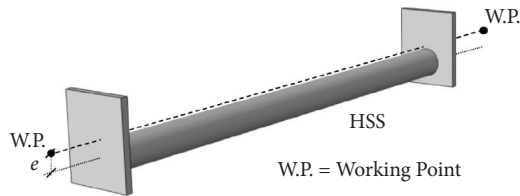


FIGURE 1: Configuration of the BIE [10].

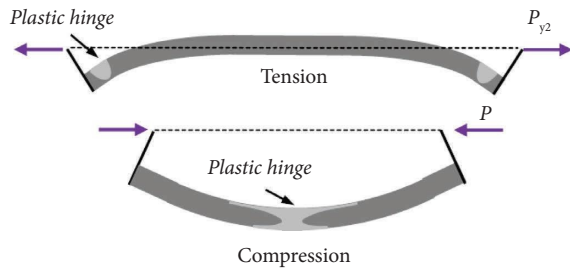


FIGURE 2: Deformed shape of brace under tensile and compressive loads [13].

element. The generated model in ETABS is shown in Figure 3. As can be seen in the figure, the eccentricity is imposed via the rigid links at the two ends of the element.

The fiber hinges are modelled using 10 layers in each direction of the section. This fiber section is shown in Figure 4. It is assumed that the brace bends only in the out-of-plane direction.

**2.1. Axial Loading.** In order to verify the developed model in ETABS, the results obtained in a work by González Ureña et al. [12] are studied here. They used OpenSees to model BIEs and to assess their behaviour and the effects of the different parameters. Their model was verified by the experimental results of Skalomenos et al. [14] and also the shell-based finite element models in the commercial software, Abaqus. The load-displacement behaviour of an element in tension and compression is reported in their work for a HSS  $178 \times 178 \times 16$  with a 5408 mm long modelled. A nominal yield stress of 345 MPa was considered for the HSS section. A displacement control loading is performed by ETABS in this study. An axial load is exerted on the element in the left end, while the right end is constrained and 100 mm displacement in compression and 250 mm displacement in tension is applied to the element. The cross-sections and rigid elements are also shown in Figure 5.

A deformed shape of the element in compression is shown in Figure 6 in a step with a 100 mm displacement and in tension with a 126.9 mm displacement as shown in Figure 7.

Under compression, the axial hinge remains in its elastic state while the fiber hinge bends considerably. In tension, both tension and flexure contribute to the load-displacement diagrams. To verify the behaviour of the developed model, the load-displacement diagrams generated by González Ureña et al. [12] are compared with the results of the

generated model in this study as shown in Figure 8. In the figure, the dashed lines are the results obtained from the model generated in this study. It can be seen that the developed model succeeds in providing good estimates of the compressive and tensile behaviour of BIE.

**2.2. Cyclic Behaviour.** Furthermore, the cyclic behaviour of the element is verified. In the work by González Ureña et al. [12], the axial force vs. lateral drift hysteretic plots of the same HSS element with an eccentricity of 180 mm were generated. They used OpenSees to analyse a braced bay with a 6 m width and 4 m height. The loading protocol had symmetrical cycles of increasing equivalent storey drifts of 0.1, 0.25, 0.75, 1.0, 1.5, 2, and 3%. As expected, the BIE showed a significant postyield stiffness in tension, in contrast with the CCB. In the compression stage, the BIE exhibited a stabilized maximum load equal to the postbuckling force.

The single element developed in the previous part is assembled in a frame with  $e = 180$  mm eccentricity and the dimensions stated above as shown in Figure 9. A cyclic loading is applied to the upper node of the frame.

A displacement loading protocol is applied to the left-most upper node of the frame as shown in Figure 10.

The load-displacement diagram of the frame is verified with the results of González Ureña et al. [12] as shown in Figure 11. The blue line in the figure is the result obtained by the model developed in this study using ETABS. As can be seen, a good agreement is achieved in this model. It should be noted that the difference in these two results may be caused by the different assumptions in the degrading parameters of the two models.

The nonlinear moment-rotation behaviour of the hinge at the middle of the brace is shown in Figure 12. Based on the verification in this section, the developed element model will be used in the structural model to assess the seismic performance of the structures with BIEs.

### 3. 20-Storey Structure

**3.1. EBF System.** The first structural model for which the seismic performance will be assessed is a 20-storey building in an area with high seismicity. Eurocodes 3 and 8 are used to design the structure. It is assumed that the ground type is B and the seismic zone is 1 with  $a_{gr} = 0.35 g$  according to [15]. The storey heights are 3.5 m and the bay widths are 6 m. Steel materials are assumed to have a yield stress of 345 MPa. A 3D layout of the frame is shown in Figure 13. To make a comparative study, the structure is first designed by the EBF system while all beam to column connections including link beam to column connections are hinged.

**3.2. Horizontal Elastic Response Spectrum.** According to the seismic parameters for the location of the building, the horizontal elastic response spectrum will be calculated according to Eurocode 8 [16]. Here, we have  $S = 1.2$ ,  $T_B(s) = 0.15$ ,  $T_C(s) = 0.5$ ,  $T_D(s) = 2.0$ , and  $\eta = \sqrt{10/(5 + \xi)} = 1$ ,  $\xi = 5\%$ . Therefore, the elastic response spectrum will be calculated as shown in Figure 14.

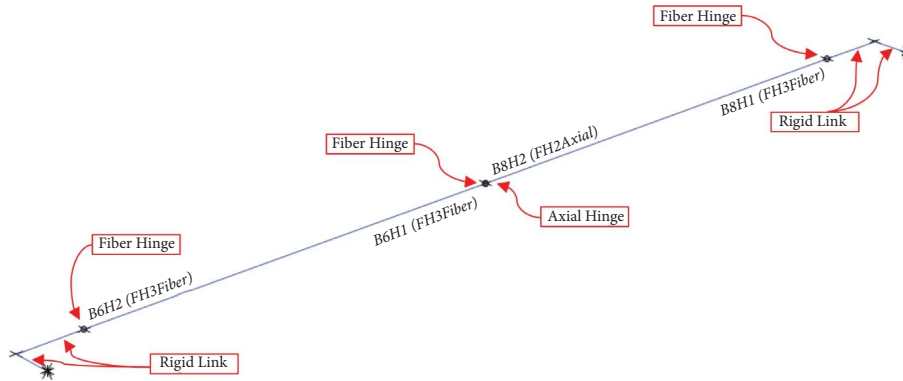


FIGURE 3: Flexural and axial hinges in the BIE element.

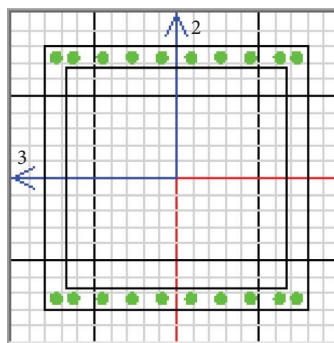


FIGURE 4: Fiber section for HSS 178 × 178 × 16.



FIGURE 5: Schematics of the element.

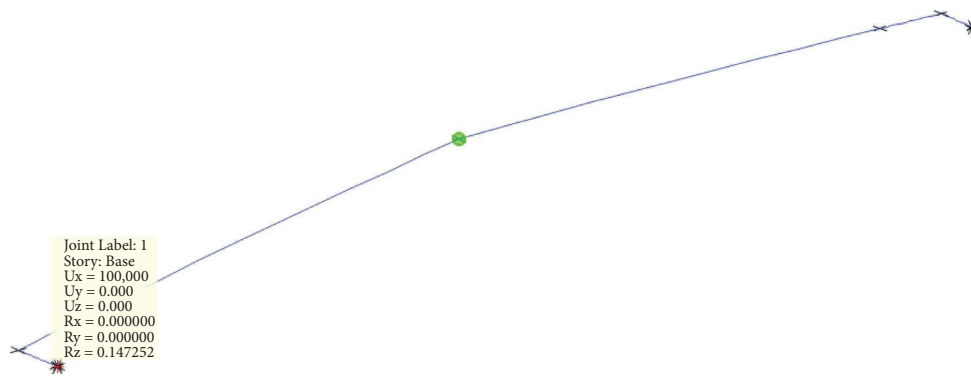


FIGURE 6: Deformed shape of the element in compression  $\delta = 100$  mm.

For the purpose of elastic design of the structure, the behaviour factor should be calculated. According to Eurocode 8 [16], the behaviour factor for the DCH ductility class

and frame with eccentric bracings would be  $5\alpha_u/\alpha_1$ , while the value of  $\alpha_u/\alpha_1$  is 1.2. Hence, the value of the behaviour factor is obtained as  $q = 6$ , and therefore, the design

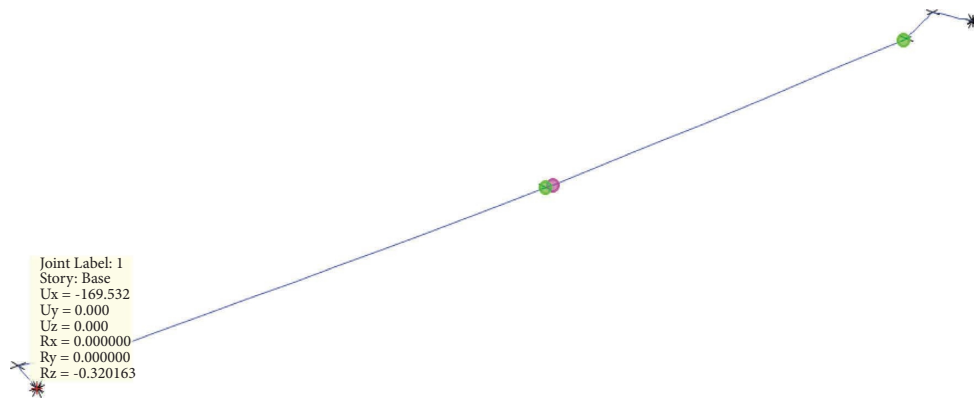


FIGURE 7: Deformed shape of the element in tension  $\Delta = 126.9$  mm.

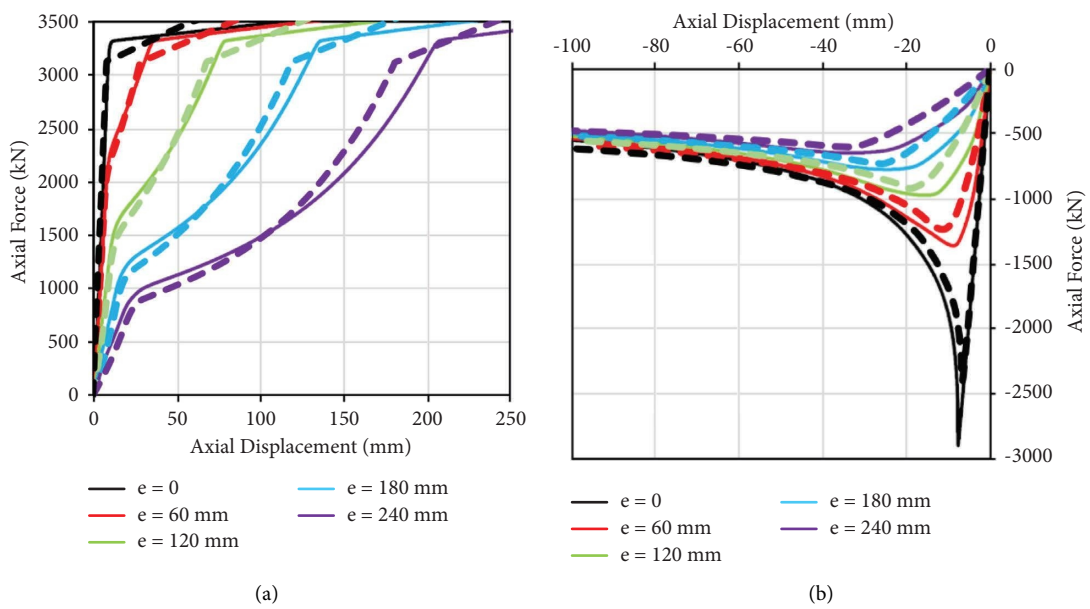


FIGURE 8: Comparison of the load-displacement diagrams generated by González Ureña et al. [12] with the results of the generated model in this study for a HSS  $178 \times 178 \times 16$  BIEs with  $L = 5408$  mm and  $Lea = 360$  mm: tension (a) and (b) compression.

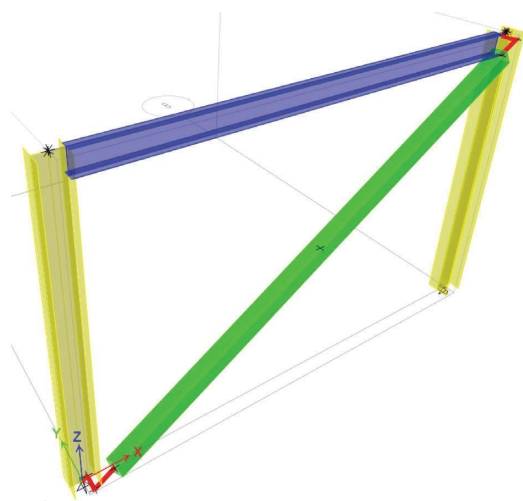


FIGURE 9: The frame with BIE element with  $e = 180$  mm.

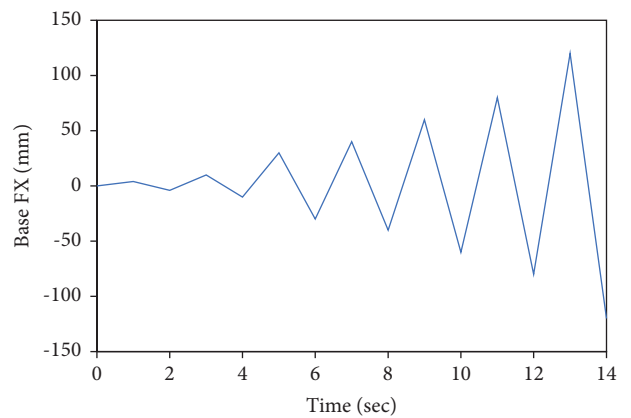


FIGURE 10: Displacement-based loading protocol.

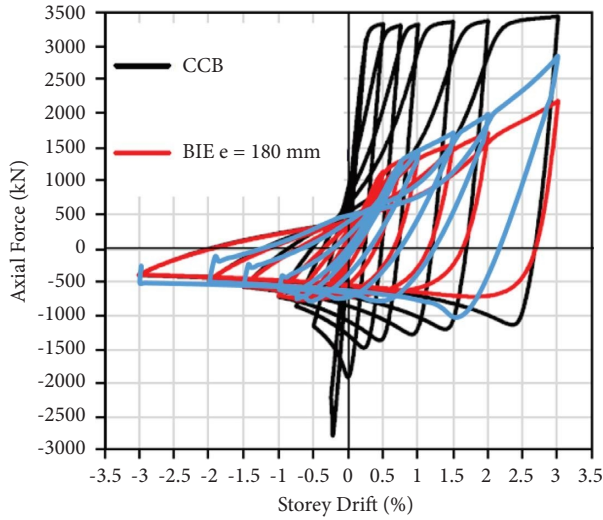


FIGURE 11: Verification of the load-displacement behaviour of the model in this study with results by González Ureña et al. [12].

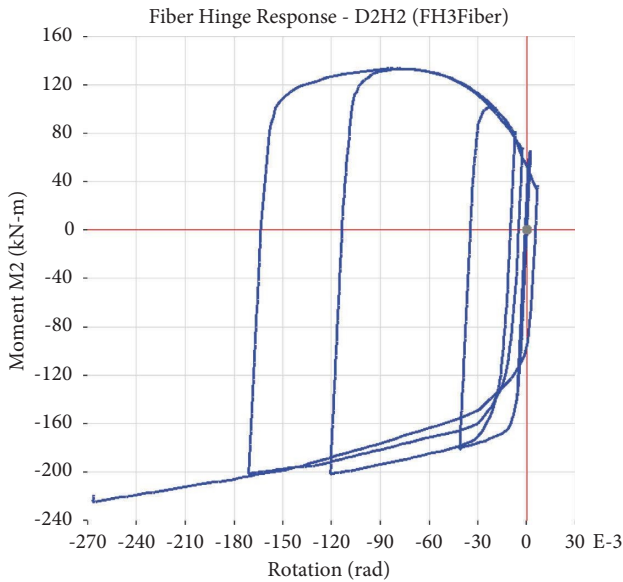


FIGURE 12: The nonlinear behaviour of the hinge at the middle of the brace.

spectrum for the elastic analysis would be calculated as shown in Figure 15.

3.3. *Structural Design.* According to the design spectrum obtained in Figure 15, the 20-storey structure is designed in ETABS (for the design details, refer to [17–21]). The cross-sections of the structural elements are shown in Figures 16 and 17.

3.4. *BIE System.* The same structure designed as EBF is equipped with the BIEs to assess and compare their seismic performance. The same HSS 178 × 178 × 16 sections with

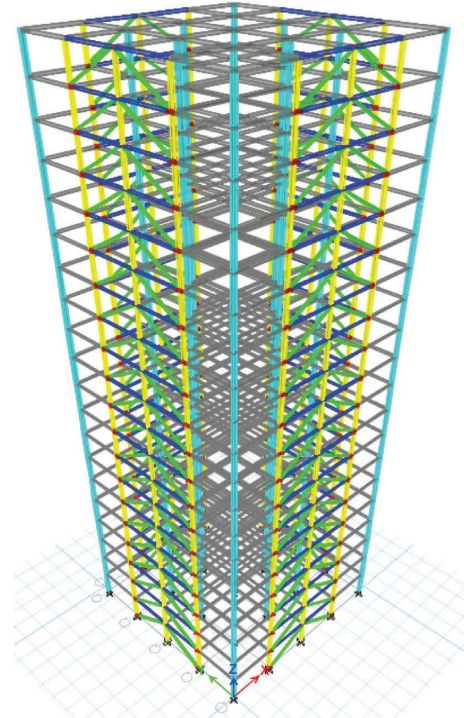


FIGURE 13: 3D layout of the 20-storey structure with EBF bracing.

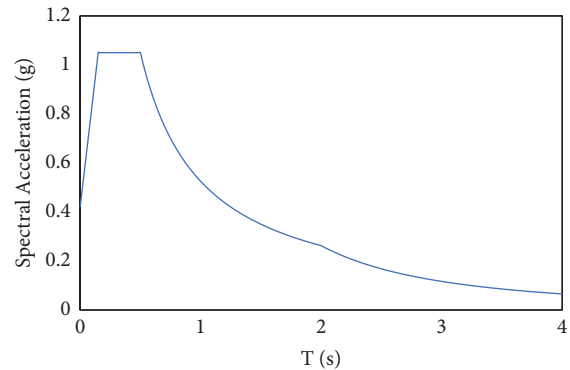


FIGURE 14: Horizontal elastic response spectrum.

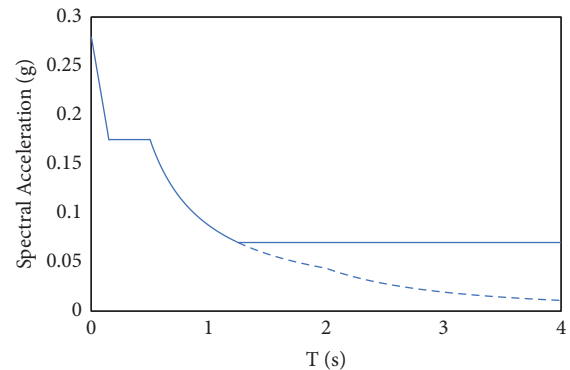


FIGURE 15: Design spectrum for elastic analysis.

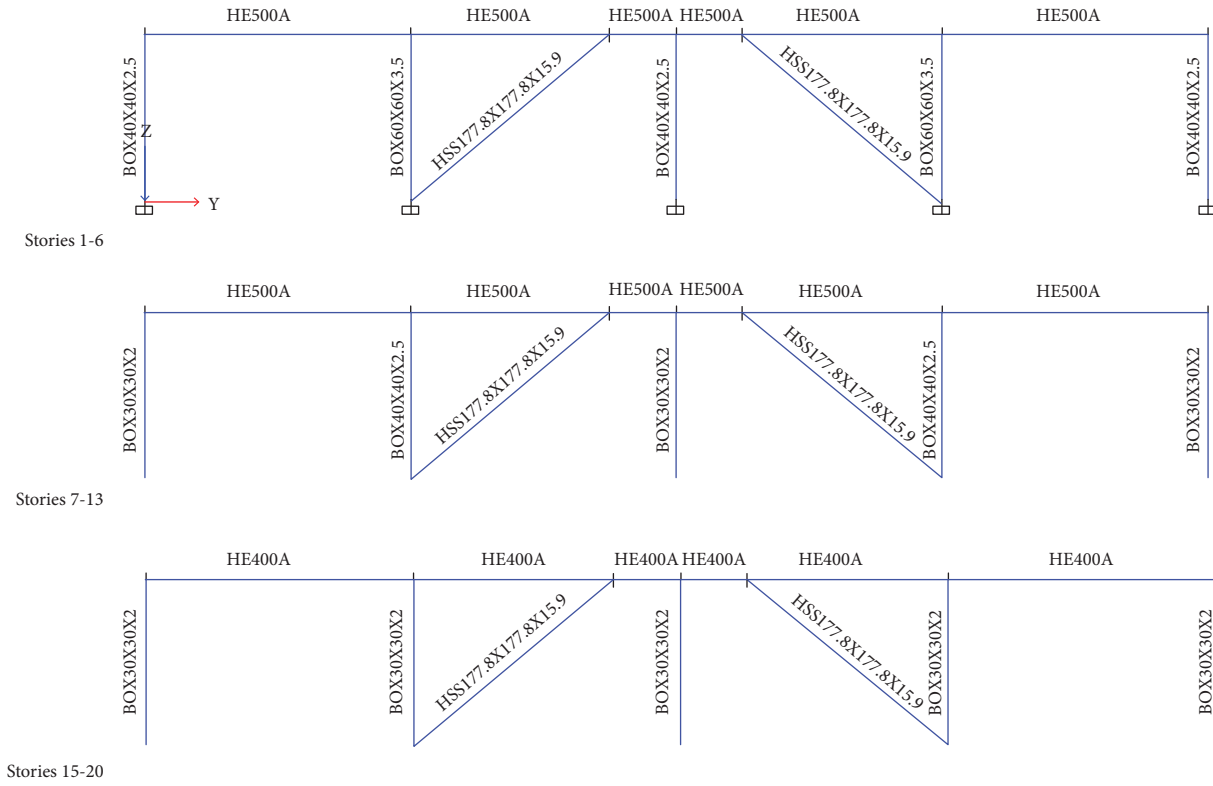


FIGURE 16: Design sections for outer frames.

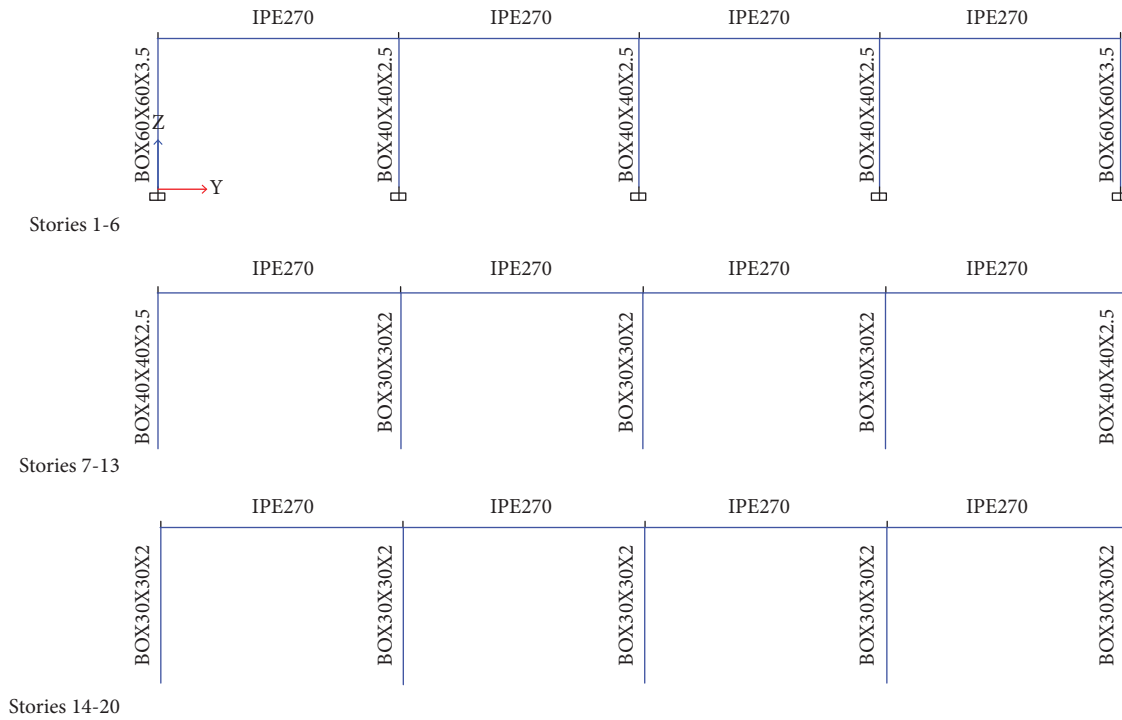


FIGURE 17: Design sections for inner frames.



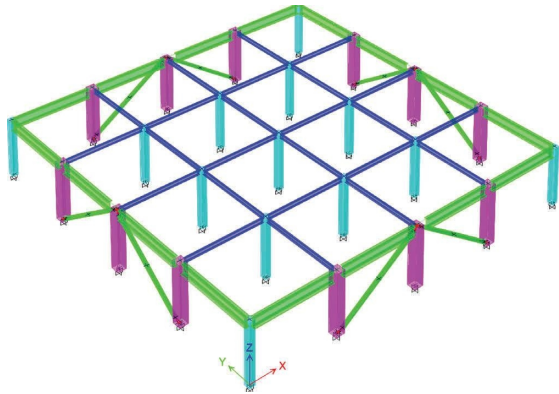


FIGURE 18: The first storey of the 20-storey structure with BIEs.

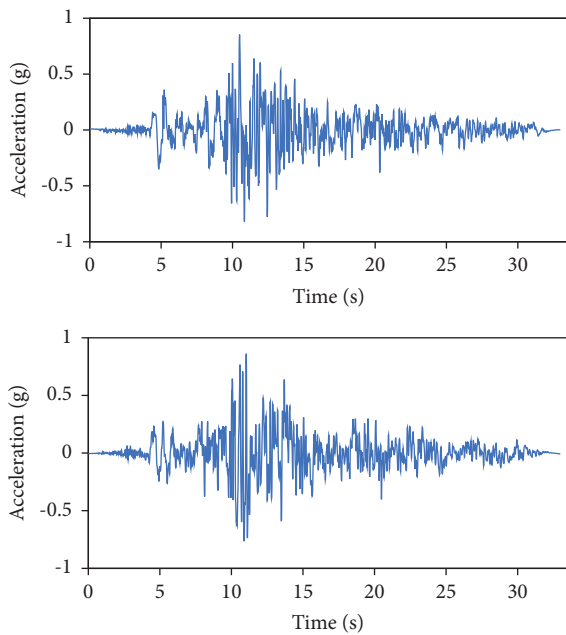


FIGURE 19: Unscaled accelerogram for the TABAS earthquake RSN143.

120 mm eccentricity are used as BIE members, and the only difference is that smaller cross-sections are used for beams in this structure since bracings are not connected to the beams in the BIE system and there is no need to use heavy beam sections. BIEs are placed in the two middle spans as shown in Figure 18. The details of the installation with rigid elements are shown in Figure 9.

**3.5. Nonlinear Time-History Analysis.** The nonlinear behaviour of the structure with two bracing systems is investigated under the TABAS earthquake. Its accelerogram is available in the PEER database by RSN143. The two unscaled horizontal components of this record are shown in Figure 19.

This earthquake record should be scaled according to Eurocode 8 [16]. The EC8 recommends that the artificial records should be generated by scaling real ground motion records. For this purpose, the spectrum of the scaled records

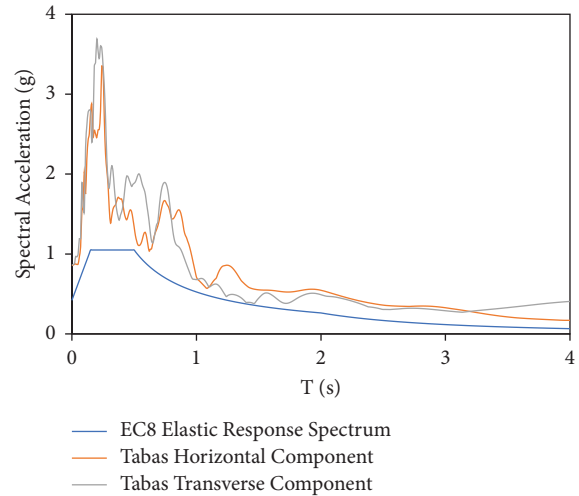


FIGURE 20: Scaling process of the TABAS accelerogram.

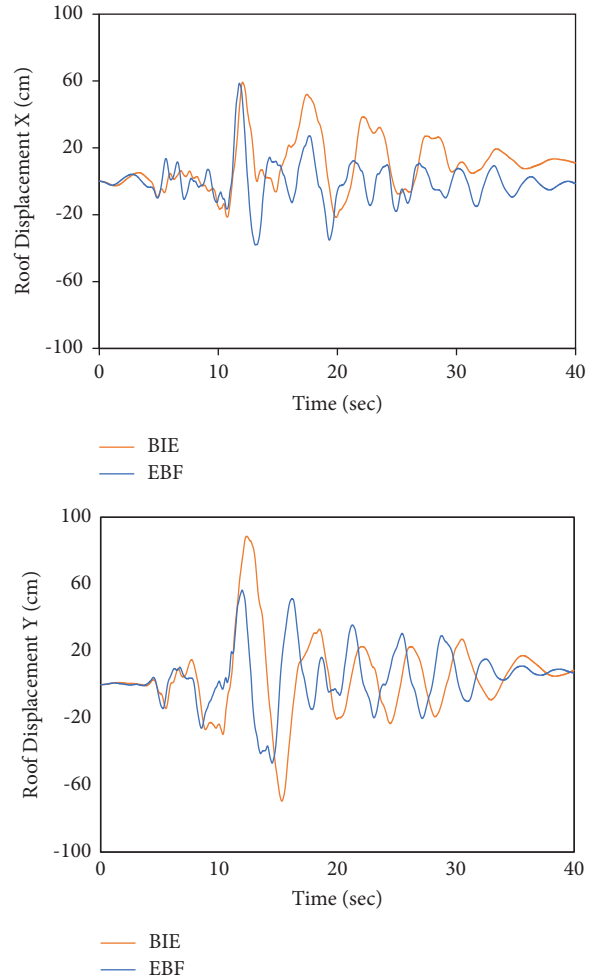


FIGURE 21: Roof displacement for BIE and EBF structures in X and Y directions.

should be always larger than 90% of the target spectrum in the periods between  $0.2 T_1$  and  $2.0 T_1$ . Here,  $T_1$  is the fundamental period of the structure in the direction where

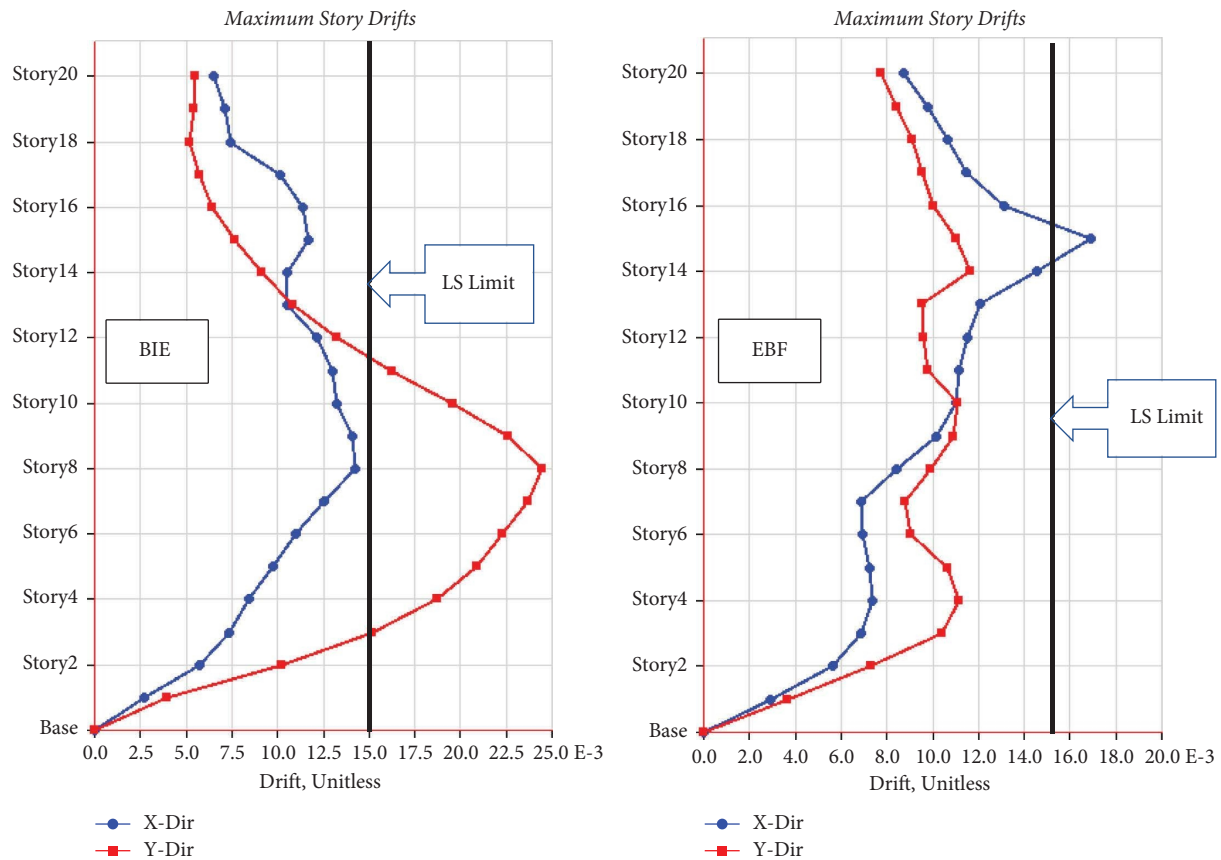


FIGURE 22: Maximum inter-story drifts along the height of the two structures.

the excitation is applied. Also, the value of the average spectrum at  $T_1 = 0$  should be larger than the value of the target spectrum at  $T_1 = 0$ . The first mode period of the structure with EBF is 3.1 seconds and for the structure with BIEs is 3.5 seconds. According to Figure 20, a 0.8 scale factor can be used for this earthquake record.

**3.6. Seismic Responses.** The structural responses of the two systems are compared in this section. Figure 21 shows the roof displacement of the two structures. As displayed in the figure, the displacement in the EBF system is smaller than the displacements in the BIE system by 39% showing the larger stiffness of the EBF system. So, very larger braces should be used in the BIE system to gain an equivalent stiffness, however, we will see in the following sections that this system has acceptable seismic performance and the use of larger braces is not required.

The drift limit for life safety (LS) performance level according to a table in ASCE41-06 (2007) is 0.015. The distribution of maximum drifts along the height of the building is shown in Figure 22. It can be seen that the interstorey drift in the BIE system is larger than the EBF system and the LS level is not satisfied in the BIE system. In order to have a comparison between the two systems, the bracing cross-sections are not changed here. It is obvious

that the drift ratios in the BIE system can be reduced by using larger cross-sections and smaller eccentricity.

The plastic hinges developed in BIEs and link beams are shown in Figure 23. It can be seen that the BIE system has provided a uniform distribution of plastic hinges along the height of the structure. Although the lateral rigidity of the structure in the EBF system is larger and the displacement of the structure is smaller in the EBF system, the concentration of damages in plastic hinges is larger in EBF link beams, and it can be verified from Figure 23. The sample hysteresis behaviour of nonlinear hinges for the two systems is shown in Figure 24.

It should be mentioned that in the BIE system, braces show large maximum out-of-plane deformation as shown in Figure 25 for an exterior frame of the structure. These deformations are more than 20 cm in some cases when the members are in compression. This large deformation is due to the geometry of the BIEs as shown in Figure 6. It can be concluded as a disadvantage of the BIE system which may affect the outer facing and claddings of the structure.

The dissipated energy in the BIE system is shown in Figure 26. Also, for the EBF system, it is shown in Figure 27. It can be seen that the dissipated energy in the BIE system (yellow colour) is larger than the EBF system by 160%.

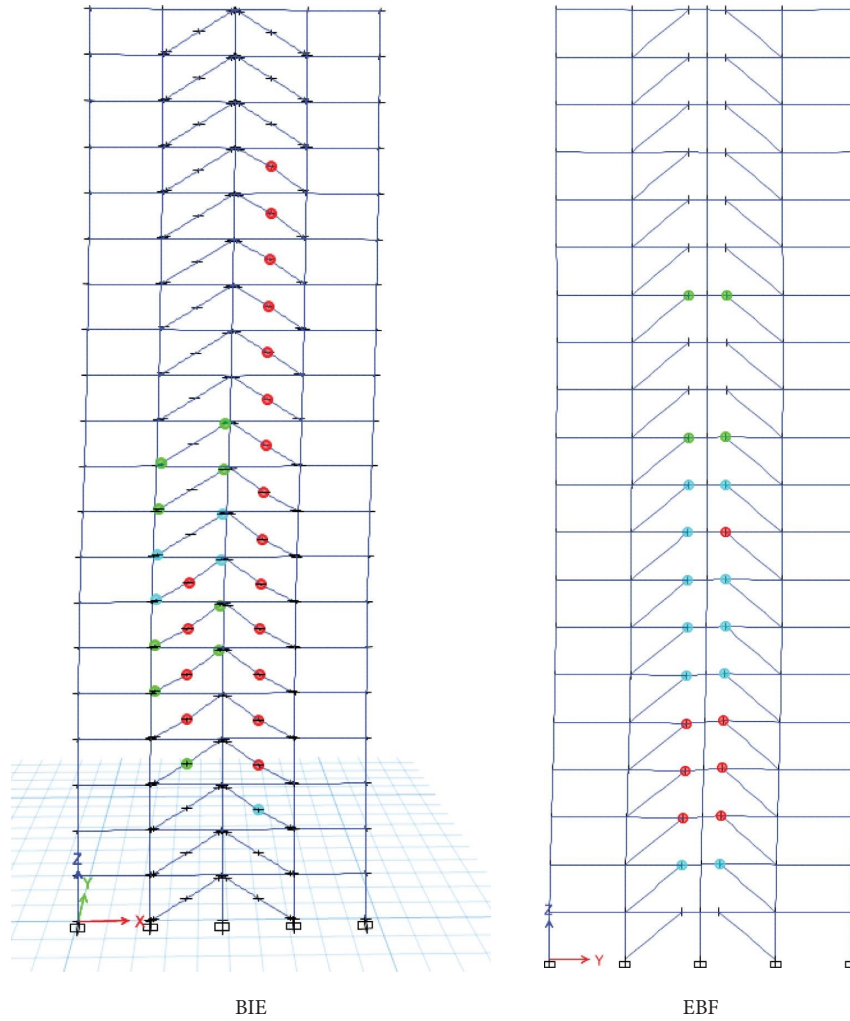


FIGURE 23: The developed hinges in BIEs and link beams.

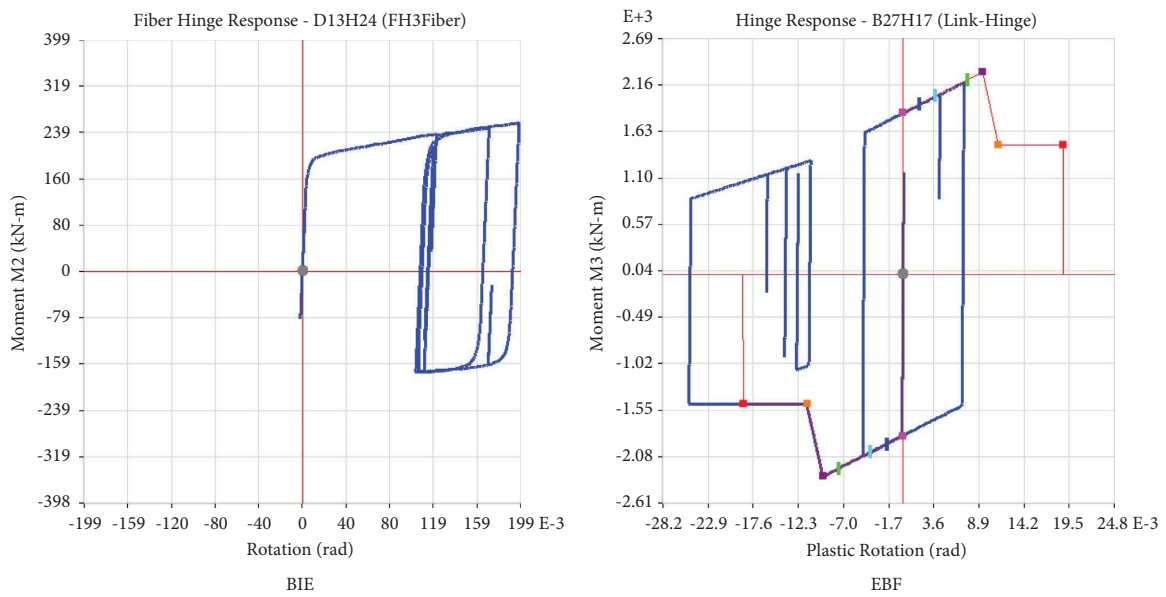


FIGURE 24: Sample hysteresis behaviour of nonlinear hinges for BIE and EBF systems.

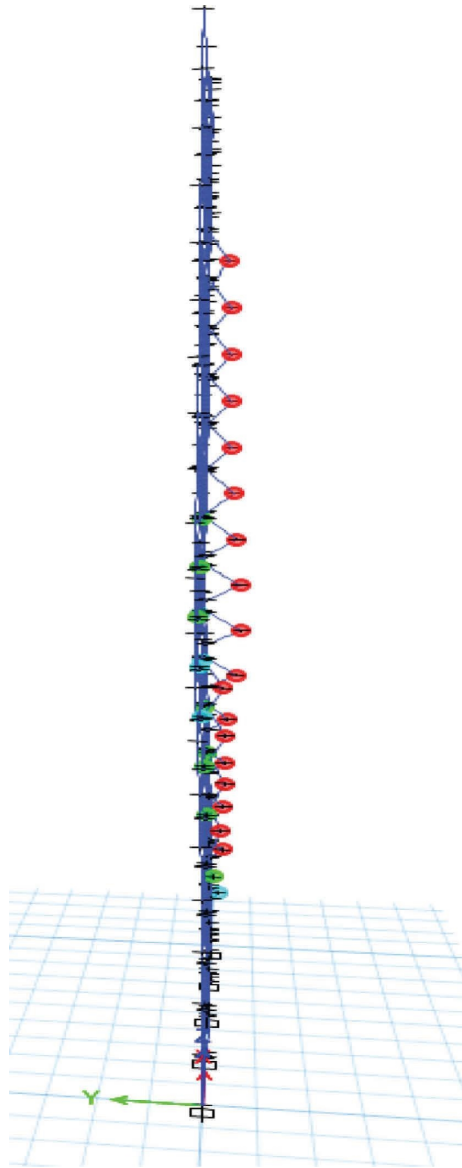


FIGURE 25: Out-of-plane deformation of braces in the BIE system (horizontal scale is doubled).

The storey shear forces for the BIE and BF systems are shown in Figure 28. It can be seen that the storey shear forces in the BIE system are less than those in the EBF system. The maximum base shears of the two systems are compared in Table 1.

The steel materials used in the two systems are compared in Table 2. It can be seen that the steel material used in the BIE system is less than the EBF system by almost 20%. This reduction is caused by the smaller beam sections in the BIE system. It is obvious that using larger BIE elements to control the storey drifts may reduce this saving.

#### 4. 25-Storey Structure with Vertical Irregularity

4.1. *Structural System.* The second structural model for which the seismic performance will be assessed is a 25-storey building with vertical irregularity. This irregularity is in the

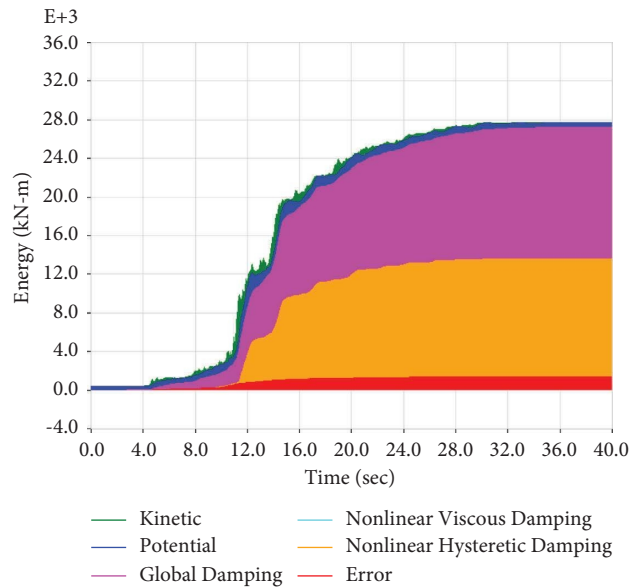


FIGURE 26: The dissipated energy in the BIE system.

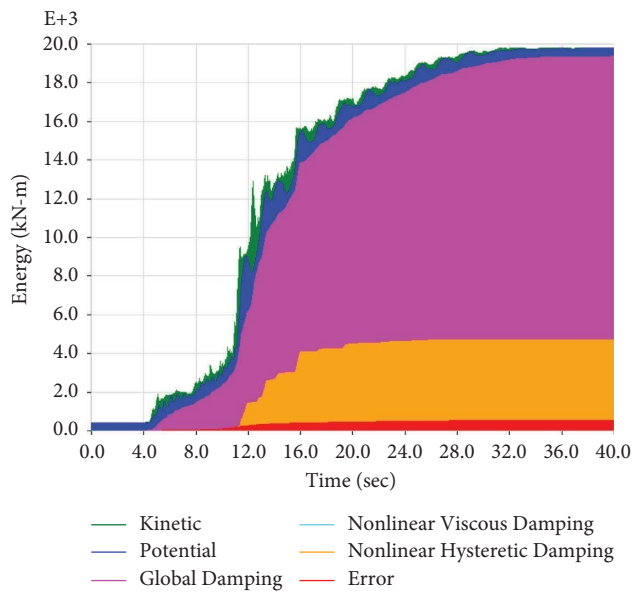


FIGURE 27: The dissipated energy in the EBF system.

form of a setback in the 11<sup>th</sup> and 19<sup>th</sup> storey of the building. This structure is considered here to assess the performance of BIEs in irregular structures and torsional effects when BIEs are located near the central core of the structure. It is assumed that the building is located in an area with high seismicity. Eurocodes 3 and 8 are used to design the structure. Similar to the previous section, it is assumed that the ground type is B and the seismic zone is 1 with  $a_{gr} = 0.35 g$  according to [15]. The storey heights are 3.5 m and the bay widths are 6 m. Steel materials are assumed to have a yield stress of 345 MPa. A 3D layout of the frame is shown in Figure 29. Also, the first storey of this structure is shown in Figure 30 to show the location of BIEs. The braces near the core of the structure are placed at all storeys

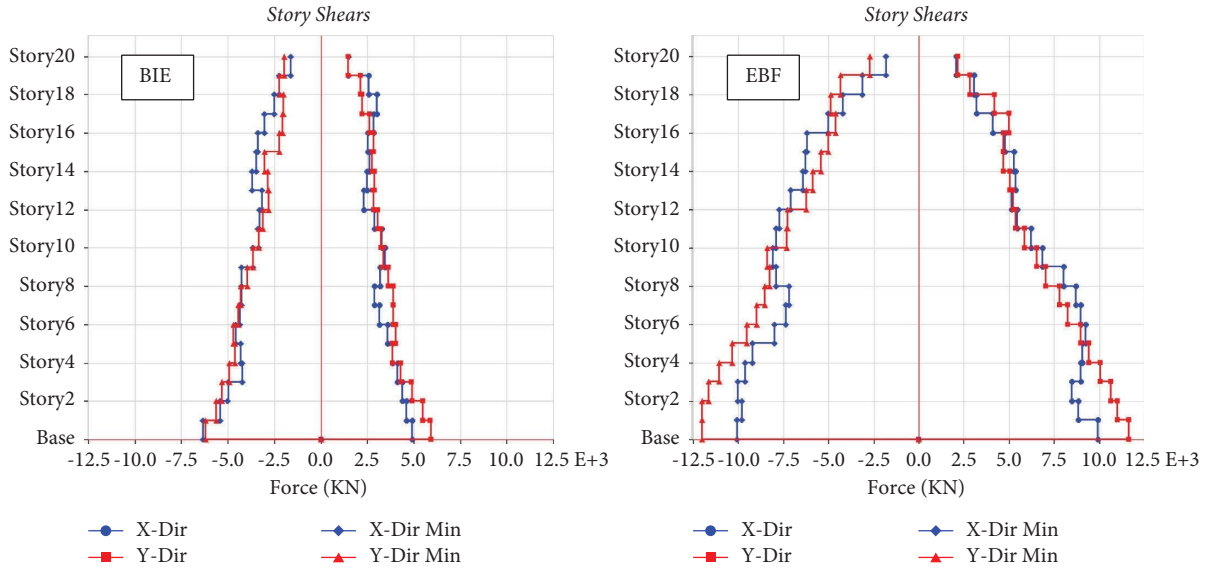


FIGURE 28: Maximum story shear forces in the 20-story structure with BIE and EBF systems.

TABLE 1: Base shears in a 20-storey structure with BIE and EBF systems.

System	Base shear	
	EBF (kN)	BIE (kN)
X direction	1043	6432
Y direction	1230	6370

TABLE 2: Steel material used in the 20-storey structure with BIE and EBF systems.

System	Steel weight	
	EBF (ton)	BIE (ton)
Column	516	516
Beam	385	162
Brace	66	72
Sum	967	750

throughout the height of the structure while the braces at the outer face of the building are continued up to the 10<sup>th</sup> storey. To highlight the seismic performance of BIEs and their capacity for energy dissipation, all beam to column connections are assumed to be hinged.

**4.2. Horizontal Elastic Response Spectrum.** Since the location of the buildings studied in this research is constant, the horizontal elastic response spectrum used for this structure is the same as that calculated in previous sections. Therefore, the elastic response spectrum will be in the form of Figure 14. It should be noted that the BIE system is not introduced in the current seismic codes and we have made a rough assumption to design the structure and acquire the

cross-sections of the beam and column elements. The value of the behaviour factor is assumed to be  $q = 6$ , and therefore, the design spectrum for the elastic analysis would be calculated as shown in Figure 15.

**4.3. Structural Design.** According to the design spectrum obtained, the 25-storey structure is designed in ETABS. The cross-sections of structural elements are shown in Figures 31 and 32. HSS  $178 \times 178 \times 16$  sections with 120 mm eccentricity are used as BIE members in this structure. It should be noted that BIEs are not displayed in these figures because they are at another elevation coordinate due to the intentional eccentricity. Instead, their locations are shown in Figure 30.

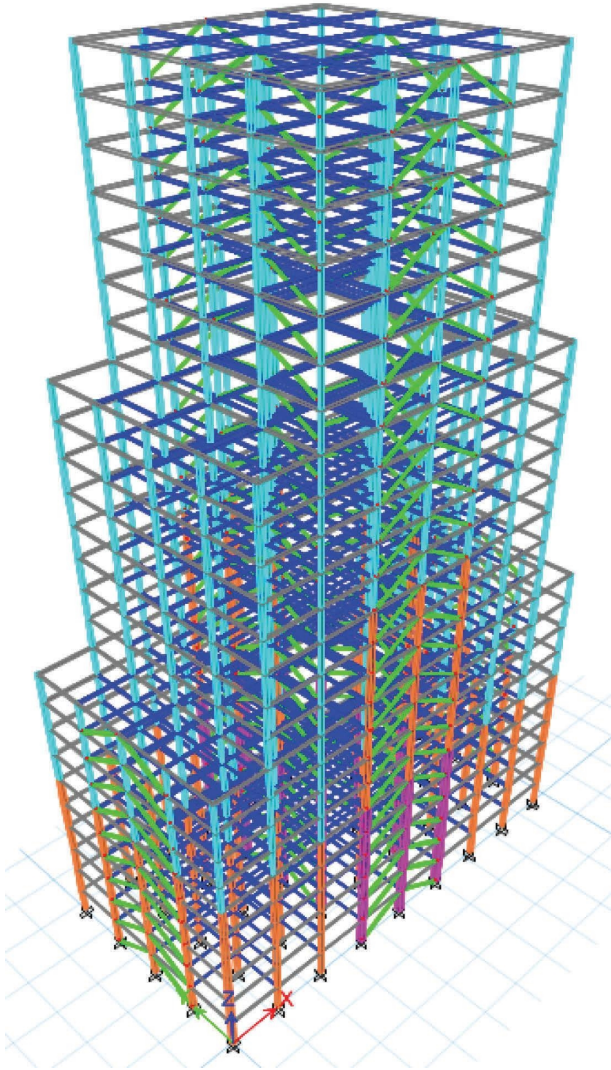


FIGURE 29: 3D layout of the 25-storey irregular structure with BIEs.

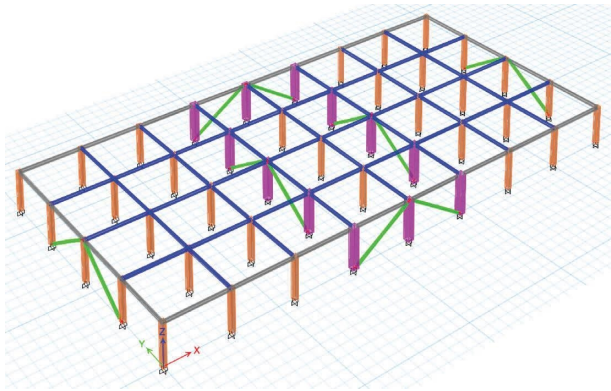


FIGURE 30: The 1<sup>st</sup> storey of the 25-storey structure and location of BIEs.



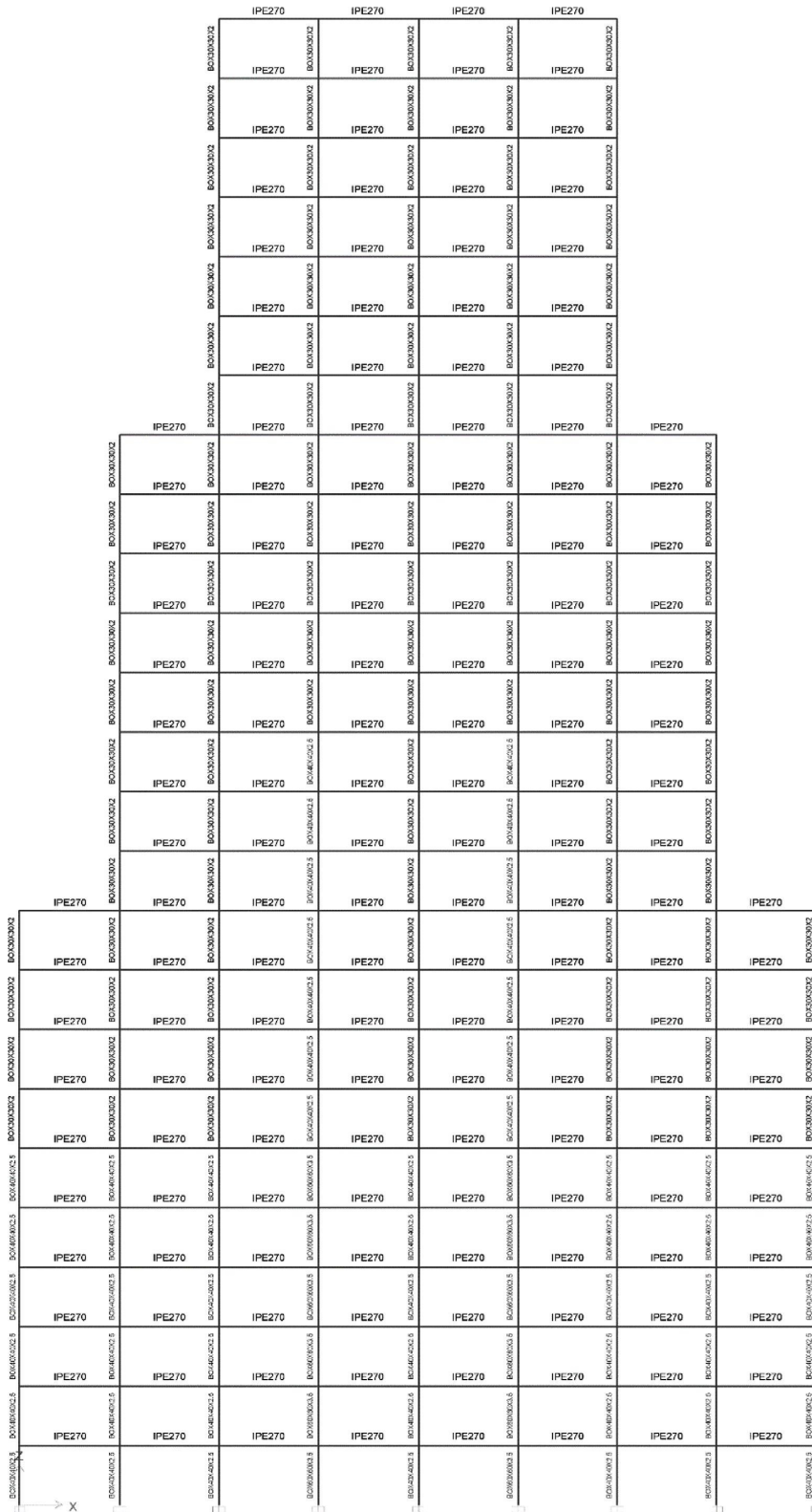


FIGURE 32: Design sections for inner frames.



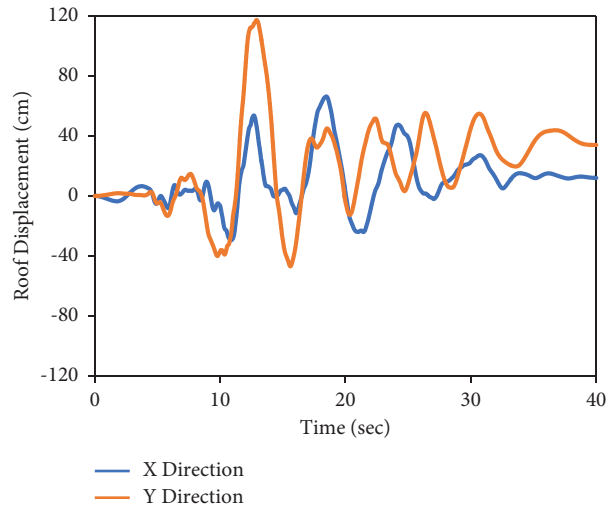


FIGURE 33: Roof displacement for the 25-story structure with BIEs in X and Y directions.

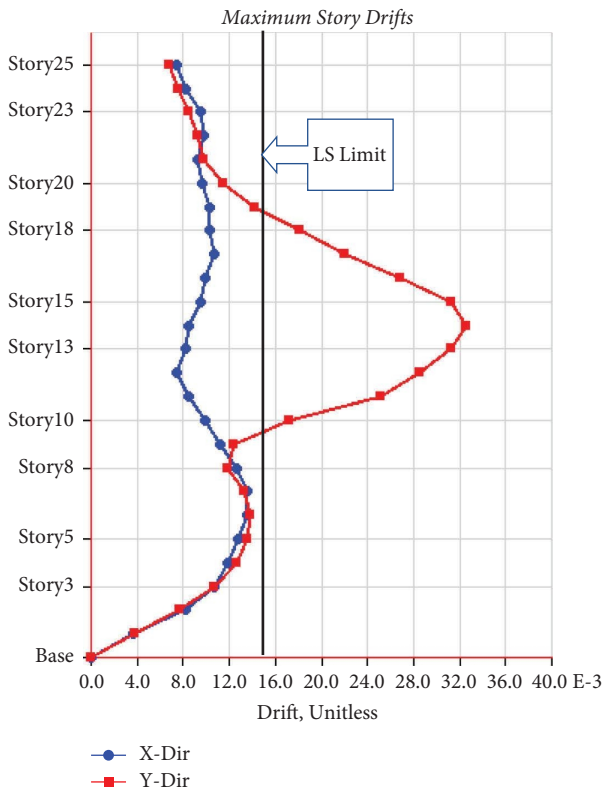


FIGURE 34: Maximum inter-story drifts along the height of the 25-story structure.

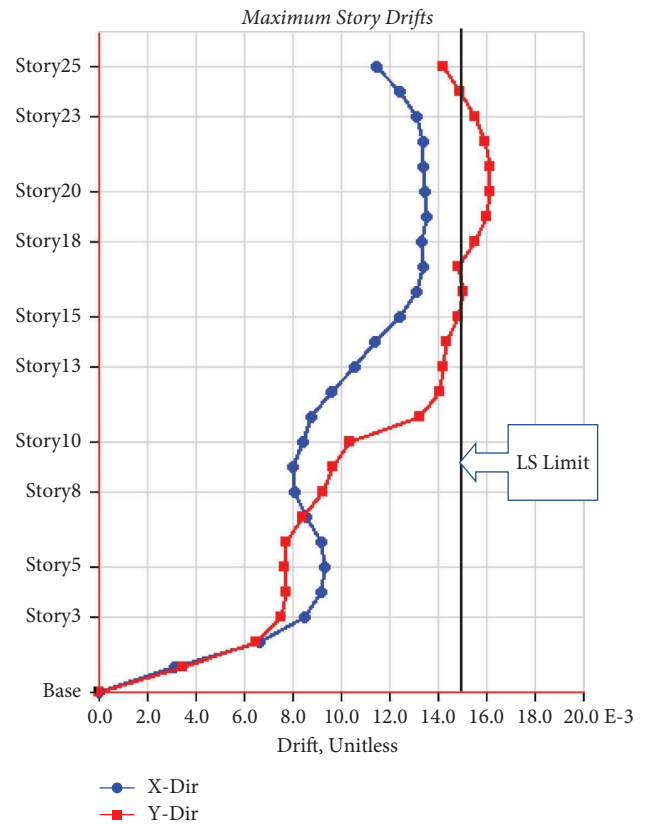


FIGURE 35: Maximum inter-story drifts along the height of the strengthened 25-story structure.

4.4. *Nonlinear Time-History Analysis.* Similar to the previous sections, the nonlinear behaviour of the 25-story structure with vertical irregularity is investigated under the TABAS earthquake. The first mode period of the 25-story structure with BIEs is 5.5 seconds. According to Figure 20, a 0.8 scale factor can be used for this earthquake record.

4.5. *Seismic Responses.* The structural response of the structure is examined in this section. Figure 33 shows the roof displacement of the 25-story structure in both directions. A considerable residual displacement in the order of 40 cm is seen in the Y direction. This may be attributed to the irregularity of the structure. Also, the distribution of maximum drifts along the height of the building is shown in

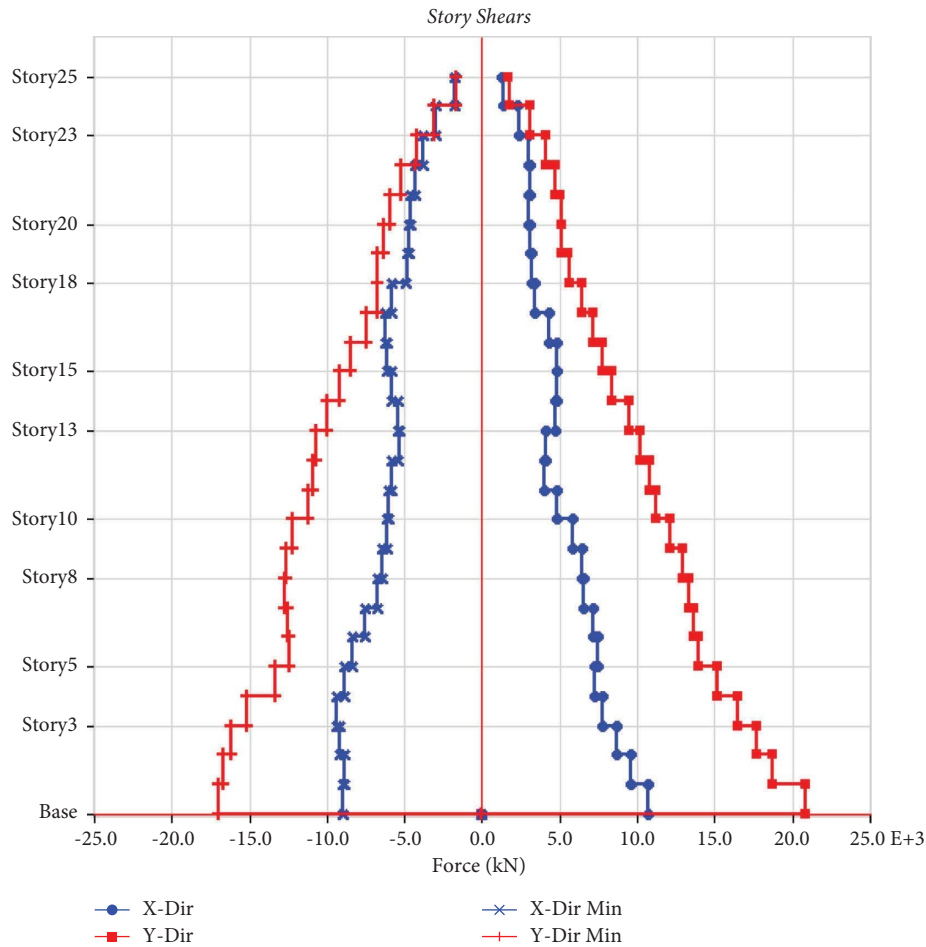


FIGURE 36: Maximum story shear forces in a 25-story strengthened structure.

Figure 34. Large interstorey drifts are seen in storeys from 10 to 19, where setbacks are applied in the architecture of the building. This issue is very important since the drift values are beyond the Life Safety (LS) limit according to ASCE41-06 (2007) and may cause instability of the structure. The LS limit (0.015) is also displayed in Figure 34.

It can be inferred that the BIEs installed at some storeys are not sufficiently stiff to reduce the storey displacements because of the effects of irregularities, and hence they should be strengthened. The setbacks at the 11<sup>th</sup> and 19<sup>th</sup> storey levels cause concentrated storey shears at these storeys. Therefore, larger sections are used as the BIEs in these storey levels which are investigated in the following section.

**4.6. Strengthened 25-Storey Structure.** Larger BIE sections are used in the  $y$  direction of the newly strengthened 25-storey structure ( $HSS\ 304 \times 304 \times 16$ ). Also, the intentional eccentricity is reduced to 80 mm for more rigidity. The effect of reducing the intentional eccentricity on the maximum storey drifts and also on the energy dissipation capacity of the BIE system may be verified here. The first mode period ( $T_1$ ) of this structure is reduced to 4.5 seconds. It is worth mentioning that the scale factor for the earthquake record

remains unchanged since the governing part of the response spectrum is at about 1.5 seconds.

The abovementioned strengthening has resulted in less interstorey drifts as shown in Figure 35. It can be seen that the LS performance level is mostly satisfied in this structure and the maximum drift ratios are reduced by almost 50%. By a trial-and-error procedure, an appropriate rigidity and strength of the structure can be achieved by selecting a proper cross-section of BIEs and proper eccentricity while maintaining the energy-dissipating capacity of the structure. It is a considerable advantage of the BIE system.

The maximum storey shear forces are shown in Figure 36. A uniform distribution of the shear forces is seen in this Figure 36. Larger sections and less eccentricity of BIEs in the  $y$  direction have resulted in larger shear forces in the  $y$  direction.

The plastic hinges developed in BIEs are shown in Figure 37. It can be seen that the BIE system has provided a uniform distribution of plastic hinges along the height of the structure up to the 14<sup>th</sup> storey.

Similar to the 20-storey structure, large out-of-plane deformations in BIEs are seen. These deformations are more than 30<sup>cm</sup> in some cases.

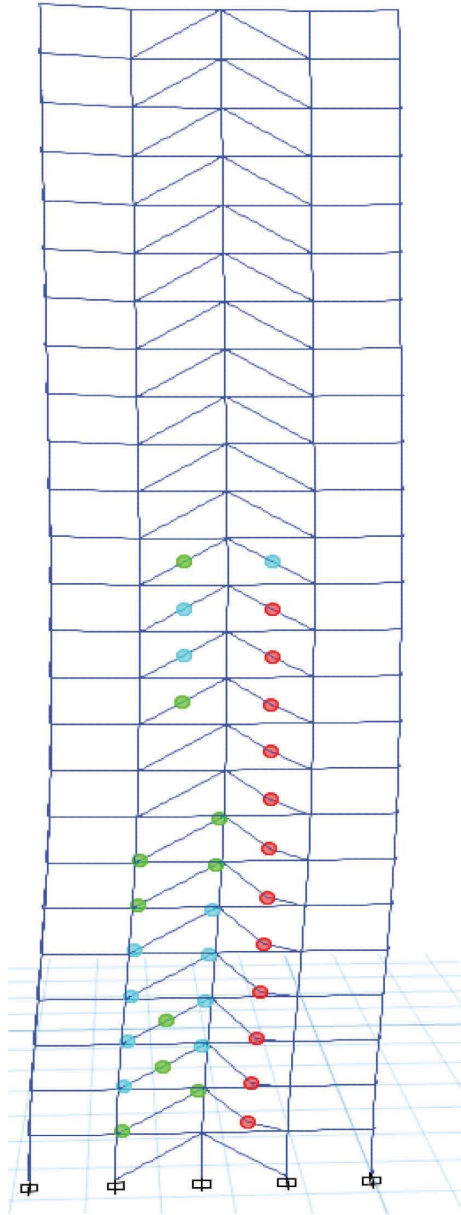


FIGURE 37: The developed hinges in BIEs and link beams.

The dissipated energy in the BIE system is shown in Figure 38. The yellow part shows the energy dissipated by BIEs.

In order to investigate the torsional effects in the irregular structure, the max/average values of storey drifts are checked. This ratio is under 1.2 for all storey levels.

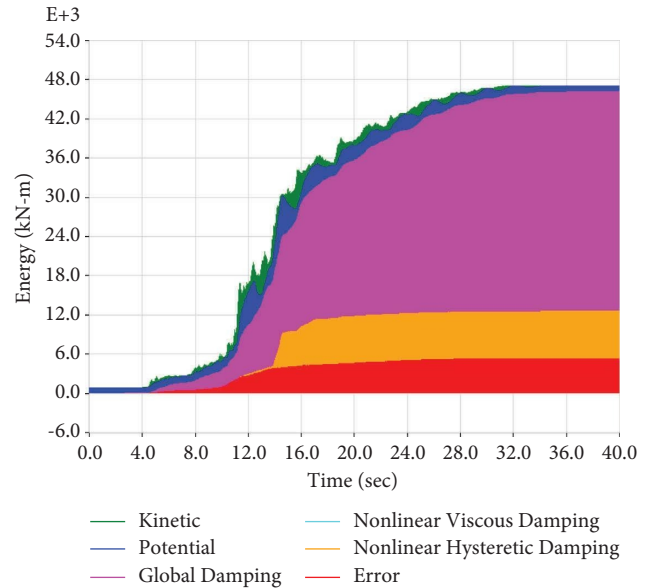


FIGURE 38: The dissipated energy in the BIE system for the strengthened 25-story building.

Therefore, no excessive torsional displacement is induced in this structure under seismic excitation.

## 5. Conclusions

In previous sections, an analytical assessment of the seismic performance of structures with the BIE system was carried out. Since the cyclic behaviour of BIEs is the main aspect of these bracing systems which affects the global behaviour of the structure under seismic loadings, as the first step, a proper model of the BIE was developed in ETABS. This model was verified by the results from previous studies to attain a proper estimate of the BIE's cyclic behaviour and backbone curve. In the second step, a 20-storey regular structure was designed by the EBF system and then, in the same structure, the bracings were replaced by BIEs. The seismic performance of the two structures was compared under the TABAS earthquake record in terms of roof displacement, storey drift ratios, dissipated energy, and steel weight. In the third step, the seismic performance of a 25-storey irregular structure was examined. The irregularity was in the form of a setback in the 11<sup>th</sup> and 19<sup>th</sup> storey of the building. The interstorey drift ratios in this structure were verified with the LS performance level, and the structure was strengthened to achieve this performance level under the TABAS earthquake record. According to the results

obtained in previous sections, the following conclusions may be derived:

- (1) The verification of the behaviour of the developed model by comparing the load-displacement diagrams generated by González Ureña et al. [12] with the results of the generated model in this study showed that the developed model succeeds in providing good estimates of the compressive and tensile behaviour of BIE. The results showed that a combination of the three fiber hinges (two at both ends and one at the middle of the element) and one axial hinge in a BIE element will result in a proper numerical model of the BIE members.
- (2) According to the results obtained for the 20-storey structure, the BIE system provides less lateral stiffness compared to the EBF system, resulting in larger lateral displacements and drifts. Larger cross-sections should be used in BIE elements to satisfy drift limits according to design codes.
- (3) The BIE system provides a uniform distribution of plastic hinges along the height of the structure preventing the concentration of damages in plastic hinges. The plastic hinges in the BIE system develop at the initial stages of seismic excitation thus providing a good energy dissipation capacity.
- (4) Stable hysteresis behaviour is seen in the BIE system resulting in a large amount of energy dissipation compared to the EBF system. BIEs start to dampen and dissipate input energy from the early levels of excitation.
- (5) The fraction of dissipated energy in the BIE system was much larger than that of the EBF system. This fraction is calculated relative to the total input energy. This shows the superiority of the BIE system in energy dissipation capacity.
- (6) Comparison between storey shear forces in the two structures with the BIE and EBF systems showed that the BIE system was subjected to less storey shear forces. This may be partly due to the less rigidity of the BIE system. However, a comprehensive conclusion requires further investigations comparing the seismic shear forces in the two systems with the same storey yield shears.
- (7) In the BIE system, braces showed large out-of-plane deformation. These deformations are more than 20 cm in some cases which can be considered as a disadvantage of the BIE system.
- (8) A comparison of the steel material weight of the two 20-storey structures with the BIE and EBF systems showed that the steel material in the structure with the BIE system is almost 20% less than the EBF system. This reduction is caused by the smaller beam sections in the BIE system. It is obvious that using larger BIE elements to control the storey drifts may reduce this saving.
- (9) The performance assessment of the 25-storey irregular structure showed a considerable residual displacement in the order of 40 cm in the  $Y$  direction. This may be attributed to the irregularity of the structure.
- (10) Large interstorey drifts were seen in storeys from 10 to 19 of the 25-storey structure before strengthening where setbacks were applied in the architecture of the building. The drift values were beyond the life safety (LS) limit according to ASCE41-06. To overcome this shortcoming, the 25-storey structure was strengthened by using larger sections and less intentional eccentricities in BIEs.
- (11) The strengthening (larger sections and less intentional eccentricities of BIEs) applied on the 25-storey structure resulted in reduced interstorey drifts by almost 50%. By a trial-and-error procedure, an appropriate rigidity and strength of the structure can be achieved by selecting a proper cross-section of BIEs and proper eccentricity while maintaining the energy-dissipating capacity of the structure. It is a considerable advantage of the BIE system.
- (12) In order to investigate the torsional effects in the structures with vertical irregularity, the max/average values of the storey drifts were explored. The ratio obtained at all storey levels was less than 1.2. Therefore, no excessive torsional displacement was induced in an irregular 25-storey structure under seismic excitation.

### Data Availability

The data used to support the findings of this study are available from the corresponding author upon request.

### Disclosure

This research was performed as part of Master project of the first author under the supervision of the second author in the City, University of London.

### Conflicts of Interest

The authors declare that they have no conflicts of interest.

### References

- [1] F. Fu, *Advanced Modelling Techniques in Structural Design*, John Wiley & Sons, Hoboken, NJ, USA, 2015.
- [2] E. J. Lumpkin, P. C. Hsiao, C. W. Roeder et al., "Investigation of the seismic response of three-storey special concentrically braced frames," *Journal of Constructional Steel Research*, vol. 77, pp. 131–144, 2012.
- [3] T. Okazaki, D. G. Lignos, T. Hikino, and K. Kajiwara, "Dynamic response of a chevron concentrically braced frame," *Journal of Structural Engineering*, vol. 139, no. 4, pp. 515–525, 2013.

- [4] J.-W. Lai and S. A. Mahin, "Steel concentrically braced frames using tubular structural sections as bracing members: design, full-scale testing and numerical simulation," *International Journal of Steel Structures*, vol. 14, no. 1, pp. 43–58, 2014.
- [5] F. Fu, *Design and Analysis of Tall and Complex Structures*, Butterworth-Heinemann, Oxford, United Kingdom, 2018.
- [6] L. Ye, "Study on the influence of post-yielding stiffness to the seismic response of building structures," in *Proceedings of the Fourteenth World Conference On Earthquake Engineering*, Shanghai, China, June 2008.
- [7] M. Baiguera, G. Vasdravellis, and T. L. Karavasilis, "Dual seismic-resistant steel frame with high post-yield stiffness energy-dissipative braces for residual drift reduction," *Journal of Constructional Steel Research*, vol. 122, pp. 198–212, 2016.
- [8] H. Iemura, Y. Takahashi, and N. Sogabe, "Two-level seismic design method using post-yield stiffness and its application to unbonded bar reinforced concrete piers," *Structural Engineering/Earthquake Engineering*, vol. 23, no. 1, pp. 109–116, 2006.
- [9] D. B. Merczel, "On the weak storey behaviour of concentrically braced frames," in *Proceedings of the 8th International Conference on Behavior of Steel Structures in Seismic Areas STESSA*, Timisoara, Romania, May 2015.
- [10] K. A. Skalomenos, H. Inamasu, H. Shimada, and M. Nakashima, "Development of a steel brace with intentional eccentricity and experimental validation," *Journal of Structural Engineering*, vol. 143, no. 8, Article ID 04017072, 2017.
- [11] K. A. Skalomenos, M. Kurata, H. Shimada, and M. Nishiyama, "Use of induction-heating in steel structures: material properties and novel brace design," *Journal of Constructional Steel Research*, vol. 148, pp. 112–123, 2018.
- [12] A. González Ureña, R. Tremblay, and C. A. Rogers, "Earthquake-resistant design of steel frames with intentionally eccentric braces," *Journal of Constructional Steel Research*, vol. 178, Article ID 106483, 2021.
- [13] K. A. Skalomenos, H. Shimada, M. Kurata, and M. Nakashima, "03.03: feasibility of hybrid simulation for testing steel connections of braces with intentional eccentricity," *Ce/Papers*, vol. 1, no. 2-3, pp. 522–529, 2017.
- [14] K. A. Skalomenos, M. Kurata, and M. Nishiyama, "Induction-heat treated steel braces with intentional eccentricity," *Engineering Structures*, vol. 211, Article ID 110461, 2020.
- [15] G. Solomos, "A Review of the Seismic hazard Zonation in National Building Codes in the Context of Eurocode 8," *JRC Scientific and Technical reports*, International Space University, Illkirch-Graffenstaden, France, 2008.
- [16] BSI, *Eurocode 8: Design of Structures for Earthquake Resistance-Part 1: General Rules, Seismic Actions and Rules for Buildings*, European Committee for Standardization, Brussels, Belgium, 2005.
- [17] K. Qian, D. Q. Lan, F. Fu, and B. Li, "Effects of infilled wall opening on load resisting capacity of RC frames to mitigate progressive collapse risk," *Engineering Structures*, vol. 223, Article ID 111196, 2020.
- [18] K. Qian, S. Liang, F. Fu, and Y. Li, "Progressive collapse resistance of emulative precast concrete frames with various reinforcing details," *Journal of Structural Engineering*, vol. 147, no. 8, Article ID 04021107, 2021a.
- [19] K. Qian, S. L. Liang, F. Fu, and Y. Li, "Progressive collapse resistance of emulative precast concrete frames with various reinforcing details," *Journal of Structural Engineering*, vol. 147, no. 8, Article ID 05021004, 2021b.
- [20] F. Fu, D. Lam, and J. Ye, "Modelling semi-rigid composite joints with precast hollowcore slabs in hogging moment region," *Journal of Constructional Steel Research*, vol. 64, no. 12, pp. 1408–1419, 2008.
- [21] F. Fu, D. Lam, and J. Ye, "Moment resistance and rotation capacity of semi-rigid composite connections with precast hollowcore slabs," *Journal of Constructional Steel Research*, vol. 66, no. 3, pp. 452–461, 2010.

## Research Article

# Seismic Performance of Concrete-Filled Square Steel Tubular Column-Steel Beam Sleeve Joint

Xiangong Huang,<sup>1</sup> Man Xu ,<sup>1</sup> Nan Guo ,<sup>1</sup> Senwen Deng,<sup>2</sup> and Le Huang<sup>3</sup>

<sup>1</sup>School of Civil Engineering, Northeast Forestry University, Harbin 150000, China

<sup>2</sup>School of Civil Engineering, Heilongjiang University, Harbin 150000, China

<sup>3</sup>Ping'an Construction Group Co., Ltd., Hangzhou 310000, China

Correspondence should be addressed to Man Xu; xuman306@126.com

Received 13 August 2021; Accepted 7 June 2022; Published 19 July 2022

Academic Editor: Manuel Aenlle Lopez

Copyright © 2022 Xiangong Huang et al. This is an open access article distributed under the Creative Commons Attribution License, which permits unrestricted use, distribution, and reproduction in any medium, provided the original work is properly cited.

The concrete-filled square steel tubular (S-CFST) structure has been widely used as a resistance system against earthquakes due to its good seismic performance. However, the application of the S-CFST structure is limited by its complex joint formulation. To overcome this shortcoming, a sleeve semirigid joint has been proposed, while its seismic performance has not been well examined. This study aims to discuss the behavior of sleeve joints with different parameters under low cyclic loading. The analysis results show that the simulation results of the finite element model established by ABAQUS were in good agreement with the experimental results, which further verified the good energy dissipation performance of the sleeve joint, and gave the design suggestions of the joint under different parameters to promote the engineering application of this type of joint.

## 1. Introduction

The concrete-filled steel tube (CFST) has various advantages, such as high bearing capacity, good plasticity and toughness, easy processing, and convenient construction [1, 2]. However, the complexity of the design and construction of beam-column joints limits its application to some extent. In addition, almost all current joints are designed as rigid joints, but the semirigid joint under the action of cyclic loading shows a better energy dissipation performance and more stable seismic characteristics, which has attracted extensive attention of researchers [3–8].

In recent years, researchers have conducted plenty of research on the types and mechanical properties of semirigid joints of concrete-filled steel tubes, and some achievements have been made. For example, Oh and Ai-Roda [9] carried out an experimental study on the connection of concrete-filled steel tubular column and H-shaped steel beam. T-cleat connections and bending steel plates with a centered hole were used to strengthen the stiffness of the connection, and the hysteretic performance of the connection was analyzed.

It was found that the joint of bending steel plates with a centered hole demonstrates good deformation ability. Ricles et al. [10] conducted low reversed cyclic loading tests on 10 full-scale joints of concrete-filled square steel tubular (CFST) column and steel beam. They found that the flange joints of the T-shaped steel bolt connection and reinforced beam meet the design principle of “strong column and weak beam,” and the bolted end-plate connection can enhance the bolt hole strength, effectively reducing the slippage and the pinch phenomenon of hysteretic curves. Yang et al. [11] studied the mechanical properties of joints through diaphragms of concrete-filled rectangular steel tubular column and H-shaped steel plate under low cyclic loading. The results showed that such type of joint has good seismic performance, and the wedge-shaped plates on both sides of the flange have a significant influence on the joint ductility. Lv and Li [12] proposed a joint form with an octagonal ring beam outside the CFST column and designed three specimens to study its mechanical properties. The obtained results indicated that the three specimens all show high bearing capacity, good ductility, and energy dissipation

capacity under cyclic loading. Mirza and Uy [13] used the experiment and finite element method to study the performance of bolted beams, columns, and horizontal end-plate joints. The mechanical properties of flat end joints of the composite beam-column under low-probability, high-consequence loading were investigated. Gao et al. [14] researched the mechanical characteristics and energy dissipation performance of different forms of large-size connections of CFST column and H-shaped steel beam. He concluded that the bearing capacity and energy dissipation performance of joints with inner diaphragms are better than those of joints with through diaphragms. France and Buick Davison [15] carried out static loading tests on the bolted end-plate joint of CFST column and steel beam and compared its performance with that of the square steel tubular column joint. Through experimental analysis, it was found that the strength and stiffness of the joint are significantly improved, but the joint ductility is reduced, and the failure mode of the joint is bolt pull out.

For the simulation model and calculation theory of the concrete-filled steel tube column-steel beam semirigid joint, the research focus is mainly on the connection with bolts, and the deformation model of the connection element is established. Huang [16] used ABAQUS to establish two-element connectors to simulate the beam-column joint used in the bolted end-plate connection. Compared with the experiment data, this finite element model (FEM) effectively simulated the force exerted on the joint under high temperatures. In such conditions, the axial force of the beam end has an obvious influence on the force exerted on the joint. Hu et al. [17] studied the performance of T-shaped steel bolted joints under low cyclic loading and proposed a new mechanical calculation model for such joints. The model diagram is shown in Figure 1, where the mechanical model simulated T-shaped steel as a nonlinear spring element, and a multiline segment cyclic stiffness model was used to simulate the hysteretic performance of T-shaped steel components. By comparing the simulated results of this model with the experimental results, it was concluded that this model can accurately simulate the mechanical behavior of T-shaped steel bolted joints [17].

Many achievements have been obtained in the connection test and theoretical study of semirigid joints of CFST column and steel beam, but the existing semirigid joint forms have their own limitations. It is difficult to find a joint form with both technical and economic advantages; thus, it is necessary to select the suitable joint type based on the application situation by developing the advantages and avoiding the disadvantages. In this paper, the sleeve joint form of concrete-filled square steel tubular column-steel beam was studied, and its mechanical properties under low cyclic loading are investigated using ABAQUS. This joint is shown in Figure 2.

## 2. Model Design

The sleeve joint is formed by sheathing the steel sleeve at the joint position of concrete-filled square steel tubular column, welding the upper and lower edges of the sleeve with the steel

tubular column, and then completely welding the steel beam with the sleeve, and the joint has clear force transmission and simple construction. To investigate the seismic performance of concrete-filled square steel tubular column-steel beam sleeve joint, three joint models of this type are designed.

*2.1. Model Dimension.* Three sleeve joint specimens of CFST column and steel beam, numbered from CFST-1 to CFST-3, were designed. The size of the square steel tubular column was  $300 \times 300 \times 8$  mm (length  $\times$  width  $\times$  thickness), and the steel beams were made of  $\text{HN}244 \times 175 \times 7 \times 11$  mm hot-rolled H-beam. Strength grade Q235 steel was used for beams, columns, and sleeves, and concrete with strength grade C30 was filled in the square steel tube. The sleeve was welded with steel plates, and the type of electrode was E43. The upper and lower flanges and web at one end of the steel beam were completely welded on the sleeve. A 5 mm weld was left on the top and bottom of the sleeve to weld the sleeve on the square steel tubular column, the periphery of which was in full contact with the square steel tubular column. The variables were the thickness and height of the sleeve. The main parameters are shown in Table 1, and the detailed joint structure is shown in Figure 3.

*2.2. Material Properties.* Steel is simulated by the conventional ideal elastic-plastic model, and Q235 steel was adopted in this model, with an elastic modulus of  $E = 2.03 \times 10^5$  N/mm<sup>2</sup>, a Poisson ratio of 0.3, and a density of 78.5 g/mm<sup>3</sup>.

The concrete constitutive model is the plastic damage model of square steel tubes proposed by Han et al. [18, 19], which considers the interaction between the inner wall of square steel tube and core concrete.

## 3. Model Validation

*3.1. Experimental Setup.* Two MTS actuators were used to apply low cyclic load to the beam ends on both sides of the specimen, and the Jack on the column top was utilized to apply the axial force, while hinged supports were placed at the column bottom and column end to simulate the hinged boundary conditions. In the test, four H-shaped steel was installed as limit beams to ensure that the components do not have out-of-plane torsion and instability before failure and to limit the lateral displacement of the specimen during loading. It is specified in the test that the pushing direction of the actuator is positive and the pulling direction is negative, and the left and right beams were marked. During the test, firstly, a vertical axial force of 770 kN (axial compression ratio of 0.23) was applied on the column top with a Jack. Then, MTS actuators were utilized to apply displacement cyclic load on the left and right beam ends at the same time, with a displacement increment of 5 mm. When the specimen yielded, cyclic loading was continued three times with the same increment until any of the following conditions occurred: (1) the load is reduced to less than 80% of the peak load; (2) the steel tube in the joint area is locally damaged by

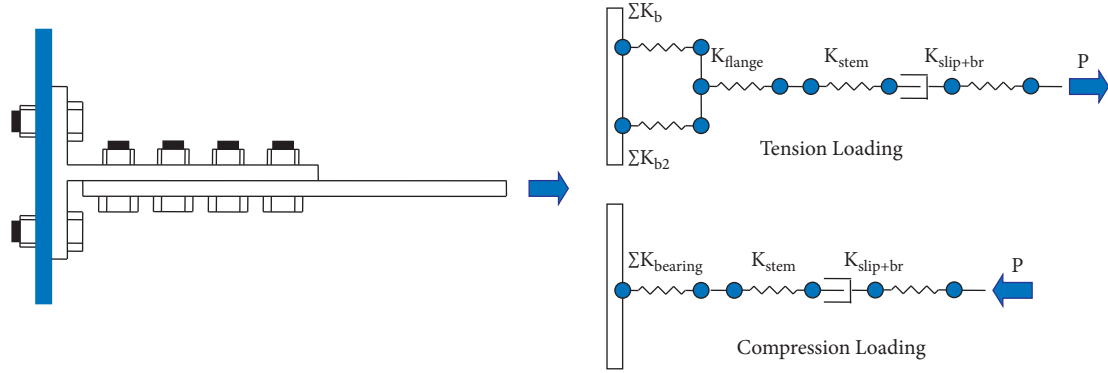


FIGURE 1: Hu calculation model.

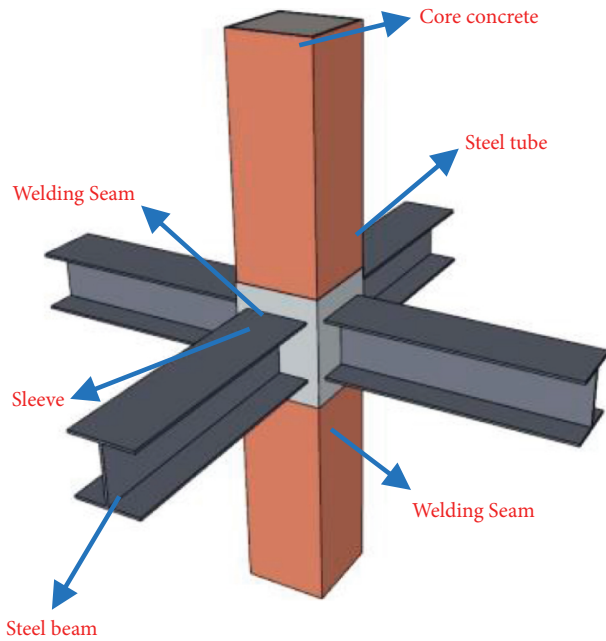


FIGURE 2: Sketch of sleeve joint.

TABLE 1: Sleeve parameters of specimens height  $\times$  side length  $\times$  thickness (mm).

CFST-1	CFST-2	CFST-3
488 $\times$ 312 $\times$ 6	600 $\times$ 312 $\times$ 6	488 $\times$ 320 $\times$ 10

shear or more than 70% of the local weld cracks; (3) the steel beam has obvious local buckling deformation or fracture, or the steel beam has out-of-plane instability.

The stress distribution in the core area of the joint was measured by both the strain gauge and the stain rosette that are arranged according to Figure 4. The displacement of the beam end was measured by a displacement sensor and collected synchronously and automatically by a computer. The test device is shown in Figure 5. Due to the sticking and measurement, the strain gauge and the stain rosette did not work well, so the measurement results of strain were not provided in this paper.

### 3.2. Material Mechanical Properties

**3.2.1. Steel.** According to the provisions in metallic materials–tensile testing–method of test at ambient temperature (GB/T 228.1–2010) [20] and steel and steel products–location and preparation of samples and test pieces for mechanical testing (GB/T 2975–2018) [21], three groups with two samples per group from the same batch of steel were taken to conduct tensile tests on the material universal testing machine. The performance parameters measured are shown in Table 2.

**3.2.2. Concrete.** When pouring C30 concrete, three 150  $\times$  150  $\times$  150 mm standard concrete test cubes and three 150  $\times$  150  $\times$  300 mm prismatic blocks were fabricated. After 28 days of curing under the same conditions as the joint specimens, the compressive test on the concrete cube was carried out, and then the average value was taken. Ultimately, the measured average compressive strength of concrete cubes was 40.59 MPa, the average axial compressive strength was 27.18 MPa, and the average elastic modulus was 31783 MPa.

**3.3. FE Model.** Solid element C3D8R in ABAQUS is used to build the model, including steel beam, steel tube, core concrete, and steel sleeve. The mesh of the connection area is encrypted by using structured mesh and considering the complex stress and calculation accuracy of the connection area. The mesh size of the joint connection area between steel tube and beam is 15 mm, and the rest parts are 60 mm. Steel sleeve is the key component of joint connection, which is divided by 15 mm. The size of core concrete is 160 mm.

The normal attribute between steel pipe and concrete is “hard” contact, the tangential direction is defined as limited sliding, and the friction coefficient is 0.3. Except the weld joint area, the contact between the steel tube and the steel sleeve is defined as “hard,” which means that there is no immersion between the two faces.

**3.4. Failure Mode.** The failure phenomena of the three specimens under different loading displacements are shown in Table 3, where 55 mm (1) represents the first circle load



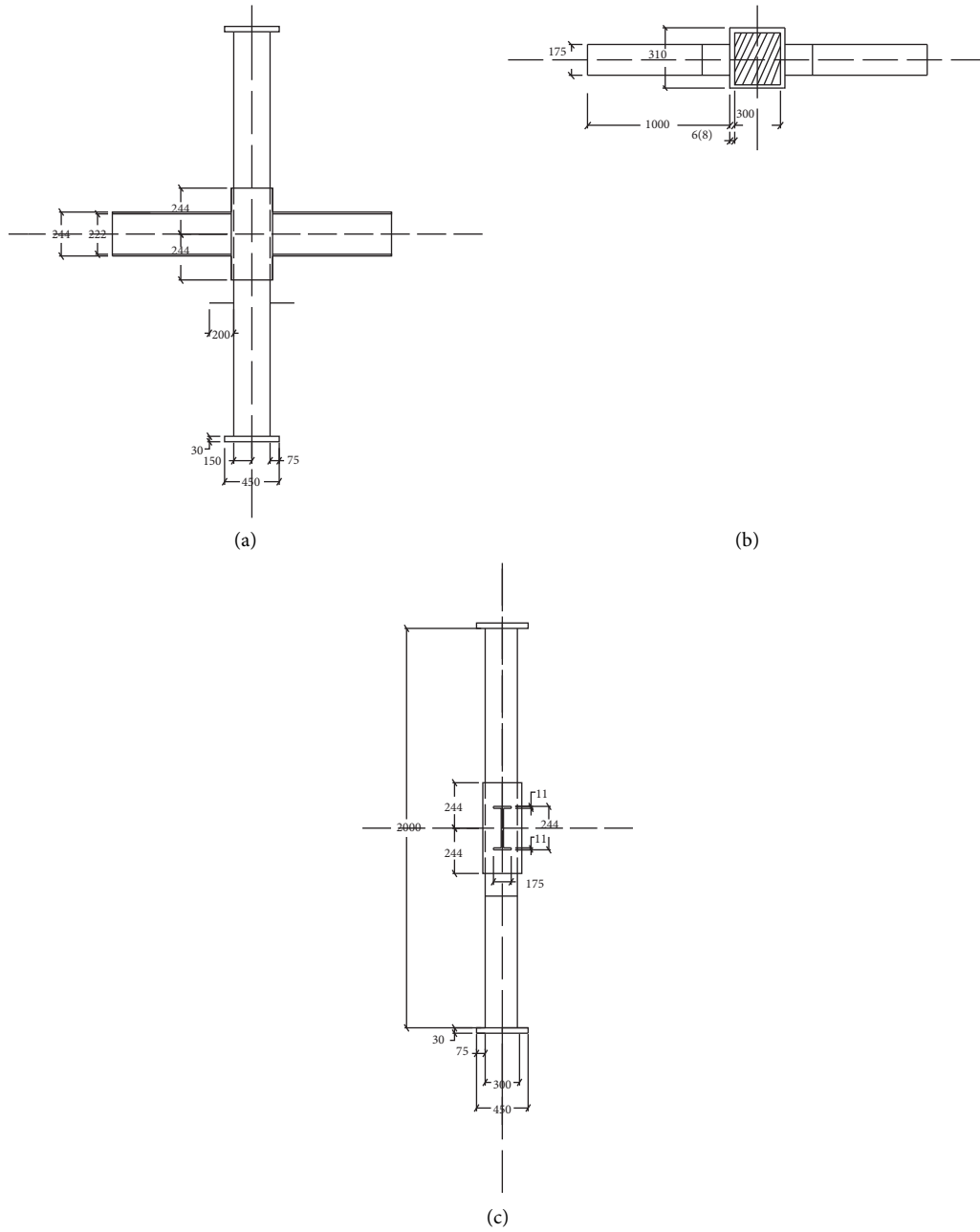


FIGURE 3: Detailed joint structure. (a) Elevation, (b) plan, and (c) profile.

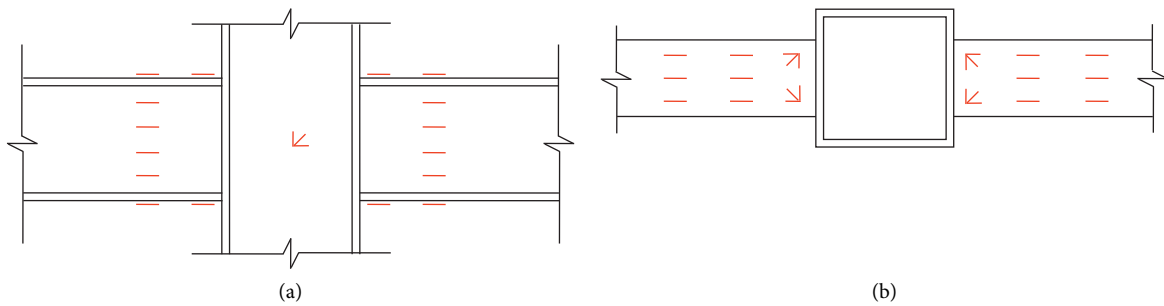


FIGURE 4: Strain gauge arrangement. (a) Front view and (b) top view.

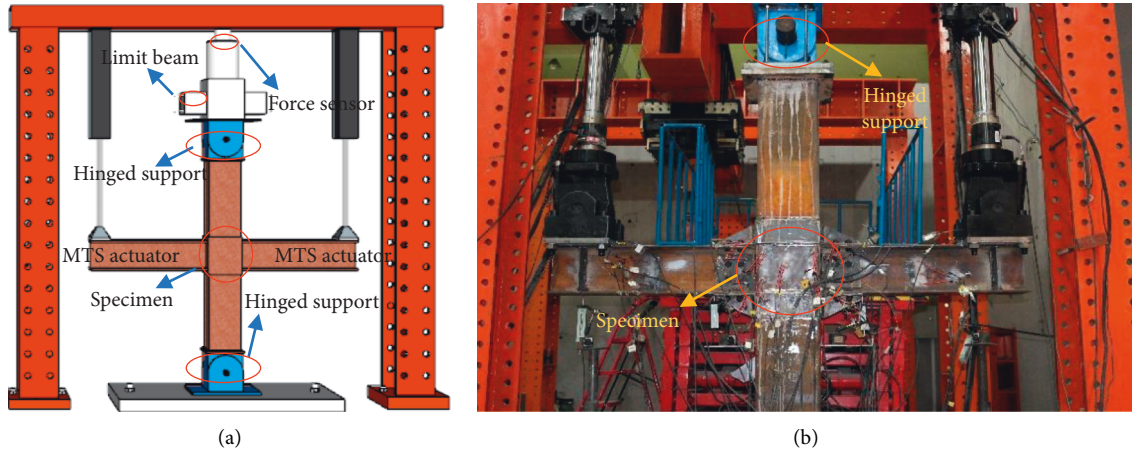


FIGURE 5: Diagram of the test device. (a) Model diagram and (b) physical diagram.

TABLE 2: Performance parameters of steel.

Thickness (mm)		Measured strength (MPa)		Average strength (MPa)
5.65	Yield strength	323.86	322.72	323.29
	Ultimate strength	474.09	473.42	473.76
7.65	Yield strength	299.50	282.88	291.19
	Ultimate strength	390.05	392.82	391.43
9.67	Yield strength	313.57	319.68	316.62
	Ultimate strength	420.86	427.45	424.15

TABLE 3: Failure phenomena of specimens.

No.	Vertical loading displacement	Failure phenomena
CFST-1	55 mm (1)	The upper flange of the right beam and the lower flange of the left beam have large local buckling
	55 mm (2)	The sleeve local buckling at the connection between the right beam and the sleeve and the left beam and the sleeve is about 15 mm and 20 mm, respectively
	55 mm (3)	The upper flange weld of the right beam and the lower flange weld of the left beam crack
	60 mm (1)	The base metals on the lower side of the right beam and the upper side of the left beam are torn
	60 mm (3)	The base metals on the upper and lower flanges are torn
	65 mm (2)	The connection between the sleeve and the upper flange and the sleeve and the lower flange of the right beam is torn about 30 mm and 8 mm, respectively; the connection between the sleeve and the upper flange of the left beam is torn about 40 mm
CFST-2	65 mm (3)	The specimen failure occurs
	55 mm (1)	The adhesion failure occurs between the concrete and steel tube wall
	60 mm (1)	The base metal on the lower flange of the right beam is torn
	60 mm (2)	The base metal on the upper flange of the left beam is torn, and the sleeve local buckling occurs
	65 mm (1)	The sleeve of the right beam has a tear of about 2 mm
	65 mm (2)	The upper flange of the left beam is partially separated from the sleeve
CFST-3	65 mm (3)	The flange on both sides of the beam is separated from the sleeve, and specimen failure occurs
	65 mm (1)	The upper flange of the right beam has a local buckling
	65 mm (2)	The sleeve of the left beam has a local buckling of about 8 mm
	65 mm (3)	The base metals on the lower side of the right beam and the upper side of the left beam are torn, and the sleeve of the left beam has a local buckling of about 12 mm
	70 mm (1)	The left beam is distorted
	70 mm (2)	The base metal has been torn, and the sleeve of the left beam has a crack of about 6 mm
	70 mm (3)	The sleeve of the left beam is slightly damaged and has a local buckling, and the whole weld is torn
	75 mm (2)	The flange on both sides of the beam is separated from the sleeve, and specimen failure occurs

when the displacement of the beam end is 55 mm. The failure modes of these specimens are shown in Figure 6.

The test phenomena, failure processes, and failure modes of three sleeve joint specimens were identical, belonging to the failure mode of semirigid joints with high stiffness. Therefore, the seismic performance of the joint can be improved by improving the design, welding process, and sequence or strengthening the strength check and quality inspection of the weld.

A full finite element model was built by ABAQUS as shown in Figure 7. The axial force was applied on the top of the column, and the cyclic load was applied on the beam end to simulate the test loading conditions. The displacement constraints in  $X$  and  $Y$  directions and rotation constraints in  $Y$  and  $Z$  directions were applied at the top of the column, and  $X$ ,  $Y$ ,  $Z$  displacement constraints and  $Y$ ,  $Z$  rotation constraints were imposed at the bottom of the column.

Figure 8 shows the comparison of joint failure modes of specimen CFST-1 between the simulated results and experimental results. It can be seen from the figure that the simulation failure mode of the sleeve joint is almost the same as the experimental result. The failure mode of the specimen is mainly the buckling and the tearing of the sleeve. However, because the material damage is not given in the material property, the tearing of the sleeve is not simulated in the finite element model. The place where the joint deformation is large is the place where the steel is torn. The ABAQUS finite element model established in this paper can accurately simulate the failure mode of joints.

Figure 9(a) shows the stress distribution of the steel beam. It can be seen from the figure that the flange of the beam is curved. This phenomenon also occurs in the specimen CFST-1, the sleeve buckling is obvious, and the flange of the beam is easier to bend. It shows that the specimen with thinner sleeve wall thickness is more prone to buckling under the same axial compression ratio.

The finite element analysis can simulate the stress distribution of the steel tube column inside the sleeve, which cannot be obtained in the test. Figure 9(b) shows the stress distribution of steel tube under ultimate load. It can be seen that when the specimen was damaged, because the sleeve is only connected with the steel tube by the upper and lower welds, the corresponding part of the steel tube is also the part with the greatest stress in the loading process, and it is also the part most prone to deformation and buckling.

Figure 10 shows a comparison of failure modes between extended end-plate joints and sleeve joints. The extended end-plate joint is a typical semirigid joint [22, 23], and its main failure modes are shown in Figure 10(a). One kind of failure is that while the upper flange of the steel beam is taken as the rotation center, the end plate at the lower flange also has bending deformation, which is consistent with the failure mode of the sleeve joint. The other kind of failure is that the end plate below the upper flange of the steel beam is basically in a straight line; that is, the end plate has no obvious bending deformation, and the failure mode is consistent with the weld tearing failure mode of sleeve joint. From the analysis of rotation capacity and failure modes, the

sleeve joint conforms to the connection characteristics of the semirigid joint.

**3.5. Hysteretic Curve.** The load-displacement hysteretic curves of the specimen beam end are shown in Figure 11, where the graph in the first and third quadrants is the hysteretic curve of the left beam end and the graph in the second and fourth quadrants is the hysteretic curve of the right beam end. Both graphs are shuttle-shaped, indicating good deformability, seismic performance, and energy dissipation capacity of the specimen. Since cyclic load is applied on both sides of the beam end, the corresponding hysteretic curves are symmetrically distributed. When the specimen reached the yield state, the hysteretic curve analysis showed that some specimens had buckled. After yielding, the first cyclic load value of each displacement level was higher than that of the next two cycles, indicating that the joint strength and stiffness degrade with loading. In terms of ultimate bearing capacity, specimen CFST-2 did not change much compared with specimen CFST-1, suggesting that increasing the sleeve height will not improve the bearing capacity. However, the area of hysteretic curves of specimen CFST-2 was larger than that of specimen CFST-1. It implicated that the energy dissipation capacity of joint specimen CFST-2 is higher than that of joint specimen CFST-1.

Figure 12 shows that the simulated hysteretic curve is in good agreement with the experimental curve, which verifies the rationality of the finite element method [24, 25]. The load value of the simulated hysteretic curve was slightly higher than that of the experimental hysteretic curve. This is because the finite element model ignores the influence of the weld quality between the sleeve and the flange of the steel beam as well as the environment of the specimen. The initial stiffness of the joint in the finite element analysis was larger than that in the test, which is because the weld of the specimen basically appears in the part where one end of the steel beam is connected with the sleeve, while the weld is not considered in the finite element analysis.

**3.6. Skeleton Curve.** When applying cyclic load on the steel beam end, the skeleton curve can be obtained by successively connecting the maximum load in each stage of the hysteretic curve. The skeleton curves of three joint specimens are shown in Figure 13. The skeleton curves of the joint specimen are basically S-shaped, and the sleeve joints undergo obvious elastic, elastic-plastic, and plastic failure processes during loading. However, the skeleton curves of the left and right beam ends are not completely symmetrical. This is because the quality of the welds on both sides of the beam end cannot be the same, and cumulative damage occurs at the joints. The initial stiffness, ultimate bearing capacity, and ultimate displacement of specimen CFST-3 were significantly higher than those of CFST-1 and CFST-2, indicating that increasing the sleeve thickness can effectively improve the seismic performance of the sleeve joint.

As shown in Figure 13, the simulated and experimental skeleton curves are both S-shaped, and the joint specimens



FIGURE 6: Failure modes of specimens. (a) Sleeve local buckling; (b) base metal tearing of the left; (c) weld cracking; (d) base metal tearing of upper; (e) sleeve tearing; (f) joint failure.

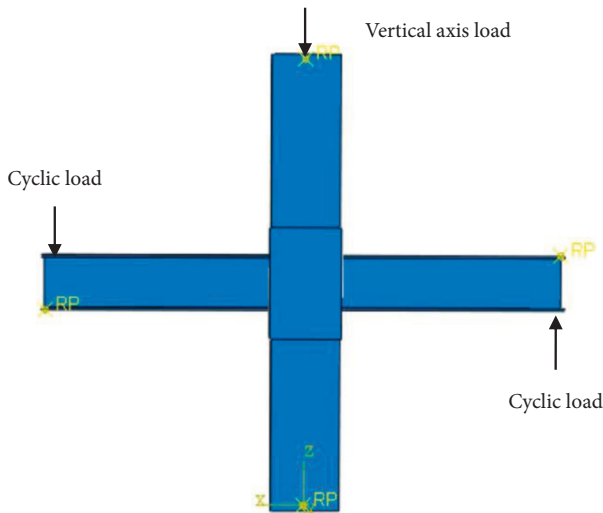


FIGURE 7: Loading conditions.

have experienced three stages under low cyclic loading, that is, elastic, elastic-plastic, and plastic failure. The simulated and experimental skeleton curves were also roughly consistent in values, with a load value error within 10%, which further illustrates the rationality of the finite element method. By comparison, the simulated skeleton curve using FEM is more symmetrical, but the symmetry of the experimental skeleton curve is slightly worse. This is because there was residual deformation during loading; thus, the

skeleton curve in positive and negative loading direction deviates slightly, but this influence factor is not considered in finite element simulation.

#### 4. Parametric Analysis

4.1. Axial Compression Ratio. Axial compression ratio is the ratio of the axial pressure of the column to the compressive strength of the entire section of the column. During the test, an axial pressure of 770 kN (axial compression ratio of 0.23) was applied to the column. Since the change in the axial compression ratio is not considered in the test, in this section, the influence of different axial compression ratios on the joint specimens was simulated and analyzed. The axial compression ratio  $n$  can be calculated according to

$$n = \frac{N}{N_u} \tag{1}$$

$$= \frac{N}{f_y A_s + f_c A_c}$$

where  $N$  represents the axial load,  $N_u$  is the ultimate bearing capacity of concrete-filled steel tube column,  $f_y$  is the yield strength of steel,  $f_c$  is the compressive strength of concrete, and  $A_s$  and  $A_c$  are the area of the steel tube and the core concrete, respectively.

Take the CFST-1 as an example. Figure 14 shows the load-displacement curves of joints with different axial compression ratios. The load-displacement curves of all

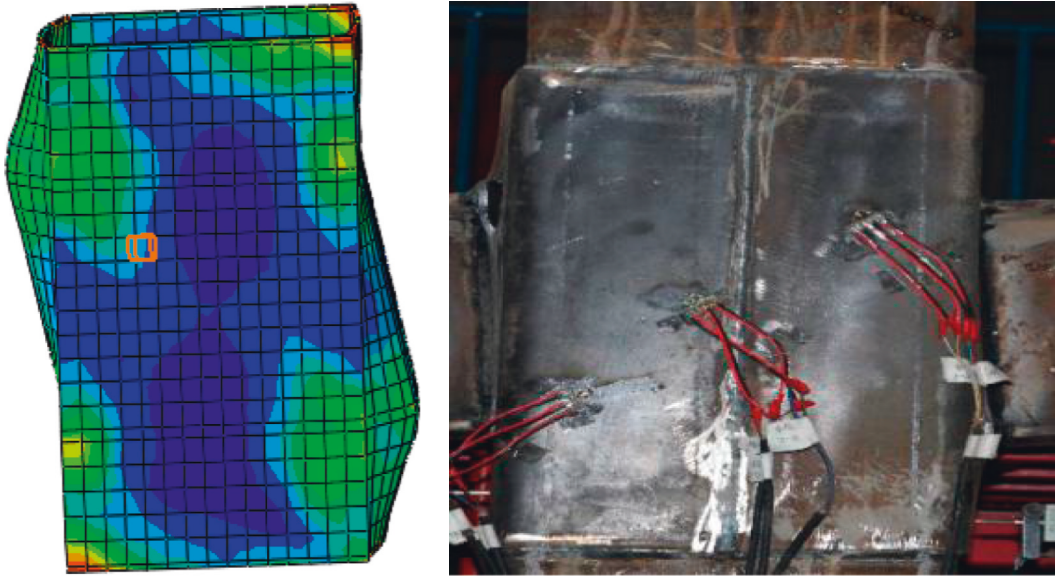


FIGURE 8: Failure mode.

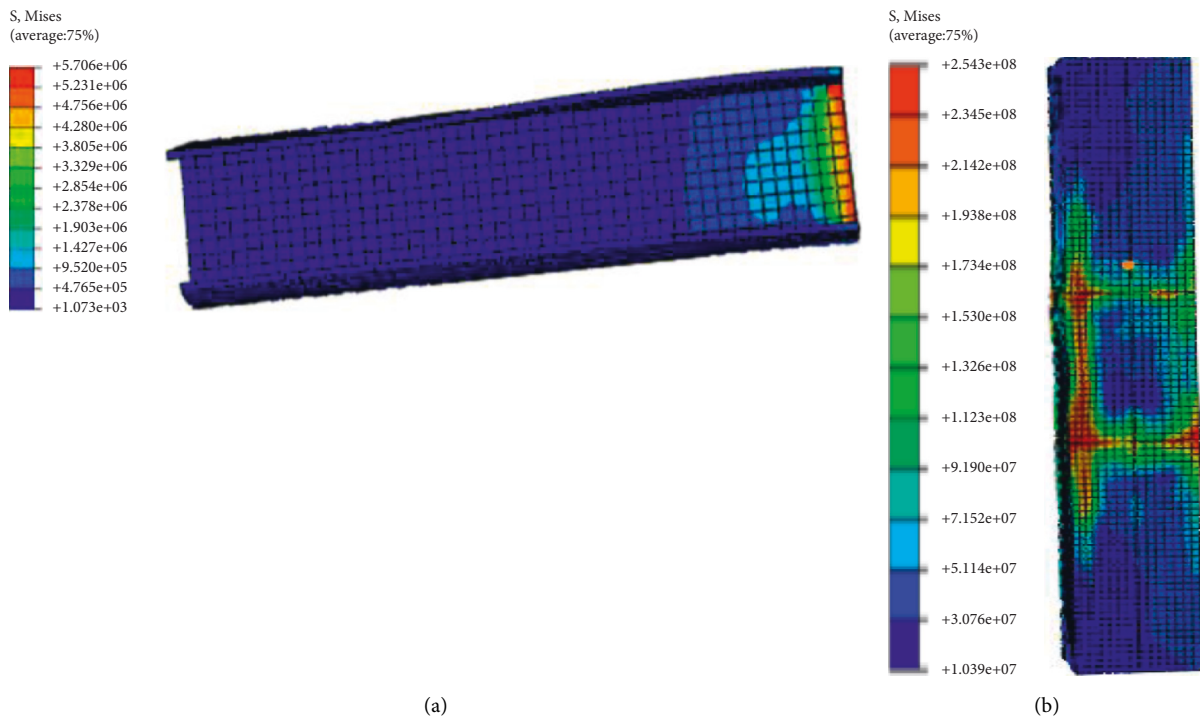


FIGURE 9: The stress distribution of steel beam and steel tube. (a) Steel beam and (b) steel tube.

parametric analyses below are obtained under monotonic loading. The initial stiffness is calculated by the slope of the elastic segment of the load-displacement curve. The slopes (initial stiffness) of the four curves are 1.116 ( $n=0.2$ ), 1.246 ( $n=0.4$ ), 1.408 ( $n=0.6$ ), and 1.334 ( $n=0.8$ ), respectively. It can be seen from the figure that, under the same boundary and loading condition, the joint

still has a good bearing capacity, and the axial compression ratio is the main factor influencing the initial stiffness of the joint. When the axial compression ratio is smaller than 0.6, the initial stiffness of the joint is positively correlated with the axial compression ratio, but when this ratio exceeds 0.6, the initial stiffness of the joint will be negatively correlated with the axial compression

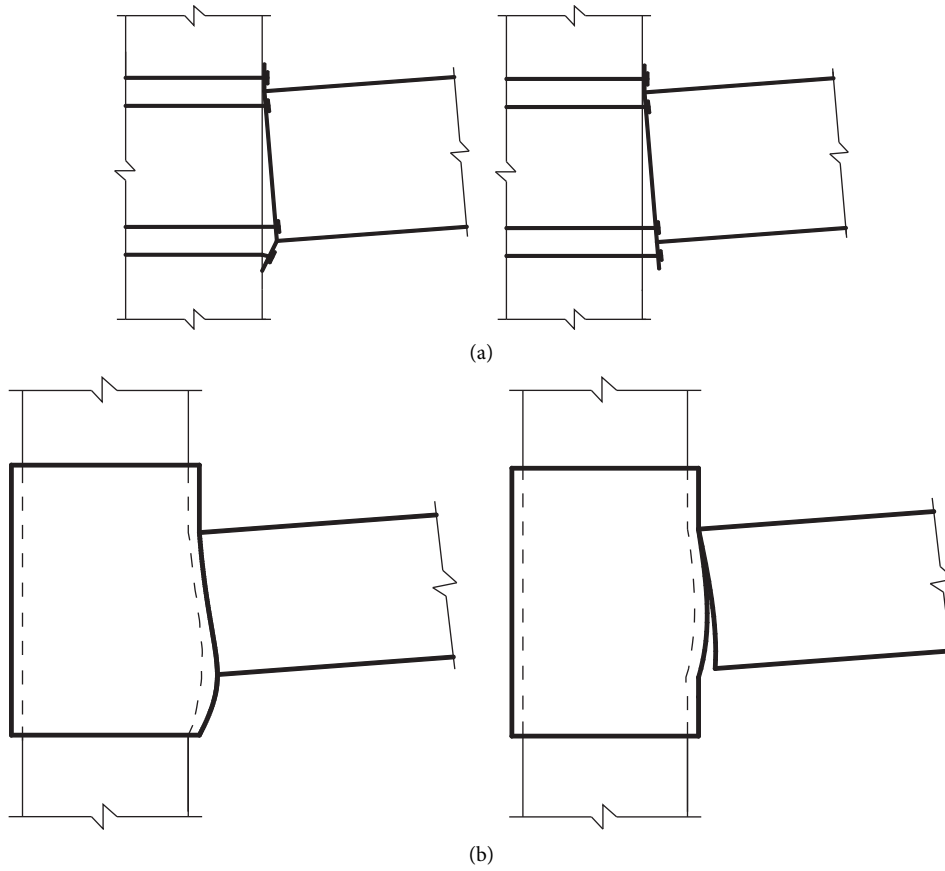


FIGURE 10: Comparison of failure modes of two semirigid joints. (a) Extended end-plate joint. (b) Sleeve joint.

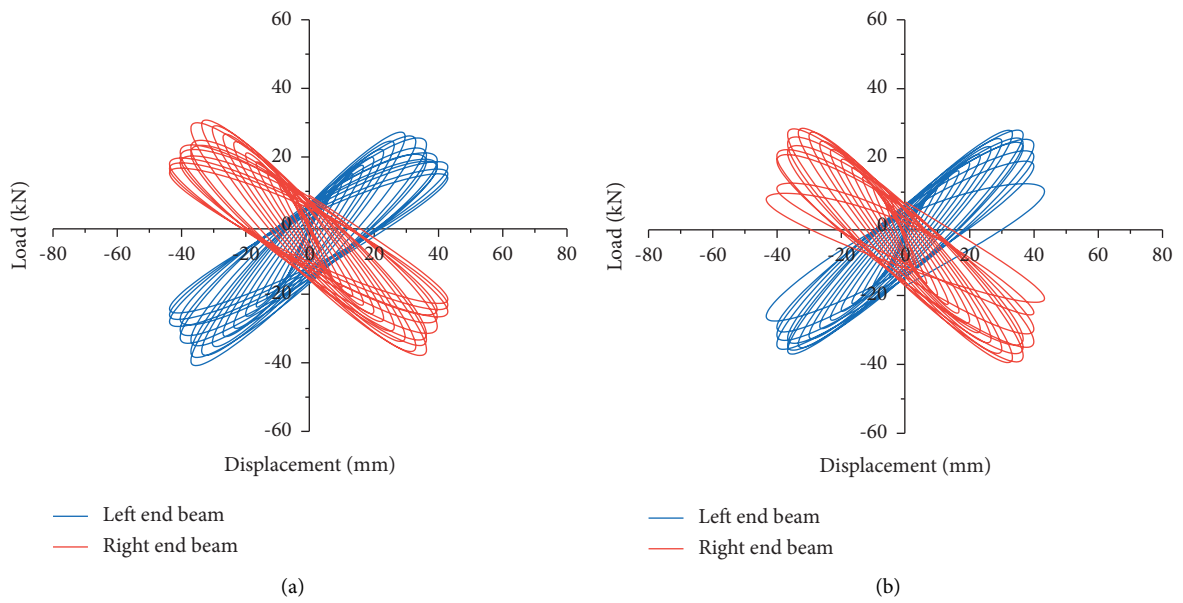
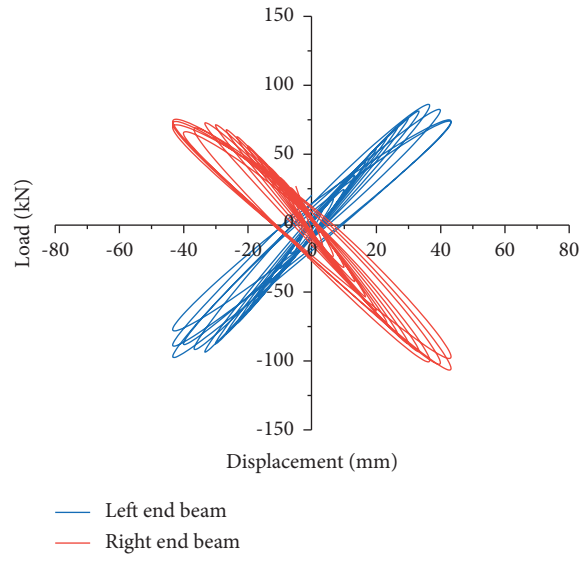
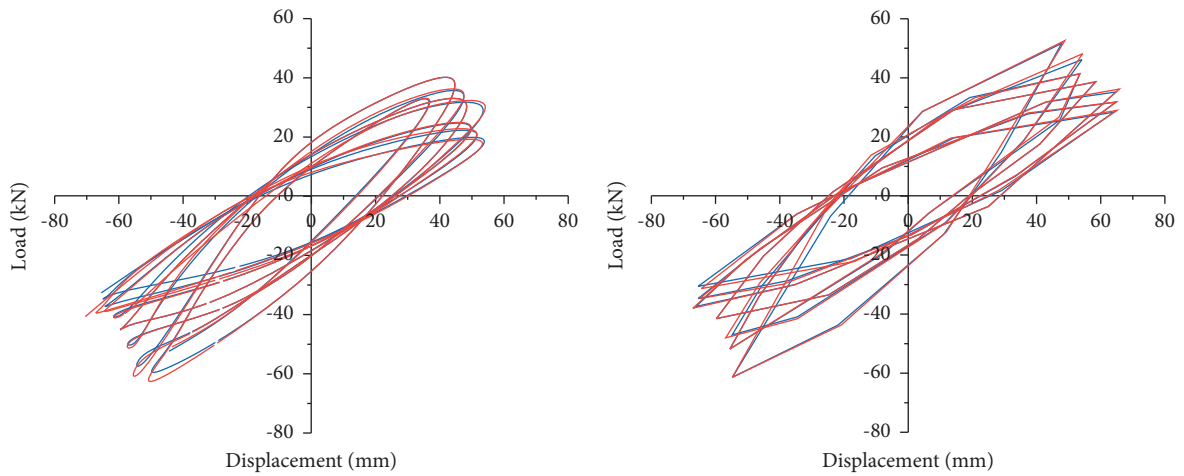


FIGURE 11: Continued.



(c)

FIGURE 11: Load-displacement hysteretic curves of the beam end. (a) CFST-1, (b) CFST-2, and (c) CFST-3.



— Test  
— Simulation

(a)

— Test  
— Simulation

(b)

FIGURE 12: Continued.

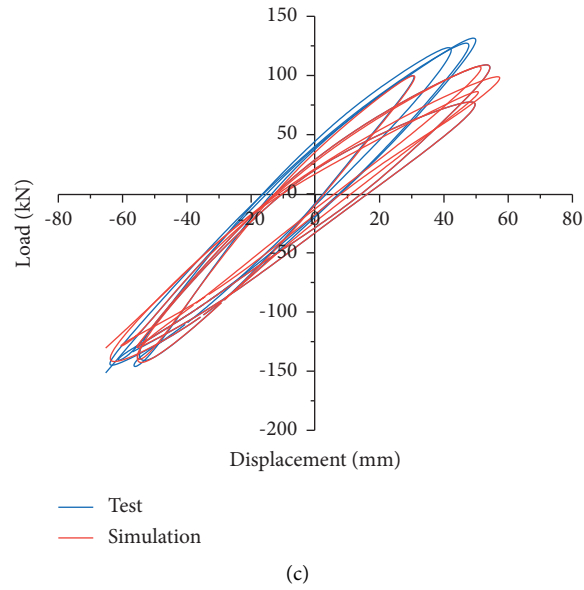


FIGURE 12: Comparison of hysteretic curves. (a) CSFT-1, (b) CFST-2, and (c) CFST-3.

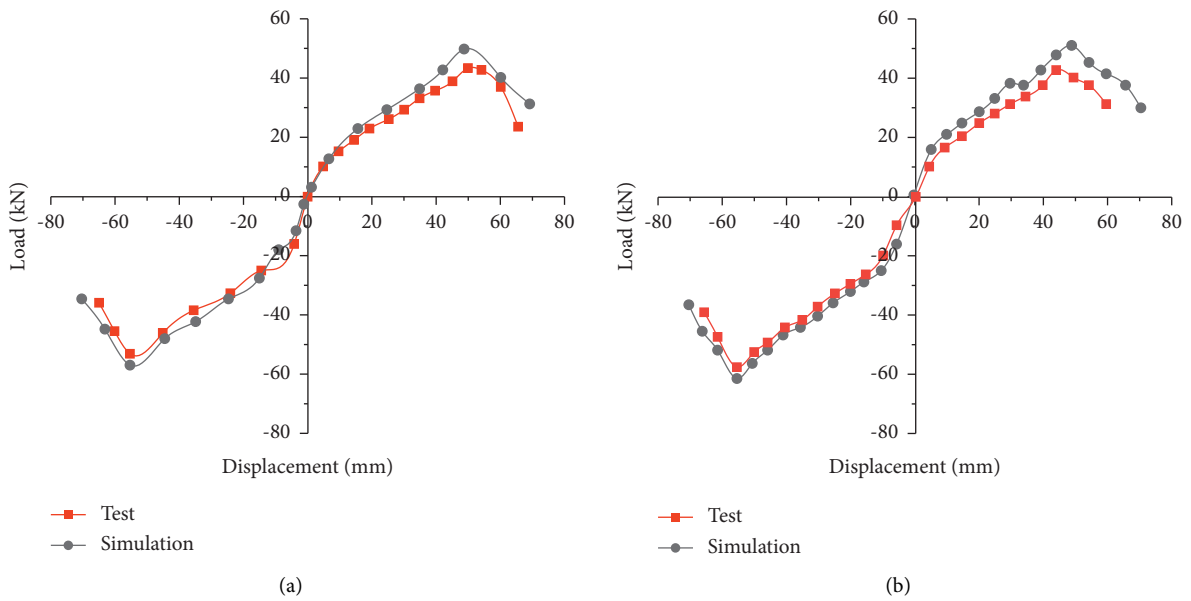


FIGURE 13: Continued.



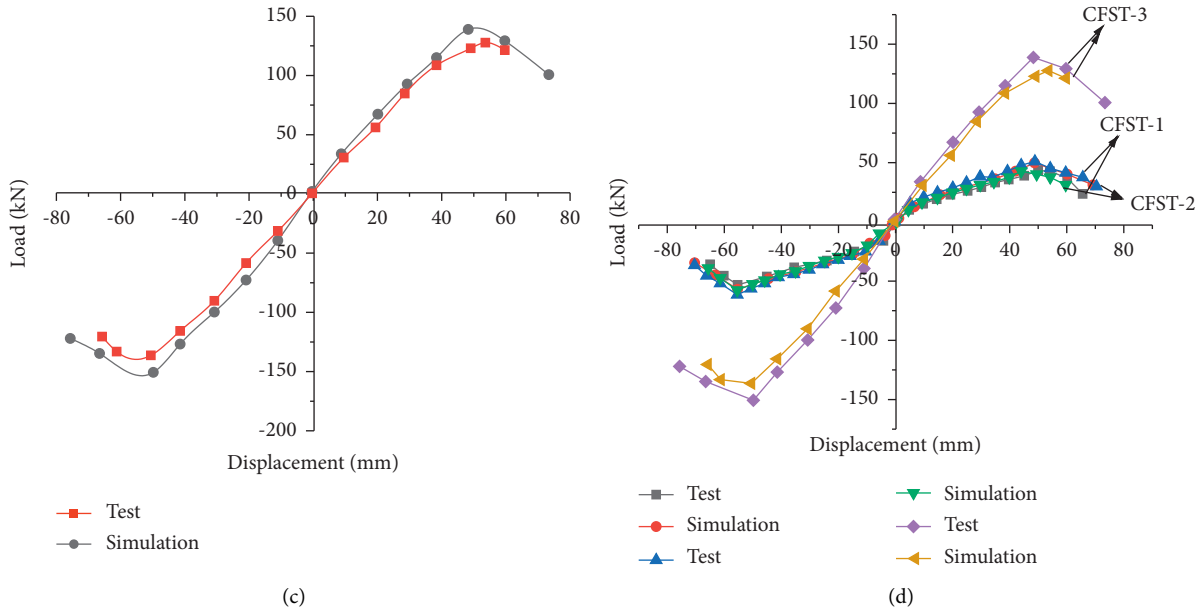


FIGURE 13: Comparison of skeleton curves. (a) CFST-1, (b) CFST-2, (c) CFST-3, and (d) comparison of skeleton curves under different parameters.

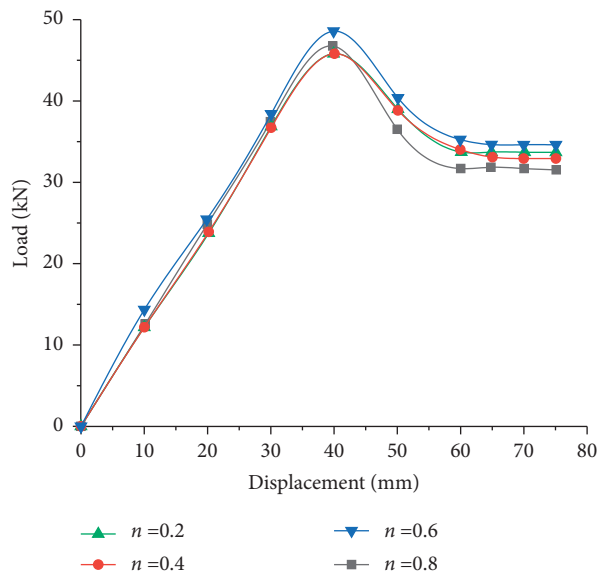


FIGURE 14: Load-displacement curves of joints with different axial compression ratios.

ratio. Therefore, it can be concluded that the joint achieves the optimal initial stiffness when the axial compression ratio  $n = 0.6$ .

It can be seen from Figure 15 that the hysteretic curves with the axial compression ratio  $n = 0.2$  and  $n = 0.4$  are almost the same, but the hysteretic curve with the axial compression ratio  $n = 0.8$  shows an obvious “pinch” phenomenon, which indicates that it is affected by slippage. When the axial compression ratio exceeds 0.6, the energy dissipation capacity of the joint will be affected.

**4.2. Influence of Concrete Strength Grade.** The influence of different concrete strength grades on sleeve joints was analyzed, and the results are shown in Figure 16. It can be seen from Figure 16 that the concrete with higher strength bears more load in the later stage of loading so that the local buckling of steel tubular wall filled with concrete of higher strength is smaller than that filled with ordinary strength concrete. Thus, it can be concluded that increasing the concrete strength has a better effect that the yielding of the steel tube will occur later.

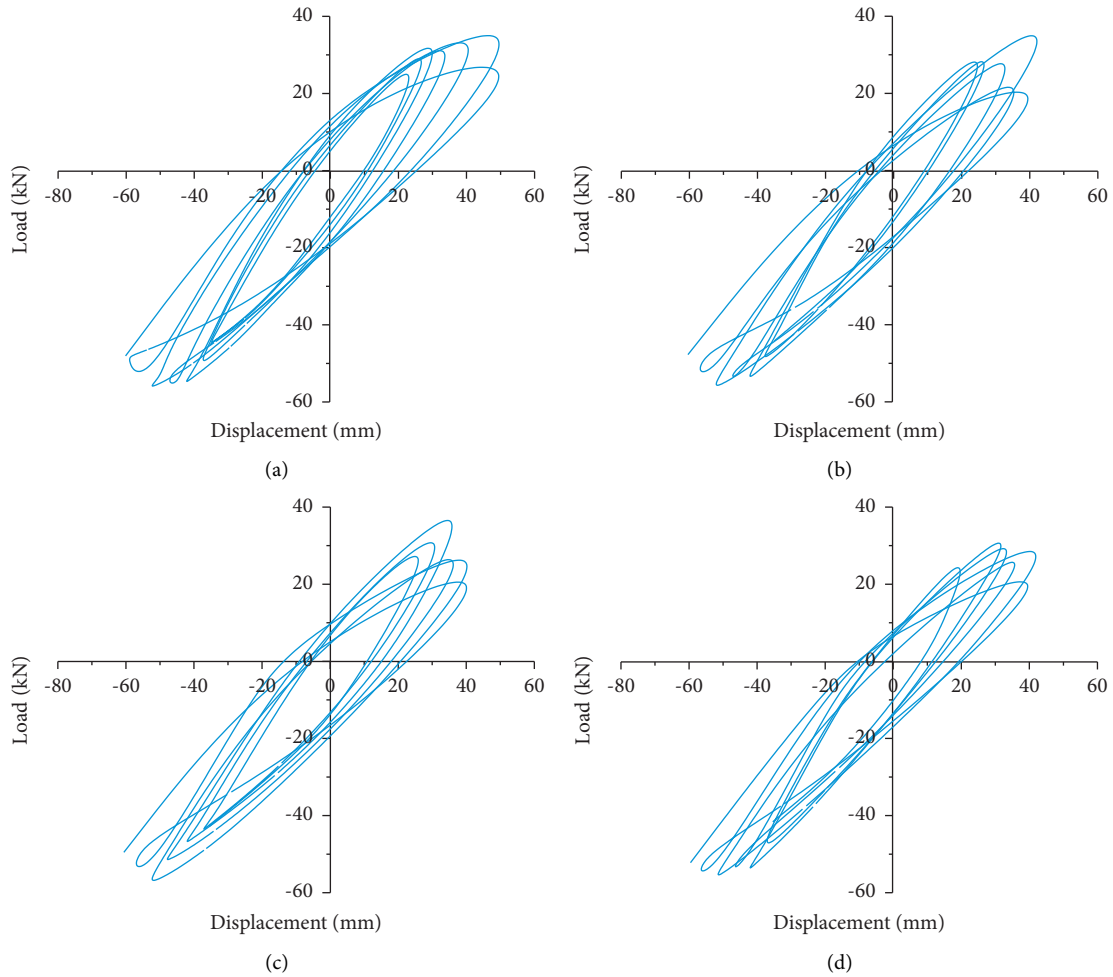


FIGURE 15: Hysteretic curves of joints with different axial compression ratios. (a)  $n=0.2$ , (b)  $n=0.4$ , (c)  $n=0.6$ , and (d)  $n=0.8$ .

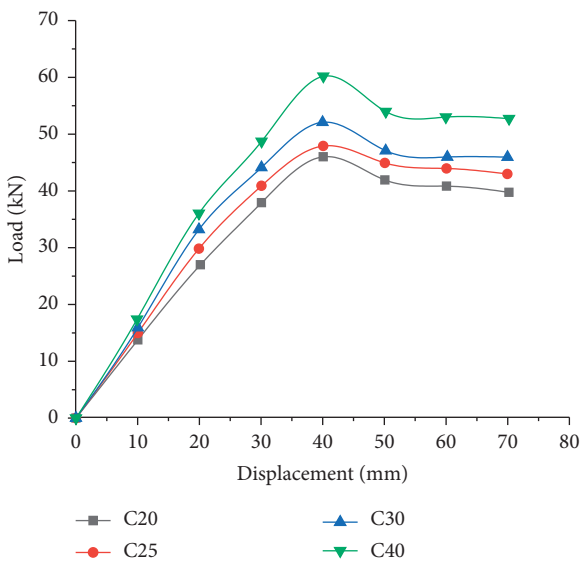


FIGURE 16: Load-displacement curves of joints with different concrete strength grades.

Figure 17 shows the hysteretic curves of joints with different concrete strengths. It can be seen from the figure that, compared with the initial hysteretic curve, the load increases by about 20% when the concrete strength increases. In addition, concrete strength has a significant influence on the overall elastic-plastic stage of the specimen, but before the elastic-plastic stage, the bearing capacity will not change significantly with increasing concrete strength.

**4.3. Influence of Sleeve Thickness.** Due to the limited test condition, only a few specimens were carried out, and the optimal sleeve thickness was not found. Therefore, in finite element analysis, the thickness of the sleeve was taken as 6 mm, 8 mm, 10 mm, 12 mm, and 16 mm for analysis and comparison, while other conditions remained constant. Figure 18 shows the load-displacement curves of joints with different sleeve thicknesses. As is observed, when the thickness of the sleeve is less than 10 mm, increasing the sleeve thickness can improve the stiffness and the ultimate bearing capacity. However, when the sleeve thickness exceeds 10 mm, the yield-bearing capacity and ultimate

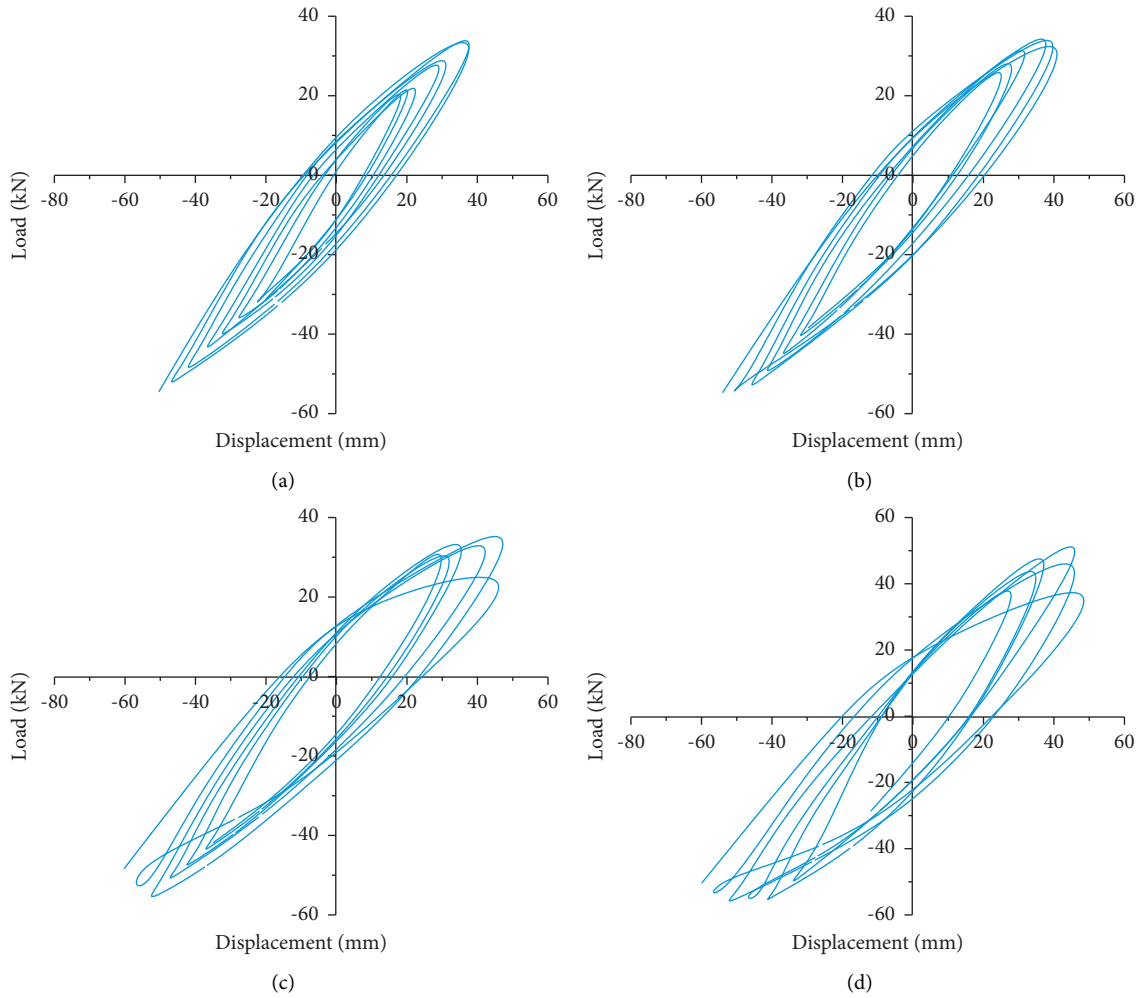


FIGURE 17: Hysteretic curves of joints with different concrete strength grades. (a) C20 concrete, (b) C25 concrete, (c) C30 concrete, and (d) C40 concrete.

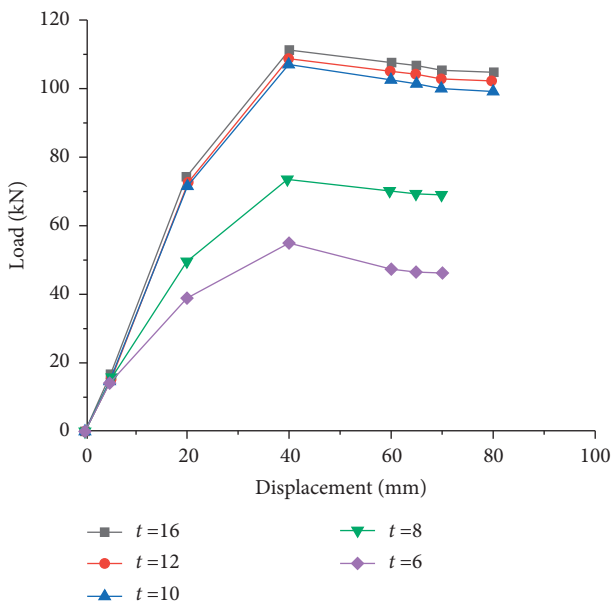


FIGURE 18: Load-displacement curves of joints with different sleeve thicknesses.

bearing capacity of the joints do not change significantly. The results show that when the thickness of the sleeve reaches 10 mm, the initial stiffness of the joint increases, but the increase is not obvious.

As shown in Figures 18 and 19, when the sleeve thickness exceeds 10 mm, the yield-bearing capacity and ultimate bearing capacity do not change significantly, and the hysteretic curves do not change much, indicating that the energy dissipation performance of the joint changes slightly. The results show that the seismic performance of joints can be improved with the increase of sleeve thickness, but the improvement effect is not obvious when the thickness exceeds a certain value. Moreover, when the thickness of the sleeve is less than 10 mm, the ultimate load increases significantly, which also leads to local buckling of the sleeve. Therefore, it is not recommended to increase the thickness of the sleeve without restriction when designing joints, which may result in unnecessary waste.

According to the test and finite element analysis, in order to meet the requirements that the joint strength should be higher than the members, the thickness of the sleeve needs to be greater than the thickness of the steel

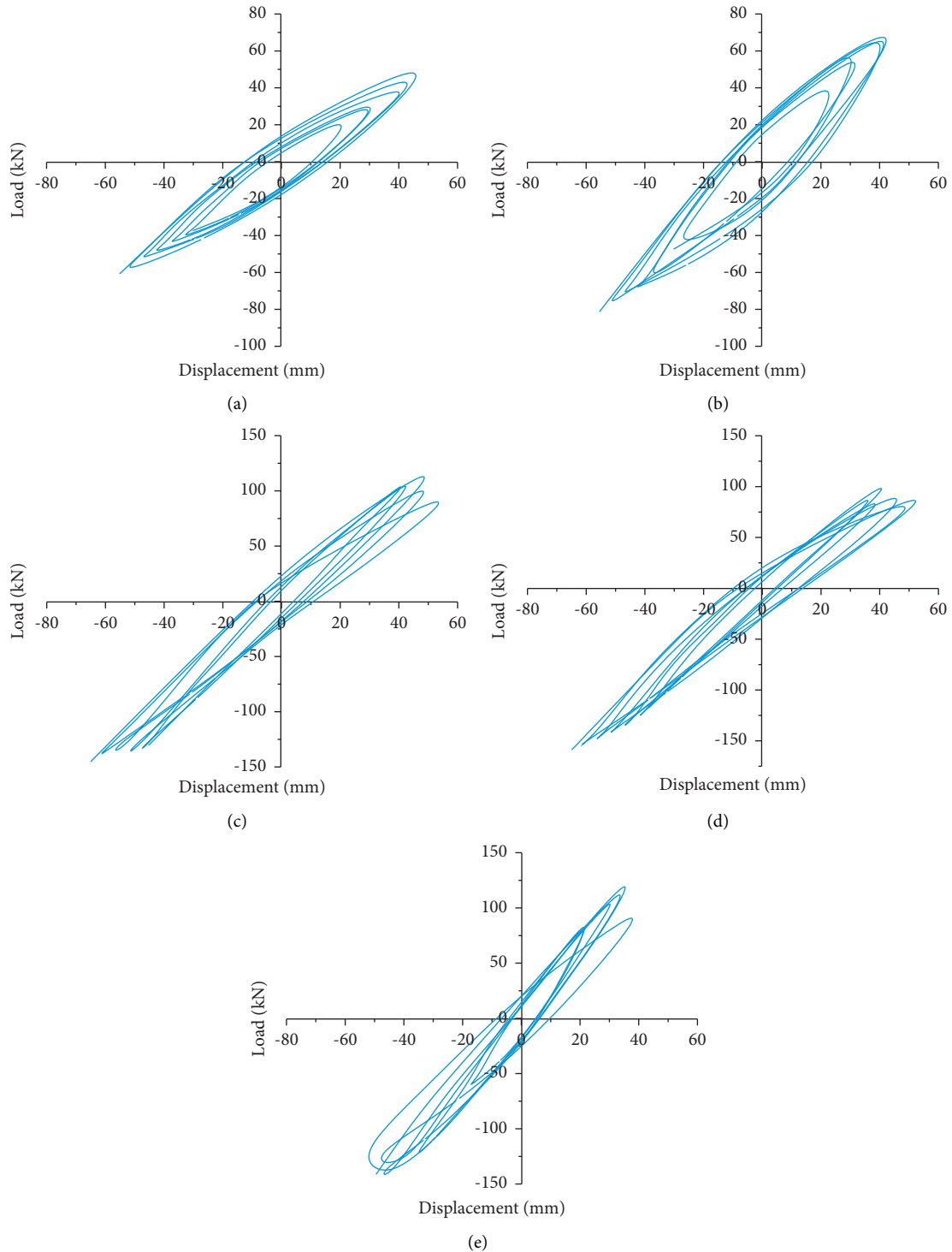


FIGURE 19: Hysteretic curves of joints with different sleeve thicknesses. (a)  $t=6$ , (b)  $t=8$ , (c)  $t=10$ , (d)  $t=12$ , and (e)  $t=16$ .

tube to ensure that the sleeve does not buckle before the column-steel tube. However, when the thickness of the sleeve reaches a certain degree, the impact on the bearing capacity of the joint decreases. At this time, increasing the thickness of the sleeve will cause a waste of materials. Therefore, it is suggested that the ratio of sleeve thickness to steel tube thickness ranges from 1.0 to 1.25.

**4.4. Influence of Sleeve Height.** Take 2 times the beam height as the initial height of the sleeve. 1.2 times, 1.5 times, and 1.8 times the sleeve height were taken to compare with the initial height. Figure 20 shows the load-displacement curves of joints with different sleeve heights. As shown in the figure, when the height of the sleeve is increased while the sleeve thickness is unchanged, the initial stiffness of the sleeve joint slowly increases. Moreover, with the increase in sleeve

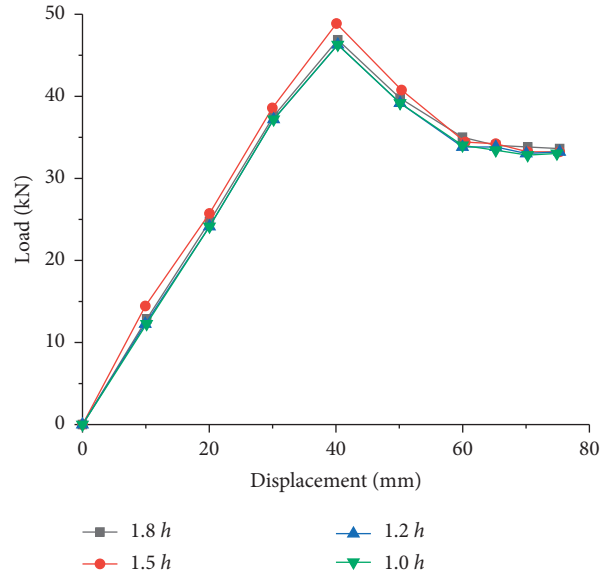


FIGURE 20: Load-displacement curves of joints with different sleeve heights.

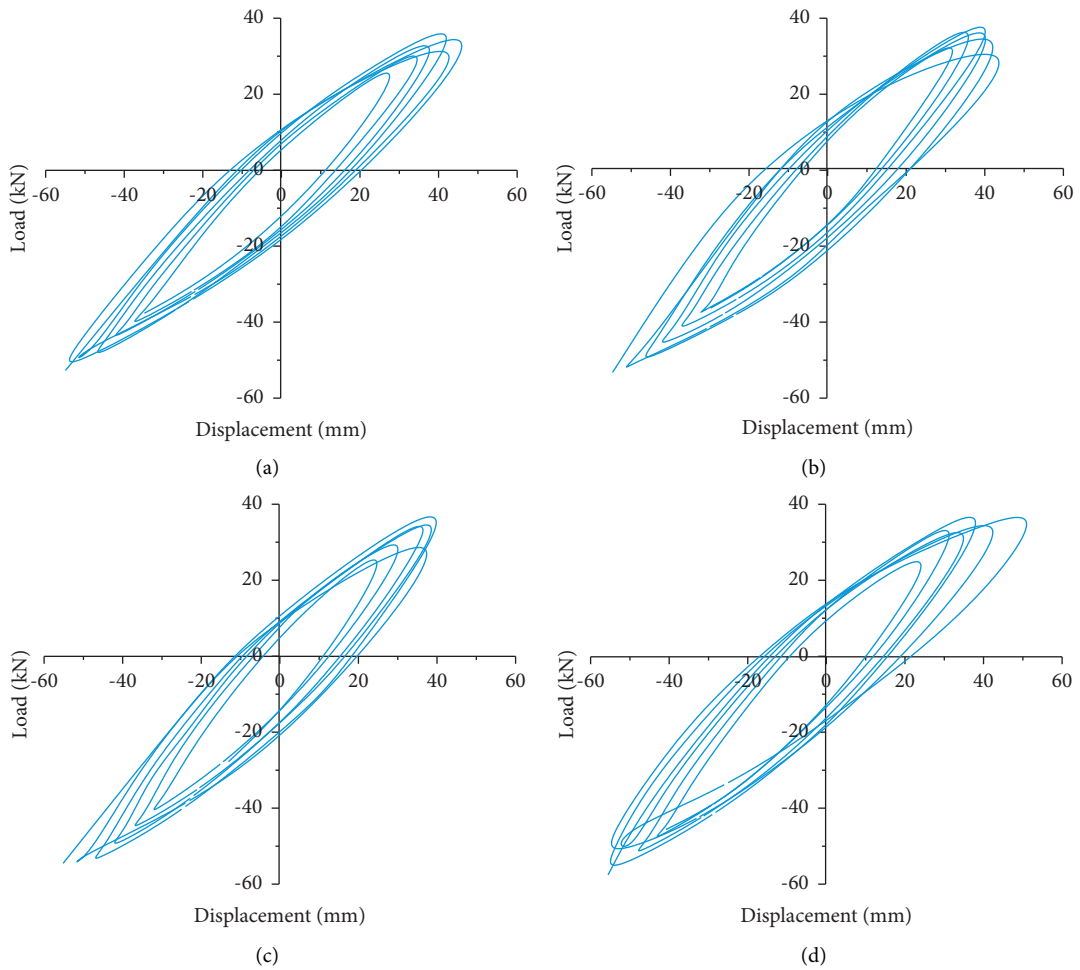


FIGURE 21: Hysteretic curves of joints with different sleeve heights. (a) 1 h, (b) 1.2 h, (c) 1.5 h, and (d) 1.8 h.

height, the ultimate load and ultimate displacement do not change significantly. Therefore, it is not economical to improve the bearing capacity of the joint by increasing the sleeve height.

Figure 21 shows the hysteretic curves of joints with different sleeve heights. By comparing the hysteretic curves of joints with each height, it is found that there is no significant change. However, as the height of the sleeve height increases, the shuttle shape becomes more obvious, and the hysteretic curve becomes fuller. It suggests that increasing the height can improve the energy dissipation capacity and ductility of the joints but has no significant effect on changing the ultimate bearing capacity and ultimate displacement. Moreover, as the height increases, the fabrication of sleeve joint specimens becomes more difficult. Therefore, the seismic requirements of joints can be met only by appropriately increasing the sleeve height.

## 5. Conclusions

In this paper, the method of numerical simulation analysis is used to design three concrete-filled steel tubular column-steel beam semirigid sleeve joints. The joint is composed of two steel plates and a sleeve welded together with the steel pipe column. The upper and lower flanges and webs at the end of the steel beam are welded by manual arc welding and completely welded on the sleeve. The validity of the finite element model is verified by comparison with experimental data, and the joints are subjected to low cyclic loading. The mechanical properties under different parameters are analyzed. Based on the analysis of this paper, the following conclusions can be drawn:

- (1) The semirigid sleeve joint model is established by ABAQUS and compared with the hysteretic curves and skeleton curves of previous experiments, which verifies the applicability of the finite element model in simulating the seismic performance of the joint under low cycle load.
- (2) The axial compression ratio and the height of the sleeve have little effect on the ultimate bearing capacity of the joint and have a small effect on the energy dissipation capacity. The design should be selected according to the economic principle.
- (3) The thickness of the sleeve and the concrete strength grade are the main factors affecting the seismic performance of sleeve joints. When the thickness of the sleeve is increased or the concrete strength grade in the column is increased, the ductility and ultimate bearing capacity of the joint increase, and the energy consumption capacity is also improved.
- (4) It is recommended that the thickness of the sleeve should be 1 to 1.25 times the thickness of the connecting steel tube. At the same time, according to the principle of economy, it is recommended that the height of the sleeve should not be greater than 2 times the height of the connecting steel beam.

## Data Availability

The data used to support the findings of this study are included within the article.

## Conflicts of Interest

The authors declare that they have no conflicts of interest.

## Acknowledgments

This project was supported by the Natural Science Foundation of Heilongjiang Province (LH2019E005), Fundamental Research Funds for the Central Universities (2572017CB02), and National Science Foundation of China (51408106), which are gratefully acknowledged.

## References

- [1] L. H. Han, W. BJORHOVDE, and R. BJORHOVDE, "Developments and advanced applications of concrete-filled steel tubular (CFST) structures: Members," *Journal of Constructional Steel Research*, vol. 100, pp. 211–228, 2014.
- [2] L. H. Han, Z. Tao, and W. D. Wang, "Advanced Composite and Mixed Structures: Testing," *Theory and design approach*, 2009.
- [3] S. Gao, L. H. Guo, and Z. Zhang, *Anti-collapse performance of composite frame with spacial-shaped MCFST columns*, Engineering Structures, vol. 245, , 2021.
- [4] S. Gao, M. Xu, F. Fu, and L. H. Guo, "Performance of bolted steel-beam to CFST-column joints using stiffened angles in column-removal scenario," *Journal of Constructional Steel Research*, vol. 159, pp. 459–475, 2019.
- [5] S. Gao, "Nonlinear finite element failure analysis of bolted steel-concrete composite frame under column-loss," *Journal of Constructional Steel Research*, vol. 155, pp. 62–76, 2019.
- [6] S. Gao and L. H. Guo, "Performance of circular bimetallic tube confined concrete slender columns under eccentric compression," *Archives of Civil and Mechanical Engineering*, vol. 21, no. 2, p. 40, 2021.
- [7] X. H. Zhou, Z. Zhou, and D. Gan, "Analysis and design of axially loaded square CFST columns with diagonal ribs," *Journal of Constructional Steel Research*, vol. 167, Article ID 105848, 2020.
- [8] D. Gan, Z. X. Li, T. Zhang, X. H. Zhou, and K. f. Chung, "Axial compressive behaviour of circular concrete-filled steel tubular stub columns with an inner bamboo culm," *Structures*, vol. 26, pp. 156–168, 2020.
- [9] Oh and Ai-Roda, "T-Cleat connection to concrete-filled tubular internal columns," *Journal of Structural Engineering*, vol. 130, 2004.
- [10] J. M. Ricles, S. W. Lu, and L. W. Lu, "Seismic behavior of composite concrete filled steel tube column-wide flange beam moment connections," *Journal of Structural Engineering*, vol. 130, no. 2, pp. 223–232, 2004.
- [11] X. L. Yang, H. L. Wang, P. Dong, and Q. C. Ren, "Experimental research on the rectangular CFST column and H-section beam connections with through diaphragms," *Journal of Hebei University of Technology*, vol. 40, no. 6, pp. 79–82, 2011.
- [12] X. L. Lv and X. P. Li, "Experimental study on ring-beam connections located outside the concrete- filled rectangular

- steel tubular columns,” *Journal of Building Structures*, vol. 24, no. 1, pp. 7–13, 2003.
- [13] O. Mirza and B Uy, “Behaviour of composite beam-column flush end-plate connections subjected to low-probability, high-consequence loading,” *Engineering Structures*, vol. 33, no. 2, pp. 647–662, 2011.
- [14] Z. Y. Gao, H. Q. Li, and Z. C. Wang, “Mechanical performance of connect node between concrete filled square tubular column and H-steel beam,” *World Earthquake Engineering*, vol. 31, no. 1, pp. 180–186, 2015.
- [15] J. E. France and J. Buick Davison, “Moment-capacity and rotational stiffness of endplate connections to concrete-filled tubular columns with flowdrilled connectors,” *Journal of Constructional Steel Research*, vol. 50, no. 1, pp. 35–48, 1999.
- [16] Z. A. Huang, “A connection element for modelling end-plate connections in fire,” *Journal of Constructional Steel Research*, vol. 67, no. 5, pp. 841–853, 2011.
- [17] J. W. Hu, R. T. Park, and T. Park, “Mechanical models for the analysis of bolted T-stub connections under cyclic loads,” *Journal of Constructional Steel Research*, vol. 78, pp. 45–57, 2012.
- [18] L. H. Han, Z. Tao, and W. D. Wang, *Advanced Composite and Mixed Structures: Testing Theory and Design Approach*, Science Press, Beijing, China, 2009.
- [19] L. H. Han, *Concrete Filled Steel Tubular Structures--Theory and practice*, Science Press, Beijing, China, 2007.
- [20] Gb/T 2975-2018, *Steel and steel products--location and preparation of samples and test pieces for mechanical testing*, China Standards Press, China, 2018.
- [21] L. L. Sun, Z. Q. Liang, Q. S. Wang et al., “Seismic response on T-head square-neck one-side bolted endplate connection of beam to square tubular column,” *Engineering Structures*, vol. 246, Article ID 113077, 2021.
- [22] L. L. Sun, Z. Q. Liang, M. Cai et al., “Seismic behaviour of TSOBs bolted I-beam to hollow section square column connection with inner stiffener,” *Journal of Building Engineering*, vol. 51, Article ID 104260, 2022.
- [23] J. B. Li and X. Li, “Realization of strong column-weak beam failure mode for concrete-filled square steel tubular frame structure,” *Advanced Materials Research*, vol. 446-449, pp. 424–428, 2012.
- [24] Y. Z. Yin and Y. Zhang, “Research on the seismic behavior of concrete-filled steel tubular column and steel beam joint,” *Applied Mechanics and Materials*, vol. 204-208, pp. 2528–2532, 2012.
- [25] Gb/T 228-2010, *Metallic materials--Tensile testing--Method of test at ambient temperature*, China Standards Press, China, 2002.

## Research Article

# Dynamic Characterization of a Reinforcement Rammed Wall for the Earthen Ruins

Bei Liu <sup>1</sup>, Yucheng Shi <sup>1</sup>, Kun Liu <sup>2</sup>, Tao Li,<sup>1</sup> and Shaopeng Wang<sup>1</sup>

<sup>1</sup>Lanzhou Institute of Seismology CEA, Lanzhou 730000, China

<sup>2</sup>Lanzhou Institute of Geotechnique and Earthquake CEA, Lanzhou 730000, China

Correspondence should be addressed to Yucheng Shi; shiyc@gdszj.gov.cn and Kun Liu; liukun@gdszj.gov.cn

Received 1 November 2021; Accepted 5 February 2022; Published 10 March 2022

Academic Editor: Shan Gao

Copyright © 2022 Bei Liu et al. This is an open access article distributed under the Creative Commons Attribution License, which permits unrestricted use, distribution, and reproduction in any medium, provided the original work is properly cited.

In recent years, the earthen ruins' cultural relics have aroused people's extensive attention, and the protection of them is more and more urgent. The aim of the paper is to present the essential results of an ongoing research on a reinforced rammed earthen wall in the Suoyang ancient city (Guazhou, China). A variety of methods to combining aerial survey, dynamic test, and numerical model is provided with the purpose of estimating the structural characteristics of the ancient rammed wall. An aerial geometric survey based on high-resolution images made by unmanned aerial vehicle (UAV) has been approached to acquiring a 3D model. An ambient vibration test has been adopted by using vibration pick-ups. The experimental data were dealt with the operational modal analysis (OMA) followed by comparing with the numerical results delivered by the model. Meanwhile, the results showed the maximum displacements and corresponding positions of the structure under the three modes by the finite element model (FEM).

## 1. Introduction

The conservation of ancient civilization architectures has received wide attention from the countries in which history carried vital cultural heritage. For instance, the earthen ruins are normally subjected to the intrinsic deterioration in time and the natural hazards [1]. Within the circumstance, they are of the greatest importance to develop and apply the reasonable methods for the sake of identifying the considerable structural parameters. Some scholars have conducted relevant research studies on the earthen ruins. For example, Li and Liu conducted field pulsation tests on the earthen site walls and obtained the spectral characteristics between the bottom and top of the walls as well as the self-oscillation period [2–4]. They correlated the structural properties of earthen sites and focused only on a certain point, i.e., obtaining the frequencies and periods at the bottom or the top of the site walls. However, the structural properties of a point for the wall usually were differed from the whole structure. The best way to access the structural dynamic characterization is to establish the dynamic monitoring system which is based on the vibration test. And, it can be

safely applied to historical structures [5]. Frequency response function curvature technique and the modal analysis have extensive usage in the structural health monitoring [6]. Given the excitation force, both methods can be effective to detect damage in civil structures, while the latter may be the better method to access the dynamic characterization in the case of unknown excitation force. One of the ways to solve the above problem is the operational modal analysis (OMA). OMA is widely adoptable to masonry civic belfry [7], the masonry tower [8, 9], and other historical masonry buildings [10–13]. Pavlovic proposed an expeditious and low-cost procedure for the structural identification of historic masonry towers [14]. Numerical simulation is a very convenient method to understand the mechanical properties of structures. This method, combining with the vibration test, is also widely taken in civil engineering. Boscatto [15, 16] has acquired the detection, localization, assessment, and prediction of damage for three different multileaf masonry specimens by the comparison between the experimental and numerical modal data calculated by the commercial finite element method (FEM). It is worth noting that the method has great advantages for nonlinear analysis [17].



The experimental work depicted in the paper followed an elementary investigation on a reinforcement rammed wall located in the Suoyang ancient city (Guazhou, China), under which actual conditions indicated that it has been strengthened and in order to avoid the loss of an ancient cultural architecture (Figure 1). We are all known that the currently conditions are the result of the restoration process against the other walls in the ancient city. While, there are ruins of the wall at different degrees of erosion damage. As the government departments pay more and more attention to the protection of cultural relics, strengthened cultural relics are processing. The wall is trapezoidal in cross section with two sides of about 6.5 m and 4.2 m; it is 10 m tall and the thickness of the rammed layer is 0.1 m. The top surface of the site is roughly terrace-shaped. Simplifying the actual situation can allow us to gain Figure 2. A trebling method is revealed combining an accurate aerial survey based on pictures processing, vibration testing, and FEM.

In the last decades, the possibility to conduct 3D surveys of intricate and inaccessible constructions has become more interesting for structural identification combining with the development of aerial measurements [18, 19]. In the paper, considerable amounts of images were taken by using unmanned aerial vehicle (UAV), which is subsequently drawn to make a 3D model. Furthermore, an ambient vibration test has been carried out using nine high-sensitivity seismic accelerometers. Measurements of velocity have been recorded for estimating dynamical parameters, including natural frequencies and mode shapes. The research is also ongoing to adjust a suitable numerical model and to access the positions and size of the maximum displacements of the reinforced rammed wall.

## 2. Aerial Photographic Survey and the 3D Model from UAV Technology

With the development of UAV technology, it is widely used in field investigations, especially in dangerous or inaccessible places [20]. Based on the high-resolution images provided by UAV technology, the size of the wall and the structural characteristics of the site provide the optimal case study for conducting architectural and geometric measurements.

The configuration used in the experiment can be epitomized into four stages: operation planning, data acquisition, data processing, and postprocessing representations. A considerable number of superimposed pictures can be obtained from the drone flight. It is commonly believed that the complete layout of the whole structure, the plan view, the one elevation, and the lower side of the wall could be generated from the datasets. Plotting the range of the flight on the remote controller, the target level of accuracy depended on the flight altitude, and as such, we must adjust the flight height. The flight was carried out using a Phantom 4 manufactured by DJI, which flew at an altitude of 80 m. Reducing the height can improve the accuracy, but it would greatly increase the cost of image processing. Thus, we need to take the height into account for processing costs. The flight range is the continuous walls in the east of Suoyang ancient city, and the object to be studied in the paper is a part



FIGURE 1: The reinforced site wall.

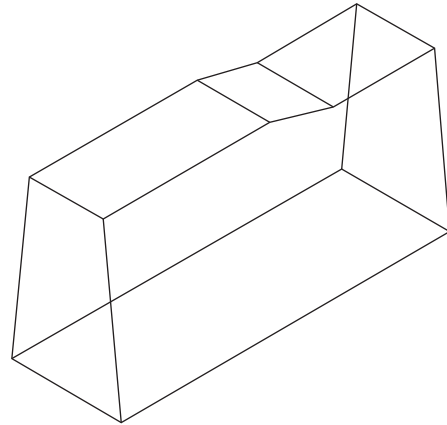


FIGURE 2: The simplified model of the wall.

of it. Therefore, it is necessary to intercept from them (Figure 3).

## 3. Data Processing and Analysis

The dynamic characterization with reference to natural frequencies and corresponding modes has carried out the OMA using vibration response action under conditions by virtue of classical measurements.

*3.1. Experimental Procedures and Methods.* The dynamic response of the reinforced wall has been measured by using nine uniaxial accelerometers. The INV 3060S intelligent signal acquisition and processing system developed by COINV were selected as the experimental equipment, and the 941 B vibration pick-ups developed by Institute of Engineering Mechanics CEA were selected as the sensors. The sensitivity of the sensor was 23 V-s/m. The 9 sensors were divided into three groups; each group has 3 sensors in which the two horizontal and one vertical direction were measured, respectively. Placing three sets of vibration pick-ups in three positions for the purpose of the identification of vertical, horizontal, and torsional vibration modes, the sensors' arrangement is reported in Figure 4. There are three experiments in the testing methodology, each recording 300 s time series with a sample rate of 204.8 Hertz. Three sets of vibration pick-ups were named as A1, 1, and 2. The one point of A1 has been installed in the bottom of the wall as a reference system for the analysis, and the others were placed on the top of the wall. Each point has three arrows



FIGURE 3: The reinforced wall in Suoyang city: virtual 3D model.

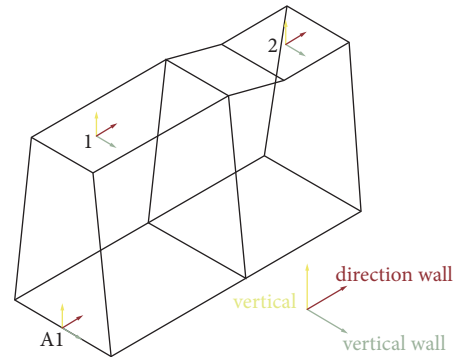


FIGURE 4: The sensors' arrangements in the wall.

representing the three directions in which it is measured (Figure 4). It should be noted that the red arrow is the direction wall, the green arrow is the vertical wall, and the yellow arrow is the vertical.

**3.2. Data Processing: SSI and EFDD.** The data obtained from the sensors were processed by the stochastic subspace identification (SSI) algorithm in the time domain and the enhanced frequency domain decomposition (EFDD) method for identifying the modal parameters [21, 22]. Since the power spectral density spectrum estimated from the raw velocity data and the corresponding references [23, 24], the range of the frequencies should be below 10 Hertz. The ambient vibration data were processed to a cut-off frequency of 10 Hertz. Natural frequencies and vibration modes of the reinforced wall were estimated by using the SSI and EFDD. Figures 5(a) and 5(b) show the stability diagram for the SSI and the singular values of the spectral matrices of the testing for the EFDD, respectively.

The paper identified the frequencies and modes of the first-three orders (Figure 6). As shown in Figure 5, the frequencies identified by the stability diagram obtained by the SSI method and the singular values obtained by the EFDD method are basically the same (Table 1).

## 4. Results and Discussion

The experimental results in terms of natural frequencies and related modes have been summarized in the previous section. The numerical modelling of masonry structure has been investigated by many researchers [25, 26]. Meanwhile, the cloud map is applied to analyze the mechanical properties, which

is widely used in masonry structures [27]. In the paper, the simplified numerical model was determined by the aerial survey carried out by direct method. The parameters with the material properties were gained from reference [28]. Due to the influence of historical and natural hazards, the material itself is damaged to varying degrees and unknowable. Hence, the parameters were acquired in the laboratory (density and elastic modulus) which need to be modified. In the study, the frequencies gained from the field test and the frequency obtained by finite element analysis were compared and analyzed. The final material property parameters (density and elastic modulus) were taken from combining specific formulas for calculation [29]. Figure 7 shows the results of the numerical modal analysis. The comparison between the results in Figures 6 and 7 revealed a good consistency between the experiment and FEM. The same can be seen when compared with the modes. The first two orders of deformation appeared in the horizontal direction. The first-order can be regarded as transverse bending, and the second order can be considered as torsional deformation occurring in the plane. The third order of deformation occurred in the vertical direction. Meanwhile, the paper reports on the results that the maximum displacements and positions correspond to each of the three modes [30]. What is interesting is that, in the maximum positions, the displacements are the same, which are all near the left top of the free surface, and the corresponding displacements are 0.071 mm, 0.077 mm, and 0.065 mm, respectively. As can be seen from the figure, the first-three orders of modes' vibration are not complicated, due to the limitations of the experimental equipment, and the OMA can only identify the lower orders of modalities. The sensors were not positioned on either side of the top surface; therefore, the torsional

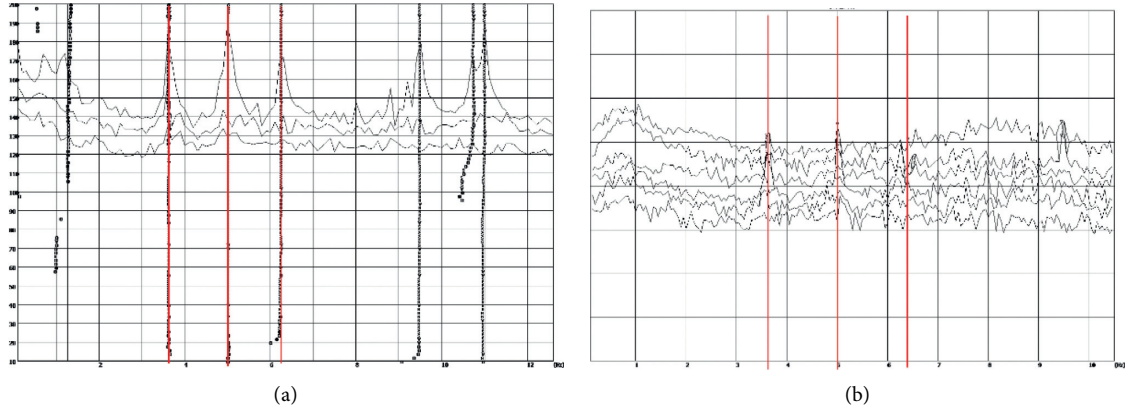


FIGURE 5: The pictures with two different techniques. (a) Stability diagram for SSI. (b) Singular value for EFDD.

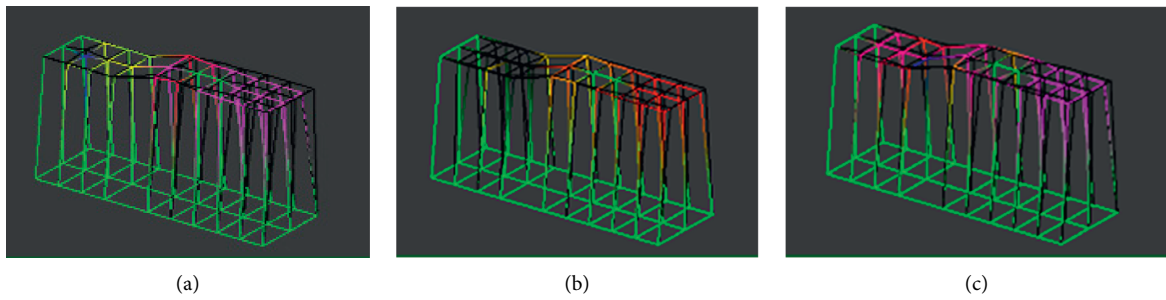


FIGURE 6: Experimental frequencies and vibration modes. (a) First-order transverse bending,  $f_1 = 3.626$  Hz, and damp = 0.861%. (b) Second-order left and right torsion,  $f_2 = 5.018$  Hz, and damp = 0.416%. (c) Third-order vertical bending,  $f_3 = 6.372$  Hz, and damp = 1.876%.

TABLE 1: The frequencies and damping for the research.

Modes (#)	SSI		EFDD		Mean	
	Freq (Hz)	Damp (%)	Freq (Hz)	Damp (%)	Freq (Hz)	Damp (%)
1	3.629	1.19	3.624	0.532	3.626	0.861
2	5.012	0.82	5.024	0.012	5.018	0.416
3	6.251	1.52	6.493	2.232	6.372	1.876

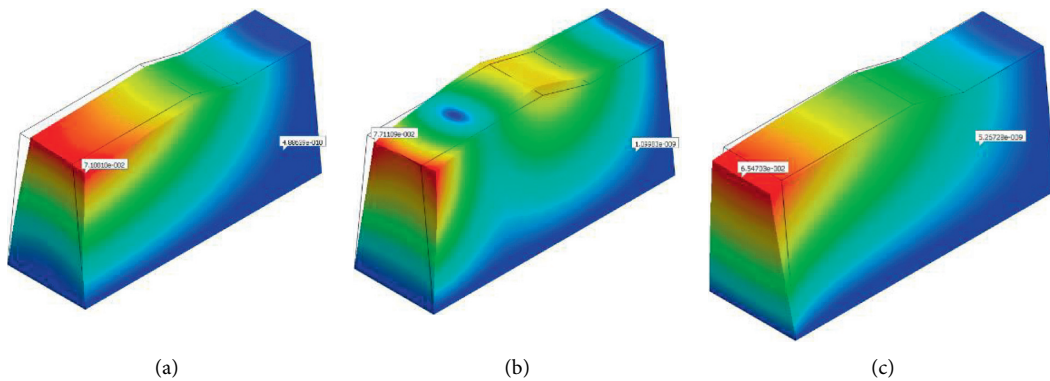


FIGURE 7: Numerical frequencies and vibration modes. (a) First-order transverse bending,  $f_{1FEM} = 3.34$  Hz, (b) second-order left and right torsion,  $f_{2FEM} = 5.417$  Hz, and (c) third-order vertical bending,  $f_{3FEM} = 6.098$  Hz.

modes in the vertical direction were not identified. In fact, there are higher order torsional modes in the vertical direction, as evidenced by the FEM results. The 3D model

obtained from the UAV flight was applied to be built as accurate as possible. Because the modelling built in the paper is regular, there are some slight differences in details from

the actual one, such as the existence of a partial gap at the top of the wall which is neglected in the finite element model. More importantly, the wall is more nonuniform and non-homogeneous on account of the effects of historical and natural disasters. This could explain the discrepancies between the experimental and FEM analyses.

## 5. Conclusion

Based on the results and discussion presented above, the conclusions are obtained as below:

- (1) It is presented by applying the UAV technology to the research object, and the classical test was performed by using high-sensitivity sensors. The vibration tests were attempted both to compare effectiveness of different techniques (SSI and EFDD) on such constructions and to conduct the dynamic structural identification.
- (2) An elementary comparison between the simplified numerical FEM and the OMA results demonstrated that we need to take the changes in material parameters caused by the damage against the structural system into account.
- (3) The experimental tests will be reported with the structural unreinforced for the purpose of investigating the change of the dynamic properties between the reinforced wall and the unreinforced. This will give us a significant amount of useful information on the seismic effect for the reinforced wall.

## Data Availability

The data were obtained by the author through practical tests, and part of the data were quoted from relevant references and indicated within the article.

## Conflicts of Interest

The authors declare that there are no conflicts of interest regarding the publication of this paper.

## Authors' Contributions

Bei Liu and Yucheng Shi were the main authors of the article. Bei Liu was the first author and participated in the whole process of the field experiment and data analysis; meanwhile, Shi Yucheng was the corresponding author of the paper and has also revised the paper. Kun Liu participated in the whole process of the experiment and modified the paper. Tao Li and Shaopeng Wang participated in the whole field experiment.

## Acknowledgments

The authors would like to thank the National Key Research and Development Program of China (2020YFC1522200) and the Fundamental Research Funds for the institute of Earthquake Forecasting, China Earthquake Administration (2019IESLZ04) for their financial support for the manuscript,

through the project "The Study on Degradation Process and Protection Technology of Earthen Ruins under multi-field coupled." The authors also acknowledge S. D. Wei, from COINV, for his support with test methods and software processing. The authors also wish to thank Y. X. Lu, P. H. and Chi et al. for their contributions to this research activity.

## References

- [1] M. L. Sun, X. D. Wang, and Z. X. Li, *A Primer on the Conservation of Earthen Sites*, Science Press, Beijing, China, 2010, in Chinese.
- [2] T. L. Li, "Disease characteristic and dynamic test analysis of jiaohe ancient city," *Journal of Seismological Research*, MSC Thesis in Chinese, Lanzhou Institute of Seismology, CEA, Lanzhou, China, 2020.
- [3] T. L. Li, Y. C. Shi, K. Liu, Y. X. Lu, C. Y. Wang, and Z. Y. Xian, "Disease characteristics and dynamic test analysis of jiaohe ancient city," *Journal of Seismological Research*, vol. 43, no. 3, pp. 456–462+601, 2020, in Chinese.
- [4] K. Liu, T. L. Li, Y. C. Shi, H. M. Tang, and Z. Y. Xian, "Dynamic response analysis of inner wall soil site in the ancient gaochang city," *Journal of Disaster Prevention and Mitigation Engineering*, vol. 40, no. 6, pp. 1–7, 2020, in Chinese.
- [5] G. Boscato, L. Z. Fragonara, A. Cecchi, E. Reccia, and D. Baraldi, "Structural health monitoring through vibration-based approaches," *Shock and Vibration*, vol. 2019, Article ID 2380616, 5 pages, 2019.
- [6] M. C. Porcu, D. M. Patteri, S. Melis, and F. Aymerich, "Effectiveness of the FRF curvature technique for structural health monitoring," *Construction and Building Materials*, vol. 226, pp. 173–187, 2019.
- [7] S. Casciati and R. Al-Saleh, "Dynamic behavior of a masonry civic belfry under operational conditions," *Acta Mechanica*, vol. 215, no. 1-4, pp. 211–224, 2010.
- [8] B. Gianni, B. Michele, and G. Saverio, "In situ static and dynamic investigations on the "Torre Grossa" masonry tower," *Engineering Structures*, vol. 52, pp. 718–733, 2013.
- [9] G. Carmelo, G. Marco, and S. Antonella, "One-year dynamic monitoring of a historic tower: damage detection under changing environment," *Mechanics*, vol. 51, pp. 2873–2889, 2016.
- [10] C. Carla, C. Rainieri, M. A. Aiello, and G. Fabbrocino, "On-site assessment of masonry vaults: dynamic tests and numerical analysis," *Geofizika*, vol. 28, no. 1, pp. 127–143, 2011.
- [11] N. Nisticò, S. Gambarelli, A. Fascetti, and G. Quaranta, "Experimental dynamic testing and numerical modeling of historical belfry," *International Journal of Architectural Heritage*, vol. 10, no. 4, pp. 476–485, 2016.
- [12] A. C. Altunisik, S. Adanur, A. F. Genc, M. Gunaydin, and F. Y. Okur, "An investigation of the seismic behaviour of an ancient masonry bastion using non-destructive and numerical methods," *Experimental Mechanics*, vol. 57, no. 2, pp. 245–259, 2016.
- [13] C. Pepi, M. Giuffrè, G. Comanducci, N. Cavalagli, A. Bonaca, and F. Ubertini, "Dynamic characterization of a severely damaged historic masonry bridge," *Procedia Engineering*, vol. 199, pp. 3398–3403, 2017.
- [14] M. Pavlovic, S. Trevisani, and A. Cecchi, "A procedure for the structural identification of masonry towers," *Journal of Nondestructive Evaluation*, vol. 38, no. 2, 2019.
- [15] G. Boscato, E. Reccia, D. Baraldi, and A. Cecchi, "Sensitivity to damage imperfection for multileaf masonry walls based on vibrational analyses," *Shock and Vibration*, vol. 2018, Article ID 2321589, 14 pages, 2018.

- [16] G. Boscato, E. Reccia, and A. Cecchi, "Non-destructive experimentation: dynamic identification of multi-leaf masonry walls damaged and consolidated," *Composites Part B: Engineering*, vol. 133, pp. 145–165, 2018.
- [17] D. Baraldi, C. B. De Carvalho Bello, A. Cecchi, E. Meroi, and E. Reccia, "Nonlinear behavior of masonry walls: FE, DE, and FE/DE models," *Composites: Mechanics, Computations, Applications, An International Journal*, vol. 10, no. 3, pp. 253–272, 2019.
- [18] E. Ippoliti, A. Meschini, and F. Sicuranza, "Structure from motion systems for architectural heritage. A survey of the internal loggia courtyard of palazzo dei capitani, ascoli piceno, Italy," *The International Archives of the Photogrammetry, Remote Sensing and Spatial Information Sciences*, vol. XL-5/W4, pp. 53–60, 2015.
- [19] M. Gioffrè, N. Cavalagli, C. Pepi, and M. Trequattrini, "Laser Doppler and radar interferometer for contactless measurements on unaccessible tie-rods on monumental buildings: santa maria della consolazione temple in todi," *Journal of Physics: Conference Series*, vol. 778, no. 1, Article ID 012008, 2017.
- [20] R. Argiolas, A. Cazzani, E. Reccia, and V. Bagnolo, "From lidar data towards hbim for structural evaluation," *ISPRS - International Archives of the Photogrammetry, Remote Sensing and Spatial Information Sciences*, vol. XLII-2/W15, no. 2/W15, pp. 125–132, 2019.
- [21] B. Peeters and G. De Roeck, "Stochastic system identification for operational modal analysis: a review," *Journal of Dynamic Systems, Measurement, and Control*, vol. 123, no. 4, pp. 659–667, 2001.
- [22] Y. G. Chen and Z. Y. Zhong, "An improved stochastic subspace method for modal parameter identification for bridge structures under ambient excitation," *Journal of Vibration and Shock*, vol. 39, no. 16, pp. 196–204, 2020, in Chinese.
- [23] D. Foti, M. Diaferio, N. I. Giannoccaro, and M. Mongelli, "Ambient vibration testing, dynamic identification and model updating of a historic tower," *NDT & E International*, vol. 47, pp. 88–95, 2012.
- [24] M. Diaferio, D. Foti, and N. I. Giannoccaro, "Non-destructive characterization and identification of the modal parameters of an old masonry tower," in *Proceedings of the IEEE Workshop on Environmental, Energy, and Structural Monitoring Systems Proceedings*, Naples, Italy, September 2014.
- [25] M. Marchi, R. Butterfield, G. Gottardi, and R. Lancellotta, "Stability and strength analysis of leaning towers," *Géotechnique*, vol. 61, no. 12, pp. 1069–1079, 2011.
- [26] D. Abruzzese, L. Miccoli, and J. Yuan, "Mechanical behavior of leaning masonry Huzhu Pagoda," *Journal of Cultural Heritage*, vol. 10, no. 4, pp. 480–486, 2009.
- [27] N. Kassotakis, V. Sarhosis, B. Riveiro et al., "Three-dimensional discrete element modelling of rubble masonry structures from dense point clouds," *Automation in Construction*, vol. 119, Article ID 103365, 2020.
- [28] Y. C. Shi, X. D. Wang, M. Q. Hu, and S. Li, "Seismic safety analysis of typical earthen archaeological sites in Northwest China," *World Earthquake Engineering*, vol. 26, pp. 148–152, 2010, in Chinese.
- [29] Y. L. Wang, "A Theoretical study on structural stability assessment for historical ramparts in dry areas," PhD Dissertation in Chinese, Xi'an University of Architecture and Technology, Xi'an, China, 2018.
- [30] M. Betti and A. Vignoli, "Modelling and analysis of a Romanesque church under earthquake loading: assessment of seismic resistance," *Engineering Structures*, vol. 30, no. 2, pp. 352–367, 2008.

## Research Article

# Probability Distribution and Determination of Blast Loading during Structural Blast Resistant Study

Taochun Yang <sup>1,2</sup>, Yaozhi Luo <sup>1</sup>, Guangqing Hu <sup>2,3</sup> and Yi Jiang <sup>3</sup>

<sup>1</sup>College of Civil Engineering and Architecture, Zhejiang University, Hangzhou 310027, Zhejiang, China

<sup>2</sup>School of Civil Engineering and Architecture, University of Jinan, Jinan 250022, Shandong, China

<sup>3</sup>Ningbo Jiangong Engineering Group Co., Ltd, Ningbo 315040, Zhejiang, China

Correspondence should be addressed to Taochun Yang; [yangtaochun@126.com](mailto:yangtaochun@126.com)

Received 11 November 2021; Accepted 10 January 2022; Published 11 February 2022

Academic Editor: Shan Gao

Copyright © 2022 Taochun Yang et al. This is an open access article distributed under the Creative Commons Attribution License, which permits unrestricted use, distribution, and reproduction in any medium, provided the original work is properly cited.

Explosion overpressure and its duration are important parameters describing blast loading. However, their values obtained using the currently available methods differ significantly. To address this problem, we simulated the overpressure reflection coefficient (i.e., the ratio of reflection overpressure to incident overpressure) and fitted the analytical expressions to the test data. We then collected a large amount of theoretical and experimental blast loading data from literature and studied the probability distribution of blast loading for different scaled distances. The results show that the probability density function of explosion overpressure obeys an exponential distribution when the scaled distance is between  $0.1 \text{ m/kg}^{1/3}$  and  $0.5 \text{ m/kg}^{1/3}$ . On the other hand, it obeys a normal distribution when the scaled distance is greater than  $0.5 \text{ m/kg}^{1/3}$ . The coefficient of variation reaches the maximum value of 1 when the scaled distance is between  $0.1 \text{ m/kg}^{1/3}$  and  $0.5 \text{ m/kg}^{1/3}$ , while it is between 0.13 and 0.2 when the scaled distance is from  $1.5 \text{ m/kg}^{1/3}$  to  $6 \text{ m/kg}^{1/3}$ . The coefficient of variation of reflected overpressure is slightly bigger than that of incident overpressure. Nevertheless, the coefficient of variation of proportional duration (i.e., the ratio of actual duration to cubic root of charge mass) is generally smaller, between 0.408 and 1.017. It was also found that there is no clear probability distribution for the blast loading duration. Finally, formulas for the explosion overpressure and proportional duration were determined together with their 95% confidence level bounds.

## 1. Introduction

With the continuous occurrence of terrorist attacks and accidental explosions, the research on blast resistance of building structures has become an important topic in civil engineering. Especially since the 9/11 incident, a significant amount of research has been carried out worldwide on blast resistance of building structures, including blast loading, structural dynamic response, failure modes, simplified calculation methods, blast resistance analysis methods, and blast resistance reinforcement measures. This led to formulating important guidelines for the blast resistance of engineering structures.

The accuracy of blast loading estimation directly affects the results of blast resistant design and is, therefore, the core consideration. A significant amount of research on the blast loading itself has been conducted, and relevant specifications have been formulated to provide efficient guidance for blast resistant design of structures. These guidelines include Fundamentals of Protective Design for Conventional Weapons TM5-855-1 [1], Structures to Resist the Effects of Accidental Explosion TM5-1300 [2], Design of Buildings to Resist Progressive Collapse UFC3-340-02 [3], Design and Assessment of Buildings Subjected to Blast Loads CSA/S850-12 [4], China National Standards Blasting Safety Regulations GB6722-2014 [5], and Code for Design of Civil Air Defense

Basement (GB50038-2005) [6]. These standards and specifications summarize theoretical research results and experimental data of blast loading in the form of formulas and graphs, which are widely used in blast resistant design and analysis.

Although calculation methods for blast loading are given in these specifications, the load values vary considerably, even by an order of magnitude, which makes selecting a design load calculation method challenging. Thus, probabilistic models of blast loading calibrated using experimental data were proposed to account for the uncertainty. Low et al. [7] performed a statistical analysis of eight commonly used blast loading determination methods (including theoretical formulas, empirical methods, and experimental data) and found that when the scaled distance was in the range of 0.24–40 m/kg<sup>1/3</sup>, the average coefficients of variation of overpressure and its duration were 0.3227 and 0.130, respectively. Bogosian et al. [8] found that the coefficient of variation of overpressure was 0.24 when the scaled distance was in the range of 1.2–23.8 m/kg<sup>1/3</sup>. Li et al. [9–11] established a relationship between the average value, standard value, and coefficient of variation of the reflected overpressure and the scaled distance from a statistical analysis of 77 samples of blast loading data and applied them to the reliability analysis of steel beams. The obtained formulas for the reflection overpressure and its duration used a 90% confidence level and can be used for the calculation of blast loading values in building structural design. Thus, these results provided a good reference for the determination of loads in blast resistant design of building structures.

In the previous studies, the mean or variance of blast loading was calculated directly from discrete random data, or the blast loading parameter variables were assumed to obey a normal distribution. The experimental values corresponding to different scaled distances were interpolated from small experimental samples. The reflection overpressure was also directly obtained from the incident overpressure using a theoretical formula without considering the actual changes in the reflection coefficient (the ratio of reflection overpressure to incident overpressure) [12]. Because of these shortcomings, in this paper, the relevant blast resistance specifications, theoretical formulas, and experimental datasets on the explosion overpressure and its duration are reviewed. The reflection overpressure is determined using the reflection coefficient obtained experimentally. The measured blast impulse is converted into an equivalent triangle impulse. From the overpressure and proportional duration (i.e., the ratio of actual duration to cubic root of charge mass) data and histograms for different scaled distances, probability distribution for the explosion overpressure and proportional duration for different scaled distances are determined and validated. The maximum likelihood estimators of the overpressure parameters are obtained and their variations are analyzed. Finally, formulas and confidence intervals for the incident overpressure, reflected overpressure, and proportional duration are given.

## 2. Blast Loading Characteristics

Explosions produce extremely high-pressure and high-temperature gases. As their volume expands rapidly, air shock waves are formed in front of the compressed gas. The overpressure is a part of the shock wave pressure exceeding the ambient air pressure. The overpressure value decays rapidly with time. When the pressure drops below the ambient air pressure, a negative pressure zone is formed. The overpressure attenuation curve of a typical shock wave is shown in Figure 1. In structural blast resistant design, this negative pressure is often ignored; thus, the main relevant physical parameters are the positive overpressure, its duration, and impulse of blast loading. The common exponential attenuation function is as follows:

$$P(t) = P_s^+ \left(1 - \frac{t}{T^+}\right) e^{-\zeta t/T^+}. \quad (1)$$

In the formula,  $P_s^+$  is the peak value of positive overpressure,  $T^+$  is the duration of positive overpressure, and  $\zeta$  is the attenuation coefficient.

In engineering applications, to simplify the calculations, the overpressure attenuation curve is often simplified as an equivalent descending triangular model [1, 2, 13, 14], as shown in Figure 2. The equivalent triangular loads have the same overpressure peak value, but different simplifications of their duration are adopted according to the expected time of the maximum response of the structure considered as follows: when the maximum response of the structure or component occurs at an early stage of the overpressure application, it is assumed that the slope of the triangular loads is tangent to the actual overpressure curve, and the equivalent action duration is denoted as  $T_{a1}$ . This method is often used for long explosion relative to the time of the maximum structural response. When the maximum response of the structure or component occurs after the overpressure drops to zero, it is necessary to ensure that the triangular impulse is consistent with the actual overpressure impulse. The equivalent action time is denoted as  $T_{a2}$ , and this method is often used for short explosion relative to the time of the maximum structural response. For the intermediate cases, it is assumed that the triangular impulse passes through  $P_s^+/2$  of the actual overpressure time history plot to calculate the duration  $T_{a3}$ . For the commonly used advanced explosives, the second simplified method for obtaining the equivalent impulse is often used because the overpressure action time is often very short compared to the relative time of structural response.

## 3. Explosion Overpressure Study

**3.1. Theoretical Overpressure Data.** A large number of researchers, including Brode [15–17], Henrych [18, 19], Mills [12], Kinney [20], and Newmark [21], studied the shock wave overpressure and derived formulas by introducing empirical coefficients under ideal air explosion conditions. However, there are still significant differences among the different formulas, especially close to the explosion center, as

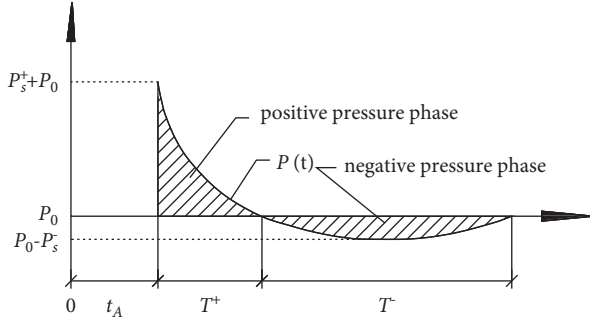


FIGURE 1: Exponential overpressure attenuation diagram.

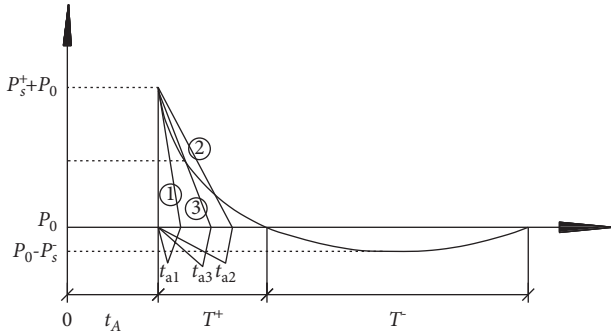


FIGURE 2: Triangle explosion overpressure equivalent diagram.

shown in Figure 3. Therefore, this study examined as many as 17 commonly used explosion overpressure formulas, as shown in (2)–(18). Of them, (2)–(17) can be used to directly calculate the incident overpressure, and (18) can be used to directly calculate the reflected overpressure.

Kinney et al. [20] gave the formula for calculating peak incident overpressure (Mpa) under free air explosion as follows:

$$\frac{P_0}{P_{\text{air}}} = \frac{808 [1 + (Z/4.5)^2]}{[1 + (Z/0.048)^2][1 + (Z/0.32)^2][1 + (Z/1.35)^2]} \quad (2)$$

Henrych et al. [18, 19] gave the expression of incident overpressure peak (bar) for ideal air explosion based on the experimental method as follows:

$$P_0 = \begin{cases} \frac{14.0717}{Z} + \frac{5.5397}{Z^2} - \frac{0.3572}{Z^3} + \frac{0.00625}{Z^4}, & 0.05 \leq Z \leq 0.3, \\ \frac{6.1938}{Z} - \frac{0.3262}{Z^2} + \frac{2.1324}{Z^3}, & 0.3 \leq Z \leq 1, \\ \frac{0.662}{Z} + \frac{4.05}{Z^2} + \frac{3.288}{Z^3}, & 1 \leq Z \leq 10. \end{cases} \quad (3)$$

Baker et al. [22] gave the expression of incident overpressure peak (MPa) for ideal air explosion as follows:

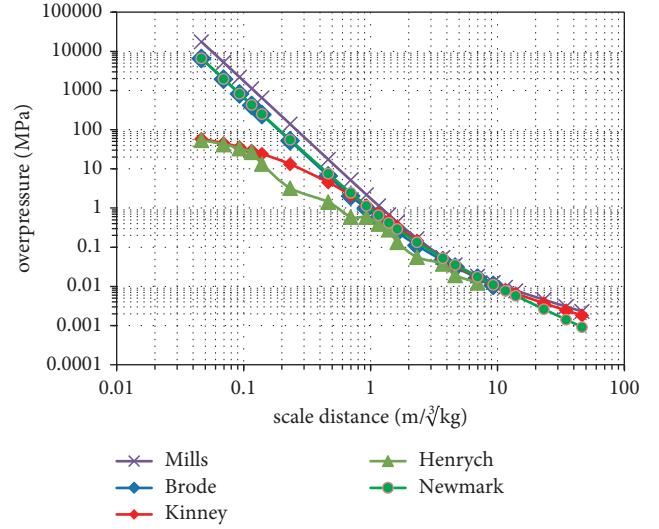


FIGURE 3: Comparison results of different overpressure formulas.

$$P_0 = \begin{cases} \frac{2.006}{Z} + \frac{0.194}{Z^2} - \frac{0.004}{Z^3}, & 0.05 \leq Z \leq 0.5, \\ \frac{0.067}{Z} + \frac{0.301}{Z^2} + \frac{0.431}{Z^3}, & 1 \leq Z \leq 10. \end{cases} \quad (4)$$

Wu and How [23] gave the expression of incident overpressure peak (MPa) during the ground explosion as follows:

$$P_0 = \begin{cases} \frac{1.059}{Z^{2.56}} - 0.051, & 0.1 \leq Z \leq 1, \\ \frac{1.008}{Z^{2.01}}, & 1 \leq Z \leq 10. \end{cases} \quad (5)$$

Naumenko et al. [19, 24, 25] gave the expression of incident overpressure peak (bar) under ideal air explosion according to the model similarity theory and determined the coefficients by experimental method. Among them, the first equation is obtained by Naumenko and Petrovsky, and the second equation is derived by Sadovskii. The specific calculation expression is as follows:

$$P_0 = \begin{cases} \frac{10.7}{Z^3} - 1, & Z \leq 1, \\ \frac{0.76}{Z} + \frac{2.55}{Z^2} + \frac{6.5}{Z^3}, & 1 \leq Z \leq 15. \end{cases} \quad (6)$$

Brode [15–17] gave the expression of incident overpressure peak (bar) for ideal air explosion by using similar model theory as follows:

$$P_0 = \begin{cases} \frac{6.7}{Z^3} + 1, & P_0 > 10\text{bar}, \\ \frac{0.975}{Z} + \frac{1.455}{Z^2} + \frac{5.85}{Z^3} - 0.019, & 0.1\text{bar} < P_0 < 10\text{bar}. \end{cases} \quad (7)$$



Mills [12] combined the similarity theory and numerical simulation and gave the expression of incident overpressure peak (MPa) for ideal air explosion as follows:

$$P_0 = \frac{0.108}{Z} - \frac{0.114}{Z^2} + \frac{1.772}{Z^3}. \quad (8)$$

Ye [26] gave the expression of incident overpressure peak (MPa) for ideal air explosion as follows:

$$P_0 = \frac{0.084}{Z} + \frac{0.27}{Z^2} + \frac{0.7}{Z^3}. \quad (9)$$

The expression of incident overpressure peak (bar) for explosive ground explosion provided in Chinese National Standard Blasting Safety Regulations [5] is as follows:

$$P_0 = \frac{1.06}{Z} + \frac{4.3}{Z^2} + \frac{14}{Z^3}, \quad \frac{H}{\sqrt[3]{W}} \leq 0.35, 1 \leq Z \leq 10 \sim 15. \quad (10)$$

The expression of incident overpressure peak (MPa) for explosive ground explosion provided in the National Standard Code for Design of Civil Air Defense Basement [6] is as follows:

$$P_0 = \frac{0.369}{Z^{3/2}} + \frac{1.316}{Z^3}. \quad (11)$$

The expression of incident overpressure peak (MPa) for ground explosion proposed by Newmark and Hansen [21] is as follows:

$$P_0 = \frac{0.294}{Z^{1.5}} + \frac{0.6784}{Z^3}. \quad (12)$$

Siddiqui [27] Ahmad [28], and Iqbal [29] gave the expressions of incident overpressure peak (MPa) for ground explosion based on experimental data as follows:

$$P_0 = 1.017 \cdot Z^{-1.91}, \quad 1 \leq Z \leq 12, \quad (13)$$

$$P_0 = 2.46 \cdot Z^{-2.67}, \quad (14)$$

$$P_0 = 1.026 \cdot Z^{-1.96}, \quad 1 \leq Z \leq 12. \quad (15)$$

The expression of incident overpressure peak (KPa) of air explosion given in the US military protection technology manual TM5-855-1 [1] is as follows:

$$P_0 = \frac{39.5}{Z} - \frac{105}{Z^2} + \frac{4120}{Z^3}, \quad 2 < P_0 < 160, 3 \leq Z \leq 20. \quad (16)$$

Held et al. [30] gave the expression of incident overpressure peak (MPa) in air explosion based on theoretical analysis as follows:

$$P_0 = A \cdot Z^{-2}, \quad 0.6 \leq A \leq 6, \bar{A} = 2. \quad (17)$$

The expression of reflection overpressure peak (KPa) for ground explosions given in the Canadian specification CSA/S 850-12 [4] is as follows:

$$\ln P_r = \begin{cases} 8.9973 - 2.6077 \ln Z - 0.5045 \ln^2 Z - 0.0588 \ln^3 Z, & 0.06 < Z \leq 1.95, \\ 9.7457 - 4.7276 \ln Z + 1.1734 \ln^2 Z - 0.1337 \ln^3 Z, & 1.95 < Z < 39.67. \end{cases} \quad (18)$$

It can be seen that there is a very limited number of theoretical or empirical formulas for the reflection overpressure; thus, more reflection overpressure data need to be obtained using the reflection coefficient and the incident overpressure. Mills proposed a theoretical expression for the reflection coefficient, as shown in (19). In the US Military Protection Technology Manual TM5-855-1 [1], the variation of reflection coefficient with the incident angle is considered (Figure 4). A comparison of the reflection coefficients obtained by (19) and Figure 4 is shown in Figure 5 for the vertical incident angle ( $0^\circ$ ). Figure 5 shows that when the incident overpressure is small, the theoretical and experimental reflection coefficients are equal. However, when the incident overpressure is large, the maximum experimental reflection coefficient is 13.2, which is much larger than the theoretical value of 8. Therefore, when the reflection overpressure is calculated using the incident overpressure and the reflection coefficient, the reflection coefficient should be determined according to the experimental value. To obtain the experimental reflection coefficient conveniently for the case of vertical incidence, a formula for the reflection coefficient,  $\mu$ , for different overpressures obtained by fitting

experimental data is shown in (20), and the regression coefficient is 0.9871, as shown in the imaginary line in Figure 5. Thus, the relationship formula equation (21) between the reflection overpressure and the incident overpressure is obtained.

$$P_r = 2P_0 \cdot \frac{7P_{\text{air}} + 4P_0}{7P_{\text{air}} + P_0}, \quad (19)$$

$$\mu = 5.3104 \cdot P_0^{0.2356} \text{ (MPa)}, \quad (20)$$

$$P_r = \mu P_0 = 5.3104 \cdot P_0^{1.2356} \text{ (MPa)}. \quad (21)$$

**3.2. Experimental Overpressure Data.** Several researchers have carried out field blast resistant tests. The test data gathered will help to analyze the explosion overpressure more accurately. In this study, 125 reliable explosion overpressure experimental datasets were collected from literature. The data cover the charge mass from 30 g to 50 kg,

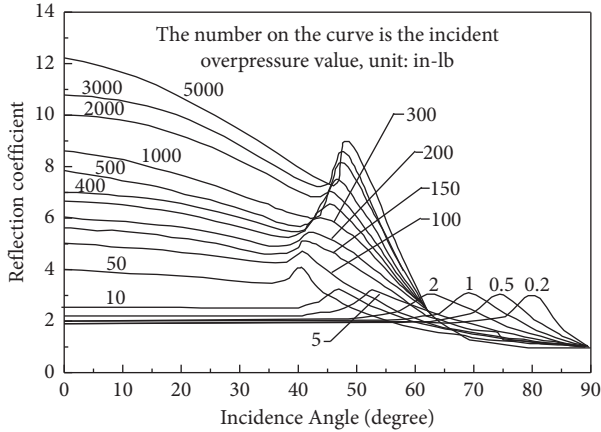


FIGURE 4: Relationship between reflection coefficient and incident angle [1].

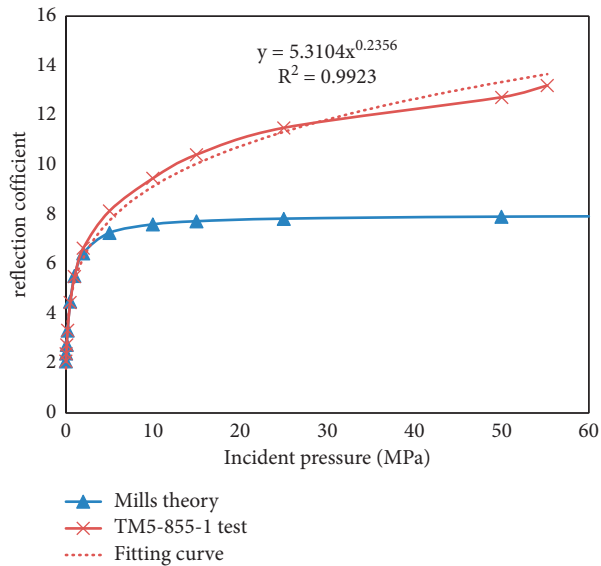


FIGURE 5: Comparison results between theory and experimental values of reflection coefficients.

and the scaled distance from 0.295 to 55 m/kg<sup>1/3</sup>, as shown in Table 1. It can be seen from the table that the blast loading is sensitive to the environmental factors, and the overpressure values obtained by multiple tests under the same conditions are different. The explosion distances in the tests were relatively small, mostly within 5 m, which was mainly because of the small equivalent explosive masses and desire to reduce the influence of environmental factors. At the same time, considering the stability and accessibility of explosives, some tests used ANFO explosives (equivalent coefficient of 0.82), emulsion explosives (0.71), Composite C-4 (1.37), and Gelamon VF80 (0.8), rather than TNT explosives, which also increased the variability of the test data. In some tests, the charge was placed at a certain height from the ground, and the reflection of the shock wave off the ground also affected the overpressure. In some tests, the charge shape was nonspherical or irregular, especially when the equivalent explosive mass was small, which had some influence on the overpressure. Therefore, for the

experimental explosion data listed in Table 1, the above factors cannot be completely avoided, and these differences are also important factors leading to explosion overpressure uncertainty.

In the collected experimental datasets, there are both vertical and nonvertical incidence cases. However, for the sake of consistency, only the vertical incidence cases were retained for analysis. Furthermore, some datasets had only the incident overpressure samples, some had only the reflected overpressure samples, and only 11 datasets had both the incident and the reflected overpressure. For the same batch of tests, 22 datasets exhibited significant differences and were excluded from the subsequent analysis. Eventually, a total of 103 datasets were used.

The existing formulas for the incident explosion overpressure (2)–(18) have the general forms as shown in (22) and (23). In each formula, there are three undetermined coefficients. Equation (22) is obtained from the mechanical explosion theory and its correlation coefficient is determined by experiments. This method has been more widely applied in the existing formula for the incident overpressure. Equation (23) is obtained by fitting the experimental data, and it also has certain applications. Therefore, the reflection coefficient formula (20) and the incident overpressure formula (22) can be used together to gain the overpressure data under certain scaled distance, which provides statistical samples for analyzing the probability distribution of the explosion overpressure.

$$P_0 = \frac{a}{Z} + \frac{b}{Z^2} + \frac{c}{Z^3}, \quad (22)$$

$$P_0 = d \cdot Z^e + f. \quad (23)$$

**3.3. Overpressure Probability Distribution.** Using the explosion overpressure data, histograms corresponding to different blast scaled distances were drawn. In addition to the distribution characteristics observed in the histograms, the K-S and Lilliefors goodness-of-fit tests of overpressure probability distribution for different scaled distances were carried out. The results showed that when the scaled distance was less than 0.5 m/kg<sup>1/3</sup>, the incident and reflected overpressure both followed exponential distributions. However, when the scaled distance was greater than 0.5 m/kg<sup>1/3</sup>, the overpressure distributions were normal. Using these probability distributions, the maximum likelihood estimates of the expectation and standard deviation of the overpressure for different scaled distances were calculated. Furthermore, the 95% confidence interval of the overpressure was obtained, as shown in Tables 2 and 3. Then, the probability density functions (exponential and normal) of overpressure for different scaled distances were drawn as shown in Figures 6 and 7. It can be seen from Tables 2 and 3 that when the scaled distance is small, the standard deviation is the largest, and thus the overpressure distribution is wider.

To compare the dispersion degree of the incident and reflected overpressure for different scaled distances, the

TABLE 1: Test data of explosion overpressure.

Sources	Explosive type	Scale distance (m/ $\text{kg}^{1/3}$ )	Incidence overpressure (MPa)	Reflection overpressure (MPa)	Sources	Explosive type	Scale distance (m/ $\text{kg}^{1/3}$ )	Incidence overpressure (MPa)	Reflection overpressure (MPa)
		1.14	0.77	3.842			0.46	4.436	33.46
Razaqpur et al. [31]	ANFO		0.753	3.741	Wang et al. [32]	Emulsion	0.46	1.627	9.690*
		1	0.962	5.059			1.5	0.252	0.967
			1.03	5.507			1.5	0.234	0.883
			0.638	3.050*	Li et al. [33]	Emulsion	0.459	4.917	38
			0.952	4.995			0.75	1.803	11
			0.942	4.933	Jin et al. [34]	Emulsified explosive	1.5	0.296	1.182
Liang et al. [35]	TNT	1.81	0.1822	0.648			0.413	5.309	41.782
		0.9	0.8607	4.412			1.368	0.763	3.8
			3.07	21.23	Li et al. [36]	TNT	1.56	0.946	4.96
			3.236	22.66			1.17	1.365	7.8
			3.236	22.66			1.086	1.736	10.5
Kim et al. [37]	ANFO	0.638	3.398	24.07	Ahmad et al. [38]	Nitroglycerin dynamite	1.72	0.6115	2.892
			4.273	31.95	ground explosion		2.28	0.2075	0.761
			3.419	24.26	Ritchie et al. [39]	TNT	1.89	0.37	1.49
			4.405	33.17	ground explosion		2.7	0.155	0.436
			1.032	5.52			0.5	0.5	2.255
		0.77	2.976	20.43	Tabatabaei et al. [41]	ANFO	2.29	0.47	2.089
			1.778	10.81	ground explosion		0.49	0.49	2.2
			0.918	4.78			0.55	0.55	2.537
		1.14	0.89	4.6			0.45	0.45	1.98
			0.776	3.88			0.3159	0.3159	1.279
Aune et al. [40]	TNT		0.426	1.85			0.4043	0.4043	1.734
		1.5	0.292	1.16	Choi et al. [42]	ANFO	1.827	0.3838	1.626
			0.459	2.03	ground explosion		0.3671	0.3671	1.539
			0.263	1.02			0.4176	0.4176	1.805
		1.82	0.244	0.93			1.5	0.269	1.05
			0.214	0.79			0.459	2.77	18.7
Safari et al. [44]	C-4	0.59	2.9138	20.0276			2.71	2.71	18.2
		0.295	9.3666	71.1276			3.321	3.321	23.4
		4.6	0.05237	0.139			2.758	2.758	18.6
Hao et al. [45]	TNT	4.77	0.04552	0.117	Zhang et al. [43]	Emulsion	4.843	4.843	37.3
		49.9	0.0013	0.001			2.758	2.758	18.6
Jacinto et al. [46]	Gelamon VF80	27.8	0.0025	0.003			9.907	9.907	90.3
ground explosion		55	0.0012	0.001			4.854	4.854	37.4
		13.9	0.0061	0.01			4.419	4.419	33.3
Cui et al. [47]	TNT	1.1	1.134	6.2					
ground explosion									

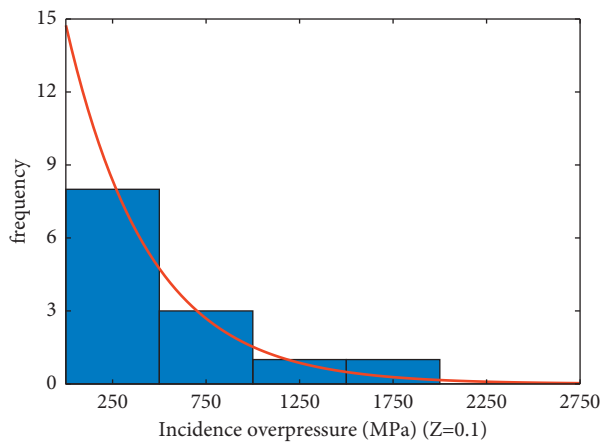
Note. The table shows only part of the experimental data. See more relevant literature.

TABLE 2: Maximum likelihood estimate of expectation and standard deviation for incident overpressure.

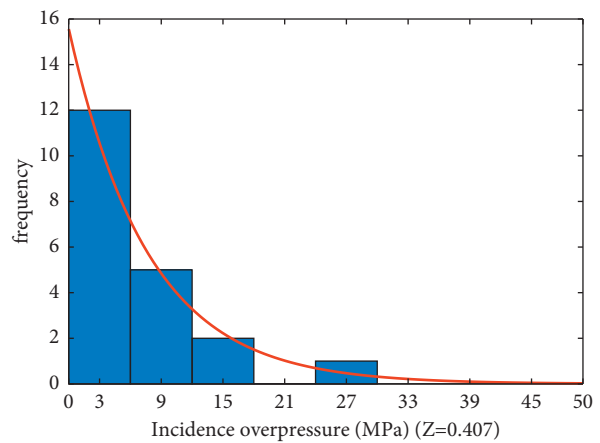
Scaled distance (m/kg <sup>1/3</sup> )	0.100	0.300	0.407	0.459	0.638	0.770	1.000
Expectation (MPa)	440.4414	20.3322	7.702	6.0207	3.1478	1.7251	0.9203
Expected confidence interval (MPa)	273.1539	12.8046	5.1916	3.9815	2.6001	1.4177	0.8079
Standard deviation (MPa)	827.1854	37.1902	12.6091	10.1586	3.6955	2.0325	1.0327
Standard deviation (MPa)	440.4414	20.3322	7.702	6.0207	1.2032	0.5769	0.2661
Scaled distance (m/kg <sup>1/3</sup> )	1.140	1.500	1.540	1.600	1.820	1.930	2.280
Expectation (MPa)	0.7078	0.354	0.3541	0.3144	0.2306	0.2012	0.1403
Expected confidence interval (MPa)	0.6328	0.3196	0.3299	0.2855	0.2142	0.1853	0.1312
Standard deviation (MPa)	0.7828	0.3884	0.3783	0.3433	0.247	0.2171	0.1494
Standard deviation (MPa)	0.1776	0.0833	0.0636	0.0617	0.037	0.0319	0.0183
Scaled distance (m/kg <sup>1/3</sup> )	3.880	4.030	5.000	8.000	10.000	11.700	15.000
Expectation (MPa)	0.0487	0.045	0.0299	0.0134	0.0096	0.0074	0.0056
Expected confidence interval (MPa)	0.0447	0.0415	0.0277	0.0119	0.0081	0.006	0.004
Standard deviation (MPa)	0.0527	0.0485	0.032	0.0148	0.0111	0.0088	0.0072
Standard deviation (MPa)	0.008	0.007	0.0042	0.0028	0.0027	0.0024	0.0022

TABLE 3: Maximum likelihood estimate of expectation and standard deviation for reflection overpressure.

Scaled distance (m/kg <sup>1/3</sup> )	0.100	0.300	0.407	0.459	0.638	0.770	1.000
Expectation (MPa)	11577.00	236.9497	70.2371	51.2193	22.3138	10.5674	4.8446
Expected confidence interval (MPa)	7180	149.2234	47.3442	33.8719	17.4063	8.2035	4.093
Standard deviation (MPa)	21742	433.4107	114.9871	86.4223	27.2214	12.9312	5.5962
Standard deviation (MPa)	11577.00	236.9497	70.2371	51.2193	10.7812	4.4361	1.7799
Scaled distance (m/kg <sup>1/3</sup> )	1.140	1.500	1.540	1.600	1.820	1.930	2.280
Expectation (MPa)	3.494	1.483	1.4789	1.2777	0.8698	0.7349	0.4701
Expected confidence interval (MPa)	3.0308	1.3041	1.3542	1.132	0.7934	0.6634	0.4328
Standard deviation (MPa)	3.9571	1.6618	1.6036	1.4233	0.9463	0.8064	0.5074
Standard deviation (MPa)	1.0968	0.4333	0.3279	0.3112	0.1724	0.1438	0.0751
Scaled distance (m/kg <sup>1/3</sup> )	3.880	4.030	5.000	8.000	10.000	11.700	15.000
Expectation (MPa)	0.1274	0.1155	0.0695	0.0258	0.0172	0.0126	0.0089
Expected confidence interval (MPa)	0.1142	0.1043	0.0634	0.0225	0.014	0.0098	0.006
Standard deviation (MPa)	0.1405	0.1268	0.0756	0.0292	0.0205	0.0154	0.0118
Standard deviation (MPa)	0.0264	0.0227	0.0118	0.0065	0.0056	0.0048	0.0041



(a)



(b)

FIGURE 6: Continued.

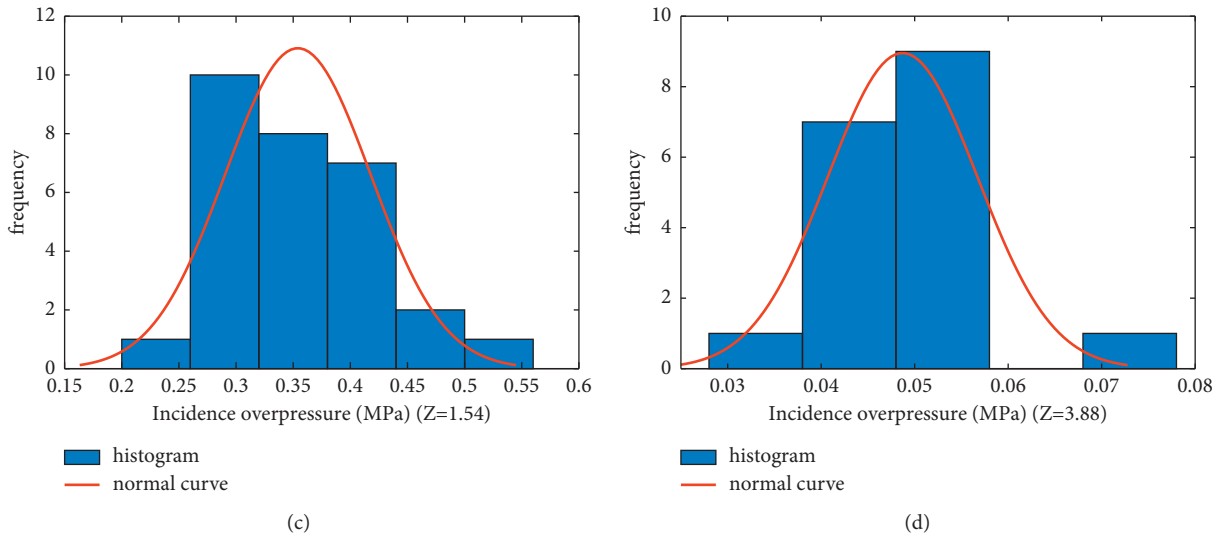


FIGURE 6: Histogram and probability density curve of incident overpressure under different scaled distance. (a)  $Z=0.1$ . (b)  $Z=0.407$ . (c)  $Z=1.54$ . (d)  $Z=3.88$ .

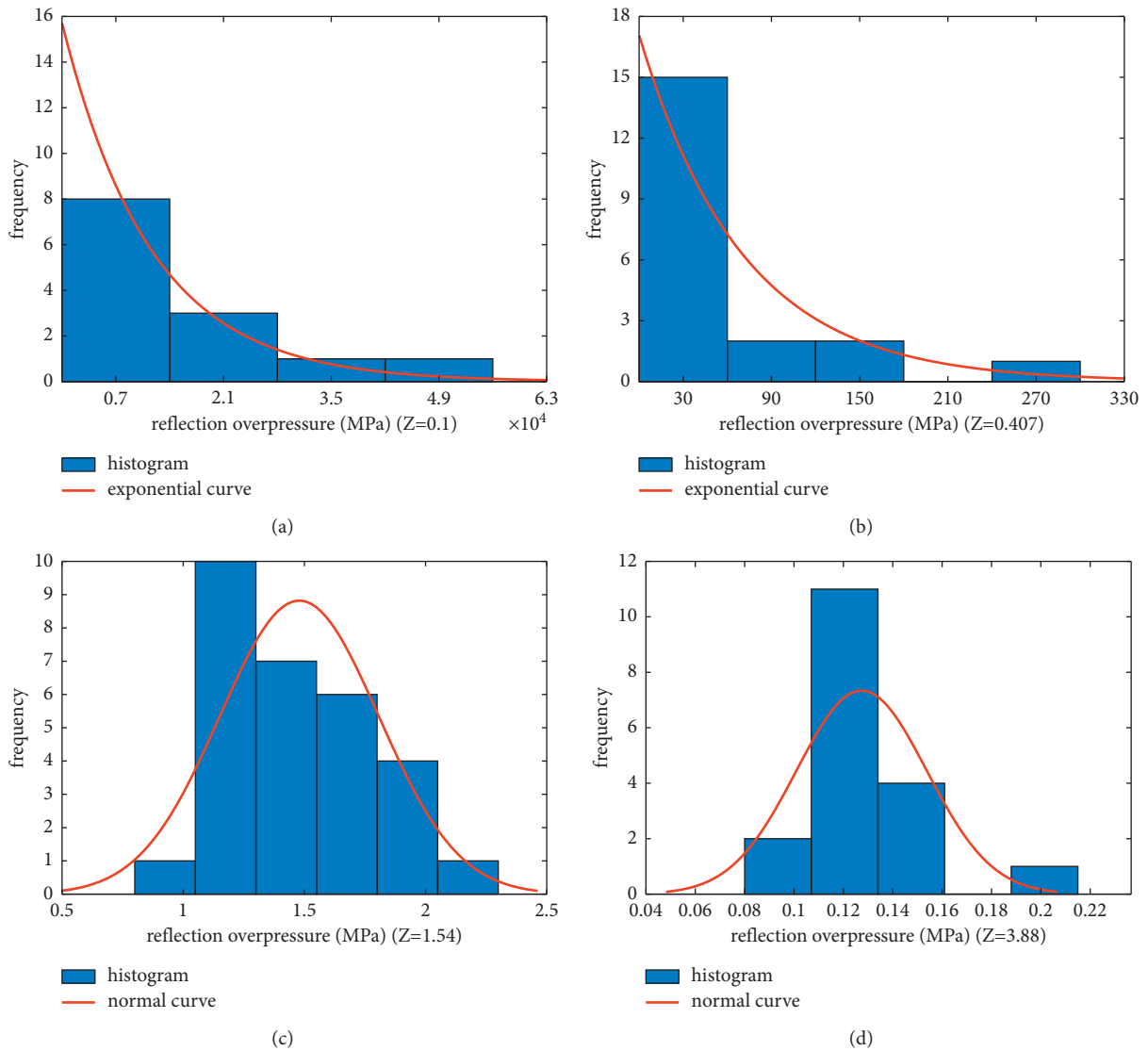


FIGURE 7: Histogram and probability density curve of reflection overpressure under different scaled distance. (a)  $Z=0.1$ . (b)  $Z=0.407$ . (c)  $Z=1.54$ . (d)  $Z=3.88$ .

coefficients of variation of overpressure distribution were obtained from the expectations and standard deviations in Tables 2 and 3, as shown in Figure 8. It can be seen from Figure 8 that when the scaled distance was less than  $0.5 \text{ m/kg}^{1/3}$ , the coefficient of variation of overpressure reached the maximum value of 1, which is constant of the exponential distribution. When the scaled distance was about  $1.5\text{--}6 \text{ m/kg}^{1/3}$ , the coefficient of variation was small due to more experimental data. In the range  $0.13\text{--}0.2 \text{ m/kg}^{1/3}$ , the coefficient of variation of the reflection overpressure was slightly larger than that of the incident overpressure.

**3.4. Determination of Overpressure Formula.** Using the maximum likelihood estimations of the overpressure expectations shown in Tables 2 and 3, the relationships between the upper and lower 95% confidence limits of the incident and reflected overpressure and the scaled distance can be obtained, as shown in Figures 9 and 10, respectively. Since the overpressure values for different scaled distances varied considerably, the scaled distances are plotted in three sections. It can be seen from the figure that the smaller the scaled distance, the more dispersed the overpressure distribution. A polynomial was fitted to the natural logarithm of the scaled distance and overpressure data using the least square method. As shown in Figures 11 and 12, the regression coefficients of the fitted curves of the incident and the reflected overpressure are greater than 0.99.

Finally, the formula for calculating incidence overpressure is as follows:

$$\ln P_0 = 0.1583 \ln^2 Z - 2.342 \ln Z - 0.0977. \quad (24)$$

The upper and lower limits of 95% confidence interval for incidence overpressure are calculated as follows:

$$\ln P_0 = 0.2149 \ln^2 Z - 2.4867 \ln Z + 0.0711 \text{ (upper.limit)}, \quad (25)$$

$$\ln P_0 = 0.1111 \ln^2 Z - 2.2428 \ln Z - 0.2506 \text{ (lower.limit)}. \quad (26)$$

Similarly, the formula for calculating reflection overpressure is as follows:

$$\ln P_r = 0.2087 \ln^2 Z - 2.9263 \ln Z + 1.5647. \quad (27)$$

The upper and lower limits of 95% confidence interval for reflection overpressure are calculated as follows:

$$\ln P_r = 0.2643 \ln^2 Z - 3.0652 \ln Z + 1.7512 \text{ (upper.limit)}, \quad (28)$$

$$\ln P_r = 0.162 \ln^2 Z - 2.8339 \ln Z + 1.3898 \text{ (lower.limit)}. \quad (29)$$

In practical engineering applications, the recommended values of incident and reflected overpressure are calculated using (24) and (27), respectively. When there is sufficient experience supported by data, (25), (26), (28), and (29) can

be used as the 95% confidence upper and lower limits of the overpressures under such conditions. It should be noted that when the scaled distance is very small ( $<0.1 \text{ m/kg}^{1/3}$ ), the explosion overpressures should be determined from special studies on the proximity or contact explosion.

## 4. Explosion Duration Study

**4.1. Theoretical Duration Data.** Duration is another important parameter of blast loading, and different formulas were proposed using theoretical derivations and experimental data, as shown in (30)–(39). The relationships between the blast loading and time use either the actual exponential form (Figure 1) or simplified triangular form (Figure 2). The Code for Design of Civil Air Defense Basement [6], Held [30], and Canadian specification CSA/S850-12 [4] all use triangular form, while some other sources use the exponential form. In the statistics of theoretical data, the most used Conwep program calculation results are included. Then, taking 25 kg and 50 kg explosive equivalents as examples, the relationships between the duration and scaled distance for different explosive equivalents are shown in Figure 13. It can be seen that the overpressure durations for the different conditions are also quite different; thus, it is necessary to carry out statistical analysis on the duration of blast loading. It can be seen from the formulas that the duration,  $t$ , is mainly related to the explosive equivalent and scaled distance. Using the similarity rate, the functional relationship between parameter  $t/\sqrt[3]{W}$  and the scaled distance can be obtained, and the statistical characteristics of the blast loading duration will be subsequently studied using this parameter.

For high-explosive TNT, Henrych [18, 19] obtained the calculation formula of overpressure duration for air explosion according to the experimental research work as follows:

$$\frac{t}{\sqrt[3]{W}} = 0.107 + 0.444Z + 0.264Z^2 - 0.129Z^3 + 0.0334Z^4, \quad 0.05 \leq Z \leq 3 \left( \frac{\text{ms}}{\text{kg}^{1/3}} \right). \quad (30)$$

Sadovskii [25] gave the calculation formula of explosion overpressure duration under the condition of air explosion as follows:

$$\frac{t}{\sqrt[3]{W}} = B \sqrt{R} \sqrt[3]{W} \left( \frac{\text{ms}}{\text{kg}^{1/3}} \right). \quad (31)$$

For coefficient B, Naumenko [24] recommended 1.0, Pokrovskii [48] considered 1.3, and Baum [49] gave 1.5.

According to Yang et al. [50], through the numerical simulation results of parameter analysis and fitting, the relationship of positive overpressure duration is as follows:

$$t = 0.079946Z^{0.85} \text{ (ascent)} + 0.71673Z^{1.3425} W^{0.3136} \text{ (downcomer) (ms)}. \quad (32)$$

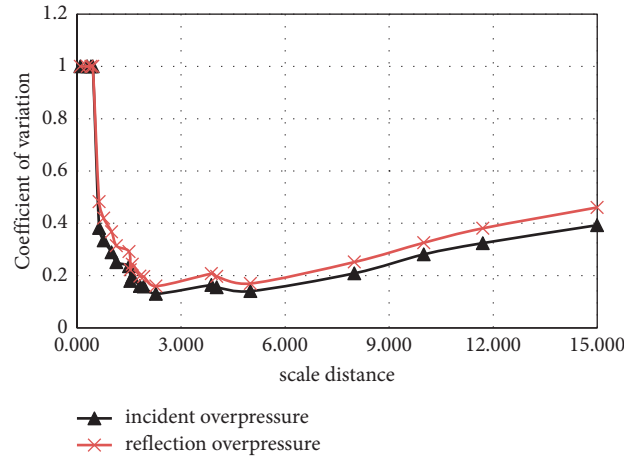


FIGURE 8: Variation coefficient of overpressure under different scaled distance.

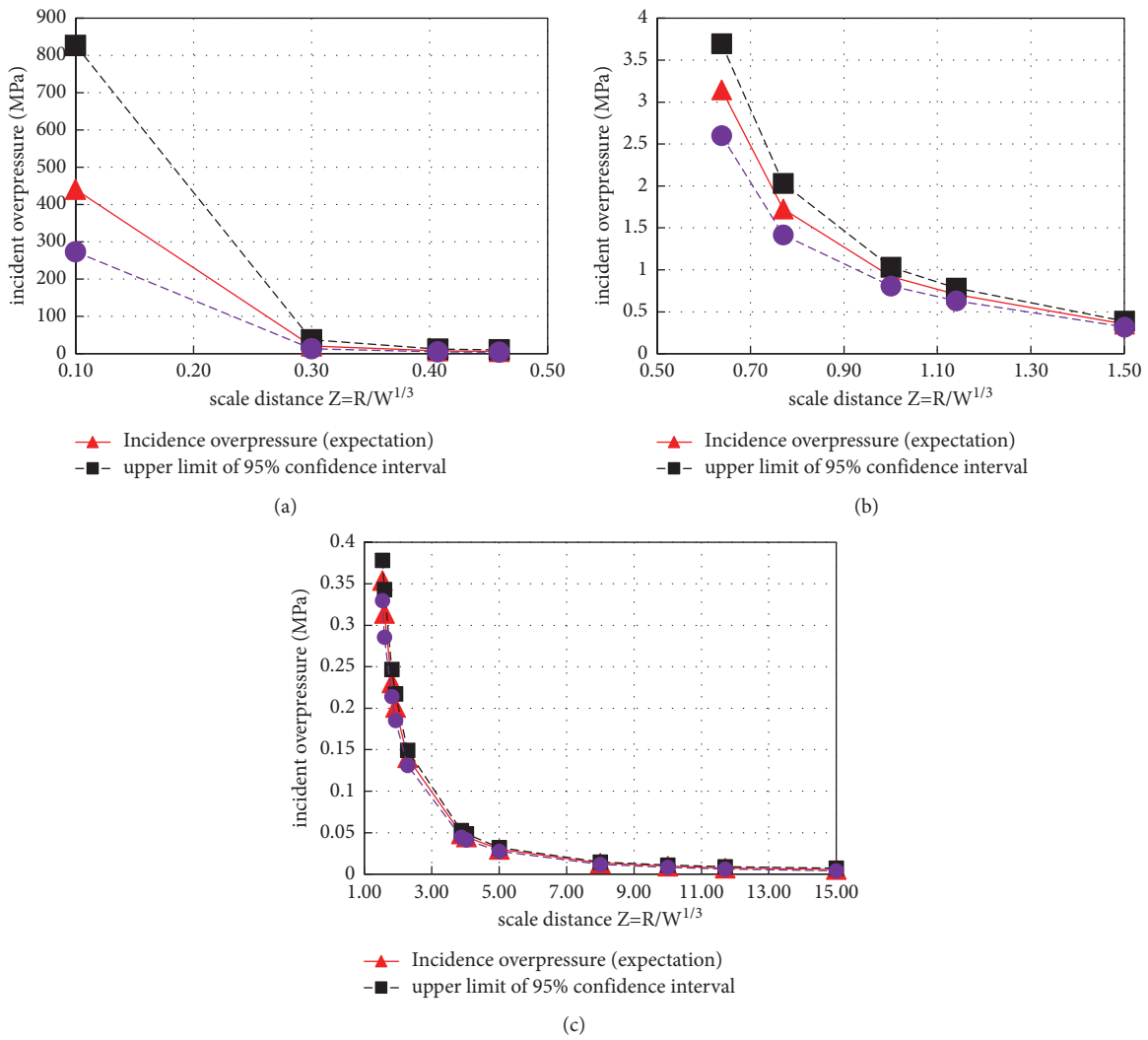


FIGURE 9: Change relation of incident overpressure, 95% confidence interval with scaled distance.

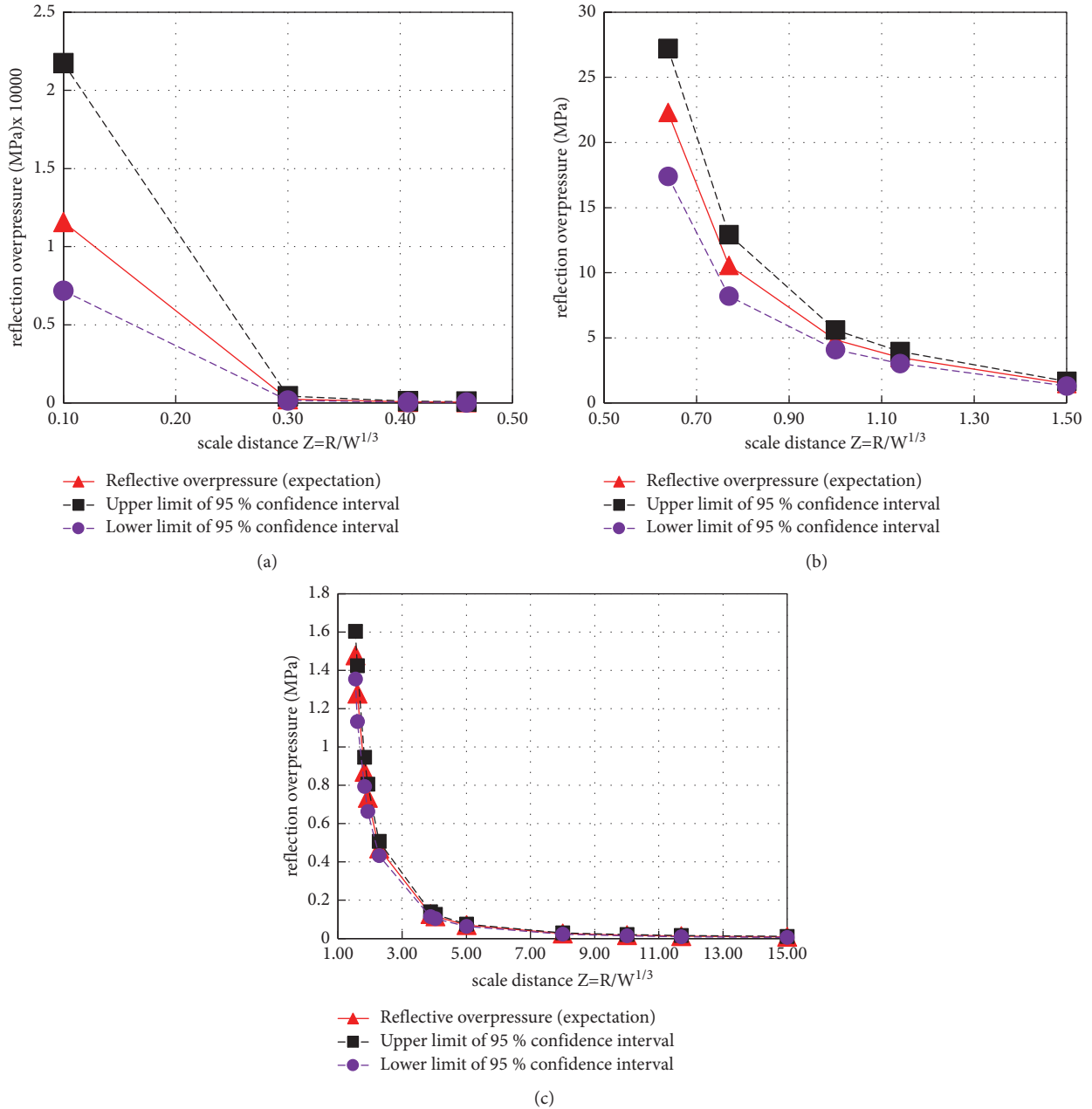


FIGURE 10: Change relation of reflection overpressure, 95% confidence interval with scaled distance. (a)  $0.1 \leq Z \leq 0.5$ . (b)  $0.5 \leq Z \leq 1.5$ . (c)  $1.5 \leq Z \leq 15$ .

In the process of data calculation, the formula has serious deviation when the scaled distance is large, so only the scaled distance less than  $3 \text{ m/kg}^{1/3}$  is considered.

In the China Code for the Design of Civil Air Defense Basement [6], the suggested overpressure duration formula for the ground explosion is as follows:

$$\frac{t}{\sqrt[3]{W}} = \frac{0.4}{\sqrt{P_r}} \quad (33)$$

where  $P_r$  is reflected overpressure, the unit is MPa, the unit of  $t$  is ms, and the unit of  $w$  is kg.

The calculation formula (triangular load) of incident overpressure and incident impulse of spherical explosive for air explosion given by Held [30] is as follows:

$$P_{so} = \frac{2}{Z^2}, \quad (34)$$

$$\frac{i_{so}}{\sqrt[3]{W}} = \frac{300}{Z}. \quad (35)$$

The duration after conversion is as follows:

$$\frac{t}{\sqrt[3]{W}} = 0.3Z. \quad (36)$$



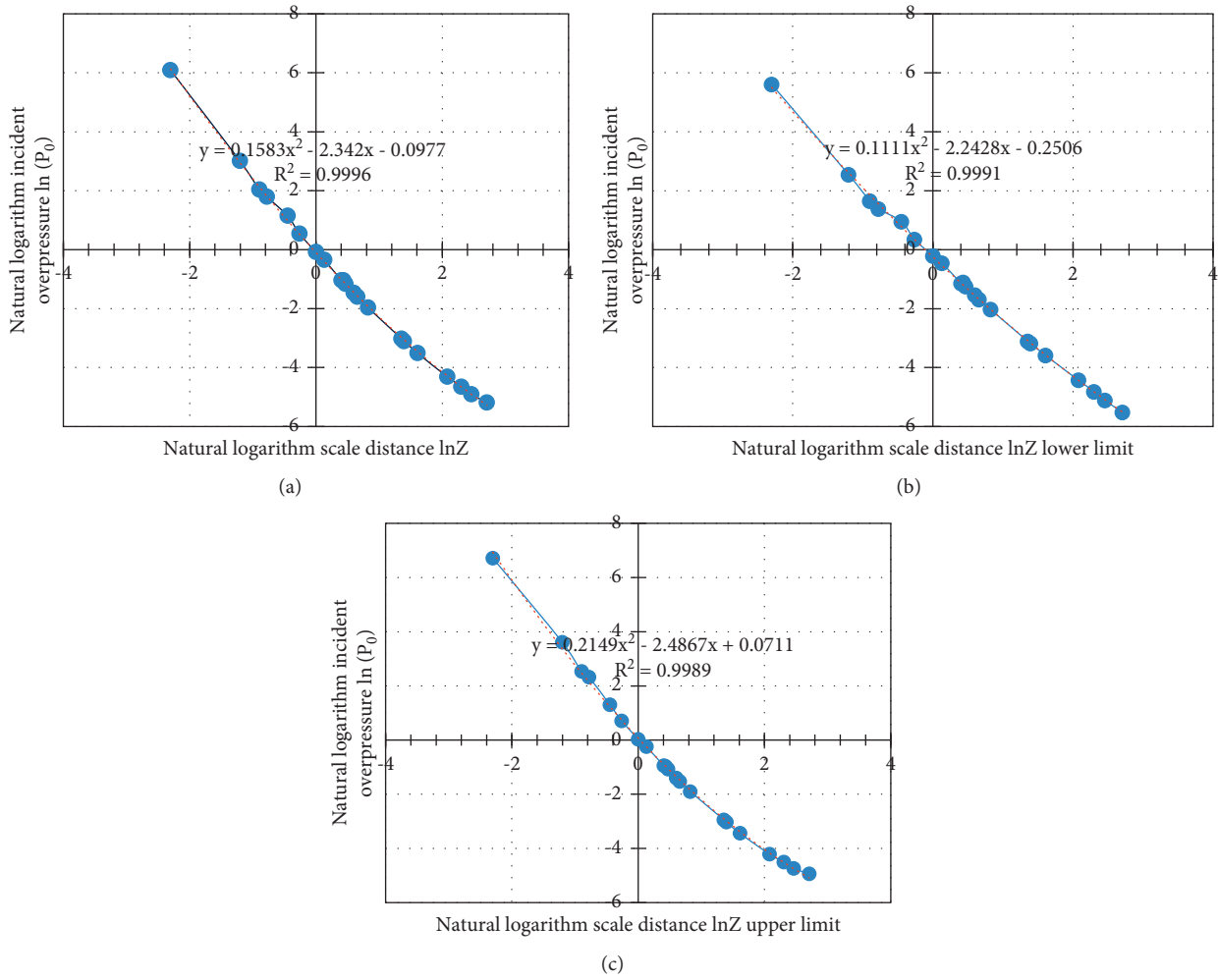


FIGURE 11: Fitting curve of incident overpressure, 95% confidence interval with scaled distance. (a) Fitting curve of incident overpressure. (b) Lower limit of incident overpressure fitting curve. (c) Upper limit of incident overpressure fitting curve.

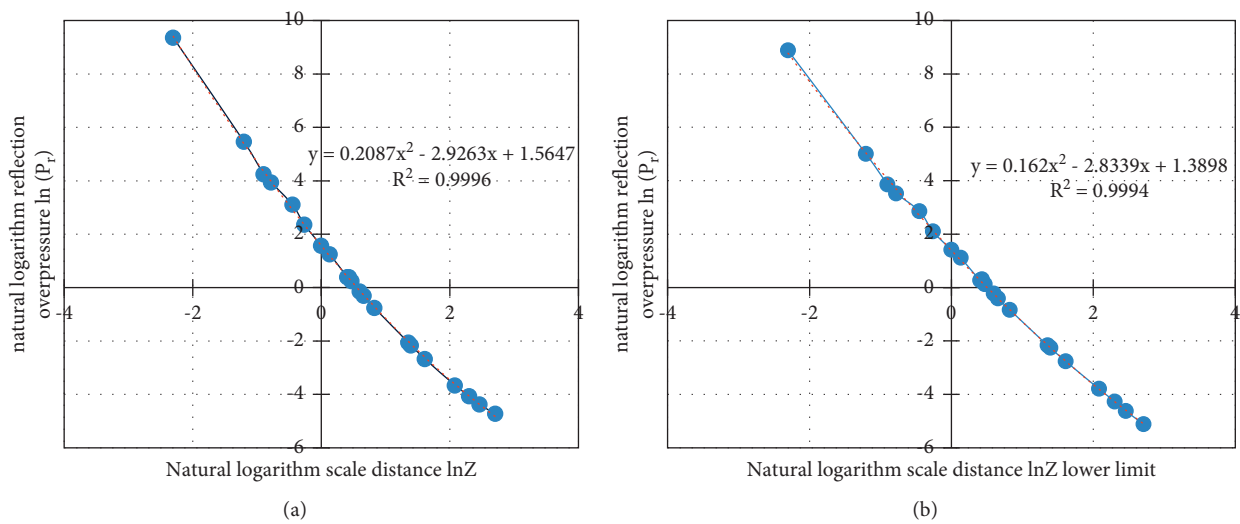


FIGURE 12: Continued.

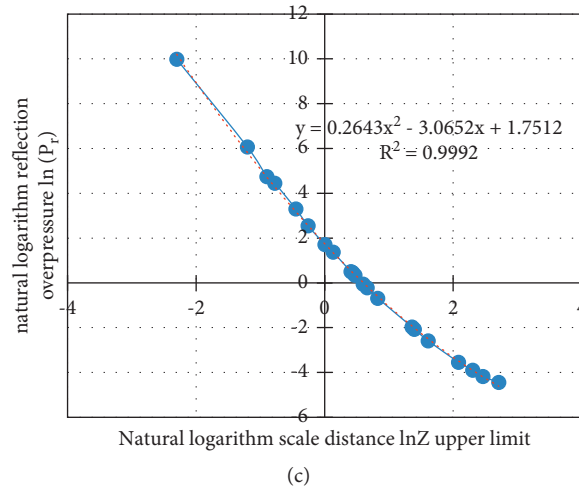


FIGURE 12: Fitting curve of reflection overpressure, 95% confidence interval with scaled distance. (a) Fitting curve of reflection overpressure. (b) Lower limit of reflection overpressure fitting curve. (c) Upper limit of reflection overpressure fitting curve.

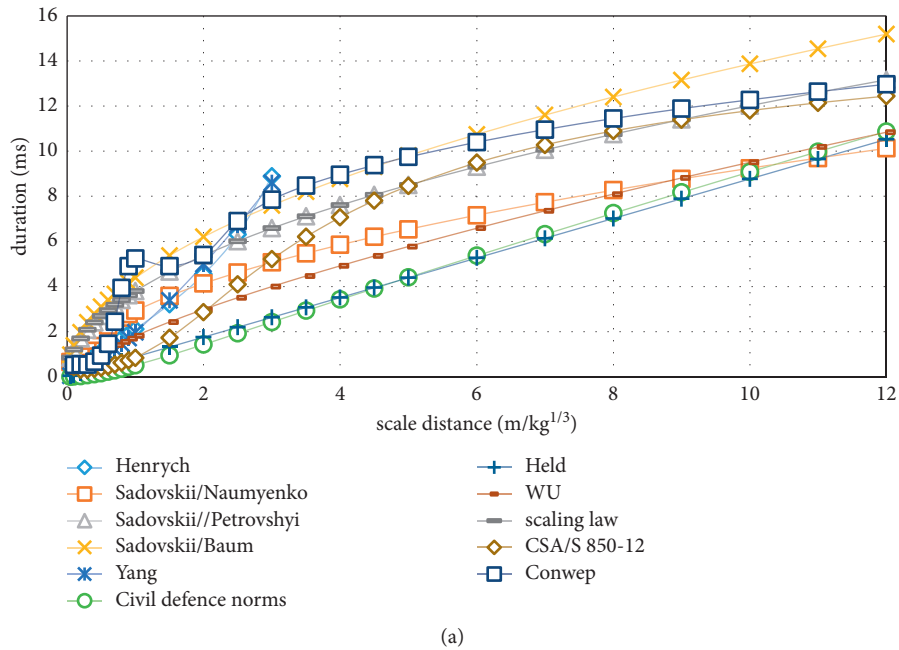


FIGURE 13: Continued.

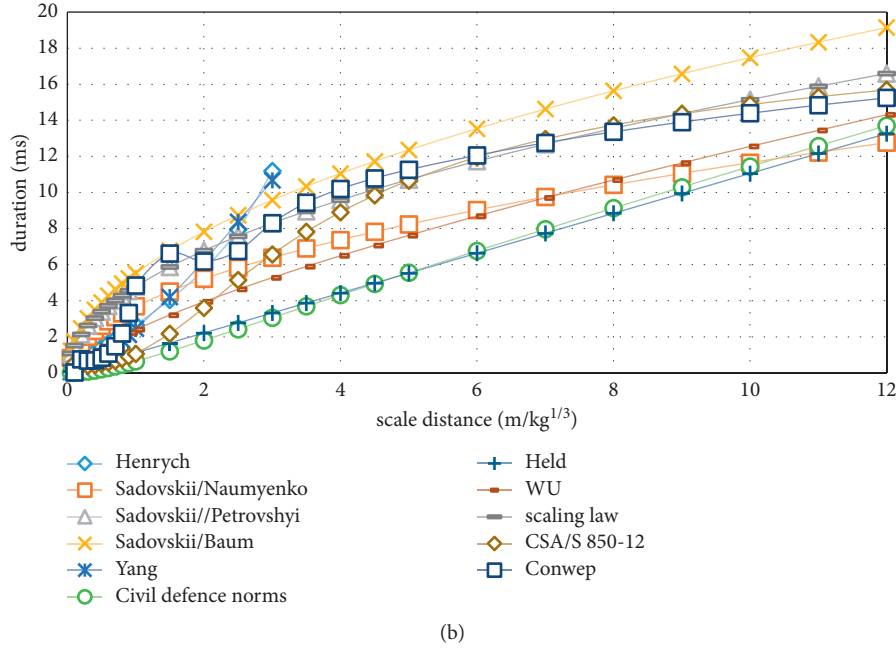


FIGURE 13: Relationship between duration and scaled distance under different explosive equivalents. (a) Explosive equivalent 25 kg. (b) Explosive equivalent 50 kg.

In the equation, the unit of  $t$  is ms, the unit of  $w$  is kg, the unit of  $P_{so}$  is MPa, and the unit of  $i_{so}$  is Pa-s.

Wu and Hao [23] suggested using Henrych's research results and giving the formula for calculating the overpressure duration of air explosions as follows:

$$t = 1.9Z^{1.3}(\text{ascent}) + 0.5Z^{0.72}W^{0.4}(\text{downcomer})(\text{ms}). \quad (37)$$

Sui [51] obtained the calculation formula of duration according to explosion similarity law as follows:

$$\frac{t}{\sqrt[3]{W}} = 1.35\sqrt{Z}, \quad R > 12R_0. \quad (38)$$

Canadian specification CSA/S 850-12 [4] gives the calculation formula of reflection overpressure and reflection impulse when the ground explosion occurs. Thus, the duration of overpressure can be inversely calculated. Among them, the calculation formula of reflection impulse is as follows:

$$\ln \frac{i_r}{\sqrt[3]{W}} = 6.7853 - 1.3466 \ln Z + 0.1010 \ln^2 Z - 0.0112 \ln^3 Z, \quad 0.06 < Z < 39.67. \quad (39)$$

The unit of  $i_r$  is KPa-ms.

**4.2. Experimental Duration Data.** Similar to the experimental overpressure data, 125 datasets were collected. The

experimental data related to the blast loading duration are shown in Table 4. Only 87 datasets were useable. In the experiments, the measured load duration is the total duration of exponentially declining overpressure. To facilitate statistical comparisons, all durations were converted into triangular durations form. The conversion principle was that the positive impulse and overpressure peak value of the exponential blast loading and triangular blast loading were consistent. It can be seen from Table 4 that, under the same conditions, the duration of blast loading has high discreteness.

By analyzing the theoretical duration formulas (30)–(39), it was found that, unlike the formulas of overpressure, the ratio of duration to the cube root of charge mass (i.e., the proportional time) was only related to the single parameter of scaled distance. Therefore, the data from theoretical calculations and experimentally measured data were changed into the proportional time data, and the relationship between the proportional time and the scaled distance was studied to determine the probability distribution of duration.

**4.3. Duration Probability Distribution and Formula Derivation.** Using the explosion overpressure duration data, the histograms of the proportional time ( $t/\sqrt[3]{W}$ ) for different scaled distances were drawn, as shown in Figure 14. Combined with the distribution characteristics of the duration histograms, the K-S and Lilliefors goodness-of-fit tests of proportional time probability distributions for different

TABLE 4: Test data for overpressure duration.

Source	Explosive	Scale distance (m/kg <sup>1/3</sup> )	Duration (ms)		$t/\sqrt{W}$ (ms/kg <sup>1/3</sup> )	Source	Explosive	Scale distance (m/kg <sup>1/3</sup> )	Duration (ms)		$t/\sqrt{W}$ (ms/kg <sup>1/3</sup> )
			Measured	Calculation					Measured	Calculation	
Razaqpur et al. [31]	ANFO	1.14	0.297	0.112	0.272	Kim et al. [37]	ANFO	0.638	0.224	0.095	0.224
			0.719	0.272	0.356				0.151	0.356	
			0.772	0.256	0.242				0.103	0.242	
		1.00	0.876	0.291	—	0.223	0.095	0.223			
			1.193	0.396	—	0.319	0.136	0.319			
			0.597	0.198	—	0.235	0.100	0.235			
		0.69	0.908	0.301	—	0.215	0.058	0.215			
			0.036	0.105	—	0.376	0.110	0.376			
			0.043	0.126	—	0.416	0.127	0.416			
		0.73	0.048	0.140	—	0.696	0.213	0.696			
			0.038	0.111	—	0.237	0.081	0.237			
			0.042	0.123	—	0.589	0.589	0.589			
0.77	0.069	0.201	—	0.648	0.648	0.648					
	0.030	0.088	—	0.552	0.552	0.552					
	0.038	0.111	—	0.306	0.119	0.306					
1.05	0.074	0.216	—	0.328	0.100	0.328					
	0.068	0.199	—	0.275	0.084	0.275					
	0.075	0.219	—	0.329	0.101	0.329					
Aune et al. [40]	TNT	1.09	0.078	0.228	0.351	Zhang et al. [43]	Emulsion	0.407	0.452	0.123	0.452
			0.078	0.228	0.376				0.351	0.351	
			0.067	0.196	0.376				0.102	0.376	
		1.14	0.064	0.187	—	0.532	0.144	0.532			
			0.070	0.204	—	0.316	0.086	0.316			
			0.073	0.213	—	0.228	0.062	0.228			
		1.42	0.078	0.228	—	0.489	0.149	0.489			
			0.118	0.344	—	0.473	0.182	0.473			
			0.119	0.347	—	0.493	0.169	0.493			
		1.46	0.140	0.409	—	0.491	0.246	0.491			
			0.130	0.379	—	1.880	0.477	1.880			
			0.131	0.382	—	1.872	0.475	1.872			
1.5	0.134	0.391	—	1.837	0.466	1.837					
	0.155	0.452	—	1.673	0.425	1.673					
	0.165	0.482	—	1.822	0.462	1.822					
1.82	0.143	0.417	—	0.0351	0.086	0.0351					
	0.161	0.470	—	0.0324	0.067	0.0324					
	0.178	0.520	—	0.038	0.059	0.038					
1.827	2.048	5.978	—	0.0333	0.053	0.0333					
	1.913	5.575	—	0.0828	0.041	0.0828					
	1.706	5.512	—	0.1108	0.038	0.1108					
Choi et al. [42] ground explosion	3.236	1.703	—	0.0611	0.028	0.0611					
	3.272	1.703	—	0.1325	0.032	0.1325					
	1.887	0.567	—	0.021	0.021	0.021					
Hao et al. [45] ground explosion	4.342	1.728	—	0.021	0.031	0.021					
	2.673	2.20	—	0.064	0.055	0.064					
	29.495	24.247	—	1.1	0.0313	1.1					

Note: The table shows only part of the experimental data. See more relevant literature.

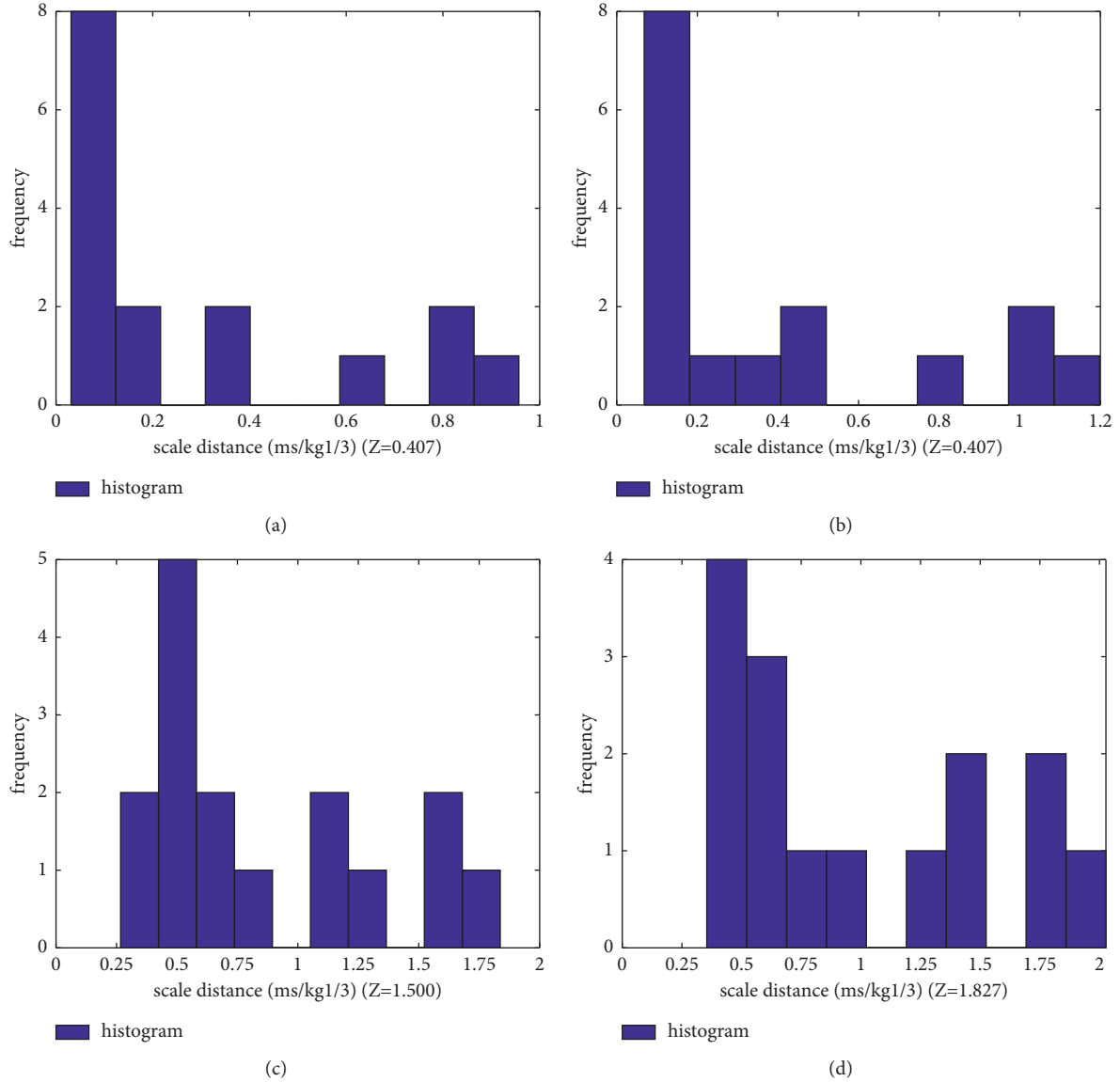


FIGURE 14: Duration histogram under different scaled distance. (a) Scale distance ( $Z=0.407$ ). (b) Scale distance ( $Z=0.638$ ). (c) Scale distance ( $Z=1.500$ ). (d) Scale distance ( $Z=1.827$ ).

scaled distances were carried out. The results showed that the proportional times for different scaled distances differed considerably and no specific probability distribution was acceptable. Therefore, the statistical data of proportional time for different scaled distances were used directly. The relationship between the proportional time and the scaled distance can be obtained by the least square method, as shown in Figure 15.

The function formula of proportional time with scaled distance is as follows:

$$\frac{t}{\sqrt[3]{W}} = 0.12821Z^3 - 0.49254Z^2 + 1.0219Z - 0.01744. \quad (40)$$

The curve formulas corresponding to the upper and lower limits of 95% confidence interval are as follows:

$$\begin{aligned} \frac{t}{\sqrt[3]{W}} &= 0.09964Z^3 - 0.39868Z^2 + 0.9184Z \\ &\quad - 0.09867 \text{ (upper limit)}, \\ \frac{t}{\sqrt[3]{W}} &= 0.15755Z^3 - 0.58869Z^2 + 1.12826Z \\ &\quad + 0.06295 \text{ (lower limit)}. \end{aligned} \quad (41)$$

To compare the dispersion degree of the proportional time for different scaled distances, the coefficient of variation of the proportional time was calculated, as shown in Figure 16. As can be seen from Figure 16, for different scaled distances, the coefficients of variation of the proportional time were overall small, between 0.408 and 1.017. The variability becomes smaller with the increase in scaled distance. At the same time, the formula for the proportional time as a function of the scaled distance was highly reliable.

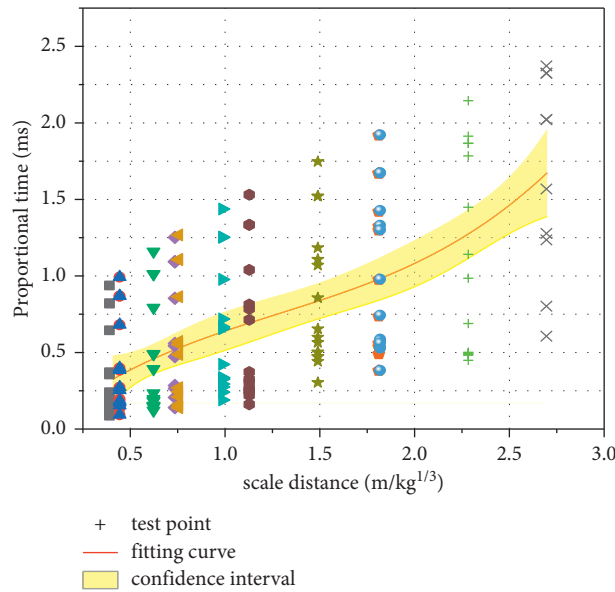


FIGURE 15: Relationship curve and confidence interval between proportional time and scaled distance.

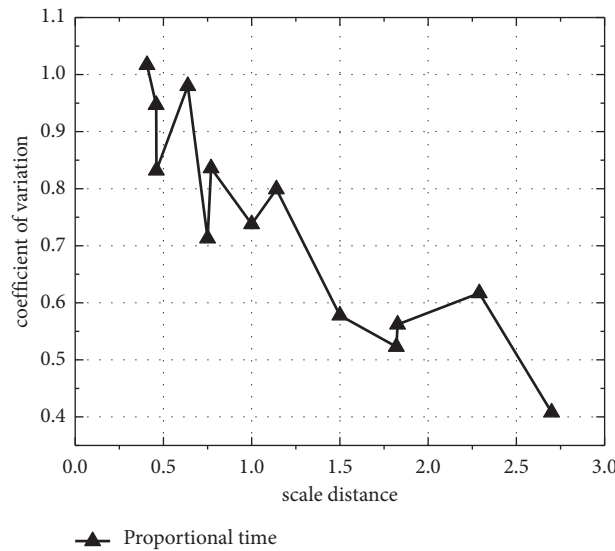


FIGURE 16: Variation coefficient of proportional time under different scaled distance.

### 5. Conclusions

By analyzing a large amount of blast loading experimental and theoretical data, the probability distribution of blast loading was studied. The main conclusions are as follows:

- (1) Blast loading test data were affected by factors such as explosive type, equivalent mass and shape, and test environment. Both the overpressure and load duration varied. The experiments mostly used small equivalent explosives. The scaled distance was mostly concentrated in the range of 0.4–2.0 m/kg<sup>1/3</sup>.
- (2) A formula for the reflection coefficient was proposed by curve fitting to the vertical incidence data, and then a formula for the reflection overpressure using the incident overpressure was obtained.
- (3) When the scaled distance was less than 0.5 m/kg<sup>1/3</sup>, the probability density of explosion overpressure followed an exponential distribution, and the coefficient of variation of overpressure reached the maximum value of 1. When the scaled distance was greater than 0.5 m/kg<sup>1/3</sup>, the probability density of explosion overpressure followed a normal distribution. When the scaled distance was about 1.5–6 m/kg<sup>1/3</sup>, the coefficient of variation was small, between 0.13 and 0.2.
- (4) For different scaled distances, no specific probability distribution function for the proportional duration could be selected, but the coefficient of variation of the proportional duration was relatively small, between 0.408 and 1.017.

- (5) Using the data of explosion overpressure and proportional duration for different scaled distances, the formulas for the explosion overpressure and proportional duration and the 95% confidence upper and lower limit formulas were derived.

## Data Availability

The data used to support the findings of this study are included within the article.

## Conflicts of Interest

The authors declare that they have no conflicts of interest.

## Acknowledgments

This work was supported by the National Natural Science Foundation of China (Grant no. 51608229). And the authors would like to express their gratitude to EditSprings (<https://www.editsprings.com/>) for the expert linguistic services provided.

## References






- [1] TM5-855-1, *Fundamentals of Protective Design for Conventional Weapons*, US Department of the Army, Washington DC, USA, 1987.
- [2] A. Castellano, J. Caltagirone, F. Sock, and N. Dobbs, *TM-5-1300, "Design of Structures to Resist the Effects of Accidental Explosions"*, Technical Manual, US Department of the Army, Washington DC, USA, 1990.
- [3] UFC 3-340-02, *Structures to Resist the Effects of Accidental Explosions*, Department of Defense Explosives Safety Board, New York, NY, USA, 2008.
- [4] CSA/S 850-12, *Design and Assessment of Buildings Subject to Blast Loads*, Canadian Standards Association, Toronto Canada, 2012.
- [5] National Standard of the People's Republic of China, *GB6722-2014, "Blasting Safety Regulations"*, China Standard Press, Beijing, China, 2014.
- [6] National standards of the People's Republic of China, *GB50038-2005, "Code for Design of Civil Air Defense Bases"*, China Plan Press, Beijing, China, 2005.
- [7] H. Y. Low and H. Hao, "Reliability analysis of reinforced concrete slabs under explosive loading," *Structural Safety*, vol. 23, no. 2, pp. 157–178, 2001.
- [8] D. Bogosian, J. Ferritto, and Y. Shi, "Measuring uncertainty and conservatism in simplified blast models," in *Proceedings of the 30th Explosives Safety Seminar*, Atlanta, Georgia, USA, August 2002.
- [9] Z. X. Li, J. H. Lu, Y. C. Shi, and Y. Ding, "Reliability analysis of steel beams under uncertain blast loading," *Engineering Mechanics*, vol. 31, no. 4, pp. 112–118, 2014.
- [10] J. H. Lu, *Reliability Analysis of Steel Beams under Uncertain Explosion Loads*, Tianjin University, Tianjin, China, 2012.
- [11] Z. X. Li, Q. W. Ren, Y. C. Shi, and Y. Ding, "Research on blast load value in design of important building structures against terrorist explosions," *Journal of Building Structures*, vol. 37, no. 3, pp. 51–58, 2016.
- [12] C. A. Mills, "The design of concrete structure to resist explosions and weapon effects," in *Proceedings of the 1st International Conference on Concrete for Hazard Protections*, Edinburgh, UK, September 1987.
- [13] R. E. Crawford, C. J. Higgins, and E. H. Bultmann, "The air force manual for design and analysis of hardened structures," *USA Handbook for Design and Analysis of Protective Structures*, Report AFWL-TR-74-102, Civil Nuclear System Corporation, New Mexico, 1980.
- [14] G. H. Li, *Anti - Explosion Dynamics of Engineering Structures*, Shanghai Science and Technology Press, Shanghai, China, 1989.
- [15] H. L. Brode, "Blast wave from a spherical charge," *Physics of Fluids*, vol. 2, no. 2, p. 217, 1959.
- [16] H. L. Brode, "Numerical solutions of spherical blast waves," *Journal of Applied Physics*, vol. 26, no. 6, pp. 766–775, 1955.
- [17] H. L. Brode, *A Calculation of the Blast Wave from a Spherical Charge of TNT*, University of Texas at Austin, Austin, TX, USA, 1961.
- [18] J. Henrych and G. R. Abrahamson, *The Dynamics of Explosion and its Use*, Elsevier Scientific Pub. Co., Amsterdam NY, USA, 1979.
- [19] J. Henrych and G. R. Abrahamson, *The Dynamics of Explosion and its Use*, Elsevier Scientific Pub. Co., Amsterdam NY, USA, 1979.
- [20] G. F. Kinney and K. J. Graham, *Explosive Shocks in Air*, Springer-Verlag, Berlin, Germany, 1985.
- [21] N. M. Newmark and R. J. Hansen, *Design of blast resistant structures*, New York: *Shock and Vibration Hand book*, Harris and Crede, McGraw-Hill, New York, NY, USA, 1961.
- [22] W. E. Baker, P. Cox, P. Westine, and J. K. R. Strehlow, *Explosion Hazards and Evaluation*, Elsevier Scientific Pub. Co., Amsterdam, The Netherlands, 1983.
- [23] C. Wu and H. Hao, "Modeling of simultaneous ground shock and airblast pressure on nearby structures from surface explosions," *International Journal of Impact Engineering*, vol. 31, no. 6, pp. 699–717, 2005.
- [24] I. A. Naumyenko and I. G. Petrovsky, *The Shock Wave of a Nuclear Explosion*, воен. издат. мии. сборки СССР, Moscow, 1956.
- [25] M. A. Sadvskii, *Mechanical effects of air shock waves from explosions according to experiments*, Nauka Press, Moscow, Explosion physics edition, 1952.
- [26] X. H. Ye, *Military Explosive Engineering*, PLA Press, Beijing, China, 1999.
- [27] J. I. Siddiqui and S. Ahmad, "Impulsive loading on a concrete structure," *Proceedings of the Institution of Civil Engineers-Structures and Buildings*, vol. 160, no. 4, pp. 231–241, 2007.
- [28] S. Ahmad, A. Elahi, J. Iqbal, M. A. Keyani, and A. G. A. Rahman, "Impulsive loading on reinforced concrete wall," *Proceedings of the Institution of Civil Engineers - Structures and Buildings*, vol. 166, no. 3, pp. 153–162, 2013.
- [29] J. Iqbal and S. Ahmad, "Improving safety provisions of structural design of containment against external explosion," in *Proceedings of the International conference on opportunities and challenges for water cooled reactors in the 21st century*, International Atomic Energy Agency (IAEA), Vienna, Austria, October 2011.
- [30] M. Held, "Blast waves in free air," *Propellants, Explosives, Pyrotechnics*, vol. 8, no. 1, pp. 1–7, 1983.
- [31] A. G. Razaqpur, A. Tolba, and E. Contestabile, "Blast loading response of reinforced concrete panels reinforced with externally bonded GFRP laminates," *Composites Part B: Engineering*, vol. 38, no. 5–6, pp. 535–546, 2007.
- [32] H. Wang, C. Wu, F. Zhang et al., "Experimental study of large-sized concrete filled steel tube columns under blast load,"

- Construction and Building Materials*, vol. 134, pp. 131–141, 2017.
- [33] J. Li, C. Wu, H. Hao, and Z. Liu, “Post-blast capacity of ultra-high performance concrete columns,” *Engineering Structures*, vol. 134, pp. 289–302, 2017.
- [34] H. W. Jin, Z. X. Liu, S. Y. Liu, and Y. Su, “Experimental study of ultra-high performance fiber reinforced concrete filled steel tube columns under blast loading,” *Building structure*, vol. 46, no. 4, pp. 45–49, 2016.
- [35] X. X. Liang, Z. Q. Wang, and R. N. Wang, “Deformation model and performance optimization research of composite blast resistant wall subjected to blast loading,” *Journal of Loss Prevention in the Process Industries*, vol. 49, pp. 326–341, 2017.
- [36] G. Q. Li, H. Y. Qu, T. C. Yang, Y. Lu, and S. W. Chen, “Experimental study on blast resistance of concrete filled steel tubular columns,” *Journal of Building Structures*, vol. 34, no. 12, pp. 69–76, 2013.
- [37] J. H. J. Kim and S. B. Kim and J. K. Choi, Experiment study on blast loading response of frp-retrofitted rc slab structures,” in *Proceedings of the Asia-Pacific Conference on FRP in Structures*, pp. 533–538, Brisbane, Australia, December 2019.
- [38] S. Ahmad, A. Elahi, H. Pervaiz, A. G. A. Rahman, and S. Barbhuiya, “Experimental study of masonry wall exposed to blast loading,” *Materiales De Construccion*, vol. 64, no. 313, p. e7, 2014.
- [39] C. B. Ritchie, J. A. Packer, M. V. Seica, and X. L. Zhao, “Behavior of steel rectangular hollow sections subject to blast loading,” *Journal of Structural Engineering-asce*, vol. 143, no. 12, Article ID 04017167, 2017.
- [40] V. Aune, E. Fagerholt, K. O. Hauge, M. Langseth, and T. Børvik, “Experimental study on the response of thin aluminium and steel plates subjected to airblast loading,” *International Journal of Impact Engineering*, vol. 90, pp. 106–121, 2016.
- [41] Z. S. Tabatabaei, J. S. Volz, J. Baird, B. P. Gliha, and D. I. Keener, “Experimental and numerical analyses of long carbon fiber reinforced concrete panels exposed to blast loading,” *International Journal of Impact Engineering*, vol. 57, pp. 70–80, 2013.
- [42] J.-H. Choi, S.-J. Choi, J.-H. J. Kim, and K.-N. Hong, “Evaluation of blast resistance and failure behavior of prestressed concrete under blast loading,” *Construction and Building Materials*, vol. 173, pp. 550–572, 2018.
- [43] F. R. Zhang, C. Q. Wu, X. L. Zhao et al., “Experimental study of CFDST columns infilled with UHPC under close-range blast loading,” *International Journal of Impact Engineering*, vol. 93, pp. 184–195, 2016.
- [44] K. H. Safari, J. Zamani, S. M. R. Khalili, and S. Jalili, “Experimental, theoretical, and numerical studies on the response of square plates subjected to blast loading,” *The Journal of Strain Analysis for Engineering Design*, vol. 46, no. 8, pp. 805–816, 2011.
- [45] Y. F. Hao, H. Hao, Y. C. Shi, Z. Q. Wang, and R. q. Zong, “Field testing of fence type blast wall for blast load mitigation,” *International Journal of Structural Stability and Dynamics*, vol. 17, no. 9, Article ID 1750099, 2017.
- [46] A. C. Jacinto, R. D. Ambrosini, and R. F. Danesi, “Experimental and computational analysis of plates under air blast loading,” *International Journal of Impact Engineering*, vol. 25, no. 10, pp. 927–947, 2001.
- [47] Y. Cui, J. H. Zhao, C. G. Zhang, and S. S. Sun, “Research on pressure distribution of blast wave on the surface of CFST column based on explosion test and numerical simulation,” *Journal of Beijing University of Technology*, vol. 40, no. 12, pp. 1828–1836, 2014.
- [48] G. I. Pokrovskii and I. S. Fedorov, *Effect of Shock and Explosion on Deformable media*, Gos. Izd, 1957.
- [49] F. A. Baum, K. P. Stanyukovich, and B. I. Shekhter, *Physics of an Explosion*, Army Engineer Research and Development Labs Fort Belvoir VA, Virginia, USA, 1959.
- [50] Y. D. Yang, X. D. Li, and X. M. Wang, “Optimized fitting of characteristic parameters of explosion shock wave propagation in air,” *Explosive Materials*, vol. 43, no. 1, pp. 13–18, 2014.
- [51] S. Y. Sui, *Terminal Effect*, National Defense Industry Press, Beijing, China, 2000.



## Research Article

# Inversion for Constitutive Model Parameters of Bird in Case of Bird Striking

Peng Yu <sup>1</sup>, Siliu Yu <sup>1</sup>, Sheng He <sup>1,2</sup>, Xinheng Huang <sup>1</sup> and Weijing Yun <sup>1</sup>

<sup>1</sup>College of Civil Engineering and Architecture,  
Key Laboratory of Disaster Prevention and Structural Safety of Ministry of Education,  
Guangxi Key Laboratory of Disaster Prevention and Structural Safety, Guangxi University, Nanning, China  
<sup>2</sup>Guangxi Bossco Environmental Protection Technology Co., Ltd, Nanning 530007, China

Correspondence should be addressed to Sheng He; [hesheng@gxu.edu.cn](mailto:hesheng@gxu.edu.cn)

Received 19 November 2021; Revised 31 December 2021; Accepted 7 January 2022; Published 9 February 2022

Academic Editor: Jingxuan Wang

Copyright © 2022 Peng Yu et al. This is an open access article distributed under the Creative Commons Attribution License, which permits unrestricted use, distribution, and reproduction in any medium, provided the original work is properly cited.

The strike between flying birds and airplanes results in the unacceptable losses of aircraft structures. The normal approach to evaluate the bird impact resistance is the combined full-scale experimental-numerical study. However, the simulation results from the current available bird constitutive models are usually not in good agreement with the experimental data. Establishing a reasonable bird constitutive model is difficult and significant to the simulation of the bird striking process. In this paper, based on the displacement measurements of an aluminum plate subjected to soft body impact, an inversion of the bird constitutive model is conducted by using backpropagation (BP) neural network. A comparative evaluation of this inversion model and other constitutive models is carried out, indicating that the proposed inversion model is more reasonable.

## 1. Introduction

The strike between flying birds and airplanes frequently results in catastrophic damage to the aircraft. According to the International Bird Strike Committee, 55 fatal accidents, in which 108 aircraft were damaged and 277 people died, were reported between 1912 and 2009 [1]. The serious events of birds striking can lead to an unacceptable loss of aircraft and the death of crewmembers. In early studies, the common method to determine the capability against bird strikes is to carry out a full-scale bird-strike experiment [2]. However, various uncertainties may lead to diversities of experiments, and the experiments cost much. The development of advanced numerical techniques and computing technologies makes it possible to perform the coupling analysis and simulate the whole process of bird strike problems. However, the numerical results of current models are not in good agreement with the experimental data. Establishing a reasonable bird constitutive model is significant to the finite element analysis of bird strikes on aircraft structures.

The anatomic structure of birds includes several internal cavities like pneumatic bones, lungs, and peculiar air sacs,

which is a complex nonlinear system. Moreover, the identification of a bird constitutive model and the corresponding material parameters is difficult. Several authors used an elastic-plastic bird constitutive model with a defined failure strain [3–5], while others highlighted the limitations of this simplified material law [6]. It was observed that no fluid-like flow response can be achieved with such an elastic-plastic model, only if the shear modulus  $G$  is set very low [7]. In Ref. [8] a rubber-like hyper-elastic Mooney–Rivlin model was adopted to simulate the bird's behavior. A more common method is an equation of state (EoS) for the bird constitutive model, by defining the pressure-volume relationship with parameters of water at room temperature. A polynomial form of the EoS and a simpler Murnaghan EoS were used in most studies [2, 9–14]. A further approach of the Grüneisen EoS was adopted in Refs. [15, 16]. However, in Ref. [17] it was reported that the Grüneisen EoS is only valid for solid materials that remained in the solid-state during the impact process and should therefore be carefully used for bird strike simulations and the usage of Grüneisen EoS dependent on the finite element code, since there are only a few of the abovementioned algorithms available in most commercial

software codes. The material constants of all EoS have to be defined, which cannot be measured directly.

A regular technique is the parameter calibrations, for example, the elastic, elastic-plastic, or nonrevolving flow model is assumed to be the bird constitutive model, and then the plate response during the bird-plate impact experiment is used to confirm the parameters of the constitutive model. This methodology was performed in studies such as [16, 18] using optimization software to determine the parameters in conjunction with bird strike experiments on instrumented plates. Nishikawa et al. [19] impacted gelatin birds on rigid targets and confirmed that the deformation of the bird model did behave like fluid and numerical simulation results correlated well with experiment data.

In recent years, the artificial neural network (ANN) has provided a fundamentally practical and powerful approach to material modeling. The basic advantage of ANN is that it does not explicitly need physical knowledge of the deformation mechanism and mathematical model. Darryl et al. [20] used a contact algorithm based on the Lagrange multiplier method to predict appropriate impact force, this method solved the severe contact-induced deformation due to a large contact force and highly deformable projectile. Previous studies usually adopted the Lagrangian formulation to model bird strikes. However, due to element instability, refining mesh elements and narrowing the time-step method had to be used to alleviate the problem, to solve this problem, nowadays more researchers use arbitrary Lagrange-Euler (ALE) [19, 21–23] and smoothed particle hydrodynamics (SPH) [19, 24–27] method in bird strike problems [25]. However, there are few reports about the application of ANN to model the bird constitutive model by using SPH Formulation during the impact process. In this paper, based on the displacement measurement results of bird impact on the aluminum plate, an ANN model with an error backpropagation learning algorithm has been applied to an inversion on bird constitutive model parameters and the parameters are obtained by inversion. The validity and reliability of the inversion model are discussed. Furthermore, a comparative evaluation of three other constitutive equations and the trained network model is carried out.

## 2. Introduction of BP Neural Network

The artificial neural network is an intelligent information-treatment system with the characteristics of adaptive learning and treating complex relationships [28]. An artificial neural network (ANN) consists of a large number of highly connected artificial units (neurons or nodes). Each neural network comprises an input layer, an output layer, and one or more hidden layers, which are connected by the processing units, as can be seen in Figure 1. The input layer is used to receive data, while the output layer sends the output values to users. The role of the hidden layer is to provide the necessary complexity (which denotes to abstract the characteristics of the input data to another dimension space to show its more abstract features) for nonlinear problems. In the present model, sigmoid functions are employed due to the processing units for computational convenience.

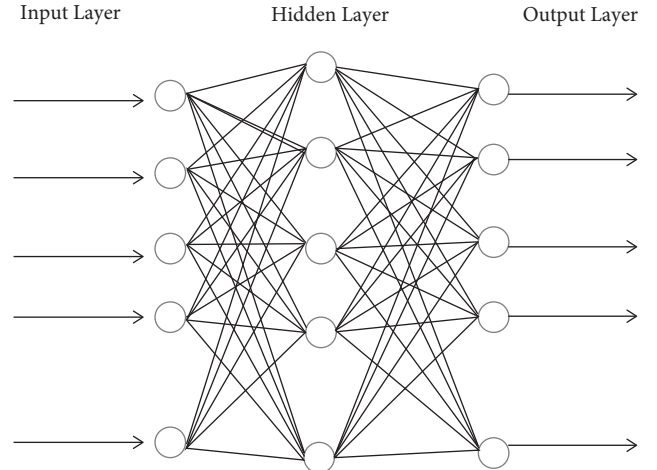


FIGURE 1: The architecture of the BP ANN model.

$$f(x) = \frac{1}{(1 + \exp(-x))}. \quad (1)$$

Among various types of ANN models, an iterative gradient algorithm called backpropagation (BP) algorithm is popular in the field in engineering applications and it is used for the present work. The training of a network by backpropagation involves three stages: the feedforward of the input training pattern, the training and backpropagation with the associated error, and the adjustment of the weights. When the artificial neural network is established for the soft body constitutive model, a feed-forward backpropagation algorithm is selected to train the network.

## 3. An Example

**3.1. Flow of Soft Body Parameter Optimization.** First of all, determine the soft body parameters to be optimized, and then according to the experience to determine the range of parameters, the values determined according to the experimental data of the soft body impact aluminum sample points. And then the sample parameters in LS-DYNA in the calculation, can get aluminum midpoint displacement curve of time, choose corresponding time point in the experimental data of the displacement, training sample is completed. After the improved BP neural network training, the required soft body model parameters are output and the stable network unit connection weights are obtained. Then network training is carried out to obtain the soft body model parameters. Lastly, the obtained parameters are put into LS-DYNA for calculation, and the calculation results are compared with the experimental results. The flow chart of soft body parameter optimization as shown in Figure 2.

**3.2. Construction of Bird Body Constitutive Model.** Newtonian fluid is selected to describe the constitutive model of the bird body, since the real bird body is a structure with flesh and blood [29]. Newtonian fluid is a viscous fluid

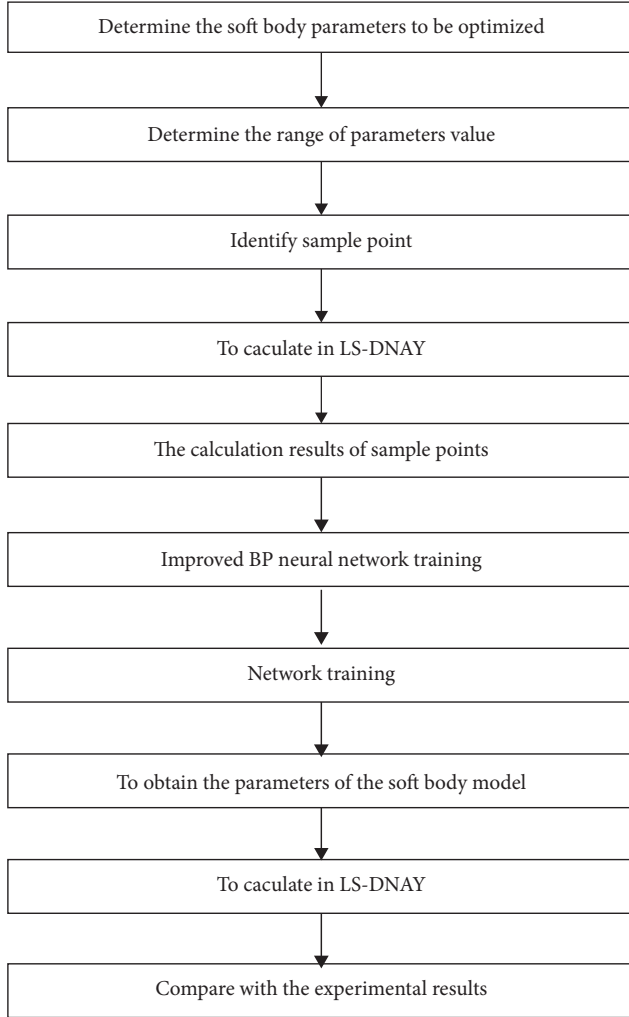


FIGURE 2: Flow chart of soft body parameter optimization.

with a linear proportional relationship between shear stress and deformation gradient, and its stress-strain relationship is determined by the following equation:

$$\sigma_{ij} = -p\delta_{ij} + D_{ijkl}V_{ij}, \quad (2)$$

where  $\sigma_{ij}$  is the stress tensor,  $V_{ij}$  is the deformation rate tensor,  $D_{ijkl}$  is the viscosity coefficient tensor of fluid, and  $P$  is the static pressure. The term  $p\delta_{ij}$  represents the state of stress in the fluid at rest (when  $V_{ij}=0$ ). Assume that static pressure  $P$  depends on the density and temperature of the fluid according to some equation of state. For Newtonian fluids, we assume that the elements of the tensor  $D_{ijkl}$  can be temperature-dependent and the stress or deformation rate is independent. Tensor  $D_{ijkl}$  is of order 4 with  $3^4=81$  elements.

If the fluid is isotropic, that is, the tensor  $D_{ijkl}$  has the same component matrix in any Cartesian rectangular system, then  $D_{ijkl}$  can be expressed by two independent constants  $\lambda$  and  $\mu$  as the following equation:

$$D_{ijkl} = \lambda\delta_{ij}\delta_{kl} + \mu(\delta_{ik}\delta_{jl} + \delta_{il}\delta_{jk}). \quad (3)$$

Then,

$$\sigma_{ij} = -p\delta_{ij} + \lambda V_{kk}\delta_{ij} + 2\mu V_{ij}. \quad (4)$$

Combining equations

$$\sigma_{kk} = -3p + (3\lambda + 2\mu)V_{kk}. \quad (5)$$

If the mean normal stress  $1/3\sigma_{kk}$  is assumed to be independent of the volume expansion rate  $V_{kk}$ , then there must be

$$3\lambda + 2\mu = 0. \quad (6)$$

Thus, the constitutive equation becomes

$$\sigma_{ij} = -p\delta_{ij} + 2\mu V_{ij} - \frac{2}{3}\mu V_{kk}\delta_{ij}. \quad (7)$$

This formula was put forward by Stokes, so the fluid subject to the above equation is called Stokes fluid, for this kind of fluid only a material constant  $\mu$  (i.e., viscosity coefficient) is enough to determine its properties.

If the fluid is incompressible, then  $V_{kk}=0$ , and the constitutive equation of incompressible viscous fluid can be obtained:

$$\sigma_{ij} = -p\delta_{ij} + 2\mu V_{ij}. \quad (8)$$

If  $\mu=0$ , the constitutive equation of inviscid fluid is obtained:

$$\sigma_{ij} = -p\delta_{ij}. \quad (9)$$

The appearance of hydrostatic pressure  $P$  marks the fundamental difference between hydrodynamics and elasticity. To accommodate the needs of this new variable, it is usually assumed that there exists some equation of state, which gives the relationship between density  $\rho$ , pressure  $P$ , and absolute temperature  $T$ , that is

$$f(p, \rho, T) = 0. \quad (10)$$

**3.3. Finite Element Model.** The bird strike setup is conducted based on the experiment of the bird-impact plate in Figure 3 by using LS-DYNA element code.

The flat plate fixed along the four edges is impacted by a soft body at the center of the flat plate at 91.1 m/s with an impact angle of  $30^\circ$ . The dimensions of the flat plate are 525 mm  $\times$  430 mm  $\times$  10 mm. The geometric model of a bird is simulated by a cylinder with a hemisphere at the two ends, the diameter of the hemisphere is 53 mm and the length of the cylinder is 156 mm. The mass of the bird is 1.8 kg.

In the finite element model, the 8-node solid and 164-element type in the LS-DYNA element library is employed for the bird and flat plate. In addition, hourglass control and single-point integration are also used. The numbers of the elements for the bird and flat plate model are 4504 and 2000.

### 3.4. Materials Properties

**3.4.1. Materials Properties of Flat Plate.** The plate is made from LY12-CZ aluminum alloy. The material parameters of the flat plate are mentioned in Table 1. The material

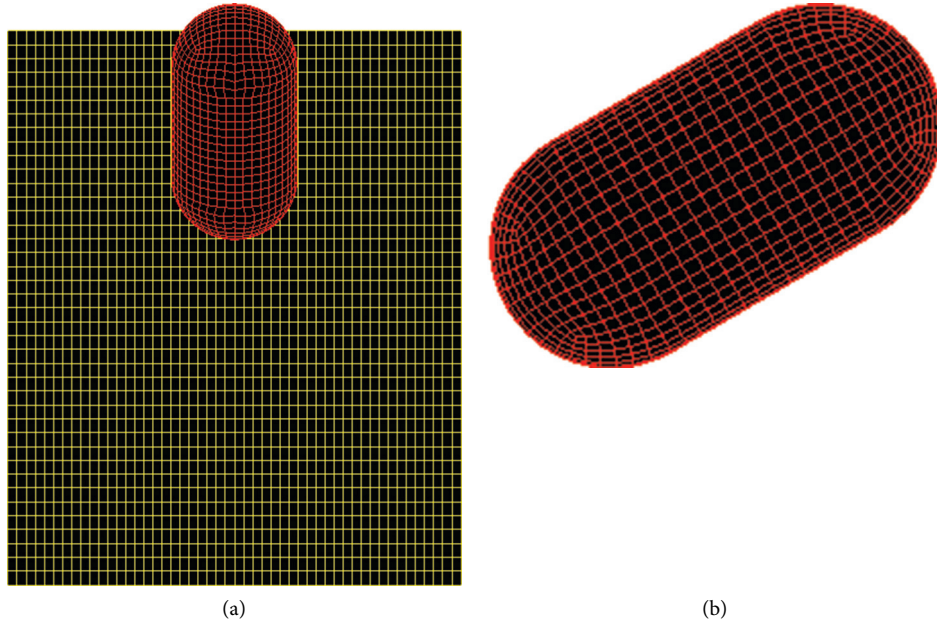


FIGURE 3: The finite element model: (a) top view; (b) front view.

TABLE 1: Material parameters of flat plate.

Young's modulus (GPa)	Poisson ratio	Density (kg/m <sup>3</sup> )	Yield stress (MPa)	Failure strain
71	0.3	2780	690	0.3

properties of the flat plate are modeled by the MAT\_PLASTIC\_KINEMATIC in LS-DYNA code where the values are set in Table 1.

**3.4.2. Material Properties of Bird.** Generally speaking, a trend is visible towards the utilization of SPH models with an equation of state for the material of bird using the properties of water-air-mixture at room temperature. A very good correlation to experimental results could be obtained with these models. For the fluid model, in LS-DYNA, the material model of NULL (empty material) is used to describe its material properties. The parameters to be input are shown in Table 2.

According to the property of the bird in the experiment, using fluid constitutive and Gruneisen state equation to describe soft body is closer to the reality. The bird model is defined by MAT\_NULL and the equation of state (EoS) is specified. The inputs of parameters are shown in Table 3.

During the impact process, the deformation of the bird is described by the equation of state. Elastic modulus and passion ratio are 0, and the density is 938 kg/m<sup>3</sup>. The four parameters of the constitutive model of the bird to be determined are shown in Table 4.

**3.5. Identification of the Bird Model and the Inversion of the Parameters.** The displacements at 12 different times are chosen as the inputs, and the outputs of the model are four constitutive parameters of the soft body. The 12 different times are based on the experimental displacement-time data

TABLE 2: Parameters of NULL model.

RO	Mass density
PC	Pressure cutoff
MU	Viscosity coefficient
TEROD	Relative vol. in tension
CEROD	Relative vol. in compression
YM	Young's modulus
PR	Poisson's ratio

TABLE 3: Parameters of Gruneisen model.

C	S1	S2	S3	GAMA0	A	E0 (J)	V0
1670	2.48	0	0	0	0	0	1

TABLE 4: Parameters to be determined.

PC	Pressure cutoff
MU	Viscosity coefficient
TEROD	Relative vol. in tension
CEROD	Relative vol. in compression

of the center of the flat plate. The experimental displacement-time data of the center of the flat plate is given in Figure 4.

Before the network training, both input and output variables are normalized within the range 0 to 1 in order to obtain a reliable form for the neural network<sup>[31]</sup>. If the number of hidden layers is too small, the trained network might not have sufficient ability to learn the process correctly. As a result, in order to choose the appropriate number

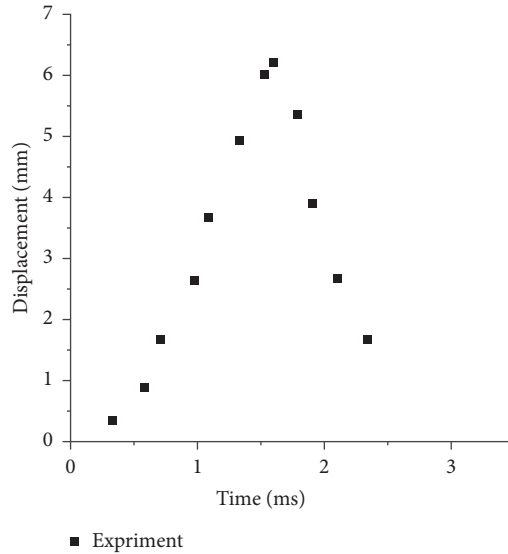


FIGURE 4: Experimental displacement-time data of the center of the flat plate.

of hidden layers, the trial-and-error procedure is started with seven neurons in the hidden layer and further carried out with up to fourteen neurons. It is found that when the number of neurons is 9, the mean square error reaches the minimum.

In the bird constitutive model, the values of the four parameters have their ranges based on the prior knowledge, specific ranges (see Table 5).

The parameters to be optimized are uniformly divided into a number of values with the space. According to the orthogonal design and uniform design principle, these values are divided into 25 groups, and each sample group contains four parameters, which is shown in Table 6.

Substituting these parameters of 25 groups into the bird constitutive model, 25 displacement-time curves of the center of the flat plate can be obtained in LS-DYNA simulation. Selecting the displacements of the center of the flat plate, the training of the network can be finished, which is shown in Table 7.

When developing the ANN model, the samples of 1, 5, 10, 15, 20, and 25 are removed to test the generalization capability of the network. The optimized ANN model consists of 12 input neurons, 4 output neurons, and a single hidden layer (with 9 neurons) and the transfer functions of the optimized ANN model are ‘tan sigmoid’ and ‘pure linear’. A feedforward backpropagation algorithm is selected to train the network. The setting of other training parameters for the neural network is listed in Table 8.

#### 4. Results and Discussion

The performance of ANN in the training stage is shown in Figure 5. It can be seen that the trend of error reduction remains unchanged after 2000 training cycles. After being trained, the ANN model can map the nonlinear relationship between the parameters of the bird constitutive model and the displacements of the center of the flat plate.

TABLE 5: The value range of the four parameters.

Optimize parameters	Label	Ranges of values	Units
PC	$X_1$	$[-0.05, -1.25]$	MPa
MU	$X_2$	$[0, 1.5]$	N·ms/mm <sup>2</sup>
TEROD	$X_3$	$[0.05, 1.25]$	—
CEROD	$X_4$	$[0.05, 1.25]$	—

TABLE 6: Parameters in sample groups.

Sample groups	$X_1$	$X_2$	$X_3$	$X_4$
1	-0.05	0	0.05	1.25
2	-0.1	0.1	0.1	1.2
3	-0.15	0.2	0.15	1.15
4	-0.2	0.3	0.2	1.1
5	-0.25	0.4	0.25	1.05
.....	.....	.....	.....	.....

The optimized parameters can be obtained, as can be seen in Table 9. The comparison of the numerical and experimental displacement of the center of the flat plate using the optimized constitutive model of bird is shown in Figure 6, indicating the simulation result using the parameters obtained from the developed network is in good agreement with experimental data. In order to verify the identification of the constitutive model after optimization, a comparative evaluation of three other constitutive equations and the present bird constitutive model is carried out. The parameters and stress distributing graphs of elastic model, plastic kinematic model, and elastic-plastic hydrodynamic Model are shown in Tables 10–12 and Figure 7, respectively, and the parameters of EOS\_LINEAR\_POLYNOMIA are shown in Table 13. As can be seen in Figure 8, the model of the bird remains in good condition while the flat plate with obvious deformation in the elastic model. The result of the plastic kinematic model and the elastic-plastic hydrodynamic model show a similar

TABLE 7: Sample groups.

Time/ms	Sample groups (Displacement/mm)					.....
	1	2	3	4	5	
0.34	0.123064	0.123165	0.123333	0.122845	0.121246	.....
0.59	1.220337	1.216867	1.216224	1.213989	1.232132	.....
0.71	2.043114	2.048179	2.048194	2.048631	2.060089	.....
0.98	4.100285	4.112417	4.128776	4.153035	4.19781	.....
1.09	4.668175	4.686835	4.689432	4.709893	4.751519	.....
1.34	5.355844	5.376423	5.394958	5.417252	5.453059	.....
1.53	5.576561	5.608154	5.628895	5.652006	5.696968	.....
1.60	5.537479	5.571992	5.605718	5.646124	5.67513	.....
1.79	4.84706	4.895124	4.93118	4.952708	4.973954	.....
1.91	4.184824	4.227517	4.255795	4.27969	4.277913	.....
2.11	3.242367	3.260473	3.273862	3.262928	3.225929	.....
2.35	2.13491	2.12319	2.114001	2.076703	2.046814	.....

TABLE 8: The setting of training parameters for network.

Name of parameters	Contents
Network	Backpropagation
Training function	Trainlm
Performance function	MSE
Training epoch	2,000
Goal	0.001

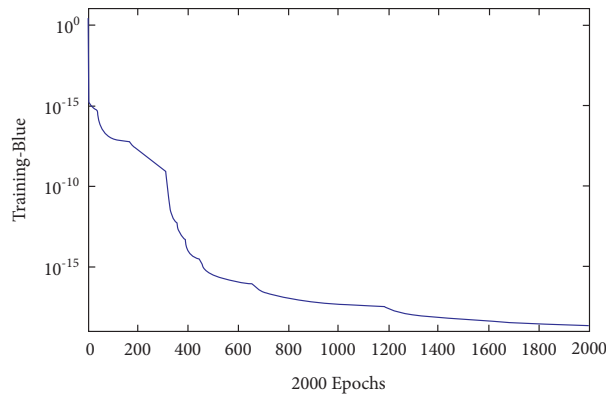


FIGURE 5: Training convergence curve of the neural network model.

TABLE 9: The results of parametric inversion.

Optimized parameters	Label	Range of values	Optimized results
PC	$X_1$	$[-0.05, -1.5]$	-0.3705
MU	$X_2$	$[0, 1.5]$	0.641
TEROD	$X_3$	$[0.05, 1.25]$	0.34
CEROD	$X_4$	$[0.05, 1.25]$	0.9295

phenomenon that the model of bird has large deformation while the flat plate with little, and the fringe levels drop significantly.

During the impact process, different bird constitutive models result in different displacement and force-time histories of the center of the flat plate. The maximum displacement and

the force of the center of the flat plate of the elastic constitutive model are the largest among the four constitutive models, in which the deviations from experimental results are also the largest. Figure 9 shows that the present bird constitutive model developed from the present network is in better agreement with experimental data than the other three constitutive models.

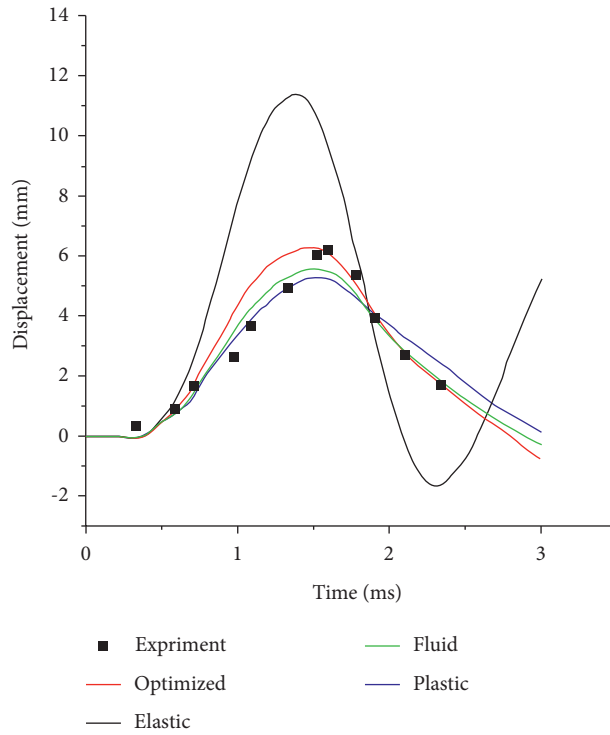


FIGURE 6: Comparisons of the numerical displacements among different constitutive models.

TABLE 10: Parameters of elastic model.

Elastic modulus/Pa	Poisson ratio	Density/kg/m <sup>3</sup>
$6.89 \times 10^7$	0.49	938

TABLE 11: Parameters of plastic kinematic model.

Elastic modulus/Pa	Poisson ratio	Density/kg/m <sup>3</sup>	Yield stress/Pa	Failure strain
$6.89 \times 10^7$	0.49	938	6894	1.25

TABLE 12: Parameters of elastic-plastic hydrodynamic model.

Density/kg/m <sup>3</sup>	Shear modulus/MPa	Hardening modulus /MPa	Pressure cutoff/MPa	Yield stress/MPa	Failure strain
938	10.2	0.13	-0.9	0.03	0.95

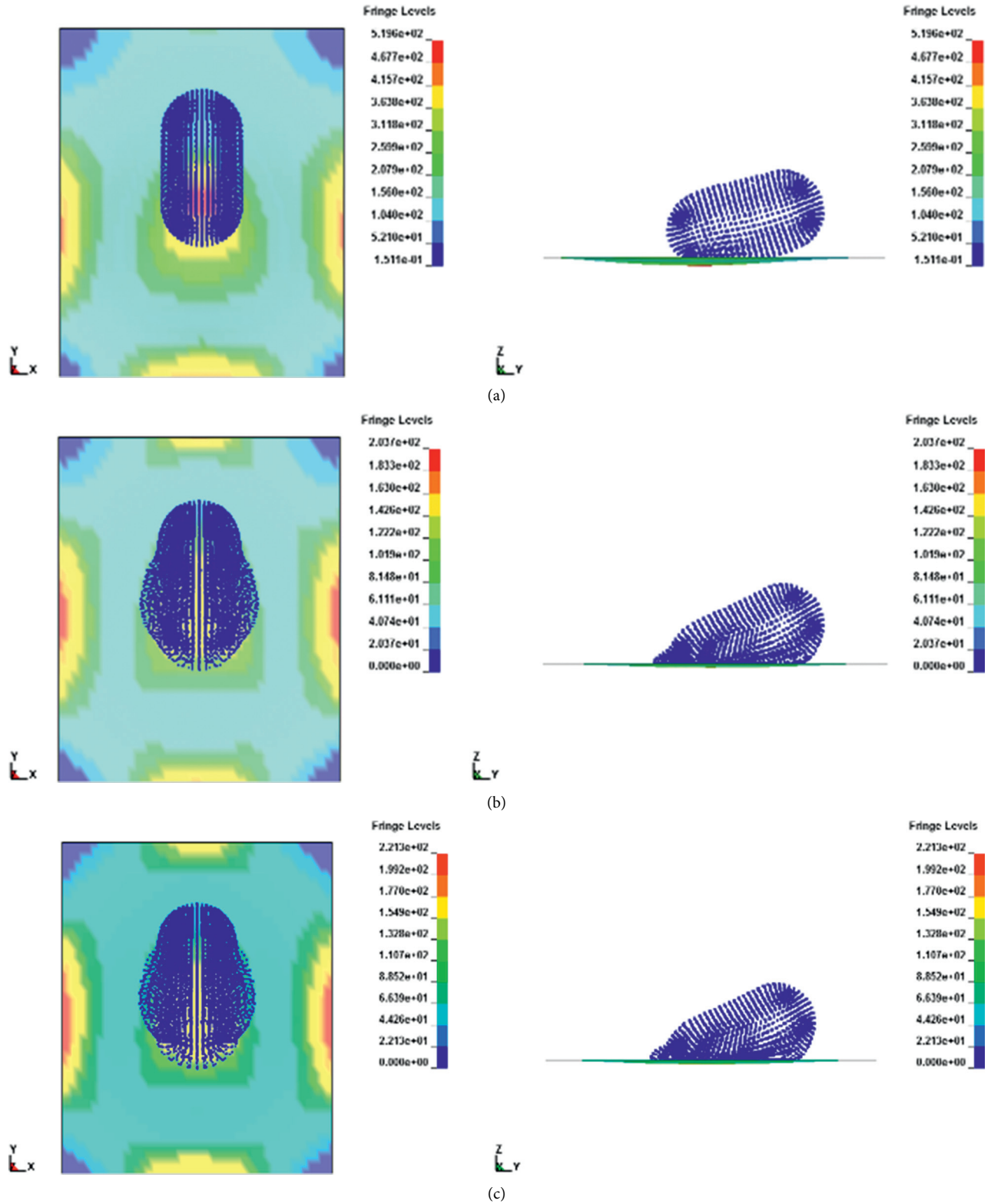


FIGURE 7: Stress distributing graphs of the top view and front view at 1.5 ms time of impact: (a) elastic model; (b) plastic kinematic model; (c) elastic-plastic hydrodynamic model.

TABLE 13: Eos linear polynomial.

$C_0$	$C_1$	$C_2$	$C_3$	$C_4$	$C_5$	$C_6$	$E_0$	$V_0$
0	2072	6217	10362	0	0	0	0	1

Unit: ( $C_0 \sim C_6$ , N/mm<sup>2</sup>;  $E_0$ , J;  $V_0$ , no unit).



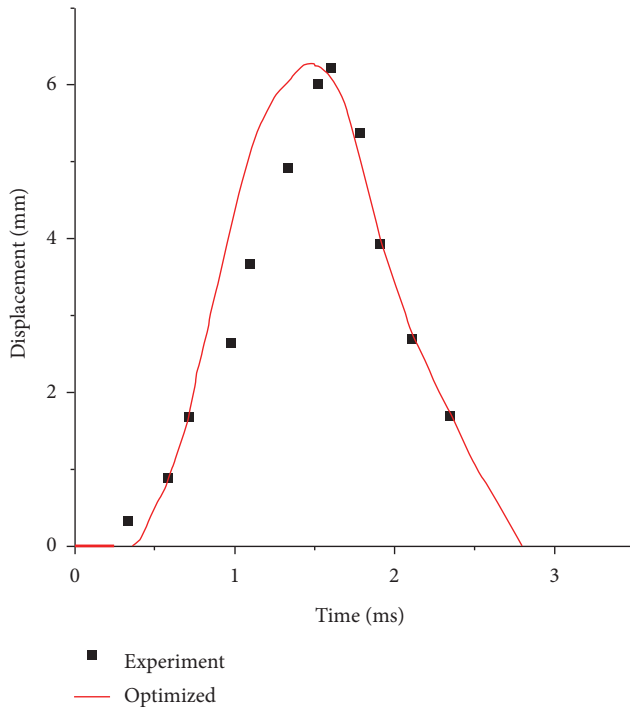


FIGURE 8: The comparison of numerical and experimental displacement of the center of the flat plate.

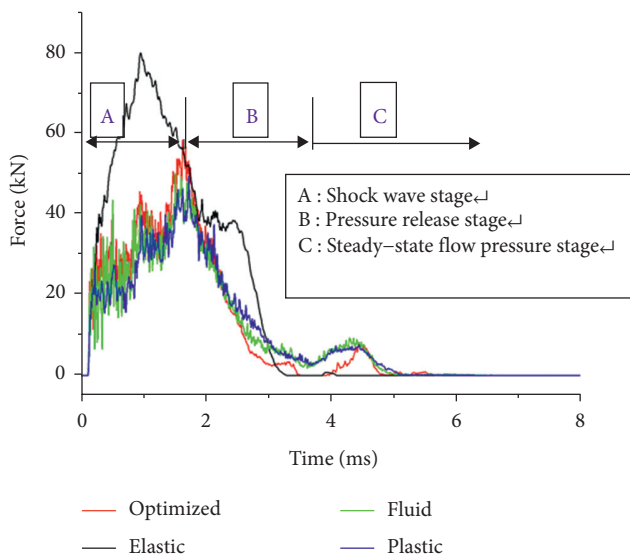


FIGURE 9: Comparisons of the force-time curves among different models.

## 5. Conclusion

In this paper, the artificial neural network model with a backpropagation learning algorithm was used to develop the constitutive relationship for the soft body during the impact process. The feasibility and practicability of this identification method were verified through a specific example. From the results of this present study, the main conclusions are drawn as follows:

- (1) Different flexible body constitutive models are used, and the impact of the soft body presents different modes, and the displacement curve and impact force curve of the aluminum plate center is also different. Among them, the displacement and impact force of the linear elastic constitutive model is the largest, but the deviation from experimental results is also the largest.
- (2) The calculated results of the soft body constitutive parameters optimized by the improved BP neural network algorithm are in good agreement with the experimental results. At the same time, it can be seen that the calculation curve optimized by BP neural network algorithm almost passes all the test points, which proves the accuracy and reliability of the optimized flexible body parameters, and the calculation convergence accuracy also meets the requirements.
- (3) As a calculation method, BP neural network can be used in the optimization calculation of constitutive parameters of soft body impact. However, it should be pointed out that each constitutive model needs to build its own neural network when it is used for calculation, and the optimization results and errors will be different due to the difference of network structure.

## Data Availability

The data used to support the findings of this study are included within the paper.

## Conflicts of Interest

The authors declare that there are no conflicts of interest regarding the publication of this paper.

## Acknowledgments

This study was funded by National Natural Science Foundation (12102095), the Scientific Research Project for Young Innovative Talents of Guangxi Province (20200312), Research grant for Talent of Guangxi Plan (100), the starting research grant for High-level Talents from Guangxi University, the Science and Technology Major Project of Guangxi Province (AA18118055), the Guangxi Natural Science Foundation (20181096), and application of key technology in building construction of prefabricated steel structure (20190528).

## References

- [1] J. Thorpe, "Update on fatalities and destroyed civil aircraft due to bird strikes with appendix for 2008 & 2009," in *Proceedings of the 29th International Bird Strike Committee Meeting*, Cairns, Australia, 2010.
- [2] D. Zhang and Q. Fei, "Effect of bird geometry and impact orientation in bird striking on a rotary jet-engine fan analysis using SPH method," *Aerospace Science and Technology*, vol. 54, no. 54, pp. 320–329, 2016.

- [3] S. Zhu, M. Tong, and Y. Wang, "Experiment and numerical simulation of a full-scale aircraft windshield subjected to bird impact," in *Proceedings of the 50th AIAA/ASME/ASCE/AHS/ASC Structures, Structural Dynamics, and Materials Conference*, Palm Springs, CA, USA, May 2009.
- [4] R. Doubrava and V. Strnad, "Bird strike analyses on the parts of aircraft structure," in *Proceedings of the 27th Congress of the International Council of the Aeronautical Sciences*, Nice, France, September 2010.
- [5] Y. K. Zhang and Y. L. Li, "Analysis of the anti-bird impact performance of typical beam-edge structure based on ANSYS/LS-DYNA," *Advanced Materials Research*, vol. 33-37, pp. 395-400, 2008.
- [6] J. L. Yang, X. J. Cai, and C. H. Wu, "Experimental and FEM study of windshield subjected to high speed bird impact," *Acta Mechanica Sinica*, vol. 19, no. 6, pp. 543-550, 2003.
- [7] F. Stoll and R. A. Brockman, "Finite element simulation of flight-speed soft-body impacts," 1997.
- [8] Y. N. Gong and S. Q. Xu, "Bird impact analysis of aircraft windshield transparency," *Chinese Journal of Aeronautics*, vol. 5, no. 2, 1992.
- [9] Y. Zhou, Y. Sun, and W. Cai, "Bird-striking damage of rotating laminates using SPH-CDM method," *Aerospace Science and Technology*, vol. 84, no. 84, pp. 265-272, 2019.
- [10] S. A. Meguid, R. H. Mao, and T. Y. Ng, "FE analysis of geometry effects of an artificial bird striking an aeroengine fan blade," *International Journal of Impact Engineering*, vol. 35, no. 6, pp. 487-498, 2008.
- [11] A. Khan, R. Kapania, and E. Johnson, "A review of soft body impact on composite structure," in *Proceedings of the 51st AIAA/ASME/ASCE/AHS/ASC Structures, Structural Dynamics, and Materials Conference 18th AIAA/ASME/AHS Adaptive Structures Conference*, Orlando, FL, USA, April 2010.
- [12] R. H. Mao, S. A. Meguid, and T. Y. Ng, "Effects of incidence angle in bird strike on integrity of aero-engine fan blade," *International Journal of Crashworthiness*, vol. 14, no. 4, pp. 295-308, 2009.
- [13] S. Q. Jia, F. S. Wang, J. J. Zhou, Z. Jiang, and B. Xu, "Study on the mechanical performances of carbon fiber/epoxy composite material subjected to dynamical compression and high temperature loads," *Composite Structures*, vol. 258, Article ID 113421, 2021.
- [14] M. Anghileri, L. L. Castelletti, and D. Molinelli, "A strategy to design bird-proof spinners," in *Proceedings of the 7th European LS-DYNA Users Conference*, Salzburg, Austria, May 2009.
- [15] M. Anghileri, L. Castelletti, and V. Mazza, "Birdstrike: approaches to the analysis of impacts with penetration," *Impact loading of lightweight structures*, vol. 49, pp. 63-74, 2005.
- [16] L. S. Nizampatnam, "Models and methods for bird strike load predictions," 2007.
- [17] M. A. McCarthy, J. R. Xiao, C. T. McCarthy et al., "Modelling of bird strike on an aircraft wing leading edge made from fibre metal laminates-part 2: modelling of impact with SPH bird model," *Applied Composite Materials*, vol. 11, no. 5, pp. 317-340, 2004.
- [18] M. A. Lavoie, A. Gakwaya, M. N. Ensan, D. G. Zimcik, and D. Nandlall, "Bird's substitute tests results and evaluation of available numerical methods," *International Journal of Impact Engineering*, vol. 36, pp. 1276-1287, 2009.
- [19] M. Nishikawa, K. Hemmi, and N. Takeda, "Finite-element simulation for modeling composite plates subjected to soft-body, high-velocity impact for application to bird-strike problem of composite fan blades," *Composite Structures*, vol. 93, no. 5, pp. 1416-1423, 2011.
- [20] L. Y. Darryl, L. C. John, M. E. Richard, and L. W. Kate, "Hazing and movements of Canada geese near Elmendorf air force base in Anchorage, Alaska," *International Biodeterioration & Biodegradation*, vol. 45, pp. 103-110, 2000.
- [21] A. F. Johnson and M. Holzap, "Modelling soft body impact on composite structures," *Composite Structures*, vol. 61, no. 1-2, pp. 103-113, 2003.
- [22] M. A. Lavoie, A. Gakwaya, and M. N. Ensan, "Validation of available approaches for numerical bird strike modeling tools," *International Review of Mechanical Engineering*, vol. 1, 2013.
- [23] F. Allaey, G. Luyckx, and W. V. Paepegem, "Characterization of real and substitute birds through experimental and numerical analysis of momentum, average impact force and residual energy in bird strike on three rigid targets: a flat plate, a wedge and a splitter," *International Journal of Impact Engineering*, vol. 99, pp. 1-13, 2017.
- [24] R. Hedayati, M. Sadighi, and M. Mohammadi-Aghdam, "On the difference of pressure readings from the numerical, experimental and theoretical results in different bird strike studies," *Aerospace Science and Technology*, vol. 32, pp. 260-266, 2014.
- [25] R. Hedayati and S. Ziaei-Rad, "A new bird model and the effect of bird geometry in impacts from various orientations," *Aerospace Science and Technology*, vol. 28, pp. 9-20, 2013.
- [26] J. Liu and Y. L. Li, "Numerical simulation of a rotary engine primary compressor impacted by bird," *Chinese Journal of Aeronautics*, vol. 4, no. 26, pp. 926-934, 2013.
- [27] J. M. Zurada, *Introduction to Artificial Neural Systems*, Jaico Publishing House, Chennai, India, 1992.
- [28] Y. Zhang and Y. Li, "Identification of the bird constitutive model," in *Proceedings of the 3rd International Conference on Mechanical Engineering and Mechanics*, Beijing China, June 2009.
- [29] K. Swingler, *Applying Neural Networks: A Practical Guide*, Morgan Kaufmann, San Francisco, CA, USA, 1996.

## Research Article

# Shaking Table Test of a New Type Insulation Decorative Block Wall under Out-of-Plane Loading

Jian Wu <sup>1,2</sup>, Yuan Yuan Lv <sup>1</sup>, Shuai Shuai Yin <sup>1</sup> and Qi Wang <sup>3</sup>

<sup>1</sup>Shaanxi Key Laboratory of Safety and Durability of Concrete Structures, Xijing University, Xi'an 710123, China

<sup>2</sup>The Youth Innovation Team of Shaanxi Universities, Xi'an 710123, China

<sup>3</sup>Zhejiang Guang'an Building Fire Inspection Co., Ltd., Hangzhou 310000, China

Correspondence should be addressed to Jian Wu; wujian2085@126.com

Received 29 July 2021; Revised 10 January 2022; Accepted 11 January 2022; Published 3 February 2022

Academic Editor: Kang Shao-Bo

Copyright © 2022 Jian Wu et al. This is an open access article distributed under the Creative Commons Attribution License, which permits unrestricted use, distribution, and reproduction in any medium, provided the original work is properly cited.

In order to solve the problems of complex construction, poor weather resistance, and environmental pollution of conventional thermal insulation materials, this paper introduces a new type of insulation decorative block (IDB) filled with insulation materials. Different anchoring methods were adopted to study the influence of anchor bolts on the out-of-plane mechanical properties of IDB walls. The test results revealed that the anchor bolts could effectively prevent the appearance and development of cracks in the specimens. With the increase of anchor bolts, the acceleration and displacement of the IDB walls decreased. Compared to rectangular arrangement, the staggered pattern of anchor bolts could reduce the relative displacement and acceleration. The structural calculation of IDB walls was carried out to determine the number of anchor bolts at different heights, and design suggestions were given to improve the performance of IDB walls. The analysis and test results indicated that the IDB is suitable for application in engineering structures.

## 1. Introduction

Nowadays, one of the problems that must be solved is how to reduce the emissions by reducing the amount of energy consumed in economic development. Based on the evaluation of energy emissions in China, the building energy consumption accounts for about 30–40% of the total energy consumption, and the trend continues to rise [1]. The maintenance components of the buildings which are in contact with the outside air, such as windows, doors, floors, and walls, are the primary reason for the energy consumption of buildings. Among these maintenance components, the walls have the largest contact area with the outdoor air, thus having the greatest impact on the building energy consumption [2]. Therefore, it is essential to take wall insulation measures to achieve the goal of the building energy saving and reduce the energy consumption of the external wall.

Thermal insulation materials are divided into organic (e.g., extruded polystyrene (XPS) and expanded polystyrene (EPS)) and inorganic materials (hydrophobic

expanded perlite (HEP)). The engineering application of XPS and EPS, as organic materials, is affected by the moisture content and high temperature: (1) the heat transfer coefficient increases with the increase of water content [3–5]; (2) the flammability of materials threatens the safety of structures [6–8]. The high temperature resistance of HEP, as an inorganic material, is relatively stable, while the thermal transfer coefficient is high due to the strong water absorption capacity. These conventional insulation materials could be used as additives in composite materials [9–12] or directly used as external thermal insulation materials of the buildings. When these insulation materials are directly used as building envelope components, structural measures and moisture control components should be proposed to improve the waterproof and fireproof properties of the materials during the construction process [13–15], which increases the construction cost and construction period. In order to deal with the defects of these conventional insulation materials in engineering application, the research on the building insulation materials should be strengthened.

A new type of thermal insulation blocks, which have high void ratio, is developed and used as the external walls of building [16–18]. The high void ratio of insulation block is helpful to reduce the dead weight and heat transfer coefficient; however, the compressive strength will be adversely affected due to the decrease of compression area. Moreover, the reinforced concrete shear walls are generally used as the external walls of high-rise buildings, indicating that it is impossible to apply the thermal insulation blocks directly. Thus, masonry veneer walls are gradually used in modern building construction. Masonry veneer walls, which consist of external masonry walls separated from the structural backing systems, are connected to the structural components using different types of ties to resist out-of-plane loads [19] and could provide the buildings with decoration and with barriers to moisture wind penetration but do not contribute to the structural resistance [20]. Desai et al. [21] studied the out-of-plane seismic properties of brick veneer wall systems in medium-rise buildings and developed analytical models of structural backing systems and masonry veneer walls. Reneckis et al. [22] described the out-of-plane performance of brick veneer walls on wood frame, and the installation methods, stiffness, and strength were found to significantly affect the seismic performance of veneer walls. Memari et al. [23] evaluated the influence of corrosion of conventional metal anchors on lateral forces, and the performances of corrosion resistant steel ties and conventional ties were compared. Marziale et al. [24] investigated the in-plane coupling between the veneer walls and concrete shear walls, and the optimum location of isolation joint was given to minimize the rocking behavior. These papers provide a reference for the study of mechanical properties of masonry veneer walls; however, the out-of-plane dynamic performance of the walls made of insulation filled masonry blocks is rarely addressed.

This paper presents the results of out-of-plane shaking table test of four full-scale specimens, which are divided by the number and arrangement modes of anchor bolts between the masonry veneer walls and backup framing (reinforced concrete walls): AB0 has no anchor bolts, AB2 is strengthened by two anchor bolts per square meter, and AB4-1 and AB4-2 are strengthened by four anchor bolts per square meter with different arrangement modes.

The structure of this paper is as follows: Firstly, the materials and experimental program, such as the dimension of the IDB, construction of specimens, arrangement of anchor bolts, and test setup, are introduced. Secondly, the mechanical tests are carried out, and the mechanical performance of specimens is obtained and analyzed, e.g., the failure pattern, development of cracks, frequency, acceleration, displacement of the specimens, and relative displacement between the IDB wall and shear wall. Finally, the reaction of IDB walls under wind load and seismic load is calculated, and design recommendations are proposed to improve the application of IDB in engineering.

## 2. Experimental Program

*2.1. Masonry Materials.* The block is made of shale and sawdust, in which the sawdust could produce a large amount of microporous inside the material, as shown in Figure 1.

The IDB is filled with conventional composite thermal insulation materials, such as XPS, EPS, and HEP, so as to achieve insulation purposes. The dimensions of the IDB are 498 mm × 120 mm × 248 mm (length × width × height), as shown in Figure 2. The density and compressive strength of the IDB are about 500 kg/m<sup>3</sup> and 2.0 MPa, respectively.

The content of mortar is cement, fly ash, sand, polymer emulsion powder, and water retaining agent. The mechanical and physical characteristics of mortar are shown in Table 1.

The anchor bolts are used to ensure the bond strength between the IDB wall and the external wall of buildings. The diameter of anchor bolt is 10 mm, and tensile strength is 0.5 MPa. The length of the anchor bolt fixed into the reinforced concrete shear wall should not be less than 50 mm.

*2.2. Construction of Specimens.* In this paper, four full-scale specimens are tested under out-of-plane dynamic loadings. The specimens are composed of ground beam, shear wall, mortar layer, and IDB walls, as shown in Figure 3.

The ground beam is used to fix the specimen on the shaking table, and the shear wall is constructed to simulate the exterior wall of the high-rise building. Materials of leveling blanket and mortar layer are both masonry mortar. The mortar layer is used to strengthen the bond between the shear wall and IDB wall. The thickness of leveling blanket, mortar layer, and mortar joint is 1–2 mm, 10 mm, and 1 mm, respectively.

The construction process of the specimens could be seen in Figure 4.

*2.3. The Arrangement of Anchor Bolt.* In order to study the influence of number and distribution of anchor bolts on the out-of-plane seismic response of the specimen, the experimental program consists of four specimens, in which one specimen has no anchor bolts, one specimen has two anchor bolts per square meter, and two specimens have four anchor bolts per unit area with different arrangement modes of anchor bolts, as shown in Figure 5. The IDB is made of sintered materials, and its brittle failure characteristics are obvious. If the anchor bolts are directly drilled on the IDB, the safety of IDB wall may be affected due to the damage caused by the drilling process.

## 3. Testing Procedure and Measurements

*3.1. Test Setup.* The performance parameters of the shaking table are shown in Table 2. The digital control system of shaking table (469D) consists of signal control of hydraulic servo system, sequence control of system procedure, and system security protection control, as shown in Figure 6.

The experiments were carried out according to Chinese code GB 50011-2010 [25]. For the normal operation of the test, the out-of-plane loading of the specimen is performed along the  $x$  direction.

In order to obtain the displacement and acceleration of the wall during the loading process, acceleration sensor and

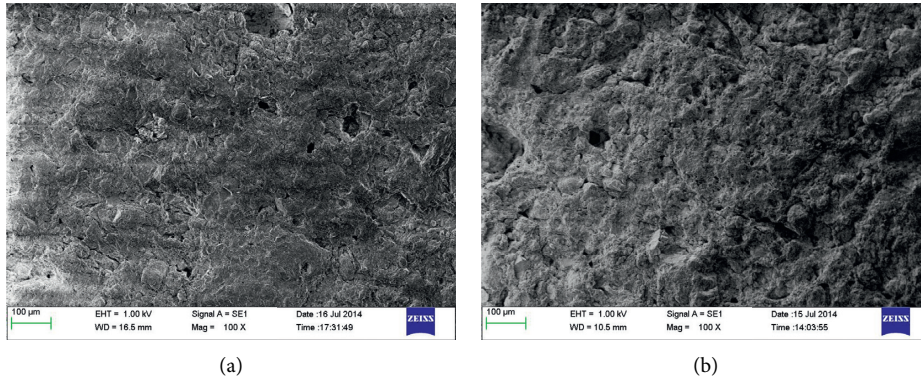


FIGURE 1: SEM graphs of sample. (a) Sintering shale sample. (b) Sintering shale sample with 6% sawdust.

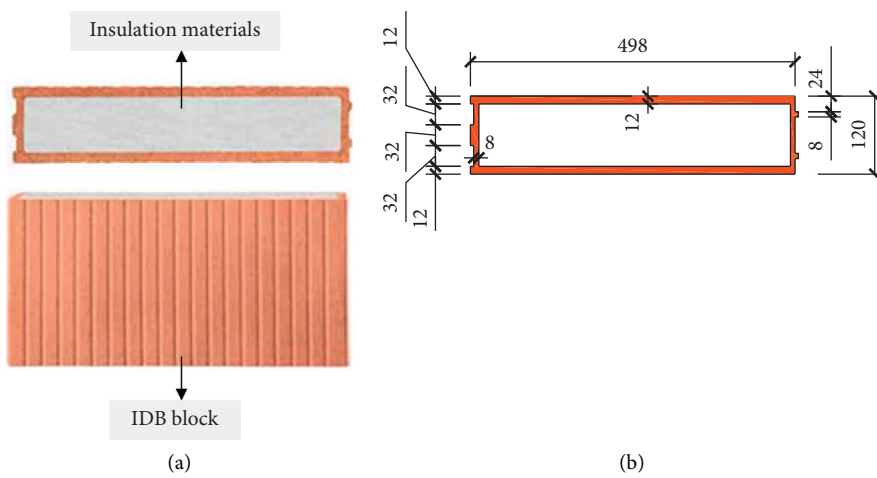


FIGURE 2: Introduction of IDB. (a) Components of IDB. (b) Dimensions of IDB.

TABLE 1: Performance parameters of mortar.

Bond strength (N/mm <sup>2</sup> )	Compressive strength (N/mm <sup>2</sup> )	Flexural strength (N/mm <sup>2</sup> )	Density (kg/m <sup>3</sup> )
0.1	15	12	1800

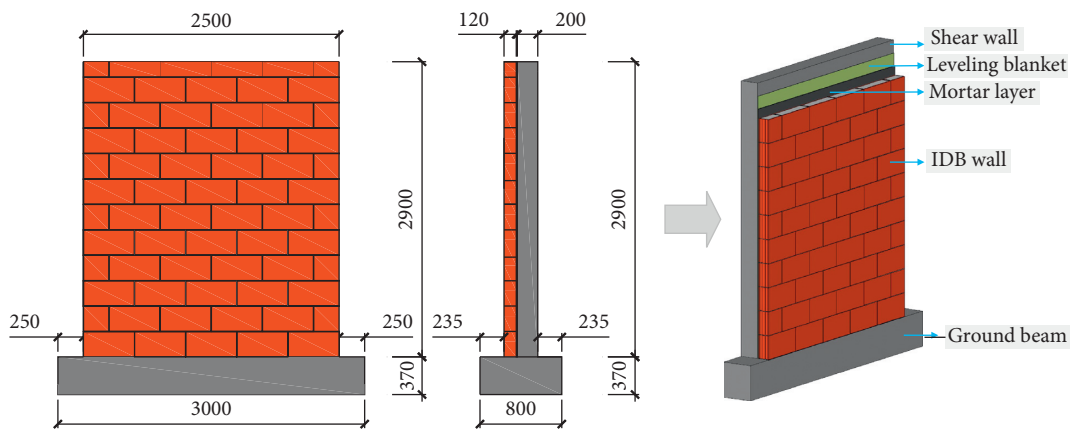


FIGURE 3: Dimensions of the specimens.



FIGURE 4: Construction process of specimens.

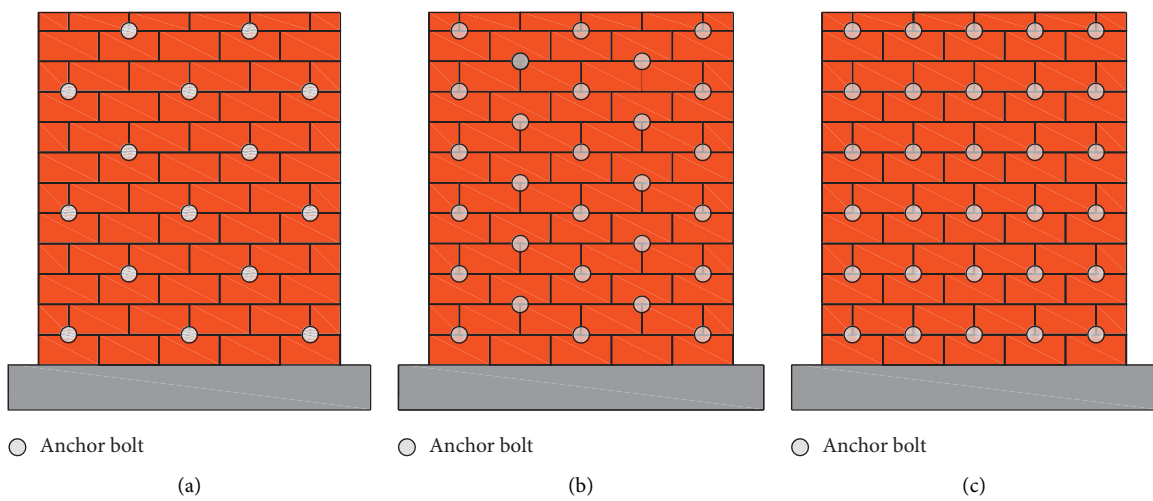


FIGURE 5: The arrangement of anchor bolts. (a) AB2. (b) AB4-1. (c) AB4-2.

TABLE 2: Technical parameters of shaking table.

Performance of shaking table	Parameter value
The dimensions of the table (m)	4.1 × 4.1
Maximum weight of the specimen (t)	20
Maximum eccentricity (m)	≥0.6
Frequency (Hz)	0.1–50
Maximum displacement (m)	x direction: ±0.15 y direction: ±0.25 z direction: ±0.10
Maximum speed (m/s)	x direction: ±0.100 y direction: ±0.125 z direction: ±0.080
Maximum acceleration (m/s <sup>2</sup> )	x direction: ±15 y direction: ±10 z direction: ±10
Maximum overturning moment (kN·m)	300
Maximum eccentric moment (kN·m)	800

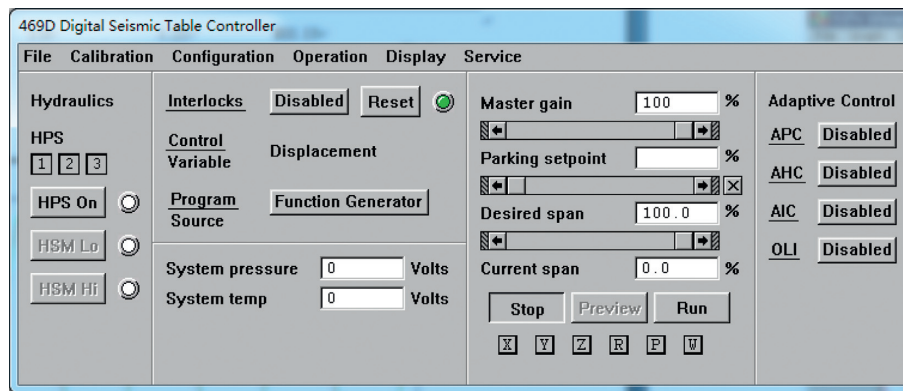


FIGURE 6: Shaking table.

displacement sensor are arranged on the specimens, as shown in Figure 7. The measure range and sensitivity of the acceleration sensor are 100 g and 10 mV/g, respectively, while the measure range and sensitivity of the displacement sensor are 50 mm and 0.1  $\mu\text{m}$ .

**3.2. Testing Procedure.** Three earthquake records, namely, two real earthquake ground motion records (El-Centro record and Taft record) and one artificial earthquake ground motion record (Ninghe record), were applied in horizontal direction. The earthquake records were selected because the characteristic periods of the earthquake records are close to the different characteristic site periods prescribed by the Chinese seismic code [25] (Table 3). The acceleration time-history curves of earthquake records are given in Figure 8.

Table 4 shows the loading process. The natural frequencies could be obtained through white noise scanning, and the accelerogram of the earthquake record was scaled in amplitude to 0.20 g, 0.30 g, 0.40 g, 0.50 g, 0.60 g, 0.70 g, and 0.80 g to satisfy the test requirements. Considering that the

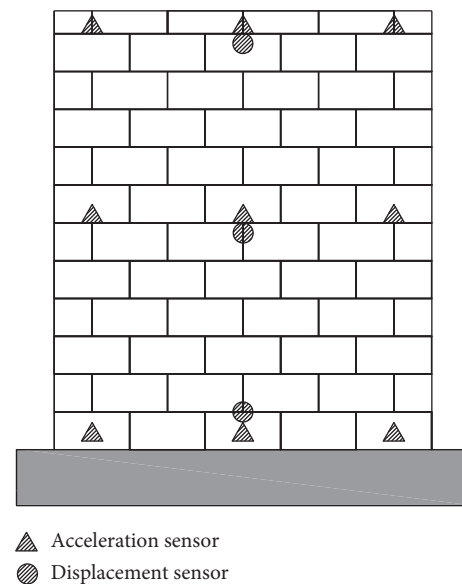


FIGURE 7: Instrumentation arrangement.

TABLE 3: Earthquake records and characteristic site period.

Earthquake	Direction	Time	Characteristic period (s)	Characteristic site period (s)
Taft record	E-W	1952.7.21	0.44	0.40
El-Centro record	N-S	1940.5.18	0.55	0.55
Ninghe record	N-S	1976.11.15	0.90	0.75

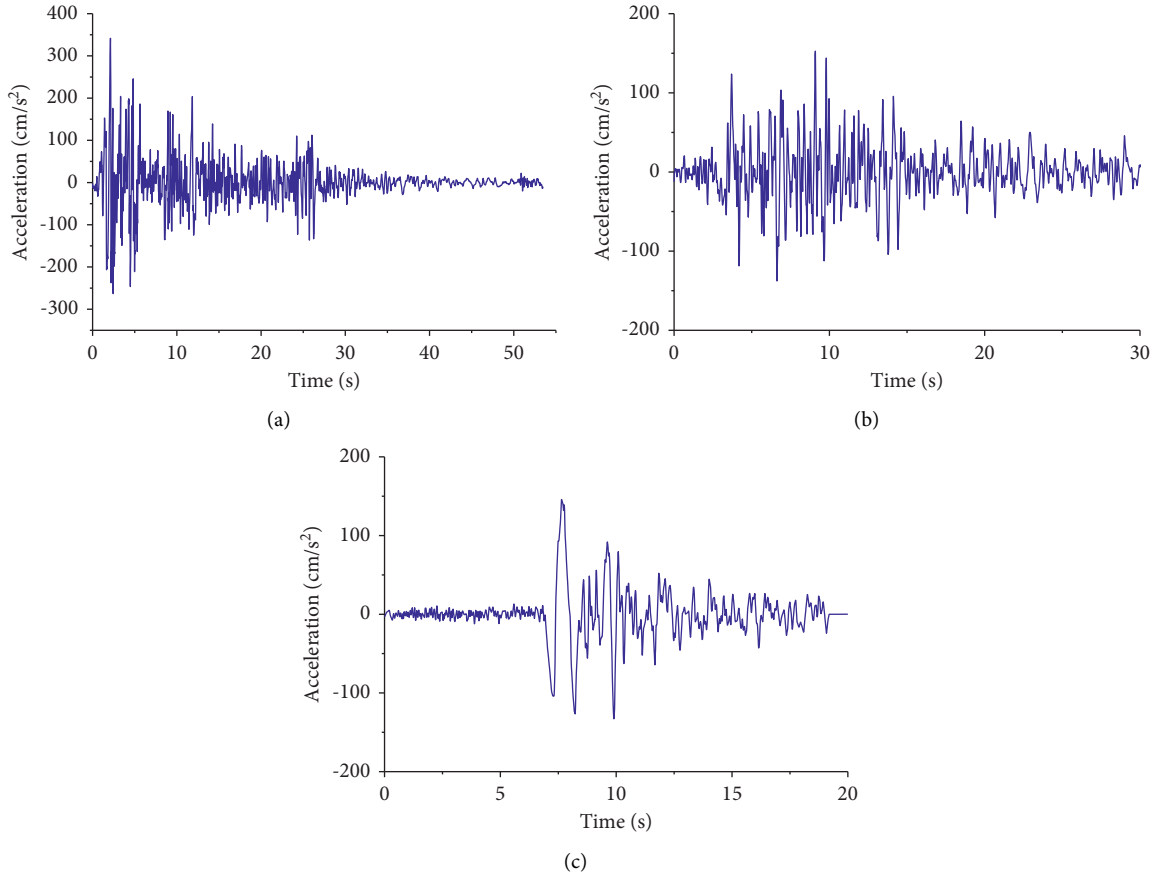


FIGURE 8: Acceleration time-history curves of earthquakes. (a) El-Centro record. (b) Taft record. (c) Ninghe record.

characteristic site period in a lot of cities of China is 0.55 s, El-Centro record is selected for elastic-plastic analysis.

## 4. Results and Discussion

**4.1. Experimental Observation and Failure Modes.** The failure pattern of the specimens is described in Table 5. The cracks on the IDB wall and IDB wall boundaries were measured. It could be concluded that the crack usually appeared firstly at the bottom of the IDB wall, and as the PGA increased, cracks began to appear in the top corner of the specimen. The cracks mainly appeared at the joint of the IDB wall, ground beam, and shear wall, and there were basically no cracks in the interior of the IDB wall. During the loading process, there was no block crushing or block peeling from the specimen.

The crack length in the top corner of the specimen reduced from 1100 mm (AB0) to 670 mm (AB4-1), and the crack width decreased with the increase of the number of anchor bolts, meaning that the anchor bolt could effectively

limit the development of cracks. Since the crack width and length of AB4-1 were smaller than AB4-2, it could be inferred that the arrangement mode had an influence on the out-of-plane mechanical performance of the IDB wall.

**4.2. Frequency of Specimens.** The natural frequencies of specimens can be obtained through white noise scanning, as given in Figure 9. When the PGA was not more than 0.20 g (AB0 and AB2) or 0.50 g (AB4-1 and AB4-2), the change of natural frequencies of the specimens was small. As the PGA continued to increase, the natural frequencies of the four specimens began to decrease significantly. For instance, when the PGA was 0.8 g, the decrease amplitude of the natural frequency of was 25.6% for AB0, 22.4% for AB2, 11.2% for AB4-1, and 12.3% for AB4-2. The following could be concluded:

- (1) The anchor bolts could effectively prevent the specimens from damage. That is for the reason that



TABLE 4: Loading procedure.

Number	Loading condition	PGA (g)
1	White noise	0.05
2	El-Centro wave	0.05
3	Taft wave	0.05
4	Ninghe wave	0.05
5	White noise	0.05
6	El-Centro wave	0.10
7	Taft wave	0.10
8	Ninghe wave	0.10
9	White noise	0.05
10	El-Centro wave	0.15
11	El-Centro wave	0.20
12	White noise	0.05
13	El-Centro wave	0.30
14	El-Centro wave	0.40
15	El-Centro wave	0.50
16	White noise	0.05
17	El-Centro wave	0.60
18	El-Centro wave	0.70
19	El-Centro wave	0.80
20	White noise	0.05
21	Two consecutive EL-Centro waves	0.80
22	White noise	0.05

TABLE 5: Test observations and failure pattern.


Specimen	Test phenomenon	Remarks/observations
AB0		<p>(i) The crack appeared firstly at the bottom of the IDB wall when the PGA was 0.3 g.</p> <p>(ii) Cracks appeared in the top corner of the IDB wall when the PGA was 0.4 g.</p> <p>(iii) At the end of the experiment, the length and width of the crack in the top corner of the specimen were 1150 mm and 3.0 mm, respectively. The crack at the bottom of the IDB wall, with a width of 2.5 mm, was basically a through crack.</p>

TABLE 5: Continued.




Specimen	Test phenomenon	Remarks/observations
AB2		<p>(i) Cracks appeared firstly in the top corner of the specimen and at the bottom of the IDB wall when PGA was 0.4 g.</p> <p>(ii) After the loading process, the length and width of the crack in the top corner of the specimen were 1000 mm and 2.5 mm, respectively, and the crack at the bottom of the IDB wall, with a width of 2.0 mm, was basically a through crack.</p>
AB4-1		<p>(i) Cracks appeared firstly in the top corner of the specimen and at the bottom of the IDB wall when PGA was 0.5 g.</p> <p>(ii) After the loading process, the length and width of the crack in the top corner of the specimen were 670 mm and 1.0 mm, respectively, and the crack at the bottom of the IDB wall, with a width of 1.5 mm, was basically a through crack.</p>

TABLE 5: Continued.

Specimen	Test phenomenon	Remarks/observations
AB4-2		<p>(i) Cracks appeared firstly in the lower part and top corner of the IDB wall when PGA was 0.5 g.</p> <p>(ii) After the loading process, the length and width of the crack in the top corner of the specimen were 850 mm and 2.0 mm, respectively, and the crack at the bottom of the IDB wall, with a width of 1.8 mm, was basically a through crack.</p>

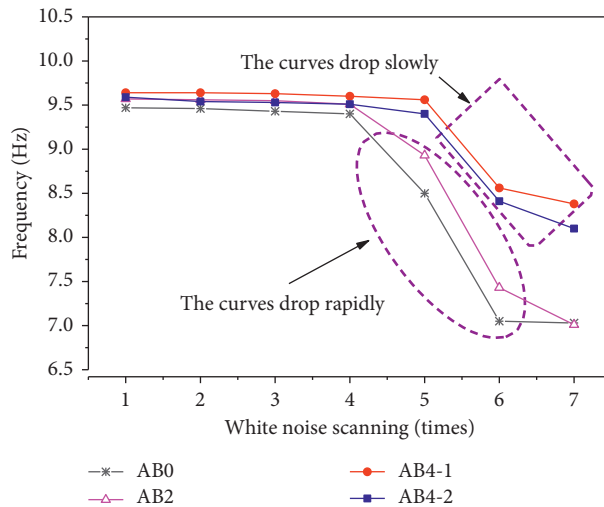


FIGURE 9: Natural frequency of the specimens.

the natural frequency of the specimen was related to the degree of damage; the more serious the damage, the smaller the natural frequency.

- (2) Although the number of the anchor bolts was the same, the reduction amplitude of natural frequency of AB4-1 was smaller than that of AB4-2, meaning that arrangement mode of anchor bolts had an influence on preventing the structure failure.

4.3. Acceleration Response Analysis. The acceleration at the bottom of the IDB wall was basically the same as the input acceleration, so this paper only gives the peak acceleration in

the middle-upper part of the IDB wall, as shown in Figure 10.

Although the cracks appeared and developed at the bottom of the IDB wall, the acceleration in the middle of the IDB wall increased linearly (Figure 10(a)), and the magnification coefficient of the acceleration response was about 1.3. The reason for these results could be that almost no cracks appeared between the IDB wall and shear wall, and the lower part of the specimens was still subjected to the out-of-plane load as a whole. However, at the top of the specimens, the cracks mainly appeared between the IDB wall and the shear wall, causing the magnification coefficient of the acceleration response to increase suddenly (Figure 10(b)).

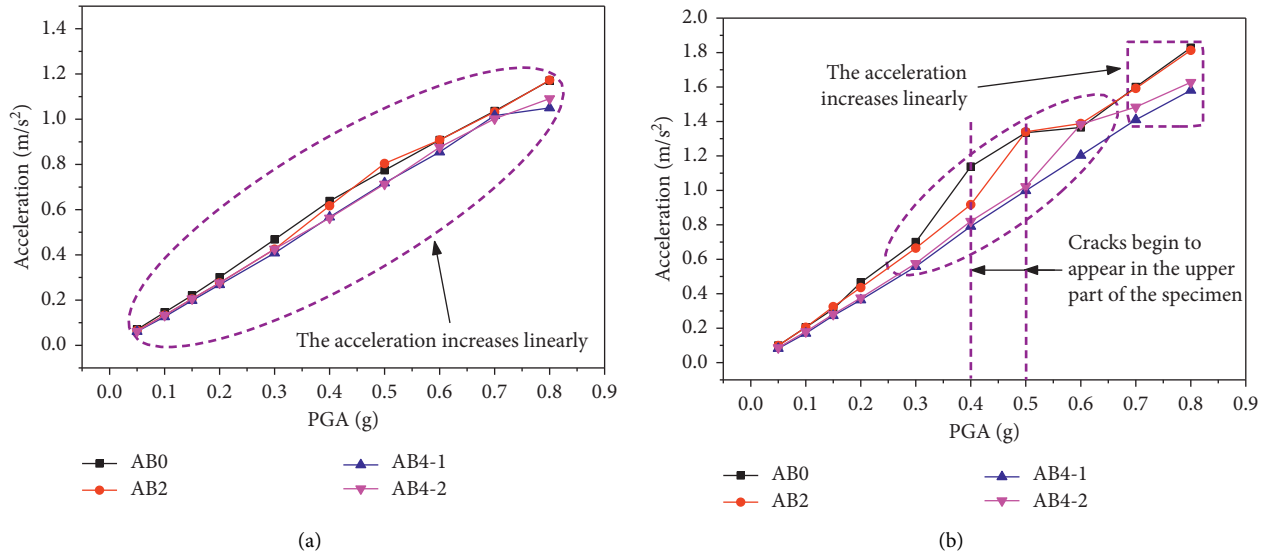


FIGURE 10: Peak acceleration of IDB wall at different positions. (a) In the middle of the IDB wall. (b) At the top of the IDB wall.

For instance, the acceleration at the top of AB0 increased linearly when the PGA was smaller than 0.4 g. As the earthquake load increased, the cracks between the IDB wall and shear wall began to appear and develop, and the magnification coefficient of the acceleration response increased from 6.7 to 9.1 when the PGA was 0.40 g and from 9.1 to 11.1 when the PGA was 0.50 g. It could also be concluded that when the crack width was small, it did not affect the global stress of the specimens. For instance, at the top of the AB4-1, the maximum width of crack between IDB wall and shear wall was only 1.0 mm, and the acceleration increased linearly all the time during the loading process.

**4.4. Displacement Response Analysis.** In order to study the seismic performance of the IDB wall, the relative displacement and maximum displacement of the IDB walls are studied. The relative displacement is the difference between IDB wall and shear wall displacements, while the maximum displacement is the difference between the middle-upper and lower displacement of the IDB wall.

The relative displacements between IDB wall and shear wall are depicted in Figure 11. Since the relative displacement at the bottom of the specimen was small, only the relative displacement of the middle-upper part of the specimen was given in Figure 11.

In the middle of the specimen, it could be observed that although the maximum relative displacement was 0.96 mm, no visible cracks appeared (Table 4). For AB0 and AB2, the relative displacement increased linearly until cracks appeared at the top of the specimens, while for AB4-1 and AB4-2, the relative displacement increased linearly all the time, which was not affected by the cracks at the top of the specimen.

At the top of the specimen, the relative displacement could directly reflect the appearance and development of the cracks. Take AB0 as example; the crack appeared firstly when

the PGA was 0.4 g, after which the relative displacement increased rapidly with the development of the cracks.

The maximum displacements of IDB wall under different conditions of PGA are given in Figure 12. From Figure 12, it could be concluded that the displacements of AB0 and AB2 were affected by the cracking at the bottom of the specimens. Once the crack appeared at the bottom of AB0 and AB2, the displacement of the specimens would increase rapidly. While for AB4-1 and AB4-2, the displacement was basically linearly increasing.

Through the analysis of Figures 11 and 12, it could be inferred that the displacement response of the IDB wall was closely related to the appearance and development of the cracks. This phenomenon was more obvious in AB0 and AB2; the displacement or relative displacement would increase rapidly after the appearance and development of the cracks. However, for AB4-1 and AB4-2, the displacement response was basically linear.

## 5. Structural Calculation and Recommendations

**5.1. Structural Calculation.** Restricted by the experimental conditions, this paper only studied the out-of-plane seismic performance of IDB walls. However, in engineering practice, we should not ignore the wind load effect on the mechanical performance of brick veneer walls. Therefore, wind load and seismic load should be considered simultaneously in structural calculation.

**5.1.1. Calculation of Seismic Action.** According to Chinese code GB 50011-2010 [25], equivalent lateral-force method can be used to evaluate the seismic load caused by the gravity of nonstructural components. Thus, the seismic load of IDB walls could be calculated as follows:

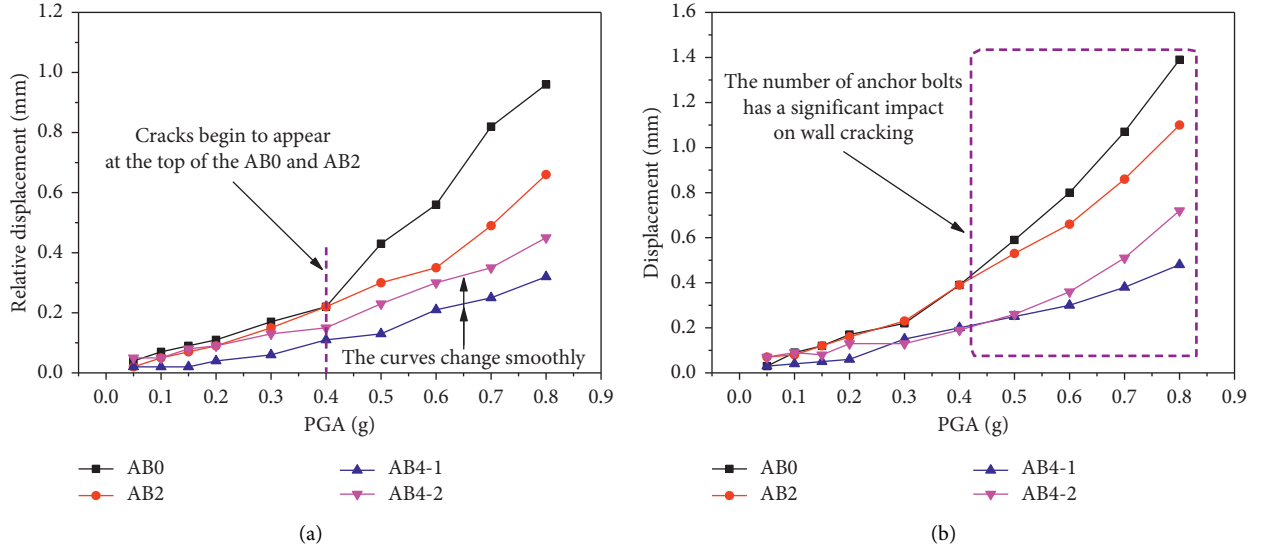


FIGURE 11: Relative displacement between IDB wall and shear wall. (a) In the middle of the specimen. (b) At the top of the specimen.

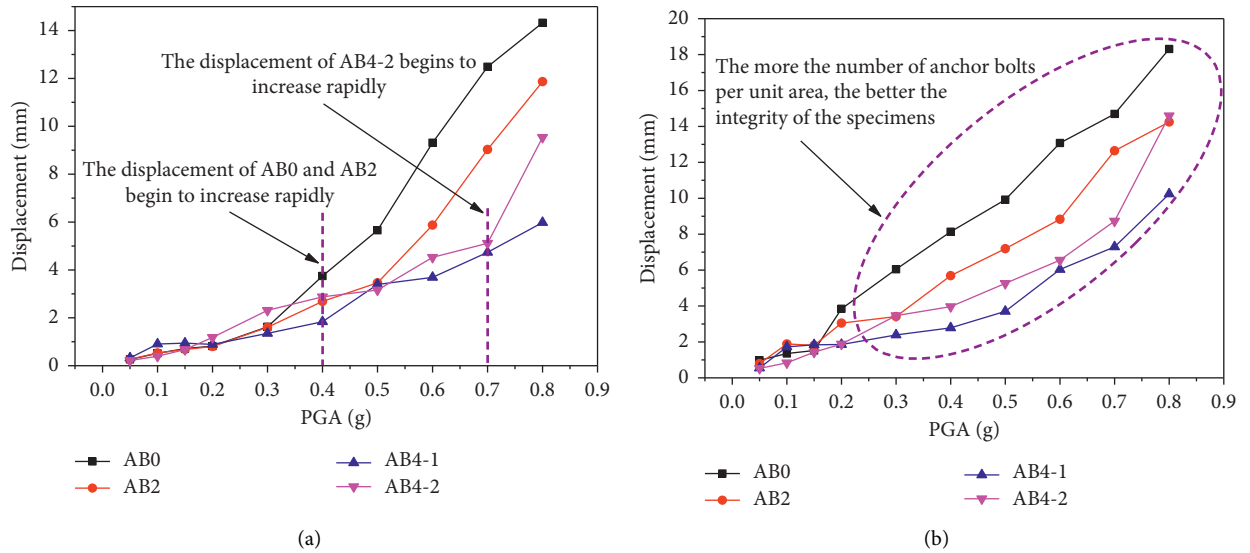


FIGURE 12: Displacement of IDB wall at different positions. (a) In the middle of the IDB wall. (b) At the top of the IDB wall.

$$F = \gamma\eta\zeta_1\zeta_2\alpha_{\max}G, \quad (1)$$

where  $\gamma$  is the functional factor of the nonstructural components and equals 1.0;  $\eta$  is the type factor of the nonstructural components and equals 1.0;  $\zeta_1$  and  $\zeta_2$  are the factor of state and location and equal 1.0 and 2.0, respectively;  $\alpha_{\max}$  is the maximum value of seismic influence coefficient and equals 0.16; and  $G$  is the gravity of nonstructural components (Table 6).

**5.1.2. Calculation of Wind Load.** The characteristic value of wind load is shown in the following equations [26]:

$$w_k = \beta_{gz}\mu_{sl}\mu_z w_0, \quad (2)$$

$$\beta_{gz} = 0.80 + 1.60\mu_f, \quad (3)$$

$$\mu_f = 0.5 \times 35^{1.8(\alpha-0.16)} \left(\frac{10}{z}\right)^\alpha, \quad (4)$$

$$\mu_z = 0.262 \left(\frac{z}{10}\right)^{0.62}, \quad (5)$$

in which  $\beta_{gz}$  is gust factor at height  $z$ ,  $\mu_{sl}$  is local shape coefficient,  $\mu_z$  is wind pressure height coefficient,  $w_0$  is basic

TABLE 6: Gravity of IDB wall insulation system.

	Mortar layer	IDB wall	Decoration layer
Thickness (mm)	10	120	—
Density (kg/m <sup>3</sup> )	1500	500	—
Gravity (N/m <sup>2</sup> )	147	588	44
Total gravity (N/m <sup>2</sup> )		779	

TABLE 7: The characteristic value of wind load at different heights.

Height (m)	$\omega_0$ (kN/m <sup>2</sup> )	$\beta_{gz}$	$\mu_z$	$\mu_{sl}$		$\omega_k$ (kN/m <sup>2</sup> )	
				Positive angle of buildings	Other locations	Positive angle of buildings	Other locations
20		2.40	0.51			1.51	2.15
50		2.20	0.69			1.87	2.67
80		2.04	0.91			2.29	3.27
100	0.88	1.98	1.04	-2.0	-1.4	2.54	3.62
150		1.87	1.33			3.06	4.38
200		1.79	1.58			3.48	4.98
250		1.74	1.81			3.88	5.54
300		1.70	2.02			4.23	6.04

TABLE 8: The number of anchor bolts.

Height (m)	Number of anchors per square meter	
	Positive angle of buildings	Other locations
≤ 20	2	4
20	4	5
50	4	6
80	5	7
100	6	8
150	7	10
200	8	11
250	9	13
300	10	14

wind pressure,  $\mu_f$  is pulsation coefficient, and  $\alpha$  is ground roughness index.

The wind load of maintenance structure for high-rise buildings is mainly wind suction, and the wind suction at the positive angle of buildings is larger than the wind suction at other locations [27]. The determination of coefficients in (2)–(5) is described in Table 7.

According to Chinese code GB 50009-2012 [26], the combination of earthquake and wind load can be expressed as

$$S = \gamma_{Q_1} S_{Q_1,k} + \gamma_{Q_2} \psi_c S_{Q_2,k} \quad (6)$$

Here, 1 and 2 represent wind and earthquake load, respectively;  $S_{Q_1,k}$  is load effect value calculated by  $w_k$ ;  $S_{Q_2,k}$  is load effect value calculated by  $F$ ;  $\gamma_{Q_1}$  and  $\gamma_{Q_2}$  are partial coefficients of load and equal 1.4 and 1.3, respectively; and  $\psi_c$  is combination value coefficient and equals 0.6.

The formula for calculating the number of anchor bolts per unit area can be given as

$$[n] = \alpha \gamma_M \frac{S}{k f_t} \quad (7)$$

where  $\alpha$  is the reduction factor considering the connection between mortar and IDB wall and equals 0.5,  $\gamma_M$  is the

anchor connection importance coefficient and equals 1.1,  $k$  is the anchorage capacity reduction coefficient under earthquake and equals 0.7, and  $f_t$  is the design value of tensile bearing capacity of anchor bolts.

Based on (1)–(7), the number of anchor bolts to be arranged at different heights is shown in Table 8. The results show that the number of anchor bolts in the test could meet the application requirements of IDB in high-rise buildings and has a good reference value.

**5.2. Recommendations.** According to the destruction features of the specimens during the test process, cracks mainly occurred at the bottom of the IDB wall and in the top corner of the specimen. When the PGA was small (0.3–0.5 g), cracks firstly appeared and developed between the IDB wall and ground beam, which was due to the bending effect of the specimens under the out-of-plane load. Premature cracks had a negative impact on the insulation effect of the IDB wall, so the bottom of the IDB wall needs to be effectively treated.

As the PGA increased, cracks began to appear between the IDB wall and the shear wall on both sides of the top of the specimens. Besides, the IDB walls were also subjected to wind loads in engineering application, and the suction in the

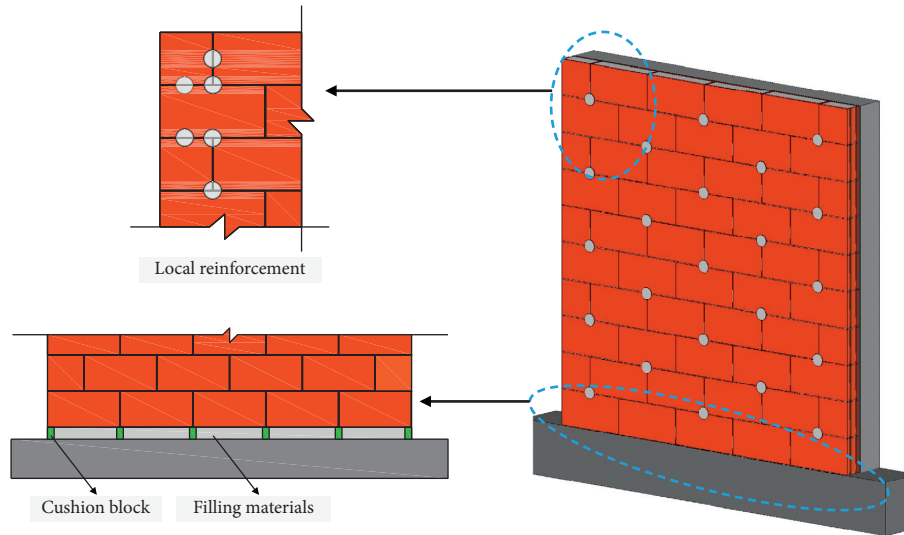


FIGURE 13: Design suggestion.

top corner, generated by negative wind pressure, was larger than that at other positions [27]; hence, attention should be paid to the reinforcement of the top corner in the structural design.

Thus, some recommendations are put forward in this paper, as shown in Figure 13.

- (1) In order to prevent the cracks at the bottom of the IDB wall from occurring too early under the action of bending, cushion blocks with certain deformation ability, such as rubber block or wooden block, should be used to bear the dead weight of the IDB wall. Foaming agent can be used as filling materials to improve the insulation performance of IDB wall.
- (2) In order to prevent cracks in the top corner of the wall from affecting the thermal insulation performance of the IDB wall, more anchor bolts should be used to strengthen the bonding between the IDB wall and shear wall at this location.

## 6. Conclusions

Shaking table tests are carried out on four specimens to investigate the out-of-plane performance of IDB walls. Failure mechanisms, frequencies, acceleration, and displacement (relative displacement) are evaluated, and the performance of anchorage mode is examined. The calculation formula of the number of anchor bolts and design suggestions are also given based on the experimental phenomena, so as to promote the application of IDB in engineering. The results obtained from the tests are briefly summarized as below:

- (1) Appearance and development of cracks between the IDB wall and shear wall are obviously affected by the number of the anchor bolts. The larger the number of anchor bolts, the smaller the seismic load at the time

of crack appearance, the shorter the crack length, and the smaller the crack width.

- (2) The anchor bolts could obviously improve the out-of-plane mechanical performance of IDB walls. Take AB0 and AB2 as example; when the seismic action is the same, the natural frequency of AB2 is larger, and the acceleration and displacement (relative displacement) are smaller.
- (3) Although the number of anchor bolts is the same, the displacement (relative displacement) and acceleration of AB4-1 are smaller than those of AB4-2, showing that the staggered pattern of the anchor bolts is a better arrangement method than rectangular arrangement.
- (4) The positive angle of the buildings should be strengthened to reduce the damage of IDB walls, and the calculation formula of the number of anchor bolts could be applied in the process of design.

Based on the test results (acceleration, displacement, and failure mode) and structural calculation, the acceleration and displacement requirements of different types of buildings could be satisfied through adjusting the number and arrangement of anchor bolts. Therefore, the study of this paper could effectively promote the application of IDB.

Computational intelligence algorithms, such as monarch butterfly optimization (MBO) [28], neutrosophic optimization (NSO) [29], artificial bee colony (ABC) [30], and ant colony algorithm (ACA) [31], are gradually used to analyze the seismic response of the structures, so as to optimize the structural design and improve the seismic performance of structures. However, the impact of these intelligent algorithms has not been considered in the specification; thus, considering the engineering application of IDB, the structural analysis method used in this paper is specified by Chinese code GB 50011-2010 [25]. Considering the optimal design of structures, the

intelligent algorithms will be used to analyze the seismic performance of structures with IDB walls in subsequent studies.

## Data Availability

The data that support the findings of this study are available on request from the corresponding author.

## Conflicts of Interest

The authors declare that they do not have any commercial or associative interest that represents conflicts of interest in connection with the work submitted.

## Acknowledgments

This research was supported by the Natural Science Foundation of Shaanxi Province (2021JQ-876) and Scientific Research Foundation for High-Level Talents (XJ17T08). The authors would like to thank Shaanxi Key Laboratory of Safety and Durability of Concrete Structures for the project testing.

## References

- [1] L. Fang, "Problems in building energy saving and application of energy saving construction technology," *Construction Material Decoration*, no. 38, pp. 41–42, 2017, in Chinese.
- [2] S. L. Yang, *Experimental Research on Bonding Behavior between XPS Insulation Board Layer and Structure Layer*, Master thesis, Wuhan University of Technology, Wuhan, China, 2011.
- [3] J. H. Crandell, "Below-ground performance of rigid polystyrene foam insulation: review of effective thermal resistivity values used in ASCE standard 32-01-design and construction of frost-protected shallow foundations," *Journal of Cold Regions Engineering*, vol. 24, no. 2, pp. 35–53, 2010.
- [4] T. Mcfadden, "Thermal performance degradation of wet insulations in cold regions," *Journal of Cold Regions Engineering*, vol. 2, no. 1, pp. 25–34, 1988.
- [5] M. Kehrer, H. Kuenzel, and K. Sedlbauer, "Ecological insulation materials—does sorption moisture affect their insulation performance?" *Journal of Thermal Envelope and Building Science*, vol. 26, no. 3, pp. 207–212, 2002.
- [6] L. Wang, C. Wang, P. Liu, Z. Jing, X. Ge, and Y. Jiang, "The flame resistance properties of expandable polystyrene foams coated with a cheap and effective barrier layer," *Construction and Building Materials*, vol. 176, pp. 403–414, 2018.
- [7] L. Jiang, D. Zhang, M. Li et al., "Pyrolytic behavior of waste extruded polystyrene and rigid polyurethane by multi kinetics methods and Py-GC/MS," *Fuel*, vol. 222, pp. 11–20, 2018.
- [8] Y. Zhou, R. Bu, J. Gong, W. Yan, and C. Fan, "Experimental investigation on downward flame spread over rigid polyurethane and extruded polystyrene foams," *Experimental Thermal and Fluid Science*, vol. 92, pp. 346–352, 2018.
- [9] A. A. Sayadi, J. V. Tapia, T. R. Neitzert, and G. C. Clifton, "Effects of expanded polystyrene (EPS) particles on fire resistance, thermal conductivity and compressive strength of foamed concrete," *Construction and Building Materials*, vol. 112, pp. 716–724, 2016.
- [10] T. Masri, H. Ounis, L. Sedira, A. Kaci, and A. Benchabane, "Characterization of new composite material based on date palm leaflets and expanded polystyrene wastes," *Construction and Building Materials*, vol. 164, pp. 410–418, 2018.
- [11] A. San-Antonio-González, M. D. R. Merino, C. V. Arrebola, and P. Villoria-Sáez, "Lightweight material made with gypsum and extruded polystyrene waste with enhanced thermal behaviour," *Construction and Building Materials*, vol. 93, pp. 57–63, 2015.
- [12] S. Ramakrishnan, X. Wang, J. Sanjayan, and J. Wilson, "Thermal performance assessment of phase change material integrated cementitious composites in buildings: experimental and numerical approach," *Applied Energy*, vol. 207, pp. 654–664, 2017.
- [13] Gb/T 30595-2014(Code of China), *External thermal Insulation Composite Systems Based on Extruded Polystyrene*, China Architecture and Building Press, Beijing, China, 2014, in Chinese.
- [14] Db21/T 1271-2003(Code of China), *Technical Specification for Exterior wall Outer thermal Insulation Based on EPS Board*, China Architecture and Building Press, Beijing, China, 2003, in Chinese.
- [15] Db34/T 5078-2017(Code of China), *Technical Specification for Application of Expanded Perlite Insulation Board Thermal Insulation Project on Building*, Anhui Engineering Construction Standard Design Office, Hefei, China, 2017, in Chinese.
- [16] K. S. Al-Jabri, A. W. Hago, A. S. Al-Nuaimi, and A. H. Al-Saidy, "Concrete blocks for thermal insulation in hot climate," *Cement and Concrete Research*, vol. 35, no. 8, pp. 1472–1479, 2005.
- [17] J. Xamán, J. Cisneros-Carreño, I. Hernández-Pérez, I. Hernández-López, K. M. Aguilar-Castro, and E. V. Macias-Melo, "Thermal performance of a hollow block with/without insulating and reflective materials for roofing in Mexico," *Applied Thermal Engineering*, vol. 123, pp. 243–255, 2017.
- [18] E. Fraile-Garcia, J. Ferreiro-Cabello, M. Mendivil-Giro, and A. S. Vicente-Navarro, "Thermal behaviour of hollow blocks and bricks made of concrete doped with waste tyre rubber," *Construction and Building Materials*, vol. 176, pp. 193–200, 2018.
- [19] P. Mendonça, *Habitar Sob uma Segunda Pele (in Portuguese)*, PhD thesis, University do Porto, Porto, Portugal, 2005.
- [20] A. Martins, G. Vasconcelos, and A. Campos Costa, "Brick masonry veneer walls: an overview," *Journal of Building Engineering*, vol. 9, pp. 29–41, 2017.
- [21] N. Desai and W. M. Mcginley, "A study of the out-of-plane performance of brick veneer wall systems in medium rise buildings under seismic loads," *Engineering Structures*, vol. 48, pp. 683–694, 2013.
- [22] D. Reneckis, J. M. Lafave, and W. M. Clarke, "Out-of-plane performance of brick veneer walls on wood frame construction," *Engineering Structures*, vol. 26, no. 8, pp. 1027–1042, 2004.
- [23] A. M. Memari, E. F. P. Burnett, and B. M. Kozy, "Seismic response of a new type of masonry tie used in brick veneer walls," *Construction and Building Materials*, vol. 16, no. 7, pp. 397–407, 2002.
- [24] S. A. Marziale and E. A. Toubia, "Analysis of brick veneer on concrete masonry wall subjected to in-plane loads," *Structures*, vol. 2, pp. 1–7, 2013.
- [25] GB 50011-2010(Code of China), *Code for Seismic Design of Buildings*, China Architecture and Building Press, Beijing, China, 2010, in Chinese.



- [26] GB 50009-2012(Code of China), *Load Code for the Design of Building Structures*, China Architecture and Building Press, Beijing, China, 2012, in Chinese.
- [27] T. C. E. Ho, D. Surry, D. Morrish, and G. A. Kopp, "The UWO contribution to the NIST aerodynamic database for wind loads on low buildings: Part 1. archiving format and basic aerodynamic data," *Journal of Wind Engineering and Industrial Aerodynamics*, vol. 93, no. 1, pp. 1–30, 2005.
- [28] O. Gardella, B. Crawford, R. Soto, J. Lemus-Romani, G. Astorga, and A. Salas-Fernández, "Bridges strengthening by conversion to tied-arch using monarch butterfly optimization," *Advances in Intelligent Systems and Computing*, vol. 1041, pp. 459–469, 2019.
- [29] M. Sarkar and T. K. Roy, "Optimization of welded beam structure using neutrosophic optimization technique: a comparative study," *International Journal of Fuzzy Systems*, vol. 20, no. 3, pp. 847–860, 2018.
- [30] M. Yassami and P. Ashtari, "Using fuzzy genetic, artificial bee colony (ABC) and simple genetic algorithm for the stiffness optimization of steel frames with semi-rigid connections," *KSCE Journal of Civil Engineering*, vol. 19, no. 5, pp. 1366–1374, 2015.
- [31] Y. B. Gong and Q. Y. Li, "Engineering structural optimization with an improved ant colony algorithm," in *Proceedings of the 10th International Conference on Enhancement and Promotion of Computational Methods in Engineering and Science*, pp. 1019–1024, Sanya, China, August 2006.

## Research Article

# Investigation of Dynamic Responses and Vibration Serviceability of Temporary Grandstands by a 3 DOF Interaction Model due to Swaying Motion

Jian Yuan,<sup>1</sup> Suhui Yu,<sup>1</sup> Cong Liu ,<sup>2</sup> Chengqiang Gao,<sup>1</sup> Wei Wang,<sup>1</sup> Lin He,<sup>3</sup> and Feng Fan<sup>3</sup>

<sup>1</sup>Academy of Combat Support, Rocket Force University of Engineering, Xi'an 710025, China

<sup>2</sup>School of Civil Engineering, Suzhou University of Science and Technology, Suzhou 215011, China

<sup>3</sup>School of Civil Engineering, Harbin Institute of Technology, Harbin 150090, China

Correspondence should be addressed to Cong Liu; [liucong618@126.com](mailto:liucong618@126.com)

Received 16 August 2021; Revised 17 November 2021; Accepted 29 November 2021; Published 6 January 2022

Academic Editor: Carlo Rosso

Copyright © 2022 Jian Yuan et al. This is an open access article distributed under the Creative Commons Attribution License, which permits unrestricted use, distribution, and reproduction in any medium, provided the original work is properly cited.

Excessive vibration of temporary grandstand by the crowd has lateral rhythmic motions, which attracted increasing attention in the recent years. This paper focuses on experiments where a temporary grandstand occupied by 20 participants is oscillated by a shaking table with a series of random waves and the crowd-induced rhythmic swaying motions at lateral direction, respectively. The dynamic forces that were induced by participants who have swayed at 0.5–1.8 Hz are recorded by a tri-axial human biomechanics force plate. A new relationship between the annoyance rate and structural acceleration at logarithmic coordinate is investigated and proposed, and the swaying load model is given. Based on these experimental results, a simplified three-degree-of-freedom lumped dynamic model of the joint human–structure system is reinterpreted. Afterwards, combined with a feasible range of crowd/structural dynamic parameters, a series of interaction models are analyzed, the vibration dose value (VDV) of the structure is obtained and discussed, and the notable parameters for interaction model are predicted. The experimental results show that the lateral serviceability limit is  $1.29 \text{ m/s}^{1.75}$  and the upper boundary is  $2.32 \text{ m/s}^{1.75}$ . The dynamic response of model indicated that the VDV of structure will be decreased with increasing the mass of static crowd and damping ratio of the dynamic crowd. The max response of the model is  $\alpha \leq 0.6, f_2 = 1.8 \text{ Hz}$  or  $\alpha > 0.6, f_2 = 1.5 \text{ Hz}$  or  $f_1 = 2.5\text{--}3.5 \text{ Hz}$ . It may be used as a reference value in vibration safety and serviceability assessment of TDGs, to estimate realistically the vibration response on the occasions when the crowds are swaying.

## 1. Introduction

The problems of vibration of structure such as in long-span floor structures [1], footbridges [2], and grandstands [3–5], which can gather large crowd, have become more prevalent in recent years. For temporary grandstand especially, excessive vibration of structure can cause crowd discomfort or panic, and what is more, it can induce the serious safety of structure due to the failure of structural component [6]. Moreover, the vibration serviceability of grandstand relates to the comfort of spectators, and human perception is of primary importance with any tendency to panic or feeling of discomfort being related to the dynamic response of the structure [7]. This seems to be a common problem in

temporary demountable grandstands (TDGs), where the lightweight structural components of TDGs can be rapidly assembled, easily dismantled, and reused, which results in low stiffness of structure at the lateral direction, and can be susceptible to vibrations caused by active crowds. So, predicting the structural dynamic responses, mitigating the excessive structural vibrations, and ensuring occupant comfort are tasks familiar to structural engineers. This has stimulated considerable interest in crowd-structure dynamics and been designated as a design problem to be tackled. In 1931, Reiher and Meister studied the effect of a shaking platform [8]. In 1971, Khan and Parmelee used a rotating display table [9]. In 1972, Chen and Robertson investigated human perception of a wheeled windowless test

room [10]. In 1974, Wiss and Parmelee investigated human perception of a rise floor [11]. All the previously mentioned researches investigated the human body vibration and the structure vibration. Thus, there are two key areas of human–structure interaction: first, the human body forces induced by crowds, which have rhythmic activities; second, the dynamic responses of structure and serviceability of human-induced vibrations. To date, a number of research projects have largely focused on producing load models to accurately represent the dynamic crowd load, and great advances have been done to investigate the human–structure interaction [3, 5, 12–16], to better understand the vibration response of grandstand structure.

This paper follows with interest the latter key area issues for predicting the dynamic responses of temporary grandstand structure. The theory of interaction model usually considers that crowd and/or structure is mathematically assumed as a mass-spring-damper SDOF system [17–20], respectively. Other researchers such as Reynolds [21–23], Caprioli [24, 25], Salyards [26], Cigada [27, 28], Comer [29], Parkhouse [30], and Jones [31] monitored and analyzed the permanent grandstands using experiments. Ibrahim [32], Mandal [33], Salyards [34], Saudi [35], Pavic [36], Jian [37], and Lin [38] investigated and analyzed the responses of grandstand by FEM. For assessing the vibration serviceability, a series of classic experiments about human perception where participants rate their feeling of the vibration were conducted [3, 8, 9, 12, 13], and as alluded to earlier, this method has been available for appraising the vibration comfort of vehicle suspension system [39, 40], high-speed train [41], pedestrian bridge [42], floor structure [43, 44], and noise annoyance [45, 46]. Some achievements have been adopted by BS6472-1 [47] and ISO2631-1 [48] standards, and the limit acceleration value for permanent grandstand was given in some standards like ISO2631-1. Both a fuzzy logic method and the probability theory and the signal detecting theory of psychophysics [49–54] were also used to assess the vibration serviceability of permanent and temporary grandstand [55, 56] structure.

What these reviews have highlighted is that vibrations induced by humans have vertical motions, and few researches analyzed the lateral vibration in the TDG. What is more, lateral vibration is more likely to be induced than vertical vibration in reality for TDG [14, 20]. This remains an open problem in the area, and the aim here is to investigate the lateral vibration of TDG.

So with this aim in mind, in this paper, an experiment to determine the human perception of horizontal vibrations at a TDG included 20 persons, where vibrations were derived from a shaking table and crowd motions, respectively. The dynamic forces that were induced by participants who have swayed 0.5–1.8 Hz are recorded using a tri-axial human biomechanics force plate. Based on these experimental results, the vibration serviceability of TDG is investigated, and then, a simplified three-degree-of-freedom lumped dynamic model of the joint human–structure system is reinterpreted under different parameters of this interaction model, which was used for analyzing the dynamic response of TDG.

Section 1 presents the lateral oscillation experiment. The evaluation method is introduced and the relationships of

evaluation parameters of structural vibration are investigated in Section 2. Based on a feasible range of human dynamic parameters and structural parameters, the structural dynamic responses of interaction models are analyzed and discussed in Section 3. The conclusions will be presented in the final chapter.

## 2. Lateral Vibration Experiments of Temporary Grandstand and Questionnaire Surveys

Experimenting was executed on the basis of a rigorous risk assessment and approval of the experiment program by the university's research ethics committee, using its standard procedures for protecting the safety of participants and acquiring sensible data. A temporary grandstand with four rows and five columns of seats that can accommodate 20 persons were selected as the test rig. A unique reference number was allotted to each participant so that their position on the structure could be logged; for example, the first row of seats is 1–5 from left to right (Figure 1(a)).

The study included forty volunteers (Figures 1(b) and 1(c)) from the university and society to consider their different life experiences and educational backgrounds. The weight of each participant was also measured, and the gross weight of the twenty participants is 1405.7 kg and 1338.7 kg, respectively. The participants consisted of 36 males with weights ranging from 54.0 to 90.5 kg (mean 70.6 kg) and four females with weights between 41.0 and 57.0 kg (mean 50.5 kg). All participants were aged between 20 and 35 years (mean age 26.2) and had a healthy body to participate in the test. All participants did not receive specialized training for perceiving the vibration. No specific posture was prescribed, and the participants sat or stood freely. Because this is a psychophysical experiment or survey by means of a category judgment method, this requires participants to rate their perception and/or comfort of the magnitude of the vibrations. Based on their perception, everyone filled in the questionnaire for rating the vibration that had been experienced during the lateral vibration tests when they sat and/or stood, respectively.

For simulating the lateral vibration of temporary grandstand, a series of random waves (Table 1) were chosen as external excitation when the test rig was occupied by participants and the test rig was fixed on a shaking table (Figure 1(b)). Table 1 shows there are three kinds of seismic waves: Chi Chi (1999s), EI Centro (1940s), and Kobe waves (1995s), including two lateral directions, West-East (W-E) and North-South (N-S), which were chosen as horizontal force to the test rig. The peak acceleration of these random waves was between  $0.16 \text{ m/s}^2$  and  $1.54 \text{ m/s}^2$  with 53 force testing sessions in total. For example, there are nine test curves of Chi Chi (W-E) from the peak acceleration 18.29 gal to 91.45 gal, increasing 0.5 times, that is, 18.29 gal, 27.43 gal ( $18.29 \times 1.5$ ), 36.58 gal ( $18.29 \times 2$ ), 45.73 gal ( $18.29 \times 2.5$ ), 54.87 gal ( $18.29 \times 3$ ), 64.02 gal ( $18.29 \times 3.5$ ), 73.16 gal ( $18.29 \times 4$ ), 82.31 gal ( $18.29 \times 4.5$ ), and 91.45 gal ( $18.29 \times 5.5$ ). Other kinds of test curves used the same increasing method like Chi Chi test waves. The shaking table was controlled by displacement curve (acceleration curves converted to displacement curves), and one of them is shown in Figure 2.

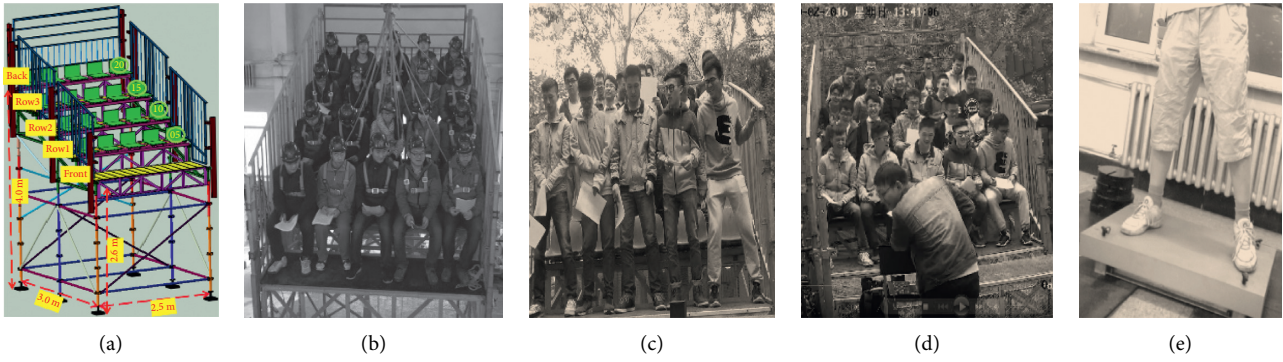


FIGURE 1: The lateral vibration experiment and single person swaying test. (a) Schematic of structure; (b) external excitation; (c) stand crowd swaying excitation; (d) seated crowd swaying excitation; (e) single person swaying.

TABLE 1: Details of test seismic waves.

Seismic wave		Peak acceleration (gal)	Duration (s)	Number
Chi Chi (1999s)	W-E	18.29–91.45	48	9
	N-S	16.26–89.43	46	10
EI Centro (1940s)	W-E	21.48–96.66	40	8
	N-S	31.29–140.81	40	8
Kobe (1995s)	W-E	30.78–153.90	30	9
	N-S	30.57–152.85	40	9

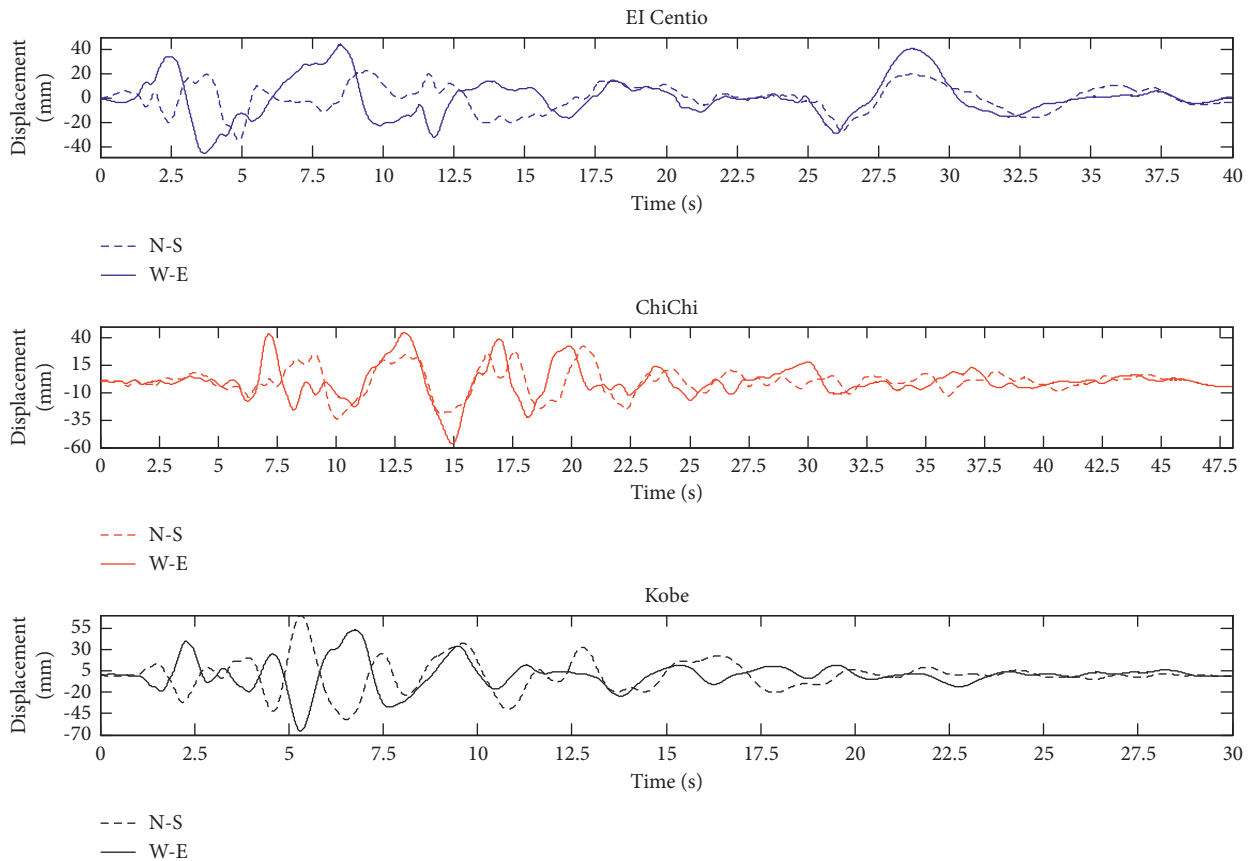


FIGURE 2: The shaking table under displacement-controlled loading.

Besides, human-induced vibration was derived in the stand/seated active crowd when they have swaying movements on temporary grandstand (Figures 1(c) and 1(d)), and eight person were swayed at a triaxial human biomechanics force plate (Figure 1(e)). (Figure 1(e)). For human internal excitation, eleven experimental conditions were designed for crowds with swaying activities at temporary grandstand. The swaying person's number, test conditions, and crowd swaying frequencies are shown in Table 2 [57]. In this paper, the passive and/or active crowd annoying levels of vibration is investigated.

In Figure 3, the main dimensions of a structure are height of front row (2.6 m), back (4.0 m), left-to-right span (2.5 m), and front-to-back span (up to 3 m). Four accelerometer points A1–A4 stand for the accelerations of each row. Also, there are three linear variable differential transformers (L1–L3) shown in this figure. The responses of structural seating system are measured by the accelerator points A1–A4 and are presumed as the responses of the crowd-TDG-coupled model. Data were collected at a sampling frequency of 1 kHz using IMC data acquisition software carrying a built-in anti-alias filter (German model IMC CRONOS compact-400-08 with robust housing) and a DH5922 (Dong Hua, China). The recorded curves were digitally filtered with a frequency content of up to 25 Hz in order to minimize the effect of background noise. Finally, the adjustable bearing of the test rig had to be sufficiently robust with a bolted connection in the shaking table and to prevent sliding due to the impact of seismic waves resulting from side-to-side motions.

As mentioned previously, only few standards or codes can provide specific clause on the assessment of human vibration acceptability for grandstand. Some researchers [3, 8, 9, 12, 13] divided the human perception and vibration level into three to six categories, which are based on the concept of equidistance followed human psychological changes. The achievements have been adopted by BS6472-1 [47] and ISO2631-1 [48] standards. Introspection is used to describe an experimental technique that was first developed by psychologist Wilhelm Wundt, in Wundt's lab, and there were two key components that made up the contents of the human mind: sensations and feelings. Wundt believed that researchers needed to do more than simply identify the structure or elements of the mind. Instead, it was essential to look at the processes and activities that occur as people experience the world around them [58]. Therefore, it is necessary to conduct a psychophysical experiment survey by means of a category judgment method [59]. So, according to these findings, the level of vibration perception (six categories) [60] and comfort are provided with vibration perception questionnaires, which require participants to select their subjective perception and/or levels of comfort during exposure to vibration. The questionnaires contain the level of vibration perception with the level comfort and shows in Table 3, and the questionnaires are shown in Figure 4.

### 3. Evaluation Method and Analysis of the Vibration Serviceability

**3.1. Annoyance Rate Method.** Although the limit acceleration value for grandstand was given in some standards like ISO2631-1 [48], the membership between the limit value and comfortable level was not reasonably extrapolated, especially for lateral vibration of temporary grandstand. The result of questionnaires includes the ambiguity of seismesthesia and the sensitivity randomness existing in participants' response to vibration environment. All these uncertainties need to be analyzed from a psychophysics view. So, first, the seismesthesia of membership function and corresponding conditional probability distribution [61] is calculated using (1) based on Table 3 and questionnaires.

$$v_j = \frac{(j-1)}{(K-1)}, \quad j = 1, 2, \dots, K, \quad (1)$$

where  $v_j$  is the seismesthesia of membership value of the  $j$ th type of the unacceptable range, and  $K$  is the class number of the subjective response, according to Table 3,  $K=6$ .

So, the subjective response corresponding to the value of  $v_j$  can be shown in Table 4.

An evaluation index annoyance rate method that is a fuzzy stochastic model for participant response to vibrations is cited [61]. The method considers these uncertainties with the fuzzy logic method and the probability theory, combined with the objective experimental data statistics. An annoyance rate is the proportion of some kind of subjective response under certain external stimulus intensity, which considers synthetically response ambiguity and randomness with fuzzy membership value. It is useful as a benchmark to determine the annoyance threshold for vibration serviceability criteria. The threshold indicates the ration of people who cannot accept the vibration to the statistical that total number. Under discrete distribution, the annoyance rate can be calculated as follows:

$$R(x=i) = \frac{\sum(v_{ij} \cdot n_{ij})}{\sum n_{ij}}, \quad (2)$$

where  $R(x=i)$  is the annoyance rate of the  $i$ th vibration intensity;  $v_{ij}$  is the membership of value is calculated using (1) at the  $i$ th vibration intensity;  $n_{ij}$  is the number of subjective response of the  $j$ th type of the  $i$ th vibration intensity;  $K$  is the class number of the subjective response,  $K=6$  (Table 3).

**3.2. Relationship of Structural Vibration Evaluation Parameters.** According to the author's paper [20], there are three common approaches to determining vibration amplitude: peak, root-mean-square (RMS), and vibration dose value (VDV). VDV approach may be more suitable for assessing the structural vibration by dynamic curves especially the curve has distinct peaks that is different from RMS approach which depends too heavily on the duration of an event to act as an accurate gauge of response severity [4]. So, the shaking table's acceleration and structural dynamic responses are quantified in terms of the vibration dose value

TABLE 2: Details of crowd rhythmic activities.

Test condition number	Test conditions	Crowd swaying frequency (Hz)
1	All standing persons swaying	0.5, 0.75, 1.0, 1.1, 1.25, 1.4, 1.5, 1.7, 1.8
2	All seated persons swaying	0.5, 0.75, 1.0, 1.1, 1.25, 1.4, 1.5, 1.7, 1.8
3	6–20 standing swaying, 1–5 seated	0.5, 0.75, 1.0, 1.1, 1.25, 1.4
4	11–20 standing swaying, 1–10 seated	0.5, 0.75, 1.0, 1.1, 1.25, 1.4
5	16–20 standing swaying, 1–15 seated	0.5, 0.75, 1.0, 1.1, 1.25, 1.4
6	6–20 standing swaying; 1–5 standing	0.5, 0.75, 1.0, 1.1, 1.25, 1.4
7	11–20 standing swaying; 1–10 standing	0.5, 0.75, 1.0, 1.1, 1.25, 1.4
8	16–20 standing swaying; 1–15 standing	0.5, 0.75, 1.0, 1.1, 1.25, 1.4
9	6–20 seated swaying; 1–5 seated	0.5, 0.75, 1.0, 1.1, 1.25, 1.4
10	11–20 seated swaying; 1–10 seated	0.5, 0.75, 1.0, 1.1, 1.25, 1.4
11	16–20 seated swaying; 1–15 seated	0.5, 0.75, 1.0, 1.1, 1.25, 1.4

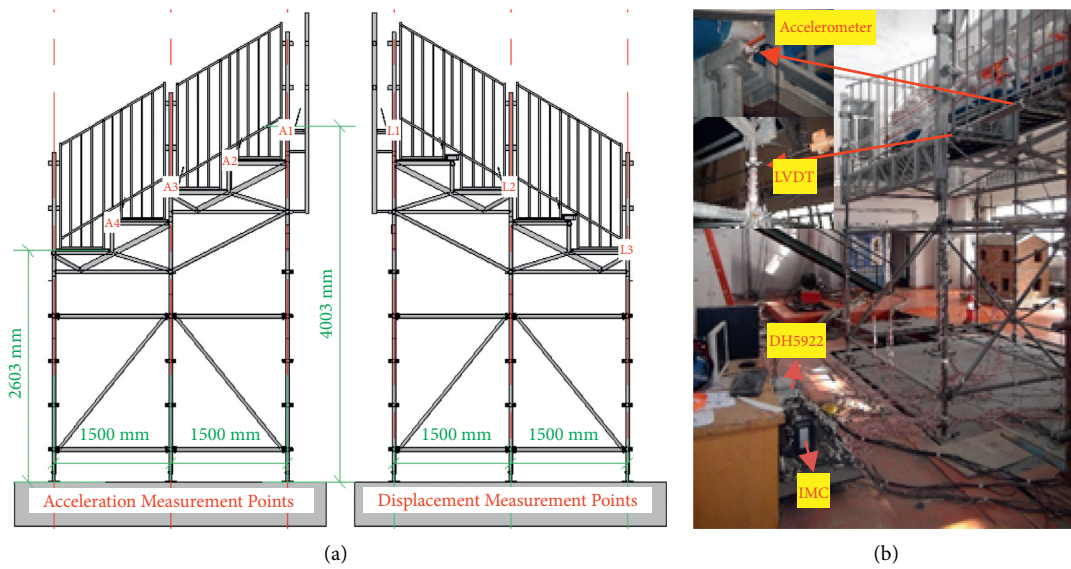


FIGURE 3: The test structure. (a) The test points of accelerometer and displacement; (b) test instruments.

TABLE 3: Human perception and comfort category.

Ordinal	Perception category	Subjective response
1	Imperceptible	No response (not uncomfortable)
2	Litter perception	Normal (a little uncomfortable)
3	Clear perception	Accept (fairly uncomfortable)
4	Little strong perception	Litter nervous (uncomfortable)
5	Strong perception	Nervous (very uncomfortable)
6	Very strong vibration	Panic (extreme uncomfortable)

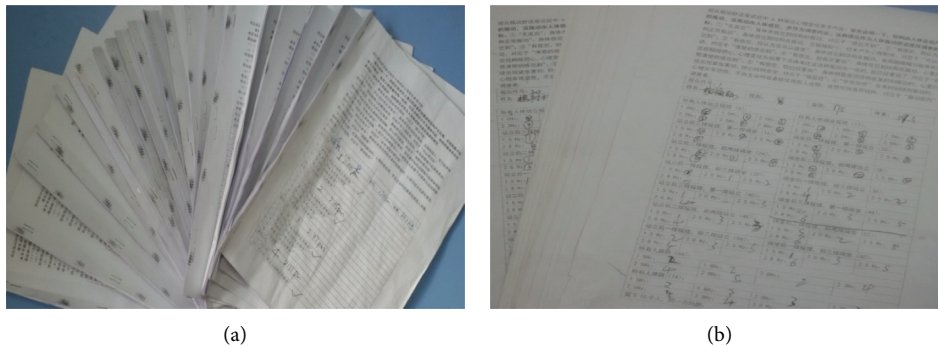


FIGURE 4: Participant response questionnaire. (a) The questionnaires of shaking table test; (b) the questionnaires of human induced vibration.

TABLE 4: Seismesthesia membership values.

Subjective response	$j=1$ No response	$j=2$ Normal	$j=3$ Acceptable	$j=4$ Litter nervous	$j=5$ Nervous	$j=6$ Panic
Membership value	0.0	0.2	0.4	0.6	0.8	1.0

(VDV), which is calculated in (3) for both continuous and digitized signal:

$$a_{\text{VDV}} = \left\{ \int_0^T a_w^4(t) dt \right\}^{1/4} = \left( \lim_{\lambda \rightarrow 0} \sum_{i=1}^n a_w^4(\zeta_i) \cdot \Delta t_i \right)^{0.25} = \left( \sum_{i=1}^n [W(f_s) \cdot a(t_i)]^4 \cdot f \right)^{0.25} \quad \lambda = \max\{\Delta x_1, \Delta x_2, \dots, \Delta x_n\}, \quad (3)$$

where  $a_{\text{vdv}}$  is the vibration dose value of acceleration  $a(t)$  in  $\text{m/s}^{1.75}$ ;  $\zeta_i$  is the integration point that equal to timing point  $t_i$ ;  $a_w(t)$  is the frequency weighted acceleration equal to  $a_w(t) \cdot W(f)$ , and  $W(f)$  is the frequency weight function from ISO2631 [62, 63];  $f_s$  is the empty structure natural frequency (Figure 5). According to the ISO2631, the value of 0.74 is used in this paper;  $a(t)$  is the digitized sample of the experimental acceleration, and it is the mean curve of A1–A4 in this paper;  $T$  is the vibration duration in seconds, and  $f$  is the sampling frequency, with  $n = T/f$  being the number of points in the signal;  $\Delta x_i$  is the  $i$ th integral interval point. In this paper, (3) is used for calculating the same kind of excitation with different amplitudes to reflect the structural dynamic performance. So, for example, the set {1, 2, 3, 4, 5, 6, 7, 8, 9, 10} and set {10, 9, 8, 7, 6, 5, 4, 3, 2, 1} are different; if both of them were evaluated by Eq. (3), they will have the same answer. However, it is incorrect to think that the two datasets are similar. In this paper, the order of the elements of  $a(t)$  is invariant, and only the size of element increases linearly, that is, {1, 2, 3, 4, 5, 6, 7, 8, 9, 10} and {2, 4, 6, 8, 10, 12, 14, 16, 18, 20} and so on.

The peak acceleration of A0 plotted against each form of structural acceleration is shown in the same window of Figure 6(a). In this figure, hollow dots stand for peak accelerations, square dots stand for RMS values, and diamond dots stand for VDV. All the dots include the results of A1 to A4. It should be noted that the fitting curve of VDV is lower than the other two, and the fitting curve of RMS is higher than the other two. For the human-induced vibration experiment, the results of excitations are derived from crowd with rhythmic activities Figure 6(b), which are different from the shaking table tests (Figure 6(a)). The peak acceleration, RMS, and VDV of each test condition results are also calculated, and the scatter plots were the three measures plotted against crowd swaying. In this figure, the hollow dots stand for peak accelerations, the square dots stand for RMS values, and the diamond dots stand for VDV. It is also found that RMS values are higher than the peak value and VDV, and the max value is about  $13.49 \text{ m/s}^2$ , which is out of the limits given by Kasperski [3], Setaerh [5], Nhleko [13], BS6472-1 [47], BS6841 [64], and some codes or guidelines [65–69]. Considering to the max value, based on the vibration perception questionnaires of these participants, it was found that they were in panic from the questionnaires.

The standard BS6472-1 [47] and ISO2631-1 [48] has given an approximate relationship between VDV and RMS when vibrations are statistically stationary, and Griffin [70] introduced the crest factor  $C_F$ , and when  $C_F = a_{\text{wp}}/a_{\text{wrms}}$  is less than 6, the VDV can be estimated using  $a_{\text{wrms}}$ . However, as can be seen in Figure 7(a), it is not applicable to the vibrations recorded in shaking table experiment as the calculated  $C_F$  are significantly smaller than 6. Ellis with Littler [71] has given a linear relationship between VDV and peak acceleration, whereas it is also not applicable to this experiment's results. Besides,  $C_F$  plotted against  $a_{\text{wvdv}}/a_{\text{wp}}$  is fitted by a linear curve and the fitting parameter R-Square is 0.74, which is different from that given by Setareh [5], a second-order relationship. This may be because Setareh researched excitations and structures that are different than that in this paper.

For human swaying experiment, the crest factor  $C_F$  values also are smaller than 6, and  $C_F$  plotted against  $a_{\text{wvdv}}/a_{\text{wp}}$  is shown in Figure 7(b). Compared with the shaking table experiment that excitations were exported with a linear increasing, even crowd-induced structure vibration has a certain randomness because the output energies of their bodies are uncertain. It is indicated that they have a linear relationship and even only a part of subjects have rhythmic swaying (such as 3–11 test conditions in Table 2). So, based on the computed  $a_{\text{wp}}$ ,  $a_{\text{wrms}}$  and  $a_{\text{wvdv}}$ , Figure 8 shows the scattered plots of  $a_{\text{wp}}$  and  $a_{\text{wrms}}$  plotted against  $a_{\text{wvdv}}$ , and a linear relationship curve was fitted, which indicated that there existed a good linear relationship between each of them.

Bearing all this in mind, the structural acceleration VDV has a linear relationship with RMS and peak acceleration, and not only the structure was oscillated by shaking table with linear increasing excitations but also it was oscillated by crowd having rhythmic activities with linear increasing swaying frequencies. And what is more, crowd swaying movements can make structure's acceleration more than  $10 \text{ m/s}^2$ , which can cause the crowd to panic.

**3.3. Acceptable VDV Limits.** The external excitation and human internal vibration for the test structure were analyzed in this paper. The structural acceleration curves had

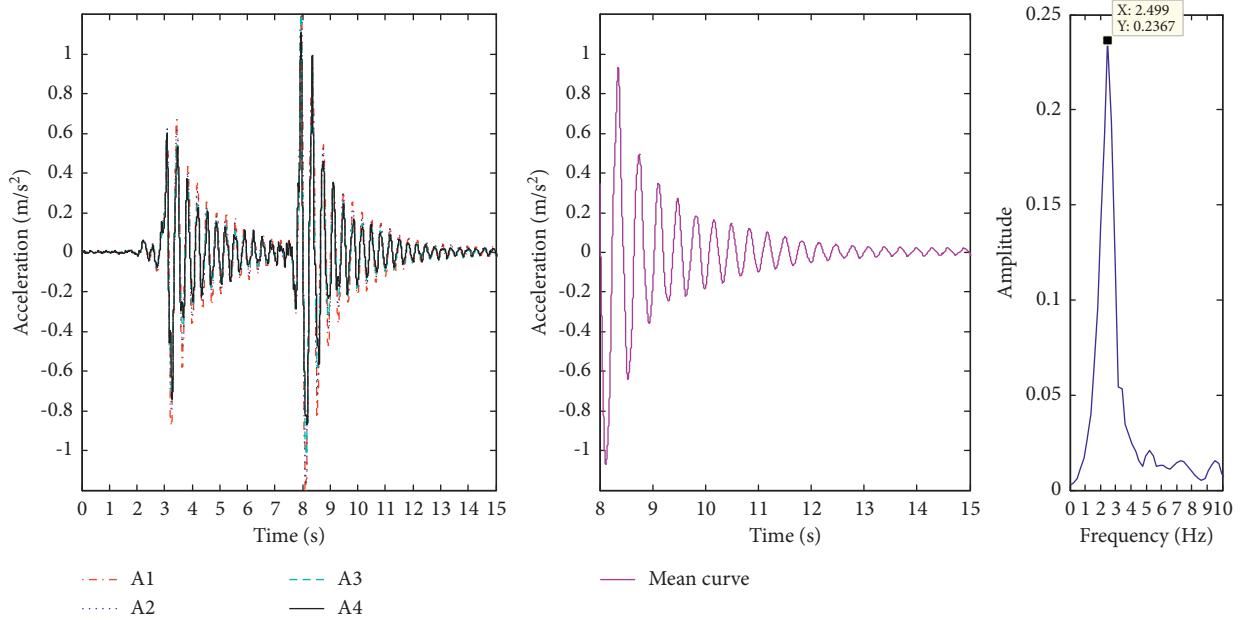


FIGURE 5: The measured points of time history and frequency domain analysis from free decaying vibration (empty structure).

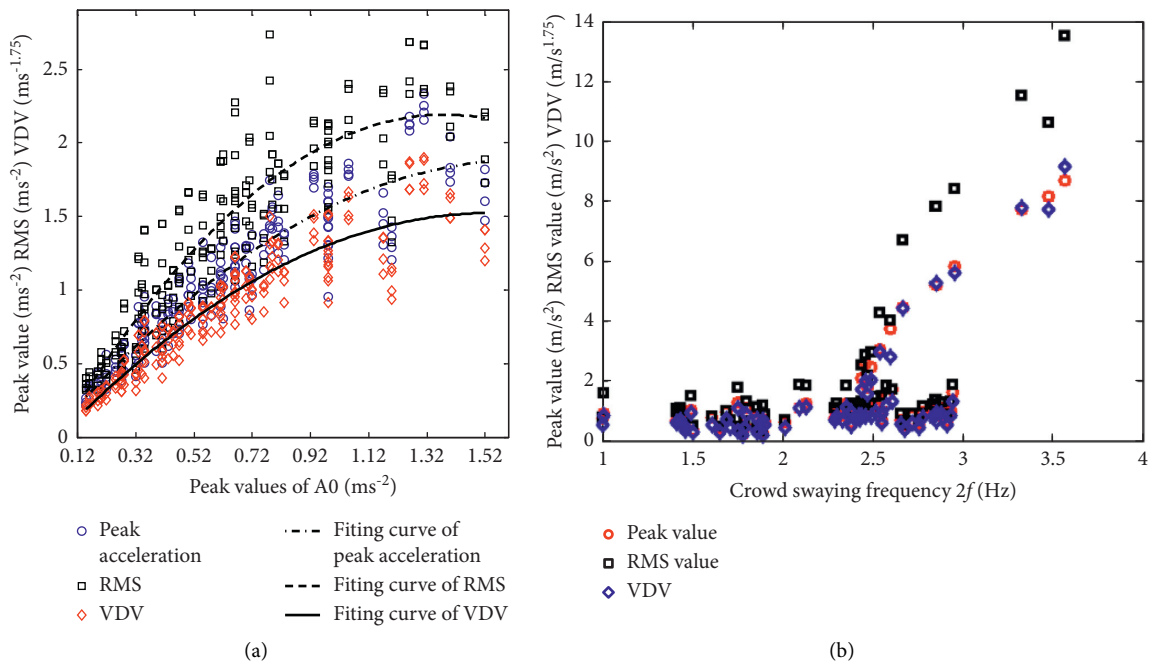


FIGURE 6: The relationship of input conditions and output accelerations: peak values, RMS values, and VDV. (a) Shaking table experiment results; (b) human-induced vibration experiment results.

characteristics that varied with time. So, VDV is more versatile than RMS and has been calculated to quantify human reactions to numerous types of vibrations, and VDV will be used for finding the relationship with annoyance ratio in this paper.

The annoyance rate  $R$  of the crowd occupying the structure when it oscillated by external excitations is calculated using (2). All the experiment data of the scattered plots annoyance rate  $R$  plotted against VDV are

shown in Figures 9 and 10. First, the distribution of annoyance rate of standing crowd experiment data (circle dots) is compared with seated crowd experiment data (star dots) in the same window, which is shown in Figure 9(a). It can be seen that the distribution of annoyance rate of the standing crowd is similar to the seated crowd when structural VDV is no more than  $1.55 \text{ m/s}^{1.75}$ . It is found that the annoyance rates of the standing crowd are lower than the seated crowd when the structure has larger VDV,



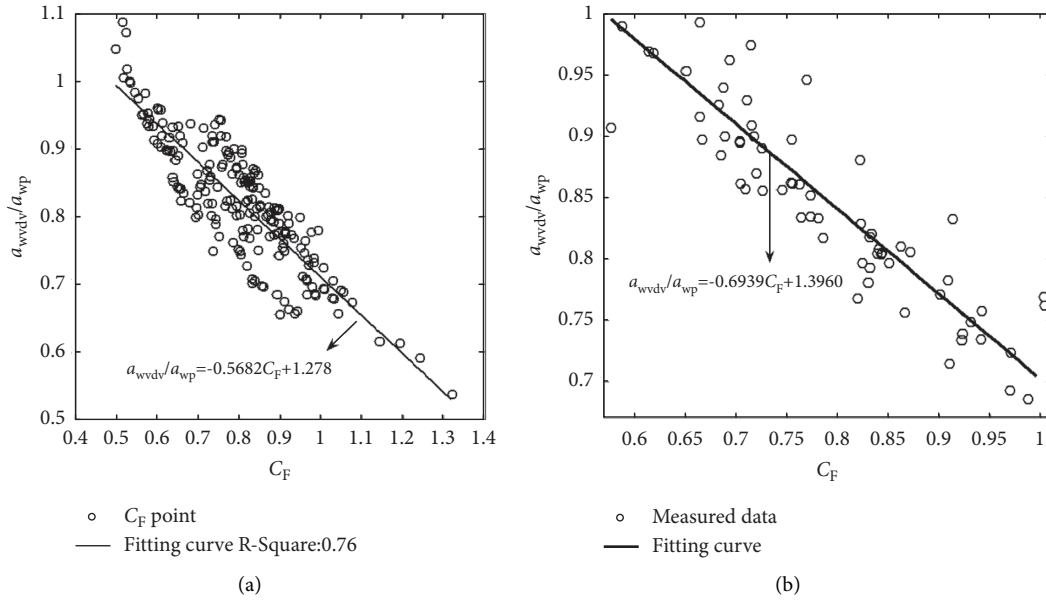


FIGURE 7:  $a_{wvdv}/a_{wp}$  plotted against  $C_F$ . (a) Measured data from shaking table tests; (b) measured data from human tests.

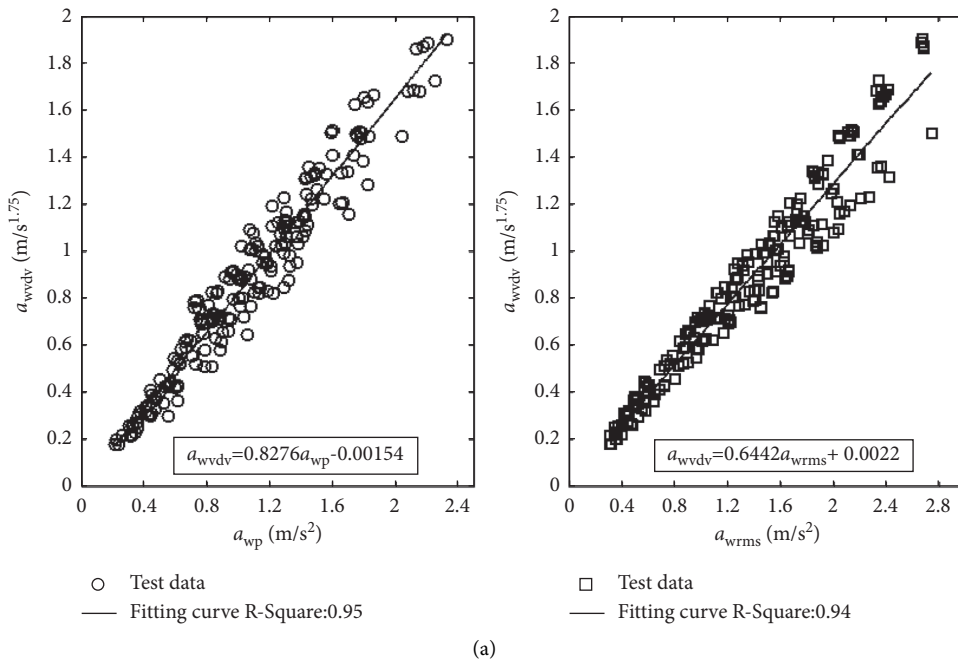


FIGURE 8: Continued.

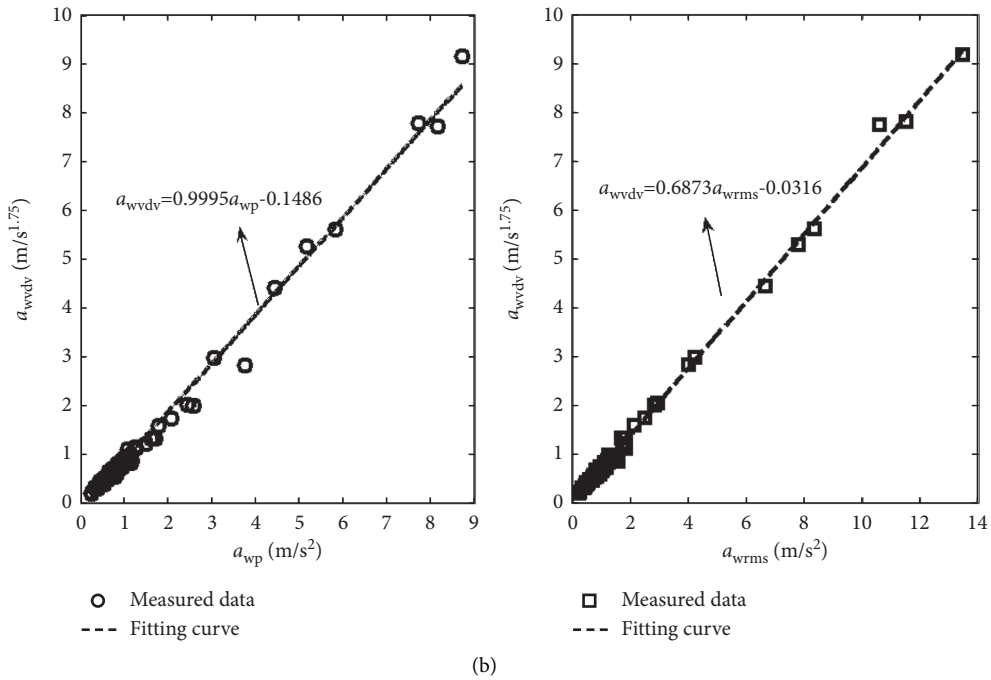


FIGURE 8:  $a_{wvdiv}$  plotted against  $a_{wp}$  and  $a_{wrms}$ . (a) Shaking table measured data; (b) crowd induced measured data.

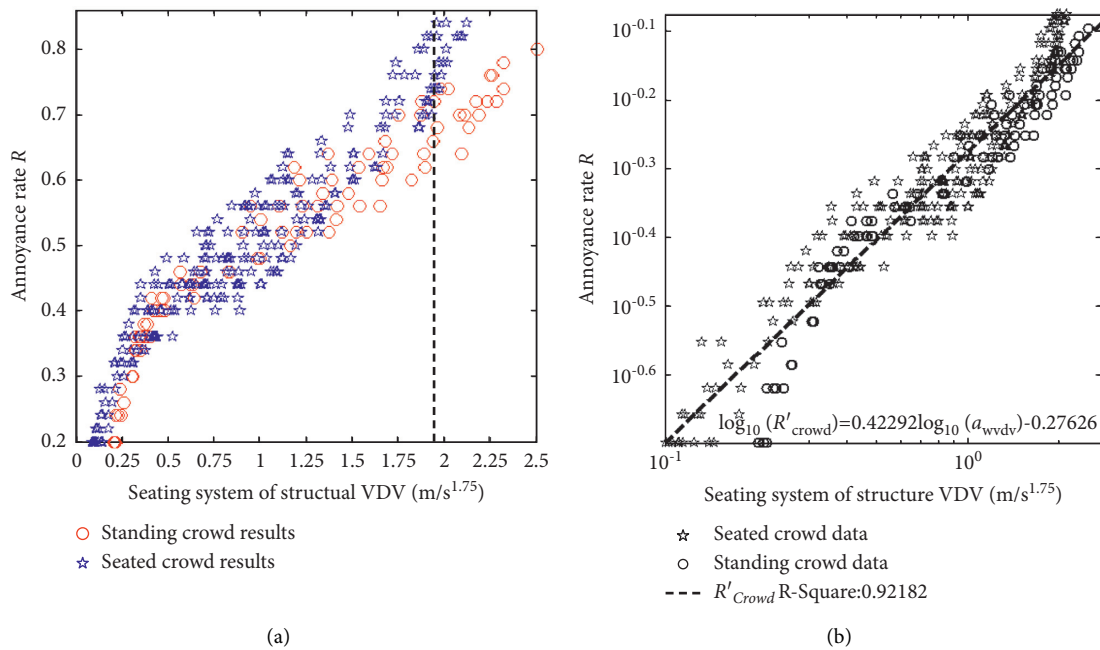


FIGURE 9: The distribution of crowds annoyance rate according to shaking table tests at logarithmic coordinate. (a) Cartesian coordinate system; (b) logarithmic coordinate system.

especially when the VDV is larger than  $2.0 \text{ m/s}^{1.75}$ , which may indicate that the standing crowd is more tolerant to vibration than the seated crowd in this kind of conditions of the experiment. Figure 9(a) shows that the crowd annoyance rate has a significant nonlinear relationship with increasing structural VDV. The distribution of annoyance rate is different in seated or standing crowds. When the

data of Figure 9(a) were shown by logarithmic coordinate system in Figure 9(b), it was found that there is a linear relationship between structural VDV and annoyance rate. So, by neglecting the slight difference found in them, the fitting curve is also given in Figure 9(b), and  $R'_{crowd}$  is the annoyance rate of the crowd at external excitation experiments.

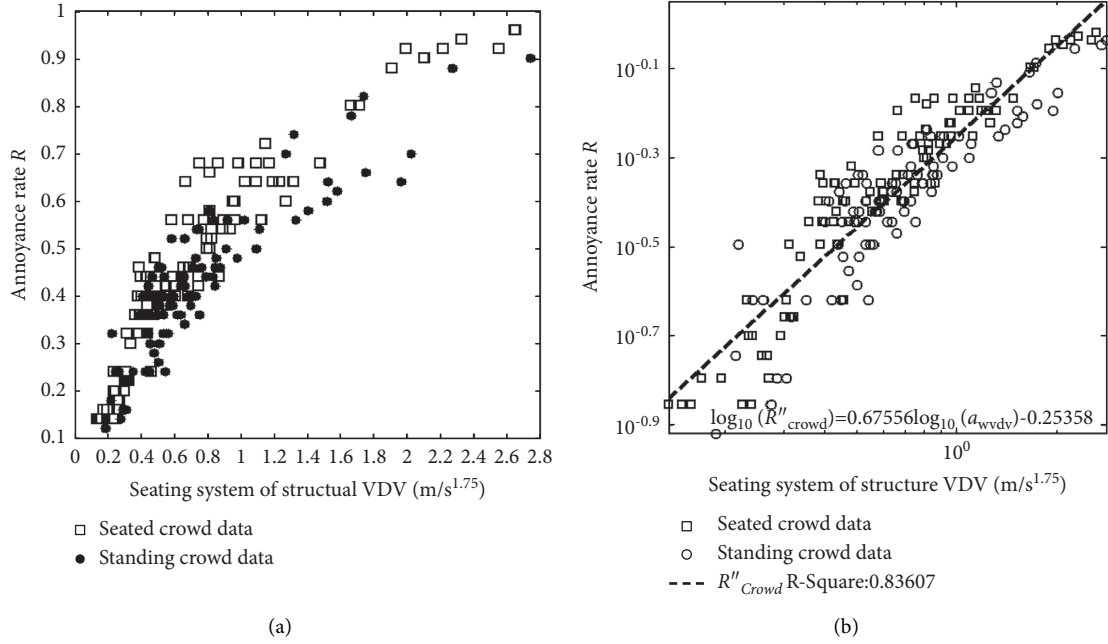


FIGURE 10: The distribution of crowds annoyance rate in human-induced structural vibration. (a) Cartesian coordinate system; (b) logarithmic coordinate system.

Second, active crowd-induced structure vibration experiment results are also investigated to find the relationship between annoyance rate and structural VDV. When the VDV is higher than  $2.8 m/s^{1.75}$ , the crowd is in panic, and the annoyance rate is 1.0. So, only the corresponding values with annoyance rate lower than 1.0 are shown in Figure 10(a). It is indicated that the distribution trend of scatters are similar to Figure 9(a), no matter what the results from standing crowd experiment data (filled dots) or seated crowd experiment data (square dots). It may also indicate that the standing crowd can tolerate more strong structural vibration than the seated crowd when the structural vibration was induced by the swaying crowd, from Figures 9(a) and 10(a), and this finding accords with Nhleko's research [13]. Also, a linear relationship between the structural VDV and annoyance rate at logarithmic coordinate system is fitted when considering the seated crowd data and standing crowd data as a whole sample. The fitting curve is shown in Figure 10(b).  $R''_{crowd}$  is the annoyance rate of crowd at human induced vibration experiment.

According to Figures 9(b) and 10(b), it is found that the trends of annoyance rate are similar no matter the structure was oscillated by the shaking table or by swaying crowd. So, both of the two experiment results were considered as a whole to evaluate the annoyance level of vibration. Figure 11 shows all the scatters of annoyance rate with structural VDV at the logarithmic coordinate system. It is clear that the distribution of annoyance rate is approximate with increasing VDV, even if there is a gap of annoyance rate between the results of seismic excitation (filled dots) and the results of human induced vibration (circle dots) when the VDV is smaller than  $0.6 m/s^{1.75}$ . A linear curve was fitted using (4a), and the formula at Cartesian coordinate system is also given in (4b):

$$\log_{10}(R) = 0.49119 \log_{10}(a_{wv dv}) - 0.27607. \quad (4a)$$

$$a_{wv dv} = 10^{0.56205} \cdot R^{1/0.49118}. \quad (4b)$$

So, when the vibration of structure was induced by stochastic and rhythmic excitations, the annoyance rate could be determined by (4a) and (4b).

$R$  is the annoyance rate of crowd on temporary grandstand, and  $a_{wv dv}$  is the acceleration VDV of seating system of temporary grandstand, and its range is 0.1 to  $2.8 m/s^{1.75}$ . In this paper,  $R$  is lower than 0.4, which indicates that the crowd is comfortable with the structure.  $R$  varying from 0.4 to 0.6 means that some people in the crowd feel uncomfortable.  $R$  varying from 0.6 to 0.8 means that most of the people feel uncomfortable, and when  $R$  is larger than 0.8 that shows that the crowd is in panic [61]. Based on this annoyance levels of vibration and according to (4a) and (4b), the structural acceleration VDV  $1.29 m/s^{1.75}$  corresponds to  $R=0.6$  as the serviceability limit, and  $2.32 m/s^{1.75}$  corresponds to  $R=0.8$  as the serviceability limit of the upper boundary.

#### 4. Parameters Analysis of Interaction Model for Structural Dynamic Response

The test results of the interaction between the static human body and temporary stand verify that the rationality of the static crowd and structure has been, respectively, simplified into an SDOF calculation system [18]. The combination with dynamic crowd not only provides load but also serves as an SDOF system, respectively [42, 43]. Thus, the proposition of a 3DOF interaction model between the crowd and

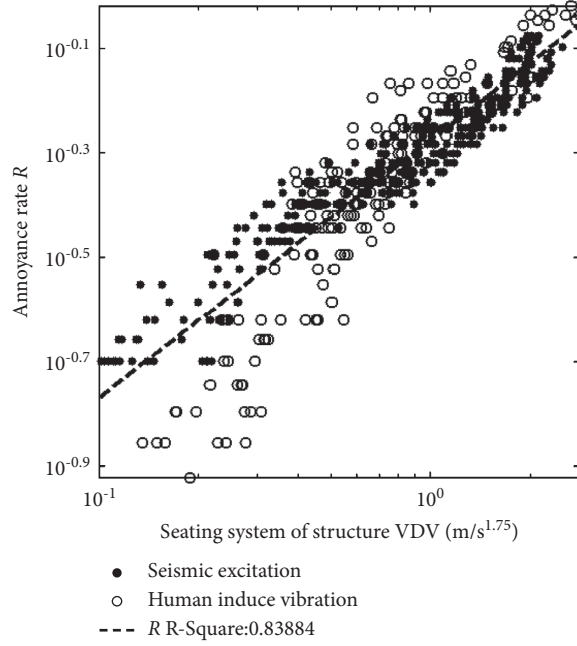


FIGURE 11: The distribution of crowds annoyance rate of TDGs.

temporary stand is presented. And for the lateral vibration,  $m_3$ ,  $f_3$ , and  $\zeta_3$  represent the mass, the first-order frequency, and the first-order damping ratio of the static crowd model,  $m_2$ ,  $f_2$ , and  $\zeta_2$  represent the relevant parameters of dynamic crowd, and  $m_1$ ,  $f_1$ , and  $\zeta_1$  represent the relevant parameters of effective area of the crowd–structure interaction. The simplified 3DOF calculation model of the crowd–structure interaction represented by these parameters is shown in Figure 12. The effective area of crowd–structure in the model refers to the seat structure area of a temporary stand in direct contact with the crowd (seating system). In view of the spatial changes in the action points of the crowd swaying, it is generally considered that the plane variables, that is, the action points, are the same. Therefore, it is assumed in the model that the crowd is a centralized mass single-point system, rather than a spatial multipoint system. The structural vibration mode  $\Phi$  in the model is simplified to 1, with its influence no longer being reflected.

Firstly, according to the experiment of swaying crowd, the swaying is loaded as the horizontal load for this model.

Second, the reasonable range values of the lateral dynamic parameters of structure and crowd are given. Based on these results [18, 40, 44, 45], it is considered that  $f_2$  varies between 1.5 and 3.3 Hz and  $\zeta_2$  varies between 0.20 and 0.25;  $f_3$  varies between 1.4 and 2.8 Hz, and  $\zeta_3$  varies between 0.3 and 0.5;  $f_1$  varies between 1.0 and 5.0 Hz and  $\zeta_1$  varies between 0.02 and 0.073. Then, the crowd and temporary stand interaction models with different parameter combinations are calculated. Finally, different parameters of the interaction model's responses are obtained, and the variation tendencies are analyzed.

In this model, the direction of displacement  $x$  is positive, the elastic force and damping force act in the opposite direction, and  $x_1$ ,  $x_2$ , and  $x_3$  are the lateral displacement of structure, dynamic crowd, and static crowd, respectively. For each mass-damping-spring system, the mechanical relationship followed by each mass is calculated with Newton's second law, as shown in (5a)–(5c):

$$\text{Mass of static crowd model } m_3: -c_3 \left( \frac{dx}{dt} - \frac{dt}{dx} \right) - k_3 (x_3 - x_1) = m_3 d^2 x_3 / dt^2 \quad (5a)$$

$$\text{Mass of dynamic crowd model } m_2: -c_2 \left( \frac{dx_2}{dt} - \frac{dx_1}{dt} \right) - K_2 (x_2 - x_1) = \frac{m_2 d^2 x_2}{dt + F(t)} \quad (5b)$$

$$\text{Mass of structure model } m_1: -c_1 \left( \frac{dx_1}{dt} - \frac{dx_1}{dt} \right) - k_2 (x_2 - x_1) = \frac{m_2 d^2 x_2}{dt + F(t)} \quad (5c)$$

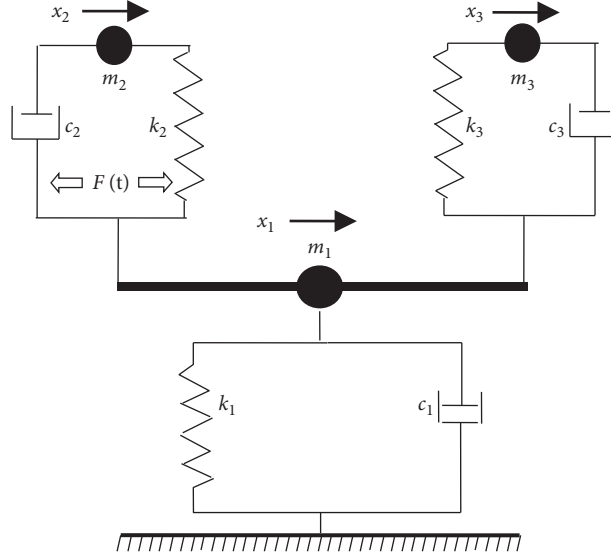


FIGURE 12: Three lumped-DOF representation of crowd-structure interaction model.

Plug equations (5a) and (5b) into (5c) and express them in matrix form as follows:

$$[M]_{3 \times 3} [\ddot{X}]_{3 \times 1} + [C]_{3 \times 3} [K]_{3 \times 3} [X]_{3 \times 1} = [F]_{3 \times 1}, \quad (6)$$

where damping  $c_i = 4\pi m_i f_i \zeta_i$ ; stiffness  $k_i = 4\pi^2 m_i f_i^2$ ,  $i = 1, 2, 3$ .

The number of dynamic and static crowds will change in the structure during the use of a temporary stand; thus, the changes in the mass of the two models  $m_2$  and  $m_3$  are considered and expressed as  $m_3 = \alpha m_2$ , wherein  $\alpha = 0$  indicates that all crowds are dynamic,  $\alpha$  approaching  $+\infty$  indicates that all crowds are static, and the structure is in a static state. It is assumed that there is a relationship  $m_1 = \beta m_2$  between the mass of the structure model and the mass of the dynamic crowd model. Dynamic crowds, especially swaying crowds in contact with the structure during movement,

provide a certain frequency and damping effect to the structure.

So, the mass matrix  $[M]$  in (6) can be expressed as (7a) using the previously mentioned parameters:

$$[M] = \begin{bmatrix} m_1 & 0 & 0 \\ 0 & m_2 & 0 \\ 0 & 0 & m_3 \end{bmatrix} = m_3 \begin{bmatrix} \beta & 0 & 0 \\ 0 & 1 & 0 \\ 0 & 0 & \alpha \end{bmatrix}. \quad (7a)$$

Considering the ratio of effective crowd model mass to effective structure model mass studied in another paper [18], there is a certain relationship between the structure mass  $m_1$  and the crowd mass  $m_2$  and  $m_3$ . In other words, there is a quantitative relationship  $m_2 + m_3 \leq 3m_1$ , and then  $m_2 + \alpha m_2 \leq 3\beta m_2$ , so  $1 + \alpha \leq 3\beta$ .

The damping matrix  $[C]$  is expressed as follows:

$$[C] = \begin{bmatrix} c_1 + c_2 + c_3 & -c_2 & -c_3 \\ -c_2 & c_2 & 0 \\ -c_3 & 0 & c_3 \end{bmatrix} = 4\pi m_2 \begin{bmatrix} \beta f_1 \zeta_1 + f_2 \zeta_2 + \alpha f_3 \zeta_3 & -f_2 \zeta_2 & -\alpha f_3 \zeta_3 \\ -f_2 \zeta_2 & f_2 \zeta_2 & 0 \\ -\alpha f_2 \zeta_2 & 0 & \alpha f_3 \zeta_2 \end{bmatrix}. \quad (7b)$$

The stiffness matrix  $[K]$  is expressed as follows:

$$[K] = \begin{bmatrix} k_1 + k_2 + k_3 & -k_2 & -k_3 \\ -k_2 & k_2 & 0 \\ -k_3 & 0 & k_3 \end{bmatrix} = 4\pi^2 m_3 \begin{bmatrix} \beta f_1^2 + f_2^2 + f_3^2 & -f_2^2 & -\alpha f_3^2 \\ -f_2^2 & f_2^2 & 0 \\ -\alpha f_3^2 & 0 & \alpha f_3^2 \end{bmatrix}. \quad (7c)$$

The dynamic differential equation (6) is transformed into a state equation using the state-space method, and the

system displacement is defined as the component of the state vector. The state vector is expressed as follows:

$$Z(t) = [z_1 \ z_2 \ z_3 \ z_4 \ z_5 \ z_6]^T = [x_1 \ x_2 \ x_3 \ \dot{x}_1 \ \dot{x}_2 \ \dot{x}_3]^T. \quad (8)$$

If the system is initially in a static state, the state equation and output equation are expressed as follows:

$$\begin{cases} \dot{Z}(t) = AZ(t) + BF, \\ y(t) = EZ(t) + DF, \end{cases} \quad (9)$$

where the transfer space matrix is  $[A] = \begin{bmatrix} 0_3 & I_3 \\ -M^{-1}K & -M^{-1}C \end{bmatrix}_{6 \times 6}$ , the input coefficient matrix is  $[B] = \begin{bmatrix} 0_{3 \times 3} \\ M^{-1} \end{bmatrix}_{6 \times 3}$ , the input matrix is  $[E] = [I_{3 \times 3} \ 0_{3 \times 3}]_{3 \times 6}$ , and the direct transfer matrix is  $[D] = [0]_{3 \times 3}$ .

The value of crowd swaying frequency is set between 1.0 and 1.8 Hz (in 0.1 Hz increments), so nine crowd swaying load curves can be simulated using (10), where the constraint parameters  $H_p$ ,  $d$ , and  $f$  are obtained from the experimental (Figures 1(c)–1(e)) data [17]. To ensure that the load is only affected by frequency, it is assumed that each swaying of the crowd is synchronized at each frequency and the most unfavorable state of the structure bearing the swaying load of the crowd is simulated. It is held that the peak value of the swaying curve generated by each frequency is the same. The swaying time is considered 20 s, so nine curves are generated and shown in Figure 13, and the peak value of the curve is  $0.2m_2g$  (N). When calculating the model, enter a time of 25 s, and the last 5 s displays the attenuation process of the model.

$$F_{ss}(t) = \frac{2H_p \sin(\pi d)}{\pi} \sin(2\pi ft) \pm \frac{2H_p \sin(3\pi d)}{3\pi} \sin(6\pi ft). \quad (10)$$

**4.1. Changing the Dynamic Crowd Parameters.** Different crowd parameters will greatly affect the response of the structure, and the crowd parameters mainly include the swaying load; frequency of static and dynamic crowd model; mass of static and dynamic crowd model; damping of static and dynamic crowd model. In order to analyze the influence of dynamic crowd parameters for structural response, the temporary stand parameters are  $f_1 = 2.7$  Hz,  $\zeta_1 = 7.3\%$ , and  $\beta = 1.0$ , and it is assumed that  $f_3 = 2.0$  Hz and  $\zeta_3 = 0.4$  [18], which is first used as a constant.

Considering the static and dynamic crowd in the use stage of the stand, the minimum value of  $\alpha$  is set to 0.2, and then, 0.8, 1.4, and 2.0 are taken as the reduction of the mass of the dynamic crowd in the total crowd. For dynamic crowd parameters,  $f_2$  forms seven frequency values in 0.3 Hz increments, from 1.5 Hz to 3.3 Hz, and  $\zeta_2$  forms three damping ratios of 0.2, 0.225, and 0.25. By substituting these parameters into (6), the mass matrix, damping matrix, and stiffness matrix expressed only in variable  $m_2$  can be obtained.

Seven hundred fifty-six coupling models are formed with nine load cases, four  $\alpha$  values, three  $\zeta_2$  values, and seven  $f_2$  values, and the model of each parameter combination is calculated using MATLAB software (the MATLAB program

in Appendix I). Figure 14 shows the acceleration curves of structure, dynamic crowd, and static crowd when  $\alpha = 2.0$ ,  $f_2 = 3.3$  Hz,  $\zeta_2 = 0.25$ , and  $f = 1.8$  Hz. As indicated by the comparison of curve peak values, although the latter two are greater than the former, more attention is paid to the response of the structure in practical application. In addition, the structural acceleration curve form obtained by theoretical calculation is similar to the structural response obtained from the measured crowd swaying test (when the crowd is seated and swaying at 1.8 Hz, and the peak value is divided by 16).

Considering that the VDV is the quantitative value of structural response in this paper, the VDV of 756 structural acceleration curves are extracted in Figure 15, where the  $x$ -axis is the swaying frequency and the  $y$ -axis is the acceleration of VDV. The seven curves in each figure correspond to the model results of the seven values, respectively. The three graphs in each row represent model results with the same  $\alpha$ ,  $\zeta_2 = 0.200, 0.225$ , and  $0.250$  respectively, and the four graphs in each column represent model results with the same  $\zeta_2$  and  $\alpha = 0.2, 0.8, 1.4$ , and  $2.0$ , respectively. Qualitative analysis on these curves shows the following tendencies: with increasing  $f$ , each curve rises first and then descends gently; each curve has only one peak, and the  $f$  corresponding to the peak increases with increasing  $f_2$ ; the larger the  $\alpha$ ,  $\zeta_2$ , and  $f_2$  are, the smaller the structural response will be.

To further determine the impact of dynamic crowd parameter changes on structural response, the relationship between the peak values of seven curves and the corresponding values in each graph of Figure 15 is plotted to form a curve. Twelve curves are shown in Figure 16(a). The curves in the graph reflect the variation tendencies: the larger the  $\zeta_2$  under the same  $\alpha$  is, the smaller the structural response will be; the curve of  $\alpha = 0.2$  rises first and then descends, while the curve of  $\alpha \geq 0.8$  descends directly. It can be seen that different  $\alpha$  cause the structural VDV to increase or decrease first or directly with increasing  $f_2$ , and that  $f_2$  corresponding to the peak are also different. Thus, the model of  $\alpha = 0.3$ – $0.7$  is calculated and the result of  $\zeta_2 = 0.2$  is shown in Figure 16(b). It shows the curve of  $\alpha \leq 0.6$  still rises first and then descends, with the peak value appearing at  $f_2 = 1.8$  Hz, while the curve after  $\alpha > 0.6$  descends directly, with the peak value appearing at  $f_2 = 1.5$  Hz. Both figures show that the structural response decreases with increasing  $\alpha$ .

The influence of variable parameters on structural response is quantitatively analyzed. Figure 17 shows the relationship curve between the maximum value of each graph in Figure 15 (the maximum value of each curve in Figure 16(a)) and each variable parameter. The four curves indicate that the structural response decreases linearly with the linear increase of  $\zeta_2$ , dropping by 19% when  $\alpha = 0.2$ ; by 21% when  $\alpha = 0.8$ ; and by 21% and 15% when  $\alpha = 1.4$  and  $2.0$ , respectively.

Similarly, the maximum reduction of structural VDV at different  $f_2$ ,  $\alpha$  and  $\zeta_2$  is given in Table 5. As shown by the data in the table, when the mass of the static crowd increases 10 times, the maximum VDV of the structure decreases by up to 90% (at 3.3 Hz), and the maximum VDV of the structure

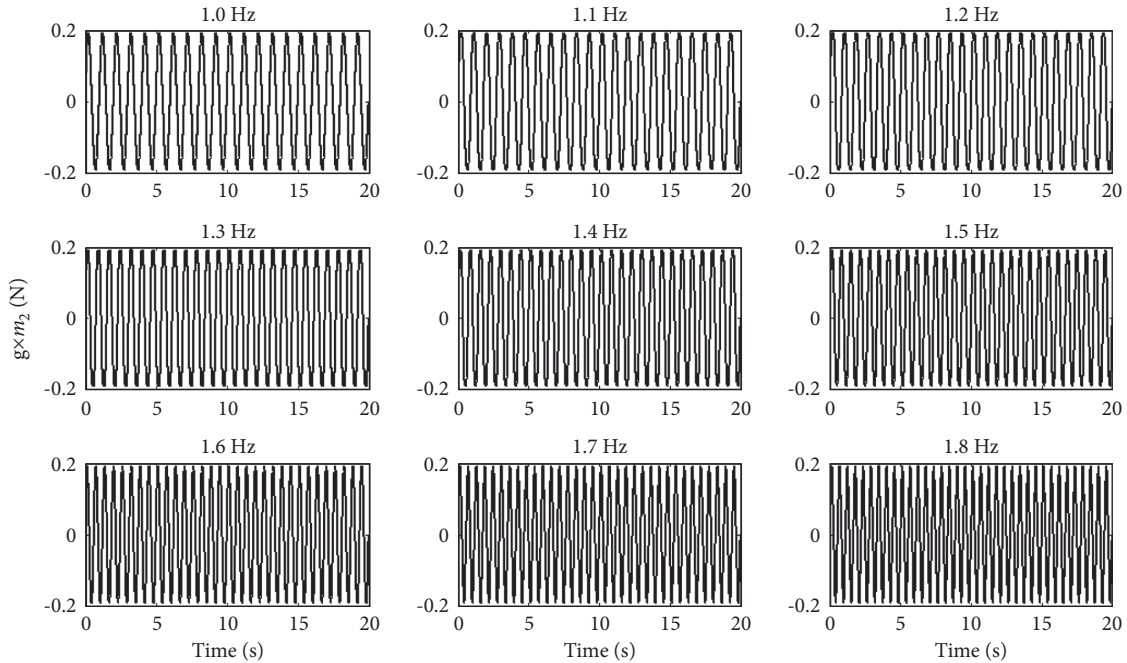


FIGURE 13: The simulated crowd swaying loads curves at nine frequencies.

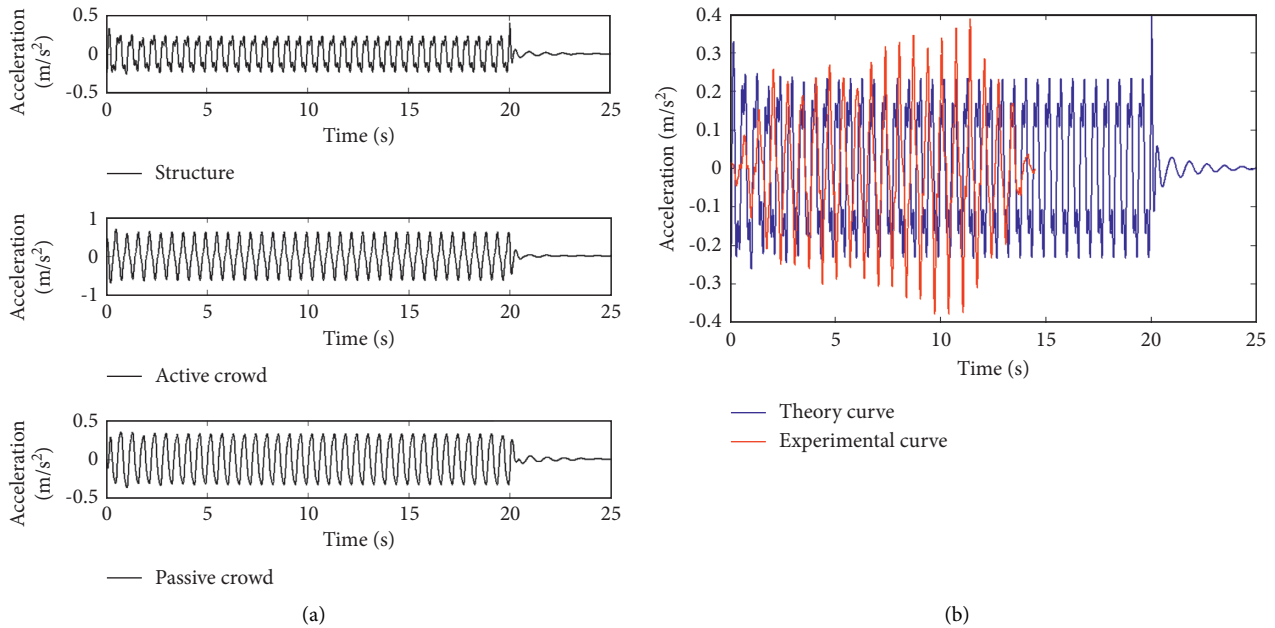


FIGURE 14: The simulated acceleration of model at swaying load. (a) The acceleration of model; (b) the theory acceleration and experimental acceleration of structure.

decreases by 23% (at 2.1 Hz) when  $\zeta_2$  increases by 25%. Besides, considering the different  $f_2$  influences on the structural response, the structural response decreases by 65–62% when  $\alpha = 0.2$ ; by 88–86% when  $\alpha = 0.8$ ; by 92–90% when  $\alpha = 1.4$ ; by 94–92% when  $\alpha = 2.0$ .

In addition, the curve in Figure 15 shows that  $f$  corresponding to the peak is different. The  $f$  corresponding to the peak of the curve is shown in Table 6.

It can be seen from the numerical trend in the table: under the same  $f_2$ , the smaller the  $\alpha$ , the larger the  $f$  that makes the structure have a greater response; the larger the  $f_2$ , the larger the  $f$  that makes the structure have a greater response, from  $f = 1.4$  Hz when  $f_2 = 1.5$  Hz to  $f = 1.7$  Hz when  $f_2 = 3.3$  Hz. The distribution of numbers in the table shows that the corresponding  $f$  varies from 1.2 to 1.7 Hz, mainly at 1.2 Hz, 1.3 Hz, and 1.4 Hz.

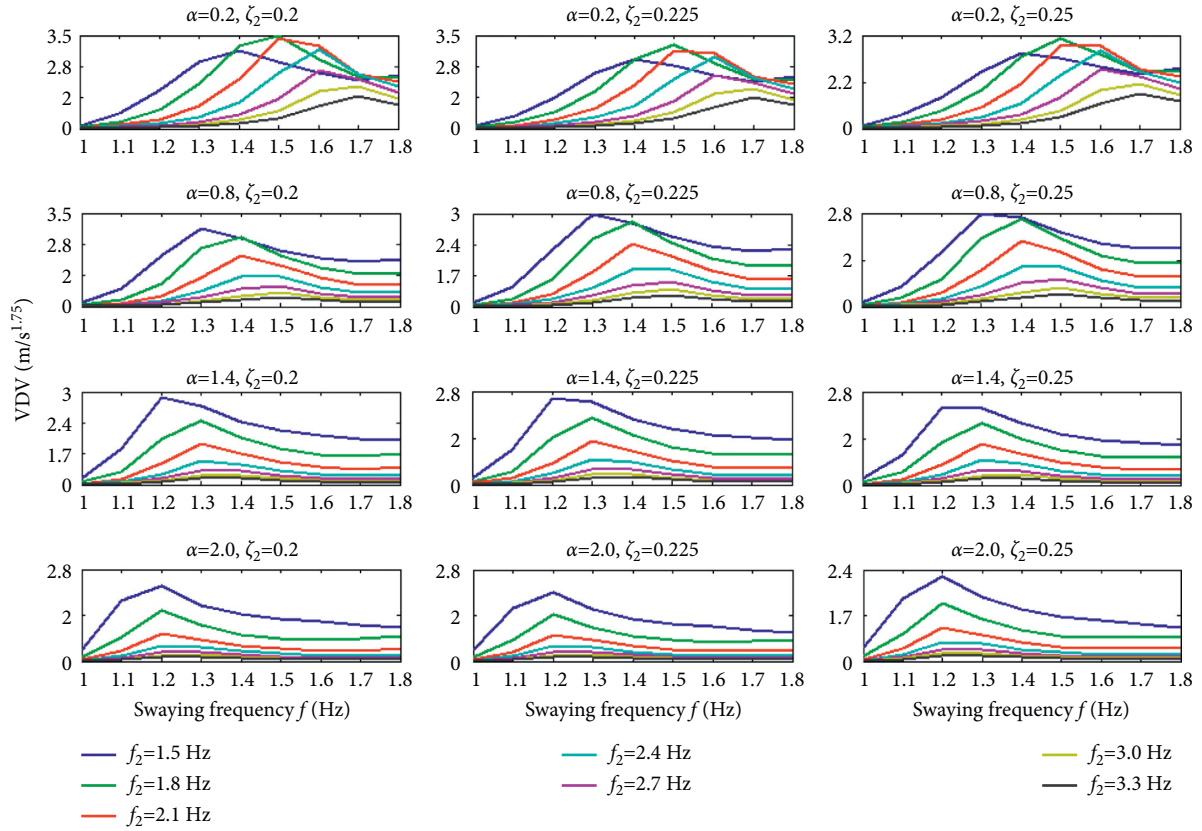


FIGURE 15: The structural dynamic responses with VDV values.

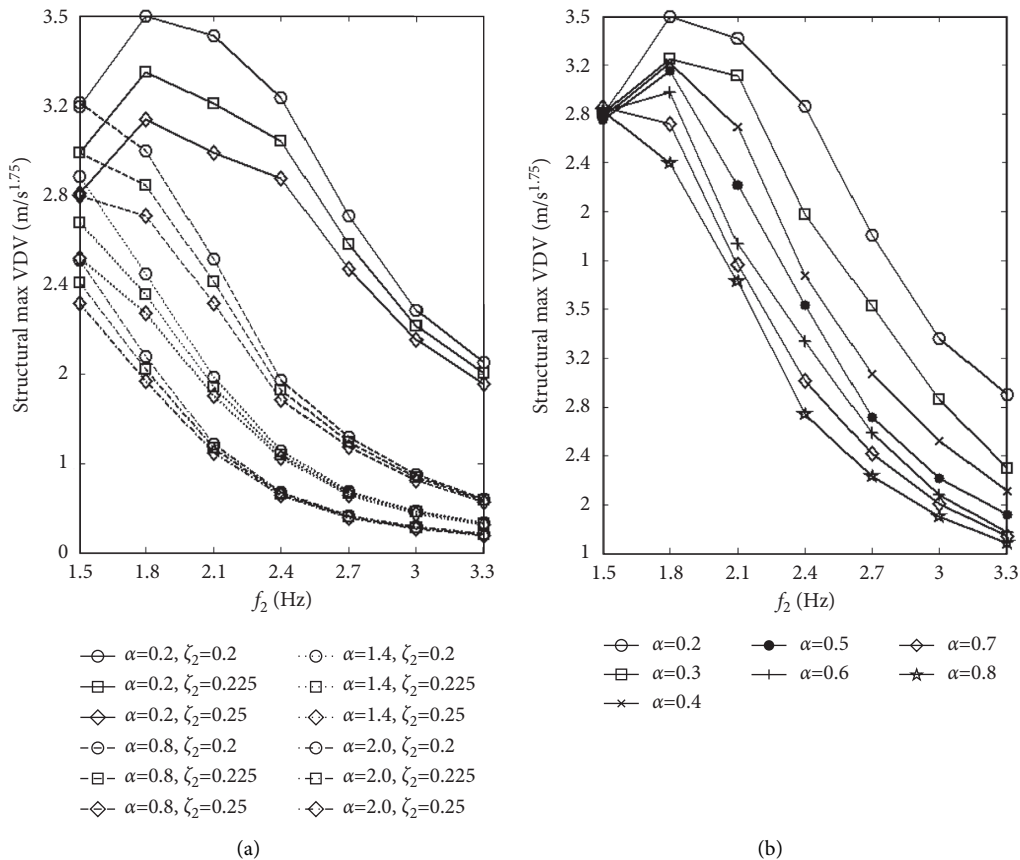


FIGURE 16: The influence of active crowd parameters on structural dynamic responses. (a) The max VDV with  $f_2 \propto \zeta_2$ ; (b) the max VDV when  $\alpha$  between 0.2 and 0.8.



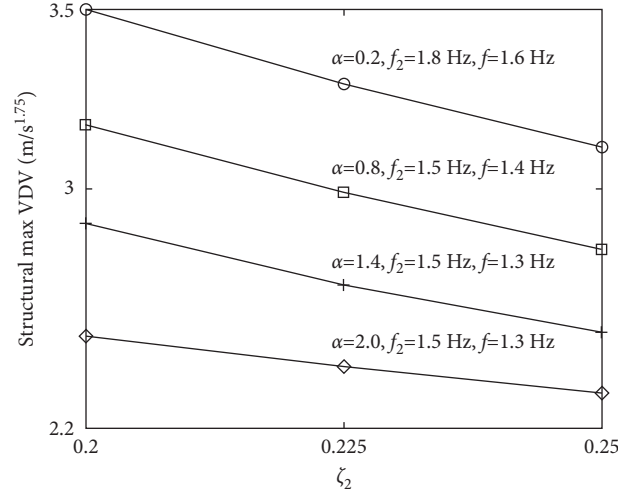
FIGURE 17: The influence of  $\zeta_2$  on structural dynamic responses.

TABLE 5: The max VDV corresponding to variate parameters of active crowd.

Parameter		The degree of reduction (%)						
		1.5 Hz	1.8 Hz	2.1 Hz	2.4 Hz	2.7 Hz	3.3 Hz	3.3 Hz
$\alpha$	0.2–2.0	34	64	79	87	89	89	90
$\zeta_2$	0.20–0.25	22	19	23	18	16	12	11

TABLE 6: The peak of structural dynamic response corresponding to swaying frequencies.

$f$ (Hz)	$f_2$ (Hz)						
	1.5	1.8	2.1	2.4	2.7	3.0	3.3
1.0							
1.1							
1.2	<i>a-l</i>	<i>j-l</i>	<i>j-l</i>	<i>j-l</i>	<i>l</i>		
1.3	<i>d-f</i>	<i>g-i</i>	<i>g-i</i>	<i>g-i</i>	<i>g-k</i>	<i>g-l</i>	<i>g-l</i>
1.4	<i>a-c</i>	<i>d-f</i>	<i>d-f</i>	<i>d-f</i>	<i>d-f</i>		
1.5		<i>a-c</i>	<i>a-c</i>			<i>d-f</i>	<i>d-f</i>
1.6				<i>a-c</i>	<i>a-c</i>		
1.7						<i>a-c</i>	
1.8							<i>a-c</i>

*a to l* stands for *a* –  $\alpha = 0.2$ ,  $\zeta_2 = 0.2$ ; *b* –  $\alpha = 0.2$ ,  $\zeta_2 = 0.225$ ; *c* –  $\alpha = 0.2$ ,  $\zeta_2 = 0.25$ ; *d* –  $\alpha = 0.8$ ,  $\zeta_2 = 0.2$ ; *e* –  $\alpha = 0.8$ ,  $\zeta_2 = 0.225$ ; *f* –  $\alpha = 0.8$ ,  $\zeta_2 = 0.25$ ; *g* –  $\alpha = 1.4$ ,  $\zeta_2 = 0.2$ ; *h* –  $\alpha = 1.4$ ,  $\zeta_2 = 0.225$ ; *i* –  $\alpha = 1.4$ ,  $\zeta_2 = 0.25$ ; *j* –  $\alpha = 2.0$ ,  $\zeta_2 = 0.2$ ; *k* –  $\alpha = 2.0$ ,  $\zeta_2 = 0.225$ ; *l* –  $\alpha = 2.0$ ,  $\zeta_2 = 0.25$ .

**4.2. Changing the Static Crowd Parameters.** The content in Section 3.1 is prepared based on  $f_3 = 2.0$  Hz and  $\zeta_3 = 0.4$ . The curve in Figure 16(a) shows that, due to different  $\alpha$ , the structure VDV may reach its maximum when  $f_2 = 1.5$  Hz and  $\zeta_2 = 0.2$  or  $f_2 = 1.8$  Hz and  $\zeta_2 = 0.2$ . According to this, for analyzing the influence of static crowd parameters of model's structural responses,  $f_3$  is set between 1.4 and 2.8 Hz and taken at 0.2 Hz intervals (eight in total),  $\zeta_3$  is set between 0.3 and 0.5 and taken at 0.1 intervals (three in total), and  $\alpha$  is set at 0.2, 0.8, 1.4, and 2.0. Then, 864 coupling model parameter combinations are formed (the program of MATLAB software is shown in Appendix I).

First, taking the model of  $f_2 = 1.5$  Hz,  $\zeta_2 = 0.2$  as an example, the structural acceleration curves of models  $f_3 = 2.8$  Hz,  $\zeta_3 = 0.5$ ,  $\alpha = 2.0$ , and  $f = 1.8$  Hz are shown in

Figure 18(a), and the curve form is still similar to the measured structural curve (crowd standing and swaying at 1.8 Hz, and the peak value is divided by 4). Just like Figure 15, the relationship curves between the VDV of all model structures and different dynamic crowd parameters are obtained, as shown in Figure 18(b). The curve variation tendencies are as follows: with increasing  $f$ , the curve first rises and then descends gently, and there is a unique peak. The larger the  $f_3$ , the greater the structural response. The  $f$  corresponding to the peak value of the curve decreases with increasing  $\alpha$ . To check whether the variation tendencies of acceleration curves in the other two forms are consistent with the previously mentioned phenomena, the RMS and peak value curve in the bottom right corner of Figure 14(b) are given in this paper, as shown in Figure 18(c). Compared

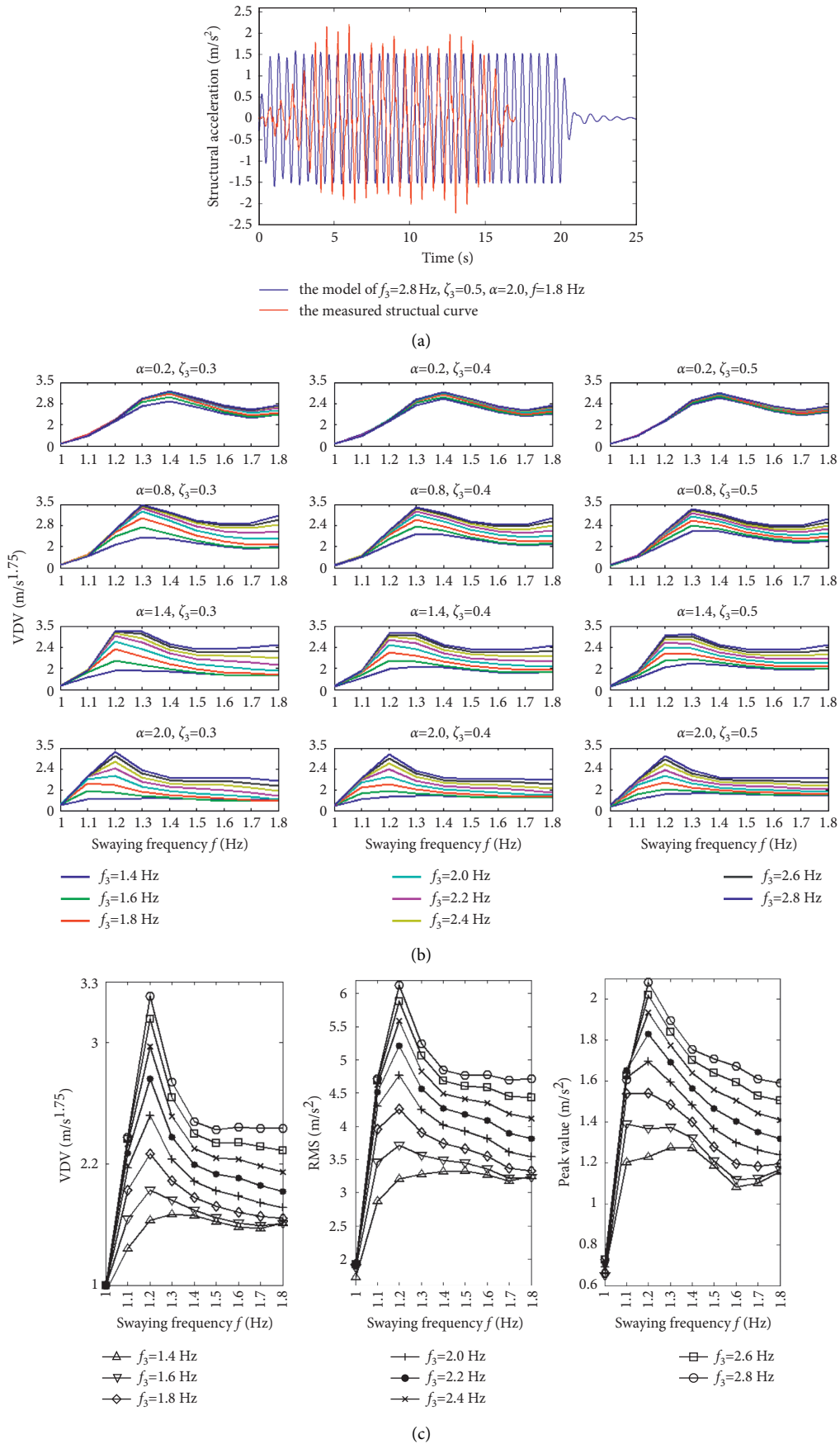


FIGURE 18: The structural dynamic responses of models with different passive crowd parameters. (a) The structural acceleration curve of one model at swaying load; (b) the structural acceleration VDV of models; (c) the acceleration VDV, RMS and peak values with swaying frequencies.

with the VDV curve, except for different values, the variation tendencies of each corresponding curve are basically the same, especially the curve represented by RMS. The rationality of analyzing the variation of static crowd parameters to structural response with VDV is hereby further proved.

Second, the relationship curve between the peak value of each curve and the  $f_3$  in Figure 18(b) is given, as shown in Figure 19. The curve in the figure shows the following variation tendencies: with increasing  $f_3$ , the structural response increases and reaches its maximum when  $f_3 = 2.8$  Hz; for the curve with the same  $\alpha$ , the higher the  $\zeta_3$  is, the larger the structural response will be. Only when  $f_3$  is greater than a certain value (e.g.,  $f_3 \geq 1.8$  Hz when  $\alpha = 0.2$ ;  $f_3 \geq 1.7$  Hz when  $\alpha = 0.8$  and 1.4; and  $f_3 \geq 2.0$  Hz when  $\alpha = 2.0$ ), the higher the  $\zeta_3$  is, the smaller the structural response will be. In addition, the structural response of the model with  $\alpha > 0.2$  is larger than that of the model with  $\alpha = 0.2$ . For example, when  $\alpha = 0.8$ , the structural response is significantly larger than that of other cases.

From the curve variations in Figure 19, it can be concluded that there is no negative correlation between the  $\alpha$  and the structure's VDV. Therefore, other  $\alpha$  (0.4, 0.6, 1.0, 1.2, 1.6, and 1.8) are also calculated. The model results of  $\zeta_3 = 0.3$  and  $\zeta_3 = 0.5$  are, respectively, shown in the left and right graphs of Figure 20. The  $x$ -axis represents the  $\alpha$ , and each curve represents the change in maximum VDV of the structure's  $f_3$ . The curves show that the VDV of the structure with  $\alpha = 0.2$  reaches its maximum when  $f_3 \leq 1.8$  Hz (red curves), the VDV of the structure with  $\alpha = 0.8$  reaches its maximum when  $f_3 = 2.0$ –2.4 Hz (blue curves), and the VDV of the structure with  $\alpha = 1.0$  reaches the maximum when  $f_3 = 2.6$ –2.8 Hz (black curves). It may be indicated that not the more static crowd the responses of structure is little, it also depends on  $f_3$ .

Third, the same drawing method is used to sort out the model results of other  $f_2$ , and the result curve of  $\zeta_3 = 0.3$  is taken as an example, as shown in Figure 21. There are six graphs in the figure, respectively, representing the model of  $f_2$  at 1.8–3.3 Hz. Compared with Figure 20, it is found that, with increasing  $f_2$ , the curve variation tendencies gradually becomes unified and decreases with increasing  $\alpha$ . Moreover, by comparing the values of each curve, it is concluded that the smaller  $f_2$  and the larger  $f_3$  are, the greater the model structure's VDV will be. Then, the result curve with  $\zeta_3 = 0.5$  is given, as shown in Figure 22. The curve variation tendencies and the structural VDV variations caused by parameters are basically the same as Figure 21.

Finally, the decrease (increase) of structural response caused by different static crowd parameters under the previously mentioned dynamic crowd parameter model is calculated. Table 7 shows the maximum structure VDV caused by difference in  $\alpha$  and  $\zeta_3$ , and the negative value indicates that the structural response is increasing. According to the data,  $\alpha$  influences on structural response are greater than  $\zeta_3$  influences, and what is interesting is that when  $f_2 = 2.7$  Hz and  $f_2 = 3.3$  Hz. The higher the  $\zeta_3$  is, the greater the model structure's VDV will be. Besides, the structural response with the  $\zeta_3$  increasing from 1.4 Hz to 2.8 Hz shows an average increase of 3.8 times.

Similarly, the  $f$  corresponding to the maximum VDV of the model structure is sorted out, as shown in Table 8. The numbers in brackets represent the model results of  $\zeta_3 = 0.3$ , and the numbers outside the brackets represent the model results of  $\zeta_3 = 0.5$ . According to the distribution of numbers, with increasing  $\alpha$ , the lower the swaying frequency, the greater the structural response, and  $f$  is mainly concentrated between 1.2–1.4 Hz. The swaying frequency range is similar to the results of dynamic crowd parameter analysis (Table 6).

To explain the reason for this phenomenon, the structural response of models  $f_2 = 1.5$  Hz,  $\zeta_2 = 0.2$ ,  $f_3 = 2.0$  Hz,  $\zeta_3 = 0.3$ , and  $\alpha = 2.0$  at  $f = 1.0$  Hz, 1.3 Hz, and 1.8 Hz are taken as examples, and the time domain curve and frequency domain results are given, as shown in Figure 23. The peak value of the time–history curve in the figure shows that the peak value of the structural acceleration appears at 1.3 Hz. As shown by the corresponding frequency domain analysis, both first-order and third-order 1.3 Hz and 1.8 Hz swaying loads contribute to the structure, while the contribution to the structure is the largest under the action of the 1.3 Hz swaying load. The reason may be that  $f_1$  in the coupling model is set to 2.7 Hz, and  $f = 1.3$  Hz is close to 1/2 of the structural frequency. The reason why the third-order frequency acts on the structure is that the contribution of the third-order frequency is considered in the calculation formula of the swaying load curve.

**4.3. Changing the Structure Parameter.** Because  $1 + \alpha \leq 3\beta$  in the first part of Section 3, and when  $\beta$  is set as 0.5,  $\alpha \leq 0.5$ , so  $\alpha$  is set as 0.2, 0.3, 0.4, and 0.5 (four in total). In order to analyze the different structure parameters influence on structural response, the crowd parameters should be regarded as constants. According to the crowd frequency without loss of generality, the  $f_2$  changes between 1.5 Hz and 3.3 Hz (in 0.3 Hz increments), for a total of seven values, and the  $f_3$  changes between 1.4 Hz–2.8 Hz (in 0.2 increments), for a total of eight values. Although  $f_2$  and  $f_3$  are variables, any combination of the two is taken as a constant in this section. For the crowd damping ratio, only the parameter values making the structure produce the maximum VDV are considered to simplify the complexity of the model parameters. Since it has been determined above that, when  $\zeta_2 = 0.2$ , the model structure VDV reaches its maximum. Considering that  $\zeta_3 = 0.3$  and  $\zeta_3 = 0.5$  have a little impact on the response of the structure,  $\zeta_3 = 0.3$  and  $\zeta_2 = 0.2$  are taken as invariants. As shown in Figure 24, the change relationship between VDV and the  $f$  of the model structure with combination parameters  $f_2 = 1.8$  Hz and  $f_3 = 2.8$  Hz is displayed. Four longitudinal graphs show the model results of  $\alpha = 0.2, 0.3, 0.4,$  and 0.5; three transverse graphs show the model results of  $\zeta_1 = 0.02, 0.05,$  and 0.073.

Furthermore, the peak value of the curve in Figure 24 and the  $f$  corresponding to other model curves are sorted out. It is concluded that when  $f_1 = 1.0$ –1.5 Hz, the peak value appears at  $f = 1.8$  Hz, and, when  $f_1 = 2.0$  Hz, the peak value appears at  $f = 1.0$  Hz. Then, with increasing the structural frequency, the  $f$  making the structure produce the maximum response increases from 1.1 Hz to 1.7 Hz.

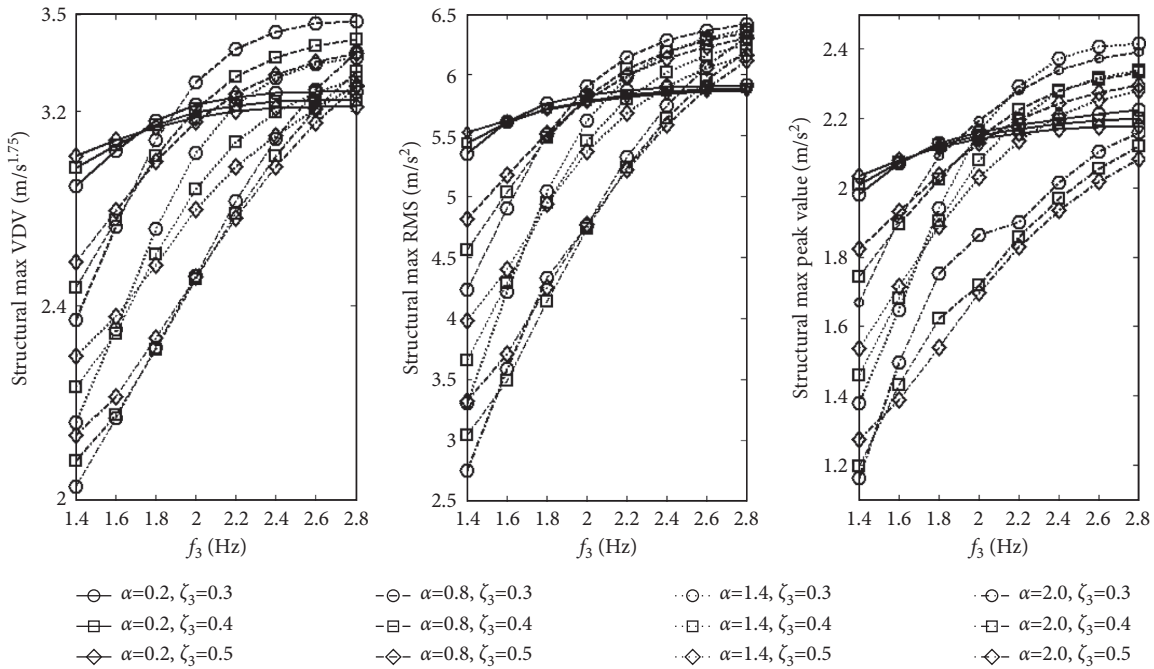


FIGURE 19: The influence of passive crowd parameters on structural dynamic responses of max acceleration VDV, RMS, and peak values.

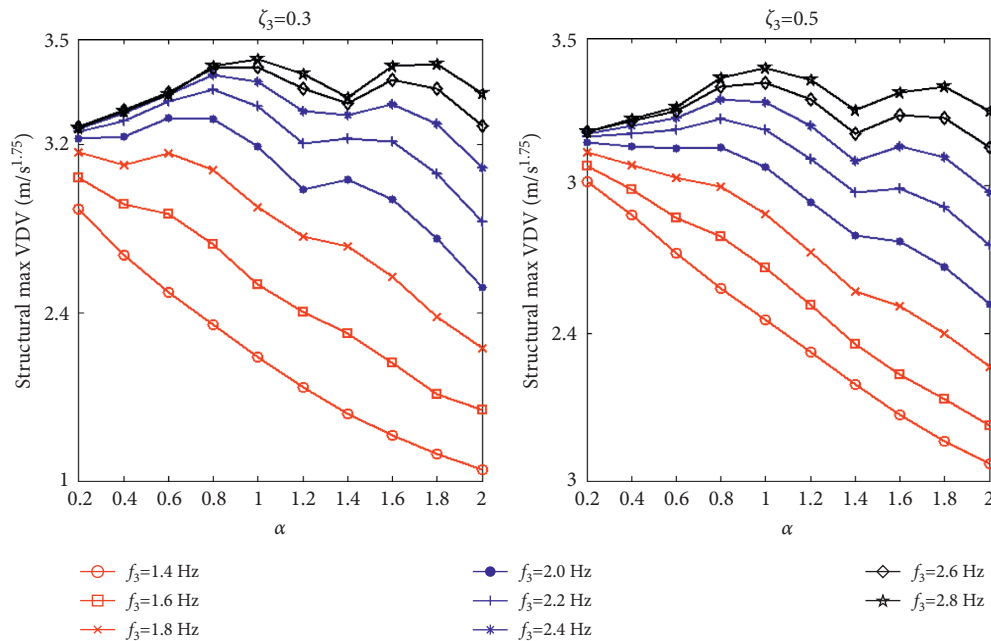


FIGURE 20: The influence of different  $\alpha$  on max acceleration VDV when  $f_2 = 1.5$  Hz.

To analyze the curve variation tendencies in more detail, for example, the model results of  $\alpha = 0.5$ ,  $\zeta_1 = 0.073$  are represented by VDV, RMS, and peak value, respectively, as shown in Figure 25. The variation tendency of the three curves are basically the same; that is, the structural response of  $f_1 \leq 1.5$  Hz increases unidirectionally with  $f_j$ , the structural response of  $f_1 = 2.0$  Hz decreases first and then increases, and the structural response of  $f_1 \geq 2.5$  Hz increases first and then decreases.

When analyzing the structure parameter influences on structural response, the relationship curve between the maximum VDV and  $f_1$  with the same  $\alpha$  and different  $\zeta_1$  is given, as shown in Figure 26. The curve in the figure shows that the smaller the  $\zeta_1$  is, the greater the structural response will be, but the influence of  $\zeta_1$  on structural response is related to  $f_1$ . Only when  $f_1$  is between 2.0 and 4.0 Hz will an increase in the  $\zeta_1$  effectively reduce the structural VDV. In addition, the curve rises first and then descends, and the

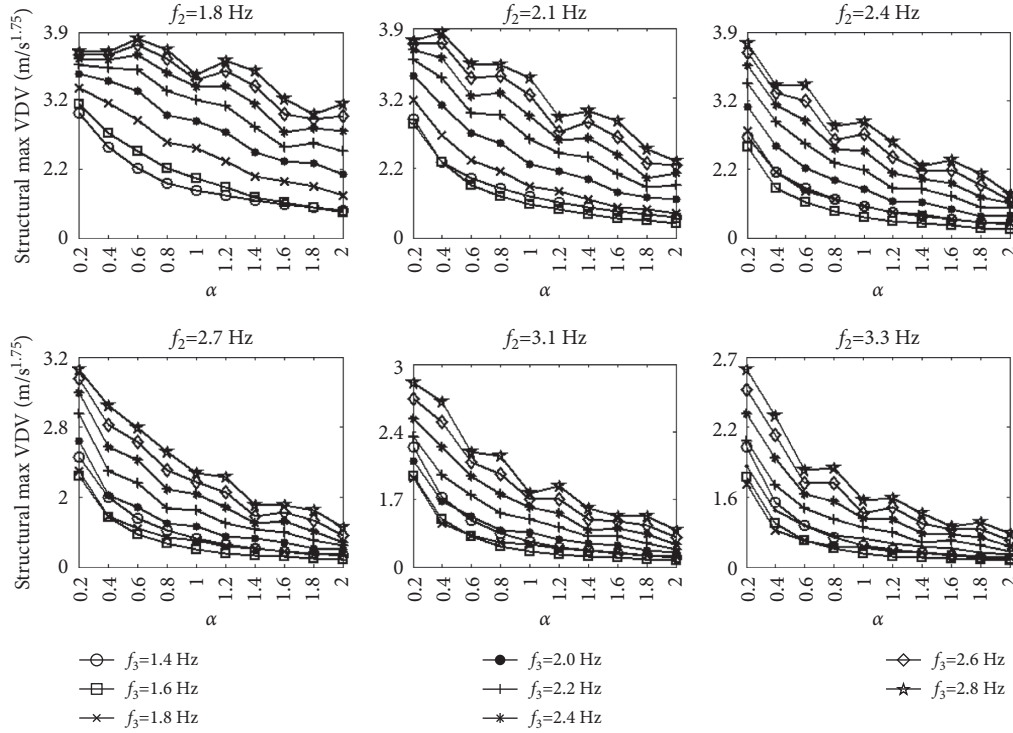


FIGURE 21: The influence of other  $f_2$  values on structural dynamic responses when  $\zeta_3 = 0.3$ .

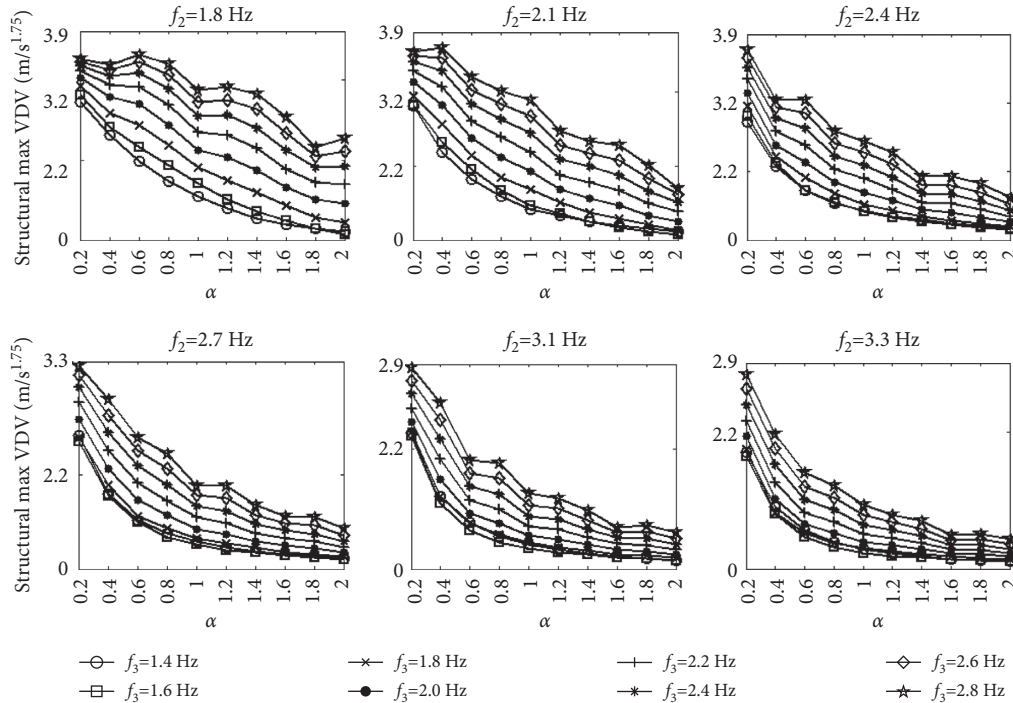


FIGURE 22: The influence of other  $f_2$  values on structural dynamic responses when  $\zeta_3 = 0.5$ .

peak value appears at  $f_1 = 2.5$  Hz or 3.0 Hz, indicating that the structure with this frequency is easy to produce a large VDV under swaying load. The model of the crowd parameter combination shows that the structure parameter corresponding to the maximum structural VDV is  $f_1 = 2.5$  Hz,  $\zeta_1 = 2\%$ , and  $\alpha = 0.5$ .

The influence of structure parameters on structural response under the combination of other  $f_2$  and  $f_3$  is further analyzed. It has been determined that the structural response is largest when  $\zeta_1 = 2\%$ ; for simplicity, only the model results corresponding to this parameter are analyzed. Figures 27(a)–27(d) show the model results of  $\alpha = 0.2, 0.3, 0.4,$  and  $0.5$ ,

TABLE 7: The max VDV corresponding to variate parameters of passive crowd.

Parameter		The degree of reduction (%)							
		1.4 Hz	1.6 Hz	1.8 Hz	2.0 Hz	2.2 Hz	2.4 Hz	2.6 Hz	2.8 Hz
$\alpha$	0.2-2.0	63	60	57	64	61	69	68	70
$\zeta_3$	0.3-0.5	-47	-12	-3	26	30	31	30	30

TABLE 8: The peak of structural dynamic response corresponding to  $f$  with three kinds of model.

$f$ (Hz)	$f_3$ (Hz)							
	1.4	1.6	1.8	2.0	2.2	2.4	2.6	2.8
1.2		$ghj-l (j-k)$	$g-l (j-l)$	$g-l (j-k)$	$g-l (j-k)$	$g-l (j-k)$	$g-l (j-k)$	$g-l (j-k)$
1.3	$d-l$	$d-fi (g-i)$	$d-f (g-i)$	$d-ff (g-i)$	$d-ff (g-i)$	$d-ff (g-i)$	$d-ff (g-i)$	$d-j (g-i)$
1.4	$a-cj (i)$	$a-c (d-f)$	$a-c (d-f)$	$a-c (d-f)$	$a-c (d-f)$	$a-c (d-f)$	$a-c (d-f)$	$a-c (d-f)$
1.5	$(a-h)$	$a-c$	$a-c$	$a-c$	$a-c$	$a-c$	$a-c$	$a-c$
1.8	$(j-l)$	$(l)$						

$a$  to  $l$  stands for  $a - \alpha = 0.2, \zeta_3 = 0.3; b - \alpha = 0.2, \zeta_3 = 0.4; c - \alpha = 0.2, \zeta_3 = 0.5; d - \alpha = 0.8, \zeta_3 = 0.3; e - \alpha = 0.8, \zeta_3 = 0.4; f - \alpha = 0.8, \zeta_3 = 0.5; g - \alpha = 1.4, \zeta_3 = 0.3; h - \alpha = 1.4, \zeta_3 = 0.4; i - \alpha = 1.4, \zeta_3 = 0.5; j - \alpha = 2.0, \zeta_3 = 0.3; k - \alpha = 2.0, \zeta_3 = 0.4; l - \alpha = 2.0, \zeta_3 = 0.5$ .

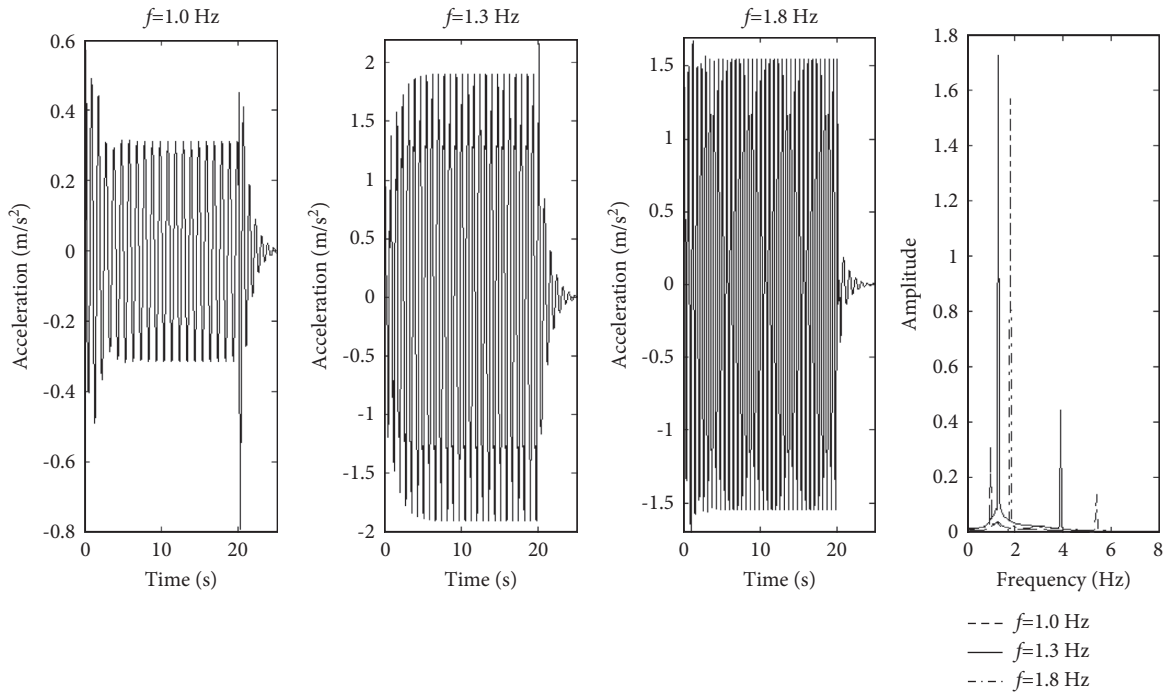


FIGURE 23: The time domain and frequency domain analysis of structure response.

respectively. There are eight curves in the graphs representing the model results of the eight  $f_3$ , and there are 56 curves in each figure. All curves rise first and then descend with increasing  $f_1$ , and the  $f_1$  corresponding to the peak value of the curve varies between 2.5 and 3.5 Hz. When comparing the curve values of different  $f_2$ , it is found that, with the change of  $\alpha$ , the maximum value of the curve is not in the model of the same  $f_2$ . For example, the curve value of  $f_2 = 2.1$  Hz is the largest in the model of  $\alpha = 0.2$ , the curve value of  $f_2 = 2.4$  Hz is the largest in the model of  $\alpha = 0.3$ , and the curve value of  $f_2 = 1.8$  Hz is the largest in the models of  $\alpha = 0.4$  and  $0.5$ . When comparing the curve values of different  $f_3$ , it can be determined that the structural VDV is the largest when  $f_3 = 2.8$  Hz.

Then, to analyze the change of structural response with different  $\alpha$ , taking the curve of  $f_3 = 2.8$  Hz in Figure 27 as an example, the change curve of structural response with  $f_1$  and  $\alpha$  under each  $f_2$  of the model is given. As shown in Figure 28, the curve values is affected by the  $f_2$  and the structural response does not strictly follow the tendency that the larger the  $\alpha$  is, the smaller the structural response is.

The structure parameters influence on structural VDV is considered. As shown in Table 9, the maximum range of structural response reduction with  $\alpha, \zeta_1$ , and  $f_1$  is given. The maximum influence of crowd mass on structural response is 83%, and this number will be reduced by 77% when the structural frequency is changed and by 56% when structural damping is increased.

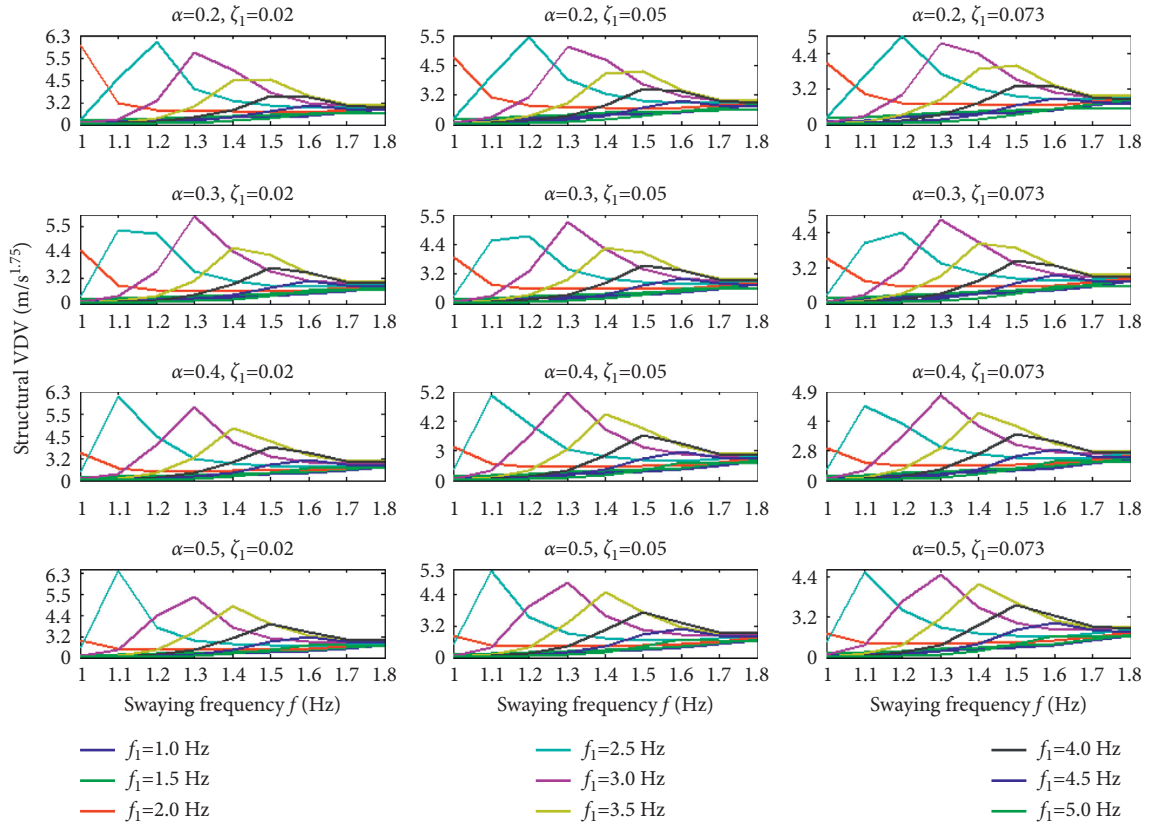


FIGURE 24: The structural VDV results when  $f_2 = 1.8$  Hz.

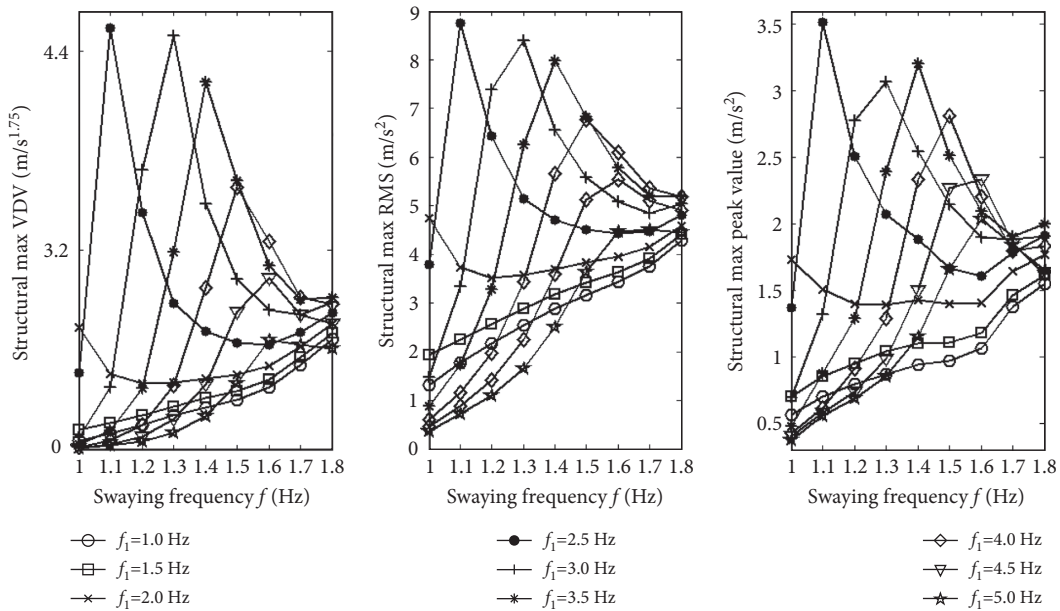


FIGURE 25: The max VDV, RMS, and peak values plotted against swaying frequencies.

When  $\beta = 1.0$ , the value range of  $\alpha$  is set between 0.2 and 2.0. In Section 3.1, the structural VDV when  $f_3 = 2.8$  Hz is calculated on the premise that  $f_1 = 2.7$  Hz. It is necessary to calculate the influence of structure parameter change on structural response under different combinations of  $f_2$  and  $f_3$ .

For example, the model results of  $f_2 = 1.8$  Hz,  $f_3 = 2.8$  Hz, and  $\alpha = 0.2, 0.8, 1.4, \text{ and } 2.0$  are taken as examples to illustrate the relationship between structural VDV and structure parameter changes. As shown in Figure 29, there is only one peak in each curve. Similarly, to analyze the curve variation

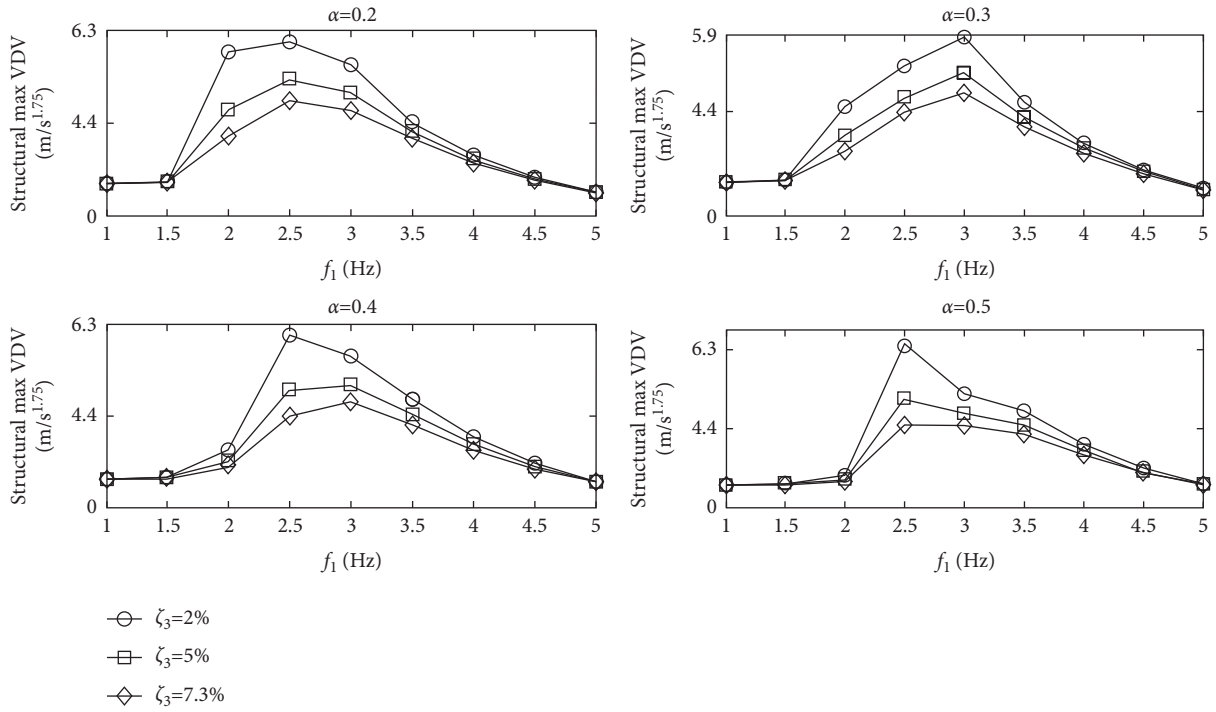
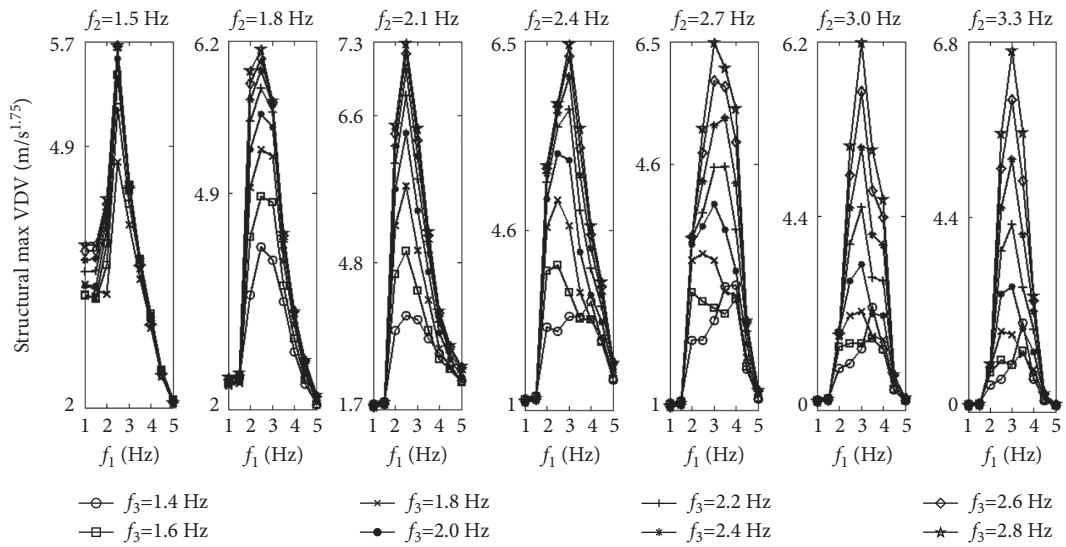


FIGURE 26: The max V DVs corresponding to structural dynamic parameters.



(a)

FIGURE 27: Continued.



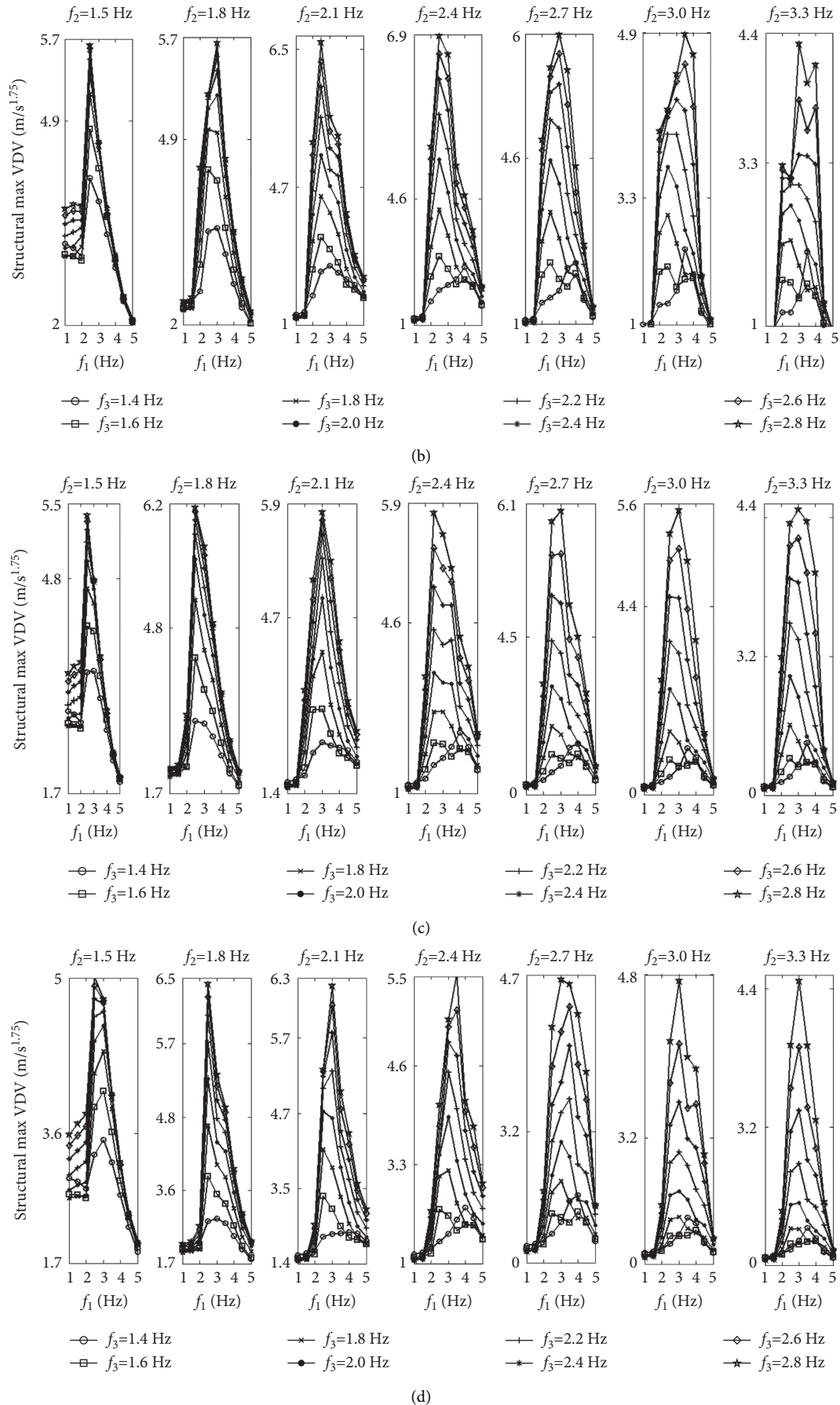


FIGURE 27: The structural parameters plotted against VDV with different  $f_2$  and  $f_3$  of models. (a) The model results when  $\alpha = 0.2$ , (b) the model results when  $\alpha = 0.3$ , (c) the model results when  $\alpha = 0.4$ , and (d) the model results when  $\alpha = 0.5$ .

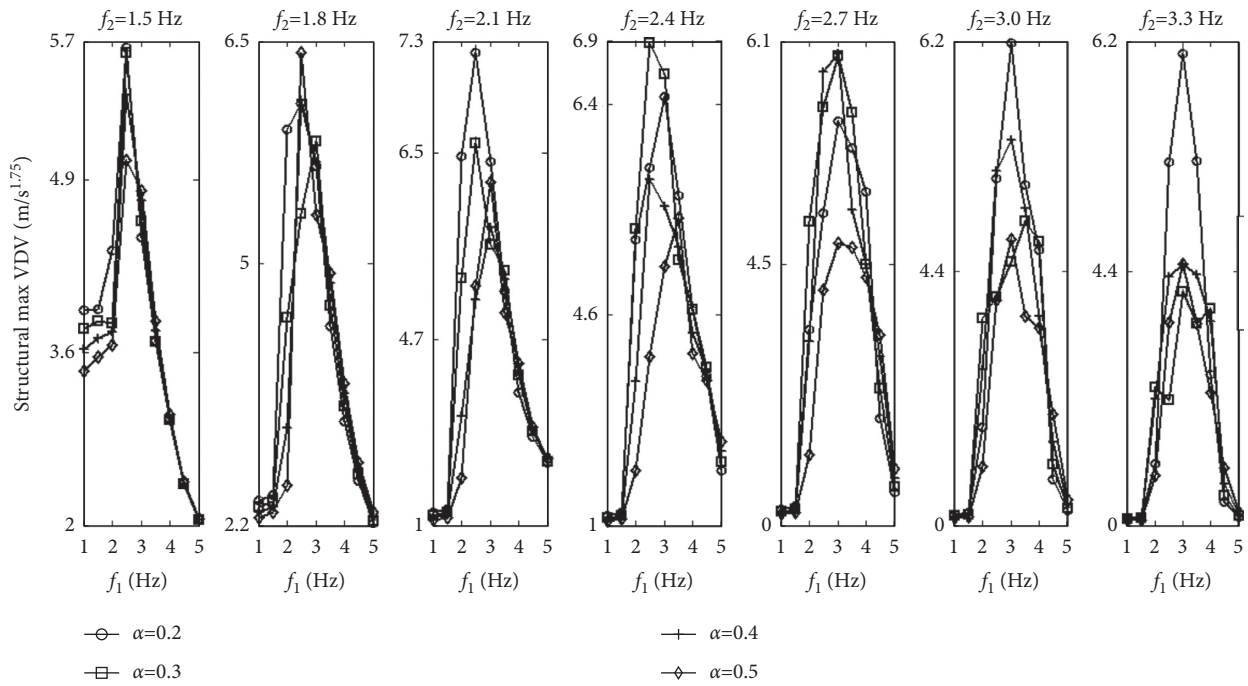


FIGURE 28: The results of model with different  $\alpha$  when  $f_3 = 2.8$  Hz.

TABLE 9: The max reduce amplitude of structural dynamic with  $\alpha$ ,  $\zeta_1$ , and  $f_1$ .

The degree of reduction	Parameter		
	$\alpha$ (0.2–0.5) (%)	$\zeta_1$ (2.0–7.3) (%)	$f_1$ (1.0–5.0 Hz) (%)
	83	56	77

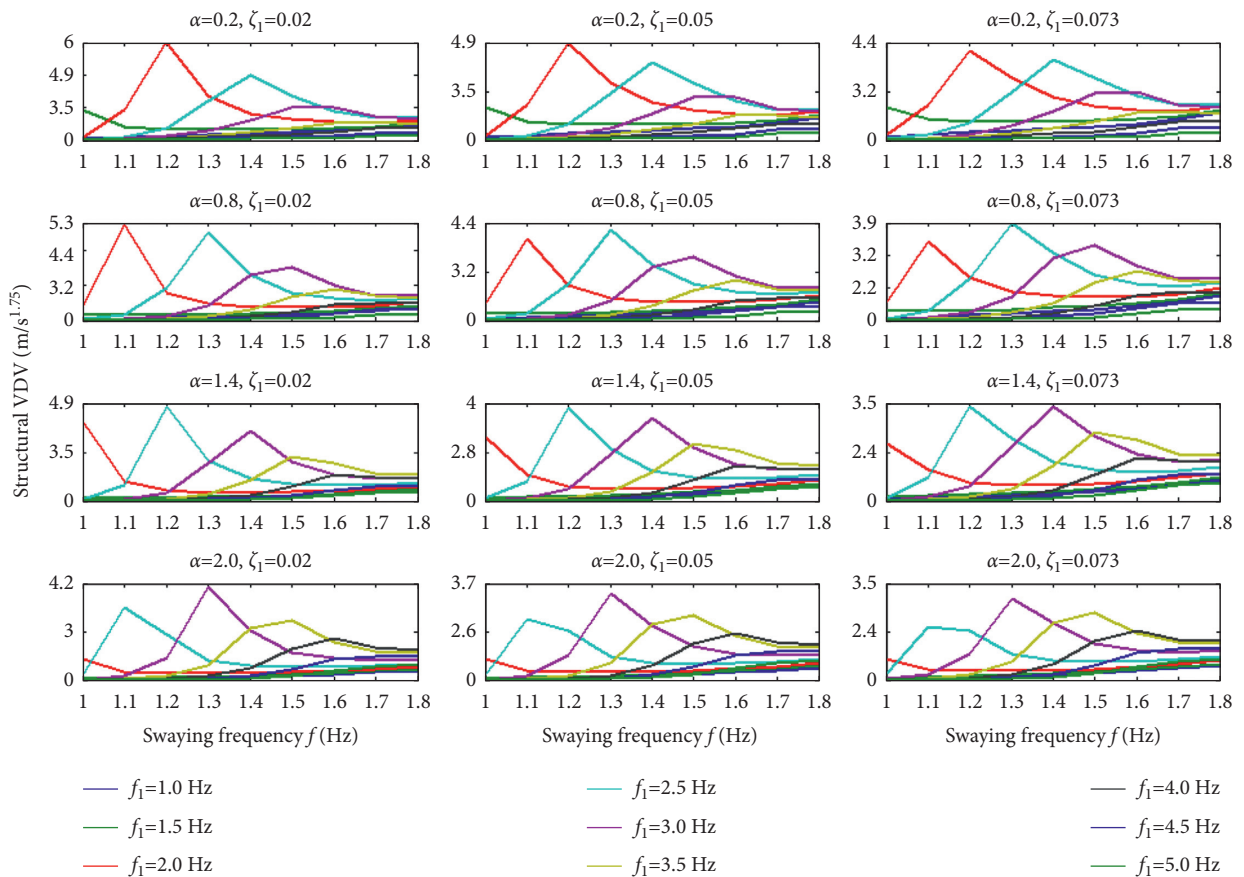


FIGURE 29: The structural VDV results when  $f_2 = 1.8$  Hz,  $f_3 = 2.8$  Hz of model.

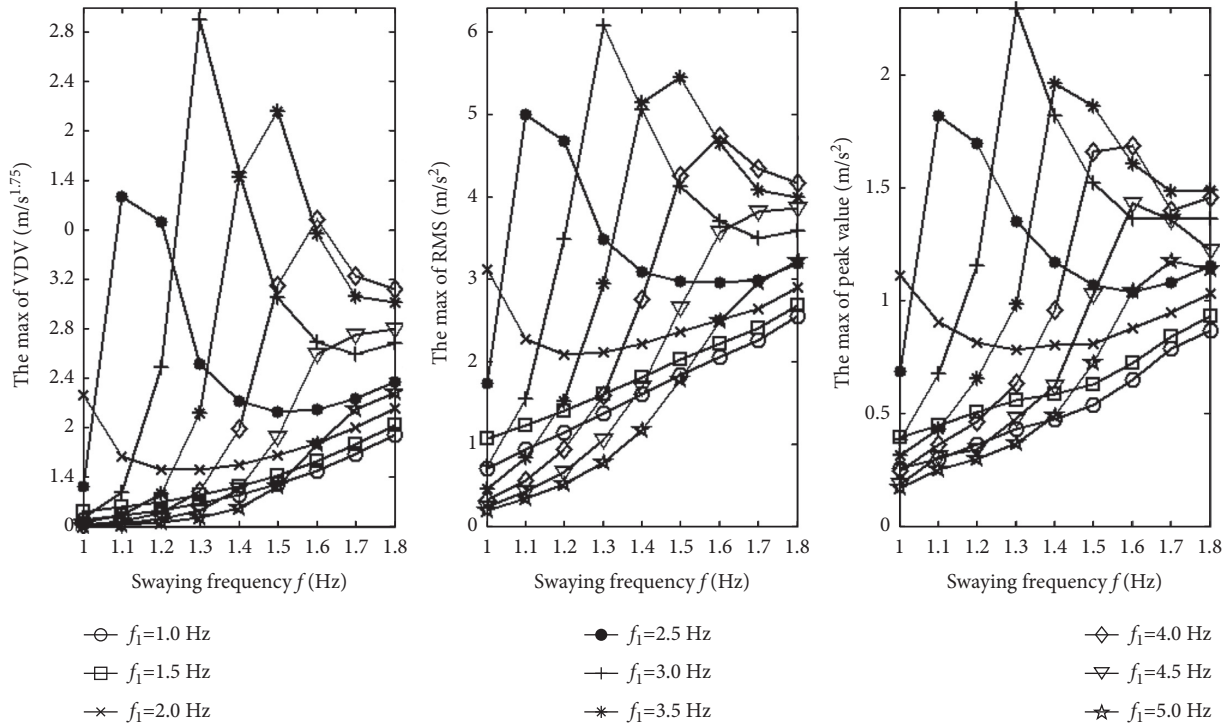


FIGURE 30: The max VDV, RMS, and peak values plotted against swaying frequencies.

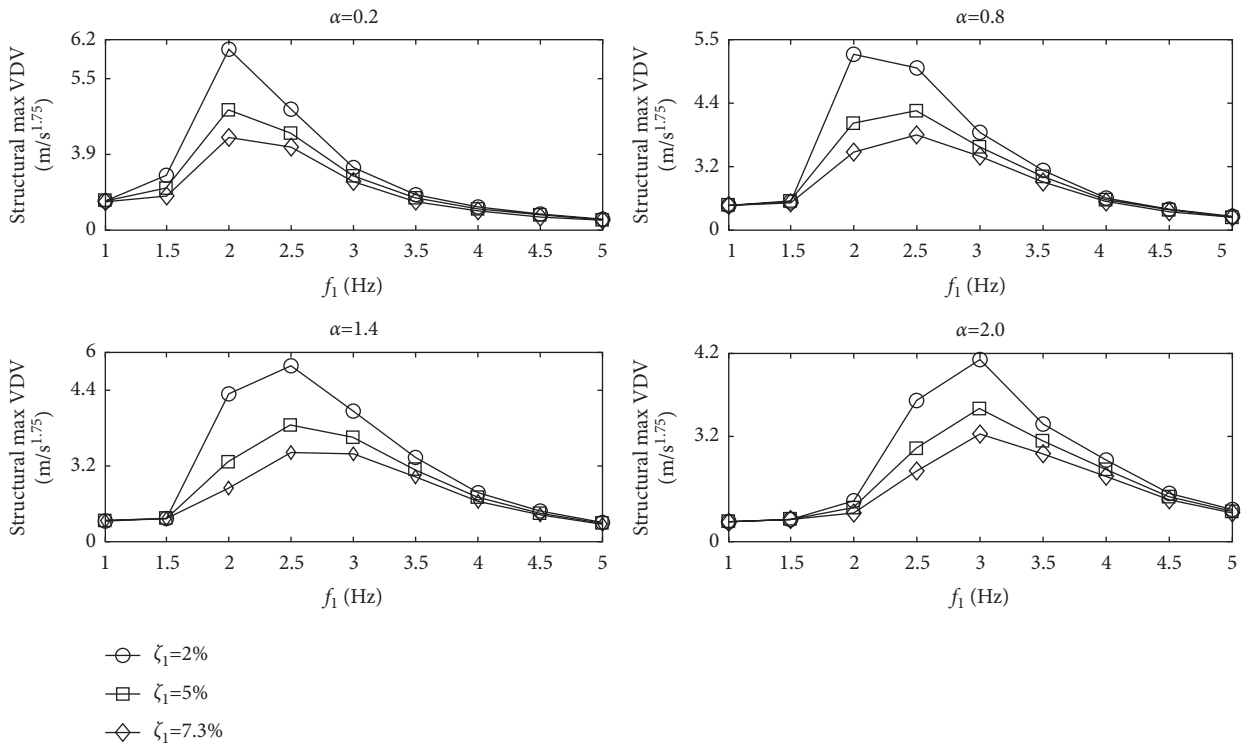


FIGURE 31: The max V DVs corresponding to structural dynamic parameters.

tendencies in more detail, the model results of  $\alpha = 2.0$ ,  $\zeta_1 = 7.3\%$  are represented by VDV, RMS, and peak value, respectively. As shown in Figure 30, three curves show the

following variation tendencies: when  $f_1 \leq 1.5$  Hz, the structural response increases roughly linearly with  $f$ ; when  $f_1 = 2.0$  Hz, the structural response decreases first and then

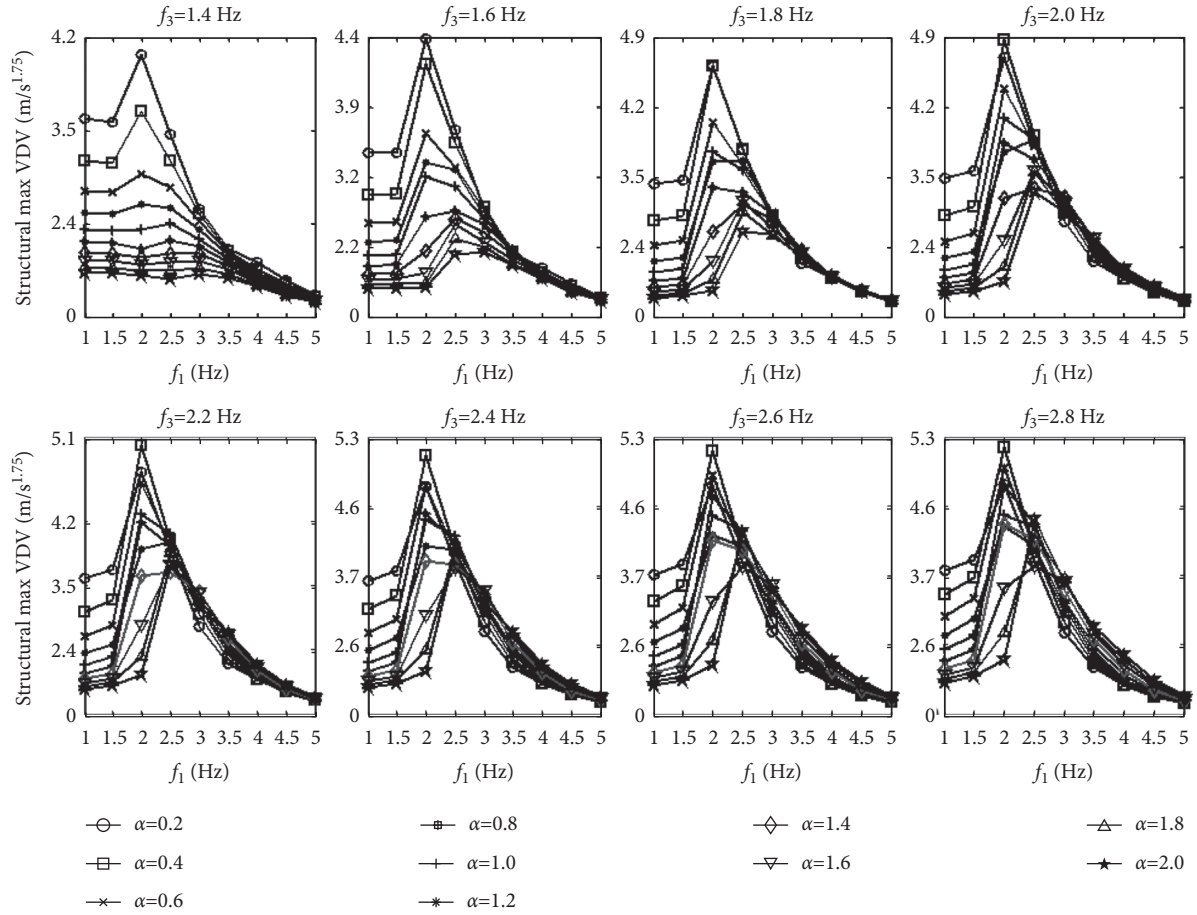


FIGURE 32: The structural VDV of models with different  $f_3$  when  $f_2 = 1.5$  Hz.

increases; when  $2.5 \text{ Hz} \leq f_1 \leq 4.0 \text{ Hz}$ , the structural response increases first and then decreases; when  $f_1 \geq 4.5 \text{ Hz}$ , the structural response increases roughly nonlinearly and unidirectionally with  $f$ .

The relationship between the peak value of each curve in Figure 29 and  $f_1$  is discussed, as shown in Figure 31. The curves in the figure show that the smaller the  $\zeta_1$ , the greater the structural response, but the influence of  $\zeta_1$  on the structural response is related to the structural frequency. An increase in the structural damping ratio will effectively reduce the structural response only when  $f_1$  is between 2.0 and 3.0 Hz. In addition, the  $f_1$  corresponding to the peak value of the curve transits from 2.5 Hz to 3.0 Hz with the increase of  $\alpha$ . The parameter model shows that the structural VDV reaches its maximum when  $\alpha = 0.2$ ,  $\zeta_1 = 2\%$ , and  $f_1 = 2.0$  Hz.

Then, the model results of different parameter combinations of  $f_2$  and  $f_3$  are calculated. Considering the maximum curve value of  $\zeta_1 = 2\%$  in Figure 31, and taking the corresponding results of this parameter as an example, the curves between the maximum VDV of the structure and the structure parameters is given for the combination of  $f_2 = 1.5$  Hz and other  $f_3$  (Figure 32). The figure shows that, with different  $f_3$  of models, the curve is slightly different with  $f_1$ . Only  $f_3 = 1.4$  Hz, and when  $\alpha = 0.2-0.6$ , the curve rise first and then descend; when  $\alpha \geq 1.4$ , the curve begins to descend after  $f_1 = 3.0$  Hz. In other  $f_3$  models. All curves first

rise and then descend with increasing  $f_1$ , and the  $f_1$  corresponding to the curve peak transits from 2.0 Hz to 2.5 Hz with increasing  $\alpha$ . By comparing the maximum value of the curve in each graph, it is found that the curve value in the model with  $f_3 = 2.8$  Hz is greater than that in the model with other  $f_3$ . When sorting out the results of the combination of six other  $f_2$  and  $f_3$ , it shows that the curve value of the combined model with  $f_3 = 2.8$  Hz is the largest. Then, the combined model curves of  $f_2 = 1.8-3.3$  Hz (six values) and  $f_3 = 2.8$  Hz are given, as shown in Figure 33. Each curve in the figure represents the model result of one  $\alpha$ . All curves first rise and then descend with increasing  $f_1$ ; the  $f_1$  corresponding to the peak value of the curve changes between 2.0 Hz and 3.0 Hz, and the  $\alpha$  corresponding to the maximum peak value of the curve is 0.2. Moreover, it is found that, after comparing the curve values in different graphs, the structural VDV of the model with  $f_2 = 1.8$  Hz is the largest.

In addition, the  $f$  corresponding to the maximum VDV of the structure is analyzed, with the results shown in Table 10. Similar to the model result of  $\beta = 0.5$ , when the  $f_1$  is 1.0–1.5 Hz, the corresponding  $f$  is 1.8 Hz or 1.0 Hz. With increasing  $f_1$ , the corresponding  $f$  transits from 1.1–1.3 Hz to 1.7–1.8 Hz. Finally, the change of structural VDV caused by the change of different structure parameters is calculated, as shown in Table 11. Only cases with the greatest impact on the

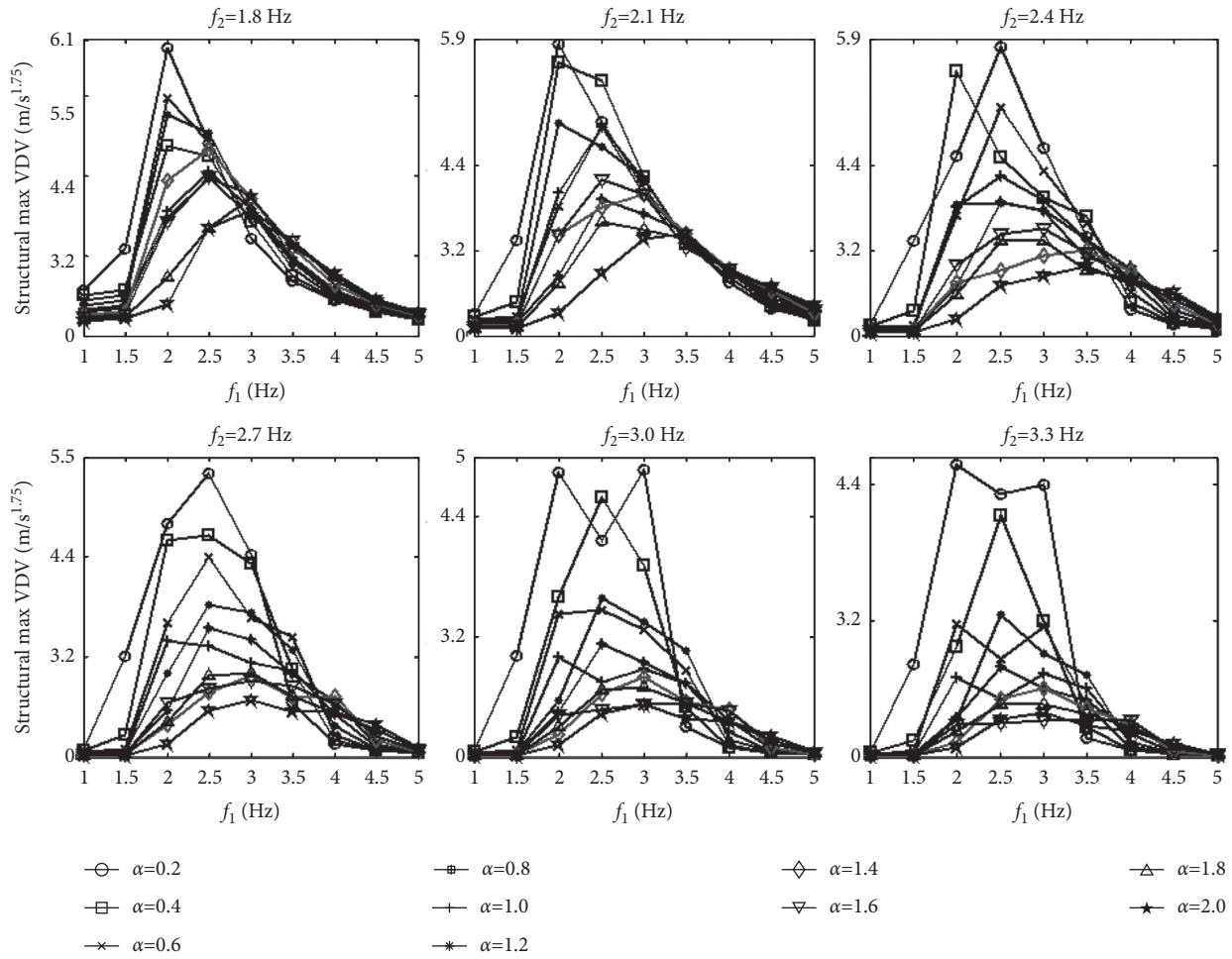


FIGURE 33: The structural VDV of models with different  $f_2$  when  $f_3 = 2.8$  Hz.

TABLE 10: The max structural VDV value corresponding swaying frequencies.

Swaying frequency	$f_1$ (Hz)								
	1.0	1.5	2.0	2.5	3.0	3.5	4.0	4.5	5.0
$f$ (Hz)	1.8	1.8, 1.0	1.1–1.3	1.3–1.6	1.4–1.8	1.5–1.8	1.5–1.8	1.6–1.8	1.7–1.8

TABLE 11: The max reduced amplitude of structural dynamic responses with  $\alpha$ ,  $\zeta_1$ , and  $f_1$ .

The degree of reduction	Parameter		
	$\alpha$ (0.2–2.0) (%)	$\zeta_1$ (2%–7.3) (%)	$f_1$ (1.0–5.0 Hz) (%)
	98	60	89

structure within the parameter range are given in the table. Increase in  $\alpha$ ,  $\zeta_1$ , and  $f_1$  will significantly reduce the structural response, with a maximum decrease of 98%, 60%, and 89%, respectively.

### 5. Discussion

Bear all this in mind; with analyzing the experiment data of crowd shocked by shaking table and swaying at temporary grandstand, respectively, it is indicated that crowd annoyance rate may not have a linear relationship with vibration, and the indicated crowd may adjust their reaction for

comfort when they under a certain range of vibration intensity. It is also indicated that the standing crowd may have more tolerance to vibration than seated crowd. The serviceability limit of  $1.29 \text{ m/s}^{1.75}$  and the upper boundary of  $2.32 \text{ m/s}^{1.75}$  suggested by VDV are obtained. There is also a need to investigate more experiments such as a big temporary grandstand with a large number of crowds (active/passive) in lab or in site. Also, through predicting dynamic structural VDV with different dynamic parameters of crowd and structure based on a simplified three-degree-of-freedom lumped dynamic model for different crowd dynamic parameters, it is considered that the VDV of structure will be

decreased with increasing  $\alpha$  and  $\zeta_2$ . The influence of  $f_2$  for structure response relates to  $\alpha$ . The max response of the model is  $\alpha \leq 0.6$ ,  $f_2 = 1.8$  Hz or  $\alpha > 0.6$ ,  $f_2 = 1.5$  Hz. The VDV of structure will be decreased with increasing  $f_3$ . The influence of  $\zeta_3$  for structure response relates to  $\alpha$  and  $f_3$ , and the notable model is not the max  $\zeta_3$  of the model. For different structural dynamic parameters, it is considered that the VDV of structure first rises and then descends with the increase of  $f_1$  (the max response of the model is  $f_1 = 2.5-3.5$  Hz) and decreases with increasing  $\zeta_1$ . The notable model is not the model that  $\alpha$  and  $\beta$  have the minimum value. It was also found that most of the predicting-peak V DVs of structure are higher than the serviceability limit value, which may indicate why the crowd can be easily susceptible to TDG's vibrations. These results are only based on a three-degree-of-freedom lumped dynamic model. While the model of structure and model of body are not a simple single-degree-of-freedom lumped model, more coupled equation system will need to be analyzed in the future and combined with more experiments.

## 6. Conclusion

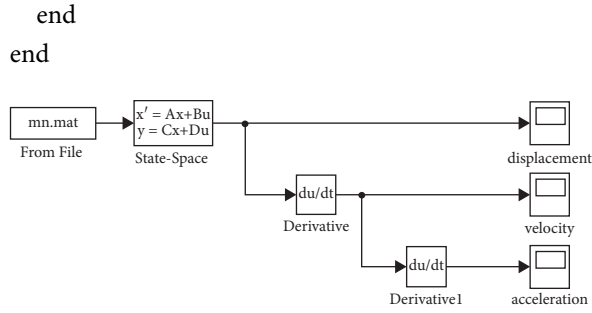
This paper tried to address the annoyance levels of lateral vibration on temporary grandstand, which is based on the lateral vibration experiments of shake table and crowds, and to analyze the responses of structure with different dynamic parameters of 3 DOF crowd and structure interaction model. For TDG, the lateral serviceability limit of  $1.29 \text{ m/s}^{1.75}$  and the upper boundary of  $2.32 \text{ m/s}^{1.75}$  are suggested. Based on the experimental data, the interaction models are calculated, and the predicting responses of structure are obtained and discussed. For different crowd parameters, with increasing  $\alpha$  and  $\zeta_2$ , the VDV of structure will be decreased. The influence of  $f_2$  for structure response relates to  $\alpha$ . With increasing  $f_3$ , the VDV of structure will be decreased. The influence of  $\zeta_3$  for structure response relates to  $\alpha$  and  $f_3$ . The notable model is not the max  $\zeta_3$  of the model. For different parameters of structure, the VDV of structure first rises and then descends with the increase of  $f_1$  and decreases with increasing  $\zeta_1$ . The notable model is not the mixture of  $\alpha$  and  $\beta$  of the model. It was also found that most of the predicting-peak V DVs of the structure are higher than the serviceability limit value. These results may be useful for analyzing the vibration serviceability of temporary grandstand.

## Appendix

### I. The part of MATLAB program for calculating the models

```
load body
ms = 119; fs = 2.7; ks = (2 * pi * fs)^2 * ms; drs = 0.073;
cs = 2 * drs * ms * 2 * pi * fs;
fh = [0.5:0.1:4.0]'; drh = [0.3:0.1:0.5]'; mh = [0.7:0.1:1]';
wh = 2 * pi * fh; wh2 = zeros(36,1);
for i = 1:36
    wh2(i, 1) = wh(i,1)^2;
```

```
end
mh = mh * 350; kh = mh * wh^2;
ch1 = 2 * 0.3 * mh * wh'; ch2 = 2 * 0.4 * mh * wh';
ch3 = 2 * 0.5 * mh * wh'; modelcd1 = zeros(18,27);
A1 = zeros(4,36); errch1 = zeros(1,36); A2 = zeros(4,36);
errch2 = zeros(1,36); A3 = zeros(4,36);
errch3 = zeros(1,36); AA = zeros(12,36); for s = 1:9
    for p = 1:18
        for i = 1:4
            M = [ms 0; 0 mh(i,1)];
            for j = 1:36
                K = [(ks+kh(i,j)) -kh(i,j); -kh(i,j) kh(i,j)]; C =
                [(cs+ch1(i,j)) -ch1(i,j); -ch1(i,j) ch1(i,j)]; A = cat(1,cat
                (2,zeros(2,2),eye(2)),cat(2,-inv(M) * K,-inv(M) * C));
                G = eye(2); B = cat(1,zeros(2,2),-inv(M) * G); C0 = cat
                (2, eye(2),zeros(2,2)); D = zeros(2,2);
                mass = zeros(48001,3); mass(:,1) = cda2(:,1); mass(:
                ,2) = (-cda2(:,s+1)) * vdvratio(p,1) * (ms+mh(i,1));
                mass = mass'; save mn mass; sim('twodof');
                err1 = zeros(48001,1); for m = 1:48001
                    err1(m,1) = abs(a1(m,3)-cda1(m,s+1))^2; errch1(1,j) =
                    sqrt(sum(err1)/48001);
                end
                C = [(cs+ch2(i,j)) -ch2(i,j); -ch2(i,j) ch2(i,j)];
                A = cat(1,cat(2,zeros(2,2),eye(2)),cat(2,-inv(M) * K,-
                inv(M) * C)); G = eye(2); B = cat(1,zeros(2,2),-inv(M) *
                G); C0 = cat(2,eye(2),zeros(2,2)); D = zeros(2,2);
                mass = zeros(48001,3); mass(:,1) = cda2(:,1); mass(:
                ,2) = (-cda2(:,s+1)) * vdvratio(p,1) * (ms+mh(i,1));
                mass = mass'; save mn mass; sim('twodof');
                err2 = zeros(48001,1); for m = 1:48001
                    err2(m,1) = abs(a1(m,3)-cda1(m,s+1))^2;
                    errch2(1,j) = sqrt(sum(err2)/48001);
                end
                C = [(cs+ch3(i,j)) -ch3(i,j); -ch3(i,j) ch3(i,j)];
                A = cat(1,cat(2,zeros(2,2),eye(2)),cat(2,-inv(M) * K,-
                inv(M) * C)); G = eye(2); B = cat(1,zeros(2,2),-inv(M) *
                G); C0 = cat(2,eye(2),zeros(2,2)); D = zeros(2,2);
                mass = zeros(48001,3); mass(:,1) = cda2(:,1); mass(:
                ,2) = (-cda2(:,s+1)) * vdvratio(p,1) * (ms+mh(i,1));
                mass = mass'; save mn mass; sim('twodof');
                err3 = zeros(48001,1); for m = 1:48001
                    err3(m,1) = abs(a1(m,3)-cda1(m,s+1))^2;
                    errch3(1,j) = sqrt(sum(err3)/48001);
                end
            end
        end
    end
    AA(1:4,:) = A1; AA(5:8,:) = A2; AA(9:12,:) = A3;
    [modelcd1(p,3 * s-2),modelcd1(p,3 * s-1)] =
    find(AA == min(min(AA)));
    modelcd1(p,3 * s) = min(min(AA));
```



```

load active
f1 = 2.7; c1 = 0.073; m1 = 1; %structure constant
f3 = 2; c3 = 0.4; %passive crowd constant
m3 = [0.2, 0.3, 0.4, 0.5]; %passive crowd mass
f2 = [1.5, 1.8, 2.1, 2.4, 2.7, 3.0, 3.3]; %active crowd frequency 7 * 1
c2 = [0.2, 0.225, 0.25]; %active crowd damping ratio 3 * 1
f2c2 = f2 * c2; %7 * 3
for m = 1:9
    for n = 1:4
        M = [m1, 0, 0; 0, 1, 0; 0, 0, m3(n,1)]; for s = 1:3
            for i = 1:7%
                C = 4 * pi * [m1 * f1 * c1 + f2c2(i,s) + m3(n,1) * f3 * c3, -
                    f2c2(i,s), -m3(n,1) * f3 * c3; -f2c2(i,s), f2c2(i,s), 0; -
                    m3(n,1) * f3 * c3, 0, m3(n,1) * f3 * c3];
                K = 4 * pi * pi * [m1 * f1 * f1 + f2(i,1) *
                    f2(i,1) + m3(n,1) * f3 * f3, -f2(i,1) * f2(i,1), -m3(n,1) *
                    f3 * f3; -f2(i,1) * f2(i,1), f2(i,1) * f2(i,1), 0; -m3(n,1) *
                    f3 * f3, 0, m3(n,1) * f3 * f3];
                A = cat(1, cat(2, zeros(3,3), eye(3)), cat(2, -inv(M) * K, -
                    inv(M) * C)); %¼ÆËä¼ÖÓóÀ
                G = eye(3); B = cat(1, zeros(3,3), -inv(M) * G);
                %¼ÆËä¼ÖÓóB
                C0 = cat(2, eye(3), zeros(3,3)); D = zeros(3,3);
                %¼ÆËä¼ÖÓóC0£-D
                mass = zeros(2501,4); mass(:,1) = t; mass(:,2) =
                    yy(:,m); %F(t)
                mass(:,3) = -yy(:,m); %-F(t)
                mass = mass'; save mn mass; sim('twodof');
                sq1 = a1(:,2); v1 = sum(sq1) * 0.01; vdv1 = sqrt(sqrt
                    (v1)); sq2 = a1(:,3); v2 = sum(sq2) * 0.01; vdv2 =
                    sqrt(sqrt(v2)); sq3 = a1(:,4); v3 = sum(sq3) * 0.01;
                    vdv3 = sqrt(sqrt(v3)); VDV1(i,s) = vdv1; VDV2(i,s) =
                    vdv2; VDV3(i,s) = vdv3; sm1 = a1(:,2); rm1 =
                    sum(sm1) * 0.01; rms1 = sqrt(rm1); sm2 = a1(:,3);
                    rm2 = sum(sm2) * 0.01; rms2 = sqrt(rm2); sm3 = a1(
                    :,4); rm3 = sum(sm3) * 0.01; rms3 = sqrt(rm3);
                    RMS1(i,s) = rms1; RMS2(i,s) = rms2; RMS3(i,s) = rms3;
                    p1 = max(a1(:,2)); p2 = max(a1(:,3)); p3 = max(a1(:,4));
                    P1(i,s) = p1; P2(i,s) = p2; P3(i,s) = p3;
            end
        end
    end
end

```

```

VDV(:, ((n-1) * 9 + 1):n * 9) =
[VDV1, VDV2, VDV3];
RMS(:, ((n-1) * 9 + 1):n * 9) = [RMS1, RMS2, RMS3];
PEAK(:, ((n-1) * 9 + 1):n * 9) = [P1, P2, P3]; end
eval(['RESULTV', num2str(m), ' = VDV', ';']);
eval(['RESULTR', num2str(m), ' = RMS', ';']);
eval(['RESULTP', num2str(m), ' = PEAK', ';']);
end

```

## Data Availability

In this paper, all the experiment data are real and available. Requests for data (6 to 12 months after publication of this article) will be considered by the corresponding author.

## Conflicts of Interest

The authors declare that they have no conflicts of interest.

## Acknowledgments

The authors are grateful for the support of Project 2014BAK14B05 of the Ministry of Science and Technology. This work was supported by Engineering Research Projects of No. 5(230103).

## References

- [1] H. Bachmann, *Vibrations of Building Structures Caused by Human Activities, Case Study of a Gymnasium*, National Research Council of Canada, Ottawa, ON, Canada, Technical Translation 2077, 1884.
- [2] P. Dallard, T. Fitzpatrick, A. Flint et al., "London millennium bridge: pedestrian-induced lateral vibration," *Journal of Bridge Engineering*, vol. 6, no. 6, pp. 412–417, 2001.
- [3] M. Kasperski, "Actual problems with stand structures due to spectator induced vibrations," in *Proceedings of the 3rd European Conference on Structural Dynamics: EURO DYN 96*, pp. 455–461, Balkema, Florence, Italy, June 1996.
- [4] C. A. Jones, P. Reynolds, and A. Pavic, "Vibration serviceability of stadia structures subjected to dynamic crowd loads: a literature review," *Journal of Sound and Vibration*, vol. 330, no. 8, pp. 1531–1566, 2011.
- [5] M. Setareh, "Evaluation and assessment of vibrations owing to human activity," *Structures and Buildings*, vol. 165, no. SB5, pp. 219–230, 2012.
- [6] A. Bolton, "Fatal mix caused stand Fall," *New Civil Engineer*, pp. 5–6, 1992.
- [7] *Interim Guidance on Assessment and Design, Dynamic Performance Requirements for Permanent Grandstands Subject to Crowd Action*, The Institution of Structural Engineers, London, UK, 2001.
- [8] H. Reiher and F. J. Meister, "Die Empfindlichkeit des Menschen gegen Erschütterungen," *Forschung auf dem Gebiete des Ingenieurwesens*, vol. 2, no. 11, pp. 381–386, 1931.
- [9] F. Khan and R. Parmelee, "Service criteria for tall buildings for wind loading," in *Proceedings of the 3rd International Conference on Wind Effects on Buildings and Structures*, Saikon, Tokyo, Japan, 1971.

- [10] P. Chen and I. L. Robertson, "Human perception thresholds of horizontal motion," *Journal of the Structural Division*, vol. 98, no. ST8, pp. 1681–1695, 1972.
- [11] J. F. Wiss and M. Parmelee, "Human perception of transient vibrations," *Journal of the Structural Division*, vol. 100, no. ST4, pp. 773–787, 1974.
- [12] G. G. Browning, *Human Perception of Vibrations Due to Synchronised Crowd Loading in Grandstands*, The University of Bath, Somerset, UK, 2011.
- [13] S. Nhleko, *Human-induced Lateral Excitation of Public Assembly Structures*, The University of Oxford, Oxford, England, UK, 2000.
- [14] B. R. Ellis, T. Ji, and J. D. Littler, "The response of grandstands to dynamic crowd loads," *Proceedings of the Institution of Civil Engineers - Structures and Buildings*, vol. 140, no. 4, pp. 355–365, 2000.
- [15] S. Živanovi, "Modelling human actions on lightweight structures: experimental and numerical developments," *MATEC Web of Conferences*, vol. 24, Article ID 01005, 13 pages, 2015.
- [16] F. N. Catbas, O. Celik, O. Avci, O. Abdeljaber, M. Gul, and N. T. Do, "Sensing and monitoring for stadium structures: a review of recent advances and a forward look," *Frontiers in Built Environment*, vol. 3, no. 38, pp. 1–18, 2017.
- [17] J. H. H. Sim, *Human-structure interaction in Cantilever stands*, Ph.D. Thesis, The University of Oxford, Oxford, England, UK, 2006.
- [18] J. Sim, A. Blakeborough, and M. Williams, "Modelling effects of passive crowds on grandstand vibration," *Proceedings of the Institution of Civil Engineers-Structures and Buildings*, vol. 159, no. 5, pp. 261–272, 2006.
- [19] H. X. Han, D. Zhou, and T. Ji, "Mechanical parameters of standing body and applications in human-structure interaction," *International Journal of Applied Mechanics*, vol. 9, no. 2, 2017.
- [20] J. Yuan, L. He, F. Fan, and C. Liu, "The dynamic parameters of passive human at temporary demountable grandstands during exposure to lateral vibration," *Journal of Civil Engineering and Management*, vol. 24, no. 4, pp. 265–283, 2018.
- [21] P. Reynolds, A. Pavic, and Z. Ibrahim, *Changes of Modal Properties of a Stadium Structure Occupied by a Crowd*, *Proceeding of the 22nd International Modal Analysis Conference IMAC XXII*, Lugano, Switzerland, 2004.
- [22] P. Reynolds, A. Pavic, and Z. Ibrahim, "A remote monitoring system for stadia dynamics," *Proceedings of the Institution of Civil Engineers-Structures and Buildings*, vol. 157, no. 6, pp. 385–393, 2004.
- [23] P. Reynolds and A. Pavic, "Vibration performance of a large cantilever grandstand during an international football match," *Journal of Performance of Constructed Facilities*, vol. 20, no. 3, pp. 202–212, 2006.
- [24] A. Caprioli, A. Castellani, A. Cigada et al., "Vibration monitoring of the g. meazza stadium in milano during concerts and football matches," *Proceeding of the Society for Experimental Mechanics Series IMAC-XXIII*, in *Proceedings of the Conference and Exposition on Structural Dynamics-Structural Health Monitoring*, Orlando, FL, USA, 2005.
- [25] A. Caprioli, P. Reynolds, M. Vanali et al., "Comparison of the effects of a moving crowd on different grandstands during similar events," in *Proceedings of the Society for Experimental Mechanics Series IMAC-XXIV: Conference and Exposition on Structural Dynamic-Looking Forward*, Technologies for IMAC, St Louis, MI, USA, 2006.
- [26] K. A. Salyards, "Utilization of simple dynamic models to explore load estimation method based on in-service structural responses," in *Proceedings of the Society for Experimental Mechanics Series IMAC-XXVI: Conference and Exposition on Structural Dynamics-Technologies for Civil Structures*, Orlando, FL, USA, 2008.
- [27] A. Cigada, A. Caprioli, M. Redaelli et al., "Numerical modeling and experimental modal analysis of a concrete grandstand structure to structural health monitoring purposes," in *Proceedings of the Society for Experimental Mechanics Series IMAC-XXVI: Conference and Exposition on Structural Dynamics-Technologies for Civil Structures*, Orlando, FL, USA, 2008.
- [28] A. Cigada, A. Caprioli, M. Redaelli, and M. Vanali, "Vibration testing at meazza stadium: reliability of operational modal analysis to health monitoring purposes," *Journal of Performance of Constructed Facilities*, vol. 22, no. 4, pp. 228–237, 2008.
- [29] A. Comer, A. Blakeborough, and M. S. Williams, "Grandstand simulator for dynamic human-structure interaction experiments," *Experimental Mechanics*, vol. 50, no. 6, pp. 825–834, 2010.
- [30] G. Parkhouse and L. Ward, "Design charts for the assessment of grandstands subject to dynamic crowd action," *Institution of Structural Engineers*, vol. 88, no. 7, pp. 27–34, 2010.
- [31] C. A. Jones, A. Pavic, P. Reynolds, and R. E. Harrison, "Verification of equivalent mass-spring-damper models for crowd-structure vibration response prediction," *Canadian Journal of Civil Engineering*, vol. 38, no. 10, pp. 1122–1135, 2011.
- [32] Z. Ibrahim and P. Reynolds, "Finite element modelling for evaluating the dynamic characteristic of a grandstand," *International Journal of Engineering and Technology*, vol. 4, no. 2, pp. 235–244, 2007.
- [33] P. Mandal and T. Ji, "Modeling dynamic behaviour of a cantilever grandstand," *Structures and Buildings*, vol. 157, no. SB3, pp. 173–184, 2003.
- [34] K. A. Salyards and L. M. Hanagan, "Evaluation of a finite element model for dynamic characteristic prediction of a stadium facility," in *Proceedings of the Society for Experimental Mechanics Series IMAC-XXIII: Conference and Exposition on Structural Dynamics-Structural Health Monitoring*, Bethel, Conn, Orlando, FL, USA, January 2005.
- [35] G. Saudi, P. Reynolds, M. Zaki, and H. Hodhod, "Finite-element model tuning of global modes of a grandstand structure using ambient vibration testing," *Journal of Performance of Constructed Facilities*, vol. 23, no. 6, pp. 467–479, 2009.
- [36] A. Pavic and P. Reynolds, "Experimental verification of novel 3dof model for grandstand crowd-structure dynamic interaction," in *Proceedings of the Society for Experimental Mechanics Series IMAC-XXVI: Conference and Exposition on Structural Dynamics-Technologies for Civil Structures*, Orlando, FL, USA, January 2008.
- [37] J. Yuan, L. He, F. Fan, C. Liu, and K. Zhang, "Dynamic modeling and vibration analysis of temporary grandstand due to crowd-jumping loads," in *Proceedings of the 9th International Conference on Structural Dynamics EURO DYN 2014*, pp. 1051–1057, Porto, Portugal, June 2014.
- [38] C. Liu, L. He, Z. Wu, and J. Yuan, "Experimental study on joint stiffness with vision-based system and geometric imperfections of temporary member structure," *Journal of Civil Engineering and Management*, vol. 24, no. 1, pp. 43–52, 2018.
- [39] C. Y. Tang, T. X. Zhang, and J. Q. Song, "Evaluation of comfortability during vibration on basis of annoyance rate,"



- Journal of Northeastern University*, vol. 27, no. 7, pp. 802–805, 2006.
- [40] C. Tang, Y. Zhang, G. Zhao, and Y. Ma, “Annoyance rate evaluation method on ride comfort of vehicle suspension system,” *Chinese Journal of Mechanical Engineering*, vol. 27, no. 2, pp. 296–303, 2014.
- [41] Y. P. Guo and G. Q. Song, “Dynamic comfort evaluation of high-speed train based on annoyance rate model,” *Journal of Northeastern University*, vol. 34, no. 11, pp. 1620–1624, 2013.
- [42] A. M. Yuan, W. X. Wu, M. Xu, H.-b. Cheng, and L. Ma, “Study on pedestrian bridge’s vibration comfort evaluation based on annoyance rate,” *Journal of Water Resources and Architectural Engineering*, vol. 11, no. 4, pp. 135–140, 2013.
- [43] X. Z. Shen and J. Teng, “Vibration serviceability assessment method for floor structures based on random walking force and annoyance rate,” *Journal of Vibration and Shock*, vol. 31, no. 22, pp. 71–75, 2012.
- [44] J. Wei, R. Chen, J. Wu, and M. Hu, “Appraisal of the vibration serviceability for a long-span pre-stressed floor based on annoyance rate,” *Zhejiang Construction*, vol. 32, no. 1, pp. 19–23, 2015.
- [45] Y. F. Huang, G. Q. Di, Y. T. Zhu, Y. P. Hong, and B. G. Zhang, “Pair-wise comparison experiment on subjective annoyance rating of noise samples with different frequency spectrums but same a-weighted level,” *The Science of the Total Environment*, vol. 69, no. 12, pp. 1205–1211, 2018.
- [46] R. H. Bakker, E. Pedersen, G. P. Van Den Berg, R. E. Stewart, W. Lok, and J. Bouma, “Impact of wind turbine sound on annoyance, self-reported sleep disturbance and psychological distress,” *The Science of the Total Environment*, vol. 425, no. 5, pp. 42–51, 2012.
- [47] Bs 6472-1, *Guide to Evaluation of Human Exposure to Vibration in Buildings-Part 1: Vibration Sources Other than Blasting*, British Standards Institution, Chennai, Tamil Nadu, India, 2008.
- [48] Iso 2631-1, *Mechanical Vibration and Shock-Evaluation of Human Exposure to Whole-Body Vibration, Part 1: General Requirement*, 1997.
- [49] Z. G. Song and W. L. Jin, “A fuzzy-stochastic model for human response to vibrations,” *Journal of Basic Science and Engineering*, vol. 10, no. 3, pp. 287–294, 2002.
- [50] Z. G. Song, *A New Annoyance-Based Vibration Comfort Design Theory on Engineering Structures*, Zhejiang University, Zhejiang, China, 2003.
- [51] Z. G. W. Song and L. Jin, “Serviceability design of ice induced platform vibration based on ice zoning map of Bohai sea-acceptable acceleration levels,” *Ocean Engineering*, vol. 123, no. 12, pp. 61–65, 2005.
- [52] Z. Li, Q. Zhang, F. Fan, and S. Shen, “Analysis of dynamic properties and vibration comfort of large-scale stands,” *Building Research & Information*, vol. 48, no. 7, pp. 802–816, 2020.
- [53] Z. Li, Q. Zhang, F. Fan, and S. Shen, “A method for calculating uncomfortable rates of people due to vertical floor vibrations using corresponding assessment values based on fuzzy reliability theory,” *Journal of Building Engineering*, vol. 28, Article ID 101061, 2020.
- [54] Q. Zhang, Z. Li, Y. Zhang, and T. Ji, “Parameter identification of the interaction body model using available measurements,” *Engineering Review*, vol. 40, no. 3, pp. 1–12, 2020.
- [55] S. Yu, J. Yuan, W. Wang, W. Wang, C. Gao, and C. Liu, “Analysis the lateral vibration serviceability of temporary grandstand and human comfort based on experiment,” in *Proceedings of the XI International Conference on Structural Dynamics EUROLYN 2020*, Athens, Greece, 2020.
- [56] L. He, J. Yuan, F. Fan, and C. Liu, “Management of lateral vibration serviceability of temporary grandstand and human health risk assessment based on experiment,” <https://www.preprints.org/manuscript/201805.0468/v1>.
- [57] L. He, J. Yuan, F. Fan, and C. Liu, “Dynamic forces of swaying human and responses of temporary demountable grandstands and based on experiment and simulation,” *Shock and Vibration*, vol. 2018, no. 1, Article ID 2791491, 22 pages, 2018.
- [58] K. Cherry, “A look at introspection Wundt’s experimental technique,” 2018, <https://www.verywell.mind.com/what-is-introspection-2795252>.
- [59] J. P. Guidford, *Psychometric Methods*, McGraw-Hill, New York, NY, USA, 1954.
- [60] G. G. Browning, *Human Perception of Vibrations Due to Synchronised Crowd Loading in Grandstands*, Ph.D Thesis, University of Bath, England, UK, 2011.
- [61] Z. Song, *A New Annoyance-Based Vibration comfort Design Theory on Engineering Structures*, Ph.D. Thesis, Zhejiang University, Zhejiang, China, 2003.
- [62] ISO 2631 *Mechanical Vibration and Shock-Evaluation of Human Exposure to Whole-Body Vibration. Part 1: General Requirement*, International Organization for Standardization (ISO), Geneva, Switzerland, 1997.
- [63] ISO 2631 *Mechanical Vibration and Shock-Evaluation of Human Exposure to Whole-Body Vibration. Part 1: Vibration in Buildings (1 Hz to 80 Hz)*, International Organization for Standardization (ISO), Geneva, Switzerland, 2003.
- [64] Bs 6841, *Guide to Measurement and Evaluation of Human Exposure to Whole Body Mechanical Vibration and Repeated Shock*, British Standards Institution, Chennai, Tamil Nadu, India, 1987.
- [65] Nbcc, *User’s Guide National Building Code of Canada 2005, Structural Commentaries (Part 4 of Division B) Commentary D, National Building Code of Canada*, NBCC, Chennai, Tamil Nadu, India, 2005.
- [66] Bs 7085, *Medical Contra-indications to Participation in Experiments Involving Whole-Body Mechanical Vibration*, British Standards Institution, Chennai, Tamil Nadu, India, 1987.
- [67] Bs 6472, *Guide to Evaluation of Human Exposure to Vibration in Buildings (1 Hz to 80 Hz)*, British Standards Institution, Chennai, Tamil Nadu, India, 1992.
- [68] ISO 10137, *Basis for the Design of Structures-Serviceability of Buildings against Vibration*, International Organization for Standardization (ISO), Geneva, Switzerland, 2007.
- [69] Bre Digest 426, *The Response of Structures to Dynamic Crowd Loads*, BRE, Bricket Wood, UK, 2nd edition, 2004.
- [70] M. J. Griffin, *Handbook of Human Vibration*, Academic Press, London, UK, 1990.
- [71] B. R. Ellis and J. D. Littler, “Response of cantilever grandstands to crowd loads. Part 1: serviceability evaluation,” *Proceedings of the Institution of Civil Engineers-Structures and Buildings*, vol. 157, no. 4, pp. 235–241, 2004.

## Research Article

# Experimental Research on Damping Effect of Double-Layer Tuned Mass Damper for High-Rise Structure

Botan Shen,<sup>1</sup> Jin Wang <sup>1</sup>, Weibing Xu <sup>1,2</sup>, Yanjiang Chen,<sup>1</sup> Weiming Yan,<sup>1</sup> Jianhui Huang,<sup>1</sup> and Zhenyun Tang<sup>2</sup>

<sup>1</sup>Beijing Key Laboratory of Earthquake Engineering and Structure Retrofit, Beijing University of Technology, Beijing 100124, China

<sup>2</sup>The Key Laboratory of Urban Security and Disaster Engineering of Ministry of Education, Beijing University of Technology, Beijing 100124, China

Correspondence should be addressed to Jin Wang; wangjin418@126.com

Received 19 September 2021; Revised 4 November 2021; Accepted 10 November 2021; Published 2 December 2021

Academic Editor: Jingxuan Wang

Copyright © 2021 Botan Shen et al. This is an open access article distributed under the Creative Commons Attribution License, which permits unrestricted use, distribution, and reproduction in any medium, provided the original work is properly cited.

A double-layer tuned mass damper (DTMD) has advantages of wide damping frequency band and strong robustness. At present, there is a lack of seismic design methods for high-rise structures based on DTMDs. In this study, a DTMD parameter optimisation method was proposed, with the objective of minimising the peak displacement response of a first N-order vibration modal with a vibration mass participation factor of 85%. Then, a scale model of a high-rise structure was fabricated, along with a corresponding DTMD. Different types of excitations were chosen to clarify the dynamic responses of the model with and without the DTMD, including Site-II ground motions, long-period (LP) ground motions without pulses, and near-fault pulse-type (NFPT) ground motions. The results indicate that the dynamic responses of high-rise structures under LP and NFPT ground motions are much greater than those under Site-II ground motions. The DTMD can effectively reduce the absolute displacement response, acceleration response, and strain response at the top floor of the test model. However, the DTMD has a time delay in providing the damping effect. A smaller damping ratio between the upper TMD and the controlled structure will lead to a more significant damping effect for the DTMD.

## 1. Introduction

With the rapid development of urbanisation and the economy, high-rise structures play an important role in urban modernisation. High-rise structures provide convenience to the society but also bring new challenges in engineering. With the continuous innovation of construction technologies and building materials, high-rise structures have become lighter and more flexible and required less damping; moreover, the structures mainly experience low-frequency vibrations. Owing to the characteristics of high-rise structures, such as a long natural vibration period, multiorder modes participating in vibration, sensitivity to wind, and earthquake-induced responses [1–4], seismic design has always been the focus. Therefore, researchers have conducted a series of studies on improving the seismic performance of high-rise structures, focusing on the

application of steel-concrete composite structures and the introduction of energy dissipation measures.

Steel-reinforced concrete (SRC) and concrete-filled steel tubes (CFSTs) have been widely used in high-rise structures in recent years. The core tube of the Shanghai Centre Tower adopted the SRC structure, and through a shaking table test of a 1/40-scale model, Tian et al. [5] showed that the structure could meet the seismic performance target required by the design. Cao [6,7] took Beijing China Zun as a prototype and, through a series of seismic performance tests, found that the CFST mega-column (with a complex cross section and multiple cavities) could significantly improve the bearing capacity and elastic deformation capacity of the structure. Guangzhou's New TV Tower [8] and Tianjin's Jin Tower [9] adopted CFST mega-columns as the main bearing members. Through theoretical analysis and experimental research, it was concluded that these structures had a good

deformation capacity and good ductility, along with a certain seismic reserve capacity. Nie et al. [10], Wang et al. [11], Uy et al. [12], and other scholars also conducted a series of studies on the bearing capacity and seismic performance of steel-concrete composite structures and demonstrated their effectiveness in applications for high-rise structures. At present, studies worldwide have shown that SRC and CFSTs can evidently improve the seismic performance of a structure; nevertheless, with a continuous increase in building height, it also leads to higher requirements for its mechanical performance. The connection performance between the steel and concrete is a key parameter affecting the seismic performance of steel-concrete composite structures, but the quantitative evaluation method for the connection mechanism between them remains imperfect.

Therefore, the introduction of energy dissipation measures in high-rise structures has become a research hotspot. Tang [13] set 30 viscous dampers in the sightseeing tower of the Nanjing Olympic Sports Centre for wind-induced vibration control. The dynamic responses of the structure decreased, and the comfort requirements for the sightseeing platform were met. Venanzi [14] effectively reduced the dynamic responses of a high-rise structure under a wind load by setting an optimised tuned mass damper (TMD). Fan et al. [15] used a high-level fire water tank as a mass block and combined it with viscous dampers to form a TMD system for effectively suppressing the resonance responses of the Beijing Olympic Tower caused by dense crowd excitations. Armali et al. [16] studied the vibration control of a 40-story building with friction dampers and optimised the number and location of the dampers. The results showed that the friction dampers can significantly reduce the dynamic response of the structure under seismic load and verified the effectiveness of friction dampers in high-rise structures. Liang [17] studied the seismic control of a high-rise structure with a metal damper. The results showed that the metal damper had good seismic performance and achieved the expected seismic control effect. Qian and Ding [18] took the Beijing CCTV Tower as a prototype and analysed the influence of an annular tuned liquid damper (TLD) on the tower through a shaking table test of a 1/150-scale model. The results indicated that the TLD could effectively decrease the resonance response of the first mode of the structure. Both the Zhuhai Jinshan Building [19] and Dalian International Trade Building [20] set a rectangular TLD water tank on top of their main structure; this evidently reduced the acceleration response of the top and improved the comfort in the building under a wind load. Naeim et al. [21] introduced a high-rise structure with particle dampers in the centre of Santiago, which suffered from the 2010 Chilean earthquake. To some extent, the study indicated that particle dampers can be applied on high-rise structures. Lu et al. [22] applied tuned particle damper technology for the wind-induced vibration control of high-rise structures and indicated that the tuned particle damper could be used to decrease the wind-induced vibration response of the top of a high-rise structure. Wang [23–25] introduced an adaptive TMD which can retune its frequency and damping ratio in real time based on the vibration state of the structure. The

adaptive TMD was applied to a wind-sensitive concrete chimney. And, the results showed that the adaptive TMD had better control effect and robustness than that of passive TMD. Wang et al. [26] introduced a Tuned Liquid Column Damper-Inerter (TLCDI) system to control the seismic response of adjacent high-rise buildings. The results indicated that the optimum TLCDI system can significantly reduce the peak acceleration of both adjacent high-rise buildings. The recent findings show that different types of dampers have achieved some beneficial performance in the seismic control of high-rise structures. Energy dissipation measures can reduce the seismic response, wind-induced response, and human-induced vibration of high-rise structures to a certain extent. However, owing to the multiorder modes participating in the vibration of high-rise structures, all of the above dampers have certain limitations in seismic control. A single TMD or TLD can only reduce the vibration of a low order (or one certain order) of the controlled structure, and their robustness is poor. The soft steel members in the metal dampers may yield when the deformation is large. In addition, as compared to a single-story building, with the high stiffness of the high-rise structure, the ability to improve the stiffness of the metal damper is limited and the local energy dissipation is not evident. The friction damper may produce a permanent displacement after an earthquake, thereby requiring maintenance and protection in the later stage; moreover, the permanent displacement will greatly weaken the damping performance of the damper. The damping effect of viscous dampers is closely related to the displacement and velocity of the controlled structure, and the energy dissipation and damping capacity are limited for long-period and low-frequency high-rise structures. The particle dampers have good robustness and good control effects on the multiorder modes of structures, but their damping effects are poor before the damping particles start to vibrate. The adaptive TMD can avoid the disadvantage of poor robustness of traditional passive TMD, and the TLCDI system can provide a certain damping effect on both adjacent buildings. However, the design and practical operability of the adaptive TMDs and the TLCDI systems are more complex than those of passive TMDs. The adaptive method and simply application method of the adaptive TMDs and the TLCDI systems are still a hotspot study.

In recent years, the theory and technologies for multiple TMDs (MTMDs) have been developed rapidly [27–30]. Compared with TMD, a MTMD has a wider damping frequency band, has better robustness, and provides a certain damping effect under microvibration. Li [31], Bandivadekar and Jangid [32], and Tharwat [33] et al. had studied applications of MTMDs in engineering, and the results showed that the MTMD has superior application prospects for structural seismic control. Moreover, Wang et al. [34] introduced an adaptive-passive variable mass multiple TMD (APVM-MTMD) system, and a large-span floor structure was proposed as a case study. The results indicated that the damper system could retune itself and had better vibration control effect. De [35] studied a multi-TMDI (MTMDI) system and applied it on the vibration

control of adjacent high-rise buildings. The MTMDI system was arranged between the adjacent buildings. The relative acceleration response of the adjacent structures can introduce a large reaction force on the inserter device in MTMDI. And, the reaction force of the MTMDI can decrease the dynamic response of adjacent buildings. The optimised MTMDI provided a better acceleration damping control for adjacent high-rise buildings than a traditional MTMD or a single TMDI. However, owing to the complex structure of the MTMD and the MTMDI systems, the application method for the MTMD and MTMDI need to be further studied. As a special case of MTMD, a double-layer TMD (DTMD) is not only simple in structure but also has mature theoretical analysis. In addition, DTMD also has an evident damping control ability and a better robustness for structural seismic control [36–38]. However, the application method and damping effect of DTMD for practically structures were still unclear, especially for high-rise structures under the ground motions with long-period characteristics.

Herein, through the establishment of a DTMD-single-degree of freedom (SDOF) system and parameter optimisation theory, a DTMD with optimised parameters was designed and manufactured. Then, the DTMD was set in a scale model of a high-rise structure. Different types of ground motions were selected as excitation inputs, such as Site-II ground motions, long-period (LP) ground motions without pulses, and near-fault pulse-type (NFPT) ground motions with different velocity periods. And, a series of shaking table tests were conducted to analyse the damping effect of the DTMD for high-rise structure.

## 2. Experimental Program

*2.1. Description of the Scaled Model.* The experimental prototype is the Liuan Tower in China, with a height of 308 m and a weight of 133588 kN. The material of the main structure is Q345 steel (yielding stress was 345 MPa). According to the full-scale finite element model of the structure (excluding the mast), the natural frequencies of the first three order translational formations were obtained, as shown in Table 1.

Considering the bearing capacity of the shaking tables in the Beijing University of Technology, the dimension scale of the model was set to 1/20. The model tower was welded with a steel plate counterweight along the height direction to make its equivalent mass density reach 2.0. The height of the model was 11 m without the mast. And, the weight of the model was 32.2 kN with the counterweight. The scaled model was made of the same material as the prototype. The other physical quantities were strictly simulated based on the similarity relationships [39] shown in Table 2. Because the weight and height of the model was high and the test model was axisymmetric, the excitations were only input along the  $X$ -direction. The acceleration, displacement, and strain sensors were used to monitor the dynamic response of the model. The layout of measuring points is shown in Figure 1(a), and the designed test model is shown in Figure 1(b).

TABLE 1: Natural vibration parameters.

Frequency	Value (Hz)	Vibration mass participation factor (%)
$\omega_1$	0.132	67
$\omega_2$	0.719	76
$\omega_3$	1.340	86

*2.2. Dynamic Characteristics of the Model.* Table 3 gives the natural frequencies of the model tower obtained by inputting white noise signal, as well as the frequencies of the finite element analysis (FEA) results and the theoretical analysis results. To obtain the frequencies of the FEA and the theoretical analysis results, firstly, the prototype finite element model (FEM) was constructed based on the Midas Gen V2019 platform. Then, the frequencies of the prototype FEM were analysed (shown in Table 1). Secondly, the theoretical frequencies of the scaled model can be obtained through multiplying the frequencies of the prototype FEM by the similarity coefficient (shown in Table 2). However, the FEA frequencies of the scaled model can be directly obtained through the analysis results of the scaled FEM based on the Midas Gen V2019 platform.

According to the data in Table 3, the deviation of the first-order frequency obtained from the scaled FEA and similarity theory is within 8% and the deviations of the second-order and third-order frequencies are less than 5%. Moreover, the deviations between the frequency of the scaled test model and the data of the scaled FAM are also within 10%. Considering the setting error of the additional mass and the manufacturing error of the scaled model, both the scaled test model and scaled FEA model can reflect the actual stress and deformation state of the prototype [2].

*2.3. Test Conditions.* Liuan Tower was located in a Class-II site (Site-II), with a 7-degree fortification zone. And, the designed earthquake group was the first group. In this case, the designed seismic response spectrum of the model tower was firstly determined according to the code for seismic design of buildings (GB 50011-2010), and the typical period range of the design response spectrum was also determined as 4s–9s based on the basic vibration period of the prototype tower. Then, three Site-II ground motions were chosen from the database of the PEER. Moreover, in order to study the dynamic response law of the SHR structures under the NFPT and LP ground motions, three NFPT ground motions and three LP ground motions without pulses with the same site conditions were also chosen. The response spectrum curves of the ground motions are shown in Figure 2.

As Figure 2 shows, the selected NFPT and the LP ground motions all have the characteristic of long-period effect. The spectrum value of the NFPT and LP ground motions is relatively large in the long-period range (4 s–9 s), which can easily induce larger dynamic response of the prototype structure (the first-order vibration period is about 7.5 s). Compared with the NFPT and LP ground motions, the spectrum value of the selected Site-II ground motions is relatively small in the long-period range (4 s–9 s). Detailed

TABLE 2: Similarity relationships.

Physical quantity	Unit	Similarity relationship	Similar coefficient
Scale	(L)	$S_L$	1/20
Displacement	(L)	$S_\delta = S_L$	1/20
Elastic modulus	(FL <sup>-2</sup> )	$S_E$	1
Equivalent mass density	(FL <sup>-4</sup> T <sup>2</sup> )	$S_{\rho_e}$	2
Strain	—	$S_\epsilon$	1
Stress	—	$S_\sigma = S_E S_\epsilon$	1
Frequency	(T <sup>-1</sup> )	$S_\omega = 1/S_T$	14.142
Acceleration	(LT <sup>-2</sup> )	$S_a = S_E / (S_L S_{\rho_e})$	10

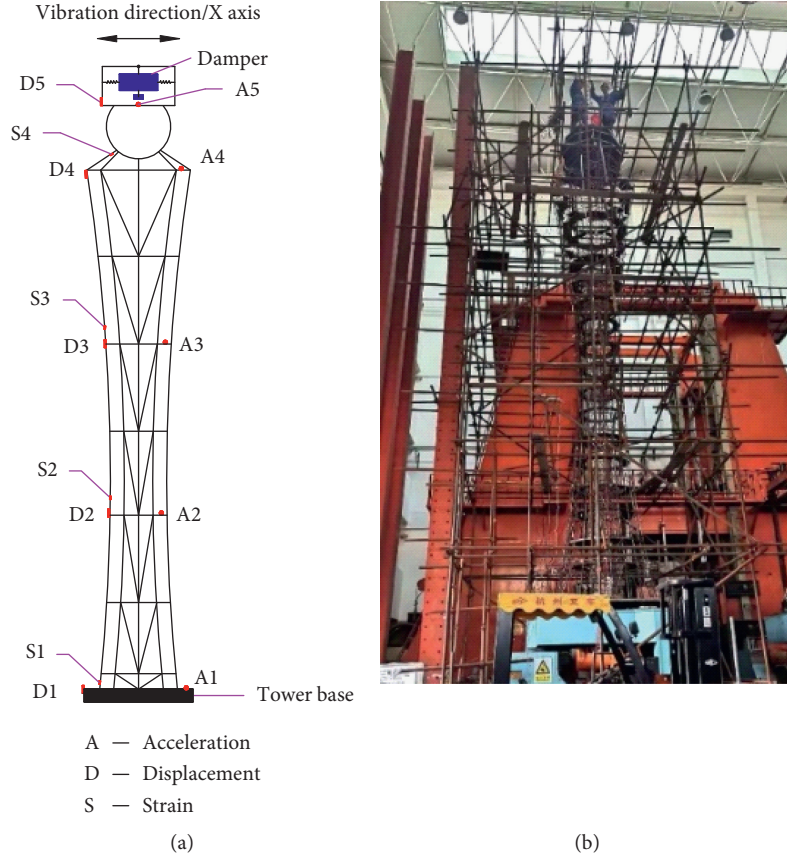


FIGURE 1: Model tower and its measuring points. (a) Layout of measuring points. (b) Test model.

TABLE 3: Comparison of the dynamic characteristics of the model.

Frequency	FEA value (Hz)	Theory value (Hz)	Test value (Hz)	Deviation rate (%)	
				(FEA-theory)/theory	(Test-FEA)/FEA
$\omega_1$	1.730	1.870	1.640	7.50	5.20
$\omega_2$	9.810	10.170	9.200	3.50	6.20
$\omega_3$	18.030	18.950	16.490	4.90	8.50

information on each ground motion is shown in Table 4. Notably, the three NFPT ground motions had different velocity pulse periods (VPPs). However, the VPP of 7.50 s was basically the same with the natural vibration period of the original structure (7.58 s). Moreover, it can also be seen that the bracketed and energy duration of the LPs are much longer than that of the NFPTs and Site-II motions. Accordingly, with the same PGA, the dynamic response of the

controlled structure under the LPs will supposedly be larger than that of under the NFPTs and Site-II motions.

Because the seismic fortification intensity was 7°, the peak accelerations corresponding to the frequent earthquake E1 and fortification earthquake E2 were 0.035 g and 0.1 g, respectively. Considering the safety of the test process and effectiveness of the damper, only the above two acceleration peaks were considered. According to Table 2, the peak

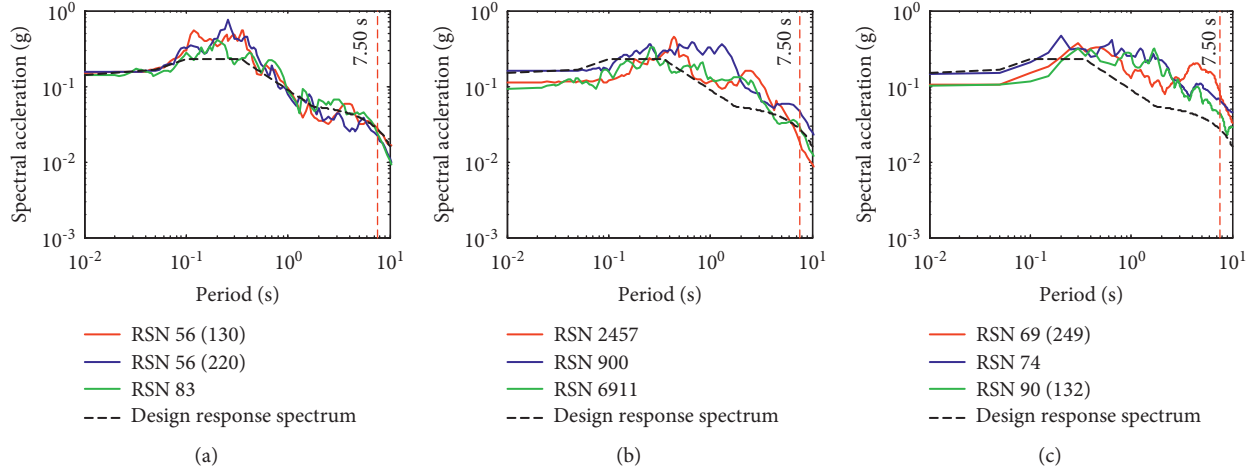


FIGURE 2: Acceleration response spectra of selected ground motions compared with the design response spectrum. (a) Site-II ground motions. (b) NFPT ground motions. (c) LP ground motions.

TABLE 4: Information of the ground motions.

Excitation types	Record sequence number (RSN)	Name	VPP (s)	M	Bracketed duration ( $\geq 1/3A_{\max}$ ) (s)	Energy duration (5%–95%) (s)	Peak ground acceleration (PGA) (g)
Site-II	56 (130)	San Fernando	—	6.61	11.6	18.9	0.071
	56 (220)	San Fernando	—	6.61	14.7	18.9	0.071
	83	San Fernando	—	6.61	8.4	14.3	0.074
Near-fault pulse-type (NFPT)	2457	Chi-Chi_Taiwan-03	3.18	6.20	5.7	12.9	0.187
	900	Landers	7.50	7.28	8.3	18.9	0.245
	6911	Darfield_New Zealand	9.92	7.00	7.6	9.5	0.450
Long period (LP)	69 (249)	San Fernando	—	6.61	51.7	52.4	0.029
	74	San Fernando	—	6.61	33.6	29.6	0.007
	90 (132)	San Fernando	—	6.61	51.4	49.3	0.017

accelerations of E1 and E2 were adjusted to 0.35 g and 1.0 g, respectively. The ground motions were input along the horizontal direction ( $X$ -direction), which was the same as the vibration direction of the damper.

### 3. Design of the Damping Scheme

#### 3.1. Optimisation Method of Damper Parameters

**3.1.1. Mechanical Model of Double-Layer Tuned Mass Damper (DTMD).** As shown in Figure 3(a), the DTMD comprises an upper TMD and lower TMD in series and the upper TMD is connected to the controlled structure. The work of the DTMD is as follows: the upper tuned mass can swing around the controlled structure through the universal hinge C (it can be adjusted as a one-direction hinge when the vibration is unidirectional, the same as below) and connecting rod D. The lower tuned mass can swing around the upper tuned mass through the universal hinge E and connecting rod F.

According to the Code for Seismic Design of Buildings, when the mode decomposition response spectrum method is adopted, the horizontal seismic effect can only take the first

2-3 modes for structures without using a torsional coupling calculation. The number of modes can be appropriately increased when the natural vibration period is greater than 1.5 s or when the height-width ratio of the buildings is greater than 5. By neglecting the coupling effect of every translational formation of the high-rise structure and taking the first  $n$ -order translational DOFs as an example, the  $i$ -order translational formation can be regarded as a SDOF structure with the same vibration participation mass and same frequency as the  $i$ -order formation. We assumed that the mass, the stiffness, and the damping coefficient of a SDOF structure were  $m_0$ ,  $k_0$ , and  $c_0$ , respectively. The upper tuned mass had a mass of  $m_1$  and was connected to the controlled structure, and its stiffness  $k_1$  and damping coefficient  $c_1$  were provided by the universal hinge C and connecting rod D. The mass of the lower tuned mass was  $m_2$ , and its stiffness  $k_2$  and damping coefficient  $c_2$  were provided by the universal hinge E and connecting rod F. The external harmonic excitation was  $F = P_0 \exp(i\omega t)$  ( $i = \sqrt{-1}$ ). The relative displacement response between the controlled structure and the ground was  $x_0(t)$ , and the corresponding displacement response of the upper and lower tuned masses was  $x_1(t)$  and  $x_2(t)$ , respectively. According to the DTMD

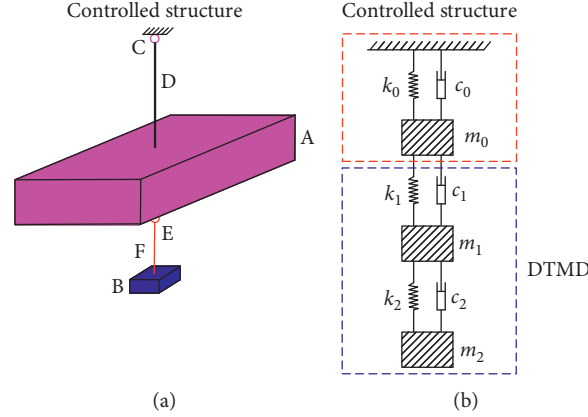


FIGURE 3: Double-layer tuned mass damper (DTMD) model. (a) Model sketch. (b) Mechanical model.

mechanical model in Figure 3(b), equation (1) could be obtained [36,38,40,41] as follows:

$$M\ddot{X} + C\dot{X} + KX = F, \quad (1)$$

$$\text{where } \mathbf{M} = \begin{bmatrix} m_0 & 0 & 0 \\ 0 & m_1 & 0 \\ 0 & 0 & m_2 \end{bmatrix}, \quad \mathbf{C} = \begin{bmatrix} c_0 + c_1 & -c_1 & 0 \\ -c_1 & c_1 + c_2 & -c_2 \\ 0 & -c_2 & c_2 \end{bmatrix},$$

$$\mathbf{K} = \begin{bmatrix} k_0 + k_1 & -k_1 & 0 \\ -k_1 & k_1 + k_2 & -k_2 \\ 0 & -k_2 & k_2 \end{bmatrix}, \quad \mathbf{X} = \begin{Bmatrix} x_0(t) \\ x_1(t) \\ x_2(t) \end{Bmatrix}, \quad \text{and } \mathbf{F} = \begin{Bmatrix} P_0 \exp(i\omega t) \\ 0 \\ 0 \end{Bmatrix}.$$

If  $x_j(t) = h_j(\omega)\exp(i\omega t)$  ( $j = 0, 1, 2$ ), then a calculation can be made as follows:

$$(-\omega^2 M + i\omega C + K)h(\omega) = F_0. \quad (2)$$

Here, the variables are determined as follows:  $h(\omega) = \begin{Bmatrix} h_0(\omega) \\ h_1(\omega) \\ h_2(\omega) \end{Bmatrix}$  and  $F_0 = \begin{Bmatrix} P_0 \\ 0 \\ 0 \end{Bmatrix}$ ; let  $\mu_1 = (m_1/m_0)$ ,  $\mu_2 = (m_2/m_0)$ ,  $\lambda_1^2 = (\omega_1^2/\omega_0^2)$ ,  $\lambda_2^2 = (\omega_2^2/\omega_0^2)$ ,  $\xi_j = (c_j/2m_j\omega_j)$ ,  $\lambda^2 = (\omega^2/\omega_0^2)$ , and  $\Delta_{st} = (P_0/k_0)$ .

Equation (2) can be expressed as follows:

$$(-\mathbf{A}_1 + \mathbf{A}_2 + \mathbf{A}_3)h(\omega) = \Delta. \quad (3)$$

Here, the variables are determined as follows:

$$\mathbf{A}_1 = \begin{bmatrix} \lambda^2 & 0 & 0 \\ 0 & \mu_1 \lambda^2 & 0 \\ 0 & 0 & \mu_2 \lambda^2 \end{bmatrix},$$

$$\mathbf{A}_2 = 2\lambda i \begin{bmatrix} \xi_0 + \xi_1 \mu_1 \lambda_1 & -\xi_1 \mu_1 \lambda_1 & 0 \\ -\xi_1 \mu_1 \lambda_1 & \xi_1 \mu_1 \lambda_1 + \xi_2 \mu_2 \lambda_2 & -\xi_2 \mu_2 \lambda_2 \\ 0 & -\xi_2 \mu_2 \lambda_2 & \xi_2 \mu_2 \lambda_2 \end{bmatrix},$$

$$\mathbf{A}_3 = \begin{bmatrix} 1 + \mu_1 \lambda_1^2 & -\mu_1 \lambda_1^2 & 0 \\ -\mu_1 \lambda_1^2 & \mu_1 \lambda_1^2 + \mu_2 \lambda_2^2 & -\mu_2 \lambda_2^2 \\ 0 & -\mu_2 \lambda_2^2 & \mu_2 \lambda_2^2 \end{bmatrix}, \quad \text{and } \Delta = \begin{pmatrix} \Delta_{st} \\ 0 \\ 0 \end{pmatrix}.$$

In this study, we let  $s_j = 2\xi_j \mu_j \lambda_j \lambda i + \mu_j \lambda_j^2$  ( $j = 0, 1, 2$ ) and  $\mu_0 = 1$  and  $\lambda_0 = 1$ . Then, the displacement dynamic

magnification factor (DDMF) of the controlled structure can be obtained as follows:

$$\text{DDMF} = \frac{-\mu_1 \mu_2 \lambda^4 + I_0(\mu, s)\lambda^2 - s_1 s_2}{\mu_1 \mu_2 \lambda^6 - I_1(\mu, s)\lambda^4 + I_2(\mu, s)\lambda^2 - s_0 s_1 s_2}. \quad (4)$$

The values of the variables are calculated as follows:

$$I_0(\mu, s) = s_2 \mu_1 + s_1 \mu_2 + s_2 \mu_2,$$

$$I_1(\mu, s) = \mu_1 s_2 + \mu_2 s_1 + \mu_2 s_2 + s_0 \mu_1 \mu_2 + s_1 \mu_1 \mu_2,$$

$$I_2(\mu, s) = s_1 s_2 + s_0 s_2 \mu_1 + s_0 s_1 \mu_2 + s_1 s_2 \mu_1 + s_0 s_2 \mu_2 + s_1 s_2 \mu_2. \quad (5)$$

**3.1.2. Parameter Optimisation Method.** Based on the MTMD parameter optimisation method, the DTMD was optimised using a numerical optimisation method [38,42-46]. Then, two important evaluation parameters of the SDOF structure with  $n$ -order TMDs can be given as follows:

$$P_1 = \sum_{i=1}^{n+1} \frac{P_{\max}(i)}{n+1}, \quad (6)$$

$$P_2 = \sum_{j=1}^{n+1} \left\{ \sum_{i=1}^{n+1} \frac{P_{\max}(i)}{n+1} - P_{\max}(j) \right\}^2. \quad (7)$$

Here,  $P_{\max(i)}$  denotes the peaks of the displacement response curve,  $P_1$  denotes the average value of the peaks, and  $P_2$  denotes the deviation value of the peaks. Shen [47] introduced an optimised method for a double-layer tuned particle damper. However, that method did not consider the effect of multimode participation. According to Table 1, the cumulative vibration mass participation factor for the first three modes of the prototype reaches 86%. Accordingly, the optimisation method of DTMD for HRS must consider the effect of multimode participation. Then, according to equations (6) and (7), the optimisation parameter expression of the DTMD is as follows:

$$Z(\mu, \mu_1, \mu_2, \xi_0, \xi_1, \xi_2, \lambda_1, \lambda_2, \lambda) = \min[\phi_1(P_{11} + P_{12}) + \phi_2(P_{21} + P_{22}) + \phi_3(P_{31} + P_{32})]. \quad (8)$$

Here,  $P_{i1}$  and  $P_{i2}$  represent the optimisation indexes 1 and 2 of the displacement response peak of the  $i$ -order mode, respectively.  $\phi_i$  represents the ratio of the vibration mass participation factor of the  $i$ -order mode to the total vibration mass participation factor for the first  $N$ -order modes. In this study,  $i = 1, 2, 3$  and  $N = 3$ , and the corresponding values of  $\phi_1$ ,  $\phi_2$ , and  $\phi_3$  are 0.779, 0.105, and 0.116, respectively. Because the additional mass of the damper has a significant influence on the stress state of the controlled structure [14,15,18–22] and that the damping effect will be poor when the additional mass ratio is excessively small, the additional mass ratio of the tuned damper is mostly controlled to be in the range of 2%–5%. In this study, the additional mass ratio  $\mu$  of the optimised DTMD was 5%. The test model was a steel structure, and the damping ratio  $\xi_0$  of the controlled structure was set at 0.02, according to the measured value. It should be pointed out that the controlled structure was assumed to be in an elastic state and the damping variation of the controlled structure (including the soil damping and structure damping) was not considered.  $\xi_1$  and  $\xi_2$  were the damping ratios of the upper and lower tuned masses, respectively, and their values were in the range of 0–0.15 and 0–0.4.  $\lambda_1$  and  $\lambda_2$  represented the ratios of the natural frequencies of the upper and lower tuned masses to the controlled structure, respectively. And, their values were all in the range of 0.6 to 1.4.  $\lambda$  was the ratio of natural frequency of the controlled structure to the excitation and was within the range of 0.60 to 1.40. Moreover, there may be some local minimum and saddle point of the optimisation results. To avoid the local minimum and saddle point, we usually draw all the displacement responses of the controlled system with different optimisation results and select a best one as the optimisation parameters. Figure 4(a) shows a comparison of the optimisation results for TMD, MTMD, and DTMD. The theoretical optimisation results of the DTMD-SDOF system are shown in Figure 4(b).

As shown in Figure 4(a), the damping frequency band of the optimised TMD is about  $0.16\lambda_0$ , while the damping frequency band of the optimised DTMD is greatly increased to  $0.30\lambda_0$  under the same optimisation conditions. The frequency range of the optimised DTMD is wider than that of the TMD. The optimised DTMD has essentially the same damping frequency band as the optimised MTMD. In addition, it can be seen from Figure 4(b) that the damping effect and robustness of the DTMD decrease with an increase in the damping ratio of the upper TMD.

**3.2. Damper Design.** The experimental validation work is also a data support and methodological reference for the future application of shock absorbers. Transforming theoretical optimisation parameters into practical available parameters has always been hotspot study in engineering field. The application method (including design and manufacture method) of optimisation parameters is also necessary to be verified by experiments. According to the dynamic

parameters of the prototype tower and optimisation method described in Section 3.1, the optimised parameters of the DTMD in this study were determined, as shown in Table 5.

According to Table 5, the mass of the upper TMD can be determined as  $m_1 = 0.0462m_0$  and the natural frequency is  $f_1 = f_0 = 1.64$  Hz, in which  $m_0$  is the first-mode participation mass of the prototype model. Also, the maximum angular displacement of the upper TMD without damping was always less than  $\pi/18$  (10 degrees) in this study. The influence of the angular displacement can be ignored. Then, the connection stiffness between the upper TMD and controlled model can be simplified as equation (9).

$$\omega_1 = \sqrt{\frac{g}{L} + \frac{k_1}{m_1} \left(\frac{h}{L}\right)}, \quad (9)$$

Here,  $\omega_1$  is equal to 10.24 rad/s and it represents the natural frequency of the upper TMD without damping. The acceleration of gravity is  $g = 9.8$  m/s<sup>2</sup>.  $L$  is the effective pendulum length and was 370 mm in this test.  $h$  represents the distance between the upper connection point and the lower connection point and in this study, it was the same as the effective pendulum length  $L$ . The external spring stiffness was obtained through equation (9) and was equal to 7780 N/m. The stiffness of the outer spring was obtained by customising the tension spring and met the deformation requirement of the pulling length.

The mass and natural frequency of the lower TMD are  $m_2 = 0.0038m_0$  and  $f_2 = 0.91 f_0 = 1.49$  Hz, respectively. Because the mass of the lower TMD was relatively small, its natural frequency was determined by the pendulum length. Then, the pendulum length of the lower TMD was obtained through  $\omega_2 = \sqrt{g/L}$  and was equal to 111 mm. Based on the optimised parameters in Table 5, the equivalent damping ratio of the lower TMD was approximated by

$$\xi_2 = \frac{C_2}{2m_2\omega_2}. \quad (10)$$

Here,  $C_2$  is the equivalent damping coefficient and can be calculated from the required equivalent damping ratio. In this study, the equivalent damping at the unidirectional hinge was provided by its friction. According to the principle of energy equivalence, if the areas of the friction-displacement curve and equivalent viscous damping-displacement curve are the same under the same harmonic excitation, then they are equivalent. The friction coefficient  $\mu$  between the unidirectional hinge of the upper TMD and lower TMD was obtained based on their area equivalence.

$$\mu = \frac{\pi C_2 (\omega_2 s)}{4m_2 g}. \quad (11)$$

In this study, the DTMD mainly concerned the first-order vibration mode and the displacement response amplitude  $s$  in equation (11) was determined according to the displacement response amplitude of the DTMD. Because the



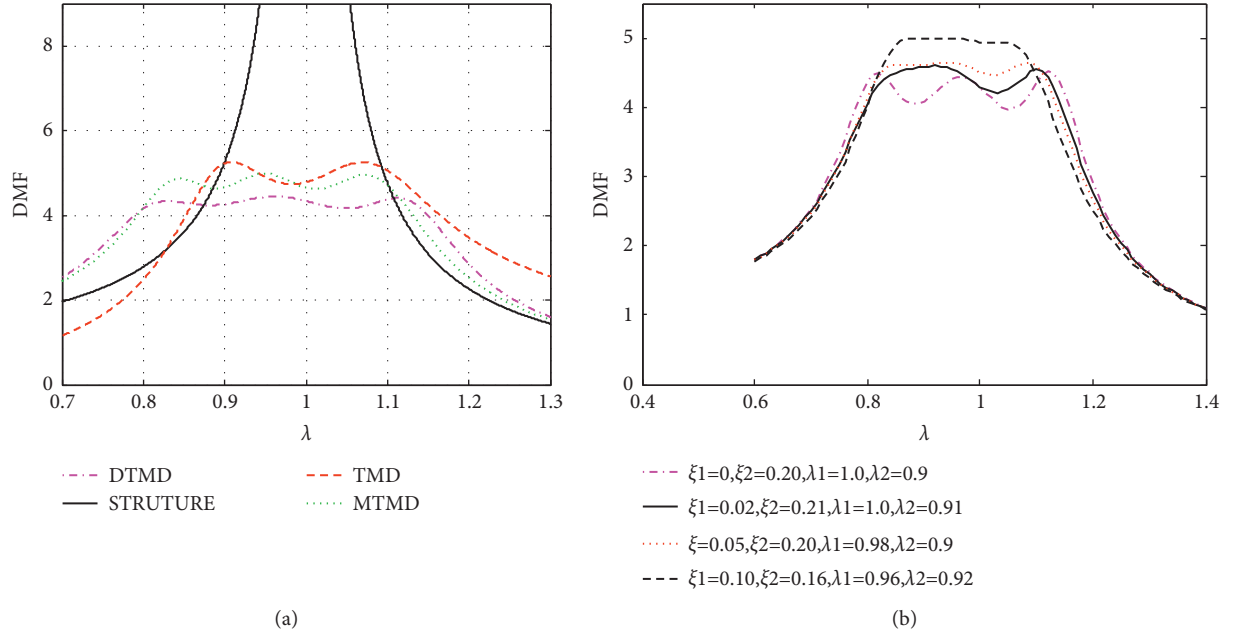


FIGURE 4: Typical optimisation results of the damper ( $\mu = 0.05$ ;  $\xi_0 = 0.02$ ). (a) Comparison of DTMD, TMD, and multiple TMD (MTMD). (b) Optimised DTMD.

TABLE 5: Optimised parameters of the double-layer tuned mass damper (DTMD).

Parameter	$\mu$	$\xi$	$\lambda$
Upper tuned mass damper	0.0462	0.02	1.00
Lower tuned mass damper	0.0038	0.21	0.91

first-mode participation mass of the model and the additional mass of the DTMD satisfied  $m_0 = nm$ , the first-order stiffness between them satisfied  $k_0 = nk$ . The peak displacement  $d_0$  of the model and the peak displacement  $d$  of the DTMD must satisfy an equation, as follows:

$$\frac{d}{d_0} = \frac{1}{2} \pm \sqrt{n + \frac{1}{4}} \quad (12)$$

Since the parameter  $n$  is equal to 20,  $d_0$  was approximately 7.0 mm under frequent earthquakes E1 and 15.0 mm under fortification earthquakes E2, respectively. The friction coefficient was equal to 0.10 and 0.22, respectively. In this study, the friction coefficient was obtained by using a steel unidirectional hinge and applying lubricant.

Considering the top space of the model tower, installation position of the damper, length of the springs, and optimised design parameters in Table 5, the upper TMD was composed of the steel box and counterweight. The counterweight was arranged at the centroid position of the steel box, and the total weight of the upper TMD was 99.24 kg. The designed DTMD is shown in Figure 5.

The numerical optimisation showed that a smaller damping ratio of the connection would lead to a more significant damping effect for the DTMD. To verify the theoretical results, this study also considered different boundary conditions for the connection when studying the damping effect of the DTMD. They were (1) case-I (the connection was

filled with the polytrifluorochloroethylene (PTFE), and the equivalent damping ratio was in the range of 0.26 to 0.56); (2) case-II (the connection had no treatment, and the equivalent damping ratio was in the range of 0.12 to 0.25); (3) case-III (the connection was lubricated with oil, and the equivalent damping ratio was in the range of 0.04 to 0.08).

In addition, the displacement response of the upper TMD and the lower TMD were monitored by the displacement sensors. And, a GoPro camera was also used to record the motion state of the damper in real time, as shown in Figure 5(c).

#### 4. Experimental Results and Analysis

To better evaluate the seismic performance and control effect of the DTMD, the absolute displacement response (ADR), root mean square (RMS) of the absolute displacement response (RMS-ADR), acceleration response (AR), and strain response (SR) of the top floor were analysed. For effective and efficient calculations, the lower limits of the ADR, AR, and SR were determined as 0.5 mm, 20 cm/s<sup>2</sup>, and 1  $\mu\epsilon$ , respectively. The expressions for the effective RMS and decreasing ratios of each parameter are as follows:

$$\lambda_d = \text{sqrt} \left( \sum_{\text{if } x_i \geq x_0}^n \frac{x_i^2}{n} \right), \quad (13)$$

$$\eta_j = \left( \frac{\lambda_{j0} - \lambda_j}{\lambda_{j0}} \right) \times 100\%.$$

Here,  $x_i$  denotes the dynamic response at  $i$  moment and  $\lambda_{j0}$  denotes the responses of the model without DTMD for each parameter.  $j$  can take the values of 1, 2, 3, and 4 and represent ADR, RMS-ADR, AR, and SR, respectively.

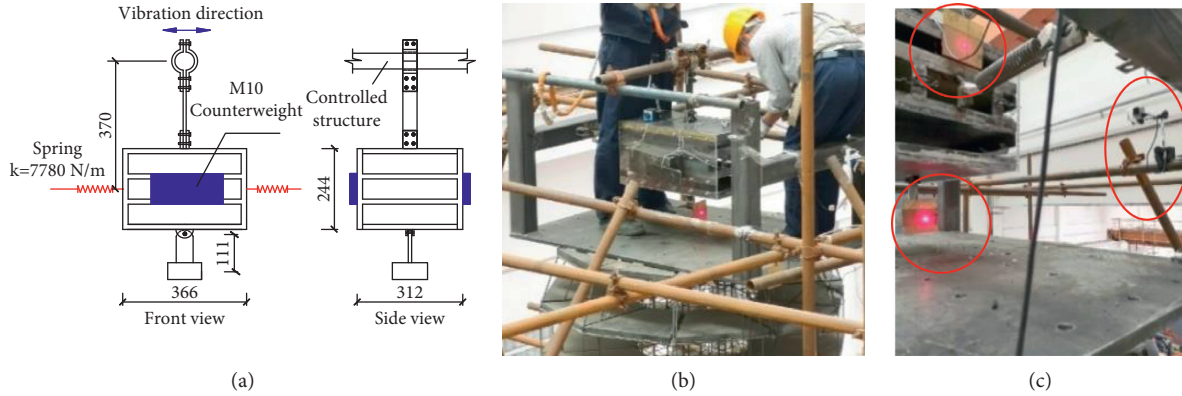


FIGURE 5: DTMD model and measurement layout. (a) Dimension (mm). (b) DTMD model. (c) Sensors and camera.

**4.1. Experimental Results of the Original Model.** According to the three types of ground motions selected in Section 2.3, shaking table tests of the original model were firstly carried out. Figure 6 shows the dynamic response curves of the top floor under three typical ground motions.

As shown in Figure 6, the displacement response of the model tower is mainly a low-frequency response under the three typical ground motions, conforming to the response characteristics of high-rise structures. For the E1 and E2 excitations, the ADRs under the NFPT ground motion (RSN900) and the LP ground motion (RSN74) are significantly larger than those under the Site-II ground motion (RSN56 (130)). Moreover, this phenomenon becomes much more evident as the excitation peaks increase. For the E1 and E2 excitations, the amplitudes of ADRs under the RSN74 wave are 1.09 times and 1.89 times larger than those under the RSN56 (130) wave, respectively. Meanwhile, the amplitudes of the ADRs under the RSN900 wave are 1.21 times and 1.85 times larger than those under the RSN56 (130) wave, respectively. In addition, the ADR, RMS-ADR, AR, and SR of the model without the DTMD are given in Table 6.

As shown in Table 6, under the three types of ground motions, the ADR, RMS-ADR, AR, and SR values of the model significantly increase with the increase in amplitude of the excitations. The dynamic response of the model under the NFPT and LP ground motions is more significant than that under the Site-II ground motions. Taking the E2 earthquake as an example, the average peak of the ADRs under Site-II ground motions is 7.87 mm. The corresponding values reach 11.87 mm and 15.33 mm under NFPT ground motions and LP ground motions, respectively.

When the velocity pulse period of the NFPT ground motion is close to the natural vibration period of the original model, the dynamic response of the model will be more significant; this is consistent with the research results of Shen et al. [47] and Xu et al. [48]. Owing to the influence of the long natural vibration period of high-rise structures, the high-frequency component of the ground motions is gradually filtered out in the transmission process and the low-frequency component at the top floor of the structure is greater than that at the bottom floor. Thus, the resonance phenomenon will cause an evident whipcord phenomenon at the top floor of the structure under the LP and NFPT

ground motions. For example, under the E2 earthquake, the peaks of the SRs (the S4 measurement point) at the top floor are  $378.65 \mu\epsilon$ ,  $1331.92 \mu\epsilon$ , and  $1646.60 \mu\epsilon$  under Site-II ground motion RSN56 (130), NFPT ground motion RSN900, and LP ground motion RSN74, respectively. In contrast, the values (the S1 measuring point) at the bottom floor are  $63.24 \mu\epsilon$ ,  $193.72 \mu\epsilon$ , and  $239.43 \mu\epsilon$  under the same cases, respectively.

#### 4.2. Experimental Results of the Damping Model

**4.2.1. Basic Dynamic Characteristics.** Table 7 shows the first-order frequency of each model with and without the DTMD. It can be seen that the first-order frequency of the scaled model has negligible changes before and after the test. Thus, the model tower is always in the elastic stage during the test, and the analysis data show high reliability. Compared with the original structure, the vibration frequencies of the test model with the DTMD decrease slightly. The connection case of the DTMD has little effect on the dynamic characteristics of the DTMD model system. In addition, owing to the small weight of the lower TMD, the acceleration sensor is only installed on the upper TMD. Under case-III, it can be seen that the first natural vibration frequency of the upper TMD is basically consistent with the design frequency. Accordingly, both the design and processing of the DTMD are effective.

**4.2.2. Site-II Ground Motions.** Figure 7 gives the ADR and AR of the model before and after the DTMD installation under the RSN56 (130) wave. The connection case of the DTMD was case-III.

As shown in Figure 7, the DTMD can effectively reduce the displacement and acceleration responses at the top of the test model. At the initial stage, both the displacement response and acceleration response curves of the model with and without the DTMD partially overlap and the difference in the dynamic response between them gradually increases in the later stages. This phenomenon shows that the DTMD has the same characteristics as the tuned damper; that is, the damping effect is not evident in the early stage but is evident in the later stages. Table 8 provides

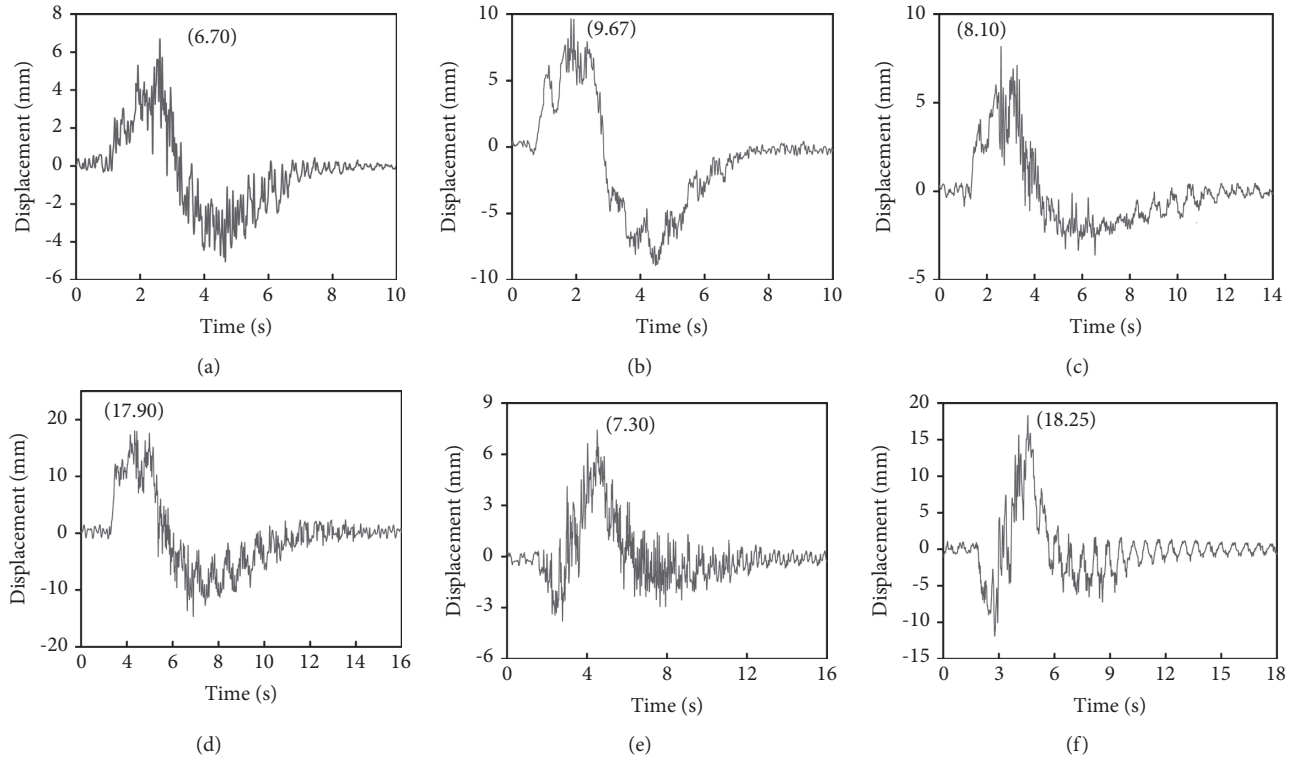


FIGURE 6: ADR of the original model. (a) RSN56 (130) with E1. (b) RSN56 (130) with E2. (c) RSN900 with E1. (d) RSN900 with E2. (e) RSN74 with E1. (f) RSN74 with E2.

TABLE 6: Statistics of the dynamic response.

Types	RSN	Peak acceleration	ADR (mm)	RMS-ADR (mm)	AR ( $m/s^2$ )	SR ( $\mu\epsilon$ )	
						Bottom-S1	Top-S4
Site-II	56 (130)	0.35 g	6.70	2.37	1.73	28.48	117.61
	56 (220)		2.52	0.84	1.27	14.17	66.54
	83		4.63	1.86	1.62	23.14	96.63
	Average		4.62	1.69	1.54	21.93	93.59
	56 (130)	1.00 g	9.67	4.77	4.21	63.24	378.65
	56 (220)		5.44	3.39	3.48	49.45	273.23
	83		8.50	4.66	4.00	60.59	349.66
	Average		7.87	4.27	3.90	57.76	333.85
NFPT	2457	0.35 g	4.68	1.62	3.01	30.71	207.97
	900		8.10	2.64	5.13	54.63	387.68
	6911		6.02	2.03	4.30	46.38	262.29
	Average		6.27	2.10	4.15	43.91	285.98
	2457	1.00 g	7.79	3.74	7.01	130.75	843.62
	900		17.90	5.6	12.07	193.72	1331.92
	6911		9.93	4.57	10.19	145.08	755.22
	Average		11.87	4.64	9.76	156.52	976.92
LP	69 (249)	0.35 g	7.57	2.33	3.56	62.33	358.25
	74		7.30	2.52	5.27	70.78	416.33
	90 (132)		6.91	1.89	4.79	70.12	407.38
	Average		7.26	2.25	4.54	67.74	393.99
	69 (249)	1.00 g	16.72	4.42	10.29	156.52	1004.33
	74		18.25	5.91	13.16	239.93	1646.60
	90 (132)		11.03	4.17	12.81	191.00	1482.56
	Average		15.33	4.83	12.09	195.82	1377.83

TABLE 7: First-order frequency of each model (Hz).

Model	Before the test	With DTMDs in different boundary conditions			After the test	DTMD	Case-III
		Case-III	Case-II	Case-I			
First-order frequency	1.64	1.53	1.56	1.58	1.67	First-order frequency	1.60

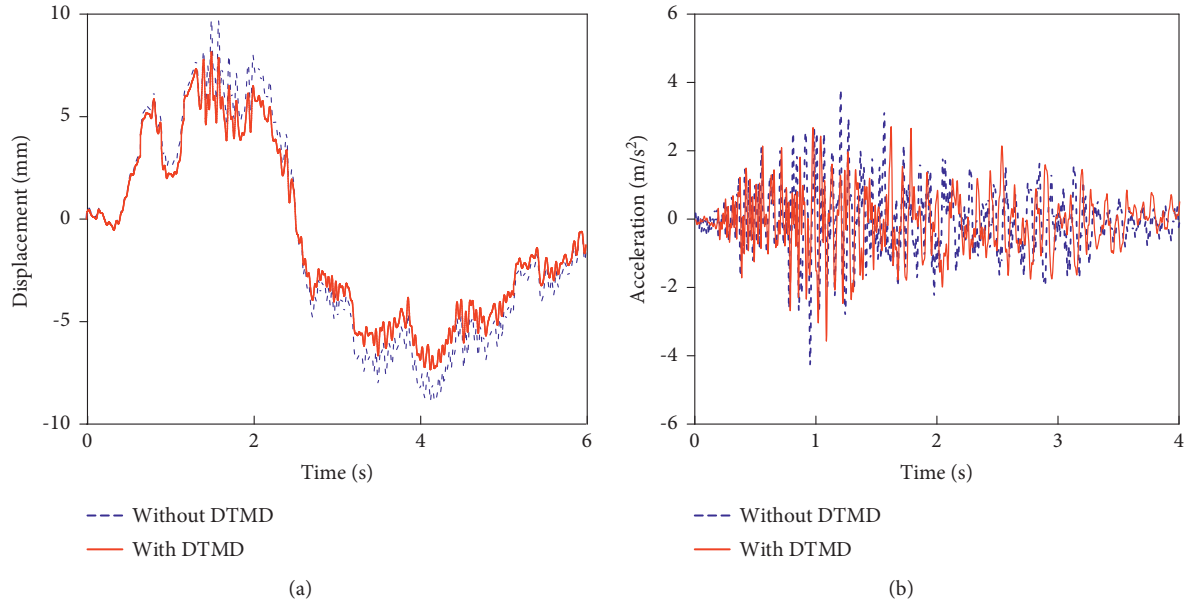


FIGURE 7: ADR and AR of the model before and after the DTMD installation under the Site-II ground motions (case-III, E2). (a) Absolute displacement. (b) Acceleration.

TABLE 8: Decreasing ratios of the model with the DTMD under Site-II ground motions.

Parameters	RSN	Peak (g)	Connection cases			Decreasing ratio (%)					
			I	II	III	I	Average	II	Average	III	Average
ADR (mm)	56 (130)	0.35	6.28	6.11	5.89	6.3	6.0	8.8	9.0	12.1	11.1
	56 (220)		2.37	2.37	2.27	5.9		5.8		9.8	
	83		4.36	4.06	4.10	5.8		12.4		11.5	
	56 (130)	1.00	8.64	8.47	8.14	10.7	5.6	12.4	11.1	15.8	15.0
	56 (220)		5.66	4.82	4.76	-4.1		11.4		12.5	
83	7.63	7.69	7.09	10.2	9.6	16.6					
RMS-ADR (mm)	56 (130)	0.35	2.14	2.15	2.05	9.7	7.1	9.4	9.7	13.6	11.6
	56 (220)		0.77	0.76	0.76	7.9		9.4		9.4	
	83		1.79	1.67	1.64	3.6		10.3		11.9	
	56 (130)	1.00	4.17	4.06	3.95	12.6	10.0	14.9	12.3	17.2	14.5
	56 (220)		3.18	3.08	3.08	6.3		9.1		9.2	
83	4.14	4.05	3.86	11.2	13.0	17.1					
AR (m/s <sup>2</sup> )	56 (130)	0.35	1.60	1.55	1.53	7.8	6.5	10.5	7.7	11.8	10.5
	56 (220)		1.20	1.22	1.16	5.4		3.9		8.7	
	83		1.52	1.48	1.44	6.4		8.8		11.0	
	56 (130)	1.00	3.80	3.65	3.52	9.8	7.5	13.2	11.3	16.4	13.7
	56 (220)		3.31	3.14	3.14	4.9		9.8		9.7	
83	3.69	3.56	3.39	7.9	11.0	15.1					
SR ( $\mu\epsilon$ )	56 (130)	0.35	107.65	105.28	104.55	8.5	6.5	10.5	8.9	11.1	10.3
	56 (220)		62.27	60.67	59.43	6.4		8.8		10.7	
	83		92.35	89.59	87.83	4.5		7.3		9.1	
	56 (130)	1.00	330.13	323.42	312.34	12.8	11.1	14.6	12.9	17.5	14.5
	56 (220)		246.15	245.06	244.30	9.9		10.3		10.6	
83	312.19	301.52	295.63	10.7	13.8	15.5					

the decreasing ratios of the model with the DTMD under the Site-II ground motions.

As shown in Table 8, except for a few cases under case-I, the DTMD can provide a good damping effect. Taking the RSN56 (130) wave under the E2 earthquake as an example, the decreasing ratios of the ADR, RMS-ADR, AR, and SR of the test model under case-III are 15.8%, 17.2%, 16.4%, and 17.5%, respectively.

The average decreasing ratio of each dynamic response parameter basically follows the variation law that decreasing ratios are the largest under case-III, the second largest under case-II, and the smallest under case-I. Taking the RMS-ADR parameter under the E2 earthquake as an example, the average decreasing ratio of the DTMD with case-I is only 10.0%. However, the corresponding decreasing ratios of the DTMD with case-II and case-III are 12.3% and 14.5%, respectively. The experimental results are similar to the optimisation results; that is, the smaller damping ratio of the connection will lead to a better damping effect for the DTMD. Based on the experimental phenomena, the reason may be that the response amplitude of the DTMD decreases with an increase in the damping of the upper TMD. The energy absorption capacity of the DTMD was significantly impacted by the damping ratio of the upper tuned mass damper (described in detail in Section 4.2.5).

In addition, the damping effect of the DTMD is also influenced by the excitation intensity. The larger excitation intensity will lead a better damping effect of the DTMD. Taking case-III as an example, under E1 and E2 excitations, the average decreasing ratios of the ADR, RMS-ADR, AR, and SR of the DTMD are 11.1% and 15.0%, 11.6% and 14.5%, 10.5% and 13.7%, and 10.3% and 14.5%, respectively. This is related to the damping mechanism of the TMD [14,27–30]. With an increase in the excitation amplitude, the structural response is greater and the dynamic response and energy dissipation of the DTMD increase.

**4.2.3. Near-Fault Pulse-Type (NFPT) Ground Motions.** Figure 8 shows a comparison of dynamic response of the model before and after the DTMD installation under a typical NFPT ground motion of RSN900. The connection condition was case-III.

As Figure 8 shows, when the time of earthquake excitation is less than 0.5 s, the absolute displacement of the test model is less than 8 mm and the control effect of the DTMD on the displacement response is not evident. When the acceleration response of the test model is less than  $5 \text{ m/s}^2$  (the time of earthquake excitation  $< 0.3 \text{ s}$ ), the control effect of the DTMD on the acceleration response is also not evident. However, after a period of earthquake excitation, the DTMD will not only decrease the ADR and AR of the model but will also rapidly attenuate its dynamic response. The DTMD has a time delay before providing the damping effect. Table 9 lists the dynamic response and decreasing ratios of the model with the DTMD under the NFPT ground motions.

As shown in Table 9, the DTMD has an obvious damping effect for the model under NFPT ground motions and the damping effect of the DTMD under RSN900 is the most

significant. Taking case-III under the E2 earthquake as an example, the decreasing ratios of the ADR, RMS-ADR, AR, and SR under the RSN900 wave reach 22.8%, 24.9%, 25.0%, and 22.1%, respectively, which are significantly higher than the corresponding values under the other NFPT ground motions. That is, when the VPP of the NFPT ground motion is close to the natural vibration period of the structure, the dynamic response of the structure amplified and then the DTMD will provide better damping effect.

The influence law of a DTMD with different boundary cases under the NFPT ground motions is similar to that under the Site-II ground motions. The DTMD has the best damping effect under case-III and a poor damping effect under case-I. Taking the ARs under the E2 excitation as an example, the average decreasing ratio of the DTMD with case-I is only 10.9%. In contrast, the corresponding average decreasing ratios of the DTMDs with case-II and case-III are 15.1% and 19.0%, respectively. The decreasing ratios of each dynamic response parameter increase with increasing excitation intensity. Taking case-III as an example, under E1 and E2 excitations, the average decreasing ratios of the ADR and RMS-ADR increase from 12.6% to 17.3% and 13.0% to 20.4%, respectively. In this case, the average decreasing ratios of the AR and SR increase from 12.4% to 19.0% and 12.7% to 17.5%, respectively.

**4.2.4. Long-Period (LP) Ground Motions.** Figures 9(a) and 9(b) show the ADR and AR of the model before and after the DTMD installation under the RSN74 wave of case-III.

Figure 9 shows that the DTMD can obviously decrease the amplitude of ADR and AR of the model under the LP ground motions. The dynamic response and decreasing ratios of the model with the DTMD under LP ground motions are presented in Table 10.

As shown in Table 10, except for the negative decreasing rate in a few cases, the DTMD can provide good energy dissipation capacity under LP ground motions. Taking case-III under E2 excitation as an example, the decreasing ratio of each dynamic response of the test model is more than 22% under the RSN74. Similar to the boundary condition law under the NFPT ground motions and Site-II ground motions, the damping effect of the DTMD will be limited when the damping ratio of the connection increases. Taking the RMS-ADR under the E2 excitation as an example, the average decreasing ratio of the DTMD with case-I is only 15.2%. However, the corresponding average decreasing ratios of the DTMDs with cases II and III are 20.1% and 23.7%, respectively. The excitation intensity also has the same influence law as that under the NFPT and Site-II ground motions, and the decreasing rates of each dynamic parameter under the LP ground motions increase with an increase in excitation intensity. Taking case-III as an example, the average decreasing ratios of the ADR, RMS-ADR, AR, and SR under the E1 excitation are 13.6%, 14.5%, 13.7%, and 13.6%, respectively. In contrast, the corresponding decreasing ratios of the DTMD are up to 21.1%, 23.7%, 22.4%, and 22.1% under the E2 excitation, respectively.

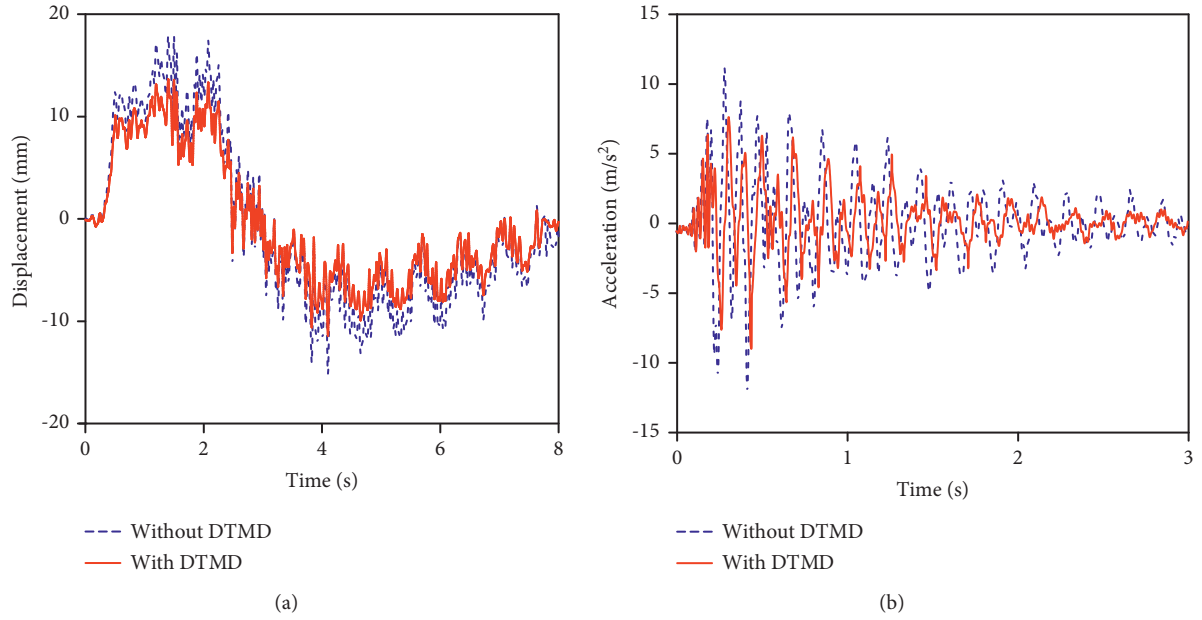


FIGURE 8: ADR and AR of the model before and after the DTMD installation under the NFPT ground motions (case-III, E2). (a) Absolute displacement. (b) Acceleration.

TABLE 9: Decreasing ratios of the model with DTMD under NFPT ground motions.

Parameters	RSN	Peak (g)	Connection cases			Decreasing ratio (%)					
			I	II	III	I	Average	II	Average	III	Average
ADR (mm)	2457	0.35	4.31	4.27	4.23	7.9	8.9	8.8	11.3	9.6	12.6
	900		7.23	6.95	6.80	10.8		14.2		16.1	
	6911		5.53	5.37	5.30	8.1		10.8		12.0	
	2457	1.00	7.31	6.99	6.65	6.2	10.4	10.2	13.7	14.6	17.3
	900		15.18	14.46	13.81	15.2		19.2		22.8	
	6911		8.96	8.77	8.48	9.7		11.7		14.6	
RMS-ADR (mm)	2457	0.35	1.49	1.46	1.45	7.8	9.1	9.6	11.5	10.3	13.0
	900		2.36	2.31	2.23	10.5		12.6		15.5	
	6911		1.85	1.78	1.76	8.9		12.4		13.1	
	2457	1.00	3.32	3.26	3.17	11.3	12.9	12.8	16.9	15.1	20.4
	900		4.75	4.39	4.20	15.1		21.6		24.9	
	6911		4.01	3.82	3.60	12.3		16.3		21.2	
AR (m/s <sup>2</sup> )	2457	0.35	2.93	3.03	2.79	2.7	8.3	-0.6	8.7	7.1	12.4
	900		4.51	4.39	4.26	12.0		14.5		16.9	
	6911		3.86	3.78	3.74	10.2		12.1		13.1	
	2457	1.00	6.38	6.29	5.97	8.9	10.9	10.3	15.1	14.8	19.0
	900		10.50	9.73	9.05	13.0		19.4		25.0	
	6911		9.08	8.60	8.45	10.9		15.6		17.1	
SR ( $\mu\epsilon$ )	2457	0.35	193.21	190.85	187.91	7.1	8.8	8.2	10.3	9.6	12.7
	900		346.53	339.29	325.85	10.6		12.5		15.9	
	6911		239.11	235.30	229.45	8.8		10.3		12.5	
	2457	1.00	745.11	717.58	721.65	11.7	12.8	14.9	16.2	14.5	17.5
	900		1143.42	1055.55	1037.37	14.2		20.8		22.1	
	6911		660.44	656.81	634.22	12.5		13.0		16.0	

4.2.5. Comparison of the Damping Effect of DTMD under Three Types of Ground Motions. To further study the damping effect of the DTMD under the three types of ground motions, Figure 10 provides a comparison of the average decreasing ratios of the DTMD with different connection cases and under different ground motions.

As shown in Figure 10, except for some cases under case-I, the damping effect of the DTMD under the LP ground motions is better than that under the NFPT and Site-II ground motions; among the three, the damping effect of the DTMD under Site-II ground motions is relatively poor. In addition, the larger excitation intensity

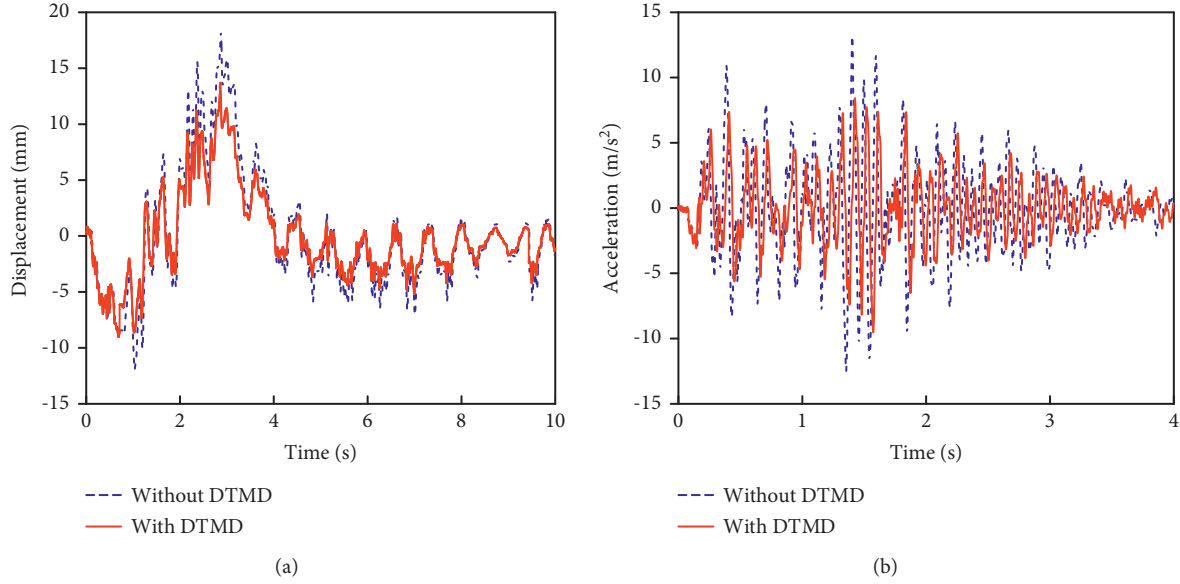


FIGURE 9: ADR and AR of the model with and without the DTMD under the LP ground motions (case-III, E2). (a) Absolute displacement. (b) Acceleration.

TABLE 10: Decreasing ratios of the model with DTMD under LP ground motions.

Parameters	RSN	Peak (g)	Connection cases			Decreasing ratio (%)					
			I	II	III	I	Average	II	Average	III	Average
ADR (mm)	69 (249)	0.35	6.88	6.74	6.72	9.1		10.9		11.2	
	74		6.49	6.37	6.15	11.1	10.1	12.7	11.6	15.8	13.6
	90 (132)		6.21	6.14	5.95	10.2		11.2		13.8	
	69 (249)	1.00	14.74	14.58	14.23	11.8		12.8		14.9	
	74		15.14	14.24	13.74	17.1	13.2	22.0	18.1	24.7	21.1
	90 (132)		9.86	8.87	8.41	10.6		19.5		23.8	
RMS-ADR (mm)	69 (249)	0.35	2.10	2.02	1.98	9.9		13.4		15.1	
	74		2.24	2.12	2.11	11.0	10.0	15.8	12.9	16.5	14.5
	90 (132)		1.72	1.71	1.66	9.0		9.4		12.0	
	69 (249)	1.00	3.83	3.67	3.46	13.4		17.0		21.7	
	74		5.00	4.60	4.33	15.4	15.2	22.1	20.1	26.8	23.7
	90 (132)		3.47	3.28	3.22	16.7		21.2		22.7	
AR ( $m/s^2$ )	69 (249)	0.35	3.57	3.39	3.24	-0.3		4.8		9.1	
	74		4.55	4.52	4.40	13.6	8.2	14.2	10.7	16.5	13.7
	90 (132)		4.25	4.16	4.04	11.3		13.1		15.6	
	69 (249)	1.00	9.31	9.12	8.44	9.5		11.3		17.9	
	74		10.82	9.92	9.47	17.8	13.6	24.6	18.4	28.0	22.4
	90 (132)		11.09	10.34	10.08	13.4		19.3		21.3	
SR ( $\mu\epsilon$ )	69 (249)	0.35	329.84	317.44	316.58	7.9		11.4		11.6	
	74		364.71	353.18	352.34	12.4	10.2	15.2	12.9	15.4	13.6
	90 (132)		365.57	357.60	351.39	10.3		12.2		13.7	
	69 (249)	1.00	846.33	824.36	803.16	15.7		17.9		20.0	
	74		1427.85	1310.53	1269.36	13.3	14.5	20.4	20.1	22.9	22.1
	90 (132)		1267.53	1157.73	1134.60	14.5		21.9		23.5	

(more significant dynamic response) will lead to a better damping effect for the DTMD. For the LP ground motions and Site-II ground motions under case-III, the differences in the average decreasing rates of the ADR, RMS-ADR, AR, and SR under E1 excitation are 2.5%, 2.9%, 3.2%, and 3.3%, respectively. However, the corresponding differences reach 6.2%, 9.2%, 8.7%, and 7.6% under E2 excitation, respectively. Similarly, there is little difference between the LP

ground motions and NFPT ground motions in regards to the decreasing ratios of the DTMD for the above parameters under the E1 excitation. However, under the E2 excitation, the damping effect of the DTMD under LP ground motions is evidently better than that under NFPT ground motions. Taking case-III as an example, the difference between the average decreasing ratios of the DTMD under the NFPT ground motions and the LP ground

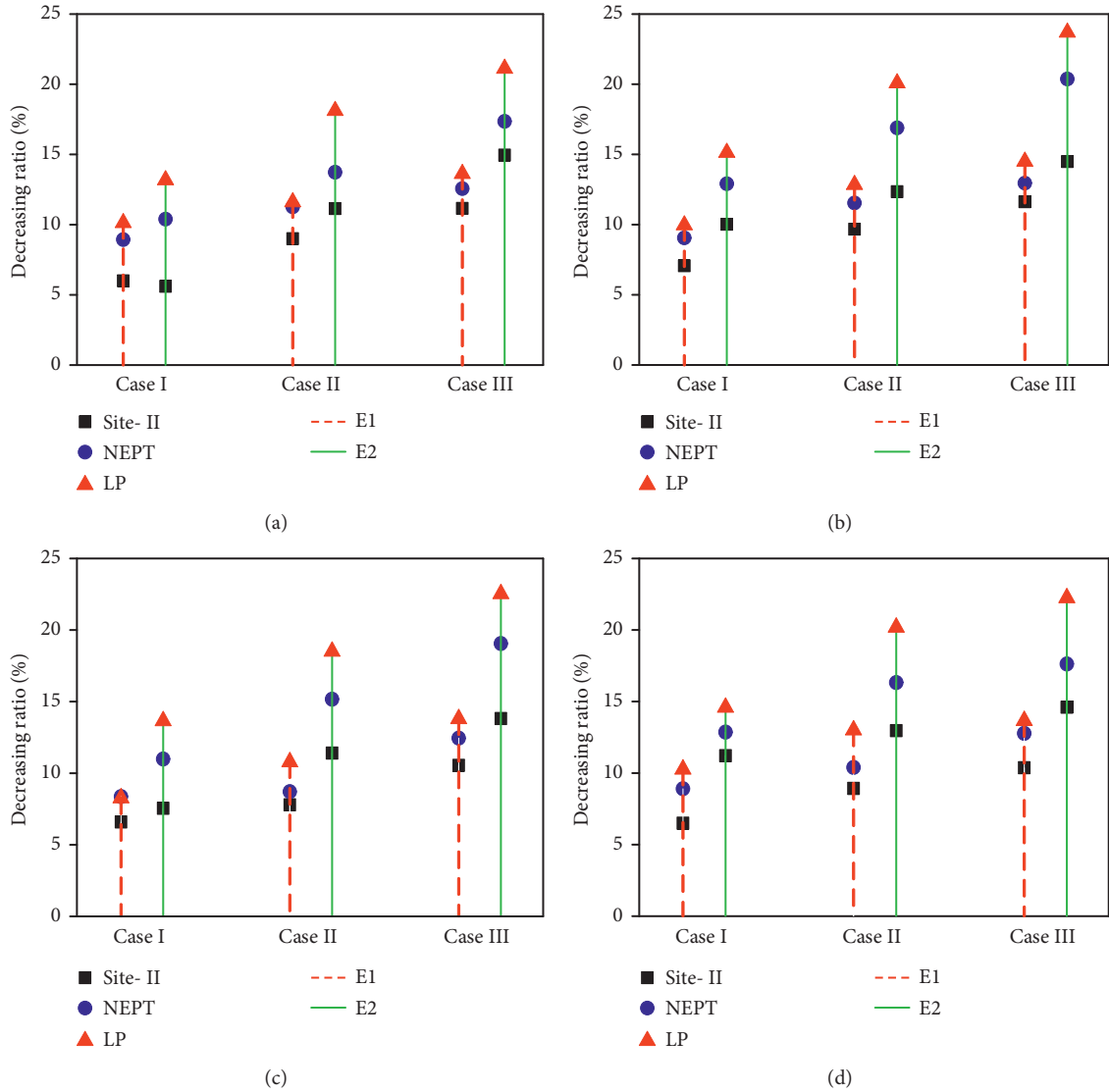


FIGURE 10: Comparison of the damping effect of the DTMD. (a) ADR. (b) RMS-ADR. (c) AR. (d) SR.

motions is in the range of 0.9% to 1.5% under the E1 excitation. However, the corresponding difference reaches 3.3% to 4.6% under the E2 excitation. In addition, the damping effect of the DTMD under NFPT ground motions is also evidently better than that under Site-II ground motions. Except for individual parameters in case-I, the difference in the average decreasing rates of the DTMD between them also increases with the increase in excitation intensity. Taking case-III as an example, the difference in the average decreasing ratios between the NFPT and Site-II ground motions under E1 excitation is approximately 1.8%. The corresponding difference reaches 4.1% under E2 excitation. To further study the damping mechanism of the DTMD, Figures 11(a) and 11(b) show the displacement response time history of the upper TMD under the Site-II ground motion RSN56 (130) and LP ground motion RSN74. Figure 11(c) and 11(d) show a comparison of the ADR decreasing ratios under two typical ground motions with different boundary cases.

As shown in Figures 11(a) and 11(b), the displacement response of the upper TMD under the LP ground motion RSN74 is evidently greater than that under the Site-II ground motion RSN56 (130) and this phenomenon becomes more evident with the increase in excitation intensity. For example, the difference in the displacement amplitude between them under the E1 condition is 2.94 mm, whereas that under the E2 condition is 7.03 mm. For the same excitation, the displacement response of the upper TMD under the E2 condition is evidently larger than that under the E1 condition. Taking RSN74 as an example, the displacement amplitudes of the upper TMD under the E1 and E2 conditions are 10.80 mm and 20.73 mm, respectively.

It can be seen from Figures 11(c) and 11(d) that the smaller damping ratio of the connection will lead a more significant damping capacity of the DTMD. Combined with Figures 11(a) and 11(b), it can also be concluded that the dynamic response of the DTMD has a significant impact on its own damping capacity. A greater response of the upper



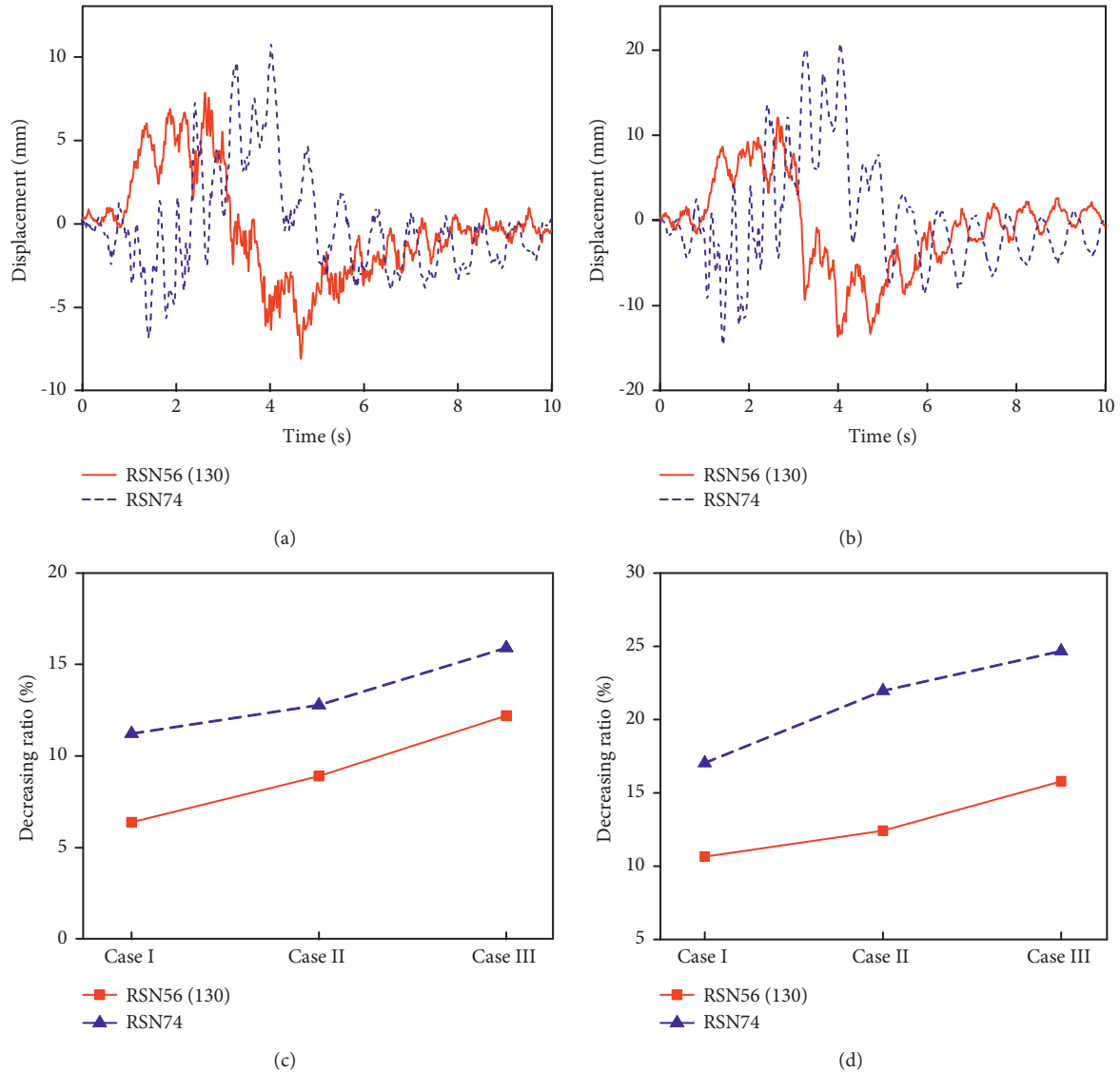


FIGURE 11: Comparison of damping effect of DTMD under two typical ground motions. (a) E1 (case-III). (b) E2 (case-III). (c) E1. (d) E2.

TMD will result in a significant damping capacity for the DTMD. Taking case-III under E2 excitation as an example, under the Site-II ground motion RSN56 (130) and LP ground motion RSN74, the decreasing rates of ADR are 15.8% and 24.7%, respectively. Combined with the analysis in Section 4.1, it can be seen that the dynamic response of the structure under ground motions with long-period characteristics (LP and NFPT ground motions) is larger, the corresponding response of DTMD is larger, and the damping effect of the DTMD is better. It can also be seen that the vibration of the DTMD requires a certain duration time through the dynamic response curve of the DTMD itself. For the test results of this study, the response of the DTMD is very small ( $<0.5$  mm) when the excitation duration is less than 0.5 s, showing that the DTMD requires a certain excitation duration to exert the damping effect. Further optimisation methods for decreasing the time delay of the DTMD damping effect will be the focus of future studies. It should be pointed out that the time delay of the DTMD is

also related to the bracketed and energy duration of the ground motion. However, the damping property of the DTMD is mainly affected by the relative dynamic response of the DTMD and the controlled structure. It is much complex to construct the relationship between the bracketed or energy duration of the ground motions and the time delay property of the damping effect of the DTMD.

Moreover, the idea of the mode shape decomposition response method was used to optimize the DTMD [49]. However, the actual seismic response of the HRS is much more complex due to the participation of multiple modes and unharmonic ground motions. Therefore, the actual damping effect of the DTMD may have significant difference with the optimised damping effect. As Tables 8–10 show, the dynamic response of structures may be amplified after the DTMD arrangement under some cases. And, the actual average decreasing rate was in the range of 5%~15%. By contrast, the theoretical decreasing ratio of the DDMF for the optimised DTMD can reach 80% under resonance

harmonic excitation and the damping effect of the optimised DTMD for the controlled structure can also exceed 50% after considering the mass participation ratio of the first three modes. Thus, the effectiveness of the parameter optimisation method for the DTMD based on the harmonic excitation is uncertain. In practical seismic design, the nonlinear time history analysis or model testing is required to verify the optimised parameters.

## 5. Discussion

**5.1. Comparison of the Damping Effect of UTMD and DTMD for HRSs.** To compare the damping effect of the UTMD (with the same mass as the DTMD) and the DTMD for HRSs, shaking table tests of the model with the UTMD were also carried out. The settlement position of the UTMD was selected as the same as the DTMD. The arrangement of the UTMD is shown in Figure 12. The ground motions were selected as the same from the previous description in Table 4. Figure 13 provides the dynamic response time history curves of the model without the damper, with the UTMD, and with the DTMD under typical ground motions. The connection cases of the UTMD and the DTMD were the same and were case-III.

As Figure 13 shows, the UTMD can also effectively reduce the displacement and acceleration response of the model under RSN69 (249). However, the UTMD increases the dynamic response of the model under RSN74. Taking the E2 excitation as an example, the decreasing ratios of the UTMD are 16.1% and -12.7% under RSN69 (249) and RSN74, respectively. However, the DTMD can both effectively decrease the dynamic response of the model. Thus, the damping robustness of the DTMD is better than that of the UTMD. In addition, the response attenuation of the model with the DTMD is faster than that of with the UTMD during the later excitation stage. Figure 14 gives the comparison of the decreasing ratios of the UTMD and the DTMD for the scaled model.

As Figure 14 shows, compared with the average damping effect of DTMD (14.9% for ADR, 15.5% for AR), the UTMD has a poorer average damping effect (2.1% for ADR, 2.4% for AR). The DTMD can provide more effective damping effect for HRSs than UTMD. To further analyse the damping effect of the UTMD and the DTMD, Figure 15 provides the comparison of the PSD (power spectral density) for accelerations of the model with the UTMD and the DTMD under typical ground motions.

As Figure 15 shows, the UTMD only has a better damping effect for the first-order vibration of the model. The UTMD cannot provide effective damping effect for higher-order vibration of the model. Thus, the damping robustness of the UTMD is poor. The DTMD can both effectively reduce the first-order vibration response and the higher-order vibration responses of the model. The damping frequency band of the DTMD is significantly larger than that of the UTMD. The reason is that the damping frequency band or robustness of the DTMD is mainly affected by the lower mass damper. The lower tuned mass damper is applied as a tuning system to control the dynamic response of the upper

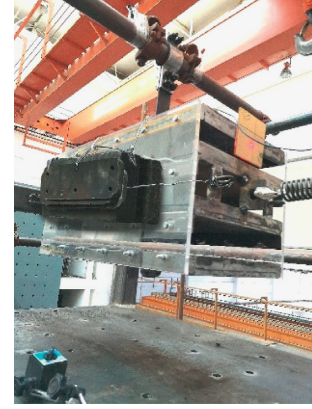


FIGURE 12: Arrangement of the UTMD.

tuned mass damper which can improve the damping frequency band of the upper tuned mass damper.

**5.2. Method for Obtaining the Equivalent Additional Damping Ratio.** The equivalent damping ratio of the controlled structure can be approximated by (14) under the free vibration test.

$$\xi = \frac{1}{2\pi m} \frac{A_n}{A_{n+m}}, \quad (14)$$

where  $A_n$  and  $A_{n+m}$  represent two selected amplitudes separated by  $m$  vibration cycles, respectively.  $\pi$  is the circular constant. It should be noted that the above calculation method for the equivalent damping ratio can be hardly used in practice. The free vibration test of the practical structure is extremely difficult. Taking the model tower in this study as an example, the height of the test model is 11 m and the total weight of the model is 32.2 kN. It is almost impossible to apply an initial displacement at the top of the test model. On the other hand, it cannot simply use a harmonic excitation or a ground motion to simulate the excitation of an initial displacement. Moreover, the additional damping ratio of the DTMD is related to the dynamic response and damage state of the controlled structure. The equivalent additional damping ratio of the DTMD is nonlinear. Therefore, the equivalent damping ratio of the system cannot be obtained in practice.

At present, the Code for Seismic Design of Buildings (GB 50011-2010) provides the calculation method of the effective damping ratio for displacement-related (metal, frictional dampers, etc.) and velocity-related (viscous, viscoelastic dampers, etc.) energy absorbers. The effective damping ratio of displacement-related and nonlinear velocity-related energy absorbers attached to structures can be estimated by the following equation:

$$\xi_a = \sum_j \frac{W_{c_j}}{(4\pi W_s)}, \quad (15)$$

where  $\xi_a$  denotes the effective damping ratio of the energy absorbers.  $W_{c_j}$  represents the energy consumed by the  $j$ -th energy absorber in a loading cycle under an expected

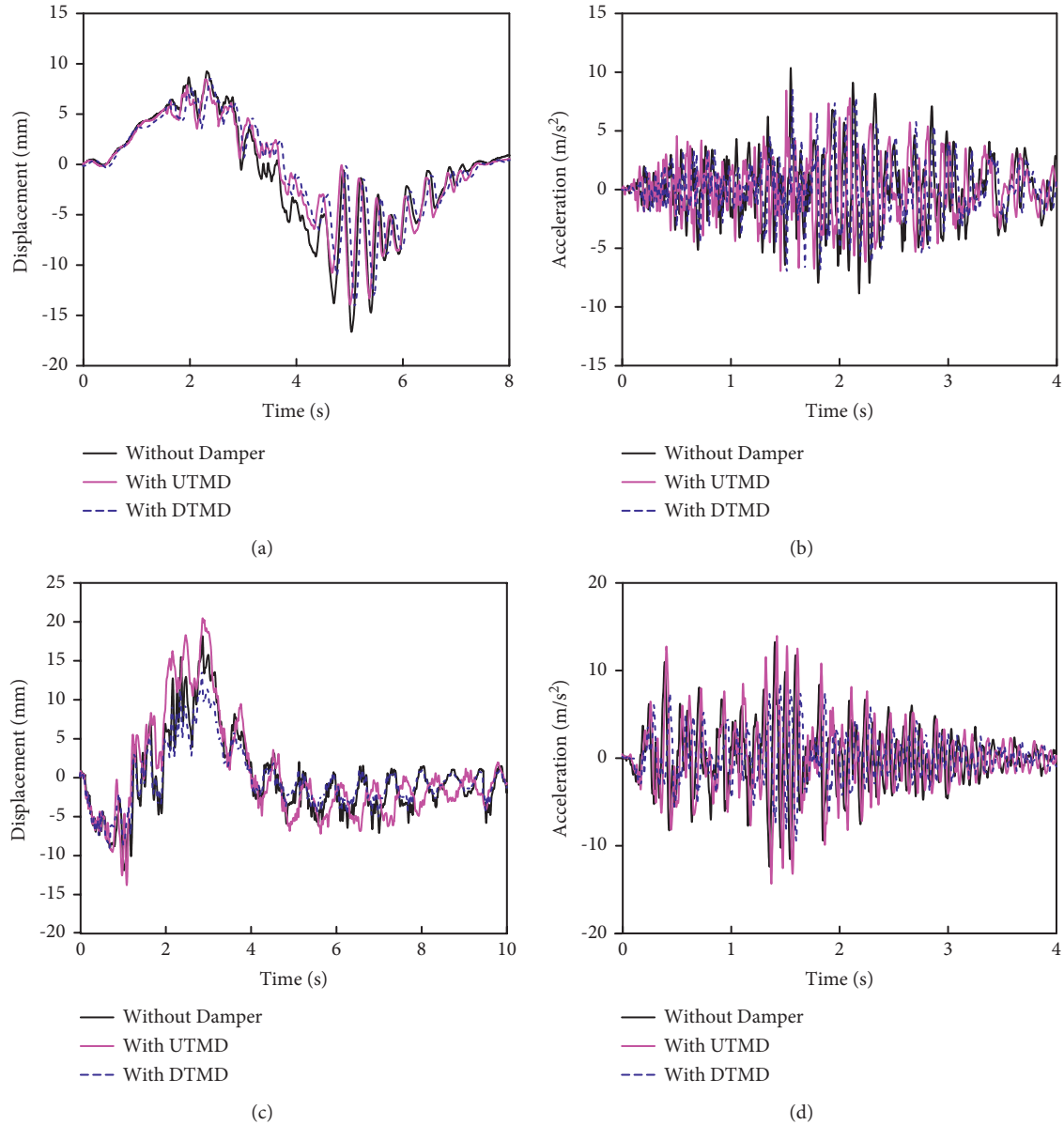


FIGURE 13: Comparison of the dynamic response time history curves of the model before and after the dampers installation (case-III). (a) ADR (RSN69 (249)). (b) AR (RSN69 (249)). (c) ADR (RSN74). (d) AR (RSN74).

interstory displacement  $\Delta u_j$ . And,  $W_s$  represents the total strain energy of the structure with energy absorbers under the same expected interstory displacement. In addition, the effective damping ratio of the energy absorbers attached to the structure can be determined by the forced decoupling method when the energy absorbers distribute uniformly on the structure, as well as the effective damping ratio is less than 20%.

As the above mentioned discussion, to calculate the effective damping ratio, the dissipating energy of the absorber in a loading cycle and the total strain energy of the controlled structure under an expected interstory displacement need to be determined. Therefore, the equivalent additional damping ratio of an absorber attached to a structure is normally obtained as follows:

- (1) Carry out the mechanical performance (hysteretic performance) test of the absorber. Obtain the energy dissipation capacity of the absorber under an expected displacement.
- (2) Parameterize the hysteretic energy dissipation capacity of the damping device. Construct the finite element model of the controlled structure with the absorber.
- (3) Perform the nonlinear time history analysis of the finite element model. Obtain the expected displacement of the structure with absorber, as well as the dissipating energy of the absorber under the expected displacement.
- (4) Conduct the pushover analysis or the simplified theory calculation of the structure model with the

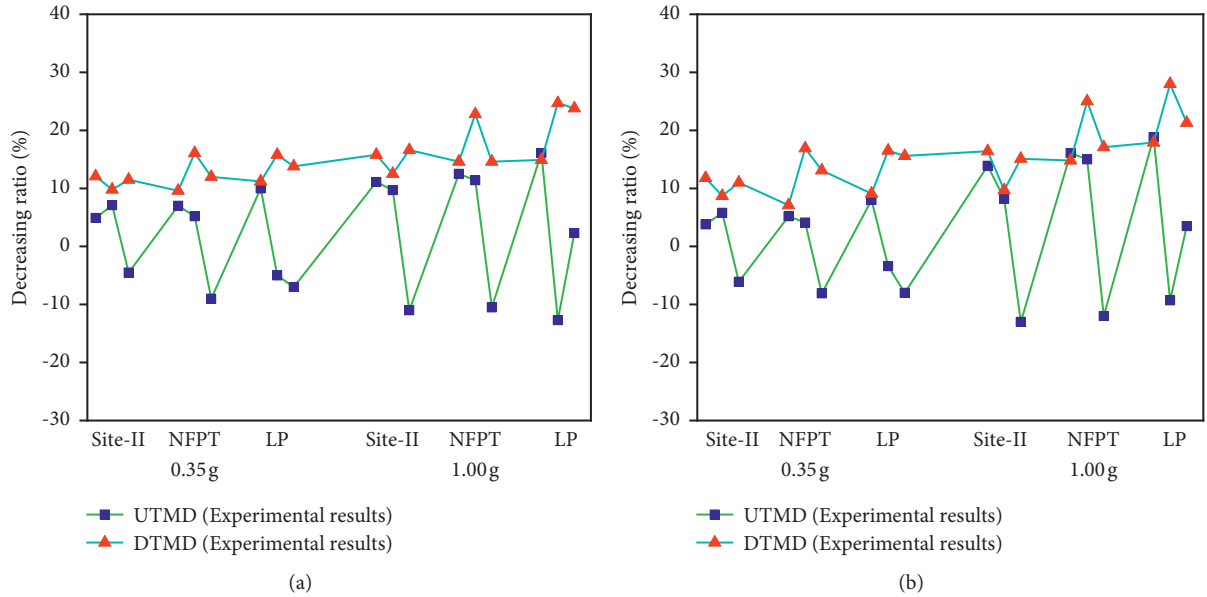


FIGURE 14: Comparison of the damping effect of the UTMD and the DTMD. (a) ADR. (b) AR.

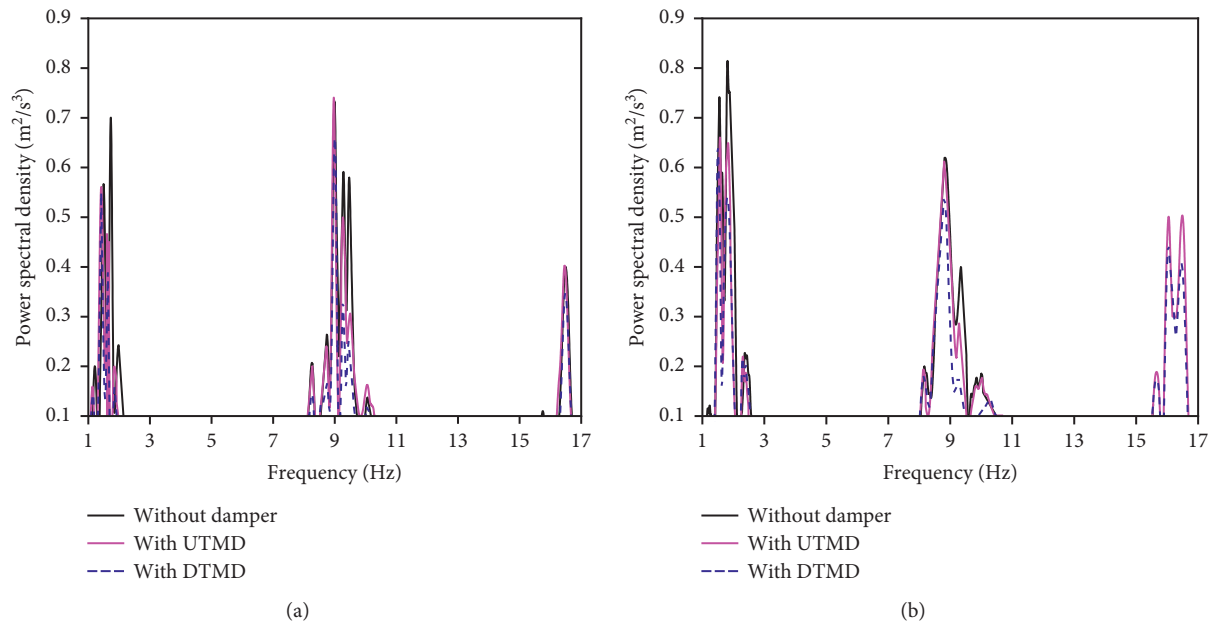


FIGURE 15: PSDs for accelerations of the model with the UTMD and the DTMD. (a) RSN69 (249). (b) RSN74.

absorber, and obtain the total strain energy of the controlled system under the expected displacement.

- (5) Finally, calculate the additional effective damping ratio of the energy absorber by equation (15).

As we all know, the damping effect of tuned mass dampers (such as DTMD, TMD, and MTDM) is not only related to the tuning effect of the tuned mass (absorbed kinetic energy of the controlled structure) but also related to the energy dissipation of the damping device installed on it (dissipated kinetic energy of the controlled structure). There is energy exchange between the tuned mass damper and controlled structure

during the whole vibration process. Therefore, under harmonic excitation, we can obtain the additional equivalent damping ratio of the tuned mass damper following the above procedure. However, under actual ground motions, the energy dissipation capacity of the tuned mass damper at an expected displacement is not uniform, which is related to the acceleration, velocity, and displacement time history of the system. And, the total strain energy of the system also cannot be obtained by a simple pushover or simplified calculation method (it is difficult to consider the contribution of the tuned mass damper to the system stiffness). Thus, the seismic design method of DTMD is still in the exploratory stage.

## 6. Conclusions

In this study, a scale model of a typical high-rise structure was fabricated. Numerous excitations were chosen to clarify the dynamic responses of high-rise structures, including Site-II ground motions, NFPT ground motions with different velocity pulse periods, and LP ground motions. Then, based on minimising the peak displacement of a first N-order vibration modal with a mass participation factor of 85%, a parameter optimisation method was proposed for the DTMD. Furthermore, a DTMD with optimised parameters was designed and manufactured. Finally, a lot of shaking table tests were carried out for the scale model with and without the DTMD. The main findings of this study are as follows:

- (1) The dynamic responses of high-rise structures under the LP and NFPT ground motions are significantly greater than those under Site-II ground motions. When the velocity pulse period of the NFPTs is close to the natural vibration period of the high-rise structure, the ADR, AR, and SR of high-rise structures are much more significant. Under an E2 earthquake excitation, the average amplitudes of the ADRs under LP and NFPT ground motions were 1.95 times and 1.51 times larger than those under Site-II ground motions, respectively. Moreover, the amplitudes of the SRs at the top floor of the structure reached  $1646.60 \mu\epsilon$  and  $1331.92 \mu\epsilon$  under LP and NFPT ground motions, respectively, i.e., much greater than those of the bottom floor ( $239.40 \mu\epsilon$  and  $193.72 \mu\epsilon$ ).
- (2) The optimised DTMD provides a wide damping frequency band and an excellent robustness. Larger excitation intensities will lead a better damping effect of the DTMD. However, the DTMD also has some damping capacity when the external excitation intensities are small. Under an E2 earthquake excitation, the average decreasing ratios of the ADR, RMS-ADR, AR, and SR are 15.0%, 14.5%, 13.7%, and 14.5% under Site-II ground motions, respectively. The average decreasing ratios of the above four parameters are 17.3%, 20.4%, 19.0%, and 17.5% under NFPT ground motions, respectively. The corresponding values are 21.1%, 23.7%, 22.4%, and 22.1% under LP ground motions, respectively. The damping capacity of the DTMD under LP and NFPT ground motions is more significant than that under Site-II ground motions. Furthermore, the DTMD will provide a better damping effect when the velocity pulse period of the NFPT ground motion is close to the natural vibration period of the structure.
- (3) The smaller damping ratio of the connection of the upper TMD will result in a better damping effect of the DTMD. An excessive damping ratio for this connection will induce the damper to become whole with the structure. Thus, the DTMD will not be able to respond adequately to the variations in the vibration state of the controlled structure. And, the

damping capacity of the DTMD will decrease. The DTMD requires a certain excitation duration time to exert its damping control effect. In this study, when the excitation duration time is less than 0.5 s, the dynamic response of the DTMD is relatively small. Therefore, the damping capacity of the DTMD cannot be fully realised. Further optimisation methods for decreasing the time delay of the DTMD damping effect will be the focus of future studies.

## Data Availability

Data are available on request to the corresponding author.

## Conflicts of Interest

The authors declare that they have no conflicts of interest.

## Authors' Contributions

Botan Shen and Weibing Xu contribute equally to the article.

## Acknowledgments

This study was partly supported by the National Natural Science Foundation of China (Grant nos. 51978021 and 51908015). The Beijing Municipal Education Commission (Grant nos. IDHT20190504 and KM201910005020) is greatly appreciated. This work was also supported by the National Key R&D Program of China (Grant nos. 2017YFC1500604 and 2017YFE0103000). Their support is gratefully acknowledged.

## References

- [1] R. Enokida, T. Nagae, K. Kajiwara, M. Nakashima, and X. Ji, "Development of shaking table test techniques to realize large responses and evaluation of safety of a high-rise building," *Journal of Structural & Construction Engineering*, vol. 74, no. 74, pp. 467–476, 2009.
- [2] Y.-L. Chung, T. Nagae, T. Hitaka, and M. Nakashima, "Seismic resistance capacity of high-rise buildings subjected to long-period ground motions: e-defense shaking table test," *Journal of Structural Engineering*, vol. 136, no. 6, pp. 637–644, 2010.
- [3] R. Sehhati, A. Rodriguez-Marek, M. Elgawady, and W. F. Cofer, "Effects of near-fault ground motions and equivalent pulses on multi-story structures," *Engineering Structures*, vol. 33, no. 3, pp. 767–779, 2011.
- [4] I. Takewaki, K. Fujita, and S. Yoshitomi, "Uncertainties in long-period ground motion and its impact on building structural design: case study of the 2011 Tohoku (Japan) earthquake," *Engineering Structures*, vol. 49, no. 2, pp. 119–134, 2013.
- [5] C. Tian, H. Zhang, C. Xiao, and J. Cao, "Experimental research on shaking table test of Shanghai Center tower," *Building Structure*, vol. 41, no. 11, pp. 47–52, 2011.
- [6] G. Yang, W. Cao, H. Dong, W. Yang, and S. Tian, "Experimental study on eccentric compressive behavior of special-shaped multi-cavity mega-bifurcated concrete filled steel tubular columns," *Journal of Building Structures*, vol. 39, no. 6, pp. 41–52, 2018.

- [7] H. Wu and W. Cao, "Seismic performance of pentagonal concrete-filled steel tube megacolumns with different bottom constructions," *The Structural Design of Tall and Special Buildings*, vol. 28, no. 10, 2019.
- [8] D. Zhou, J. Han, H. Yang et al., "Structural design of guangzhou tower," *Building Structure*, vol. 42, no. 6, pp. 1–12, 2012.
- [9] D. Wang, D. Lu, L. Huang, J. Wang, L. Xu, and J. Zhu, "Structure design of jinta in tianjiin," *Journal of Building Structures*, vol. 30, no. S1, pp. 1–7, 2009.
- [10] J.-g. Nie, Y.-h. Wang, and J.-s. Fan, "Experimental research on concrete filled steel tube columns under combined compression-bending-torsion cyclic load," *Thin-Walled Structures*, vol. 67, no. 2, pp. 1–14, 2013.
- [11] Y. Wang, J. Fan, Y. Guo, and Y. Yang, "Loading capacity of steel reinforced concrete fish bone-shaped column," *Journal of Tsinghua University*, vol. 50, no. 6, pp. 810–814, 2010.
- [12] B. Uy, Z. Tao, and L.-H. Han, "Behaviour of short and slender concrete-filled stainless steel tubular columns," *Journal of Constructional Steel Research*, vol. 67, no. 3, pp. 360–378, 2011.
- [13] R. Tang, "Design of sightseeing tower in nanjing olympic Sports technology center," *Progress in Steel Building Structures*, vol. 11, no. 6, pp. 56–60, 2009.
- [14] I. Venanzi, F. Ubertini, and A. L. Materazzi, "Optimal design of an array of active tuned mass dampers for wind-exposed high-rise buildings," *Structural Control and Health Monitoring*, vol. 20, no. 6, pp. 903–917, 2013.
- [15] Z. Fan, K. Yang, H. Chai et al., "Structural design and research on beijing olympic tower," *Journal of Building Structures*, vol. 40, no. 3, pp. 106–117, 2019.
- [16] M. Armali, H. Damerji, J. Hallal, and M. Fakhri, "Effectiveness of friction dampers on the seismic behavior of high rise building VS shear wall system," *Engineering Reports*, vol. 1, no. 6, 2019.
- [17] W. Liang, "Application of shear-type metal damper in a high-rise project," *Building Structure*, vol. 49, no. S1, pp. 403–407, 2019.
- [18] J. Qian and X. Ding, "Shaking table experiment study on the suppression dynamic response of a TV Tower with TLD," *Journal of Building Structures*, vol. 16, no. 5, pp. 32–39, 1995.
- [19] W. Qu, B. Song, C. Yangui, and Z. Xinmin, "Design of controlled wind vibration response of the main building of Jinshan Mansion in Zhuhai with TLD," *Journal of Building Structures*, vol. 16, no. 3, pp. 21–28, 1995.
- [20] Q. Jing, H. Li, L. Wang, and F. Li, "Wind-induced vibration control of International Trade Building of Dalian using tuned liquid dampers," *Earthquake Engineering and Engineering Vibration*, vol. 26, no. 2, pp. 111–118, 2006.
- [21] F. Naeim, M. Lew, L. D. Carpenter et al., "Performance of tall buildings in Santiago, Chile during the 27 February 2010 offshore Maule, Chile earthquake," *The Structural Design of Tall and Special Buildings*, vol. 20, no. 1, pp. 1–16, 2011.
- [22] Z. Lu, D. Wang, and Y. Zhou, "Experimental parametric study on wind-induced vibration control of particle tuned mass damper on a benchmark high-rise building," *The Structural Design of Tall and Special Buildings*, vol. 26, no. 8, Article ID 1359, 2017.
- [23] L. Wang, W. Shi, Z. Ying, and Q. Zhang, "Semi-active eddy current pendulum tuned mass damper with variable frequency and damping," *Smart Structures and Systems*, vol. 25, no. 1, pp. 65–80, 2020.
- [24] L. Wang, S. Nagarajaiah, W. Shi, and Y. Zhou, "Study on adaptive-passive eddy current pendulum tuned mass damper for wind-induced vibration control," *The Structural Design of Tall and Special Buildings*, vol. 29, no. 15, Article ID e1793, 2020.
- [25] L. Wang, W. Shi, X. Li, Q. Zhang, and Y. Zhou, "An adaptive-passive retuning device for a pendulum tuned mass damper considering mass uncertainty and optimum frequency," *Structural Control and Health Monitoring*, vol. 26, no. 7, Article ID e2377, 2019.
- [26] Q. Wang, H. Qiao, D. De Domenico, Z. Zhu, and Y. Tang, "Seismic response control of adjacent high-rise buildings linked by the Tuned Liquid Column Damper-Inerter (TLCDI)," *Engineering Structures*, vol. 223, Article ID 111169, 2020.
- [27] G. Cai, F. Sun, J. Huang, and C. Wang, "Characteristic analysis of MTMD for seismically excited structures," *Engineering Mechanics*, vol. 17, no. 3, pp. 55–59, 2000.
- [28] M. Gu, S. R. Chen, and C. C. Chang, "Parametric study on multiple tuned mass dampers for buffeting control of Yangpu Bridge," *Journal of Wind Engineering and Industrial Aerodynamics*, vol. 89, no. 11–12, pp. 987–1000, 2001.
- [29] W. Tu and Y. Zou, "Analysis of multistory structures with MTMD in frequency domain," *Engineering Mechanics*, vol. 20, no. 3, pp. 78–88, 2003.
- [30] M. Shahrouzi, G. Nouri, and N. Salehi, "Optimal seismic control of steel bridges by single and multiple tuned mass dampers using charged system search," *International Journal of Civil Engineering*, vol. 15, no. 2, pp. 309–318, 2017.
- [31] C. Li, "Multiple active-passive tuned mass dampers for structures under the ground acceleration," *Earthquake Engineering & Structural Dynamics*, vol. 32, no. 6, pp. 949–964, 2003.
- [32] T. P. Bandivadekar and R. S. Jangid, "Dual-layer multiple tuned mass dampers for vibration control of structures," *International Journal of Advanced Structural Engineering*, vol. 2, no. 2, pp. 91–113, 2010.
- [33] A. Tharwat and Sakr, "Vibration control of buildings by using partial floor loads as multiple tuned mass dampers," *HBRC Journal*, vol. 13, no. 2, pp. 133–144, 2017.
- [34] L. Wang, W. Shi, Q. Zhang, and Y. Zhou, "Study on adaptive-passive multiple tuned mass damper with variable mass for a large-span floor structure," *Engineering Structures*, vol. 209, Article ID 110010, 2020.
- [35] D. De Domenico, H. Qiao, Q. Wang, Z. Zhu, and G. Marano, "Optimal design and seismic performance of Multi-Tuned Mass Damper Inerter (MTMDI) applied to adjacent high-rise buildings," *The Structural Design of Tall and Special Buildings*, vol. 29, no. 14, Article ID e1781, 2020.
- [36] C. Li, B. Han, and D. Du, "Control strategy of double tuned mass dampers for structures," *China Civil Engineering Journal*, vol. 38, no. 5, pp. 1–9, 2005.
- [37] F. Teng, W. Yan, and W. Xu, "Analysis of parameters of Double Tuned Mass Damper and its design method for multi-degree-of-freedom structures," *Industrial Construction*, vol. 44, no. S1, pp. 309–312, 2014.
- [38] M. Ni, W. Yan, W. Xu, and J. Wang, "Fundamental characteristics of a double-tuned mass damper under simple-harmonical excitations," *Journal of Vibration and Shock*, vol. 34, no. 17, pp. 213–219, 2015.
- [39] T. Wang, *Civil Engineering Structural Test*, Wuhan University Press, Wuhan, China, (in Chinese), 2014.
- [40] W. Yan, J. Wang, H. Jia, W. Xu, and Y. Chen, "Parameter optimization method for tuned particle dampers and its effectiveness evaluation," *Journal of Vibration and Shock*, vol. 35, no. 7, pp. 145–151, 2016.

- [41] T. Chandrasekhara and R. Debbarma, "Seismic vibration control of skew bridges using multiple tuned mass dampers," *International Journal of Engineering Technology, Management and Applied Sciences*, vol. 4, pp. 16–28, 2016.
- [42] T. T. Soong and G. F. Dargush, *Passive Energy Dissipation Systems in Structural Engineering*, Wiley & Sons, Incorporated, John, Hoboken, NJ, US, 1997.
- [43] R. Rana and T. T. Soong, "Parametric study and simplified design of tuned mass dampers," *Engineering Structures*, vol. 20, no. 3, pp. 193–204, 1998.
- [44] C. Li, "Performance of multiple tuned mass dampers for attenuating undesirable oscillations of structures under the ground acceleration," *Earthquake Engineering & Structural Dynamics*, vol. 29, no. 9, pp. 1405–1421, 2000.
- [45] C. Li and Y. Liu, "Optimum multiple tuned mass dampers for structures under the ground acceleration based on the uniform distribution of system parameters," *Earthquake Engineering & Structural Dynamics*, vol. 32, no. 5, pp. 671–690, 2003.
- [46] I. Halperin, Y. Ribakov, and G. Agranovich, "Optimal viscous dampers gains for structures subjected to earthquakes," *Structural Control and Health Monitoring*, vol. 23, no. 3, pp. 458–469, 2016.
- [47] B. Shen, W. Xu, J. Wang et al., "Seismic control of super high-rise structures with double-layer tuned particle damper," *Earthquake Engineering & Structural Dynamics*, vol. 50, no. 3, pp. 791–810, 2021.
- [48] W. Xu, Z. Luo, W. Yan, Y. Chen, and J. Wang, "Impact of pulse parameters on the seismic response of long-period bridges," *Structure and Infrastructure Engineering*, vol. 16, no. 10, pp. 1461–1480, 2020.
- [49] National Standard of People's Republic of China, *Code for Seismic Design of Buildings (GB 50011-2010)*, China Architecture & Building Press, Beijing, China, 2010.

## Research Article

# Modeling Research and Test Verification of the Seismic Response of a Multistage Series Liquid Tank

Xiaoguang Yao , Lijun Meng , Peng Chu , and Liang Yao 

School of Mechanical Engineering, Xijing University, Xi'an 710123, China

Correspondence should be addressed to Xiaoguang Yao; xgyao\_1980@sina.com

Received 11 August 2021; Accepted 29 October 2021; Published 17 November 2021

Academic Editor: Honghao Li

Copyright © 2021 Xiaoguang Yao et al. This is an open access article distributed under the Creative Commons Attribution License, which permits unrestricted use, distribution, and reproduction in any medium, provided the original work is properly cited.

Liquid storage tanks are lifeline structures and strategically very important. Heavy damages or even collapse of these facilities subjected to strong earthquakes may cause disastrous consequences. In this paper, the seismic response of a multistage series liquid storage tank was simulated by a finite element method and verified by a scaled-down experiment. The structural flexibility of the tank and the liquid-structure coupling characteristics between the liquid and tank wall were considered in the research. A multimass-block and spring model was employed to be equivalent to the longitudinal vibration of the liquid in the storage tank. The relationships between the connection springs and the elements of the stiffness matrix were explicitly deduced. The seismic response analysis of a four-stage series liquid tank was carried out, and the acceleration response, the stress response of the tank, and the vertical vibration of the liquid were obtained. The experimental results are in good agreement with the simulation results, which verifies the effectiveness of the modeling method in this paper.

## 1. Introduction

Liquid storage tanks are lifeline structures and strategically very important since they have vital use in industries and nuclear power plants [1]. Heavy damages or even collapse of these facilities subjected to strong earthquakes may cause disastrous consequences such as explosions, fires, and environmental contaminations [2]. The seismic safety performance of a large liquid storage tank is crucial and has a direct effect on the economic performance, reliability, and service life of the tank [3]. Analytical solutions for the seismic fluid-structure interaction of tanks are used by analysts and engineers for a number of purposes, including preliminary sizing, risk assessment, and verification of numerical models [4].

The seismic behavior of the liquid storage tank is highly complex due to liquid-structure interaction, leading to a tedious design procedure from an earthquake-resistant design point of view. To improve the structural seismic response of the liquid storage tank, in the past few decades, scholars have proposed many effective research methods including the concentrated mass method, the distributed

mass method, and the test analysis method. Housner [5] and Rosenblueth and Newmark [6] developed a lumped mass model of rigid liquid storage tanks and investigated its seismic response. These models were modified by Haroun [7], which takes into account the flexibility of the tank wall in the seismic analysis. In the concentrated mass method, the contained liquid is considered as incompressible and inviscid and has irrotational flow. The typical models include the single-degree-of-freedom model [8], two-degree-of-freedom model [9–11], and three-degree-of-freedom model [12–18]. In [8], a simplified one-degree-of-freedom idealization was set up and particular attention was paid to the sloshing effects. In the two-degree-of-freedom model, as described in [9–11], the liquid mass was considered as a convective mass which caused the sloshing phenomenon and an impulsive mass which accelerated along with the tank. In the three-degree-of-freedom lumped mass model, the entire tank liquid mass vibrates in three distinct patterns: sloshing mass, impulsive mass, and rigid mass.

In the research using the distributed mass model [19–27], the finite element method is generally used to establish the model of the liquid storage tank for liquid-structure coupling



analysis. The tank wall is always regarded as the structure element, and the liquid is regarded as the fluid element. According to the relative motion relationship between the tank and the liquid, the motion coordination constraints of the structure element and fluid element are established. Then, the seismic excitation is applied to analyze the dynamics of the tank and fluid. Aiming at calculating sloshing frequencies, as well as sloshing transient response under horizontal seismic excitation, Karamanos [20, 21] presented a finite element formulation for earthquake-induced sloshing in horizontal-cylindrical industrial vessels. Jingyuan Li [23] adopted the finite element software ABAQUS to trace the dynamic response history of a large reinforced concrete storage tank during different seismic excitations. The dynamic characteristics and failure modes of the tank's structure were investigated by considering the rebar's effect. Aruna Rawat [24, 25] investigated the three-dimensional ground-supported cylindrical and rectangular rigid liquid storage tanks filled with water and subjected to seismic base excitation. The analyses of the tanks were carried out using coupled acoustic-structural and coupled Eulerian-Lagrangian approaches of the finite element method. In [26], the numerical seismic response of liquid storage tanks isolated by bilinear hysteretic bearing elements was investigated under long-period ground motions. Finite shell elements for the tank structure and boundary elements for the liquid region were employed. Fluid-structure equations of motion were coupled with the governing equation of the base-isolation system to represent the whole system behavior. In [27], numerical analyses were performed by means of a detailed finite element model, considering the exact geometry of the elevated steel tank structure and the fluid-structure interaction effects for an arbitrary level of fluid filling, as well as the nonlinearities introduced by the various bracing systems.

In the research using the test analysis method [28–30], a real or scaled model of the liquid tank is generally processed, and the test research is carried out by using the earthquake occurrence test bed. In [28], a series of forced vibration tests, whose measured response was considered as a benchmark, were carried out on a cylindrical tank experimental model. All of the test parameters were scaled according to similitude laws. Jang Ho Park [29] presented dynamic test results of a cylindrical liquid storage tank under horizontal earthquake excitation to investigate its dynamic behavior characteristics, including beam-type and oval-type vibrations. Bae and Ho Park [30] presented the results of shaking table tests performed to examine the dynamic behavior of a scaled cylindrical steel tank model considering the presence or absence of a fixed roof and added mass at the top of the tank for various fluid levels.

At present, there are many studies about the seismic response analysis of a single tank; however, research on the analysis of a multistage series tank is not deep enough. Different from the single-stage tank, the multistage series tank is tall, and the slenderness ratio is relatively large. Therefore, the structural flexibility of the tank needs to be considered. The “forced vibration” effect caused by the liquid-structure interaction should also be considered. In addition, the research literature mostly considers only the

lateral sloshing effect of the liquid, and the longitudinal vibration characteristic is ignored. Aiming at the seismic response analysis of the multistage series liquid storage tank, this paper constructed a finite element model including the liquid-structure coupling effect of the tank wall and liquid, as well as the longitudinal vibration characteristic of the liquid. The research on the modeling method and experimental verification were simultaneously carried out in this paper.

## 2. Mass Matrix and Longitudinal Stiffness Matrix

*2.1. Mass Matrix.* Due to the structural flexibility and the coupling effect, the multistage series tank will form a tower effect when it encounters an earthquake; that is, the ground excitations will be multiplied on the tank. The important feature of the liquid-structure coupling problem is the interaction of the two-phase medium. The solid structure will deform or move under the action of the fluid load, and this deformation or movement will in turn affect the amplitude and distribution of the fluid load. In this investigation, the liquid is considered incompressible and inviscid and has irrotational motion. For the quasistatic flow field and linear elastic structure with small deformation, the equation of the displacement-pressure format of the liquid-structure coupling system can be expressed as

$$\begin{bmatrix} \mathbf{M}_s & 0 \\ -\mathbf{Q}^T & \mathbf{M}_f \end{bmatrix} \begin{Bmatrix} \ddot{\mathbf{u}} \\ \ddot{\mathbf{p}} \end{Bmatrix} + \begin{bmatrix} \mathbf{K}_s & \frac{\mathbf{Q}}{\rho_f} \\ 0 & \mathbf{K}_f \end{bmatrix} \begin{Bmatrix} \mathbf{u} \\ \mathbf{p} \end{Bmatrix} = \begin{Bmatrix} \mathbf{F}_s \\ 0 \end{Bmatrix}, \quad (1)$$

where  $\mathbf{p}$  is the pressure vector of the fluid node;  $\mathbf{u}$  is the displacement vector of the solid node;  $\mathbf{Q}$  is the liquid-structure coupling matrix;  $\mathbf{M}_f$  and  $\mathbf{K}_f$  are the mass matrix and stiffness matrix of the fluid, respectively;  $\mathbf{M}_s$  and  $\mathbf{K}_s$  are the mass matrix and stiffness matrix of the structure, respectively;  $\mathbf{F}_s$  is the external load vector; and  $\rho_f$  is the density of the liquid.

If the influences of fluctuation and compressibility of the liquid are ignored, the dynamics problem of the liquid-filled tank can be simplified as the structural dynamics problem with additional mass. The dynamic equation (1) can be rewritten as

$$\begin{bmatrix} \mathbf{M}_s & 0 \\ -\mathbf{Q}^T & 0 \end{bmatrix} \begin{Bmatrix} \ddot{\mathbf{u}} \\ \ddot{\mathbf{p}} \end{Bmatrix} + \begin{bmatrix} \mathbf{K}_s & \frac{\mathbf{Q}}{\rho_f} \\ 0 & \mathbf{K}_f \end{bmatrix} \begin{Bmatrix} \mathbf{u} \\ \mathbf{p} \end{Bmatrix} = \begin{Bmatrix} \mathbf{F}_s \\ 0 \end{Bmatrix}. \quad (2)$$

Substituting equation (2) into (1) and eliminating vector  $\mathbf{p}$ , one can obtain

$$(\mathbf{M}_s + \mathbf{M}'_s)\ddot{\mathbf{u}} + \mathbf{K}_s\mathbf{u} = \mathbf{F}_s, \quad (3)$$

where  $\mathbf{M}'_s = \mathbf{Q}\mathbf{K}^{-1}\mathbf{f}\mathbf{Q}^T/\rho_f$  is the additional mass matrix representing the effect of the fluid on the solid structure. The key to the dynamic problem, therefore, lies in the processing of the additional mass matrix.

Since the quality characteristics of the tank structure and liquid are different, the quality of the two is treated separately in the modeling process. When calculating the mass attributes of the tank structure, it is assumed that the structural mass is uniformly distributed. According to the inviscid feature of the liquid, when the storage tank is bent and deformed laterally, most of the liquid will move in parallel with the structure of the tank, except for the liquid near the free surface. Besides, when the tank is deformed longitudinally, the liquid will only follow the movement of the tank bottom, provided that the influence of the longitudinal deformation of the tank on the diameter is ignored. Accordingly, the liquid in the tank is only counted as the translational mass, and the moment of inertia is ignored. The mass matrix of the liquid unit can be written as

$$\mathbf{M}_s^e = \mathbf{M}_f^e = \begin{bmatrix} m_f^e & 0 & 0 & 0 & 0 & 0 \\ & m_f^e & 0 & 0 & 0 & 0 \\ & & m_f^e & 0 & 0 & 0 \\ \text{symm} & & & 0 & 0 & 0 \\ & & & & 0 & 0 \\ & & & & & 0 \end{bmatrix}, \quad (4)$$

where  $m_f^e = \int_{V_f^e} \rho_f dV_f^e$ , in which  $m_f^e$  is the mass of the liquid unit and  $V_f^e$  is the volume of the liquid unit.

**2.2. Longitudinal Stiffness Matrix.** In order to simulate the longitudinal vibration characteristics of the multistage series

liquid storage tank, a multimass-block model is employed to equivalent the longitudinal vibration of the liquid. Taking the three-mass-block model of a single-stage liquid-filled storage tank as an example, its structure diagram, mechanical model, and calculation model are shown in Figure 1. The liquid in the tank is divided into three mass blocks marked as  $m_{11}$ ,  $m_{12}$ , and  $m_{13}$ , respectively. The tank is equivalent to a massless beam, and the mass properties of the tank are assigned to the nodes of the beam elements in the form of concentrated mass. Taking the mass assignment process of a certain section of the tank as an example, as illustrated in Figure 1(a), the mass of the tank wall between nodes  $a$  and  $g$  is divided into three parts according to its structural characteristic. Then, the mass marked as  $m_{i-1}$  between nodes  $a$  and  $c$  is assigned to node  $b$ , and the mass marked as  $m_i$  between nodes  $c$  and  $e$  is assigned to node  $d$ . Similarly, the mass marked as  $m_{i+1}$  between nodes  $e$  and  $g$  is assigned to node  $f$ . By repeating this, the equivalent process of tank mass to the nodes of the massless beam can be completed.

The position of the storage tank at the free surface of the liquid is marked as 5, as illustrated in Figure 1(c). The positions of centroids of the three liquid mass blocks are marked as 4, 3, and 2, respectively. The connecting part of the tank barrel section and tank bottom is marked as 1. The symbols  $l_1$ ,  $l_2$ , and  $l_3$  represent the liquid heights corresponding to the three mass blocks, respectively. The tank is cylindrical with the inner diameter  $2a$ , the thickness of the wall is  $h$ , the elastic modulus of the material is  $E$ , and Poisson's ratio is  $\mu$ . The flexibility coefficient matrix [31] of the three-mass-block model is defined as

$$\mathbf{F} = \begin{bmatrix} f_{22} & f_{23} & f_{24} & f_{25} \\ f_{32} & f_{33} & f_{34} & f_{35} \\ f_{42} & f_{43} & f_{44} & f_{45} \\ f_{52} & f_{53} & f_{54} & f_{55} \end{bmatrix}, \quad (5)$$

$$= \begin{bmatrix} \frac{4}{3K_1} + \frac{1}{K_B} & \frac{2}{K_1} + \frac{1}{K_B} & \frac{2}{K_1} + \frac{1}{K_B} & \frac{\mu}{K_1} \\ & \frac{4}{K_1} + \frac{4}{3K_2} + \frac{1}{K_B} & \frac{4}{K_1} + \frac{2}{K_2} + \frac{1}{K_B} & \frac{2\mu}{K_1} + \frac{\mu}{K_2} \\ & & \frac{4}{K_1} + \frac{4}{K_2} + \frac{4}{3K_3} + \frac{1}{K_B} & \frac{2\mu}{K_1} + \frac{2\mu}{K_2} + \frac{\mu}{K_3} \\ \text{symm} & & & \frac{1}{K_1} + \frac{1}{K_2} + \frac{1}{K_3} \end{bmatrix}$$

where  $K_1 = 2\pi a E h / l_1$ ,  $K_2 = 2\pi a E h / l_2$ , and  $K_3 = 2\pi a E h / l_3$  are the axial rigidities of the tank wall surrounding the mass

blocks  $m_1$ ,  $m_2$ , and  $m_3$ , respectively;  $K_B$  is the rigidity of the tank bottom.

The stiffness coefficient matrix  $\mathbf{K}$  of the three-mass-block model can then be obtained by solving the inverse of matrix  $\mathbf{D}$  as

$$\mathbf{K} = \mathbf{D}^{-1},$$

$$= \begin{bmatrix} k_{22} & k_{23} & k_{24} & k_{25} \\ k_{32} & k_{33} & k_{34} & k_{35} \\ k_{42} & k_{43} & k_{44} & k_{45} \\ k_{52} & k_{53} & k_{54} & k_{55} \end{bmatrix}. \quad (6)$$

The relationships between the springs in Figure 1(c) and the elements of the stiffness matrix  $\mathbf{K}$  are shown in the following equation:

$$\begin{aligned} K_{23} &= -k_{23}; \\ K_{24} &= -k_{24}; \\ K_{25} &= -k_{25}; \\ K_{34} &= -k_{34}; \\ K_{35} &= -k_{35}; \\ K_{45} &= -k_{45}; \\ K_{12} &= k_{22} + k_{23} + k_{24} + k_{25}; \\ K_{13} &= k_{32} + k_{33} + k_{34} + k_{35}; \\ K_{14} &= k_{42} + k_{43} + k_{44} + k_{45}; \\ K_{15} &= k_{52} + k_{53} + k_{54} + k_{55}. \end{aligned} \quad (7)$$

### 3. Simulation Results

**3.1. Model of the Liquid Storage Tank.** The structure of the four-stage series liquid storage tank is shown in Figure 2, which is composed of four cylindrical flat bottom tanks I–IV, a connection segment, and a conical head. The bottom of the tank is fixed on the foundation by bolts. The structural dimensions and material properties of the tank are shown in Table 1. The four storage tanks I–IV are filled with a liquid, and the liquid mass in each tank is 35 tons, 45 tons, 25 tons, and 10 tons, respectively.

The mechanical model of the storage tank established by the aforementioned method is shown in Figure 3. According to the geometric attributes of the tank wall and the connection segment, the whole structure is assumed to be a hollow circular beam element with variable thickness and cross section. In the finite element model, the structure of the tank is meshed by the three-dimensional and three-node Timoshenko beam elements. The elastoplastic characteristic of the material is considered. The connecting segments and the tanks are connected by flanges and bolts, and the strength and rigidity of the connecting parts have been predesigned with sufficient margin. The connection segments are also treated as the hollow cylindrical structure, and the thickness is obtained by the stiffness equivalent method. Therefore, the connection segments can also be meshed by the Timoshenko beam elements, and according to its structural characteristics, the mesh of the section is locally refined. The finite element model of the four-stage

series liquid storage tank established in ANSYS is shown in Figure 4.

The assignment process of liquid mass effects can be implemented as follows: taking the liquid mass  $m_{l1}$  as an example, as illustrated in Figure 1, the horizontal mass effects  $m_{l1x}$  and  $m_{l1z}$  are equally distributed to the nodes from  $m_3$  to  $m_i$  near the liquid; its vertical mass effect  $m_{l1y}$  is connected to the liquid mass  $m_{l2}$ ,  $m_{l3}$ , and the related beam nodes through the springs  $K_{14}$ ,  $K_{24}$ ,  $K_{34}$ , and  $K_{45}$ . The spring-mass system is composed of the concentrated mass  $m_{l1}$ ,  $m_{l2}$ , and  $m_{l3}$ , and the springs can then be used to simulate the vertical seismic response of the liquid mass in the storage tank.

**3.2. Adjustment of the Seismic Wave.** Seismic amplitude (or intensity) includes peak acceleration, peak velocity, and peak displacement of the seismic wave. In seismic analysis, the peak value of the acceleration of ground motion is generally used as the strength standard. The selected ground motion record should be adjusted according to an appropriate proportion so that the peak acceleration of the selected wave is equivalent to that of the corresponding seismic fortification intensity. The adjustment formula is

$$a'(t) = \frac{A'_{\max}}{A_{\max}} a(t), \quad (8)$$

where  $a'(t)$  and  $A'_{\max}$  represent the adjusted seismic acceleration curve and peak value, respectively;  $a(t)$  and  $A_{\max}$  represent the original recorded seismic acceleration curve and peak value, respectively.

The acceleration curve of the adjusted El Centro earthquake wave with 8° fortification intensity is shown in Figure 5, and its peak acceleration is set to be 0.2 g. The seismic waves along the  $x$ -,  $y$ -, and  $z$ -axis are all used as input excitations, and the peak acceleration ratio among them is set as  $x : y : z = 1 : 0.65 : 0.85$ .

**3.3. Seismic Response Curve of the Top Node.** Taking the top node  $o$ , as illustrated in Figure 3, of the liquid storage tank as the study object, the curves of displacement and acceleration of this node along the horizontal direction ( $x$ -axis and  $z$ -axis) and the vertical direction ( $y$ -axis) are shown in Figures 6–11, respectively.

It can be seen from Figures 6–8 that, under the action of earthquake excitation, the top node  $o$  has endured large vibration displacements. The maximum amplitude along the  $x$ -axis is 0.264 m, which occurred at the time  $t = 6.5$  s. The vibration displacement along the  $z$ -axis is similar to that of the  $x$ -axis, but the overall amplitude is slightly smaller, which is due to the fact that the amplitude of seismic acceleration input along the  $z$ -axis is smaller than that along the  $x$ -axis. The displacement responses in these two directions firstly increase with the increase of the seismic acceleration and then attenuate. In the entire time history, the waves generally present a “spindle” structure with a short front and a long rear, which is caused by the fact that the energy of the seismic wave is mainly concentrated in the early stage. In Figure 7,

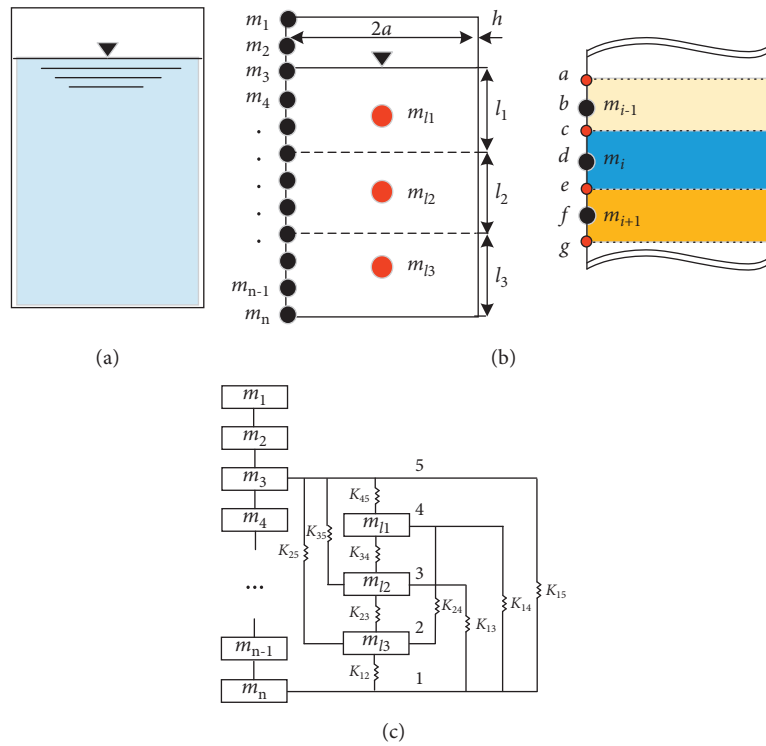


FIGURE 1: Three-mass-block model of the single-stage liquid storage tank. (a) Structure diagram. (b) Mechanical model. (c) Calculation model.

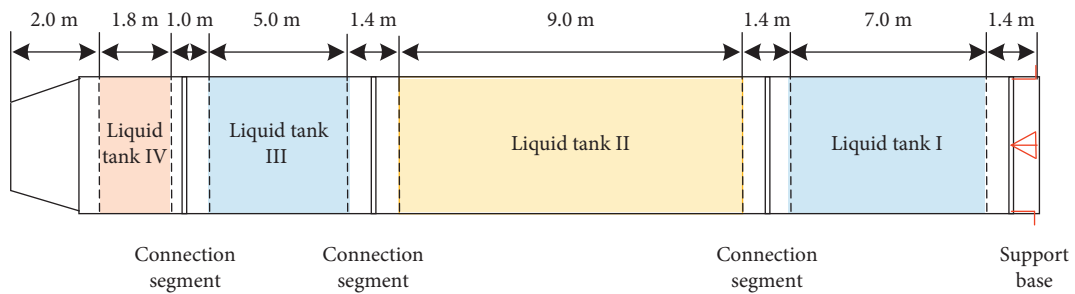


FIGURE 2: Structure of the four-stage series liquid storage tank.

TABLE 1: Structural dimensions and material properties of the liquid storage tank.

Parameter	Length (m)	Diameter (m)	Thickness (mm)	Elastic modulus (GPa)	Yield strength (MPa)	Tensile strength (MPa)	Poisson's ratio
Value	30	3.0	3.5	70	300	420	0.33

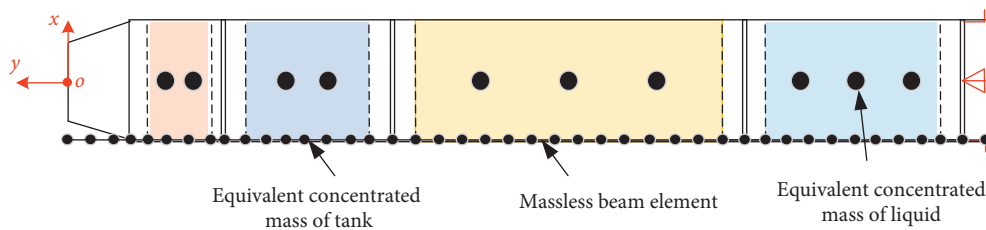


FIGURE 3: Mechanical model of the liquid storage tank (the springs are omitted).

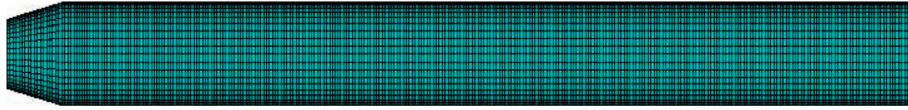


FIGURE 4: Finite element model of the liquid storage tank.

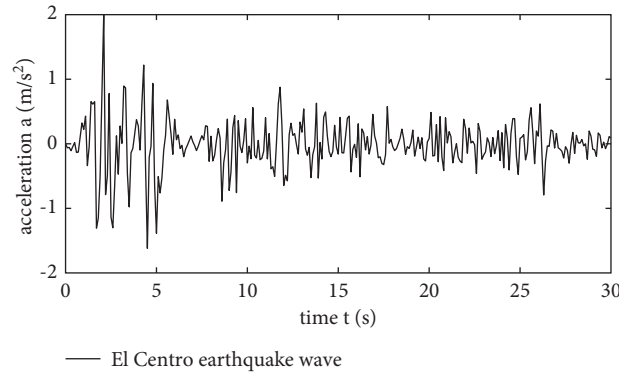


FIGURE 5: Adjusted El Centro seismic wave with 8° fortification intensity.

due to the large axial stiffness of the storage tank, the vibration displacement of the node along the  $y$ -axis is very tiny and within 0.5 mm most of the time. The reason for the notable displacement in the initial stage is that the gravity acceleration is applied to the liquid storage tank in the form of a step function at the initial time of calculation. The notable displacement fluctuation is the step response of the system to the gravity acceleration.

The peak value of the vibration acceleration of the node  $o$  along the  $x$ -axis is about  $3.382 \text{ m/s}^2$ , which occurred at time  $t = 2.1 \text{ s}$ . It is consistent with the peak time of the input seismic wave, and the amplification factor of peak acceleration of the node along this direction is  $\beta_x = 1.691$ . The peak value of the vibration acceleration of the node along the  $z$ -axis is about  $2.875 \text{ m/s}^2$ , which also occurred at  $t = 2.1 \text{ s}$ . The amplification factor of the peak acceleration of the node along this direction is  $\beta_y = 1.438$ . Ignoring the step effect of the tank on the gravity acceleration at the initial stage, the longitudinal vibration acceleration of the node caused by the ground motion is relatively small, which is basically within the range of  $\pm 0.2 \text{ m/s}^2$ . The calculation results show that the seismic wave has a greater impact on the lateral vibration of the tank and less impact on the longitudinal vibration. This is mainly due to that the longitudinal tensile and compression stiffness of the storage tank is much greater than its lateral bending stiffness.

**3.4. Vertical Vibration of the Liquid in the Tank.** The seismic responses of the acceleration of the liquid mass center in tanks I–IV are shown in Figures 12–15. It can be seen that the liquid has obvious vibration fluctuations along the vertical direction since the influence of the flexibility of the tank on the liquid is considered, as illustrated in Figure 1(c). The acceleration values of the mass center of liquid in tanks I and II are obvious and reach about  $0.9 \text{ m/s}^2$ . However, the values of the mass center of the liquid in tanks III and IV are

neglectable within the range of  $\pm 0.2 \text{ m/s}^2$ , which is equivalent to the value of the top node  $o$ . The differences of the vibration acceleration of the liquid mass center in different tanks can be explained as follows: in equations (5)–(7), the stiffness coefficient matrix  $K$  of the three-mass-block model includes the rigidity of the tank wall and the bottom. Compared with the storage tanks III and IV, the lengths of the storage tanks I and II are much longer, as illustrated in Figure 2, which result in the two tanks having lower rigidities. In addition, the liquid mass in the two tanks is much heavier. The lower tank rigidity and heavier liquid mass inevitably cause more significant seismic responses of the liquid in tanks I and II. On the contrary, the lengths of the tanks III and IV are much shorter, which result in the higher rigidities of the two tanks. Moreover, the liquid mass in the tanks is much lighter. Therefore, the higher tank rigidity and lighter liquid mass cause minor seismic responses of the liquid in tanks III and IV.

**3.5. Diagram of Combined Deformation-Axial Coordinate (the Moment of Maximum Deformation).** It can be seen from Figures 6 and 8 that the maximum deformation of the whole structure of the tank occurred at the time  $t = 6.5 \text{ s}$ . At this moment, the combined deformation curve of the nodes along the axial direction of the tank is shown in Figure 16. The combined deformation of the tank increases with the height of its body. The overall deformation of the tank presents the deformation characteristic of a vertical cantilever beam subjected to a horizontal load. The maximum combined deformation of the tank is 0.331 m at the coordinate  $y = 0$ .

**3.6. Time History Curve of Stress at the Supporting Point of the Tank.** The time history curve of the stress of the grid point, where the supporting point of the tank is located, on the beam element is shown in Figure 17. The maximum stress is

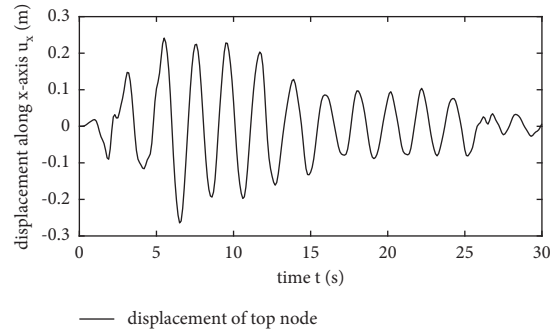


FIGURE 6: Displacement of top node (o) along the (x)-axis.

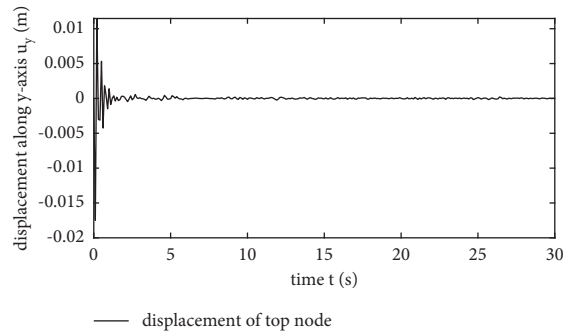


FIGURE 7: Displacement of top node (o) along the (y)-axis.

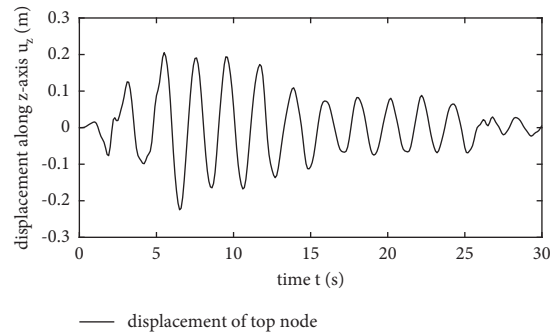


FIGURE 8: Displacement of top node (o) along the (z)-axis.

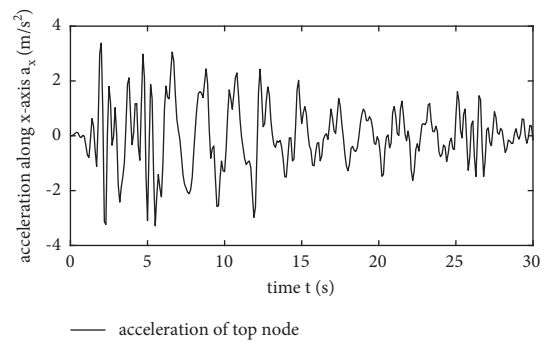


FIGURE 9: Acceleration of top node (o) along the (x)-axis.

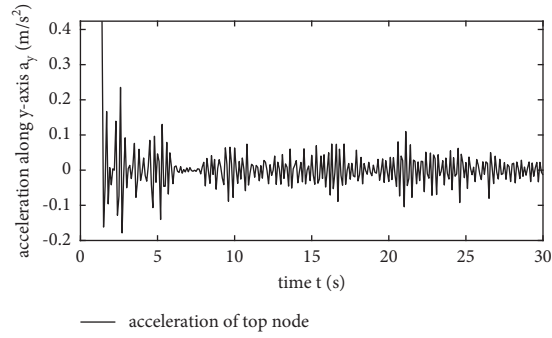


FIGURE 10: Acceleration of top node (o) along the (y)-axis with ignoring the step effect of gravitational acceleration at the initial moment.

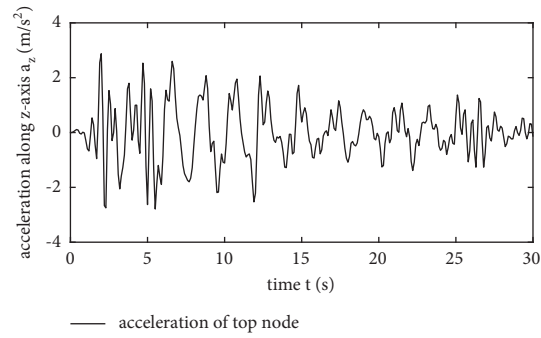


FIGURE 11: Acceleration of top node (o) along the (z)-axis.

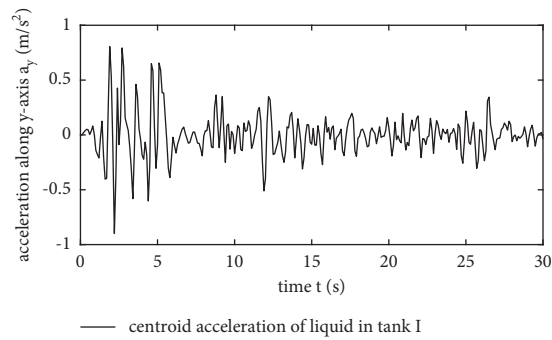


FIGURE 12: Acceleration curve of mass center of the liquid in tank I.

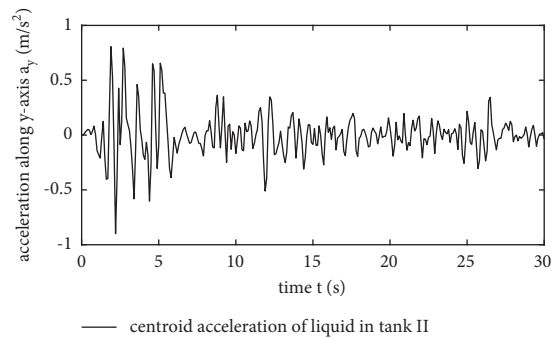


FIGURE 13: Acceleration curve of mass center of the liquid in tank II.

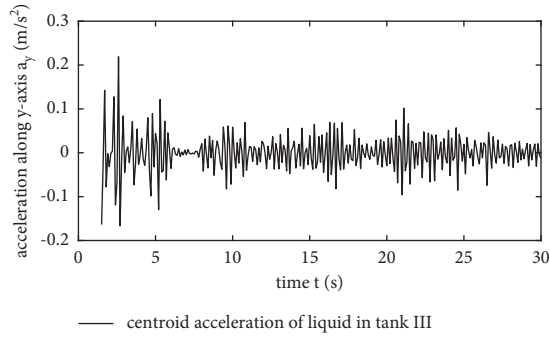


FIGURE 14: Acceleration curve of mass center of the liquid in tank III.

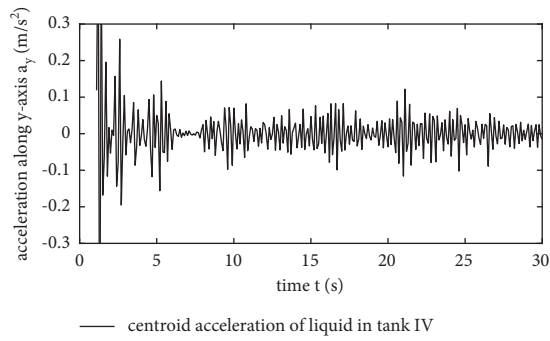


FIGURE 15: Acceleration curve of mass center of the liquid in tank IV.

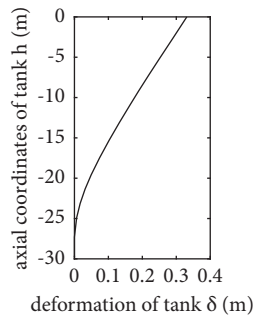


FIGURE 16: Diagram of the combined deformation-axial coordinate (the moment of maximum deformation).

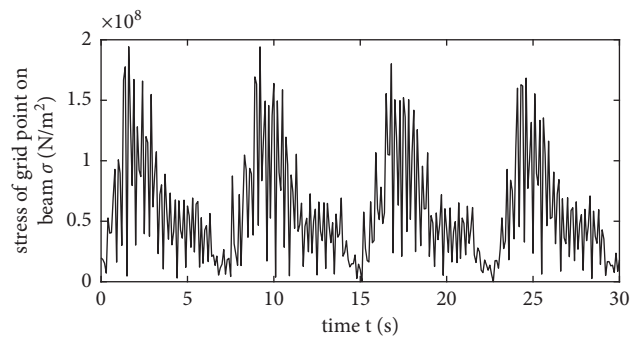


FIGURE 17: Time history curve of stress of the supporting point.





FIGURE 18: The scaled-down model of the four-stage storage tank.

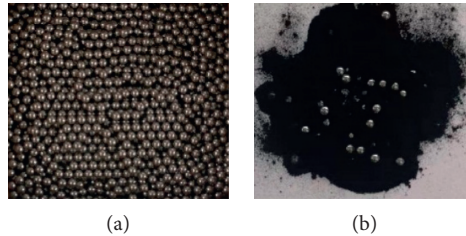


FIGURE 19: Equivalent filling material for liquid. (a) Lead balls. (b) Mixture of lead balls and iron powder.

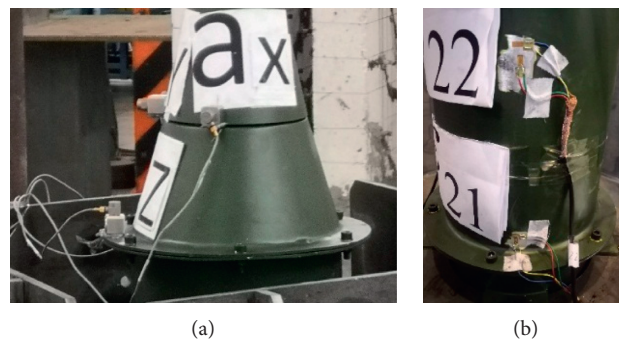


FIGURE 20: Layout of measuring sensors. (a) Measuring position of the acceleration sensor. (b) Measuring position of the strain gauge (a pair of strain gauges in a T-shaped arrangement).

194.24 MPa, which is less than the yield stress of the material. The stress curve presents the characteristic of periodic fluctuations, and the overall trend of the attenuation is consistent with the decrease of the input intensity of the seismic wave.

#### 4. Test Verification

A scaled-down test model of the four-stage series storage tank, as shown in Figure 18, is manufactured to verify the

accuracy of the research model presented in this paper. The scaled model is mainly composed of the conical top, four-stage storage tanks I–IV, and end support. Different sections of the test model are connected by flanges and bolts. In order to simulate the coupling effect of the liquid in the tank, lead balls and a mixture of lead balls and iron powder, as shown in Figure 19, are filled in different tanks. Tanks II and IV are filled with lead balls, and tanks I and III are filled with a mixture of lead balls and iron powder. The experiment was carried out on the earthquake occurrence test bed of

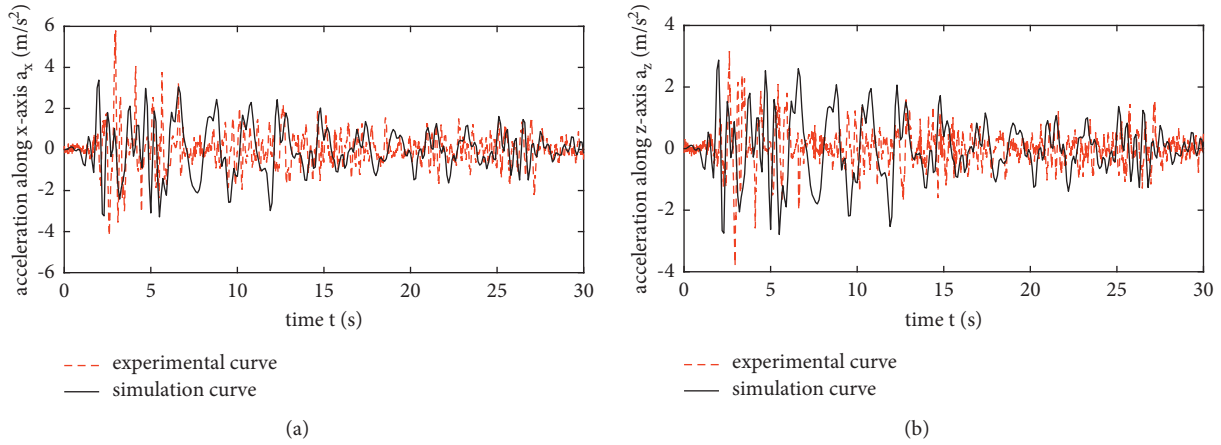


FIGURE 21: Comparison of lateral acceleration results of the top node. (a) Acceleration curve along the (x)-axis. (b) Acceleration curve along the (z)-axis.

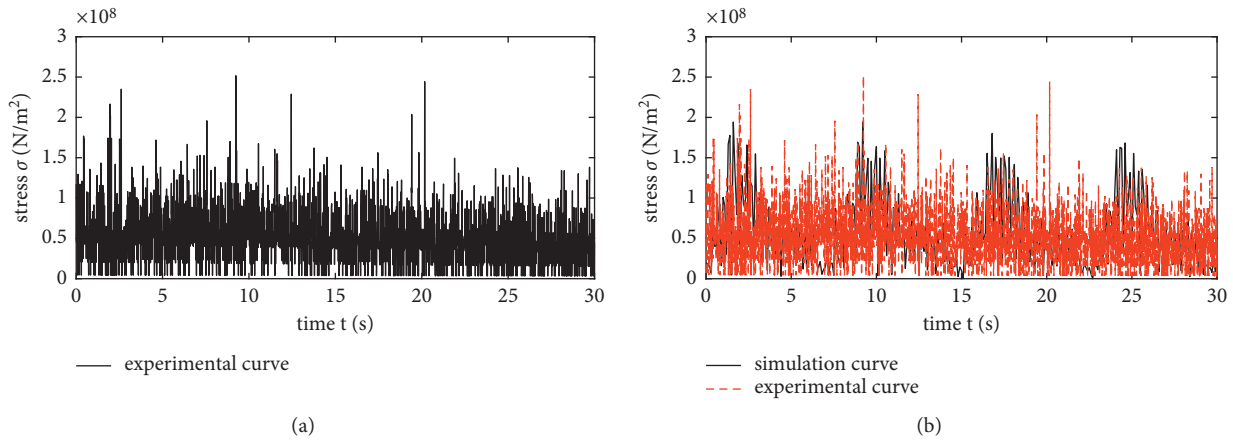


FIGURE 22: Comparison of stress results of supporting point. (a) Test result curve. (b) Comparison curves between the test model and calculation model.

Lanzhou University of Technology. The measuring positions of the acceleration sensor and the strain gauge are shown in Figure 20.

**4.1. Comparison of Acceleration Results.** The comparisons between the test curve and the calculated curve of acceleration of the top node  $o$  along the  $x$ -axis and the  $z$ -axis are shown in Figure 21. It can be seen that the two curves are in good agreement with the trend of the waveform amplitude. However, the oscillating periods of them are significantly different. The main reason for this can be analyzed as follows: (1) In the numerical model, the frequency of the input seismic wave is set lower ( $f=10$  Hz) to reduce the calculation cost, while in the test model, the frequency is set much higher ( $f=50$  Hz). The differences in the input frequency of seismic excitation lead to the forced vibration frequency of the test model being much greater than that of the calculation model. (2) Due to the limitation of machining technology, the rigidity of the scaled model is greater than that of the calculation model, which leads to the higher

natural frequencies and response frequencies in the test model.

**4.2. Comparison of Stress Results.** The time history curve of the stress of the supporting part on the test model is shown in Figure 22(a), and the comparison between the test curve and the calculated curve is shown in Figure 22(b). It can be seen that the two curves have similar attenuation and periodic characteristics, and the amplitudes of them are also in good agreement. Compared with the stress curve of the calculation model, the curve of the test model has more peak burrs, which is mainly caused by the interference of external signals on the sensors.

## 5. Conclusions

The seismic response of the multistage series liquid storage tank was simulated and verified in this paper. The structural flexibility of the tank and the liquid-structure coupling characteristics between the tank wall and the liquid were considered

in the study. The additional mass matrix representing the effect of the liquid on the structure was obtained by assuming that the liquid is incompressible and inviscid and has irrotational motion. In order to simulate the longitudinal vibration characteristics of the liquid storage tank, a multimass-block and spring model was employed to equivalent the longitudinal vibration of the liquid. The relationships between the connection springs and the elements of the stiffness matrix of the spring-mass model were explicitly deduced.

The seismic response analysis of the four-stage series liquid tank was carried out in ANSYS. The acceleration, deformation, and stress responses of the tank were obtained. In addition, because the influence of the flexibility of the tank wall on the longitudinal vibration of the liquid was considered in the model, the vertical vibrations of the liquid were also obtained. A scaled-down model of the four-stage series storage tank was processed and manufactured, and the seismic test was subsequently carried out. The experimental results are in good agreement with the simulation results, which verified the effectiveness of the modeling method in this paper.

### Data Availability

The data used to support the findings of this study are available from the corresponding author upon request.

### Conflicts of Interest

The authors declare no potential conflicts of interest with respect to the research, authorship, and/or publication of this article.

### Acknowledgments

The authors wish to express their sincere thanks to the sponsors and to the reviewers for useful and important comments. This research was financially supported by the National Natural Science Foundation of China (Grant no. 51505485), the Basic Research Program of Natural Science in Shaanxi Province (Grant no. 2020JM-640), the Special Item Funds for High-level Personnel of Xijing University (Grant no. XJ18B08), and the Youth Innovation Team of Shaanxi Universities.

### References

- [1] M. K. Shrimali and R. S. Jangid, "Seismic analysis of base-isolated liquid storage tanks," *Journal of Sound and Vibration*, vol. 275, no. 1-2, pp. 59–75, 2004.
- [2] X. Meng, X. Li, X. Xu, J. Zhang, W. Zhou, and D. Zhou, "Earthquake response of cylindrical storage tanks on an elastic soil," *Journal of Vibration Engineering & Technologies*, vol. 7, no. 5, pp. 433–444, 2019.
- [3] M. Bovo, A. Barbaresi, and D. Torreggiani, "Definition of seismic performances and fragility curves of unanchored cylindrical steel legged tanks used in wine making and storage," *Bulletin of Earthquake Engineering*, vol. 18, no. 8, pp. 3711–3745, 2020.
- [4] C.-C. Yu and A. S. Whittaker, "Review of analytical studies on seismic fluid-structure interaction of base-supported cylindrical tanks," *Engineering Structures*, vol. 233, Article ID 111589, 2021.
- [5] G. W. Housner, "The dynamic behavior of water tanks," *Bulletin of the Seismological Society of America*, vol. 53, no. 2, pp. 381–387, 1963.
- [6] E. Rosenblueth and N. M. Newmark, *Fundamentals of Earthquake Engineering*, Prentice-Hall, Englewood Cliffs, NJ, USA, 1971.
- [7] M. A. Haroun, "Vibration studies and tests of liquid storage tanks," *Earthquake Engineering & Structural Dynamics*, vol. 11, no. 2, pp. 179–206, 1983.
- [8] A. Fiore, C. Rago, I. Vanzi, R. Greco, and B. Briseghella, "Seismic behavior of a low-rise horizontal cylindrical tank," *International Journal of Advanced Structural Engineering*, vol. 10, no. 2, pp. 143–152, 2018.
- [9] D. K. Fotini and G. D. Hatzigeorgiou, "Water and wastewater steel tanks under multiple earthquakes," *Soil Dynamics and Earthquake Engineering*, vol. 100, pp. 445–453, 2017.
- [10] G. W. Housner, "Earthquake pressures on fluid containers, eighth technical report under office of naval research," California Institute of Technology, Pasadena, CA, USA, Project Designation No. 081-095, 1954.
- [11] G. W. Housner, "Dynamic pressures on accelerated fluid containers," *Bulletin of the Seismological Society of America*, vol. 47, pp. 313–346, 1957.
- [12] A. Rawat, V. Matsagar, and A. K. Nagpal, "Coupled acoustic-structure interaction in cylindrical liquid storage tank subjected to bi-directional excitation," in *Advances in Structural Engineering*, Springer, New Delhi, India, 2015.
- [13] M. K. Shrimali and R. S. Jangid, "Earthquake response of isolated elevated liquid storage steel tanks," *Journal of Constructional Steel Research*, vol. 59, no. 10, pp. 1267–1288, 2003.
- [14] O. Curadelli, "Equivalent linear stochastic seismic analysis of cylindrical base-isolated liquid storage tanks," *Journal of Constructional Steel Research*, vol. 83, pp. 166–176, 2013.
- [15] S. K. Saha, V. A. Matsagar, and A. K. Jain, "Seismic fragility of base-isolated water storage tanks under non-stationary earthquakes," *Bulletin of Earthquake Engineering*, vol. 14, no. 4, pp. 1153–1175, 2016.
- [16] A. S. Ayman and M. El-Sharkawy, "Seismic response of base isolated liquid storage ground tanks," *Ain Shams Engineering Journal*, vol. 2, pp. 33–42, 2011.
- [17] L. Yuan, J. Sun, and Z. Sun, "Simplified mechanical model for seismic design of horizontal storage tank considering soil-tank-liquid interaction," *Ocean Engineering*, vol. 198, Article ID 106953, 2020.
- [18] V. R. Panchal and R. S. Jangid, "Variable friction pendulum system for seismic isolation of liquid storage tanks," *Nuclear Engineering and Design*, vol. 238, no. 6, pp. 1304–1315, 2008.
- [19] V. Ozsarac, E. Brunesi, and R. Nascimbene, "Earthquake-induced nonlinear sloshing response of above-ground steel tanks with damped or undamped floating roof," *Soil Dynamics and Earthquake Engineering*, vol. 144, Article ID 106673, 2021.
- [20] S. A. Karamanos, "Sloshing effects on the seismic design of horizontal-cylindrical and spherical vessels," in *Proceedings of the 2004 ASME Pressure Vessels and Piping Division Conference*, San Diego, CA, USA, July 2004.
- [21] M. A. Platyrrachos and S. A. Karamanos, "Finite element analysis of sloshing in horizontal-cylindrical industrial vessels under earthquake loading," in *Proceedings of the 2005 ASME Pressure Vessels and Piping Division Conference*, Denver, CO, USA, July 2005.

- [22] L. A. Patkas and S. A. Karamanos, "Variational analysis of sloshing in spherical industrial vessels under earthquake loading," in *Proceedings of the 2006 ASME Pressure Vessels and Piping Division Conference*, Vancouver, Canada, July 2006.
- [23] J. Li, X. You, H. Cui, Q. He, and J. Ju, "Analysis of large concrete storage tank under seismic response," *Journal of Mechanical Science and Technology*, vol. 29, no. 1, pp. 85–91, 2015.
- [24] A. Rawat, V. Mittal, T. Chakraborty, and V. Matsagar, "Earthquake induced sloshing and hydrodynamic pressures in rigid liquid storage tanks analyzed by coupled acoustic-structural and Euler-Lagrange methods," *Thin-Walled Structures*, vol. 134, pp. 333–346, 2019.
- [25] A. Rawat, V. A. Matsagar, and A. K. Nagpal, "Numerical study of base-isolated cylindrical liquid storage tanks using coupled acoustic-structural approach," *Soil Dynamics and Earthquake Engineering*, vol. 119, pp. 196–219, 2019.
- [26] M. R. Shekari, N. Khaji, and M. T. Ahmadi, "On the seismic behavior of cylindrical base-isolated liquid storage tanks excited by long-period ground motions," *Soil Dynamics and Earthquake Engineering*, vol. 30, no. 10, pp. 968–980, 2010.
- [27] J. C. Drosos, S. V. Tsiniopoulos, and D. L. Karabalis, "Seismic retrofit of spherical liquid storage tanks with energy dissipative devices," *Soil Dynamics and Earthquake Engineering*, vol. 119, pp. 158–169, 2019.
- [28] E. María and O. Curadelli, "Experimental and numerical study of the response of cylindrical steel tanks under seismic excitation," *International Journal of Civil Engineering*, vol. 16, pp. 793–805, 2018.
- [29] J. H. Park, D. Bae, and C. K. Oh, "Experimental study on the dynamic behavior of a cylindrical liquid storage tank subjected to seismic excitation," *International Journal of Steel Structures*, vol. 16, no. 3, pp. 935–945, 2016.
- [30] D. Bae and J. Ho Park, "Shaking table test of steel cylindrical liquid storage tank considering the roof characteristics," *International Journal of Steel Structures*, vol. 18, no. 4, pp. 1167–1176, 2018.
- [31] D. Wenbin and Y. Tang, "Study on application of dynamical models for the longitudinal vibration of liquid-propellant launch vehicles," *Structure & Environment Engineering*, vol. 42, no. 6, pp. 1–10, 2015.

## Research Article

# Overlapping Decentralized Control Strategies of Building Structures' Vibration with Time Delay Based on $H_\infty$ Control Algorithms under Seismic Excitation

Xiaofang Kang <sup>1,2,3</sup>, Jian Wu,<sup>1</sup> Yewei Zhang,<sup>1</sup> Guoliang Liu,<sup>1</sup> Suhui Zhang,<sup>1</sup> Xueting Tao <sup>4</sup>, Guanghui Xia <sup>1,2,3</sup>, Dawei Man <sup>1,2,3</sup> and Qinghu Xu<sup>1,2,3</sup>

<sup>1</sup>School of Civil Engineering, Anhui Jianzhu University, Hefei 230601, China

<sup>2</sup>BIM Engineering Center of Anhui Province, Hefei 230601, China

<sup>3</sup>Prefabricated Building Research Institute of Anhui Province, Hefei 230601, China

<sup>4</sup>Nanjing Urban Construction Secondary Specialized School, Nanjing 210018, China

Correspondence should be addressed to Xueting Tao; 837359772@qq.com and Dawei Man; mandawei1989@126.com

Received 24 August 2021; Revised 30 September 2021; Accepted 26 October 2021; Published 11 November 2021

Academic Editor: Bing Zhang

Copyright © 2021 Xiaofang Kang et al. This is an open access article distributed under the Creative Commons Attribution License, which permits unrestricted use, distribution, and reproduction in any medium, provided the original work is properly cited.

A decentralized control strategy can effectively solve the control problem of the large-scale time delayed structures. In this paper, combining the overlapping decentralized control method, linear matrix inequality (LMI) method, and  $H_\infty$  control algorithm, overlapping decentralized  $H_\infty$  control approach of the time delayed structures has been established. The feedback gain matrixes of all subsystems are obtained by this method based on genetic algorithm optimization tools and the specific goal of optimization control. The whole vibration control system of the time delayed structures is divided into a series of overlapping subsystems by overlapping decentralized control strategy. The feedback gain matrixes of each subsystem can be obtained by using  $H_\infty$  control algorithm to calculate each subsystem. The vibration control of a twenty layers' antiseismic steel structure Benchmark model was analyzed with the numerical method. The results show that the proposed method can be applied to control system with time delay. The overlapping decentralized control strategies acquire the similar control effects with that of the centralized control strategy. Moreover, the flexibility of the controller design has been enhanced by using overlapping decentralized control strategies.

## 1. Introduction

With the construction of super-high, long-span, and other complex large-scale civil structures, the traditional passive control strategy has some limitations in its application, which is difficult to meet the requirements. In 1972, Yao had put forward the concept of active control technology and applied it to the structural vibration control system [1]. There are inevitably time-delay problems in the operation of the active control system, such as the actuator process, sensor signal transmission and communication, and controller data processing [2–4]. These phenomena will lead to the time delay of control force and the decline of control effect and even lead to the failure of the control system [5–7]. Cai and Huang [8] proposed a traditional discrete LQR

control method for the building structure vibration control system under earthquake excitation. The obtained controller not only contains the state feedback of the current step but also includes the linear combination of some previous control steps. Udwadia et al. [9] derived the design principle of the time-delay controller for single degree-of-freedom structure active control and developed the theory to multi-degree-of-freedom structure time-delay control. The theory is applied to the design of time-delay controller for the vibration of multistorey building structures. Chen [10] combined control  $H_\infty$  algorithm with the Tagagi–Sugeno (T-S) fuzzy control method, and a fuzzy robust control method for nonlinear structural systems with time delay was proposed. Du et al. [11] studied the parameter uncertainty and time delay of active vibration control of building

structures and proposed a robust saturation control method. Using genetic algorithm as optimization tool, Xue et al. [12] solved the corresponding control gain according to the specific optimization control objective and proposed a structural vibration control method with time delay based on genetic algorithm.

The vibration control system of large-scale civil structures under the action of earthquake and wind is a complex multi-degree-of-freedom system, and the centralized control method has some defects, such as large amount of calculation and unstable control performance [13]. Decentralized control strategy can effectively solve the problem of building structure vibration control. Intelligent optimization algorithm and decentralized control strategy are used to solve the vibration control problem of building structures under earthquake excitation [14]. The decentralized control strategy based on the homotopy method is used to transform a typical centralized controller into multiple decoupled decentralized controllers [15]. The benchmark model of twenty-story steel structure is used to verify the stability of decentralized control strategy [16]. The time-delay problem of control systems has been widely studied. Decentralized control strategy is also applied to solve complex time-delay control systems [17–23]. Fallah and Taghikhany [24] proposed an overlapping decentralized  $H_2/LQG$  control method for cable-stayed bridge with time delay and divided the cable-stayed bridge into two overlapping subsystems for control. Wang and Law [25] proposed a time-delay decentralized  $H_\infty$  control method for vibration of building structures under seismic excitation, and a six-story building structure was taken as an example to verify the method. The contraction principle and overlapping dispersion strategy are applied to the vibration control system of intelligent buildings to minimize the damage caused by earthquake [26]. Karimi et al. [27] and Palacios-Quiñonero et al. [28] proposed a multioverlapping LQR control method for high-rise building structures based on LQR control algorithm and inclusion principle. This method only needs the control information of adjacent floors to realize control. A good control effect is obtained in the example. However, there is little research on overlapping decentralized control methods to solve the vibration control problem of structures with time delay. The overlapping decentralized control strategy divides the whole structural vibration control system into a series of overlapping subsystems according to certain rules, and each subsystem uses local information to control independently.

In order to study the control effect of overlapping decentralized control method to solve the vibration problem of structures with time delay based on  $H_\infty$  control algorithm, first, in this study, the overlapping decentralized control strategy, linear matrix inequality (LMI) method, and  $H_\infty$  control algorithm are combined to propose an overlapping decentralized control method for structures with time delay based on  $H_\infty$  control algorithm. Secondly, based on the inclusion principle and decomposition principle, the whole vibration control system of building structure with time delay is divided into a series of subsystems, and each subsystem is controlled by  $H_\infty$  control algorithm. In the process of solving

the feedback gain matrix of each subsystem, the  $H_\infty$  control algorithm is transformed into linear matrix inequality (LMI). In this paper, genetic algorithm is used to solve the linear matrix inequality (LMI) of each subsystem, so as to obtain the feedback gain matrix of each subsystem. Finally, the feedback gain matrix of each subsystem is reduced to an overlapping decentralized controller according to the contraction principle. In this study, five kinds of control strategies, including  $H_\infty$  centralized control and overlapping decentralized  $H_\infty$  control, are designed for the vibration time-delay control problem of twenty-story seismic steel structure benchmark model under seismic excitation, and the corresponding calculation results are given. The overlapping decentralized control method provides a new control approach to solve the vibration control problem of structures with time delay based on  $H_\infty$  control algorithm, and the control strategy reduces the calculation cost and increases the flexibility of the controller design.

## 2. Building Structure Model with Time Delay

Consider a vibration control system of an  $n$ -story building structure, as shown in Figure 1. Under the action of earthquake load, the motion equation of building structure with time delay can be described as follows:

$$M\ddot{q}(t) + C\dot{q}(t) + Kq(t) = T_u u(t - \tau) + T_w w(t), \quad (1)$$

where  $q(t) = [q_1(t), q_2(t), \dots, q_n(t)]^T$ ,  $q_i(t)$  is the displacement of the layer  $i$  floor structure,  $u(t) = [u_1(t), u_2(t), \dots, u_r(t)]^T$ ,  $u_r(t)$  is the control force matrix of the  $r$ th controller,  $T_u \in R^{n \times r}$  is the position matrix of the  $r$ th controller,  $w(t)$  is the direction of external load interference (i.e., seismic load acceleration),  $T_w$  is the interference input matrix, and  $M, C, K \in R^{n \times n}$  are the mass, damping, and stiffness matrices of the building structure, respectively.

$a_i (i = 1, 2, \dots, n)$  are the drive control devices in Figure 1. By using the state variable  $x_I(t) = [q^T(t) \dot{q}^T(t)]^T$  for equation (1), the system in equation (1) can be transformed into the following spatial state form:

$$S_I: \dot{x}_I(t) = A_I x_I(t) + B_I u(t - \tau) + E_I w(t), \quad (2)$$

where  $A_I = \begin{bmatrix} [0]_{n \times n} & [I]_{n \times n} \\ -M^{-1}K & -M^{-1}C \end{bmatrix}$ ,  $B_I = \begin{bmatrix} [0]_{n \times n} \\ M^{-1}T_u \end{bmatrix}$ , and  $E_I = \begin{bmatrix} [0]_{n \times 1} \\ -[1]_{n \times 1} \end{bmatrix}$ .

Now, we define a new state vector:

$$x(t) = \Gamma x_I(t), \quad (3)$$

where  $\Gamma$  is the transformation matrix.

Therefore, the system of equation (2) can be converted into

$$S: \dot{x}(t) = Ax(t) + Bu(t - \tau) + Ew(t), \quad (4)$$

where  $A = \Gamma A_I \Gamma^{-1}$ ,  $B = \Gamma B_I$ ,  $E = \Gamma E_I$ ,  $x(t) = [x_1(t), x_2(t), \dots, x_{2n}(t)]$ , and  $x_i(t)$  satisfy the following equation:

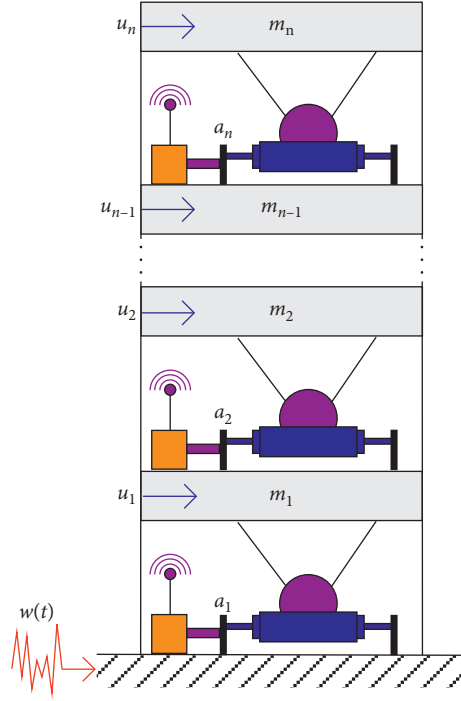


FIGURE 1: (n)-story building structural vibration control system.

$$\begin{cases} x_1(t) = q_1(t), & x_2(t) = \dot{q}_1(t), \\ x_{2j-1}(t) = q_j(t) - q_{j-1}(t), & j = 2, 3, \dots, n, \\ x_{2j}(t) = \dot{q}_j(t) - \dot{q}_{j-1}(t), & j = 2, 3, \dots, n. \end{cases} \quad (5)$$

$$\begin{cases} \dot{x}(t) = Ax(t) + Bu(t - \tau) + Ew(t), \\ z(t) = C_zx(t) + D_zu(t - \tau) + D_w w(t), \\ y(t) = C_yx(t), \end{cases} \quad (8)$$

### 3. Overlapping Decentralized H $\infty$ Control Design

**3.1. H $\infty$  Control Algorithm.** According to the basic principle of H $\infty$  norm control, the basic block diagram of standard H $\infty$  control algorithm is shown in Figure 2.

In Figure 2,  $S$  is the controlled system,  $G$  is the transfer function of the controller,  $u$  is the control input,  $y$  is the measurement output,  $w$  is the external disturbance, and  $z$  is the modulated output.

In order to design the H $\infty$  controller for building structure vibration with time delay, the following control outputs are considered to achieve the control performance index of the controller:

$$z(t) = C_zx(t) + D_zu(t - \tau) + D_w w(t), \quad (6)$$

where  $C_z$ ,  $D_z$ , and  $D_w$  are constant matrices with proper dimensions.

It is assumed that the energy of external load disturbance  $w(t) \in L_2[0, \infty)$  is finite:

$$\|w(t)\|_2 = \sqrt{\int_0^\infty w^T(t)w(t)dt} < \infty. \quad (7)$$

According to equations (4) and (6), the building structure control system can be described as

where  $y(t)$  is the measurement output and  $C_y$  is the appropriate dimension constant matrix.

The significance of the H $\infty$  controller design of equation (8) is to find the control gain matrix  $G$  so that the closed-loop system with control input  $u(t) = Gy(t) = GC_yx(t)$  is stable, and for a given constant  $\gamma > 0$ , the closed-loop system can obtain the performance  $\|T_{zw}\|_\infty < \gamma$  under nonzero disturbance  $w(t) \in L_2[0, \infty)$ , which is the closed-loop transfer function H $\infty$  norm from disturbance  $w(t)$  to control output  $z(t)$ .

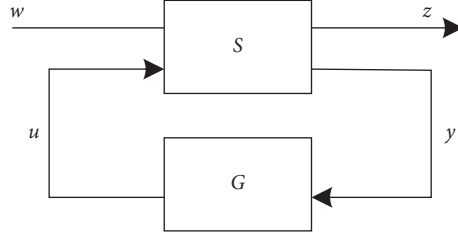
In this section, the H $\infty$  delay controller of equation (8) is designed by linear matrix inequality (LMI). Now, assuming  $D_w = 0$ , the feedback control law  $u(t - \tau) = Gy(t - \tau) = GC_yx(t - \tau)$  is substituted by equation (8):

$$\begin{cases} \dot{x}(t) = Ax(t) + BGC_yx(t - \tau) + Ew(t), \\ z(t) = C_zx(t) + D_zGC_yx(t - \tau), \\ x(t) = \varphi(t), \quad \forall t \in [-\tau, 0], \end{cases} \quad (9)$$

where  $\varphi(t)$  is the initial condition and  $G$  is the control gain matrix.

According to formula (9) and Leibniz–Newton formula, the following formula can be obtained:

$$x(t - \tau) = x(t) - \int_{t-\tau}^t \dot{x}(\theta)d\theta. \quad (10)$$

FIGURE 2: The diagram of standard H $\infty$  control algorithm.

By substituting the above formula into formula (9), we can obtain

$$\dot{x}(t) = (A + BGC_y)x(t) - BGC_y \int_{t-\tau}^t \dot{x}(\theta)d\theta + Ew(t). \quad (11)$$

Now, considering the following Lyapunov function,

$$V(x(t)) = V_1 + V_2 + V_3, \quad (12)$$

where  $V_1 = x^T(t)Px(t)$ ,  $V_2 = \int_{-\tau}^0 \int_{t+\beta}^t \dot{x}^T(\alpha)Z\dot{x}(\alpha)d\alpha d\beta$ ,  $V_3 = \int_{t-\tau}^0 \int_{t+\beta}^t x^T(\alpha)Q_c x(\alpha)d\alpha d\beta$ , and  $P$ ,  $Z$ , and  $Q_c$  are symmetric positive definite matrices.

According to the bounded real lemma and [29], it can be concluded that

$$\begin{aligned} \dot{V}(x(t)) &= \dot{V}_1 + \dot{V}_2 + \dot{V}_3 \\ &\leq x^T(t)(A^T P + PA + \bar{\tau}X + Y + Y^T)x(t) \\ &\quad + 2x^T(t)(PBGC_y - Y)x(t - \tau) \\ &\quad + \bar{\tau}[Ax(t) + Ew(t) + BGC_y x(t - \tau)]^T Z [Ax(t) + Ew(t) + BGC_y x(t - \tau)] \\ &\quad + x^T(t)Q_c x(t) - x^T(t - \tau)Q_c x(t - \tau) + w^T(t)E^T Px(t) + x(t)PEw(t). \end{aligned} \quad (13)$$

Assuming the initial condition  $\varphi(t) = 0, \forall t \in [-\tau, 0]$ , we can get  $V(x(t))|_{t=0} = 0$ .

Considering the following performance indicators,

$$J_{zw} = \int_0^{\infty} [z^T(t)z(t) - \gamma^2 w^T(t)w(t)]dt. \quad (14)$$

For any nonzero perturbation  $w(t) \in L_2[0, \infty)$ , we can obtain that

$$\begin{aligned} J_{zw} &\leq \int_0^{\infty} [z^T(t)z(t) - \gamma^2 w^T(t)w(t)]dt + V(x(t))|_{t=\infty} - V(x(t))|_{t=0} \\ &= \int_0^{\infty} [z^T(t)z(t) - \gamma^2 w^T(t)w(t) + \dot{V}(x(t))]dt \\ &= \int_0^{\infty} \eta^T(t)\Pi\eta(t)dt, \end{aligned} \quad (15)$$

where  $\eta(t) = [x(t) \ x(t - \tau) \ w(t)]^T$  and

$$\Pi = \begin{bmatrix} \Phi & PBGC_y - Y + \bar{\tau}A^T ZBGC_y + C_z^T D_z GC_y & \bar{\tau}A^T ZE + PE \\ * & -Q_c + \bar{\tau}(GC_y)^T B^T ZBGC_y + (GC_y)^T D_z^T D_z GC_y & \bar{\tau}(GC_y)^T B^T ZE \\ * & * & -\gamma^2 I + \bar{\tau}E^T ZE \end{bmatrix} < 0, \quad (16)$$

where

$$\Phi = A^T P + PA + \bar{\tau}X + Y + Y^T + Q_c + \bar{\tau}A^T ZA + C_z^T C_z. \quad (17)$$



According to the Schurz complement theorem, equation (16) can be equivalent to equation (19). Given a scalar  $\bar{\tau} > 0$ , for any constant time delay  $\tau (0 \leq \tau \leq \bar{\tau})$ , if there exists a

matrix  $G, P > 0, Q_c > 0, Z > 0$ , and  $X$  and  $Y$  satisfy equations (18) and (19); the closed-loop system equation (9) with  $H_\infty$  performance index  $\gamma (\gamma > 0)$  is asymptotically stable:

$$\begin{bmatrix} X & Y \\ Y^T & Z \end{bmatrix} \geq 0, \quad (18)$$

$$\begin{bmatrix} A^T P + PA + \bar{\tau} X + Y + Y^T + Q_c & PBGC_y - Y & PE & \bar{\tau} A^T Z & C_z^T \\ * & -Q_c & 0 & \bar{\tau} (GC_y)^T B^T Z & (GC_y)^T D_z^T \\ * & * & -\gamma^2 I & \bar{\tau} E^T Z & 0 \\ * & * & * & -\bar{\tau} Z & 0 \\ * & * & * & * & -I \end{bmatrix} < 0, \quad (19)$$

where the symbol \* denotes symmetry.

**3.2. Genetic Algorithm for Solving Linear Matrix Inequality (LMI).** Genetic algorithm is a probabilistic search process algorithm based on natural selection and natural genetic mechanism, which has been applied to solve the global optimization problems of various controllers. Arfiadi and Hadi [30] use genetic algorithm to design static output feedback controllers for  $H_2$  or  $H_\infty$  norm optimization problems. When MATLAB Robust control toolbox is used to calculate the output feedback controller, it is found that the optimization problem of bilinear matrix inequality (BLMI) (equations (18) and (19)) is not solvable. Therefore, this section uses the random search function of genetic algorithm to solve the following problems:

$$\max_{G \in R^{r \times n_u}} \bar{\tau} \text{ subject to equations (18) and (19),} \quad (20)$$

where the state variable of the controller is  $n_u$ ,  $r$  is the input vector, and the genetic algorithm generates a feedback gain matrix  $G \in R^{r \times n_u}$  at random, and the evolution is carried out according to the condition of equation (20).

If the feedback gain matrix  $G$  after evolution satisfies equation (20) and the maximum value  $\bar{\tau}$  can be obtained, then the design of the controller can be completed.

According to the following strategy, genetic algorithm solves the corresponding linear matrix inequality (LMI):

Step 1: the feedback gain matrix is encoded with a binary string.

Step 2: an initial population of  $N_p$  chromosomes was randomly generated.

Step 3: evaluate goals and assign fitness values. The initial value of Step 2 is fed back to the actual population control matrix  $G_j, j = 1, 2, \dots, N_p$ , in each decoding step. For each  $G_j$  dichotomy is used to search

the maximum delay  $\tau_j$  so that  $\tau_j$  and  $G_j$  are feasible in equation (20). According to the permutation-based allocation method, each delay  $\tau_j$  and the corresponding target value  $G_j$  are obtained, and each group  $(\tau_j, G_j)$  obtained is substituted into step 4. For  $G_j$ , there is no feasible delay  $\tau_j$  in equation (20). In order to reduce its survival chance in the next generation, the target value in line with  $G_j$  will be assigned to a larger value.

Step 4: the natural selection of Darwin's theory of biological evolution and the biological evolution process of genetic mechanism are used to select offspring.

Step 5: perform consistent crossover probability  $p_c$  and generate new offspring.

Step 6: there is a small mutation possibility  $p_m$  in chromosome population.

Step 7: select the optimal chromosome population and put it into the relevant program.

The evolutionary process of genetic algorithm will repeat Step 3 to Step 7 for  $N_g$  times. The optimal chromosome is decoded into the actual value, and the feedback gain matrix is generated here.

**3.3. Overlapping Decentralized  $H_\infty$  Control Approach.** In order to design the overlapping decentralized controller for structural vibration with time delay, the steps of the overlapping decentralized  $H_\infty$  control algorithm can be described as follows:

- (1) The motion equation of the shear model of  $n$ -story building structure with time delay can be described as equation (4). According to the inclusion principle in the overlapping decentralized control method [31], the system  $S$  in equation (4) can be extended and decoupled into a series of overlapping subsystems  $\tilde{S}_D^{(i)} (i = 1, 2, \dots, L)$ :

$$\tilde{\mathbf{S}}_D^{(i)}: \begin{cases} \dot{\tilde{\mathbf{x}}}_i(t) = \tilde{\mathbf{A}}_{ii}\tilde{\mathbf{x}}_i(t) + \tilde{\mathbf{B}}_{ii}\tilde{\mathbf{u}}_i(t - \tau) + \tilde{\mathbf{E}}_i\mathbf{w}_i(t), \\ \tilde{\mathbf{z}}_i(t) = (\tilde{\mathbf{C}}_z)_{ii}\tilde{\mathbf{x}}_i(t) + (\tilde{\mathbf{D}}_z)_{ii}\tilde{\mathbf{u}}_i(t - \tau), \\ \tilde{\mathbf{y}}_i(t) = (\tilde{\mathbf{C}}_y)_{ii}\tilde{\mathbf{x}}_i(t), \end{cases} \quad (i = 1, 2, \dots, L; 2 \leq L \leq n - 1), \quad (21)$$

where  $\tilde{\mathbf{A}}_{ii}$ ,  $\tilde{\mathbf{B}}_{ii}$ ,  $\tilde{\mathbf{E}}_i$ , and  $(\tilde{\mathbf{C}}_y)_{ii}$  are the corresponding matrices of subsystem  $\tilde{\mathbf{S}}_D^{(i)}$  ( $i = 1, 2, \dots, L$ ), respectively, and  $(\tilde{\mathbf{C}}_z)_{ii}$  and  $(\tilde{\mathbf{D}}_z)_{ii}$  are the constant matrices of appropriate dimension of subsystem  $\tilde{\mathbf{S}}_D^{(i)}$  ( $i = 1, 2, \dots, L$ ), respectively.

- (2) A series of overlapping  $\tilde{\mathbf{S}}_D^{(i)}$  ( $i = 1, 2, \dots, L$ ) subsystems in equation (21) are designed with the H $\infty$  controller. The genetic algorithm in Section 3.2 is used to solve linear matrix inequality (18) and equation (19), and the optimal feedback gain matrix  $\tilde{\mathbf{G}}^{(i)}$  ( $i = 1, 2, \dots, L$ ) of each subsystem can be obtained after several times of genetic algorithm search and evolution process.
- (3) The control law of the extended decoupled overlapping control system  $s$  can be expressed as  $\tilde{\mathbf{u}}_D(t) = \tilde{\mathbf{G}}_D\tilde{\mathbf{x}}(t)$ :

$$\tilde{\mathbf{G}}_D = \text{diag}\{\tilde{\mathbf{G}}^{(1)}, \tilde{\mathbf{G}}^{(2)}, \dots, \tilde{\mathbf{G}}^{(L)}\}, \quad (22)$$

where  $\tilde{\mathbf{G}}^{(i)}$  ( $i = 1, 2, \dots, L$ ) is the feedback gain matrix of subsystem  $\tilde{\mathbf{S}}_D^{(i)}$  ( $i = 1, 2, \dots, L$ ).

- (4) According to the contraction principle and the corresponding linear transformation [31], the feedback gain matrix  $\tilde{\mathbf{G}}_D$  after extended decoupling can be reduced to the original state overlapping control:

$$\mathbf{G}_o = \mathbf{Q}\tilde{\mathbf{G}}_D\mathbf{V}, \quad (23)$$

where  $\mathbf{Q}$  and  $\mathbf{V}$  are contraction matrices and expansion matrices, respectively.

#### 4. Controller Design and Example Analysis

In order to verify the proposed overlapping decentralized H $\infty$  control method for building structures with time delay, the benchmark model of a twenty-story steel frame structure in Los Angeles, USA, is used in this section. The structural parameters are [32]  $m_1 = 215.2 \times 10^3$  kg,  $m_2 = 209.2 \times 10^3$  kg,  $m_3 = 207 \times 10^3$  kg,  $m_4 = 204.8 \times 10^3$  kg,  $m_5 = 266.1 \times 10^3$  kg,  $k_1 = 147 \times 10^3$  kN/m,  $k_2 = 113 \times 10^3$  kN/m,  $k_3 = 99 \times 10^3$  kN/m,  $k_4 = 89 \times 10^3$  kN/m, and  $k_5 = 84 \times 10^3$  kN/m. The structural damping rate is 5%. In this section, the overlapping decentralized control method, linear matrix inequality (LMI) method, and H $\infty$  control algorithm are combined to propose the overlapping decentralized H $\infty$  control method for structures with time delay. In this section, five control strategies are set according to the overlapping information sharing mode of different floor structures, as shown in Figure 3. The seismic excitation adopts El Centro (N-S, 1940) wave and the sampling step is 0.02 s (see Figure 4). The energy distribution of the input time-history on the natural

frequency-time plane can be obtained by the principle of wavelet transform (see Figure 5). The genetic algorithm parameters' set in this section are population chromosome number,  $N_p = 100$ , crossover probability,  $p_c = 0.9$ , mutation probability,  $p_m = 0.02$ , and maximum random search times,  $N_g = 500$ .

Centralized control is to control the whole building structure as a control system (Figure 3(a)). When MATLAB robust control toolbox is used to calculate the output feedback controller, it is found that the linear matrix inequality (LMI) of the system is not solvable. According to the parameters of the genetic algorithm set in this section and using the genetic algorithm to solve equation (20), the feedback gain matrix  $\mathbf{G}_c$  of the H $\infty$  controller can be obtained.

The overlapping decentralized control scheme is shown in Figure 3(b) to Figure 3(e). Among them, Figure 3(b) shows that the control information of layer 11 structure is shared by subsystems  $S^{(1)}$  and  $S^{(2)}$ . In Figure 3(c), the control information of layer 7 structure is shared by subsystems  $S^{(1)}$  and  $S^{(2)}$  and the control information of layer 14 structure is shared by subsystems  $S^{(2)}$  and  $S^{(3)}$ . In Figure 3(d), subsystems  $S^{(1)}$  and  $S^{(2)}$  share the control information of layer 5 structure. Subsystems  $S^{(2)}$  and  $S^{(3)}$  share the control information of the 10th layer structure. Subsystems  $S^{(3)}$  and  $S^{(4)}$  share the control information of layer 15 structure. In Figure 3(e), the control information of layer  $i$  structure is shared by subsystems  $S^{(i-1)}$  and  $S^{(i)}$  ( $i = 2, 3, \dots, 19$ ). In the above different overlapping decentralized control schemes, the H $\infty$  control algorithm based on linear matrix inequality is used to solve the subsystems of each scheme. In this section, the genetic algorithm in Section 3.2 and the set genetic algorithm parameters are used to solve the linear matrix inequality (LMI) of the corresponding subsystem. After several times of random search function of genetic algorithm, the subsystem feedback gain matrix of each scheme can be obtained, and the control gain matrix  $G_{ODC1}$ ,  $G_{ODC2}$ ,  $G_{ODC3}$ , and  $G_{ODC4}$  of each overlapping decentralized control scheme can be obtained by using the feedback gain matrix of each subsystem through formulas (22) and (23).

According to formula (14) and  $\gamma_G = \|T_{zw}\|_\infty = \max \bar{\sigma}[T_{zw}(j\omega)]$ , we can obtain the maximum singular values. From the gain matrix under different control strategies, the maximum singular values under different time delays can be obtained, as shown in Figures 6 and 7. The maximum interlayer displacement and maximum control force are shown in Figures 8–11.

As can be seen from Figure 6, when the time delay  $\tau = 20$ ms, the maximum singular value  $\gamma_{G_c}$  of H $\infty$  centralized control is 0.0511, the maximum singular value  $\gamma_{G_{ODC1}}$  of overlapping decentralized H $\infty$  controller 1 is

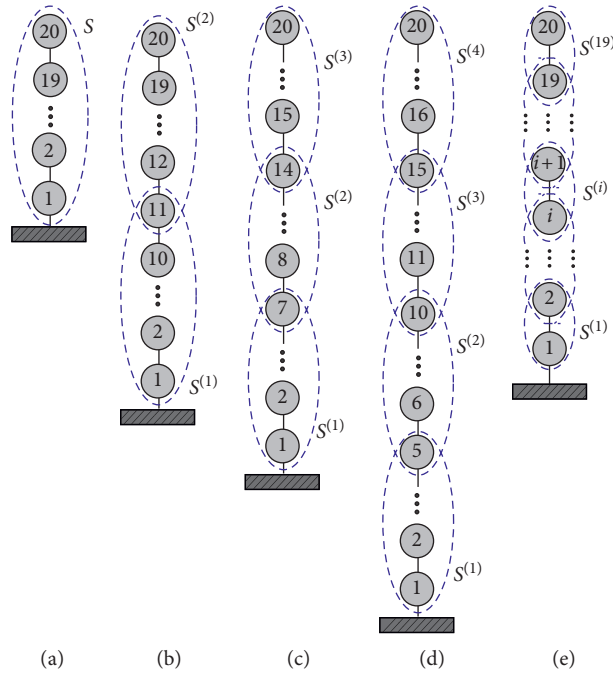


FIGURE 3: The design of controllers. (a) Centralized control. (b) ODC1 (c) ODC2. (d) ODC3. (e) ODC4.

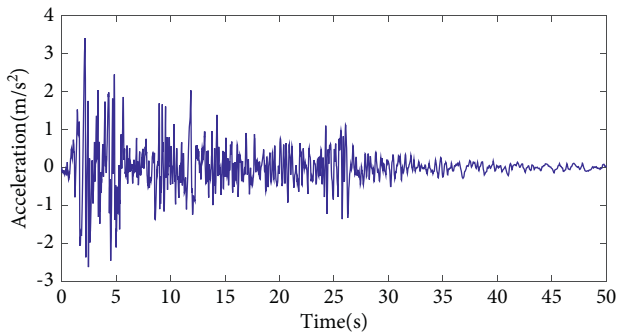


FIGURE 4: El Centro (1940) earthquake N-S component of ground motion acceleration record.

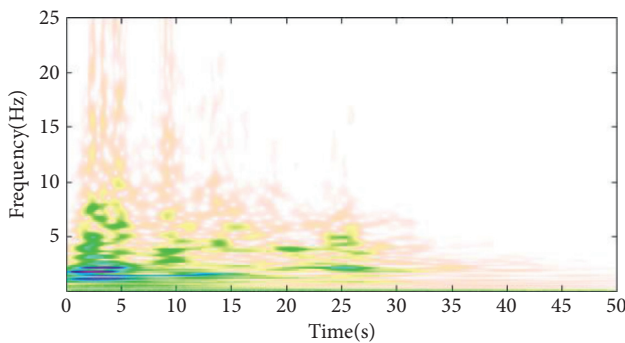


FIGURE 5: The energy distribution of input time-history on natural frequency-time plane.

0.0570, the maximum singular value  $\gamma_{G_{ODC_2}}$  of overlapping decentralized  $H_\infty$  controller 2 is 0.0748, the maximum singular value  $\gamma_{G_{ODC_3}}$  of overlapping decentralized  $H_\infty$

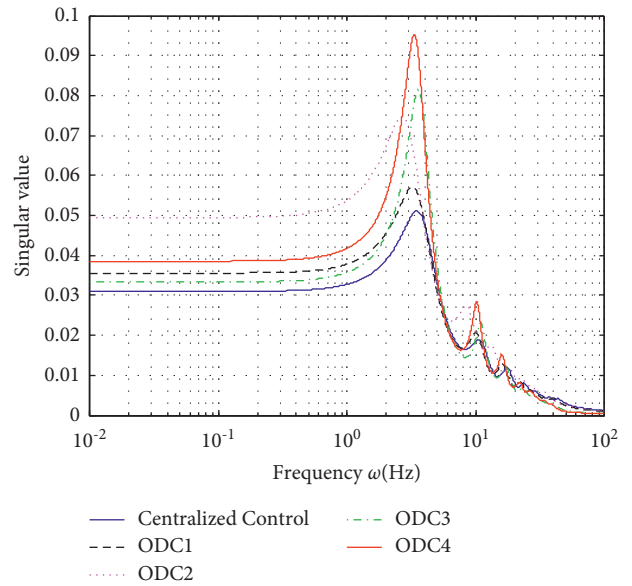
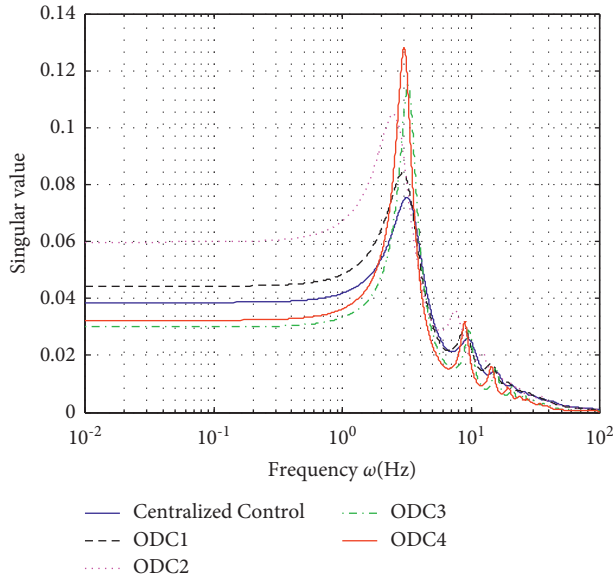
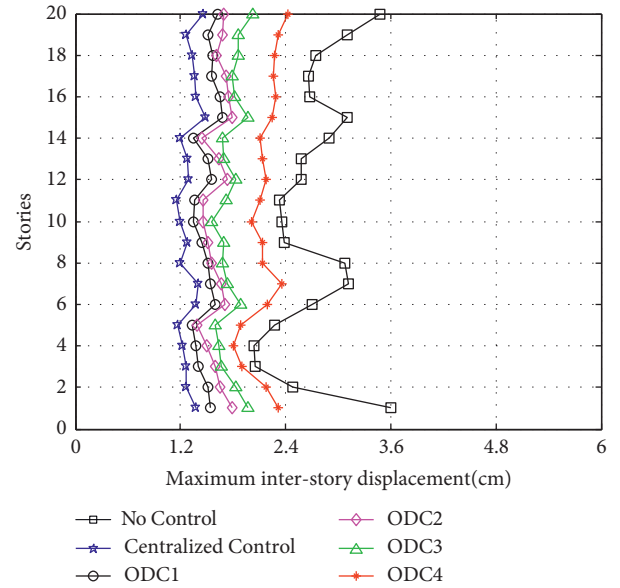
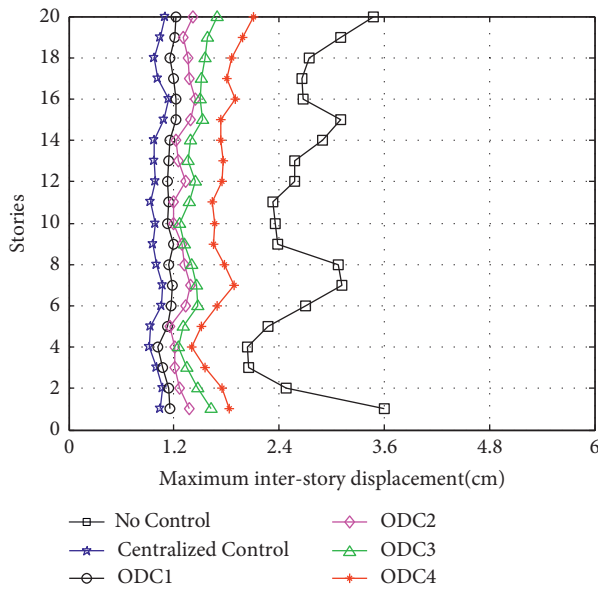
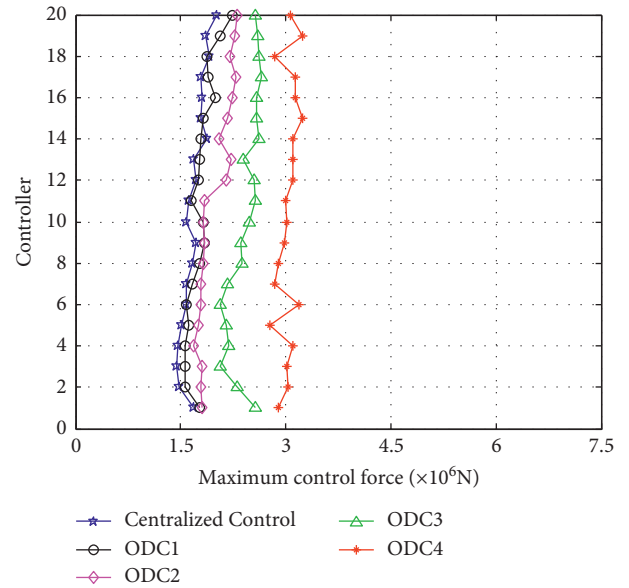


FIGURE 6: The maximum singular values of time delay  $\tau = 20\text{ms}$ .

controller 3 is 0.0814, and the maximum singular value  $\gamma_{G_{ODC_4}}$  of overlapping decentralized  $H_\infty$  controller 4 is 0.0951.

It can be seen from Figure 7 that when the time delay  $\tau = 40\text{ms}$ , the maximum singular value  $\gamma_{G_C}$  of  $H_\infty$  centralized control is 0.0756, the maximum singular value  $\gamma_{G_{ODC_1}}$  of overlapping decentralized  $H_\infty$  controller 1 is 0.0840, the maximum singular value  $\gamma_{G_{ODC_2}}$  of overlapping decentralized  $H_\infty$  controller 2 is 0.1048, the maximum singular value  $\gamma_{G_{ODC_3}}$  of overlapping decentralized  $H_\infty$  controller 3 is 0.1150, and the maximum singular value

FIGURE 7: The maximum singular values of time delay  $\tau = 40\text{ms}$ .FIGURE 9: The maximum interstory displacements of time delay  $\tau = 40\text{ms}$ .FIGURE 8: The maximum interstory displacements of time delay  $\tau = 20\text{ms}$ .FIGURE 10: The maximum control force of time delay  $\tau = 20\text{ms}$ .

$\gamma_{G_{ODC4}}$  of overlapping decentralized  $H_{\infty}$  controller 4 is 0.1280.

According to the maximum interstory displacements of time delay shown in Figure 8, when the time delay  $\tau = 20\text{ms}$ , the story drift response value of the structure in the uncontrolled state is the largest, and the control effect of  $H_{\infty}$  centralized control is the best. The overlapping decentralized  $H_{\infty}$  controller 1 to the overlapping decentralized  $H_{\infty}$  controller 4 also gets better control effect. With the deepening of the overlapping degree of building structure, the control effect of overlapping decentralized controller is getting worse and worse. Among them, the overlapping decentralized  $H_{\infty}$  controller 4 has the worst control effect,

but it also obtains better control effect. As shown in Figure 9, the maximum interstory displacement of the building structure with time delay  $\tau = 40\text{ms}$  can be obtained. The control effect of the centralized controller is the best, and the control effect of the overlapping decentralized controller is also very good. The control effect of each overlapping decentralized controller is similar to that of  $\tau = 20\text{ms}$ .

Centralized control has some defects in solving the vibration control problems of multi-degree-of-freedom structures, such as large amount of calculation, poor reliability, and unstable control performance. It is difficult to be widely used in specific large-scale building structure vibration control system. The overlapping decentralized

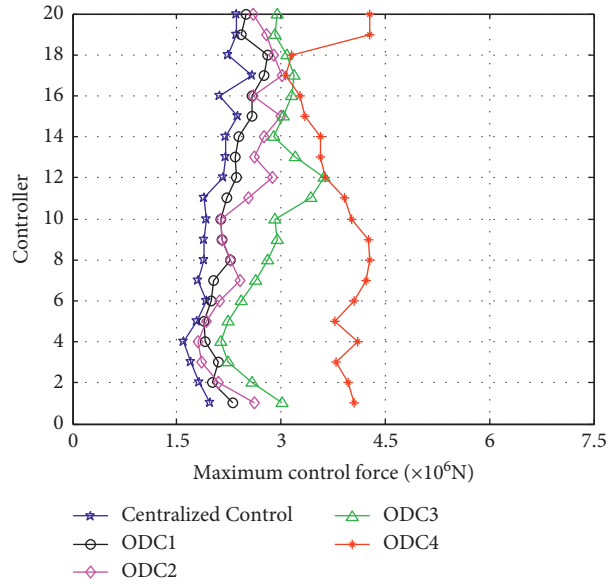


FIGURE 11: The maximum control force of time delay  $\tau = 40\text{ms}$ .

control strategy is more operable and can solve this problem. Therefore, for this kind of structural vibration control system, it is necessary to adopt an overlapping and decentralized control theory to control it. The overlapping decentralized  $H_\infty$  control strategies for structures with time delay are control methods based on overlapping decentralized control theory, which can solve the problems of centralized control strategy. The control strategy proposed in this paper provides a new way to solve the vibration control of complex multi-degree-of-freedom structures.

It can be seen from the maximum control force in Figure 10 and Figure 11 that the control force of the structure in the centralized control state is the smallest when the hysteresis are  $\tau = 20\text{ms}$  and  $\tau = 40\text{ms}$ . With the deepening of building structure overlap, the control force of overlapping decentralized controller is increasing. Among them, the overlapping decentralized  $H_\infty$  controller 4 has the largest control force. Therefore, it can be considered that with the deepening of the degree of building structure overlap, and the energy required by the overlapping decentralized controller is also more and more.

In order to describe the maximum displacement and the maximum control force of the structure under the action of time delay in more detail, limited to space, only the maximum displacement of the bottom layer of the structure (Figure 12) and the maximum control force (Figure 13) are given.

From the maximum displacement of the bottom layer of the structure under the action of time delay shown in Figure 12, it can be seen that the time delay effect should be given enough attention in the decentralized control system. Even if the time delay is very small, it may lead to the unstable state of the controlled structure. It can be seen from Figure 13 that the control force at the bottom layer of the structure increases with the time delay and finally tends to infinity.

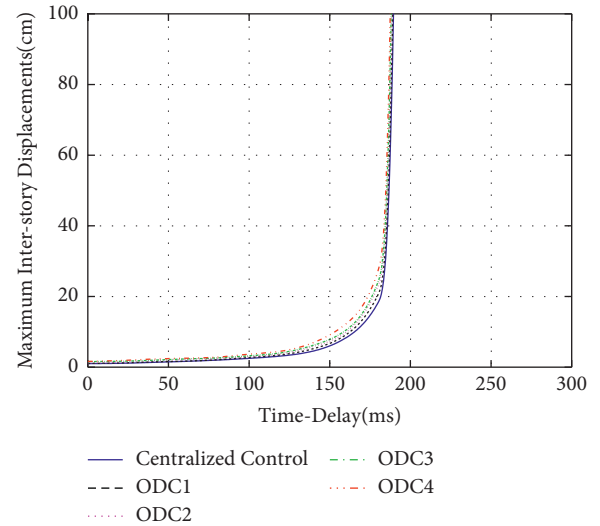


FIGURE 12: The maximum displacement value of first floor with time delay.

## 5. Discussion

- (1) In this paper, a new path is provided to solve the vibration control problem of structures with time delay based on  $H_\infty$  control algorithm: an overlapping decentralized control method, and the corresponding maximum singular values  $\gamma$  are calculated according to different overlapping decentralized control strategies. As the degree of overlap and decentralization increases, the corresponding maximum single values  $\gamma$  become larger and larger. However, when solving the time-delay problem of vibration control of practical engineering structures, the controller needs to be designed according to the time delay and the frequency of the structure itself.

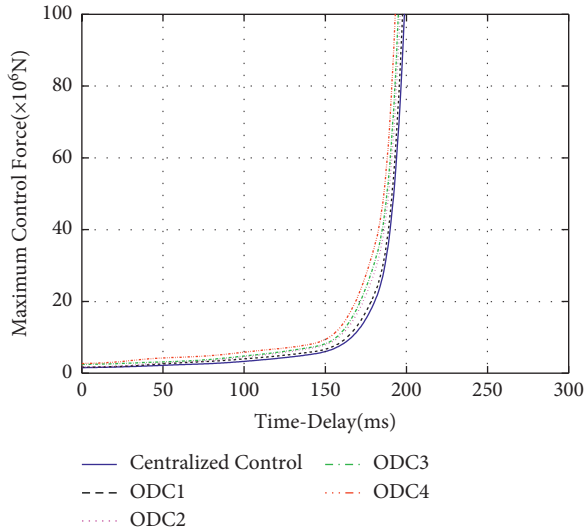


FIGURE 13: The maximum control force of first floor with time delay.

- (2) When the building structure vibration control system adopts the same control strategy, the maximum singular values  $\gamma$  are also increasing with the increase of hysteresis  $\tau$ .
- (3) Matlab R2016b software is used to program and calculate different control strategies of vibration control system of twenty-story building structure with time delay. The running time of the centralized control strategy (Figure 3(a)) is 1.5 hours. The operation time of overlapping decentralized controller 1 (ODC1) is 40 minutes. The running time of overlapping decentralized controller 2 (ODC2) is 30 seconds. The operation time of overlapping decentralized controller 3 (ODC3) is 20 seconds. The running time of overlapping decentralized controller 4 (ODC4) is 8 seconds. As the degree of overlap and decentralization increases, the cost of computer computing is also decreasing.

## 6. Conclusions and Directions

When a large number of intelligent wireless sensors and controllers are applied to the vibration control system of high-rise buildings, there will inevitably be the problem of time delay. Even if the time delay is very small, it may cause the control effect to decline and even lead to the unstable state of the controlled structure. Centralized control strategy collects and transmits data by a single central processor. Once a failure occurs, the whole control system will be paralyzed. However, decentralized control strategy can better solve this problem.

In this paper, the linear matrix inequality (LMI) method,  $H_\infty$  control algorithm, and overlapping decentralized control strategy are combined to propose the overlapping decentralized  $H_\infty$  control method for building structures with time delay. The proposed control method is used to design and calculate the controller for the benchmark model

of 20-story steel frame structure. Genetic algorithm is used to solve the corresponding linear matrix inequality (LMI) to obtain the feedback gain matrix of each subsystem, and then, the feedback gain matrix is reduced to the corresponding overlapping decentralized controller according to the overlapping decentralized control strategy. The results show that

- (1) Similar to  $H_\infty$  centralized control, overlapping decentralized  $H_\infty$  control also obtains good control effect.
- (2) Time delay overlapping decentralized control system can effectively reduce the vibration response of building structure under seismic excitation and improve the robust performance of feedback time delay of the control system.
- (3) Overlapping decentralized  $H_\infty$  control provides a new way to solve the vibration control problem of complex multi-degree-of-freedom structures with time delay. Time-delay effect should be paid enough attention in the decentralized control system, and it is worthy of further study.
- (4) In this paper, the computational efficiency of structural vibration control with time delay based on  $H_\infty$  control algorithm under earthquake is studied, and the interlayer actuator with control time-delay effect is designed. This theory may be helpful to solve the problem of vibration control of buildings under seismic excitation.
- (5) When the building structure is subjected to seismic load, its control system will produce time-delay phenomenon. However, the overlapping decentralized control method is developed based on the inclusion principle and contraction principle. The whole system is divided into a series of subsystems, and the subsystems can share the control information with overlapping structure. The number of degrees of freedom of the subsystem can be divided according to the load condition and the influence degree of time delay. Therefore, the overlapping decentralized control method increases the flexibility of the controller design.

## Data Availability

The data used to support the findings of this study are included within the article.

## Conflicts of Interest

The authors declare that they have no conflicts of interest.

## Acknowledgments

This study was financially supported by the Natural Science Research Project of Higher Education Institutions in Anhui Province (KJ2019A0747, KJ2019A0748, and KJ2020A0490), the Anhui Provincial Natural Science Foundation (Grant nos. 2008085QE245 and 2108085QA41), the National Key

Research and Development Program of China (2016YFC0701507-2), the Project of Science and Technology Plan of Department of Housing and Urban-Rural Development of Anhui Province (2019YF-029, 2020-YF20, and 2021-YF22), the Doctoral Startup Foundation of Anhui Jianzhu University (2017QD05, 2020QDZ07, and 2020QDZ38), the National College Student Innovation and Entrepreneurship Training Program Project (202110878052), the ideological and political demonstration course for the Quality Engineering Project of Anhui Province (2020szsfkc0298), the ideological and political demonstration course of Anhui Jianzhu University (2020szkc05), and the University-Industry Collaborative Education Program of the Ministry of Education (202002129042).

## References

- [1] J. T. P. Yao, "Concept of structural control," *Journal of the Structural Division*, vol. 98, no. 7, pp. 1567–1574, 1972.
- [2] A. Banaei and J. Alamatian, "New genetic algorithm for structural active control by considering the effect of time delay," *Journal of Vibration and Control*, vol. 27, no. 7, pp. 743–758, 2021.
- [3] K. Liu, L.-X. Chen, and G.-P. Cai, "Active control of a nonlinear and hysteretic building structure with time delay," *Structural Engineering & Mechanics*, vol. 40, no. 3, pp. 431–451, 2011.
- [4] K. Liu, L. X. Chen, and G. P. Cai, "Active control of buildings with bilinear hysteresis and time delay," *International Journal of Structural Stability and Dynamics*, vol. 13, no. 5, Article ID 1350027, 2013.
- [5] M. Soleymani, A. H. Abolmasoumi, H. Bahrami, A. Khalatbari-S, E. Khoshbin, and S. Sayahi, "Modified sliding mode control of a seismic active mass damper system considering model uncertainties and input time delay," *Journal of Vibration and Control*, vol. 24, no. 6, pp. 1051–1064, 2018.
- [6] X. Xue, Q. Sun, L. Zhang, and X. Wu, "Semi-active control strategy using genetic algorithm for seismically excited structure combined with MR damper," *Journal of Intelligent Material Systems and Structures*, vol. 22, no. 3, pp. 291–302, 2011.
- [7] Y.-J. Cha, A. K. Agrawal, and S. J. Dyke, "Time delay effects on large-scale MR damper based semi-active control strategies," *Smart Materials and Structures*, vol. 22, no. 1, Article ID 015011, 2012.
- [8] G. Cai and J. Huang, "Optimal control method for seismically excited building structures with time-delay in control," *Journal of Engineering Mechanics*, vol. 128, no. 6, pp. 602–612, 2002.
- [9] F. E. Udawadia, H. Von Bremen, and P. Phohomsiri, "Time-delayed control design for active control of structures: principles and applications," *Structural Control and Health Monitoring*, vol. 14, no. 1, pp. 27–61, 2007.
- [10] C. Chen, "Application of fuzzy-model-based control to nonlinear structural systems with time delay: an LMI method," *Journal of Vibration and Control*, vol. 16, no. 1, pp. 1651–1672, 2010.
- [11] H. Du, N. Zhang, and F. Naghdy, "Actuator saturation control of uncertain structures with input time delay," *Journal of Sound and Vibration*, vol. 330, no. 18, pp. 4399–4412, 2011.
- [12] X. Xue, Q. Sun, L. Zhang, and X. Wu, "Research on active control for time delayed structure using modified genetic algorithm," *Engineering Mechanics*, vol. 28, no. 3, pp. 143–149, 2011, (in Chinese).
- [13] Y. Luo, H. Sun, X. Wang, L. Zuo, and N. Chen, "Wind induced vibration control and energy harvesting of electromagnetic resonant shunt tuned mass-damper-inerter for building structures," *Shock and Vibration*, vol. 2017, Article ID 4180134, 13 pages, 2017.
- [14] K. Xu, L. Chen, M. Wang, A. M. Lopes, J. A. Tenreiro Machado, and H. Zhai, "Improved decentralized fractional PD control of structure vibrations," *Mathematics*, vol. 8, no. 3, p. 326, 2020.
- [15] Y. Wang, "Time-delayed dynamic output feedback  $\mathcal{H}_\infty$  controller design for civil structures: a decentralized approach through homotopic transformation," *Structural Control and Health Monitoring*, vol. 18, no. 2, pp. 121–139, 2011.
- [16] L. Bakule, M. Papík, and B. Reháč, "Decentralized stabilization of large-scale civil structures," *IFAC Proceedings Volumes*, vol. 47, no. 3, pp. 10427–10432, 2014.
- [17] C. Peng, Q. L. Han, and D. Yue, "Communication-delay-distribution-dependent decentralized control for large-scale systems with IP-based communication networks," *IEEE Transactions on Control Systems Technology*, vol. 21, no. 3, pp. 820–830, 2012.
- [18] F. H. Feng-Hsiang Hsiao, J. D. Jung-Dong Hwang, C. W. Cheng-Wu Chen, and Z. R. Zhi-Ren Tsai, "Robust stabilization of nonlinear multiple time-delay large-scale systems via decentralized fuzzy control," *IEEE Transactions on Fuzzy Systems*, vol. 13, no. 1, pp. 152–163, 2005.
- [19] S. Tong, W. Wang, and L. Qu, "Decentralized robust control for uncertain TS fuzzy large-scale systems with time-delay," *International Journal of Innovative Computing, Information and Control*, vol. 3, no. 3, pp. 657–672, 2007.
- [20] Y. Zhu and E. Fridman, "Predictor methods for decentralized control of large-scale systems with input delays," *Automatica*, vol. 116, Article ID 108903, 2020.
- [21] L. Liu, S. Xu, X. J. Xie, and B. Xiao, "Observer-based decentralized control of large-scale stochastic high-order feedforward systems with multi time delays," *Journal of the Franklin Institute*, vol. 356, no. 16, pp. 9627–9645, 2019.
- [22] A. Moradvandi, M. Shahrokhi, and S. A. Malek, "Adaptive fuzzy decentralized control for a class of MIMO large-scale nonlinear state delay systems with unmodeled dynamics subject to unknown input saturation and infinite number of actuator failures," *Information Sciences*, vol. 475, pp. 121–141, 2019.
- [23] F. Zhou, L. Liu, and G. Feng, "Fuzzy decentralized control for a class of networked systems with time delay and missing measurements," *Asian Journal of Control*, vol. 17, no. 1, pp. 84–98, 2015.
- [24] A. Y. Fallah and T. Taghikhany, "Time-delayed decentralized H2/LQG controller for cable-stayed bridge under seismic loading," *Structural Control and Health Monitoring*, vol. 20, no. 3, pp. 354–372, 2013.
- [25] Y. Wang and K. H. Law, "Structural control with multi-subnet wireless sensing feedback: experimental validation of time-delayed decentralized H\* control design," *Advances in Structural Engineering*, vol. 14, no. 1, pp. 25–39, 2016.
- [26] M. Z. Doghmane, M. Kidouche, S. Eladj, and B. Belahcene, "Design of optimal decentralized controller using overlapping decomposition for smart building system," in *Proceedings of the International Conference In Artificial Intelligence In Renewable Energetic Systems*, pp. 155–167, Tipaza, Algeria, December 2020.

- [27] H. R. Karimi, F. Palacios-Quiñonero, J. M. Rossell, and J. Rubió-Massegú, "Sequential design of multioverlapping controllers for structural vibration control of tall buildings under seismic excitation," *Proceedings of the Institution of Mechanical Engineers - Part I: Journal of Systems & Control Engineering*, vol. 227, no. 2, pp. 176–183, 2013.
- [28] F. Palacios-Quiñonero, J. Rubió-Massegú, J. M. Rossell, and H. R. Karimi, "Discrete-time multioverlapping controller design for structural vibration control of tall buildings under seismic excitation," *Mathematical Problems in Engineering*, vol. 2012, Article ID 636878, 20 pages, 2012.
- [29] Y. S. Moon, P. Park, W. H. Kwon, and Y. S. Lee, "Delay-dependent robust stabilization of uncertain state-delayed systems," *International Journal of Control*, vol. 74, no. 14, pp. 1447–1455, 2001.
- [30] Y. Arfiadi and M. N. S. Hadi, "Optimal direct (static) output feedback controller using real coded genetic algorithms," *Computers & Structures*, vol. 79, no. 17, pp. 1625–1634, 2001.
- [31] F. Palacios-Quiñonero, J. M. Rossell, and H. R. Karimi, "Semi-decentralized strategies in structural vibration control," *Modeling Identification and Control*, vol. 32, no. 2, pp. 57–77, 2011.
- [32] Y. Wang, J. P. Lynch, and K. H. Law, "Decentralized  $\mathcal{H}_\infty$  controller design for large-scale civil structures," *Earthquake Engineering & Structural Dynamics*, vol. 38, no. 3, pp. 377–401, 2009.



## Research Article

# Dynamic Response and Parametric Studies of Elliptical Blast-Resistant Door with the Combined Structure for Large Vacuum Explosion Containers

Saiwei Cheng <sup>1</sup>, Xiaojie Li <sup>1,2</sup>, Yang Wang <sup>1</sup>, Yuxin Wang <sup>1</sup>, and Honghao Yan <sup>1</sup>

<sup>1</sup>Department of Engineering Mechanics, Dalian University of Technology, Dalian 116024, China

<sup>2</sup>State Key Laboratory of Structural Analysis for Industrial Equipment, Dalian University of Technology, Dalian 116024, China

Correspondence should be addressed to Xiaojie Li; robinli@dlut.edu.cn

Received 12 July 2021; Revised 2 September 2021; Accepted 21 October 2021; Published 3 November 2021

Academic Editor: Bing Zhang

Copyright © 2021 Saiwei Cheng et al. This is an open access article distributed under the Creative Commons Attribution License, which permits unrestricted use, distribution, and reproduction in any medium, provided the original work is properly cited.

In recent years, with the improvement of environmental protection requirements year by year and the continuous expansion of explosive working scale, higher standards have been put forward for explosive working. It is hoped that the sphere of influence of the explosion can be limited to a minimal range. The explosion vessel is driven by such demand. As the explosion vessel's key component, studying the blast-resistant door in depth is of great significance. This paper introduces a new elliptical blast-resistant door with the combined structure (EBD), mainly welded with an elliptical panel, arc support plate, and triangle support plate. The finite element program AUTODYN was used to calculate the explosion load, and LS-DYNA was used to calculate the blast-resistant door's dynamic response. The calculation results show that the newly proposed EBD's blast-resistance capacity is better than that of the traditional structure. To further study the factors that affect the dynamic response of the EBD, a parametric study was carried out on the EBD, mainly analyzing the influence of the vacuum degree in the explosion vessel, the number of explosives, and the diameter ratio of the EBD. The parametric calculation results show that reducing the vacuum degree in the explosion vessel and the number of explosives during explosion working can improve the blast-resistance capacity of the EBD. Based on the analysis of the dynamic response of four kinds of EBD with different diameter ratios under 0.2 atm explosion load, the optimal diameter ratio of the EBD is given.

## 1. Introduction

Explosive working is a material processing method that relies on explosive detonation's high-speed and high-pressure impact to carry out plastic forming, surface modification, and metallurgical bonds between metals [1]. The common explosive working methods include explosive strengthening [2–4], explosive welding [5–7], explosive compaction [8, 9], explosive cutting [10–12], detonation synthesis [13, 14], and so on. Explosion working is often carried out outdoors. However, the strong shock wave, noise, harmful gas, and dust produced by the explosion will greatly impact the surrounding environment [15]. Nowadays, environmental problems are becoming more and more serious. Besides, with the increasing production and explosive quantity of explosive working, the single explosive

quantity of explosive working is close to 1 ton. The traditional outdoor bare explosion production mode can no longer meet the needs of industrial production. The vacuum explosion vessel can just solve these problems. At the same time, the blast-resistant door is a critical component of the vacuum explosion vessel. Its primary function is to seal the container and enter and exit the materials (i.e., meet large vehicles and machinery requirements to enter and exit the explosion vessel). The antiexplosion ability of the blast-resistant door on the explosion vessel directly affects the whole explosion vessel's antiexplosion ability. Therefore, it is crucial to study the blast-resistant door of a large explosion vessel.

Blast-resistant doors are widely used in defense engineering, civil air-defense construction, petrochemical engineering, mining industry, and other fields [16–18]. The

research of traditional blast-resistant doors is mainly from two aspects of structure and material. In the research of blast-resistant door structures, traditional blast-resistant doors are mostly made of steel, with beam slab structure [19]. The beam-slab blast-resistant door is mainly composed of panels and ribbed beams. The rib beam is arranged on the bottom of the face slab by crossing the longitudinal rib and the transverse rib. The blast-resistant door mainly bears the combined action of membrane stress and bending stress subjected to blast load [18]. There are relatively few researches on beam-slab blast-resistant doors in published materials at present. However, beam-slab blast-resistant doors can be regarded as a combination of stiffened plates/shells. Early studies on stiffened plates/shells indicate that stiffening is an effective method to improve the structure's flexural rigidity without increasing weight [20]. Some scholars have also studied the direction (longitudinal and transverse), position, shape, size, and a number of the stiffeners and found that the above factors affect stiffened plates' dynamic characteristics [21–24]. Although the application scope of the beam-slab blast-resistant door is broad, it is mostly used in protection engineering with a low resistance level.

In the blast-resistant door's material research, the beam-slab blast-resistant door is usually filled with concrete [18] or foam aluminum [25] to improve the blast-resistance capacity. With the continuous development of new materials and technology, various new composite materials have been used to research blast-resistant doors. Zhao et al. [26, 27] studied the blast-resistance capacity of sheet molding compound (SMC) blast-resistant door and basalt fiber reinforced polymers and sheet molding compound (BFRP-SMC) blast-resistant door. The research results show that SMC and BFRP-SMC materials can significantly improve the blast-resistant door's flexural rigidity and bearing capacity. They are one of the alternative materials for light-weight blast-resistant door structures. Although the new material can improve the blast-resistant door's blast-resistance ability, it does not consider its fatigue and durability.

The traditional blast-resistant door only considers the blast-resistance ability once. It allows the blast-resistant door to produce large deformation and even a certain degree of damage. The blast-resistant door to be studied in this article is different from the traditional blast-resistant door. It is the critical component of a large explosion vessel. It needs to bear long-term and repeated explosive load in the process of explosive working. Accordingly, the deformation of the blast-resistant door should always be kept in the elastic range. Under the actual production conditions of explosive working, the blast-resistant door should be designed to manufacture, install, and maintain expediently and should be at low cost and good fatigue resistance. To this end, we designed a steel elliptical blast-resistant door with a combined structure (EBD). Then, the EBD is compared with the same mass flat blast-resistant door (FBD) and the reinforced flat blast-resistant door (RFBD). The numerical results show that the blast-resistance capacity of the EBD designed in this paper is better than that of the FBD and the RFBD. Besides, we also have carried out a parametric study on the EBD and analyzed the factors affecting the blast-

resistance capacity of the EBD one by one, including the vacuum degree of the explosion vessel, the number of explosives, and the diameter ratio of the EBD.

## 2. Explosive Load

The explosive load in the confined space is different from that in the free field [28]. Due to the container wall restriction, the confined space's explosion shock wave has an apparent reflection phenomenon [29]. The back and forth reflection of the shock wave in the explosion vessel can significantly enhance the explosive load's peak pressure and impulse, which can cause more significant damage to the vessel and its attached structures [30]. However, considering that the explosion shock wave is easily affected by the environmental conditions [31, 32], the shock wave's peak pressure and impulse can be reduced by reducing the ambient pressure [33]. In this paper, the blast-resistant door on the explosion vessel with a volume of 1,600 m<sup>3</sup> is studied. The explosive vessel's designed maximum working charge is 600 kg ANFO (ammonium-nitrate/fuel-oil) explosive. The vessel is vacuumized in each explosion process to reduce the vessel's initial ambient pressure.

*2.1. Computational Model.* It is assumed that the blast-resistant door works under extreme conditions. At this time, the working charge of the explosive container is 600 kg ANFO explosive. The distance between the center of the explosive and the blast-resistant door is 7.2557 m, which is the position of gauge 1 in Figure 1. The scaled distance is given as follows:

$$\bar{R} = \frac{R}{\sqrt[3]{W}} = \frac{7.2557 \text{ m}}{\sqrt[3]{600 \text{ kg}}} \cong 0.86 \text{ m/kg}^{1/3}, \quad (1)$$

where  $\bar{R}$  is the scaled distance in m/kg<sup>1/3</sup>,  $R$  is the distance from the center of the explosive to the blast-resistant door in m, and  $w$  is the mass of ANFO explosive in kg.

In the calculation, ANFO uses the JWL (Jones–Wilkins–Lee) equation of state.

$$P = A \left( 1 - \frac{\omega\eta}{R_1} \right) e^{-R_1/\eta} + B \left( 1 - \frac{\omega\eta}{R_2} \right) e^{-R_2/\eta} + \omega\rho e, \quad (2)$$

Since both the explosive vessel and the explosive are spherical, the numerical calculation model can be simplified to a spherically symmetric model. A two-dimensional axis-symmetric wedge model similar to one-dimensional spherical symmetry is used for calculation, as shown in Figure 1. According to reference [34], it is sufficient to divide the element size into 5 mm for calculating shock wave overpressure. The model adopts the 2D multimaterial Euler algorithm of the AUTODYN-19 program. The explosive and air are filled into the wedge mesh. A rigid boundary is set at the wedge model's wide end to simulate the closed vessel's characteristics: where  $P$  is the pressure,  $\rho_0$  is the reference density,  $\rho$  is the density of detonation products, here  $\eta = \rho/\rho_0$ ,  $e$  is the internal energy per unit mass of explosive, and  $A$ ,  $B$ ,  $R_1$ ,  $R_2$ , and  $\omega$  are the parameters of the JWL equation of state. The material parameters of ANFO explosives are provided by the AUTODYN program in Table 1.

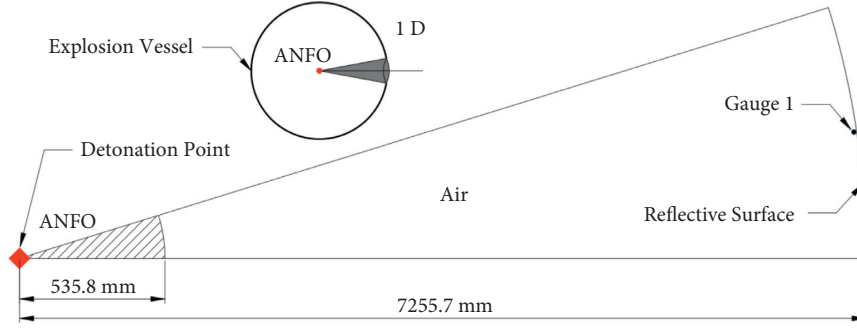


FIGURE 1: The calculation model of explosive load.

TABLE 1: Material parameters of ANFO explosive [35].

$\rho$ (kg/m <sup>3</sup> )	$D_{CJ}$ (m/s)	$P_{CJ}$ (GPa)	$E_{CJ}$ (J/m <sup>3</sup> )	$A$ (GPa)	$B$ (GPa)	$R_1$	$R_2$	$\omega$
931	4160	5.15	$2.484 \times 10^9$	49.46	1.891	3.907	1.118	1/3

The ideal gas equation of state is used for air as follows:

$$P = (\gamma - 1)\rho e, \quad (3)$$

where  $P$  is the pressure,  $\gamma$  is the adiabatic exponent,  $\rho$  is the air density, and  $e$  is the air's specific internal energy. The material parameters of air are shown in Table 2.

**2.2. Vacuum Setting.** To reduce the pressure in the explosive vessel during the actual production process, the vacuum pump was used to vacuum the vessel until the vessel's pressure dropped to 0.2 atm. In the numerical calculation, it can be seen from equation (3) that the air environment under different vacuum conditions can be approximately simulated by changing the density and specific internal energy of air in the equation of state.

Assuming that air is an ideal gas, then

$$de = c_v dT, \quad (4)$$

where  $e$  is internal energy per unit mass,  $c_v$  is the specific heat at constant volume, and  $T$  is temperature. It can be seen from equation (4) that the internal energy of the ideal gas is only a function of temperature. If the initial temperature is kept constant, the internal energy of the air must remain constant. Combined with equation (3), the pressure is a single-valued function of density under the condition of keeping the initial temperature constant. Therefore, the initial density of air at 0.2 atm can be expressed as follows:

$$\rho_{0.2} = \frac{P_{0.2}}{P_0} \rho_0, \quad (5)$$

where  $\rho_0$  is the air density under standard conditions, taking 1.225 kg/m<sup>3</sup>;  $P_0$  is the air pressure under standard conditions, taking  $1.013 \times 10^5$  Pa;  $P_{0.2}$  is the air pressure when the vacuum degree is 0.2 atm; and  $\rho_{0.2}$  is the air density when the vacuum degree is 0.2 atm. According to equation (5),  $\rho_{0.2} = 0.245$  kg/m<sup>3</sup>.

TABLE 2: Material parameters of air under standard conditions.

$\rho$ (kg/m <sup>3</sup> )	$\gamma$	$e$ (J/kg)	$T$ (K)	$c$ (J/kg·K)
1.225	1.4	$2.068 \times 10^5$	288	717.6

**2.3. Explosive Load at 0.2 atm.** In Figure 1, gauge 1 represents the position of the blast-resistant door from the center of the explosive. The explosive load at 0.2 atm at gauge 1 obtained by numerical calculation is shown in Figure 2(a). The red horizontal line indicates the residual gas pressure after explosive detonation. It can be seen from Figure 2(a) that the explosive load in the confined space fluctuates up and down along a particular value after multiple reflections. The researchers divided the internal blast loading into two stages: the shock wave reflection phase and the long quasi-static phase [36]. When the explosion shock wave is reflected inside the vessel, the latter shock wave peak overpressure and impulse are always smaller than those of the former. The final shock wave will slowly decay to the quasi-static pressure. However, considering the influence of charge shape and initiation position on shock waves during explosive working, the actual detonation process is not as utterly symmetrical as the ideal conditions. In this way, the regular reflection in Figure 2(a) cannot be generated. The internal blast loading may consist of only the first pulse wave and quasi-static pulse. Therefore, the internal blast loading is simplified in this paper. The first shock wave of the internal blast loading is taken as the input load to study the blast-resistant door's dynamic response, as shown in Figure 2(b). Here, the influence of quasi-static pressure on the dynamic response of the blast-resistant door is ignored. In the follow-up research, we will further study the influence of quasi-static pressure on the blast-resistant door's dynamic response.

**2.4. Verification of the Decoupling Algorithm.** Because of the large volume of the explosion vessel, the complete numerical

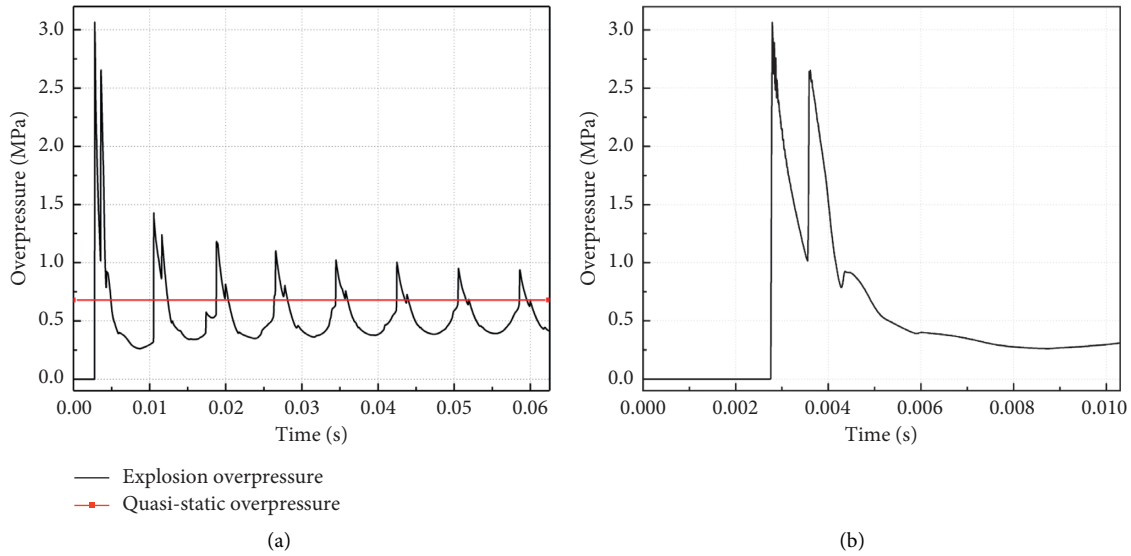


FIGURE 2: The time history curve of reflected overpressure at gauge 1: (a) explosive load at 0.2 atm and (b) simplified explosive load.

model will involve explosives, air, explosion vessels, and blast-resistant doors. The calculation model is complicated and time-consuming. To simplify the calculation, this paper uses the decoupling method to calculate the explosive load. The calculated explosive load is then applied to the blast-resistant door to calculate the blast-resistant door's dynamic response. We assume that the boundary is rigid when calculating the explosive load. However, the actual explosion vessel and blast-resistant door are deformable bodies, different from the rigid boundary. The shock wave pressure disturbance of the blast-resistant door can be calculated by the shock wave acoustic theory as follows:

$$p = \rho c u. \quad (6)$$

The yield velocity of steel is calculated as follows:

$$u_Y = \frac{\sigma_Y}{\rho_0 c_0}. \quad (7)$$

The yield strength  $\sigma_Y$  of the steel is assumed to be 400 MPa. The wave impedance  $\rho_0 c_0$  is  $4 \times 10^7 \text{ N}\cdot\text{s}/\text{m}^3$ . Then the yield velocity  $u_Y$  of the corresponding steel is 10 m/s. At this point, the disturbed air velocity  $u$  near the blast-resistant door is also 10 m/s. By substituting the air density  $\rho = 1.225 \text{ kg}/\text{m}^3$  and the sound velocity  $c = 340 \text{ m}/\text{s}$  into equation (6), the disturbance pressure  $p$  is 4165 Pa. It can be seen from Figure 2 that the peak overpressure  $\Delta p$  of the shock wave is  $3.07 \times 10^6 \text{ Pa}$ .

$$\frac{p}{\Delta p} = \frac{4165 \text{ Pa}}{3.07 \times 10^6 \text{ Pa}} \times 100\% = 0.14\%. \quad (8)$$

The calculation shows that the blast-resistant door's deformation has very little disturbance to the shock wave overpressure. The blast-resistant door can be simplified as a rigid boundary when calculating the explosive load. Therefore, the decoupling algorithm used in this paper is reasonable.

### 3. Numerical Calculation of the Blast-Resistant Door

In today's world, the rapid improvement of computer hardware performance has promoted numerical computation. The emergence of various commercial finite element software reduces the difficulty of using numerical methods to solve problems. Nowadays, the finite element method seems to have become a new calculation "standard." Many scholars compare the theoretical solutions with the finite element calculation results to verify the new theory's effectiveness [37–40]. Therefore, this paper uses the commercial finite element software LS-DYNA to calculate the blast-resistant door's dynamic response. LS-DYNA software is widely used to analyze structural impact problems because of its powerful nonlinear calculation ability and numerous material models. Many examples show that LS-DYNA is reliable in calculating structural response with damage and considerable deformation [17, 41–43].

**3.1. Structural Style.** In this paper, the elliptical blast-resistant door with the combined structure is referred to as EBD. The flat blast-resistant door is referred to as FBD. The reinforced flat blast-resistant door is referred to as RFBD. To compare the blast-resistance capacity of the EBD proposed in this paper, we compare the EBD with the common FBD and RFBD. The mass between different blast-resistant doors is equal by adjusting each part of the blast-resistant door's thickness in the research process. The FBD is made of steel plate with a thickness of 74.7 mm, as shown in Figure 3. According to the number and arrangement of stiffeners, there are five structural forms of RFBD, as shown in Figure 4. The length, height, and thickness of the RFBD's stiffener are 4,000 mm, 150 mm, and 40 mm, respectively. Its structural form is shown in Figure 4(f). The EBD is composed of an elliptical panel; four arc support plates; and four triangle support plates, with a thickness of 50 mm, as shown in

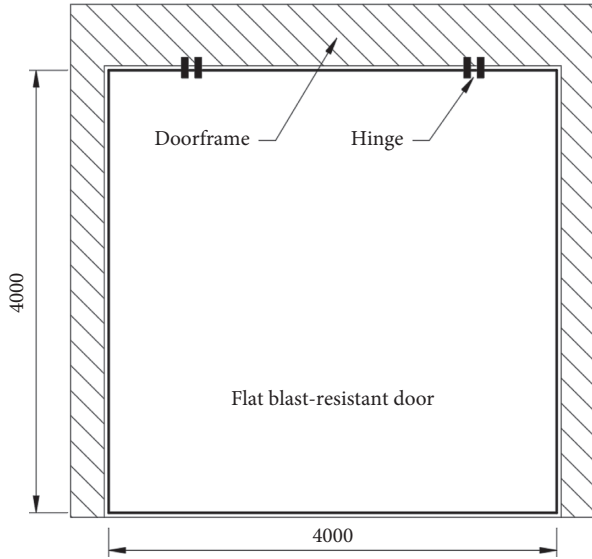


FIGURE 3: Flat blast-resistant door (FBD; unit: mm).

Figure 5. The projection dimensions of the blast-resistant doors studied in this paper are all 4,000 mm  $\times$  4,000 mm, and their specifications are shown in Table 3.

**3.2. Material Model.** The blast-resistant door is made of Q355 high-strength, low-alloy structural steel. The explosive load acting on the blast-resistant door is relatively short, about 10 ms (see Figure 2(b)). The deformation of the blast-resistant door is faster under severe dynamic load. Previous experimental studies have shown that the dynamic strength of steel is significantly higher than that of static strength, that is, the steel will show a hardening phenomenon under high-speed impact conditions. Therefore, the Johnson–Cook constitutive model in LS-DYNA is used to simulate the blast-resistant door’s dynamic behavior. The Johnson–Cook model comprehensively considers the effects of strain, strain rate, strain history, and temperature on the flow stress and multiplies and couples the parameters together. It is very suitable for the dynamic response analysis of structures under explosive load [45].

$$\sigma_y = (A + B\bar{\epsilon}_p^n)(1 + C \ln \dot{\epsilon}^*)(1 - T^{*m}), \quad (9)$$

where  $\sigma_y$  is the von Mises flow stress;  $A$ ,  $B$ ,  $C$ ,  $n$ , and  $m$  are the material parameters;  $\bar{\epsilon}_p$  is the effective plastic strain;  $\dot{\epsilon}^* = \dot{\epsilon}/\dot{\epsilon}_0$  is the normalized effective plastic strain rate;  $\dot{\epsilon}$  is the plastic strain rate;  $\dot{\epsilon}_0$  is the quasi-threshold strain rate;  $T^* = T - T_{\text{room}}/T_{\text{melt}} - T_{\text{room}}$  is the dimensionless temperature; and  $T$ ,  $T_{\text{room}}$ , and  $T_{\text{melt}}$  are the temperature during the deformation of the material, room temperature, and melt temperature, respectively. The Q355 material parameters used in the numerical calculations are shown in Table 4.

**3.3. Element, Mesh, and Boundary Condition.** Since the dimension of the thickness direction of the blast-resistant door is much smaller than that of the other two directions, the Belytschko–Tsay shell element can be used to simulate the

dynamic response of the blast-resistant door. The finite element model of the EBD is shown in Figure 6. In practical use, the blast-resistant door is fixed on the door frame by hinges and bolts. Therefore, in the numerical calculation, to approximate simulate the actual boundary conditions, the keyword \*BOUNDARY\_SPC can be used to constrain the degrees of freedom of UX, UY, and UZ around the blast-resistant door.

The accuracy of numerical calculation depends on the size of the finite element mesh. The computation result obtained by the sparse grid has a large error. Although the calculation accuracy of the dense grid is high, the calculation efficiency is low. Finite element calculation needs to find a balance between accuracy and efficiency. Therefore, to study the grid’s influence, we analyze the EBD and take the grid size of 100 mm, 50 mm, 10 mm, and 5 mm. The displacement calculation results of the mid-span node of the blast-resistant door are shown in Figure 7.

It can be seen from Figure 7 that the convergence of the calculation results is good when the grid size is reduced to 10 mm. When the grid size is further reduced to 5 mm, the calculation results of the mid-span displacement of the blast-resistant door are almost the same as those of the 10 mm grid, but the cost of computer time has increased by 12 times. From the perspective of deformation shape, the blast-resistant door mainly bears in-plane bending under the explosive load. The Belytschko–Tsay shell element adopts the single-point integration algorithm. The finer grid can more accurately simulate the bending behavior of the blast-resistant door. Hence, after comprehensively considering the accuracy and efficiency, this paper adopts a 10 mm grid to calculate the blast-resistant door’s dynamic response.

**3.4. Results and Discussion.** To determine the structure’s dynamic response under explosive load, it is necessary to calculate its displacement, stress, and strain. Figure 8 shows the displacement contour of the EBD and the RFBD2. The displacement contours of other blast-resistant doors are similar to Figure 8, which are not given here. Figure 9 shows the peak displacement in the mid-span of all blast-resistant doors. It can be seen from Figure 9 and Table 5 that the peak displacement of the RFBD is smaller than that of the FBD. It indicates that the reinforcement can improve the blast-resistant door’s blast-resistance capacity, but the improvement is relatively small compared with the EBD. Except for RFBD3, the peak displacement of other RFBD decreases gradually with the increase of the number of stiffening ribs. The reason is that the stiffening rib bears part of the explosive load, which changes the mechanical characteristics of the blast-resistant door, thus improving its overall flexural rigidity. The peak displacement response of the RFBD3 is smaller than that of the RFBD4. The reason is that the mid-span measuring point of the RFBD3 is just at the longitudinal rib and the transverse rib intersection. When the stiffening ribs are arranged as RFBD5, the peak displacement of the RFBD is the smallest, which is 66.8 mm and 11.8% less than that of the FBD. The EBD peak displacement is 5.1 mm, 93.3% less than that of the FBD, and 92.4% less than that of

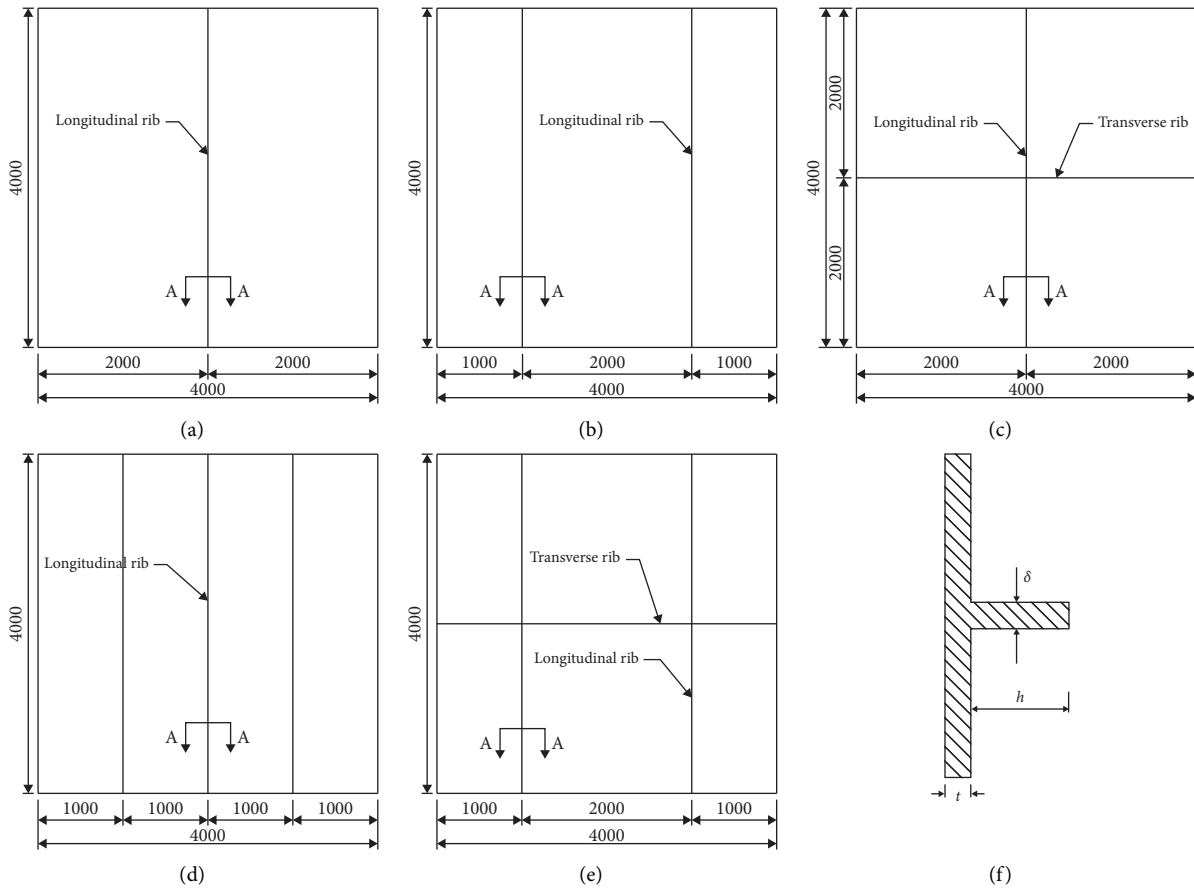


FIGURE 4: Reinforced flat blast-resistant door (RFB; unit: mm): (a) one longitudinal rib (RFB1), (b) two longitudinal ribs (RFB2), (c) one longitudinal rib and one transverse rib (RFB3), (d) three longitudinal ribs (RFB4), (e) two longitudinal ribs and one transverse rib (RFB5), and (f) section A-A.

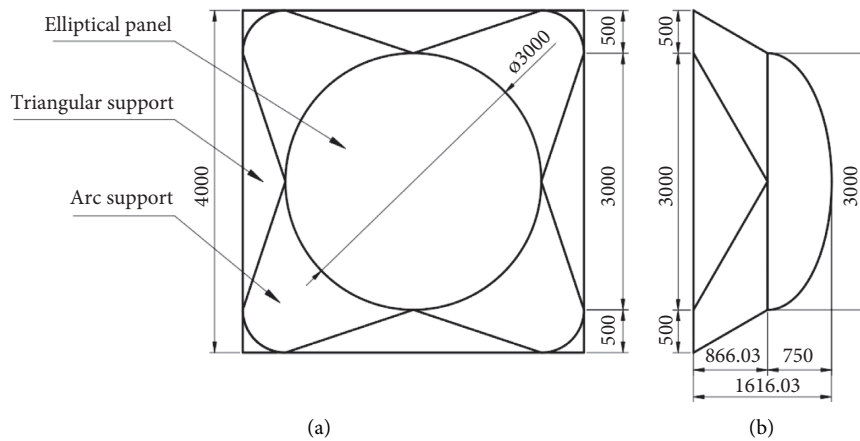


FIGURE 5: Elliptical blast-resistant door with the combined structure (EBD; unit: mm): (a) front view and (b) side view.

the RFB5. The time history curve of mid-span displacement of the blast-resistant door is shown in Figure 10. It can be seen from Figure 10 that the vibration period of the EBD is much smaller than that of the FBD and the RFB. The smaller the vibration period of the blast-resistant door with the same mass, the greater the structure's rigidity and the

stronger the ability to resist deformation, that is, the better the blast-resistance capacity. Therefore, the EBD proposed in this paper has better blast-resistance capacity.

Figures 11–13 show the maximum von Mises stress and effective plastic strain of the blast-resistant doors with different structural forms under explosive load. In Figure 11,

TABLE 3: Parameters of different blast-resistant doors.

Type	Longitudinal rib	Transverse rib	Thickness $t$ (mm)
FBD	—	—	74.7
RFBD1	1	0	73.2
RFBD2	2	0	71.7
RFBD3	1	1	71.7
RFBD4	3	0	70.2
RFBD5	2	1	70.2
EBD	—	—	50.0

TABLE 4: Material parameters of the Q355 steel [44].

$\rho$ (kg/m <sup>3</sup> )	$E$ (GPa)	$\nu$	$A$ (MPa)	$B$ (MPa)	$n$	$m$	$C$	$\dot{\epsilon}_0$	$T_{\text{room}}$ (K)	$T_{\text{melt}}$ (K)
7,850	206	0.28	339.45	620	0.403	0.659	0.02	$1.333 \times 10^{-3}$	293	1,800

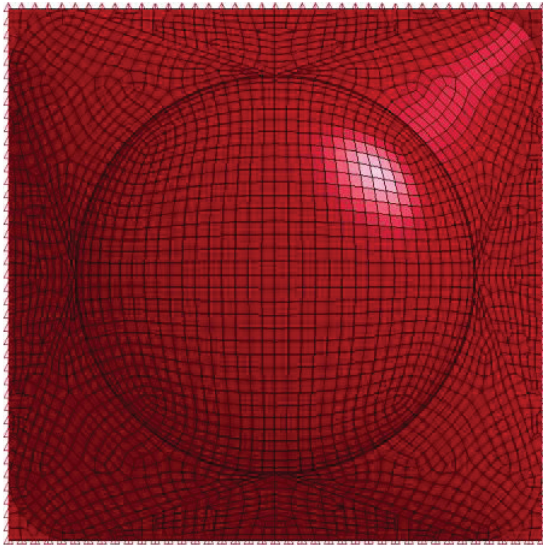


FIGURE 6: Finite element model with boundary conditions (mesh size: 100 mm).

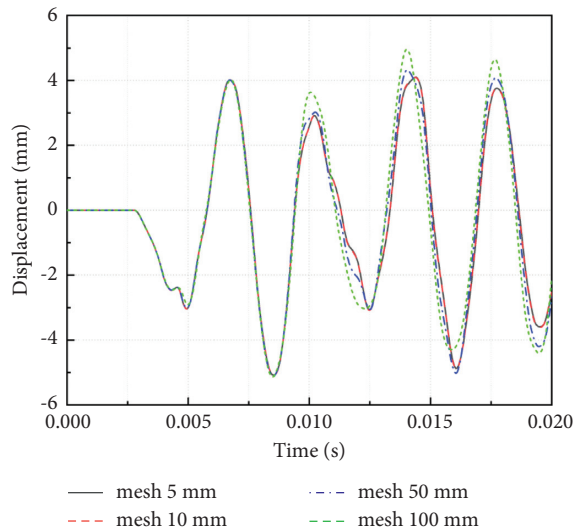


FIGURE 7: Displacement time history curves of different mesh sizes.

the stress distribution of the FBD is not uniform, but a sizeable high-stress area appears in the central area. The FBD yields from the center and extends to the surroundings with the maximum effective plastic strain of 0.14%. The von Mises stress contour and effective plastic strain contour of the RFBD5 with the smallest mid-span peak displacement are shown in Figure 12. The maximum von Mises stress of the RFBD5 occurs in the stiffening ribs with a value of 454.2 MPa, which indicates that the stiffening ribs are subjected to a large load during the blast loading and resulted in a large plastic deformation in this region with maximum effective plastic deformation of 0.52%. In Figure 13, the maximum stress occurs at the joint between the elliptical panel and the arc support plate, where the maximum von Mises stress is 437.6 MPa. None of the von Mises stresses in the rest of the EBD exceed 270 MPa, much less than the static yield strength of Q355 steel. The reason is that the horizontal reaction force is generated at the joint between the elliptical panel and the arc support plate under explosive load. This force and the vertical force together cause high stress at the joint (here is an orthogonal decomposition of the force at the joint. In fact, the joint is subjected to the resultant force). In the subsequent optimization design, the internal force at the joint between the elliptical panel and the arc support plate can be reduced by providing stiffening ribs or changing the elliptical minor axis's diameter. As shown in Figure 13 and Table 5, the maximum effective strain of the EBD occurs at the maximum stress of the blast-resistant door, with a magnitude of 0.11%. It indicates that the plastic deformation occurring here is extremely small. Except for the joint between the elliptical panel and the arc support plate, the rest of the EBD is in the state of perfect elasticity deformation. Overall, the maximum von Mises stress and effective plastic strain of the EBD are less than those of the FBD and the RFBD.

From the above analysis, it can be seen that the stress distribution of the EBD proposed in this paper is relatively uniform. Moreover, the von Mises stress in most areas of the EBD is much less than the static yield strength of the blast-resistant door material. It leaves greater safety redundancy for the blast-resistant door design. Under the same 0.2 atm vacuum explosive load, the displacement response of the

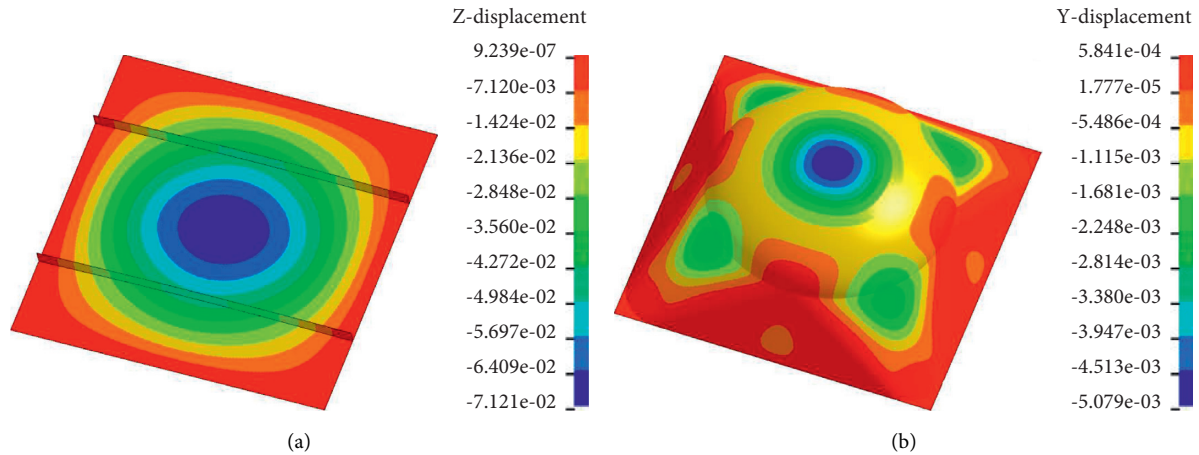


FIGURE 8: Displacement contour of the blast-resistant door: (a) RFBFD2 and (b) EBD.

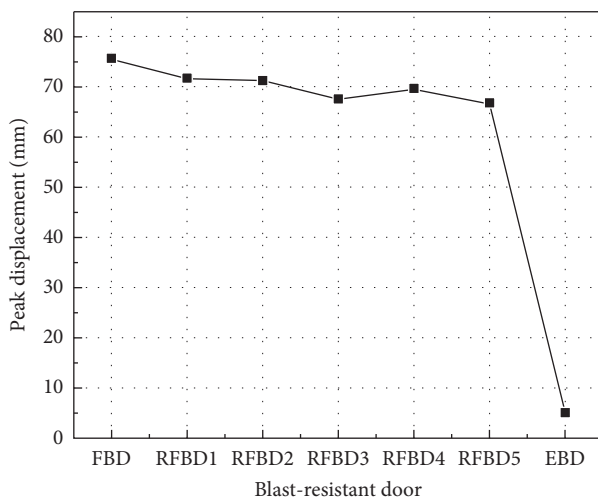


FIGURE 9: Peak displacement of different blast-resistant doors.

EBD is smaller than that of the FBD and the RFBFD. It indicates that the EBD has a better blast-resistance capacity. However, the careful analysis also found a slight plastic deformation at the joint between the elliptical panel and the arc support plate of the EBD, so it can be further optimized to achieve better blast resistance performance.

#### 4. Parametric Study of the EBD

The dynamic response of the EBD is influenced by three factors: the vacuum degree of the explosive vessel, the number of explosives during the explosion working, and the diameter ratio of the EBD. In this section; these factors are analyzed one by one to achieve the optimum blast-resistant structure for the EBD. The EBD's loading mode, material model, element type, mesh size, and boundary conditions are similar to those in the previous section.

**4.1. Effect of Vacuum Degree.** The internal blast loading under different vacuum degrees is shown in Figure 14. It can

be seen from Figure 14 that there are two distinct peaks for each explosive load pulse. The first peak is an air shock wave formed by the detonation product compressed air. The second peak is a shock wave formed by the expansion of the detonation product. With the decrease of the vacuum degree inside the explosion vessel, the first peak of the internal blast loading decreases gradually. In contrast, the second peak caused by the detonation product increases gradually. Overall, the smaller the vacuum degree is, the faster the decay of the internal blast loading is, that is, the smaller the slope of the load impulse curve in Figure 14. The explosive load under different vacuum degrees calculated in Figure 14 is applied as an input load to act on the EBD. The calculated dynamic response of the EBD is given in Table 6. The time history curve of the mid-span displacement is illustrated in Figure 15. The 1 and 2 marked in Figure 15 represent the first and second peaks of the displacement response, respectively.

As can be seen in Figure 15 and Table 6, except for the second peak of the displacement response at 0.2 atm, the peak displacement, the maximum von Mises stress, and the maximum effective plastic strain of the EBD gradually decrease with the decrease of the vacuum degree inside the explosion vessel. When the vacuum degree is 0.2 atm, the second peak displacement of the EBD is 5.08 mm. When the vacuum degree is 0.4 atm, the second peak displacement of the EBD is 4.92 mm. Here, the second peak displacement of the EBD at 0.2 atm is slightly greater than that at 0.4 atm. The reason is that when the vacuum degree inside the explosion vessel is reduced to 0.2 atm, the air becomes relatively thin, and the overpressure of shock waves caused by air is relatively small. However, the shock wave overpressure at 0.2 atm caused by the detonation product is 1.3 times higher than that at 0.4 atm. The second peak on the displacement time history curve is caused by the detonation product's shock wave overpressure.

In this section, the dynamic response of the EBD is analyzed at 0.2 atm, 0.4 atm, 0.6 atm, 0.8 atm, and 1 atm. After a comparative study, it is found that reducing the ambient pressure helps improve the blast-resistance capacity of the structure. The maximum von Mises stress contour of the EBD at 1 atm is given in Figure 16. Compared with Figure 13, the



TABLE 5: Peak displacement, von Mises stress, and effective plastic strain.

Type	Peak displacement (mm)	Maximum von Mises stress (MPa)	Maximum effective plastic strain (%)
FBD	75.7	434.7	0.14
RFBD1	71.8	453.4	0.58
RFBD2	71.2	430.6	0.47
RFBD3	67.5	455.4	0.49
RFBD4	69.6	449.5	0.48
RFBD5	66.8	454.2	0.52
EBD	5.1	437.6	0.11

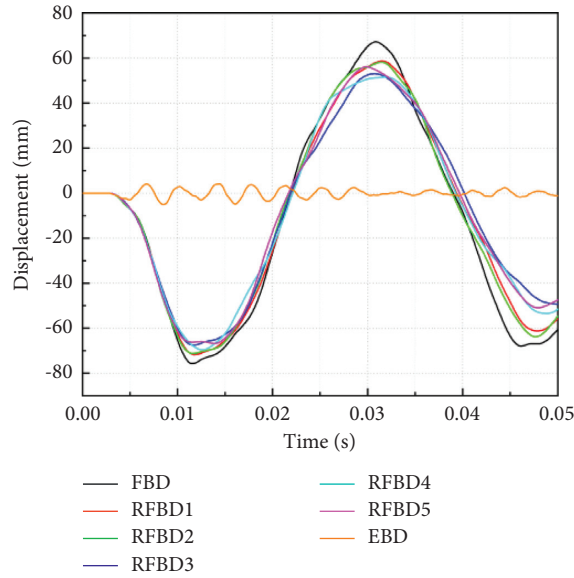


FIGURE 10: Displacement time history curves of different blast-resistant doors.

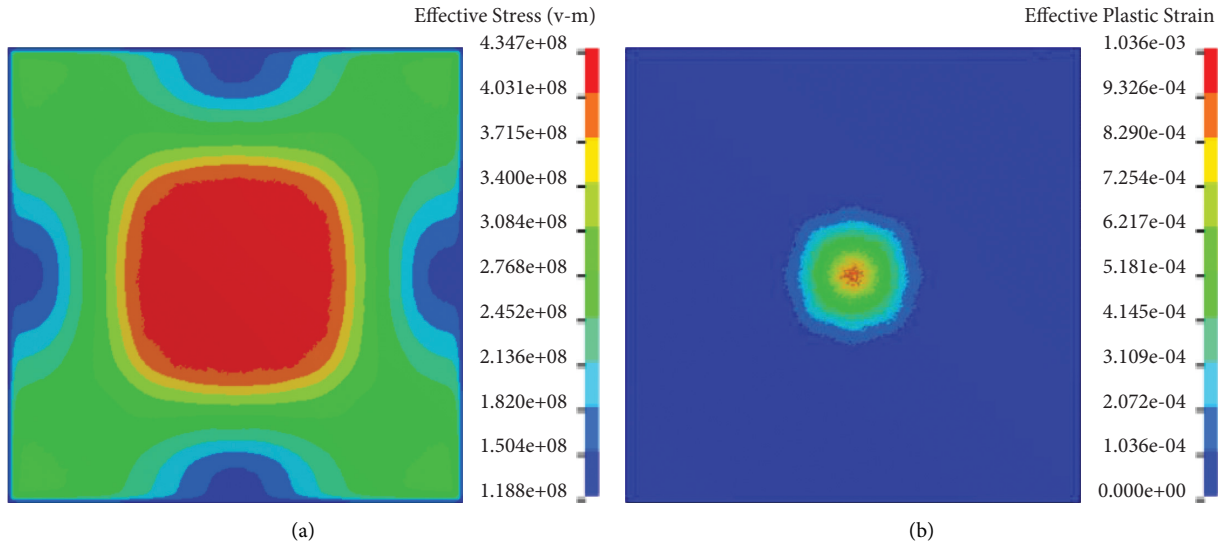


FIGURE 11: (a) von Mises stress and (b) effective plastic strain of the FBD.

EBD generates higher stress at the joint between the elliptical panel and the arc support plate and along the joint between the triangle support plate and the arc support plate. It shows the transfer process of explosive load on the EBD. That is to say, and the explosive load is first transferred from the elliptical

panel to the arc support plate, then from the arc support plate to the triangle support plate, and finally to the support. Figure 17 shows the maximum effective plastic strain contour of the EBD at 1 atm. It can be seen from Figure 17 that with the increase of explosive load, the EBD produces great plastic

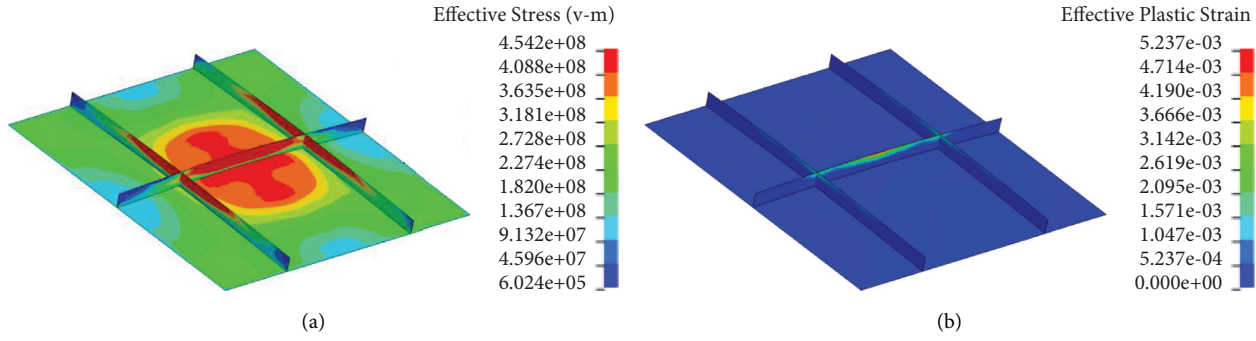


FIGURE 12: (a) von Mises stress and (b) effective plastic strain of the RFBD5.

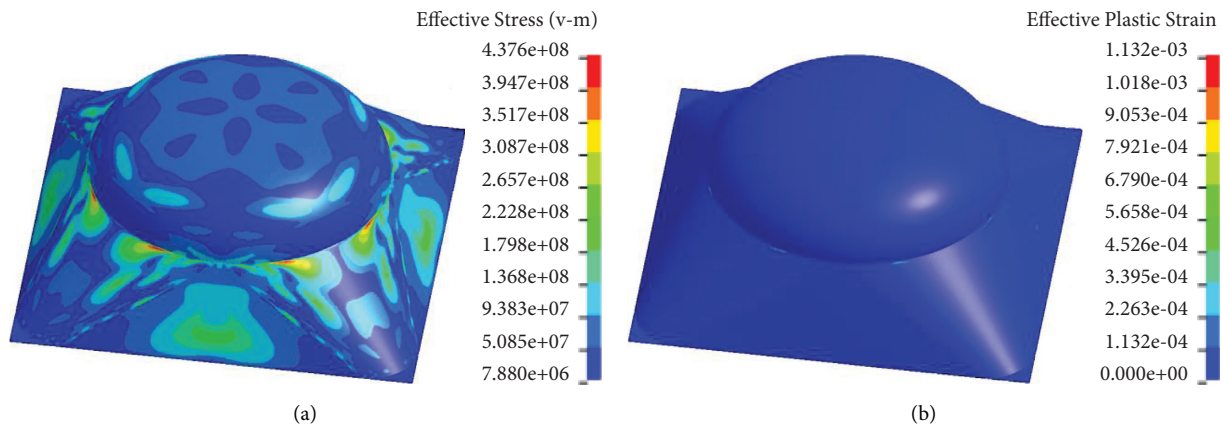


FIGURE 13: (a) von Mises stress and (b) effective plastic strain of the EBD.

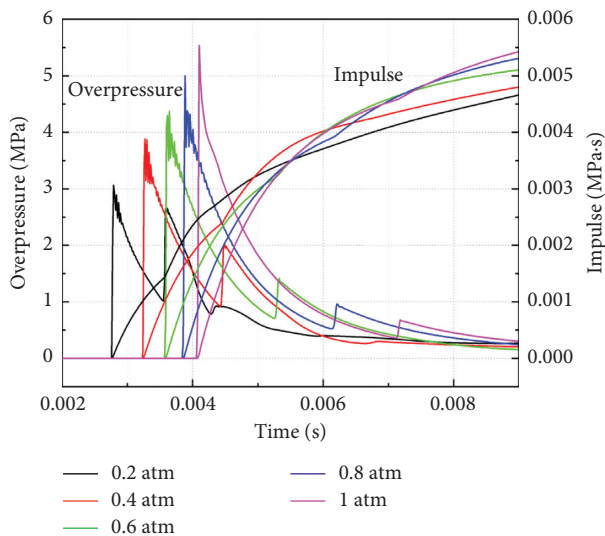


FIGURE 14: Explosive load under different vacuum degrees.

deformation in the high-stress area of the structural joint. Furthermore, the EBD also produces great plastic deformation in the middle of the triangle support plate. Therefore, these places with large plastic deformation should be strengthened in the design of the EBD.

**4.2. Effect of Explosive Quantity.** The vacuum degree in the explosion vessel is kept unchanged, which is 0.2 atm. The explosive load acting on the blast-resistant door with 200 kg, 400 kg, 600 kg, and 800 kg charges are calculated by changing the number of explosives. When the explosive quantity is 600 kg, the dynamic response of the EBD has been calculated in Section 3. Figure 18 shows the explosive load under different explosive quantities. It can be seen in Figure 18 and Table 7 that when the explosive quantity increases from 200 kg to 800 kg, the peak overpressure increases from 1.57 MPa to 4.33 MPa, which increases by 2.76 times, while the action time of the explosive load decreases slightly. The mid-span displacement time history curve of the EBD under different explosive quantities is shown in Figure 19. As can be seen from Figure 19, when the explosive quantity decreases from 800 kg to 200 kg, the first peak of the EBD's displacement decreases from 3.76 mm to 1.10 mm, reducing by 70.7%; the second peak of the EBD's displacement decreases from 6.09 mm to 1.85 mm, reducing by 69.6%. It indicates that reducing the explosive quantity can improve the blast-resistance capacity of the EBD. Table 7 gives the peak displacement, the maximum von Mises stress, and the maximum effective plastic strain of the EBD under different explosive quantities. It can be seen from Table 7 that when the explosive quantity is 200 kg, the EBD is in a state of

TABLE 6: Displacement, von Mises stress, and effective plastic strain of the EBD under different vacuum degrees.

Vacuum degree (atm)	Load (MPa)		Displacement (mm)		Maximum von Mises stress (MPa)	Maximum effective plastic strain (%)
	Air	Detonation product	First peak	Second peak		
0.2	3.07	2.65	3.03	5.08	437.6	0.11
0.4	3.88	2.04	3.27	4.92	456.6	0.22
0.6	4.37	1.42	3.32	5.36	489.4	0.54
0.8	5.00	0.96	3.51	6.62	503.7	0.93
1	5.54	0.68	3.79	7.45	510.3	1.03

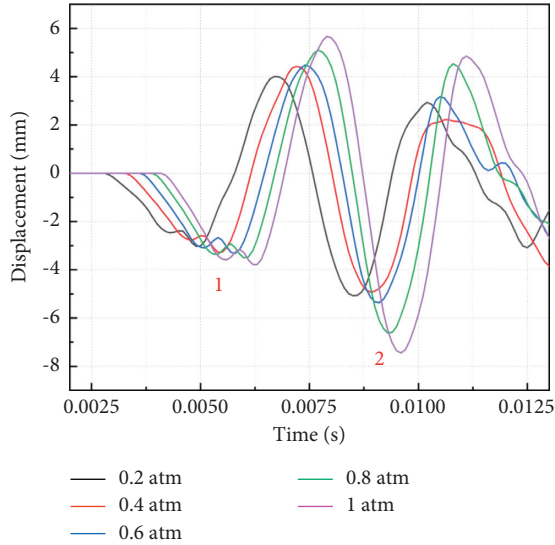


FIGURE 15: The mid-span displacement time history curve of the EBD under different vacuum degrees.

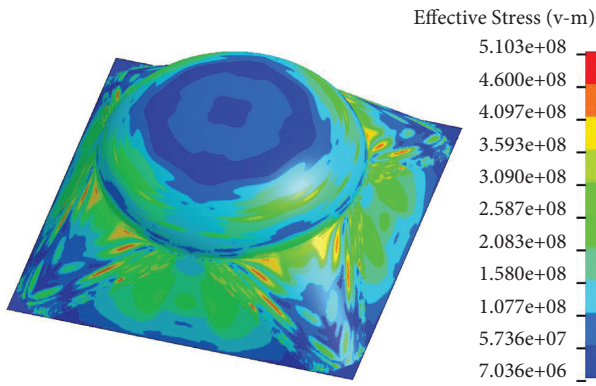


FIGURE 16: The maximum von Mises stress contour of the EBD at 1 atm.

perfect elasticity deformation. When the explosive quantity is 800 kg, the maximum von Mises stress and the maximum effective plastic strain of the EBD are 456.8 MPa and 0.24%, respectively. Although the explosion vessel's maximum design charge is 600 kg ANFO explosive, the EBD is still in a small plastic deformation state when the explosive quantity is 800 kg. Its plastic strain is far less than the fracture strain of Q355 steel, so the EBD will not fracture suddenly. Taken together, during the explosive working, the explosive load

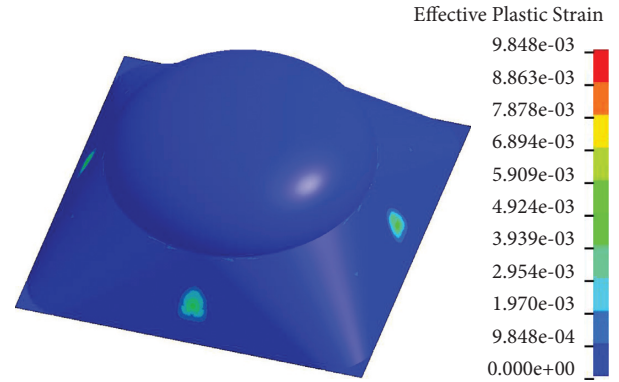


FIGURE 17: The maximum effective plastic strain contour of the EBD at 1 atm.

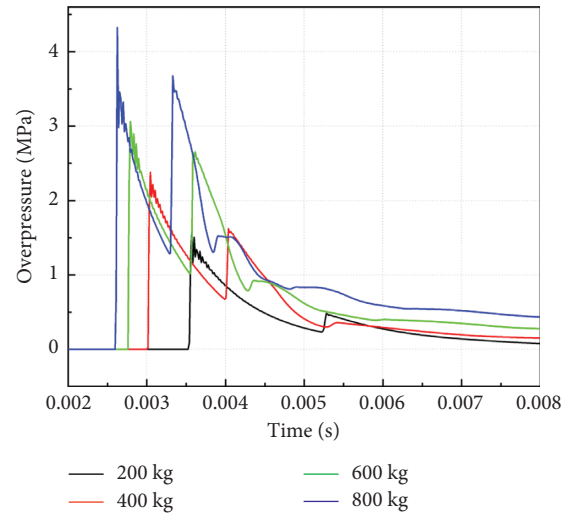


FIGURE 18: Explosive load under different explosive quantities.

acting on the blast-resistant door can be reduced by regulating the explosive quantity. In this way, it can ensure that the EBD can work under the safe explosive quantity.

4.3. *Effect of Diameter Ratio.* In this section, the blast-resistance capability of the EBD with four different diameter ratios of 1:0.25, 1:0.5, 1:0.75, and 1:1 is analyzed. The elliptical panel's major axis diameter is always 3,000 mm, and different diameter ratios are achieved by changing the minor axis diameter. When the diameter ratio is 1:0.25, 1:0.5, 1:

TABLE 7: Displacement, von Mises stress, and effective plastic strain of the EBD under the different explosive quantities.

Explosive quantity (kg)	Load		Peak displacement (mm)		Maximum von Mises stress (MPa)	Maximum effective plastic strain (%)
	Peak overpressure (MPa)	Action time (ms)	First peak	Second peak		
200	1.57	13.0	1.10	1.85	317.9	0
400	2.38	11.0	2.17	3.55	412.7	0.02
600	3.07	10.5	3.03	5.08	437.6	0.11
800	4.33	10.0	3.76	6.09	456.8	0.24

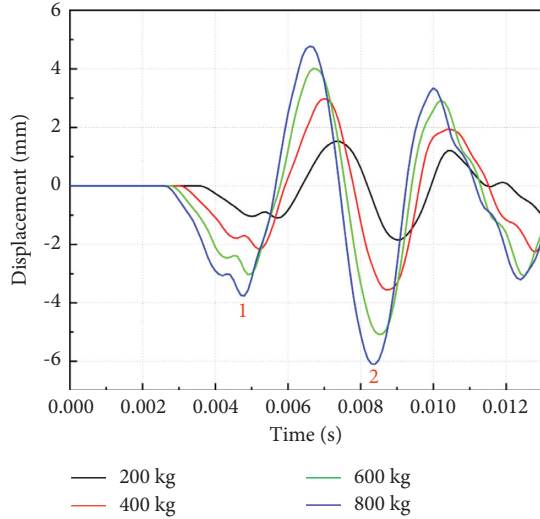


FIGURE 19: The mid-span displacement time history curve of the EBD under the different explosive quantities.

0.75, and 1:1, then the elliptical panel's corresponding minor axis diameter is 750 mm, 1,500 mm, 2,250 mm, and 3,000 mm, respectively. In this paper, the EBD's mass with different diameter ratios is kept equal by adjusting the steel plate's thickness. The thickness dimensions are shown in Table 8. The EBD with a diameter ratio of 1:0.5 has been calculated in Section 3. The mid-span displacement time history curve of the EBD with different diameter ratios is shown in Figure 20. Table 8 gives the peak displacement, the maximum von Mises stress, and the maximum effective plastic strain of the EBD with different diameter ratios. It can be seen in Figure 20 and Table 8 that by changing the EBD's diameter ratio (i.e., increasing minor axis diameter), the mid-span peak displacement of the EBD gradually decreases, and the vibration period of the displacement curve also gradually decreases accordingly. It indicates that increasing the diameter of the EBD's minor axis can improve their flexural rigidity. When the diameter ratio is 1:0.25, the maximum von Mises stress and the maximum effective plastic strain of the EBD are the smallest among the four structures, but the peak displacements are the largest. When the minor axis diameter of the EBD is greater than 750 mm, the maximum von Mises stress and the maximum effective plastic strain of the EBD with the diameter ratio of 1:0.75 are both less than those with the diameter ratio of 1:0.5 and 1:1. In summary, the optimum diameter ratio of the EBD proposed in this paper is 1:0.75.

TABLE 8: Displacement, von Mises stress, and effective plastic strain of the EBD with different diameter ratios.

Diameter ratio	Thickness (mm)	Peak displacement (mm)	Maximum von Mises stress (MPa)	Maximum effective plastic strain
1:0.25	53.9	9.44	397.3	$5.93 \times 10^{-6}$
1:0.5	50.0	5.08	437.6	$1.13 \times 10^{-3}$
1:0.75	46.0	2.85	424.3	$5.33 \times 10^{-4}$
1:1	42.3	2.76	454.1	$2.42 \times 10^{-3}$

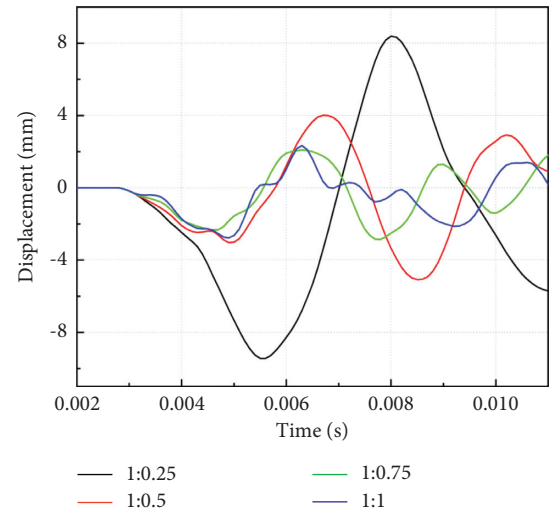


FIGURE 20: The mid-span displacement time history curve of the EBD with different diameter ratios.

## 5. Conclusions

This paper proposes an elliptical blast-resistant door with the combined structure for the large vacuum explosion container consisting of an elliptical panel, four arc support plates, and four triangle support plates. The following conclusions are drawn from the numerical calculations:

- (1) The decoupling method is reasonable for solving the dynamic response of the large vacuum explosion container's blast-resistant door. It can significantly reduce the calculation amount of the project and provide a reference for similar engineering problems.

- (2) The peak displacement of the elliptical blast-resistant door with the combined structure is 93.3% less than that of the flat blast-resistant door and 92.4% less than that of the reinforced flat blast-resistant door with the smallest peak displacement (RFBD5). By analyzing the stress and strain, the maximum von Mises stress and the maximum effective plastic strain of the elliptical blast-resistant door with the combined structure are smaller than those of the flat plate blast-resistant door and the reinforced flat blast-resistant door. It indicates that the blast-resistance capacity of the elliptical blast-resistant door with the combined structure proposed in this paper is better than that of the traditional blast-resistant door.
- (3) The parametric analysis shows that the blast-resistance capacity of the elliptical blast-resistant door with the combined structure can be improved effectively by reducing the vacuum degree in the explosion vessel and the number of explosives during the explosion working. During the production of explosion working, the vacuum degree should be controlled not greater than 0.2 atm, and the explosive quantity should not be greater than 600 kg.
- (4) By analyzing the peak displacement, the maximum von Mises stress, and the maximum effective plastic strain, it is determined that the optimum diameter ratio of the elliptical blast-resistant door with the combined structure is 1:0.75.

## Data Availability

The data used to support the findings of this study are included within the article.

## Conflicts of Interest

The authors declare that they have no conflicts of interest.

## Acknowledgments

This work was supported by the National Natural Science Foundation of China (Nos. 12172084, 12072067, and 11672067).

## References

- [1] J. S. Rinehart and J. Pearson, *Explosive Working of Metals*, Pergamon Press, New York, NY, USA, 1963.
- [2] A. Maranda, J. Nowaczewski, and A. Przetakiewicz, "Explosive strengthening of the surface layer in St72P steel rails," *Journal of Materials Processing Technology*, vol. 34, no. 1–4, pp. 241–245, 1992.
- [3] Z. Tong, Z. M. Shi, S. J. Tong, D. W. Wang, and P. F. Li, "Surface nanocrystallization, austenization and hardening of medium carbon steel by an explosive impact technique," *Surface and Coatings Technology*, vol. 251, pp. 293–299, 2014.
- [4] H. Wang, Z. Shi, X. Yaer, Z. Tong, and Z. Du, "High mechanical performance of AISI304 stainless steel plate by surface nanocrystallization and microstructural evolution during the explosive impact treatment," *Journal of materials research and technology*, vol. 8, no. 1, pp. 609–614, 2019.
- [5] B. Crossland, *Explosive Welding of Metals and its Application*, Clarendon Press, Oxford, England, 1982.
- [6] Y. Wang, X. Li, X. Wang, and H. Yan, "Fabrication of a thick copper-stainless steel clad plate for nuclear fusion equipment by explosive welding," *Fusion Engineering and Design*, vol. 137, pp. 91–96, 2018.
- [7] X.-y. Zeng, X.-j. Li, X. Chen, X.-h. Wang, and H.-h. Yan, "Numerical and experimental studies on the explosive welding of plates with different initial strength," *Welding in the World*, vol. 63, 2019.
- [8] X. Chen, X. Li, X. Wang, H. Yan, K. Li, and X. Zeng, "Bonding mechanism of explosive compaction-welding sintering," *Journal of Manufacturing Processes*, vol. 46, pp. 1–15, 2019.
- [9] S. Vorozhtsov, A. Vorozhtsov, O. Kudryashova, I. Zhukov, and V. Promakhov, "Structural and mechanical properties of aluminium-based composites processed by explosive compaction," *Powder Technology*, vol. 313, pp. 251–259, 2017.
- [10] A. Y. Cui, F. Y. Hu, H. K. Wei, H. D. Liu, Z. Wang, and X. L. Dong, "Research on rapid shaped-charge cutting technology of aircraft damaged thin-wall structures," *Strength of Materials*, vol. 48, no. 1, pp. 58–62, 2016.
- [11] N. Narimanzadeh, A. Darvizeh, M. Darvizeh, and H. Gharababaei, "Modelling of explosive cutting process of plates using GMDH-type neural network and singular value decomposition," *Journal of Materials Processing Technology*, vol. 128, no. 128, pp. 80–87, 2002.
- [12] H. Wegener, H. U. Freund, and S. Schumann, "Explosive cutting of thick-walled steel pipes in the reactor HDR," *Nuclear Engineering and Design*, vol. 118, no. 1, pp. 87–97, 1990.
- [13] X. Li, X. Li, X. Wang, X. Pan, and H. Yan, "Characterization of carbon-encapsulated permalloy nanoparticles prepared through detonation," *Materials Research Express*, vol. 4, no. 7, Article ID 075024, 2017.
- [14] K. V. Volkov, V. V. Danilenko, and V. I. Elin, "Synthesis of diamond from the carbon in the detonation products of explosives," *Combustion, Explosion and Shock Waves*, vol. 26, no. 3, pp. 366–368, 1990.
- [15] Q. Xiaoyong, *The Study on Large Scale Hemispherical Shock-Waves Trap Structure for Explosive Welding*, Dalian University of Technology, Dalin, China, 2008.
- [16] X. Luo, X. Qian, H. Zhao, and P. Huang, "Simulation analysis on structure safety of refuge chamber door under explosion load," *Procedia Engineering*, vol. 45, pp. 923–929, 2012.
- [17] W. Chen and H. Hao, "Numerical study of a new multi-arch double-layered blast-resistance door panel," *International Journal of Impact Engineering*, vol. 43, pp. 16–28, 2012.
- [18] C. G. Koh, K. K. Ang, and P. F. Chan, "Dynamic analysis of shell structures with application to blast resistant doors," *Shock and Vibration*, vol. 10, no. 4, pp. 269–279, 2003.
- [19] G. Dong, L. Jinbo, and Z. Xiaobo, "Resistance parameters analysis and dynamic response for a steel blast door subjected to blast loading," *Journal of Vibration and Shock*, vol. 32, no. 03, pp. 134–140+156, 2013.
- [20] R. P. Mcbean, *Analysis of Stiffened Plates by the Finite Element Method*, p. 164, Stanford University, Stanford, CA, USA, 1968.
- [21] M. M. Alinia and S. H. Moosavi, "A parametric study on the longitudinal stiffeners of web panels," *Thin-Walled Structures*, vol. 46, no. 11, pp. 1213–1223, 2008.
- [22] E. Maiorana, C. Pellegrino, and C. Modena, "Influence of longitudinal stiffeners on elastic stability of girder webs,"

- Journal of Constructional Steel Research*, vol. 67, no. 1, pp. 51–64, 2011.
- [23] Y. Pan and L. A. Louca, “Experimental and numerical studies on the response of stiffened plates subjected to gas explosions,” *Journal of Constructional Steel Research*, vol. 52, no. 2, pp. 171–193, 1999.
- [24] P. R. Sahoo and M. Barik, “Free vibration analysis of stiffened plates,” *Journal of Vibration Engineering & Technologies*, vol. 8, 2020.
- [25] Z. Boyi, Z. Dongxian, S. Jian, and W. Wei, “Numerical simulation on dynamic response of blast-resistant door with built-in aluminum matrix syntactic foam,” *Acta Armamentarii*, vol. 35, no. S2, pp. 263–267, 2014.
- [26] Z. Zhao, B. Zhang, F. Jin, J. Zhou, H. Chen, and H. Fan, “BFRP reinforcing hierarchical stiffened SMC protective structure,” *Composites Part B: Engineering*, vol. 168, pp. 195–203, 2019.
- [27] Z. Zhao, B. Zhang, J. Zhou et al., “Quasi-far-field blast responses of hierarchical orthogrid-stiffened sheet molding compound (SMC) protective door structures,” *Engineering Structures*, vol. 168, pp. 431–446, 2018.
- [28] W. E. Baker, P. A. Cox, P. S. Westine, J. J. Kulesz, and R. A. Strehlow, *Explosion Hazards and Evaluation*, Elsevier Scientific Pub. Co, Amsterdam, Netherlands, 1983.
- [29] P. C. Chan and H. H. Klein, “A study of blast effects inside an enclosure,” *Journal of Fluids Engineering*, vol. 116, no. 3, pp. 181–189, 1994.
- [30] C. Geretto, S. Chung Kim Yuen, and G. N. Nurick, “An experimental study of the effects of degrees of confinement on the response of square mild steel plates subjected to blast loading,” *International Journal of Impact Engineering*, vol. 79, no. may, pp. 32–44, 2015.
- [31] W. Olson, I. Patterson, and J. Williams, “The effect of atmospheric pressure on the reflected impulse from air blast waves,” *Army Ballistic Research Lab Aberdeen Proving Ground, MD*, 1960.
- [32] R. G. Sachs, “The dependence of blast on ambient pressure and temperature,” *Army Ballistic Research Lab Aberdeen Proving Ground, MD*, 1944.
- [33] R. L. Veldman, M. W. Nansteel, C. C.-T. Chen, and B. A. Toner, “The effect of ambient pressure on blast reflected impulse and overpressure,” *Experimental Techniques*, vol. 41, no. 3, pp. 227–236, 2017.
- [34] J. Shin, A. S. Whittaker, D. Cormie, and W. Wilkinson, “Numerical modeling of close-in detonations of high explosives,” *Engineering Structures*, vol. 81, pp. 88–97, 2014.
- [35] L. Davis and L. Hill, *ANFO cylinder Tests, AIP Conference Proceedings*, pp. 165–168, American Institute of Physics, College park, MD, USA, 2002.
- [36] C. E. Anderson, W. E. Baker, D. K. Wauters, and B. L. Morris, “Quasi-static pressure, duration, and impulse for explosions (e.g. HE) in structures,” *International Journal of Mechanical Sciences*, vol. 25, no. 6, pp. 455–464, 1983.
- [37] W.-K. Sun, L.-W. Zhang, and K. M. Liew, “A smoothed particle hydrodynamics-peridynamics coupling strategy for modeling fluid-structure interaction problems,” *Computer Methods in Applied Mechanics and Engineering*, vol. 371, Article ID 113298, 2020.
- [38] S. C. White, G. Raju, and P. M. Weaver, “Initial post-buckling of variable-stiffness curved panels,” *Journal of the Mechanics and Physics of Solids*, vol. 71, pp. 132–155, 2014.
- [39] D. M. Li, C. A. Featherston, and Z. Wu, “An element-free study of variable stiffness composite plates with cutouts for enhanced buckling and post-buckling performance,” *Computer Methods in Applied Mechanics and Engineering*, vol. 371, Article ID 113314, 2020.
- [40] K. Liew and T. Teo, “Modeling via differential quadrature method: three-dimensional solutions for rectangular plates,” *Computer Methods in Applied Mechanics and Engineering*, vol. 159, no. 3-4, pp. 369–381, 1998.
- [41] R. Barauskas and A. Abraitienė, “Computational analysis of impact of a bullet against the multilayer fabrics in LS-DYNA,” *International Journal of Impact Engineering*, vol. 34, no. 7, pp. 1286–1305, 2007.
- [42] W. Rust and K. Schweizerhof, “Finite element limit load analysis of thin-walled structures by ANSYS (implicit), LS-DYNA (explicit) and in combination,” *Thin-Walled Structures*, vol. 41, no. 2-3, pp. 227–244, 2003.
- [43] B. A. Gama and J. W. Gillespie, “Finite element modeling of impact, damage evolution and penetration of thick-section composites,” *International Journal of Impact Engineering*, vol. 38, no. 4, pp. 181–197, 2011.
- [44] Z. Yu, *Research on Dynamic Constitutive Relationship of Q355B Steel Based on Johnson-Cook Model*, Harbin University of Science and Technology, Harbin, China, 2019.
- [45] G. R. Johnson and W. H. Cook, “Fracture characteristics of three metals subjected to various strains, strain rates, temperatures and pressures,” *Engineering Fracture Mechanics*, vol. 21, no. 1, pp. 31–48, 1985.

## Research Article

# A Case Study on the Deformation of Metro Foundation Pit in Silt Stratum in North China

Yonggang Zhang <sup>1</sup>, Yonghong Wang,<sup>2</sup> and Yuanyuan Zhao <sup>3</sup>

<sup>1</sup>School of Civil Engineering, Beijing Jiaotong University, Beijing 100044, China

<sup>2</sup>Key Laboratory of Urban Underground Engineering, Ministry of Education, Beijing Jiaotong University, Beijing 100044, China

<sup>3</sup>School of Civil Engineering, Hebei University of Science and Technology, Shijiazhuang 050000, Hebei, China

Correspondence should be addressed to Yuanyuan Zhao; zhaoyuanyuan@hebestu.edu.cn

Received 27 July 2021; Accepted 24 September 2021; Published 28 October 2021

Academic Editor: Shan Gao

Copyright © 2021 Yonggang Zhang et al. This is an open access article distributed under the Creative Commons Attribution License, which permits unrestricted use, distribution, and reproduction in any medium, provided the original work is properly cited.

Geological conditions of urban subway foundation pits are controllable factors in determining the deformation of pits. In this paper, the monitoring data and statistical data of a subway deep foundation pit in North China are presented and compared with those of Tianjin subway. The deformation characteristics of the proposed pit, open excavated with triple-layer steel supports, are introduced in detail. Based on the aforementioned information, the energy conservation equation of the mobilized strength design (MSD) method in which the compression deformation energy of internal support is considered is applied to predict the maximum lateral movement. The maximum lateral movement turns out to be 22.2 mm according to the improved MSD method, which is very close to the measured value.

## 1. Introduction

In the construction of metro, the deformation control of deep pit is one of the most crucial topics. Excessive large deformation of the stratum will lead to the accidents of foundation pit and surrounding buildings. The deformation of foundation pit should be strictly controlled to reduce the impact of excavation on the surroundings.

Researchers and engineers have conducted extensive research on the deformation mode and failure mechanism of deep and large foundation pits, including the deformation prediction method of foundation pits and the estimation of ground settlement and horizontal displacement of wall.

Peck [1] conducted a detailed study on the ground settlement caused by the excavation of soft soil foundation pit and obtained the estimated value of the soil settlement outside the pit. Clough and O'Rourke [2] and O'Rourke [3] studied the deformation of the wall in the foundation pit of hard clay, residual soil, and sand. Wang et al. [4] and Yang and Lu [5], respectively, used numerical analysis methods to analyze the relationship between the deformation mode of

support structure and the settlement range, settlement distribution form, the maximum value of settlement, and the location of the soil around the foundation pit. Wang et al. [6], Xu et al. [7,8], and Jiang et al. [9] collected the deformation data of Shanghai deep foundation pit engineering and discussed the deformation characteristics of foundation pit retaining structure from the statistical point of view.

In order to reduce the influence of deep foundation pit excavation on the surrounding environment, the deformation of supporting structure needs to be strictly controlled. In order to reflect the development of stress and displacement in the process of foundation pit deformation, Bolton et al. [10] proposed the design method of foundation pit retaining structure, namely, MSD (Mobilized Strength Design), based on the plastic deformation mechanism and virtual work principle. Bolton et al. [11, 12] and Osman and Bolton [13, 14] applied the MSD method to the cantilever deformation foundation pit of retaining wall. Wang et al. [15] introduced elastic strain energy of retaining wall to improve the MSD method. Liu et al. [16] introduced the influence of compression deformation energy of internal

support, bending deformation energy of retaining structure above excavation surface, and buried depth of excavation surface into energy conservation equation and proposed the curve form of variable wave peak cosine function. Xu et al. [17] proposed the improved MSD rigidity of the deep foundation pit support structure, which was verified in the support structure of the deep foundation pit of Nanjing Metro.

Based on the monitoring data of the deep foundation pit in a metro project of Shijiazhuang city in North China, this paper analyzes the deformation characteristics of the deep foundation pit under the condition of open excavation plus three steel supports, taking a two-story three-span box type underground frame structure station in Shijiazhuang city subway project as an example. The deep foundation pit project of Tianjin metro project which is located 260 km away from Shijiazhuang city in North China is used as a companion object. In the energy conservation equation of the MSD method, the compression deformation energy of internal support is introduced to predict the deformation characteristics of foundation pit and compared with the measured value.

## 2. Deformation Statistics of Metro Foundation Pit

*2.1. Foundation Pit Retaining Structure.* Shijiazhuang city is located in the Piedmont inclined plane, with a total terrain of 1.5~2.0‰ from west and northwest to east and southeast. The total length of the Metro Line 1 is 36.626 km where the first phase of the project is 23.9 km, with 20 underground stations and the average station spacing is about 1.2 km. Table 1 shows the basic information of the metro foundation pit. The strata in this area are artificial fill layer ( $Q^{ml}$ ), Neogene sedimentary layer ( $Q_4^{al}$ ), quaternary Holocene alluvial proluvial layer ( $Q_4^{al+pl}$ ), and quaternary upper Pleistocene alluvial proluvial layer ( $Q_3^{al+pl}$ ).

As shown in Figure 1, the excavation length of foundation pit in Shijiazhuang city is between 100 and 300 m, the width is between 20 and 45 m, and the length-width ratio is 8~14, among which the foundation pit with the length-width ratio of 10~12 accounts for 47.1%. In contrast, the ratio of length to width of the foundation pit of Tianjin Metro Line 6 is more evenly distributed than that of Shijiazhuang city Metro Line 1. The proportion of foundation pit with the ratio of length to width of 10~12 accounts for 12.2%. With the increase in the ratio of length to width, the proportion of foundation pit with open excavation method decreases.

The ratio between the depths of the retaining wall inserted into the pit bottom to the depth of the pit bottom is defined as the insertion ratio, which represents the soil condition of the area. The maximum insertion ratio of 17 metro stations in Metro Line 1 of Shijiazhuang city is 0.35 while the average insertion ratio is 0.21, as shown in Figure 2. Compared with Tianjin, the distribution is relatively concentrated. The insertion ratio in Metro Line 6 of Tianjin is obviously larger than that of Metro Line 1 of Shijiazhuang city. The maximum insertion ratio of Tianjin Metro is 1.15,

the minimum is 0.62, and the average is 0.89. Moreover, when the depth of foundation pit is 20~25 m, the distribution of insertion ratio is relatively scattered.

*2.2. Settlement of Foundation Pit.* The maximum ground settlement behind the foundation retaining structures of Shijiazhuang city is shown in Figure 3. The maximum settlement is less than 40 mm, of which 15 30 mm accounts for 70%, and the distribution of each section is relatively uniform. The maximum ground settlement behind the foundation structures of Tianjin Metro is more than 40 mm, of which 30~40 mm accounts for 17.3%, far greater than that of Shijiazhuang city.

Figure 4 shows the distribution of the maximum lateral movement of foundation pit retaining structures of Shijiazhuang city metro. The largest lateral movement is between 10 mm and 24 mm, of which 14 mm to 18 mm accounts for 64.7%, while the proportion of lateral movement larger than 20 mm is very small, and the distribution is relatively concentrated. The maximum lateral movement of foundation pit retaining structures in Tianjin is between 10 mm and 40 mm, of which 30 mm to 40 mm accounts for 71.05%. It can be seen that the deformation of foundation pit of Shijiazhuang city subway is quite different from that of Tianjin subway. This reflects the leading role of geological conditions in the deformation of urban subway foundation pit.

## 3. Foundation Pit Condition of Representative Station No. 1

Station No. 1 in Metro Line 1 is an underground double deck island station, with a total length of 287 m, a standard section width of 21.1 m, a roof covering of 3.1 m, a standard section floor depth of 17.19 m, and a shield shaft section floor depth of 18.64 m. The main structure of the station is constructed by the open excavation method, and the structural type is the underground two-layer three-span box type frame structure. The average ground elevation within the construction scope of the station is 82.54 m, and the average covering soil thickness of the station structure is 3.1 m. The upper part of the main retaining structure of the station is the concrete retaining wall, while the lower part is the retaining pile plus steel support type. Three supports are installed in the open excavation standard section, as shown in Figure 5.

The stratum of the site is alluvial and diluvial stratum, and the lithology is quaternary Holocene cohesive soil and sand soil. There are collapsible loess like silt and loess like silty clay in the site. The self-weight collapsible amount is less than 70 mm; therefore, the collapsible type of the site is non-self-weight collapsible loess site (Table 2).

According to the mechanical properties, the foundation soil in the 55.00 m insertion depth range of station 1 can be divided into 10 sublayers, and the stratum profile and physical and mechanical properties of soil layer are shown in Figure 6.

When the insertion depth is less than 7.5 m and more than 17.5 m, the sensitivity of soil layer is lower ( $S_t < 2$ ). The soil layer between 7.5 and 17.5 m is highly sensitive, which



TABLE 1: Basic information of the metro foundation pit.

	Length (m)	Width (m)	Length-width ratio	Pit depth (m)	Wall depth (m)	Insertion ratio
Max.	287.00	41.40	13.60	22.59	25.19	0.35
Min.	194.12	19.60	5.86	14.80	18.50	0.12
Average	230.36	22.78	10.36	17.28	21.15	0.23
Std.	24.15	4.80	1.63	1.85	1.93	0.05
CV	0.10	0.21	0.16	0.11	0.09	0.23

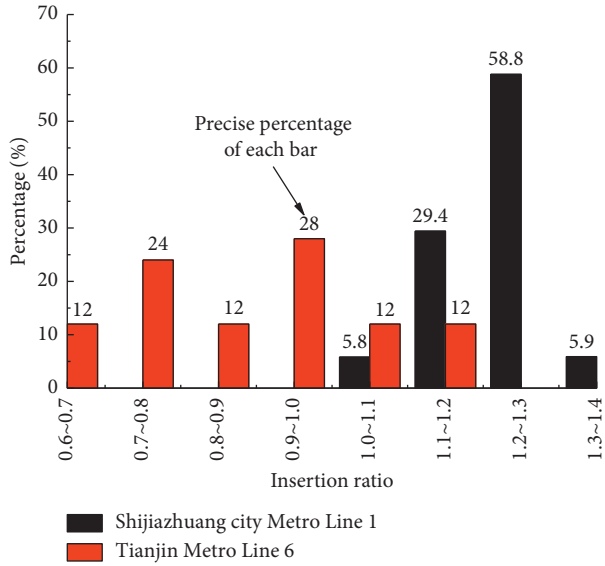


FIGURE 1: Length-width ratio distribution.

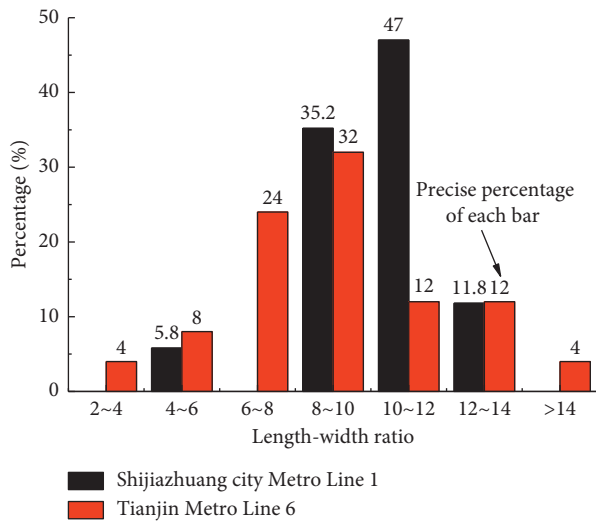


FIGURE 2: Insertion ratio distribution.

indicates that the strength and rigidity of soil in this range are easily disturbed by construction and significantly reduced.

From  $0.1 < a_{s1-2} < 0.5$ , it can be seen that within 55 m of the insertion depth, all are medium compressible soil. The shear strength indexes  $C_u$  and  $\phi_u$  of soil are obtained from the direct shear test, for the stress-strain curve provided by

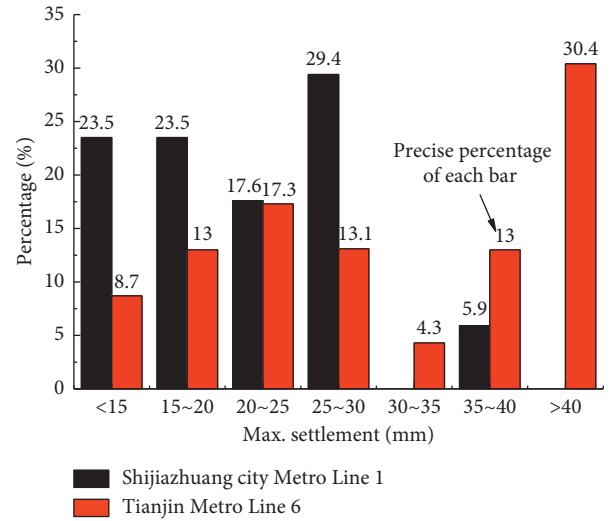


FIGURE 3: Distribution of maximum ground surface settlement behind retaining structures.

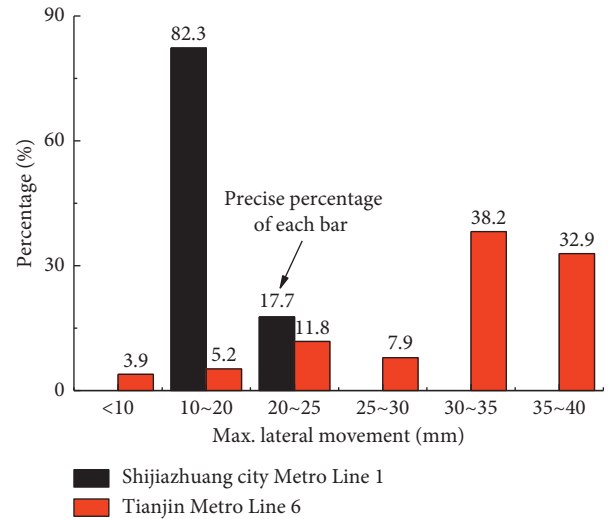


FIGURE 4: Distribution of maximum lateral movement of foundation pit retaining structures.

the direct shear test which is closest to the in situ test results. It can be seen from the above parameters that the stratum of the foundation pit of Station No. 1 is medium hard clay, and its void ratio is less than 1. Due to the high compressibility of the stratum, the undrained shear strength is less than 75 kPa.

The triaxial test was carried out in the site field. The stress-strain curve of each layer is shown in Figure 7. The peak shear strength increases with the increase in insertion

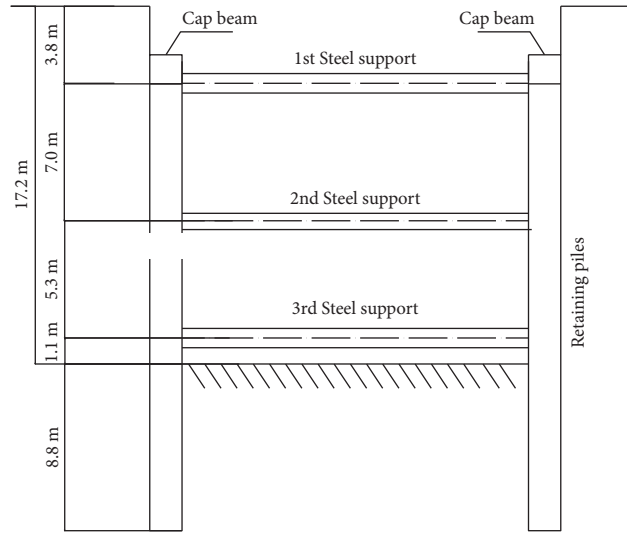


FIGURE 5: Retaining structures of Station No. 1.

TABLE 2: Feature of the stratum.

Stratum no.	Lithology	Density (g/cm <sup>3</sup> )	Cohesion (kPa)	Friction angle (°)	Standard value of bearing capacity (kPa)	Static lateral pressure factor	Natural water content (%)
2-2	Loess silty clay	1.81	35	20	150	0.33	13.6
2-3	Loess silt	1.83	14	29	160	0.32	13.6
3-1	Loess silty clay	1.94	35	21	160	0.35	21.5
3-2	Loess silt	1.86	25	29	180	0.31	13.9
5-1	Silty clay	1.99	37	18	190	0.41	23.5
5-2	Silty soil	2.00	23	24	190	0.33	19.6
5-4	Medium coarse sand	2.03	0	31	200	0.30	—
6-3	Pebble	2.12	0	35	350	0.25	—

depth. In the nonyielding stage, with the increase in soil strain, there is a one-to-one relationship between stress and strain.

## 4. Deformation Analysis

*4.1. Analysis of Deformation Monitoring Data.* At the ends and middle point of the long side of the foundation pit, total 6 inclined holes for the retaining structure were evenly arranged to monitor the lateral movement curve at the depth of 15 m, as shown in Figure 8.

The foundation pit was constructed from the left end first, and the lateral movement of the retaining structure tended to be stable on May 18, 2014, lasting for 69 days; the final lateral movement was between 18 mm and 20 mm. The construction of the middle and right ends of the foundation pit started at the same time, and the lateral movement of the right end of the retaining structure tended to be stable on June 6, 2014, lasting 71 days; the final lateral movement was between 17 mm and 23 mm. The lateral movement of the retaining structure in the middle of the foundation pit tended to be stable on July 24, 2014, lasting for 118 days; the final lateral movement was between 18 mm and 20 mm, and the change gradient is relatively gentle.

The lateral movement duration curves of point  $M_{up}$  at the retaining structure are shown in Figure 9. The maximum lateral movement of the retaining structure occurs at the depth of 10 mm, while the minimum lateral movement occurs at the toe of the retaining structure.

There are 54 lateral movement monitoring points in the foundation pit. The relationship between the maximum lateral movement and the excavation depth is shown in Figure 10. It can be seen from the figure that the maximum lateral movement of the retaining structures is between 0.026%H and 0.240%H, with an average of 0.165%H (H is the excavation depth).

The relationship between the maximum lateral movement depth of the retaining structures and the excavation depth is shown in Figure 11. The maximum lateral movement depth of the retaining structures is between 7.5 m and 17.5 m, accounting for 90.17%. With the increase in excavation depth, the maximum lateral movement depth of the retaining structure tends to decrease whilst the distribution is more centralized, with an average depth of about 13 m, about 0.42H.

The ground surface settlement curves at 3 meters away from the retaining structures of the foundation pit are shown in Figure 12. It can be seen from the figure that behind the left lower side wall, the surface was uplifted; behind the

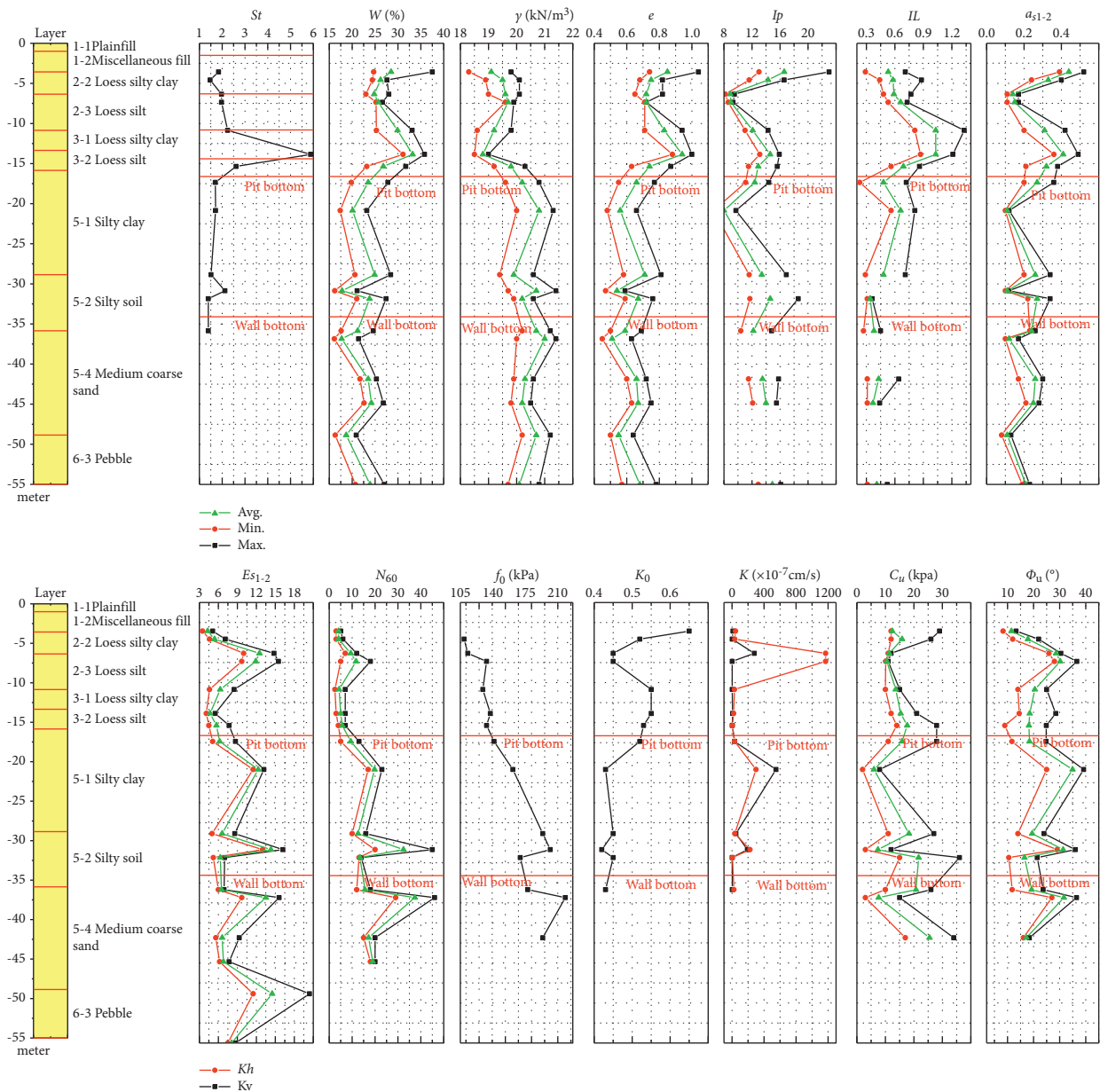


FIGURE 6: Physical and mechanical properties of soil layers.

middle lower side wall, the surface settlement was very small; and the maximum surface settlement behind the retaining structures was located at the right lower side wall, about 22 mm.

After excavation, the lateral movement of the retaining wall is shown in Figure 13. There is no obvious change rule of the lateral movement of the retaining wall. Due to the restraint of the internal support, the foundation pit does not show the characteristics of large deformation at the midpoint of the long side and small deformation at both sides, such as the cantilever foundation pit.

**4.2. Improved Mobilized Strength Design.** In this paper, the mobilized strength design (MSD) method, considering the

compression deformation energy of the internal support, is used to predict the maximum lateral movement of the retaining structures with following steps:

- (1) Determine the soil stress-strain curve: collect the representative soil around the foundation pit for the indoor triaxial compression test and obtain the soil strength characteristic curve.
- (2) Determine the cantilever type deformation: obtain the mobilization rate of undrained shear strength of soil through known parameters such as the buried depth of retaining structure, the excavation depth of foundation pit, and the weight of soil; obtain its undrained shear strain through the soil stress-strain curve; then obtain the deflection angle of the retaining wall and the maximum displacement of

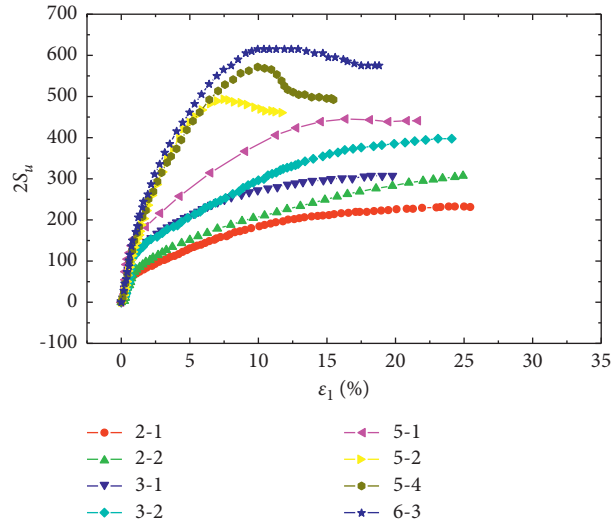


FIGURE 7: Stress-strain curves of the consolidated undrained triaxial test for each layer of soil.

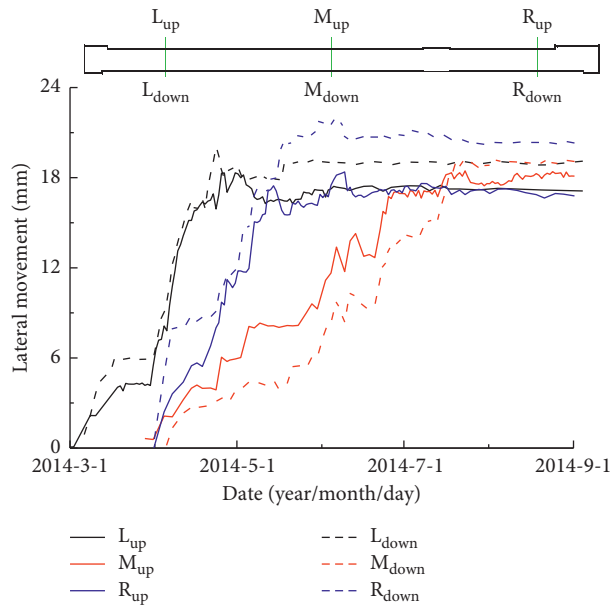


FIGURE 8: Lateral movement of retaining structures at the depth of 15 m.

wall top  $\delta_{wm1}$ , as well as the cantilever type deformation curve:

$$\Delta_{w1}(y) = \Delta_{wm1} + \frac{\Delta_{wm1}y}{\lambda}; -\lambda \leq y \leq 0. \quad (1)$$

- (3) Determine the excavation deformation in the second step: the influence wavelength of deformation is  $\lambda$ , and the excavation incremental deformation in the second step is approximated to the segment cosine function, namely:

$$\delta_{w2}(y) = \begin{cases} \frac{\delta_{wm2}}{2} \left[ 1 - \cos\left(\frac{\pi y}{k_2 \lambda}\right) \right]; -k_2 \lambda \leq y < 0 \\ \frac{\delta_{wm2}}{2} \left[ 1 - \cos\left(\frac{\pi(y - (1 - 2k_2)\lambda)}{(1 - k_2)\lambda}\right) \right]; -\lambda \leq y < -k_2 \lambda \end{cases} \quad (2)$$

In the second step, the total deformation curve is as follows:

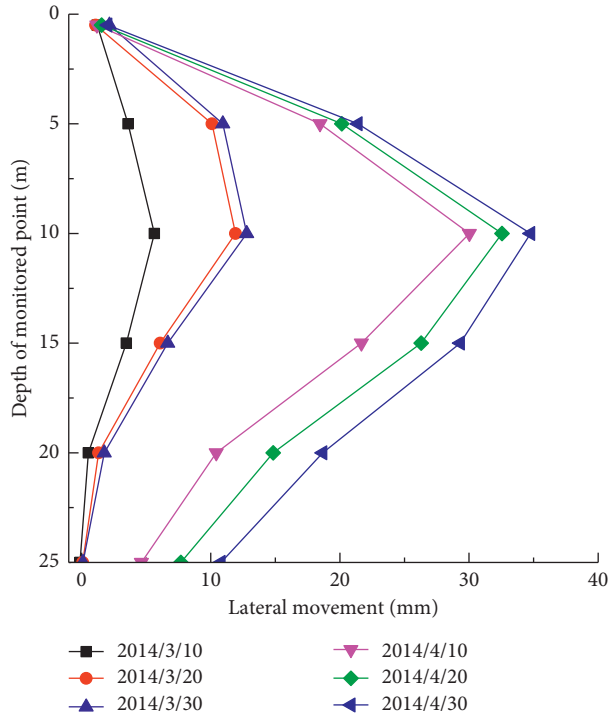


FIGURE 9: Lateral movement duration curves of point  $M_{up}$  at the retaining structures.

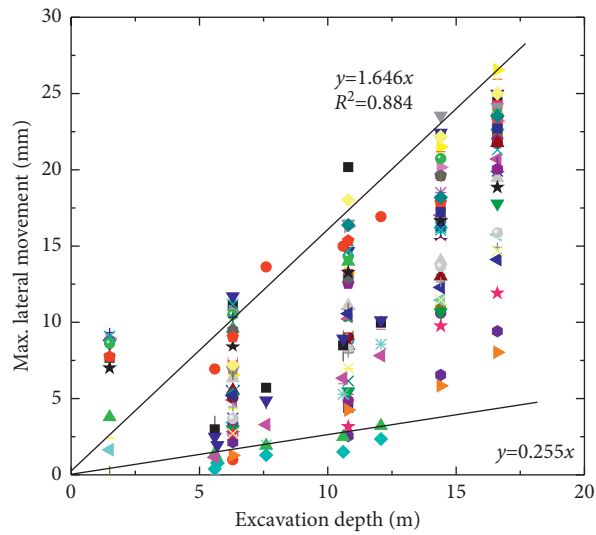


FIGURE 10: Relationship between the maximum lateral movement and the excavation depth.

$$\Delta_{w2}(y) = \begin{cases} \frac{\delta_{wm2}}{2} \left[ 1 - \cos\left(\frac{\pi y}{k_2 \lambda}\right) \right] + \left( \Delta_{wm1} + \frac{\Delta_{wm1} y}{\lambda} \right); & -k_2 \lambda \leq y < 0 \\ \frac{\delta_{wm2}}{2} \left[ 1 - \cos\left(\frac{\pi(y - (1 - 2k_2)\lambda)}{(1 - k_2)\lambda}\right) \right] + \left( \Delta_{wm1} + \frac{\Delta_{wm1} y}{\lambda} \right); & -\lambda \leq y < -k_2 \lambda \end{cases} \quad (3)$$

The derivative of  $\Delta_{w2}(y)$  is as follows:

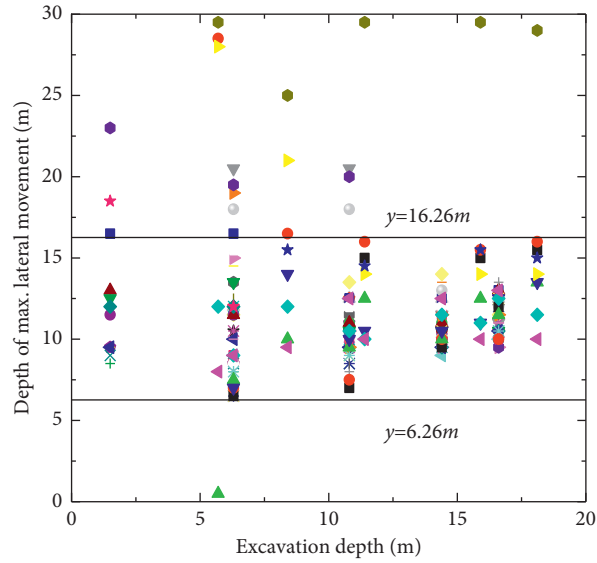


FIGURE 11: Relationship between the depth of the maximum lateral movement and excavation depth.

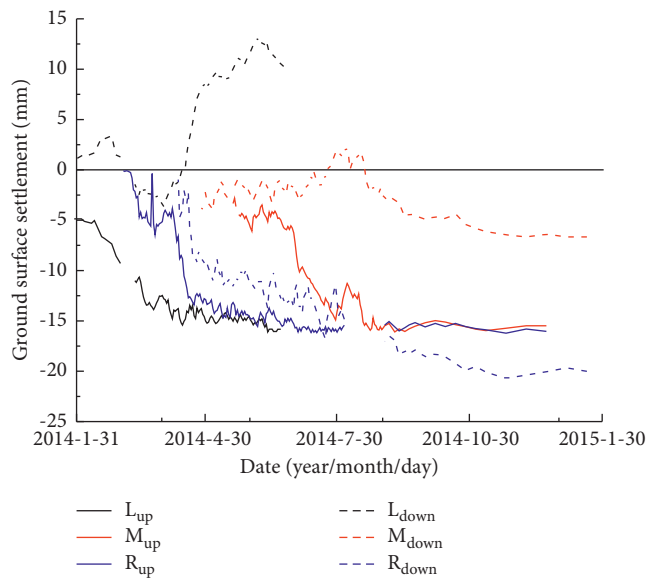


FIGURE 12: Ground surface settlement duration curves at 3 m distance from the retaining structures.

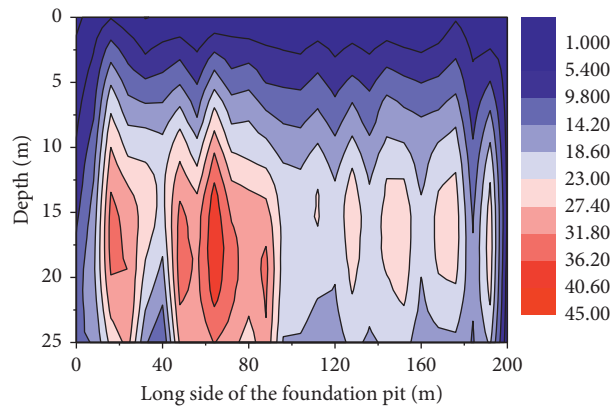


FIGURE 13: Lateral movement contour of the retaining structures after excavation.

$$\Delta'_{w2}(y) = \begin{cases} \frac{\delta_{wm2}}{2} \frac{\pi}{k_2\lambda} \sin\left(\frac{\pi y}{k_2\lambda}\right) + \frac{\Delta_{wm1}}{\lambda}; & -k_2\lambda \leq y < 0 \\ \frac{\delta_{wm2}}{2} \frac{\pi}{(1-k_2)\lambda} \sin\left(\frac{\pi(y - (1-2k_2)\lambda)}{(1-k_2)\lambda}\right) + \frac{\Delta_{wm1}}{\lambda}; & \lambda \leq y < -k_2\lambda \end{cases} \quad (4)$$

The value of the maximum lateral displacement of the retaining structure is the same as that of the excavation surface; then, when  $y=H$ , the value of  $\Delta'_{w2}(y)=0$ :

$$\begin{cases} \frac{\pi H}{k_2\lambda} \sin\left(\frac{\pi H}{k_2\lambda}\right) = -\frac{2\Delta_{wm1}}{\lambda\delta_{wm2}} H; & -k_2\lambda_2 \leq y < 0 \\ \frac{\pi(H - (1-2k_2)\lambda)}{(1-k_2)\lambda} \sin\left(\frac{\pi(H - (1-2k_2)\lambda)}{(1-k_2)\lambda}\right) = -\frac{2\Delta_{wm1}}{\lambda\delta_{wm2}} [H - (1-2k_2)\lambda_2]; & -\lambda_2 \leq y < -k_2\lambda_2 \end{cases} \quad (5)$$

By equation (5),  $k_2$  which makes the total deformation reach the maximum value can be obtained. The obtained  $k_2$  is substituted into the incremental deformation curve, and the horizontal and vertical deformations of the soil mass on both sides of the foundation pit are calculated according to equations (4) and (5), and then the soil gravity potential energy  $\Delta P$  expressed by  $\delta_{wm2}$  is obtained.

When the width of the foundation pit  $B < 2[2(\lambda-h_0)]^{1/2}$ , the foundation pit is a narrow foundation pit, and the influence range of the soil outside the pit is the same as that of the wide foundation pit. The influence range of the soil inside the pit is rectangular and obeys the two-dimensional shear state as follows:

$$\delta_y = \begin{cases} \frac{\lambda' \delta_m}{4B} \left( \pi + \frac{\pi y}{k\lambda'} - \sin \frac{\pi y}{k\lambda'} \right) \sin\left(\frac{\pi x}{B}\right); & 0 \leq y \leq k\lambda', \\ \frac{\lambda' \delta_m}{4B} \left( \pi + \frac{\pi y}{(1-k)\lambda'} - \sin \frac{\pi y}{(1-k)\lambda'} \right) \sin\left(\frac{\pi x}{B}\right); & -(1-k)\lambda' \leq y < 0, \end{cases} \quad (6)$$

$$\delta_x = \begin{cases} \frac{\delta_m}{2} \left( 1 + \cos \frac{\pi y}{k\lambda'} \right) \cos\left(\frac{\pi x}{B}\right); & 0 \leq y \leq k\lambda', \\ \frac{\delta_m}{2} \left( 1 + \cos \frac{\pi y}{(1-k)\lambda'} \right) \cos\left(\frac{\pi x}{B}\right); & -(1-k)\lambda' \leq y < 0, \end{cases} \quad (7)$$

According to the relationship between the maximum incremental deformation and the shear strain of the soil and the stress-strain curve of the soil, the internal energy  $\Delta W$  consumed by the shear action of the soil expressed by  $\delta_{wm2}$  is obtained. According to the flexural rigidity of the wall and the compressive rigidity of the internal support, the flexural deformation energy of the wall  $\Delta U$  expressed by  $\delta_{wm2}$  and the compressive deformation energy of the internal support  $\Delta V$  are obtained. The external work produced by the self-weight of the soil behind the wall is equal to the internal energy dissipated by the shear action of the soil behind the wall and the strain energy produced by the bending deformation of the wall and the compression deformation of the support:

$$\Delta P = \Delta W + \Delta U + \Delta V,$$

$$\begin{aligned} \int_{\text{vol}} \gamma_v \delta_v d\text{vol} &= \int_{\text{vol}} c_{mob} \delta_y d\text{vol} + \frac{EI}{2} \int_0^h \left[ \frac{d^2 w_x}{dy^2} \right]^2 dx \\ &+ \sum_{p=1}^P \frac{E_p A_p}{2l_p} (w_p)^2, \end{aligned} \quad (8)$$

where  $\Delta P$  is the work done by external force;  $\Delta W$  is the energy consumption of soil mass;  $\Delta U$  is the elastic strain energy stored in the wall;  $\Delta V$  is the elastic strain energy stored in the support;  $\gamma_v$  is the unit volume weight of soil mass;  $\delta_v$  is the vertical displacement of soil mass behind the wall;  $c_{mob}$  is the mobilization value of soil strength;  $\delta_y$  is the

TABLE 3: The energy increment of each step.

Items	Construction steps			
	2	3	4	5
$\Delta P$ (J/m)	4.21	9.425	38.745	53.82
$\Delta W$ (J/m)	3.95	9.005	35.24	52.775
$\Delta U$ (J/m)	0.26	0.06	0.075	0.035
$\Delta V$ (J/m)	0	0.365	3.43	1.01
$\Delta U/\Delta P$ (%)	3.09	0.32	0.095	0.035
$\Delta V/\Delta P$ (%)	0	1.935	4.425	0.94

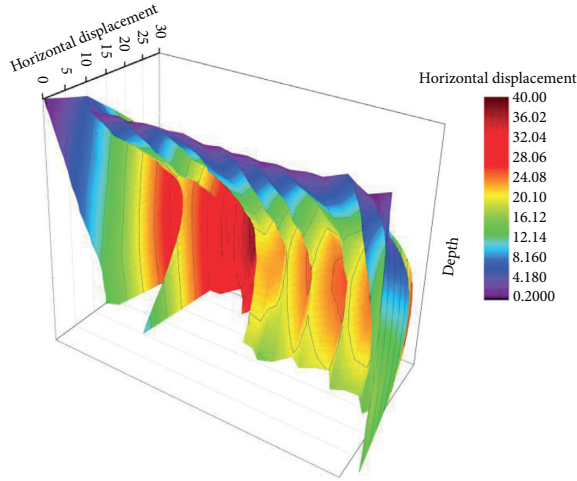


FIGURE 14: Horizontal displacement of the retaining wall.

increment of shear strain;  $EI$  is the elastic modulus of retaining wall;  $dw_x$  is the increment of horizontal deformation of retaining structure along the wall depth;  $h$  is the depth of retaining wall;  $F_s$  is the supporting axial force;  $l$  is the supporting length; and  $EA$  is the tensile rigidity of the member.

According to Equation (6), the maximum lateral displacement value  $\delta_{wm2}$  of the wall is obtained, and whether it meets the design standard is judged, and the parameters are adjusted until the satisfactory result is obtained. The solution  $\delta_{wm2}$  is substituted into Equation (3) to get the deformation curve of the second excavation step.

**4.3. Validation of Improved MSD.** In the proposed pit, the intermediate pile, bored pile, and internal corner reinforcement were constructed as Step 1. From Step 2 to Step 4, the proposed pit was excavated layer by layer, each time 0.5 m below the steel support. In Step 5, the pit was totally excavated. Table 3 gives the energy parameters calculated by the improved MSD method where  $\Delta P$  is the work done by external force;  $\Delta W$  is the energy consumption of soil mass;  $\Delta U$  is the elastic strain energy stored in the wall; and  $\Delta V$  is the elastic strain energy stored in the support. Horizontal displacement of retaining wall is shown in Figure 14. Vertical displacement of surface behind the wall is shown in Figure 15.

According to the improved MSD method in this section, the lateral movement curves of the wall are compared with

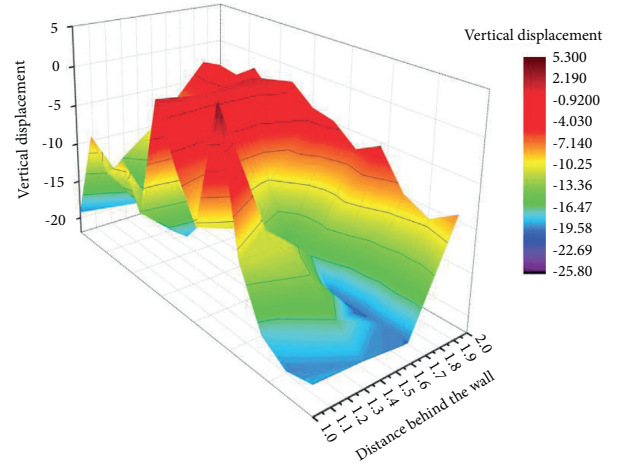


FIGURE 15: Vertical displacement of the surface behind the wall.

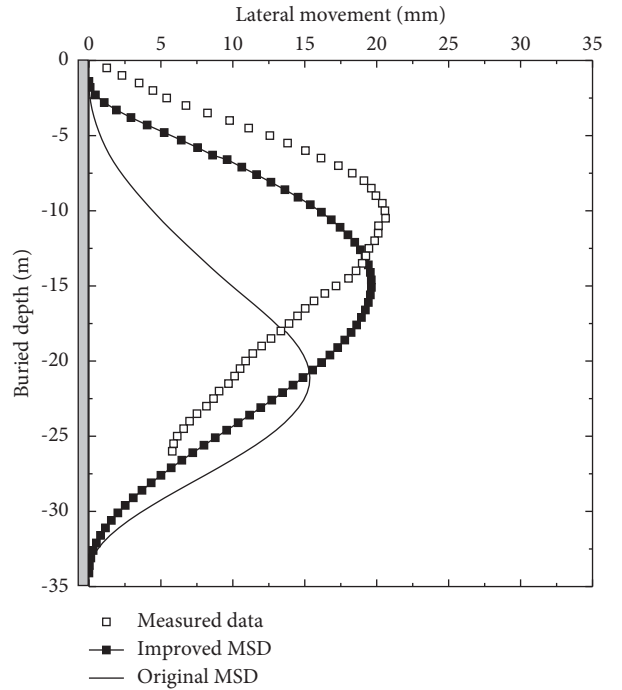


FIGURE 16: Comparison of measured data and calculated values.

the original MSD method and the measured data, as shown in Figure 16. It can be seen that the deformation curves obtained by the improved MSD are closer to the measured data than the original MSD method. In the proposed pit, the maximum lateral movement  $\delta_{hm} = 23.4$  mm and the corresponding buried depth  $H_{\delta hm} = 7.0$  m. It is predicted by the improved MSD method that  $\delta_{hm} = 22.2$  mm and  $H_{\delta hm} = 10.1$  m, while  $\delta_{hm} = 17.4$  mm and  $H_{\delta hm} = 14.1$  m according to the original MSD method.

## 5. Conclusions

- (1) The average insertion ratio in Tianjin Metro is 0.89, which is significantly greater than that in Shijiazhuang city; the maximum lateral movement of



the foundation pit in Tianjin Metro is between 30 mm and 40 mm, while the maximum lateral movement of the wall is between 14 mm and 18 mm in Shijiazhuang city.

- (2) In the proposed pit, the maximum lateral movement of the wall is about 0.165%H; the maximum lateral movement buried depth is between 7.5 m and 17.5 m.
- (3) The compression deformation energy of internal support is considered in the energy conservation equation of the MSD method, and the maximum lateral movement  $\delta_{hm} = 22.2$  mm, and the corresponding buried depth  $H_{\delta hm} = 10.1$  m while  $\delta_{hm} = 17.4$  mm and  $H_{\delta hm} = 14.1$  m according to the original MSD method. In the proposed pit,  $\delta_{hm} = 23.4$  mm and  $H_{\delta hm} = 7.0$  m, the improved MSD method is more acceptable than the original MSD method.

### Data Availability

The data used to support the findings of this study are included within the article.

### Conflicts of Interest

The authors declare that there are no conflicts of interest.

### Acknowledgments


This project was supported by the National Natural Science Foundation of China (51478037), which is gratefully acknowledged.

### References

- [1] R. B. Peck, "Deep excavation and tunneling in soft ground," in *Proceedings of the 7th International Conference on Soil Mechanics and Foundation Engineering*, pp. 225–290, State-of-the-Art-Volume, Mexico City, 1969.
- [2] G. W. Clough and T. D. O'Rourke, "Construction induced movements of in situ wall," in *Proceedings of the ASCE Conference on Design and Performance of Earth Retaining Structures*, pp. 439–470, Geotechnical Special Publication No. 25, ASCE, New York, 1990.
- [3] T. D. O'Rourke, "Base stability and ground movement prediction for excavations in soft clay. Retaining-structures," in *Proceedings of the International Conference on Retaining Structures*, pp. 657–686, Tomas Telford, London, July 1993.
- [4] J. H. Wang, Z. H. Xu, and W. D. Wang, "Analysis of deformation behavior of deep excavations supported," *Chinese Journal of Geotechnical Engineering*, vol. 29, no. 12, pp. 1899–1903, 2007.
- [5] M. Yang and J. Y. Lu, "Estimation of ground settlement aroused by deep excavation," *Chinese Journal of Geotechnical Engineering*, vol. 32, no. 12, pp. 1821–1828, 2010.
- [6] B. J. Wang, J. H. Xiong, and B. T. Zhu, "Influence of deformation modes of retaining structures on surface settlements," *Structural Engineers*, vol. 23, no. 3, pp. 47–52, 2007.
- [7] Z. H. Xu, J. H. Wang, and W. D. Wang, "Deformation behavior of diaphragm walls in deep excavations in Shanghai," *China Civil Engineering Journal*, vol. 41, no. 8, pp. 89–94, 2008.
- [8] Z. H. Xu, J. H. Wang, and W. D. Wang, "Deformation behavior of excavations retained by bored pile wall in soft soil," *Rock and Soil Mechanics*, vol. 30, no. 5, pp. 165–169, 2009.
- [9] X. F. Jiang, G. B. Liu, W. L. Zhang, and X. Y. Li, "Deformation characteristics of ultra-deep foundation pit in Shanghai based on measured data," *Chinese Journal of Geotechnical Engineering*, vol. 32, no. S2, pp. 570–573, 2010.
- [10] M. D. Bolton, S.-Y. Lam, P. J. Vardanega, C. W. W. Ng, and X. Ma, "Ground movements due to deep excavations in Shanghai: design charts," *Frontiers of Structural and Civil Engineering*, vol. 8, no. 3, pp. 201–236, 2014.
- [11] M. D. Bolton, W. Powrie, and I. F. Symons, "The design of stiff in-situ walls retaining over-consolidated clay part 1, short term behavior," *Ground Engineering*, vol. 23, no. 1, pp. 34–39, 1989.
- [12] M. D. Bolton, W. Powrie, and I. F. Symons, "The design of stiff in-situ walls retaining over-consolidated clay part 2, long term behavior," *Ground Engineering*, vol. 23, no. 2, pp. 22–28, 1990.
- [13] A. S. Osman and M. D. Bolton, "A new design method for retaining walls in clay," *Canadian Geotechnical Journal*, vol. 41, no. 3, pp. 451–466, 2004.
- [14] A. S. Osman and M. D. Bolton, "Ground movement predictions for braced excavations in undrained clay," *Journal of Geotechnical and Geoenvironmental Engineering*, vol. 132, no. 4, pp. 465–477, 2006.
- [15] H. R. Wang, W. D. Wang, M. S. Huang, and Z. H. Xu, "Modified mobilizable strength design (MSD) method on deformation predictions of foundation pit," *Chinese Journal of Rock Mechanics and Engineering*, vol. 30, no. S1, pp. 3245–3251, 2011.
- [16] M. L. Liu, Q. Fang, D. L. Zhang, and Y. J. Hou, "Prediction of transient deformation due to excavation based on improved MSD method," *Chinese Journal of Rock Mechanics and Engineering*, vol. 37, no. 7, pp. 1700–1707, 2018.
- [17] H. Z. Xu, P. P. Sun, W. S. Cui, and Y. J. Sun, "MSD synthetic system stiffness and deformation prediction of support structure for deep excavation in Nanjing subway," *Journal of China University of Mining & Technology*, vol. 47, no. 4, pp. 907–912, 2018.

## Research Article

# Elaborate Modeling and Fragility Assessment of a Multiframe PC Box-Girder Bridge with Intermediate Hinges in California

Tong Wu,<sup>1,2</sup> Zhan Li,<sup>3</sup> and Shengchun Liu <sup>1</sup>

<sup>1</sup>School of Electronic Engineering, Heilongjiang University, Harbin 150080, China

<sup>2</sup>School of Civil Engineering, Heilongjiang University, Harbin 150080, China

<sup>3</sup>China Institute of Marine Technology & Economy, Beijing 100081, China

Correspondence should be addressed to Shengchun Liu; liushengchun@hlju.edu.cn

Received 23 July 2021; Accepted 7 September 2021; Published 8 October 2021

Academic Editor: Shan Gao

Copyright © 2021 Tong Wu et al. This is an open access article distributed under the Creative Commons Attribution License, which permits unrestricted use, distribution, and reproduction in any medium, provided the original work is properly cited.

Multiframe PC box-girder bridge with intermediate hinges is a kind of bridge having complex structural characters, which is very quintessential in California. In this study, a typical bridge was adopted to establish a nonlinear dynamic model through OpenSees platform. Intermediate hinge and inhibiting devices in it were elaborately simulated. Meanwhile, pushover analysis was used to reinstate a specimen of column test, which has the similar ratio of reinforcement to the typical bridge, and the hysteretic model parameters of the longitudinal steels inside columns were obtained. The damage indexes of column and hinge, which are primary components, under different limit states were acquired by moment-curvature analysis. Taking into account the uncertainty, nonlinear time-history analysis of the bridge was carried out through a suite of synthetic ground motions. Subsequently, a probabilistic seismic demand model was developed, and fragility curves were further focused on. According to fragility assessment, the conclusion shows that columns and hinge restrainers exhibit high fragility, and bridge system fragility is gradually determined by column fragility along with aggravating of the damage state. Unseating of girder can hardly occur at abutments and intermediate hinges. Moderate limit state could be exceeded in the positions of plug-type concrete structures in intermediate hinges, which tends to create transverse and vertical cracks, furthermore causing reinforcements yield. It indicates that it would severely underestimate the seismic fragility of intermediate hinges without considering the elaborate simulation of hinges.

## 1. Introduction

California, where the prestressed concrete viaducts were generally designed to the form of column-girder consolidation, is located in the San Andreas fault [1, 2], which is the part of the Circum-Pacific seismic belt. In order to release the freedom of bridges and reduce the number of cracks, the intermediate hinges [3, 4] were designed in some spans of bridges [5], shown in Figure 1. Hinges are generally located next to 1/6~1/4 point of span length, which were designed to the form of upper-lower and left-right occlusion, called plug-type, shown in Figure 2. Moreover, inhibiting devices were designed inside hinges to limit displacement, including longitudinal restrainers, vertical elastomeric bearings, and transverse elastomeric pads. This type of bridge, called multiframe prestressed concrete box-girder bridge, has been

widely used in California and even throughout the United States, due to its perfect integrity and large spanning ability.

In the process of vibration, the bending moment of the bridge decreases to zero at the point of hinges. Hinge, taken as the boundary, makes the column-girder consolidation on both sides of it present the vibration characteristic, which is the similar to frame. The overall vibration form of the bridge can be outlined as follows: the individual vibration of each frame is connected into the overall vibration of the bridge by hinges. Consequently, the vibration characteristic and vibration rule of hinge, as a key component of connecting every single frame, are particularly crucial. Several studies [6–8] have stated that the linear elastic model was often used to simulate the elements of girder due to rare occurrence of plastic failure here. In addition, in order to simplify finite element calculation, relative displacement at the point of



FIGURE 1: Intermediate hinge.

hinge was neglected in vertical and transverse directions [7, 8]. Thus, the hinge points belonging to adjacent frames were imitated to be fixed in vertical and transverse directions, and only tensile and compressive action of longitudinal restrainers between adjacent frames was considered [9, 10]. The previously mentioned simplification tended to ignore the potential damage at the point of hinge, which may have a considerable impact on fragility analysis and risk assessment of the bridges.

Meanwhile, the provided concrete uniaxial material and steel uniaxial material, such as Concrete07 and reinforcing steel in OpenSees [11], are often combined to simulate the columns. This combination does not take into account the diversity of column sections, which will undoubtedly reduce the accuracy of the hysteretic performance of the columns and increase the error. Because of the important influence of columns on the overall dynamic characteristics of the bridge [12–15], the column experiment, which matches with the actual columns, should be used to obtain the material constitutive relationship of the columns, so that the obtained column hysteresis model will be more reliable.

The previously mentioned findings collectively demonstrate that the multiframe prestressed concrete box-girder bridge has complex characteristics combined with consolidation of girder and column and frame structure. For the bridge with large spans, high columns, and multihinges, especially, its structural complexity should be very prominent. Consequently, it is indispensable to assess the seismic fragility of this type of bridge in depth. In spite of quite a few relevant researches being done, the unsolved question, particularly regarding the refined intermediate hinge modeling, still needs to be solved. If this question is neglected, some damage positions may be missed, and the potential hidden danger may be caused.

The fragility analysis is a method of risk assessment for structures [16, 17], which combines two kinds of uncertainties, the ground motion intensity uncertainty and structural parameters uncertainty, organically by probability and statistics algorithm [18]. Damage indexes to limit states are obtained by the experimental and empirical statistical results, while seismic demands of structures are obtained through time-history analysis, and further probabilistic seismic demand models are established. The fragility analysis, used for predisaster prevention and postdisaster loss assessment, has become the most efficient and effective approach to risk assessment of structures

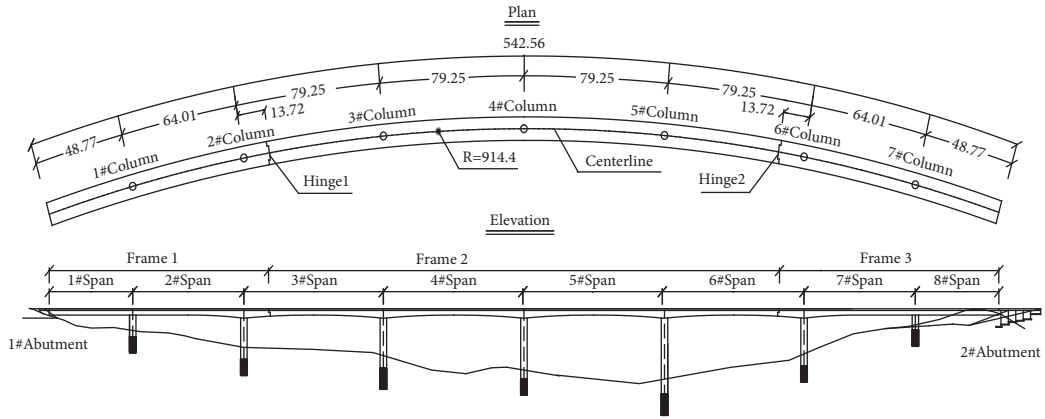
and is adopted extensively in the field of disaster prevention and mitigation [19, 20].

Considering the limitation of previous works, this study focuses on a multiframe prestressed concrete box-girder bridge with eight spans and double intermediate hinges. Elaborate nonlinear analytical models of this bridge, serving as a template of simulation to the similar type of bridge, which accounts for the nonlinear behavior of girders, plug-type hinges, columns, bearings, and abutments, are developed in the OpenSees platform. The damage indexes of bridge components are selected scrupulously through data screening and Xtract analysis. Subsequently, fragility curves of bridge components and bridge system are developed, while seismic damage exceedance probabilities are acquired. The study can provide data reference and theoretical basis for seismic damage assessment and pre-earthquake protection of the same type of bridges.

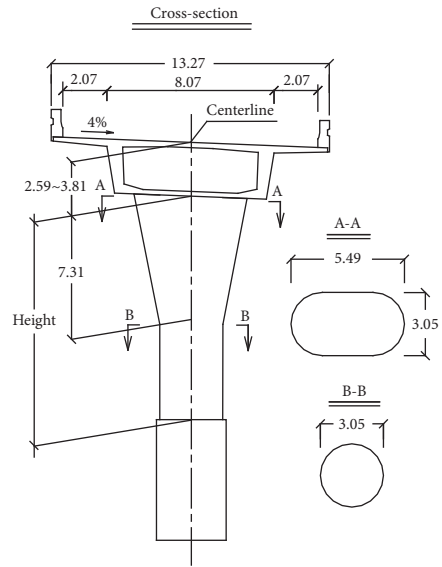
## 2. Numerical Modeling of the Bridge

**2.1. Characteristics.** A typical bridge (Figure 2(a)), designed in 1991, built in 1993, and located in California, US, is a prestressed concrete curved box-girder bridge with eight spans (Table 1). The superstructure for this prestressed concrete box-girder curved bridge has a degree of curvature  $34^\circ$  (0.593 rad) and a centerline radius of 914.4 m. Between the midspan of #2 span and the midspan of #7 span, the depth of deck section changes from 2.59 m at the midspan to 3.81 m at the supported point through parabola, and the depth of section for any other parts of superstructure is 2.59 m. Figure 2(b) shows the cross section of the two-lane box girder rigidly connected by bridge columns. All the columns have different heights with a range from 8.53 m to 42.67 m (Table 2), each connected to a single pile foundation. On each abutment (Figure 2(c)), two elastomeric pads with the size of 914 mm  $\times$  610 mm  $\times$  51 mm are used to support the vertical loads while allowing horizontal translation through a frictional surface. Also, two shear keys near the elastomeric pads in each abutment are placed to restrain the transverse translation of the superstructure. Each abutment is supported by a rectangular footing. Figures 2(d)–2(f) show the plan, cross section, and elevation of the intermediate hinges, located in the #3 and #6 spans, which divide the bridge into three frames (Figure 2(a)). Two horizontal elastomeric bearings (Figure 2(e)) are installed to sustain vertical compression and restrain horizontal shear deformation (i.e., the relative horizontal displacement between the adjacent decks in the intermediate hinge). Besides, four transverse compressive pads (Figure 2(e)) are designed to sustain transverse compression and restrain vertical shear deformation (i.e., the relative vertical displacement between the adjacent decks in the intermediate hinge). Figure 2(f) shows that the girder deck ends in the intermediate hinge and is connected by longitudinal restrainers. Polystyrene is stuffed into the gap in the intermediate hinge (Figures 2(d) and 2(f)).

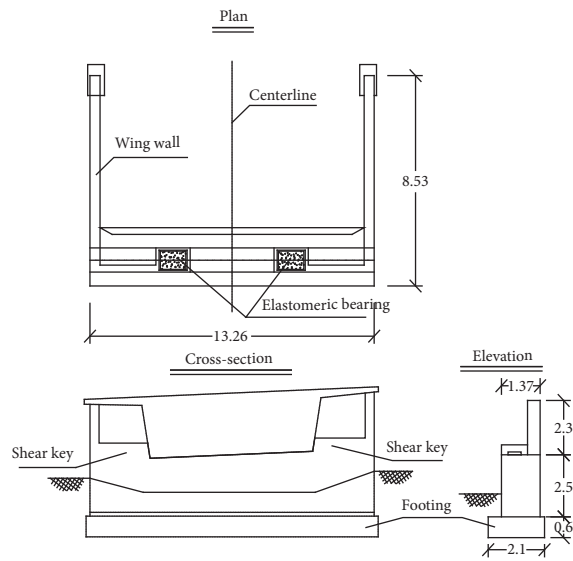
**2.2. Numerical Simulation.** In this study, OpenSees program [21] was employed to simulate the typical bridge. A three-dimensional numerical model of the typical bridge, the



(a)



(b)



(c)

FIGURE 2: Continued.

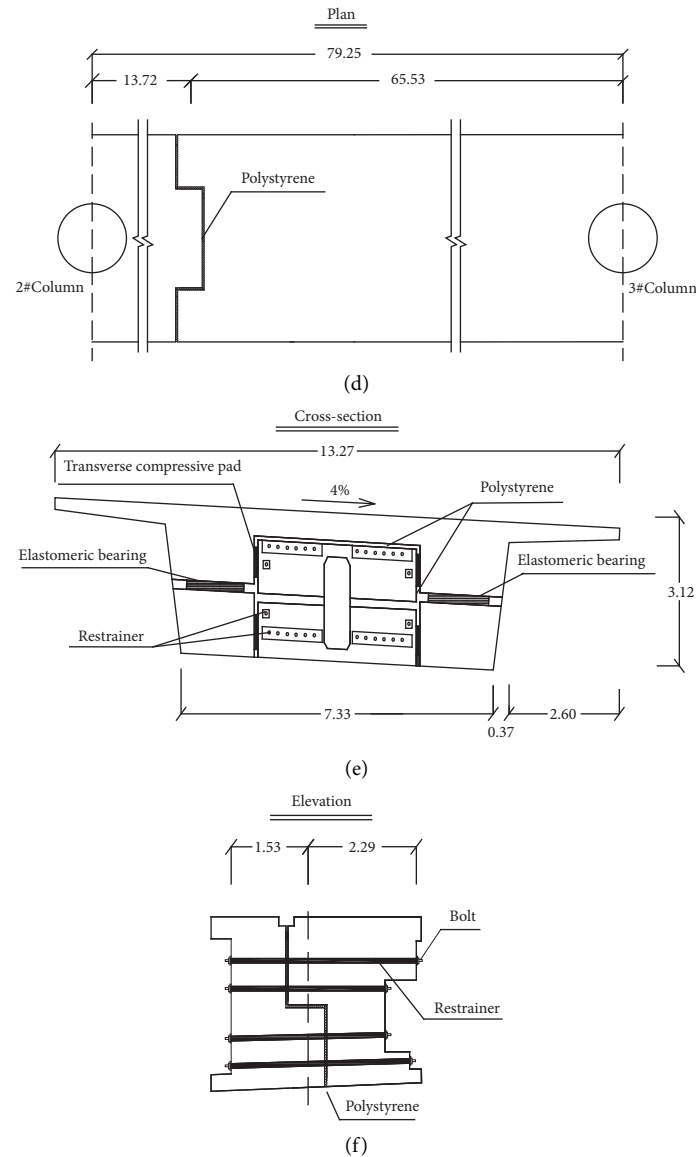


FIGURE 2: Schematic view of the typical bridge (m). (a) Bridge plan and elevation. (b) Girder and column cross section. (c) Abutment plan, elevation, and cross section. (d) Hinge span plan. (e) Hinge cross section. (f) Hinge elevation.

constitutive relation of the materials, and the force-displacement relation of the component models are shown in Figure 3. In order to acquire the response of intermediate hinge under seismic load, the girder elements were set as a displacement-based beam-column element considering elastic and plastic properties. So girders, hinges, columns and prestressing tendons were all modeled by the elastic-plastic element, which is different from previous studies [6–10].

A concrete model, Concrete07, developed by Chang and Mander [22, 23], was used to simulate the confined and unconfined concrete in girders, hinges, and columns, illustrated in Figure 3(b).

The column is the most important component that affects the overall seismic performance of the bridge. In order to improve the accuracy of the column simulation, the

longitudinal steels of columns were modeled through hysteretic material in OpenSees, while the concrete was modeled by Concrete07. The hysteretic material parameters were determined by the following process. An experiment of column, Lehman 415S [24], with the similar reinforcement ratio to the typical bridge columns, was simulated by OpenSees. The hysteretic process of the experimental column was obtained through pushover analysis. Obviously, different hysteretic parameters of the longitudinal steels corresponded to different hysteretic results. Through a large amount of pushover analysis and trials to column models with different hysteretic parameters, the hysteretic process of a simulative column, which was most matching with the hysteretic process of the experimental column, was screened out. The hysteretic process of the simulative column and the backbone curves between the simulative and the

TABLE 1: Span length (m).

Spans	1#	2#	3#	4#	5#	6#	7#	8#	Total
Length (m)	48.77	64.01	79.25	79.25	79.25	79.25	64.01	48.77	542.56

TABLE 2: Column height (m).

Columns	1#	2#	3#	4#	5#	6#	7#
Height (m)	12.19	23.16	28.04	34.14	42.67	26.82	8.53

experimental columns are shown in Figures 4(a) and 4(b), respectively. The hysteretic parameters of the longitudinal steel model of the most matching simulative column are presented in Table 3. The model of longitudinal steels in columns is illustrated in Figure 3(c).

A uniaxial Giuffre-Menegotto-Pinto steel material object [25] with isotropic strain hardening, which can simulate the initial tensile stress, was used to model the prestressing tendons through Steel02 material in OpenSees. \$sigInit was used to load the initial stress value of tendons. The prestressing tendon elements were connected to the girder elements through rigid links.

The model developed by Muthukumar [26] was used to represent the shearing force and displacement of elastomeric bearings located at abutments and hinges. Steel01 material was chosen to establish the bilinear relationship of bearing zero-length elements, illustrated in Figure 3(d).

In consideration of the supporting reaction in hinges, the vertical compressive state of the elastomeric bearings in hinges was simulated. The relationship of compressive force and displacement of elastomeric bearings in hinges was captured through the experimental report, "Nonlinear Finite Element Analysis of Elastomers" [27]. The compressive stress-strain relationship of the experimental rubber bearing is listed in Figure 5 [27]. The compressive force and displacement relationship of simulative bearing is listed in Figure 3(e), where initial stiffness and compressive yield stiffness was modeled by elastic material and ElasticPPGap material, respectively. Meanwhile, the parallel material made two previously constructed materials together.

The bilinear model derived from Hertz model considering hysteretic damping, referring to the study of Muthukumar [26] and DesRoches et al. [28], was used to simulate the pounding performance between abutment and girder, as well as hinge and girder, illustrated in Figure 3(f). The bilinear model was modeled using ElasticPPGap material in OpenSees platform, and pounding stiffness parameters were suggested from Nielson's study [29], where  $K_{t1} = 586.3(\text{kN/mm})/\text{m}$ ,  $K_{t2} = 201.73 (\text{kN/mm})/\text{m}$ ,  $K_{\text{eff}} = 238.5(\text{kN/mm})/\text{m}$ ,  $\Delta_y = 2.54 \text{ mm}$ , and  $\Delta_m = 25.4 \text{ mm}$ .

Abutment components, including passive performance, footing transverse response, bearings, and shear keys, were simulated in detail below.

The force vs. displacement response of the abutment backfill was simulated by HyperbolicGap material in OpenSees, which was proposed by Shamsabadi et al. [30, 31]. The nonlinear relationship between the passive force and the abutment displacement was tested by using an abutment

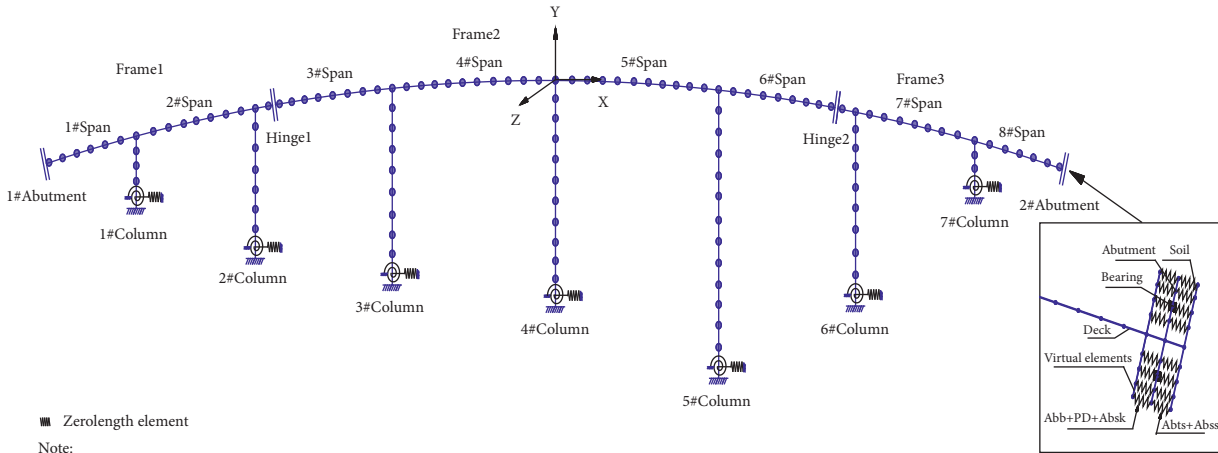
model with a backwall height of 1.68 m. The curve between the passive force and displacement is shown in Figure 3(g), where,  $F_{\text{ult}}$  represents the passive force corresponding to the maximum passive displacement  $\Delta_{\text{max}}$ ,  $\Delta_{\text{ave}}$  represents passive displacement corresponding to 1/2 of  $F_{\text{ult}}$ , and  $K_{\text{Ini}}$  represents mean stiffness of soil.

The transverse force vs. displacement response of the footings beneath the abutments was modeled through soil springs using hysteretic material in OpenSees, shown in Figure 3(h), where the yield stiffness and yield displacement were calculated based on the study of Gazetas and Tassoulas [32], as well as Gadre and Dobry [33].

The shear keys play an important role in resisting the transverse seismic load and limiting the transverse displacement of the bridge. In the event of an earthquake, the shear keys transfer the inertial force of the superstructure to the abutments and the bent caps; sequentially, the abutments and the bent caps transfer the force to the foundations. If the response of the superstructure exceeds the shearing strength of the shear keys, the transferring function of the shear keys can be instantly lost. The ElasticPPGap material in OpenSees was used to simulate the force vs. displacement relationship of shear keys in abutments, illustrated in Figure 3(i), which was based on a strut-and-tie analogous model proposed by Megally et al. [34, 35].

The hinges are located in the #3 and #6 spans of the bridge, which is about 1/6 span length away from the supporting point. The form of hinge is upper-lower and left-right occlusion, called plug-type. The inhibiting devices, set in the hinges, are used to limit the potential moving displacement, and the gap between hinge and girder is filled with polystyrene. Longitudinally, restrainers, composed of 28 high strength steel bundles with the diameter of 3.175 cm, anchored on the concrete on both sides of the hinges. The restrainers, bearing longitudinal tension, and compression are used to connect the left and right frames, limit the longitudinal relative displacement, and restrain the longitudinal collision. Transversely, four transverse compressive pads, with the size of 838.2 mm × 381 mm × 76.2 mm, are used to alleviate the lateral relative displacement in order to restrain the lateral collision, as well as providing vertical shear strength to inhibit the vertical relative displacement. Vertically, two elastomeric rubber bearings, with the size of 1447.8 mm × 609.6 mm × 177.8 mm, are used to bear the compression of the vertical supporting reaction, resist the transverse shear deformation, and restrain the lateral collision.

Previous studies [6–10] believed that the overlimited curvature of concrete cannot occur in hinges, so the hinges were simulated to linear elastic elements. Meanwhile, most of the inhibiting devices in hinges were ignored through connecting the elements rigidly in transverse and vertical direction, except for the longitudinal restrainer being



■ Zerolength element

Note:

- Abb : abutment bearing
- Absk: abutment shear key
- Abts: abutment transverse response
- Abss: abutment passive response
- PD : pounding

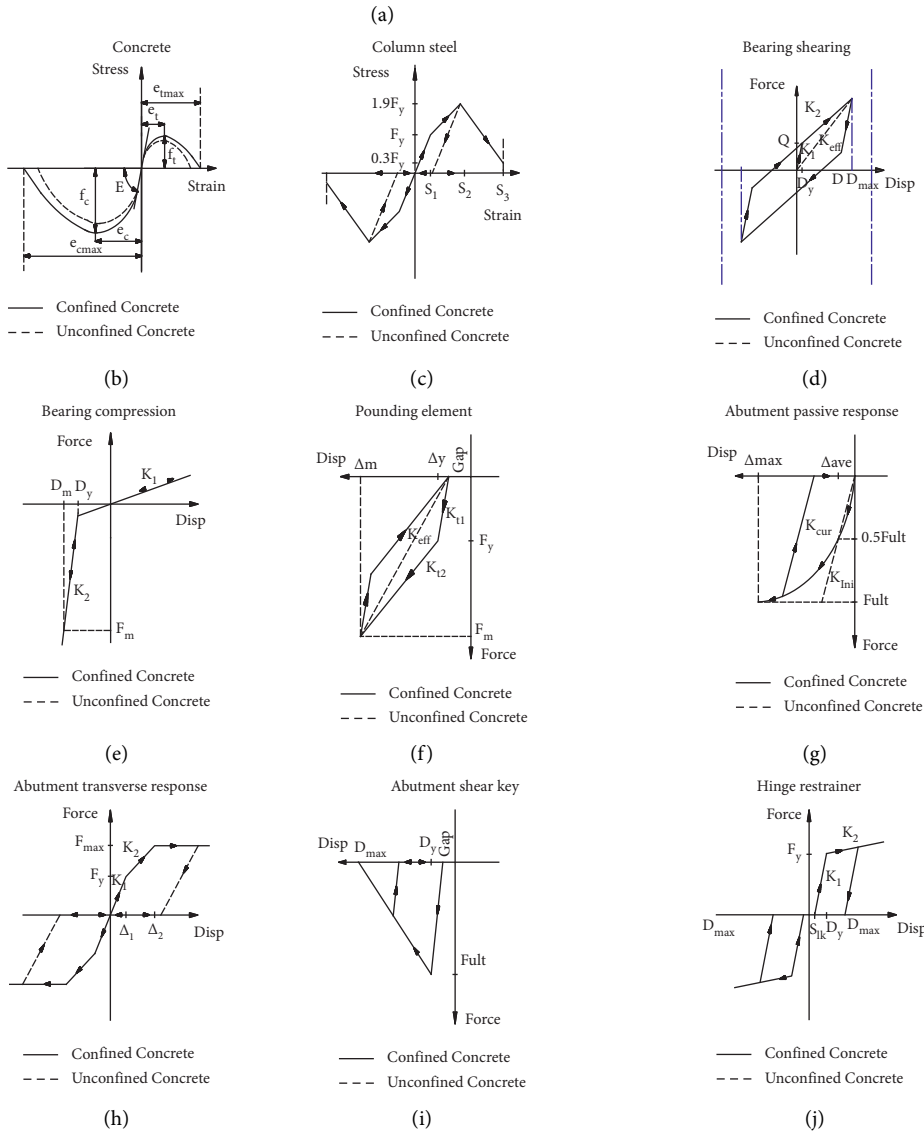


FIGURE 3: Schematic representation and global coordinate of the numerical model. (a) Bridge. (b) Concrete. (c) Longitudinal steel in column. (d) Bearing (shearing). (e) Bearing (compression). (f) Pounding. (g) Abutment passive performance. (h) Abutment transverse response. (i) Shear key. (j) Hinge restrainer.

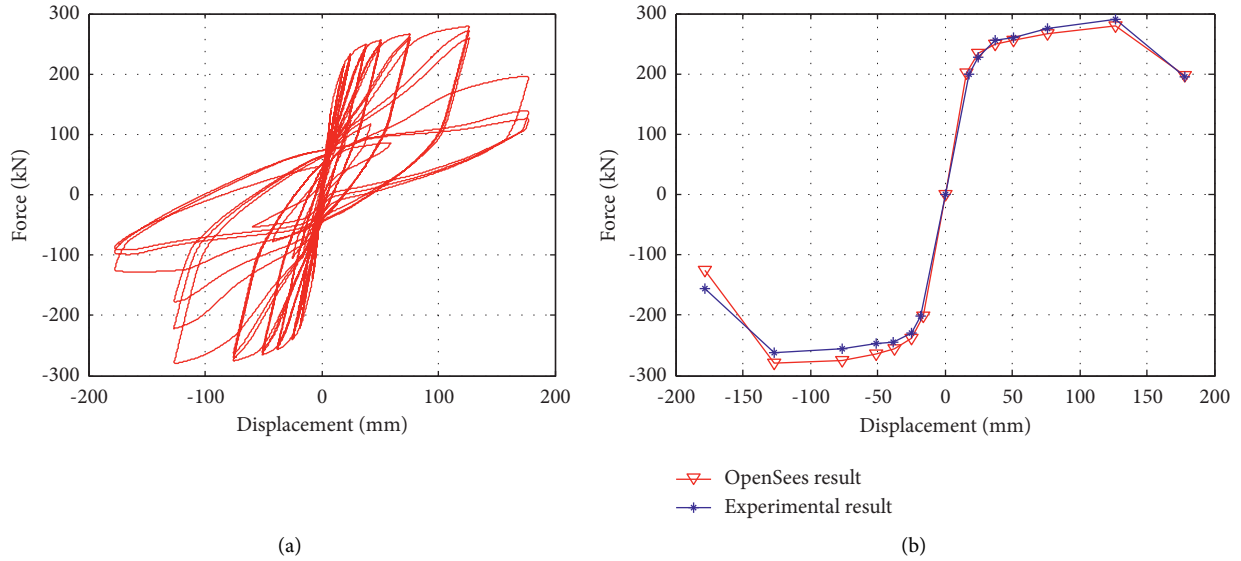


FIGURE 4: Hysteretic process of column. (a) Hysteresis curve of the simulative column. (b) Comparison of backbones between simulation and experiment.

TABLE 3: Parameters of hysteretic material for longitudinal steels in columns.

Number	Parameters	Values
1	$\$s1p$	$\$fys$
2	$\$e1p$	0.003
3	$\$s2p$	$1.9*\$fys$
4	$\$e2p$	0.13
5	$\$s3p$	$0.3*\$fys$
6	$\$e3p$	0.28
7	$\$s1n$	$-\$fys$
8	$\$e1n$	-0.003
9	$\$s2n$	$-1.9*\$fys$
10	$\$e2n$	-0.13
11	$\$s3n$	$-0.3*\$fys$
12	$\$e3n$	-0.28
13	$\$Pinchx$	0.7
14	$\$Pinchy$	0.85
15	$\$damage1$	0.00
16	$\$damage2$	0.33
17	$\$beta$	0.05

<sup>1</sup> $\$fys$  represents the yield strength of steel.

simulated. The previously mentioned simulation can miss the possibility of bending failure of occlusion concrete in hinges. However, in the event of earthquake, the huge inertial load, aggravating the reaction force of the supporting point, results in great bending moment at the root of occlusion concrete in hinge, which can cause the risk of overlimited curvature [36].

In view of the previously mentioned analysis, the hinges were simulated elaborately, shown in Figure 6, using displacement-based beam-column element. The slave elements, generated from the slave nodes, were established to reproduce the precise positions of the occlusion concrete of the hinges. In order to integrate the slave nodes with the master nodes in hinges, Rigidlink constraint was used to connect

two kinds of nodes. Zero-length elements were used to simulate inhibiting devices, such as elastomeric bearings, transverse compressive pads, longitudinal restrainers, and pounding elements in the hinges, as shown in Figure 6.

In the simulation of restrainers, the high strength steel bundles, which are closely bonded to concrete in most length range, are considered having an initial slack in the cables. Once deformation exceeds the slack, the restrainers bear the tension and compression load. According to the study of Ramanathan [37], the initial slack conformed to a uniform distribution bounded between 6.35 mm and 25.4 mm. Meanwhile, the length and the material strength of high strength steel bundle were both considered in simulation, illustrated in Figure 3(j). UniaxialMaterials of ElasticPPGap and Parallel were used simultaneously to capture the force deformation response of restrainer cables.

The pile foundations were simulated through lumped translational and rotational springs at the bases of the columns, calculated by LPILE2018 [38].

**2.3. Modeling Uncertainties.** During the process of design, the designed parameter of bridge was adopted in a certainty form, but during the process of construction and serving, some parameters, like strength, stiffness, geometry, damp, mass, and so on, showed uncertainty within a range [39, 40]. This kind of uncertainty, called cognitive uncertainty, is implemented through imitating the uncertainty of parameter in finite element model when performing the probabilistic seismic demand analysis. Multidimensional stratified sampling method, Latin hypercube sampling (LHS), was adopted to sample the uncertain parameters. The LHS sample data of 10 selected uncertain parameters, including the strength of concrete, yield strength of reinforcement, shear modulus of elastomeric pad, longitudinal gap of abutment, transverse gap of shear key, gap inside hinge, length of restrainer, restrainer initial slack, mass, damping



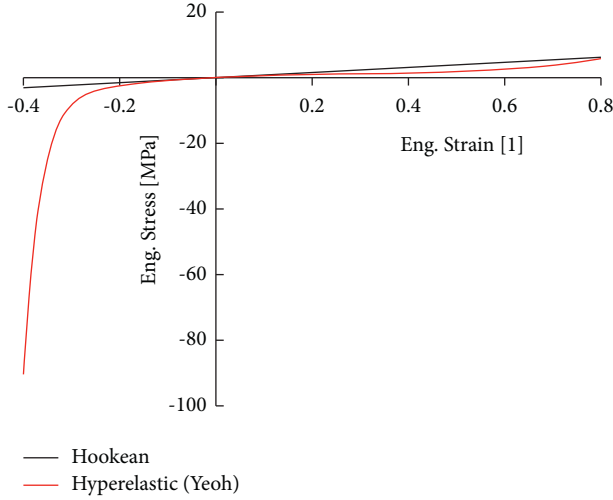


FIGURE 5: Experimental compression curve for elastomeric bearing.

coefficient, were proposed by the work of Ramanathan [37] and Yang et al. [41], as shown in Table 4.

In Table 4,  $\mu$  and  $\sigma$  are mean value and dispersion for normal distribution, and  $\lambda$  and  $\zeta$  are mean value and dispersion for log-normal distribution, respectively. Meanwhile, up and lo are the upper limit value and lower limit value for uniform distribution, respectively.

### 3. Methodology

**3.1. Probabilistic Seismic Demand Model.** In order to estimate the damage to structure during earthquake, fragility analysis has been investigated to represent the probability that the seismic response ( $D$ ) of an engineering demand parameter (EDP) reaches or exceeds a certain limit state ( $L_s$ ) under the ground motion with a given intensity index (IM). The demand and capacity both follow a logarithmic normal distribution [37, 41], and a peak ground acceleration (PGA) was selected to be the IM of ground motions [41–43]. Single component fragility can be acquired as follows:

$$P[D_{\text{EDP}} > L_s | \text{IM}] = \Phi \left[ \frac{\ln S_D - \ln S_{L_s}}{\sqrt{\beta_{D|\text{IM}}^2 + \beta_{L_s}^2}} \right], \quad (1)$$

where  $D_{\text{EDP}}$  and  $L_s$  represent the demand and capacity,  $S_D$  and  $\beta_{D|\text{IM}}$  represent the median value and the logarithmic standard deviation of demand,  $S_{L_s}$  and  $\beta_{L_s}$  represent the median value and the logarithmic standard deviation of capacity, and  $\Phi[*]$  represents the standard normal cumulative distribution function.

The relationship between IM and  $S_D$  can be formulated based on the following:

$$S_D = a (\text{IM})^b, \quad (2)$$

where  $a$  and  $b$  are the regression coefficients, determined by a linear regression from a series of  $D_i$  and  $\text{IM}_i$  corresponding to each time-history analysis of the bridge model and  $D_i$  represents the mean value of peak response of an EDP among the same component of structure under a seismic

load. The logarithmic standard deviation of demand can be formulated based on the following:

$$\beta_{D|\text{IM}} \cong \sqrt{\frac{\sum_{i=1}^N [\ln(D_i) - \ln(a\text{IM}_i^b)]^2}{N-2}}. \quad (3)$$

Therefore, the fragility of every bridge component can be expressed by the probability distribution of demand, which is a function related to IM [11], called the probabilistic seismic demand model (PSDM). In previous studies [44, 45], the fragility curves of single component such as curvature of column and displacement of girder were often used to represent the fragility of the entire bridge system, which could underestimate the fragility of bridge system [46, 47] through replacing the system with a single component. In order to take into account the influence of each component accurately during the seismic evaluation, the joint probability distribution function of seismic demand for the components should be established. In this study, more consideration was given to the correlation between component failure states, so Monte Carlo sampling method [48, 49], due to the strong ability to deal with nonlinear problems and high estimation accuracy [50, 51], was used to develop the fragility of bridge system.

**3.2. Components' Selection.** The fragility of bridge components affects not only the evaluation for local damage state of the bridge, but also the evaluation for overall damage state of the bridge. Therefore, bridge components need to be investigated elaborately. In this study, column, abutment passive performance, abutment transverse response, abutment bearing, abutment shear key, hinge restrainer, and plug-type concrete structure in hinge were selected to be assessable components.

The influence of column on the stability and the load capacity of the bridge is prominent, so the curvature ductility was unquestionably classified as the primary component. Longitudinal deformation of bearing at abutment is severely related to the unseating of the bridge, so abutment bearing was categorized as the primary component, accompanied by setting unseating size as the complete limit state median value. Hinge restrainer, a key component that drives the two adjacent frames vibrating collectively, which greatly influences the overall vibration characteristics and the seismic damage state of the bridge, can be categorized as the primary component. The plug-type concrete structure of hinge, a position that is often overlooked and rarely investigated in detail, is subjected to a large vertical supporting reaction in the static state [36]. When an earthquake occurs, the large curvature in  $z$  direction in this position, produced by bending moment resulting from the supporting reaction, is liable to give rise to bending failure. In the ultimate limit state, the bending fracture is likely to occur in this position, which can result in unseating in hinge. In consideration of the importance of this position, the curvature ductility in  $z$  direction of elements 2 and 3 of the hinge model, shown in Figure 6, was set to be the primary component, called HmcZ for short. Under seismic load, the character of deviation to



column in order to simplify the fragility analysis. Although the data tended to be reasonable within a certain range, the diversity in the form of reinforcement, the size of steel bar, and the size of cross section for columns led to the difference in median values of the limit states for different columns. Therefore, this study performed moment-curvature analysis for seven columns, and the analysis results were regarded as median value of limit states for columns. According to the research of Zhang [54], the damage states of four limit states of columns can be quantified as follows: longitudinal reinforcement yields, concrete compressive strain reaching 0.005, concrete compressive strain reaching 0.011 and the curvature reaching  $0.8 \mu_{\max}$  (ultimate curvature). Moment-curvature analysis [55] of column #1 to column #7 was performed, using Xtract, to acquire the effective yield curvature and ultimate curvature, shown as Table 5. During analysis, axial load is equal to the dead load of the bridge assigned to every column. Moment-curvature analysis for columns is illustrated in Figure 7. According to the definition of curvature ductility,  $\mu$  is the quotient of actual curvature divided by corresponding effective yield curvature during moment-curvature analysis. Table 6 lists the quantified value  $\mu$  of each limit state from column #1, column #3, column #5, and column #7, which corresponds to the result of Ramanathan [37] for post-1990 ductile column. Therefore, the mean values of  $\mu$  from column #1 to column #7 are used as the proposed median values eventually.

For the component of abutment passive performance, 19.5 mm is the proposed median value of slight state, which corresponded to the placement of 1/2 ultimate force of Shamsabadi's model [30, 31], shown in Figure 3(g). Referring to the specification of Hazus®MH 4 Technical Manual [56], 50.8 mm is used to represent the median value of moderate state, summarized from the following provision: "moderate damage of the abutment is defined by moderate movement (<2)". 76.2 mm corresponds to the median value of extensive state, which was used to represent CDT-0 by Ramanathan [37]. The median value, 228.6 mm, of complete state is obtained from displacement of  $y_{\max}$  that came from Shamsabadi's model [30, 31].

The median value of slight, moderate, and extensive states for the component of abutment footing transverse response, referred from Gadre and Dobry's model [33], shown in Figure 3(h), is 7.6 mm, 25.4 mm, 50.8 mm respectively. 101.6 mm, which came from Ramanathan [37] proposed value for CDT-1, is used to represent the median value of complete state.

According to the study by Ramanathan [37], the bearing pads remain elastic until about 100% shear strain and experience significant damage and tearing over 300 to 350% shear strain. According to the thickness of abutment bearings, 51.0 mm, the median values of bearings for the slight and extensive states are proposed to be 51.0 mm and 153.0 mm. Based on the provision of "the maximum shear strain resisted by elastomeric pads prior to failure is estimated at  $\pm 150\%$ " from "Caltrans Seismic Design Criteria Version 1.6" [57], 76.5 mm is used to represent the median value of moderate state. The size of unseating in abutment, 914.4 m, is used to represent the median value of the complete state.

The proposed median values of shear keys for four limit states are calculated from Megally's model [34], shown as Figure 3(i). The calculation is as follows:  $(D_y + \text{Gap})/2 = 17.2$  mm, which is for median value of slight state;  $D_y = 21.6$  mm, which is for median value of moderate state;  $(D_{\max} + D_y)/2 = 542.3$  mm, which is for median value of extensive state;  $D_{\max} = 1063.0$  mm, which is for median value of complete state.

The median values of hinge restrainers are as follows: according to the study by Ramanathan [37], "the CDT-0 and CDT-1 values are set at 75% and 200% of the yield displacement," and therefore, the median values of the slight and extensive state are proposed to be 27.3 mm and 46.4 mm. The median value of moderate state is equal to the yield displacement of restrainers, 31.1 mm. The ultimate deformation of restrainers, 358.8 mm, which corresponds to the ultimate tensile strain of 0.09, is used to represent the median value of the complete state. The proposed median values include the slack of restrainers.

Similar to the columns, Xtract was used to implement moment-curvature analysis for hinges 1 and 2; the effective yield curvature and the ultimate curvature are obtained, shown in Table 7. Axial load is equal to the longitudinal axial force of the bridge. Moment-curvature analysis for hinge elements is illustrated in Figure 8. Through moment-curvature analysis, concrete compressive strain at the root of occlusion concrete in hinge (elements 2 and 3) cannot reach 0.011, so the damage states of four limit states of the hinges can be quantified as follows: cracking, longitudinal reinforcement yields, concrete compressive strain reaching 0.005, and the curvature reaching  $0.8 \mu_{\max}$  (ultimate curvature). Curvature ductility of hinge is defined as the quotient of actual curvature divided by effective yield curvature, which was transplanted from column. Table 8 lists HmcZ and HmcY from the moment-curvature analysis and the corresponding damage description. Moreover, the proposed median values of curvature ductility for every limit state were extracted referring to analysis result.

Followed from Ramanathan [37] and Abbasi and Moustafa [11], 0.35 was adopted to represent the dispersion values of log-normal distribution for every component in four limit states, which was proved to be the good estimated value. The proposed median values (med) and dispersion values (disp) of bridge components are listed in Table 9.

## 4. Seismic Fragility Assessment

**4.1. Ground Motions.** A bin of 48 ground motions, collected from the Rix and Fernandez [58], was used to perform the nonlinear time-history analysis to the typical bridge model. Through each model paired with a set of parameters from Latin hypercube sample, shown as Table 4, 48 groups of typical bridge models, with different material, stiffness, geometry, damp, and mass parameters, were formed to match with 48 ground motions. Therefore, a set of 48 time-history analyses was performed in the typical bridge model to acquire the peak demand of every component.

TABLE 5: Moment-curvature analysis qualitative description of columns.

Columns	#1	#2	#3	#4	#5	#6	#7
Axial load (kN)	16424	21472	25059	25255	27839	22209	15607
Effective yield curvature ( $10^{-6}$ 1/mm)	1.44	1.46	1.48	1.48	1.55	1.47	1.43
Ultimate curvature ( $10^{-6}$ 1/mm)	29.04	27.24	25.66	25.60	23.34	26.95	29.65

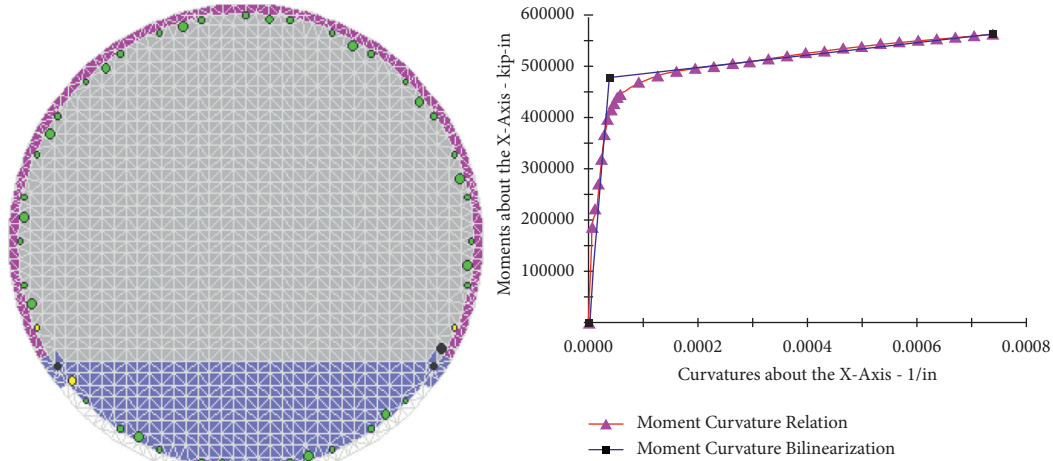


FIGURE 7: Schematic diagram of moment-curvature analysis for columns.

TABLE 6: Curvature ductility of columns for each limit state.

Limit state	Description	Calculated values				Ramanathan's proposed values	Proposed values
		Column #1	Column #1	Column #5	Column #7		
Slight	Longitudinal reinforcement yields	0.9	1.0	0.8	0.9	1.0	0.9
Moderate	Concrete compressive strain reaches 0.005	4.3~5.2	3.2~3.9	2.9~3.6	4.4	4.0	4.0
Extensive	Concrete compressive strain reaches 0.011	10.8~11.8	9.5~10.2	8.3	11.1	8.0	9.0
Complete	Curvature reaches $0.8\mu_{max}$	16.0	13.9	12.1	16.5	12.0	14.0

TABLE 7: Moment-curvature analysis qualitative description of hinges.

Hinges 1, 2	My	Mz
Axial load (kN)	1598	1598
Effective yield curvature ( $10^{-6}$ 1/mm)	1.66	2.20
Ultimate curvature ( $10^{-6}$ 1/mm)	50.79	66.34

4.2. *Seismic Fragility Parameters.* The fragility curves in each limit state are mainly determined by two parameters, median value ( $\lambda_f$ ), and dispersion value ( $\beta_f$ ) of log-normal distribution. The corresponding parameters for bridge system and components are listed in Table 10.

The difference of fragility curves for the system and components can be intuitively evaluated by the histograms of median IM value in fragility function. The median PGA values of bridge system and each component are shown in Figure 9. As illustrated in Figure 9, the bridge system has the lowest median PGA value, compared with any other components, across the four limit states, which indicates that the system is more vulnerable than any other components that

are consistent with the research results of previous studies [11, 37, 41].

As found in Figure 9(a), the median PGA values of Abts and Hs are low and closest to the median PGA value of bridge system in the slight and moderate limit states, which demonstrates that the probabilities of exceeding slight and moderate limit states to the abutment transverse response and the hinge restrainers are large, while these two components are dominant to bridge system fragility in the previously mentioned two states. The median PGA value of HmcZ is low and much lower than that of HmcY, which indicates that, in the slight and moderate limit states, curvature ductility in z direction of plug-type concrete structure in hinge exhibits a higher fragility than that in y direction.

With reference to Figure 9(b), column and Hs have the lowest median PGA values in the extensive limit state, which demonstrates that the components have the greatest probability of exceeding the extensive limit state. Further, the median PGA value of Hs is the closest to that of bridge system, indicating that the hinge restrainers have the most dominant influence on the vulnerability of

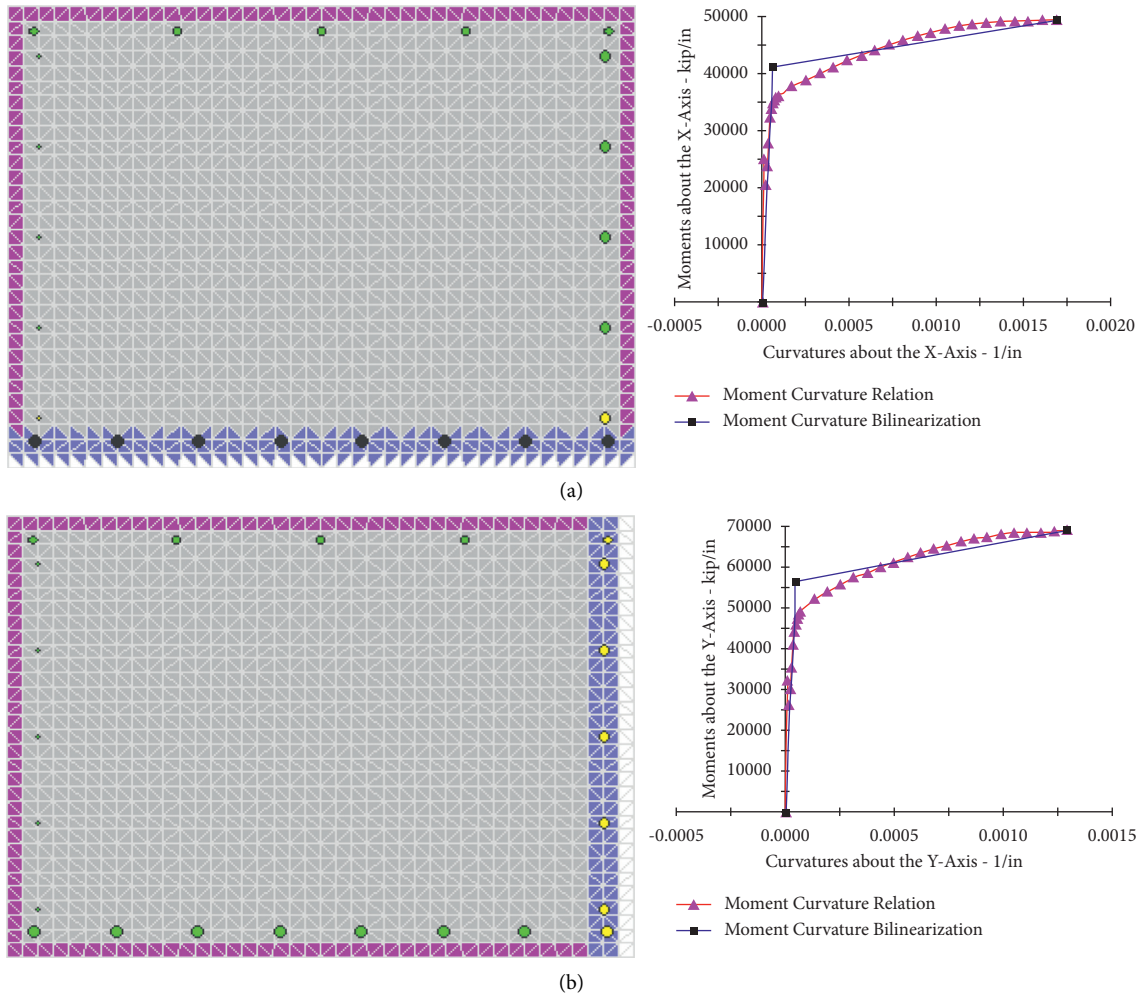


FIGURE 8: Schematic diagram of moment-curvature analysis for hinges. (a) HmcZ. (b) HmcY.

bridge system in the previously mentioned state. Figure 9(b) also shows that the median PGA value of column, among all primary components, is the lowest in the complete limit state, indicating that the probability of exceeding the complete limit state to column is the largest and column exhibits maximum vulnerability. Based on Figures 9(a) and 9(b), along with the aggravating of the damage state gradually, the median PGA values of column and that of bridge system match gradually and are nearly equal in the complete limit state, which demonstrates that, according to the damage degree aggravation, column is increasingly dominant to bridge system fragility. According to Figure 9(b), in the extensive and complete limit state, both HmcZ and HmcY exhibit the high median PGA values, suggesting that the damage probabilities of curvature ductility of plug-type concrete structure in hinge are intensely low. Abb exhibits the intensely large median PGA values in the previously mentioned two states, indicating that the probability of exceeding the extensive state and complete state to abutment bearings is extremely low so that the probability of unseating failure hardly happens at abutment. The large median PGA value of Hs in the complete limit

state signifies the probability of deformation of the hinge restrainers attaining to the ultimate is exceedingly low.

**4.3. Seismic Fragility Assessment.** The probabilistic seismic demand model of the typical bridge subjected to the suite of synthetic seismic loads was established through performing nonlinear time-history analysis, and the seismic fragility curves of bridge system and components are developed in Figures 10 and 11. The fragility analysis is discussed as follows.

As illustrated in Figure 10(a), column, Hs, and HmcZ exhibit the high probability of exceeding the slight limit state. Although Abb and HmcY are not the most vulnerable components, they still have a certain damage exceedance probability in the slight limit state. The fragility curves shown in Figure 10(a), along with the description of the limit states for HmcZ and HmcY discussed in Table 8, demonstrate that the hinge has the risk of the transverse and vertical cracks generating at the root of element next to the supporting point. The risk probability of transverse cracks generating is higher than that of vertical cracks due to the large supporting reaction.

TABLE 8: Curvature ductility of hinges for every limit state.

Limit state	Description	HmcY		HmcZ	
		Calculated values	Proposed values	Calculated values	Proposed values
Slight	Cracking	0.15	0.15	0.15	0.15
Moderate	Longitudinal reinforcement yields	1.0	1.0	0.8	1.0
Extensive	Concrete compressive strain reaches 0.005	18.9~23.3	19.0	18.7~23.0	19.0
Complete	Curvature reaches $0.8\mu_{max}$	24.4	24.0	24.2	24.0

TABLE 9: Limit states of bridge components.

Components	Abbreviation	Units	Slight		Moderate		Extensive		Complete				
			Med	Disp	Med	Disp	Med	Disp	Med	Disp	Med	Disp	
1 Pri	Column	Column	$\mu$	0.90	0.35	4.0	0.35	9.0	0.35	14.0	0.35		
2 Sec	Abutment passive	Abss	mm	19.5	0.35	50.8	0.35	76.2 (1000)	0.35	228.6 (1000)	0.35		
3 Sec	Abutment trans	Abts	mm	7.6	0.35	25.4	0.35	50.8 (1000)	0.35	101.6 (1000)	0.35		
4 Pri	Abutment bearing	Abb	mm	51.0	0.35	76.5	0.35	153.0	0.35	914.4	0.35		
5 Sec	Abutment shear key	AbSk	mm	17.2	0.35	21.6	0.35	542.3 (1000)	0.35	1063.0	0.35		
6 Pri	Hinge restrainer	Hs	mm	27.3	0.35	31.1	0.35	46.4	0.35	358.8	0.35		
7 Pri	Hinge My (Ele2, 3)	HmcY	$\mu$	0.15	0.35	1.0	0.35	19.0	0.35	24.0	0.35		
8 Pri	Hinge Mz (Ele2, 3)	HmcZ	$\mu$	0.15	0.35	1.0	0.35	19.0	0.35	24.0	0.35		

<sup>1</sup>The values in ( ) are used for fragility analysis of bridge components.

<sup>2</sup>The values outside ( ) are used for fragility analysis of bridge system.

TABLE 10: Fragility parameters for bridge system and components.

System and components	Slight		Moderate		Extensive		Complete	
	$\lambda_f (g)$	$\beta_f$	$\lambda_f (g)$	$\beta_f$	$\lambda_f (g)$	$\beta_f$	$\lambda_f (g)$	$\beta_f$
System	0.022	0.418	0.059	0.524	0.246	0.878	1.128	0.395
Column	0.180	0.399	0.504	0.399	0.882	0.399	1.197	0.399
Abss	0.219	0.971	0.490	0.971	—	—	—	—
Abts	0.023	0.458	0.065	0.458	—	—	—	—
Abb	0.377	1.490	1.726	1.490	23.26	1.490	Huge	1.490
AbSk	1.297	2.075	2.350	2.075	—	—	—	—
Hs	0.097	1.040	0.122	1.040	0.240	1.040	7.956	1.040
HmcY	0.846	0.755	4.191	0.755	50.21	0.755	61.143	0.755
HmcZ	0.130	0.624	0.634	0.624	7.407	0.624	9.002	0.624

Based on Figure 10(b), in the moderate limit state, column and Hs are the most vulnerable components, while Abb and HmcZ have certain vulnerability in contrast to the low vulnerability of HmcY. The previously mentioned results indicate that, under seismic load, the deformation of abutment bearings has a risk of exceeding 1.5 times thickness and the hinge has a risk of longitudinal steels yielding at the root of element next to the supporting point. The risk probability of longitudinal steels yielding is greater at the bottom of section than that at its side in hinge.

As shown in Figure 10(c), in the extensive limit state, column and Hs are still the most vulnerable components. Abb, HmcZ, and HmcY are less vulnerable and have a low probability of exceeding the limit state. The results demonstrate that the deformation of abutment bearings has a low risk of exceeding 3.0 times thickness, and hinges exhibit a low risk of reaching states like shearing cracks, concrete spalling, and section cracks expanding.

According to Figure 10(d), in the complete limit state, the fragility of column, which is high, is close to that of bridge system. Nevertheless, the vulnerabilities of other

primary components are low, indicating that the damage of Abb, Hs, HmcY, and HmcZ could hardly exceed the complete limit state. The discussion demonstrates that the probability of the unseating failure at abutment and hinge is extremely low and the fracture failure at the intermediate hinge can hardly be generated.

Figures 11(a) and 11(b) illustrate that the fragility curves of bridge system and the fragility curves of Abts overlap fundamentally in the slight and moderate limit states, which indicates that Abts has the most prominent influence on the fragility of bridge system in these two limit states.

According to Figures 11(c) and 11(d), in the extensive and complete limit states, the fragility of AbSk is basically zero, which demonstrates the probabilities that shear keys exceed the extensive and complete limit states are very little. Shear keys with lateral large stiffness transfer the inertial force from superstructure to abutment smoothly, which cannot generate the relative lateral misplaced failure between abutment and superstructure. Nevertheless, the inertial force from superstructure will be transmitted to the abutment foundation through the

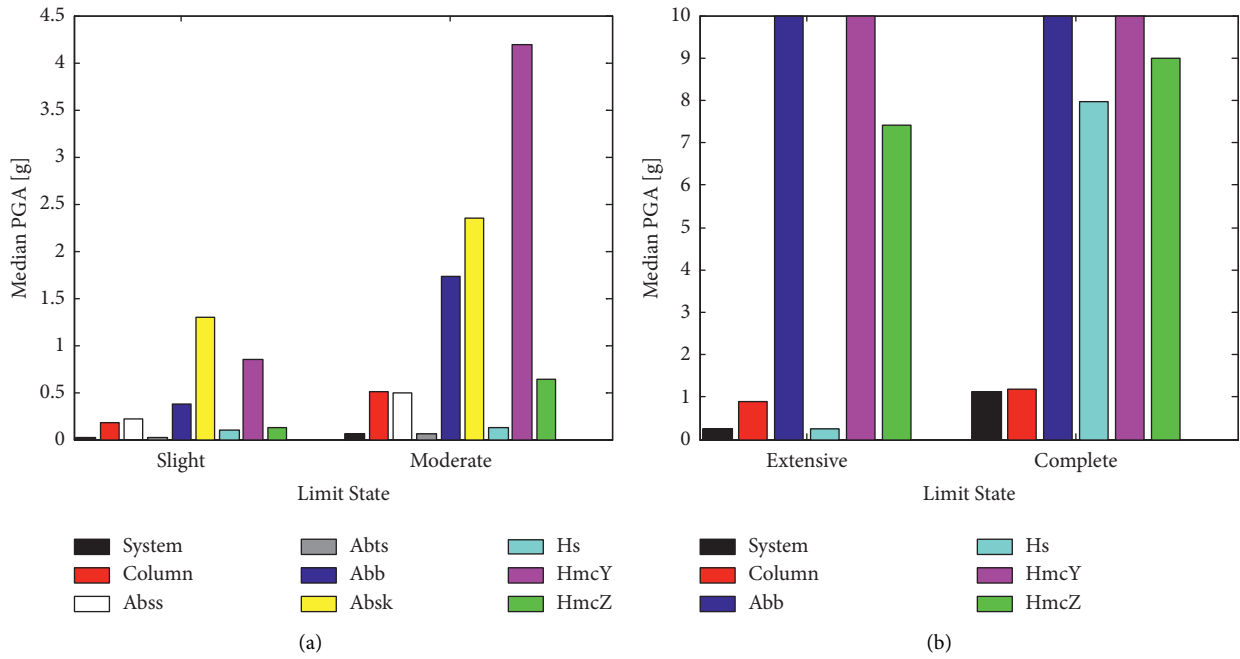


FIGURE 9: Median PGA values of calculated fragility functions for bridge system and all components in the (a) slight and moderate limit states and (b) extensive and complete limit states.

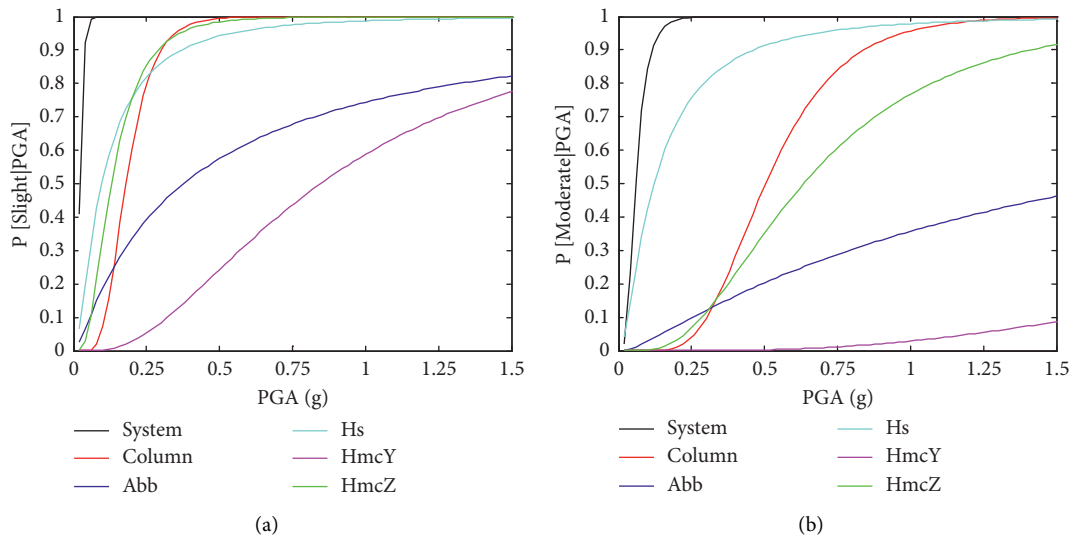


FIGURE 10: Continued.

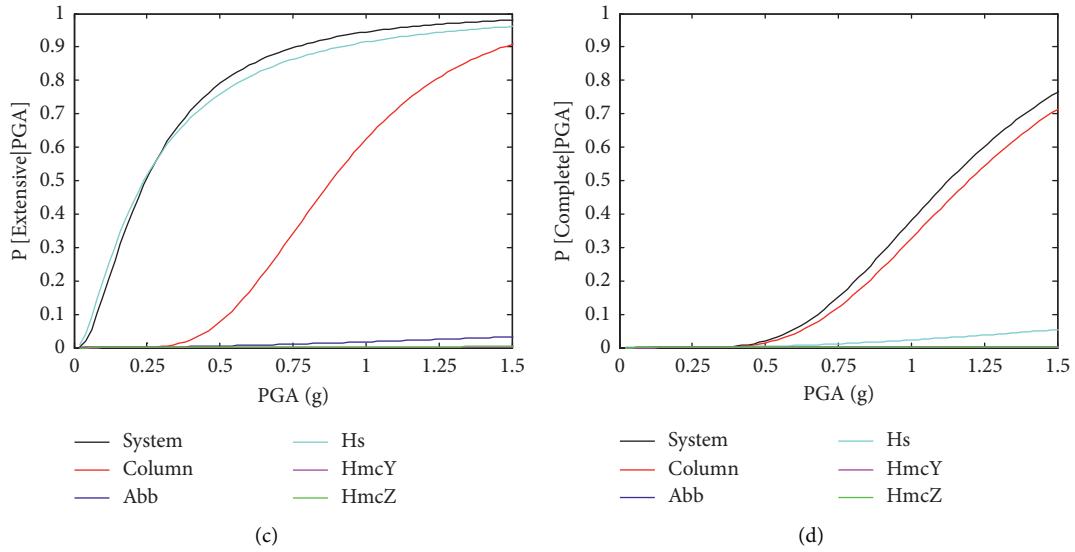


FIGURE 10: Seismic fragility curves of the system and primary components in the (a) slight, (b) moderate, (c) extensive, and (d) complete limit states.

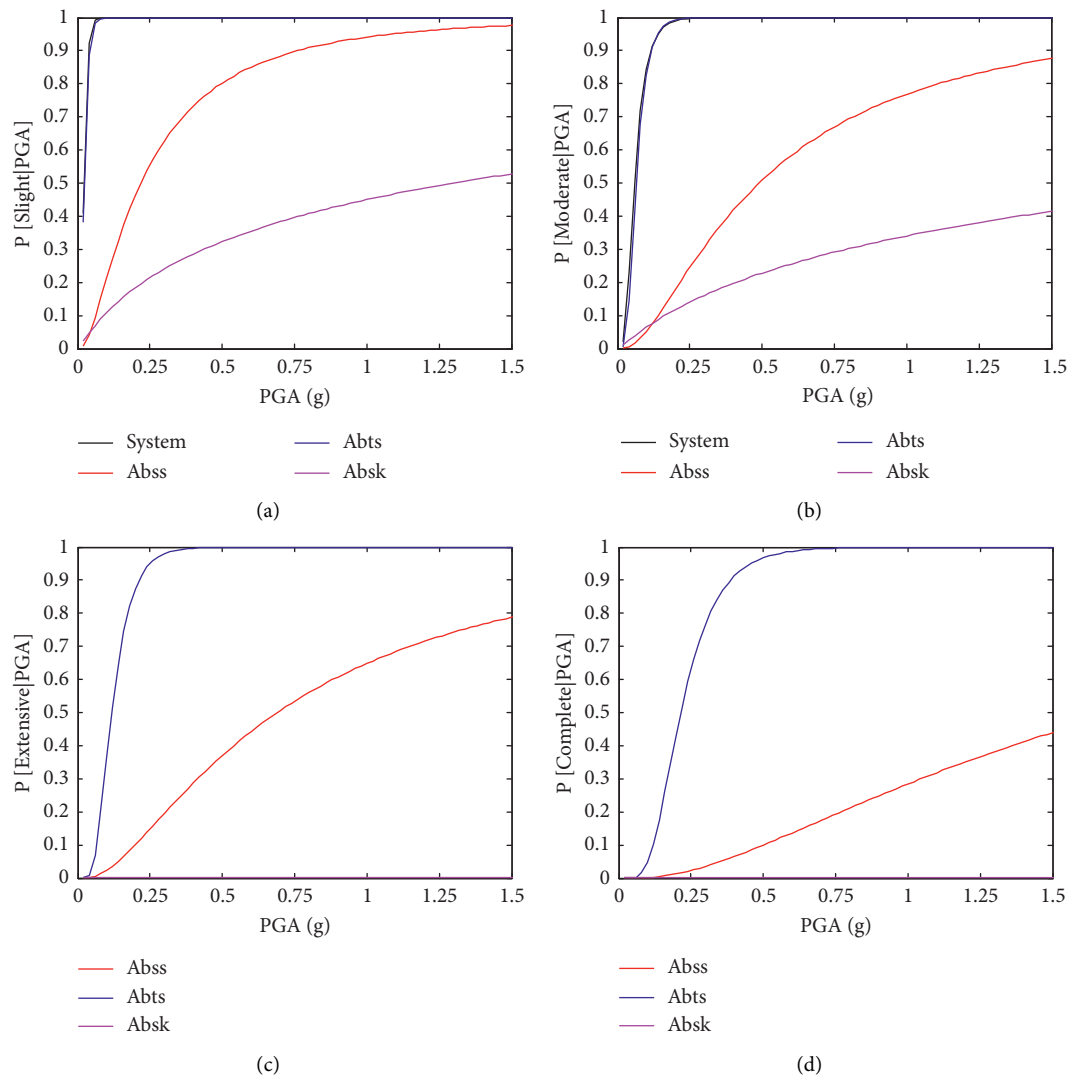


FIGURE 11: Seismic fragility curves of the system and secondary components in the (a) slight, (b) moderate, (c) extensive, and (d) complete limit states.



shear keys, which could result in the huge damage of abutment transverse response.

## 5. Summary and Conclusions

Fragility assessment of a multiframe prestressed concrete box-girder bridge with intermediate hinges, located in California, was performed in this study. Elaborate modeling along with definition of damage indexes for components could be used as a template to the similar type of bridge. Through fragility analysis of bridge system and components, the following conclusions can be obtained.

Column exhibits high fragility across all four limit states. Moreover, in the complete limit state, column fragility is extremely close to bridge system fragility, which indicates that bridge system fragility is gradually determined by columns along with aggravating of damage state. Abb exhibits certain fragility in the slight and moderate limit states, while the fragility is intensely low, almost zero, in the extensive and complete limit states, which manifests that the deformation of abutment bearings is arduous to exceed 3.0 times thickness, and the probability of unseating occurring at abutment is virtually impossible. Hs has high fragility across the three limit states of slight, moderate, and extensive, while, in the complete limit state, the fragility is intensely low, almost zero, which indicates that the probability of ultimate deformation occurring at intermediate hinge is extremely low. HmcZ has high fragility in the slight limit state, certain fragility in the moderate state, and almost no fragility in the extensive and complete state. HmcY has certain fragility in the slight limit state, low fragility in the moderate state, and almost no fragility in the extensive and complete state.

The fragility results demonstrate that transverse and vertical cracks are generated at intermediate hinges with a high probability during earthquake; meanwhile, the probability of generating transverse cracks is greater than that of generating vertical cracks. Besides, there is a risk of longitudinal steels yielding in these positions, which is greater at the bottom of section than that at its side. It can be speculated that the large reaction force from supporting point could give rise to the large bending moment at the bottom of intermediate hinges, which would raise the risk of fracture failure in these positions. Obviously, seismic damage probability in the plug-type hinge exists deterministically, especially in the slight limit state and moderate limit state, which cannot be ignored. Construction errors, which may result in size deviation of hinges or installation deviation of inhibiting devices in hinges, could greatly affect the fragility of intermediate hinges and even threaten the safety of the whole bridge. Among all errors, the deviation of elastomeric bearings in hinges could lead to the most serious influence on the bridge.

## Data Availability

The data used to support the findings of this study are included within the article.

## Conflicts of Interest

The authors declare that there are no conflicts of interest regarding the publication of this paper.

## Acknowledgments

This research was supported by (i) the Basic Research Expense Project of Heilongjiang Provincial Colleges and Universities (Grant no. 2020-KYYWF-1039) and (ii) the National Natural Science Foundation of China (NSFC) (Grant no. 11774081).

## References

- [1] B. A. Castillo, S. F. McGill, K. M. Scharer et al., "Prehistoric earthquakes on the banning strand of the san andreas fault, north palm springs, California," *Geosphere*, vol. 17, no. 3, pp. 685–710, 2021.
- [2] K. Blisniuk, K. Scharer, W. D. Sharp, R. Burgmann, C. Amos, and M. Rymer, "A revised position for the primary strand of the pleistocene-holocene san andreas fault in southern California," *Science Advances*, vol. 7, no. 13, p. 14, Article ID eaaz5691, 2021.
- [3] M. Mehr and A. E. Zaghi, "Modified elastic dynamic analysis (eda) for seismic demand on in-span hinge shear keys in multi-frame bridges," *Transportation Research Record: Journal of the Transportation Research Board*, vol. 2672, no. 41, pp. 75–86, 2018.
- [4] E. Aboutorabian and M. Raissi Dehkordi, "Numerical study of seismic response of irregular multi-frame reinforced concrete bridges," *Proceedings of the Institution of Civil Engineers - Structures and Buildings*, vol. 173, no. 11, pp. 783–798, 2020.
- [5] M. A. Hube and K. M. Mosalam, "Experimental and computational evaluation of current and innovative in-span hinge details in reinforced concrete box-girder bridges," *Report PEER 2008/103, Pacific Earthquake Engineering Center*, PEER, Berkeley, CA, USA, 2008.
- [6] J.-S. Jeon, S. Mangalathu, J. Song, and R. Desroches, "Parameterized seismic fragility curves for curved multi-frame concrete box-girder bridges using bayesian parameter estimation," *Journal of Earthquake Engineering*, vol. 23, no. 6, pp. 954–979, 2019.
- [7] M. Mehr and A. E. Zaghi, "Seismic response of multi-frame bridges," *Bulletin of Earthquake Engineering*, vol. 14, no. 4, pp. 1219–1243, 2016.
- [8] J.-S. Jeon, R. DesRoches, T. Kim, and E. Choi, "Geometric parameters affecting seismic fragilities of curved multi-frame concrete box-girder bridges with integral abutments," *Engineering Structures*, vol. 122, no. 1, pp. 121–143, 2016.
- [9] R. DesRoches and G. L. Fenves, "Simplified restrainer design procedure for multiple-frame bridges," *Earthquake Spectra*, vol. 17, no. 4, pp. 551–567, 2001.
- [10] G. L. Fenves and M. Ellery, "Behavior and failure analysis of a multiple-frame highway bridge in the 1994 northridge earthquake," *Report PEER 1998/08, Pacific Earthquake Engineering Research Center*, PEER, Berkeley, CA, USA, 1998.
- [11] M. Abbasi and M. A. Moustafa, "Time-dependent seismic fragilities of older and newly designed multi-frame reinforced concrete box-girder bridges in California," *Earthquake Spectra*, vol. 35, no. 1, pp. 233–266, 2019.
- [12] Y. Youb, A. Kadid, and H. Lombarkia, "Analysis of the post-mainshock behavior of reinforced concrete bridge pier

- columns subjected to aftershocks,” *Jordan Journal of Civil Engineering*, vol. 15, no. 2, pp. 193–208, 2021.
- [13] M. Sajed and P. Tehrani, “Effects of column and superstructure irregularity on the seismic response of four-span RC bridges,” *Structure*, vol. 28, pp. 1400–1412, 2020.
- [14] X. Li, K. D. Chen, P. Hu, W. He, L. Xiao, and R. Zhang, “Effect of ECC jackets for enhancing the lateral cyclic behavior of RC bridge columns,” *Engineering Structures*, vol. 219, Article ID 110714, 2020.
- [15] C. Y. Jiao, J. Z. Li, B. Wei, P. Long, and Y. Xu, “Experimental investigations on seismic responses of RC circular column piers in curved bridges,” *Earthquakes and Structures*, vol. 17, no. 5, pp. 435–445, 2019.
- [16] S. Kurino, W. Wei, and A. Igarashi, “Seismic fragility and uncertainty mitigation of cable restrainer retrofit for isolated highway bridges incorporated with deteriorated elastomeric bearings,” *Engineering Structures*, vol. 237, Article ID 112190, 2021.
- [17] R. Sarkar and K. Pareek, “Influence of stratification and assessment of fragility curves for mountain tunnels,” *Proceedings of the Institution of Civil Engineers–Geotechnical Engineering*, vol. 174, no. 3, pp. 279–290, Article ID 1900134, 2021.
- [18] S. Song, S. Wang, G. Wu, and B. S. Xu, “Seismic vulnerability analysis of small and medium span girder bridges,” *Journal of Vibration and Shock*, vol. 39, no. 9, pp. 118–125, 2020.
- [19] Z. Zhao, X. W. Lu, Y. Guo, and X. Zhao, “Seismic fragility assessment of base-isolated steel water storage tank,” *Shock and Vibration*, vol. 2020, Article ID 8835943, 13 pages, 2020.
- [20] H. Derakhshan, K. Q. Walsh, J. M. Ingham, M. C. Griffith, and D. P. Thambiratnam, “Seismic fragility assessment of non-structural components in unreinforced clay brick masonry buildings,” *Earthquake Engineering & Structural Dynamics*, vol. 49, no. 3, pp. 285–300, 2019.
- [21] F. McKenna and G. L. Fenves, *Open System for Earthquake Simulation Framework (OpenSees) Ver. 2.4.4*. Pacific Earthquake Engineering Research Center (PEER), University of California, Berkeley, CA, USA, 2014.
- [22] G. A. Chang and J. B. Mander, “Seismic energy based fatigue damage analysis of bridge columns: part I- evaluation of seismic capacity,” Technical Report 94-0006, NCEEER, Buffalo, NY, USA, 1994.
- [23] J. D. Waugh, “Nonlinear analysis of T-shaped concrete walls subjected to multidirectional displacements,” Ph.D. Thesis, Iowa State University, Ames, IA, USA, 2009.
- [24] D. Lehman, J. Moehle, S. Mahin, A. Calderone, and L. Henry, “Experimental evaluation of the seismic performance of reinforced concrete bridge columns,” *Journal of Structural Engineering*, vol. 130, no. 6, pp. 869–879, 2004.
- [25] F. C. Filippou, E. P. Popov, and V. V. Bertero, *Effects of Bond Deterioration on Hysteretic Behavior of Reinforced Concrete Joints*, Report EERC 83-19, Earthquake Engineering Research Center, University of California, Berkeley, CA, USA, 1983.
- [26] S. Muthukumar, *A contact element approach with hysteresis damping for the analysis and design of pounding in bridges*, Ph.D. Thesis, Georgia Institute of Technology, Atlanta, GA, USA, 2003.
- [27] MSC Software Corporation, *Nonlinear Finite Element Analysis of Elastomers*, MSC Software: Whitepaper Report, Santa Ana, CA, USA, 2000.
- [28] R. DesRoches and S. Muthukumar, “Implications of seismic pounding on the longitudinal response of multi-span bridges—an analytical perspective,” *Earthquake Engineering and Engineering Vibration*, vol. 3, no. 1, pp. 57–65, 2004.
- [29] B. G. Nielson, *Analytical fragility curves for highway bridges in moderate seismic zones*, Ph.D. Thesis, Georgia Institute of Technology, Atlanta, GA, USA, 2005.
- [30] A. Shamsabadi, K. M. Rollins, and M. Kapuskar, “Nonlinear soil-abutment-bridge structure interaction for seismic performance-based design,” *Journal of Geotechnical and Geoenvironmental Engineering*, vol. 133, no. 6, pp. 707–720, 2007.
- [31] A. Shamsabadi and L. Yan, “Closed-form force-displacement backbone curves for bridge abutment-backfill systems,” *Geotechnical Earthquake Engineering and Soil Dynamics Congress*, vol. IV, 2008.
- [32] G. Gazetas and J. L. Tassoulas, “Horizontal stiffness of arbitrarily shaped embedded foundations,” *Journal of Geotechnical Engineering*, vol. 113, no. 5, pp. 440–457, 1987.
- [33] A. Gadre and R. Dobry, “Lateral cyclic loading centrifuge tests on square embedded footing,” *Journal of Geotechnical and Geoenvironmental Engineering*, vol. 124, no. 11, pp. 1128–1138, 1998.
- [34] S. H. Megally, P. F. Silva, and F. Seible, “Seismic response of sacrificial shear keys in bridge abutments,” *Structural Systems Research Project, Report No. SSRR-2001/23*, University of California, San Diego, CA, USA, 2002.
- [35] A. Bozorgzadeh, S. Megally, J. I. Restrepo, and S. A. Ashford, “Capacity evaluation of exterior sacrificial shear keys of bridge abutments,” *Journal of Bridge Engineering*, vol. 11, no. 5, pp. 555–565, 2006.
- [36] T. Wu and Q. S. Sun, “Study and analysis for seismic response of hinge in frame-style curved girder bridge,” *Engineering Mechanics*, vol. 33, no. 10, pp. 155–163, 2016, (in Chinese).
- [37] K. N. Ramanathan, *Next generation seismic fragility curves for California bridges incorporating the evolution in seismic design philosophy*, Ph.D. Thesis, Georgia Institute of Technology, Atlanta, GA, USA, 2012.
- [38] W. M. Isenhower, S. T. Wang, and L. G. Vasquez, *A Program to Analyze Deep Foundations under Lateral Loading, User’s Manual for LPile 2018*, 2018.
- [39] X. B. Hu, C. Lu, and X. Q. Zhu, “A simplified model for dynamic response analysis of framed self-centering wall structures under seismic excitations,” *Shock and Vibration*, vol. 2019, Article ID 2360150, 14 pages, 2019.
- [40] S. Hamidpour and M. Soltani, “Probabilistic assessment of ground motions intensity considering soil properties uncertainty,” *Soil Dynamics and Earthquake Engineering*, vol. 90, pp. 158–168, 2016.
- [41] C.-S. W. Yang, S. D. Werner, and R. DesRoches, “Seismic fragility analysis of skewed bridges in the central southeastern United States,” *Engineering Structures*, vol. 83, pp. 116–128, 2015.
- [42] F. Che, C. Yin, J. L. Zhou et al., “Embankment seismic fragility assessment under the near-fault pulse-like ground motions by applying the response surface method,” *Shock and Vibration*, vol. 2021, Article ID 8849043, 15 pages, 2021.
- [43] Z. P. Song, J. C. Mao, X. X. Tian, Y. Jang, and J. Wang, “Optimization analysis of controlled blasting for passing through houses at close range in super-large section tunnels,” *Shock and Vibration*, vol. 2019, Article ID 1941436, 16 pages, 2019.
- [44] A. Kibboua, M. Naili, D. Benouar, and F. Kehila, “Analytical fragility curves for typical Algerian reinforced concrete bridge piers,” *Structural Engineering & Mechanics*, vol. 39, no. 3, pp. 411–425, 2011.
- [45] J. Simon, J. M. Bracci, and P. Gardoni, “Seismic response and fragility of deteriorated reinforced concrete bridges,” *Journal of Structural Engineering*, vol. 136, no. 10, pp. 1273–1281, 2010.

- [46] S. Song, Y. J. Qian, and G. Wu, "Research on seismic fragility method of bridge system based on copula function," *Engineering Structures*, vol. 33, no. 11, pp. 193–200, 2016.
- [47] K. F. Zheng, L. B. Chen, W. L. Zhuang, H.-S. Ma, and J. J. Zhang, "Bridge vulnerability analysis based on probabilistic seismic demand models," *Engineering Mechanics*, vol. 30, no. 5, pp. 165–171, 2013.
- [48] Y. H. Gu, Y. C. Liu, and C. D. Lu, "Brake noise reduction method based on Monte Carlo sampling and particle swarm optimization," *Shock and Vibration*, vol. 2021, Article ID 8878223, 11 pages, 2021.
- [49] X. Q. Chen, Z. P. Shen, and X. Liu, "A copula-based and Monte Carlo sampling approach for structural dynamics model updating with interval uncertainty," *Shock and Vibration*, vol. 2018, Article ID 3958016, 11 pages, 2018.
- [50] B. G. Nielson and R. DesRoches, "Seismic fragility methodology for highway bridges using a component level approach," *Earthquake Engineering & Structural Dynamics*, vol. 36, no. 6, pp. 823–839, 2007.
- [51] E. Choi, R. DesRoches, and B. Nielson, "Seismic fragility of typical bridges in moderate seismic zones," *Engineering Structures*, vol. 26, no. 2, pp. 187–199, 2004.
- [52] K. K. Moridani, P. Zarfam, and M. G. Ashtiany, "Seismic failure probability of a curved bridge based on analytical and neural network approaches," *Shock and Vibration*, vol. 2017, Article ID 2408234, 18 pages, 2017.
- [53] C. Zhang, C. W. Wu, and P. G. Wang, "Seismic fragility analysis of bridge group pile foundations considering fluid-pile-soil Interaction," *Shock and Vibration*, vol. 2020, Article ID 8838813, 17 pages, 2020.
- [54] Y. Zhang, P. Tan, J. X. Zheng, and F. L. Zhou, "Seismic fragility analysis on isolated bridges with flexible column piers," *Journal of Vibration and Shock*, vol. 34, no. 16, pp. 48–54, 2015.
- [55] H. J. Zhao, Q. N. Li, J. Zhao, S. F. Li, and Y. Zheng, "Calculation method for moment-curvature of high strength concrete shear wall confined with high strength rectangle spiral reinforcements," *Engineering Mechanics*, vol. 37, no. 9, pp. 123–132, 2020.
- [56] Earthquake model technical manual, *Department of Homeland Security, Federal Emergency Management Agency*, Vol. 4, Hazus-MH MR, Mitigation Division, Washington, D.C, 2003.
- [57] Caltrans 1.6, *Caltrans Seismic Design Criteria*, California Department of Transportation, Sacramento, CA, USA, 2010.
- [58] G. J. Rix and J. A. Fernandez, "Synthetic ground motions for memphis," TN [http://geosystems.ce.gatech.edu/soil\\_dynamics/research/groundmotionsembay/](http://geosystems.ce.gatech.edu/soil_dynamics/research/groundmotionsembay/), 2004.

## Research Article

# The research into the propagation law of the shock wave of a gas explosion inside a building

Shu-Chao Lin,<sup>1,2,3</sup> You-Chun Xu,<sup>1</sup> Pei-Dong Yang,<sup>1</sup> Shan Gao ,<sup>4,5</sup> Yi-Jun Zhou,<sup>3</sup> and Jin Xu<sup>1</sup>

<sup>1</sup>Shaanxi Key Laboratory of Safety and Durability of Concrete Structures, Xijing University, Xi'an 710123, China

<sup>2</sup>Post-Doctoral Mobile Station of Civil Engineering, School of Civil Engineering, Tianjin University, Tianjin 300072, China

<sup>3</sup>College of Civil and Architectural Engineering, North China University of Science and Technology, Tangshan 063210, China

<sup>4</sup>School of Civil Engineering, Harbin Institute of Technology, Harbin 150000, China

<sup>5</sup>Postdoctoral Station of Civil Engineering, Chongqing University, Chongqing 400000, China

Correspondence should be addressed to Shan Gao; 13833185232@139.com

Received 21 June 2021; Revised 29 July 2021; Accepted 23 September 2021; Published 7 October 2021

Academic Editor: Arturo Garcia-Perez

Copyright © 2021 Shu-Chao Lin et al. This is an open access article distributed under the Creative Commons Attribution License, which permits unrestricted use, distribution, and reproduction in any medium, provided the original work is properly cited.

Based on the dissipation rate conservation equations of turbulent kinetic energy in the  $k-\varepsilon$  turbulence model, a complicated three-dimensional finite element model of a kitchen filled with gas mixture is developed by using the open source field operation and manipulation (OpenFOAM). Two representative kitchens were used to investigate the propagation law of the shock wave of a gas explosion inside a building by considering the key characteristics of the blast shock wave. The influence of some crucial parameters, such as initial conditions and kitchen parameters, on the properties of the blast shock wave is investigated. The basic steps to predict the peak pressure of the blast shock wave are given in consideration of the initial condition and the kitchen whilst the injury effect of the blast shock wave on the humans and animals is evaluated. The research results indicate that the pressure time history and the peak pressure space distribution are greatly influenced by the kitchen design layout. The coupled interaction between the initial temperature and gas volume concentration, especially at the upper and lower explosion limits of the gas, significantly affects the peak pressure. The peak pressure varies significantly with the opening and the buffer; however, it has little relation with the width, length, and height of the kitchen. The proposed method can accurately and effectively predict the peak pressure of the blast shock wave inside buildings. In terms of the peak pressure space distribution of the explosion shock wave, the peak pressure is much higher than the threshold of the killing pressure, which is unsafe for the humans and animals in the building.

## 1. Introduction

With the acceleration of the urbanization process, urban gas gradually becomes an important part of the energy in citizen's daily life over the last few decades [1, 2] resulting from its irreplaceable advantages, such as high efficiency, cleanliness and cheapness. Urban gases mainly include natural gas, manufactured gas, liquefied petroleum gas and marsh gas which are flammable and explosive. Urban gas leakage in the process of being used is very likely to cause an explosion inside a building and easily leads to a chain of disastrous consequences [3, 4]. Therefore, the research into the propagation law of the shock wave of a gas explosion inside

buildings has been widely concerned by the researchers and engineers in this field [5].

Many theoretical analyses, experiment studies and numerical simulations have been conducted to investigate the injury effect on the living beings based on North Atlantic Treaty Organization and Department of Defense specifications [6, 7]. The basic characteristics of the blast shock wave in free air have been investigated, such as the time and space attenuation model of the pressure [8] and the impulse [8, 9]. However, the researches concerning the propagation law of the blast shock wave caused by an explosive charge or gas explosion inside a building are few. As far as the building structures are concerned, considering the multiple

propagation patterns of the blast shock wave and the geometrical conditions of the underground transportation infrastructure, Pennetier et al. [10] determined the position of this transition spherical-to-planar wave propagation in a tunnel using both numerical simulations and scale model tests and verified the dedicated law proposed by himself. By considering the effects of stairs, pillars, and wall materials, Ma et al. [11] discussed the propagation law of the blast shock wave in a metro station, and estimated the harm on the human health. A few prevention measures against an explosion scenario to reduce the killing effect on the humans were proposed. Edri et al. [12] conducted experimental, analytical, and numerical studies to investigate an explosion in an enclosed space, which significantly benefitted the advancement of knowledge regarding this subject.

Additionally, the studies regarding the propagation law of the blast shock wave resulted from a gas explosion are very few. By using the reliable commercial computational fluid dynamics (CFD) software FLACS, Ji and Wang [13, 14] successfully predicted the formation process of the natural gas cloud due to the pipeline leakage inside and outside the building and accurately reproduced the gas explosion accident scene that had happened. With the help of the CFD numerical simulation method, Wang et al. [15] mainly analyzed the gas leakage and diffusion, blast shock wave, and flame propagation process of a real gas explosion inside the building, and discussed about the reason for this accident through it. Based on the characteristics of the building structure, Li et al. [16] proposed a hybrid method that combines the numerical simulation and the analytical solutions to predict the internal and external pressures from the vented gas explosion in a large enclosure, and verified the reliability and accuracy of this method by the experimental data.

From the aforementioned reference review, the existing researches on this subject mainly concentrate on the propagation process of the blast shock wave in a particular space, but lack of the properties of the blast shock wave itself. Concurrently, several research problems associated with the propagation law of the blast shock wave caused by a gas explosion remain unclear as a result of the limitations of the study subjects and the experimental conditions.

In view of the above and some typical urban gas explosion incidents [13–15, 17] in recent years, a series of numerical simulation analyses are conducted on kitchen to investigate the influence of the initial condition on the properties of the blast shock wave. A new method is proposed herein to estimate the properties of the blast shock wave inside the building. This present study can provide the technological support and theoretical basis for the potential risk assessment on the living beings [18].

## 2. Finite element model of the kitchen

**2.1. Kitchen scheme.** In order to explore the propagation law of the shock wave of a gas explosion inside a building, two representative kitchens [19–22] are introduced in this study, as shown in Figure 1. As far as Scheme 1 is concerned, the

kitchen is enclosed on three sides by the filling wall and faces the dining and living room on the fourth side. It can be defined by three parameters: kitchen width,  $w_k = 2500$  mm; kitchen length,  $l_k = 2500$  mm; and kitchen height,  $h_k = 3600$  mm. As for Scheme 2, three sides are also surrounded by the filling wall and one side is adjacent to the buffer zone, which is often used as the toilet, storage room, etc. It can be defined by four parameters: kitchen width,  $w_k = 2500$  mm; kitchen length,  $l_k = 2500$  mm; kitchen height,  $h_k = 3600$  mm; and buffer length,  $l_b = 2000$  mm. The dimensions of the door and window openings are  $1000$  mm  $\times$   $2400$  mm and  $900$  mm  $\times$   $1800$  mm, respectively. Thus, the window hole ratio of the wall is as follows:  $\lambda_k = 18\%$ . The air is mixed with the urban gas in certain proportion to form the gas mixture with the initial temperature of  $25$  °C and initial pressure of  $101.325$  kPa. The kitchen is filled with the gas mixture that is ignited with temperature of  $2000$  °C at the center of it.

**2.2. Basic theory.** Along with the development of modern computers, the computational fluid dynamics is widely used in solving a variety of complicated problems in fluid mechanics. It can accurately predict a wide range of physical phenomena of the fluid, such as fluid flow, heat transfer, mass transfer, chemical reaction and so on.

**2.2.1. Governing equations.** Urban gas explosion in the kitchen can be regard as a swift and violent combustion process [23]. This section describes the mathematical model for it, which mainly includes a set of the governing equations [24, 25], such as the equations for conservation of mass, momentum, energy, chemical specie, turbulent kinetic energy and its dissipation rate. In the Cartesian coordinate system, these equations are presented in partial differential form as follow.

The mass conservation equation (continuity equation) is:

$$\frac{\partial}{\partial t}(\rho) + \frac{\partial}{\partial x_i}(\rho v_i) = 0, \quad (1)$$

where  $\rho$  is the mass density;  $v_j$  is the velocity component in  $i$ -direction;  $x_j$  is the global Cartesian coordinate; and  $t$  is the time.

The momentum conservation equation (Navier-Stokes equation) is:

$$\frac{\partial}{\partial t}(\rho v_j) + \frac{\partial}{\partial x_i}(\rho v_i v_j) = \frac{\partial}{\partial x_j}(p) + \frac{\partial}{\partial x_i}(\tau_{ij}) + \rho \sum_{k=1}^N Y_k f_{k,j}, \quad (2)$$

where  $p$  is the static pressure;  $\tau_{ij}$  is the deviatoric stress tensor;  $Y_k$  is the mass fraction of chemical specie  $k$ ; and  $f_{k,j}$  is the volume force acting on the chemical specie  $k$  in  $j$ -direction.

In the above equation, the deviatoric stress tensor can be defined as follows:

$$\tau_{ij} = -\frac{2}{3}\mu \frac{\partial v_k}{\partial x_k} \delta_{ij} + \mu \left( \frac{\partial v_i}{\partial x_j} + \frac{\partial v_j}{\partial x_i} \right), \quad (3)$$

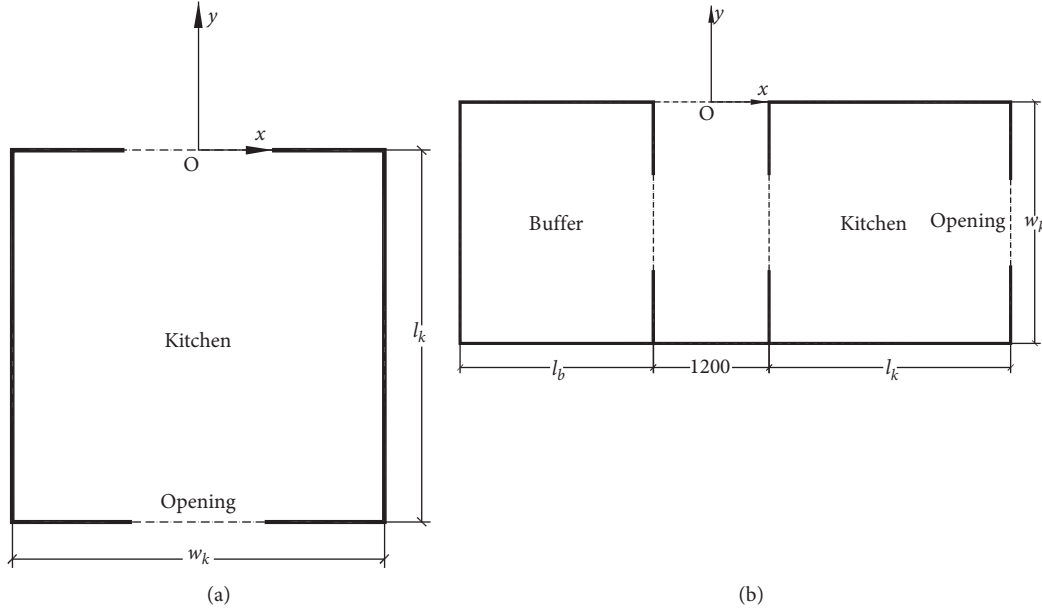


FIGURE 1: Kitchen prototype. (a) Scheme 1 (b) Scheme 2

where  $\mu$  is the dynamic viscosity; and  $\delta_{ij}$  is the Kronecker Delta function.

The energy (enthalpy) conservation equation is:

$$\frac{\partial}{\partial t} (\rho h) + \frac{\partial}{\partial x_i} (\rho v_i h) = \frac{Dp}{Dt} - \frac{\partial q_i}{\partial x_i} + \tau_{ij} \frac{\partial u_i}{\partial x_j} + \dot{Q} + \rho \sum_{k=1}^N Y_k f_{k,i} V_{k,i}, \quad (4)$$

where  $h$  is the enthalpy;  $D/Dt$  is the substantial derivative operator;  $q_i$  is the energy flux;  $\dot{Q}$  is the heat source term; and  $V_{k,i}$  is the  $i$ -component of the diffusion velocity  $V_k$  of chemical specie  $k$ .

The conservation equation of mass fraction of chemical specie is:

$$\frac{\partial}{\partial t} (\rho Y_k) + \frac{\partial}{\partial x_i} [\rho (v_i + V_{k,i}) Y_k] = \dot{w}_k, \quad (5)$$

where  $\dot{w}_k$  is the reaction rate of chemical specie  $k$ .

In addition, the turbulent kinetic energy and its dissipation rate conservation equations [26] need to be satisfied in the  $k$ - $\varepsilon$  turbulence model, and can be written as follows:

$$\begin{aligned} \frac{\partial}{\partial t} (\rho k) + \frac{\partial}{\partial x_i} (\rho v_i k) &= \frac{\partial}{\partial x_i} \left[ \left( \mu + \frac{\mu_t}{\sigma_k} \right) \frac{\partial k}{\partial x_i} \right] + P_k - \rho \varepsilon, \\ \frac{\partial}{\partial t} (\rho \varepsilon) + \frac{\partial}{\partial x_i} (\rho v_i \varepsilon) &= \frac{\partial}{\partial x_i} \left[ \left( \mu + \frac{\mu_t}{\sigma_\varepsilon} \right) \frac{\partial \varepsilon}{\partial x_i} \right] + \frac{\varepsilon}{k} (C_1 P_k - C_2 \rho \varepsilon), \end{aligned} \quad (6)$$

where  $k$  and  $\varepsilon$  are the turbulent kinetic energy and its dissipation rate, respectively;  $\sigma_k$  and  $\sigma_\varepsilon$  are the  $k$ - $\varepsilon$  model constants, respectively;  $\mu_t$  is the turbulent viscosity;  $P_k$  is the production rate of the turbulent kinetic energy; and  $C_1$  and  $C_2$  are all the non-dimensional constants.

The un-burnt gas is pushed ahead of the flame and the flame consumes the un-burnt gas. It produces a large

amount of high temperature and high pressure gases in accompany with the complicated chemical kinetic equilibrium processes between these detonation products. Thus, the turbulent flow field is generated. The explosion pressure rises sharply and the detonation products expand dramatically. After that, the explosion pressure decreases greatly with the increase in volume expansion of the detonation products. Simultaneously, they are converted gradually to the ideal gas. This expansion can be up to 8–9 times the initial volume.

The equation of state of the detonation products is a complicated function of pressure, density and temperature. Up to now, the empirical or semi-empirical equation of state is mainly used. The main reason for this is that it is difficult to be determined directly by using the test method. The BKW equation of state [27] is introduced in this study and can be described as follows:

$$\frac{pV_m}{RT} = 1 + x e^{\beta x}, \quad (7)$$

where

$$x = \frac{k}{V_m (T + \theta)^{\alpha}}, \quad (8)$$

$$k = \kappa \sum_{n=1}^N x_n k_n.$$

Here  $V_m$  is the molar gas volume;  $R$  is the universal gas coefficient;  $T$  is the absolute temperature;  $x_n$  is the mole fraction of component  $n$ ; and  $\alpha$ ,  $\beta$ ,  $\kappa$ ,  $\theta$ , and  $k_n$  are the constants.

The ideal gas is used in many applications of the existing finite element analysis software, for instance, FLACS, AutoReaGas, LS-DYNA and AUTODYN. The corresponding equation of state is derived from the laws of Boyle and Gay-Lussac [28] and can be expressed as follows:

$$pW_m = \rho RT, \quad (9)$$

where  $W_m$  is the molar weight of the gas mixture.

**2.2.2. Other details.** The solution algorithm used in the software OpenFOAM is the PIMPLE (merged PISO-SIMPLE) algorithm that is a combination of the pressure-implicit with splitting of operators (PISO) algorithm [29] and the semi-implicit method for pressure-linked equations (SIMPLE) algorithm. This algorithm has one predictor and two or three correctors. Thus, the mass and momentum conservation equations can be better satisfied, and simultaneously the convergence is accelerated at each iteration step. It is iterative procedure for solving the governing equations for the velocity and the pressure, which are used as the dependent variables. The practice has proved that it requires some extra storage space, but it is very fast and efficient. It is well-suited for the gas explosion scenario in OpenFOAM.

The turbulence models (e.g. standard  $k-\varepsilon$  model, RNG Turbulence model, NKE Turbulence model, GIR Turbulence model, SZL Turbulence model, standard  $k-\omega$  model, SST Turbulence model, etc.) are invalid immediately adjacent to the wall, since the viscous force dominates the inertial effect. Therefore, the wall function is introduced in this context to improve the modeling of the flow field in the near-wall region. The wall function has been tested on the low Reynolds number benchmark cases, and the good agreement between the published benchmark results and the OpenFOAM results is obtained [30].

The boundary conditions of the gas and air computation domain next to the filling wall and floor slab are the wall boundary for the velocity, meaning a fixed or stationary wall. All the others (including the door and window openings) are the zeroGradient boundary for the pressure, with the implication that the normal gradient of the pressure is the zero.

### 3. Model validation

In order to verify the validity of the finite element model and the corresponding analysis method, the propagation process of the shock wave of a methane/air or hydrogen/air mixture explosion reported in the reference [31] is simulated by using the finite element analysis method mentioned above.

In this validation study, there are two test chambers, which are measured to be  $4.6 \text{ m} \times 4.6 \text{ m} \times 3.0 \text{ m}$  and about  $64 \text{ m}^3$  in volume. They all have a square vent on the wall. Chamber I is  $2.7 \text{ m}^2$  and Chamber II is  $5.4 \text{ m}^2$ . They are filled with the premixed hydrogen/air, methane/air or propane/air mixture, and the hydrogen, methane or propane gas volume concentration is about 18%, 9.5% or 4%, respectively. There is one pressure sensor (PS) to monitor the pressure on the wall. PS is attached to the wall at a height of 1.5 meters above the ground, as depicted in Fig. 2. In addition, there are two ignition points (IP1 for Chamber I and IP2 for Chamber II) that are all at a height of 1.5 m above the ground, as shown in Figure 2. The electric ignition system is used in the gas explosion experiment, and

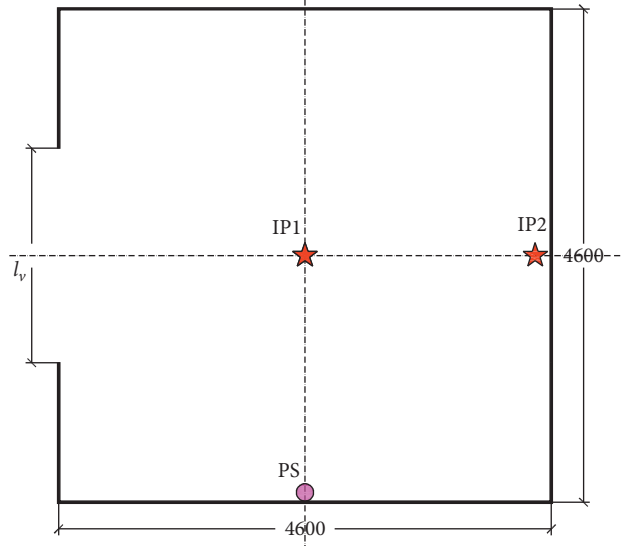


FIGURE 2: Test chamber.

the energy of the ignition is around 1000 J. High-speed line-scanning cameras are applied to capture more details of the gas explosion experiment.

Figure 3 describes the pressure time histories from experimental data and numerical simulation results. The maximum relative deviations between them are all less than 5% indicating that the numerical simulation results are in good agreement with the experimental data. There are three main reasons accounting for the difference between the test and simulated results. Firstly, the chamber is easy to deform slightly due to the gas explosion, thus affecting the measurement accuracy of the pressure sensor. Secondly, the ignition system is very hard to be simulated perfectly by using an ignition temperature. Thirdly, in general, a tiny quantity of the combustible and explosive gases of other type except the methane or hydrogen gas exists in the test.

### 4. Characteristics of the blast shock wave

Figure 4 describes the pressure time history of the blast shock wave of the measured point O in Fig. 1. The pressure increases immediately and reaches a maximum, after then it decreases rapidly, and gradually fluctuates around the zero, and finally tends to zero. It usually lasts for no more than 0.30 s. The peak pressures of Schemes 1 and 2 are 160 kPa and 97 kPa, respectively, and the peak pressure of Scheme 2 is only 61% of that of Scheme 1. Hence, it can be concluded that the pressure time history is greatly influenced by the kitchen design layout [32].

Figure 5 depicts the peak pressure space distributions of Schemes 1 and 2 whilst  $x$  and  $y$  are the Cartesian coordinates, and  $z = p / p_{Op}$ , where  $p$  and  $p_{Op}$  are the peak pressures of the measured point  $(x, y)$  and the measured point O, respectively. It can be seen that the peak pressure decreases significantly with the distance away from the measured point O. In addition, the peak pressure space distribution is greatly influenced by the kitchen design layout [33].

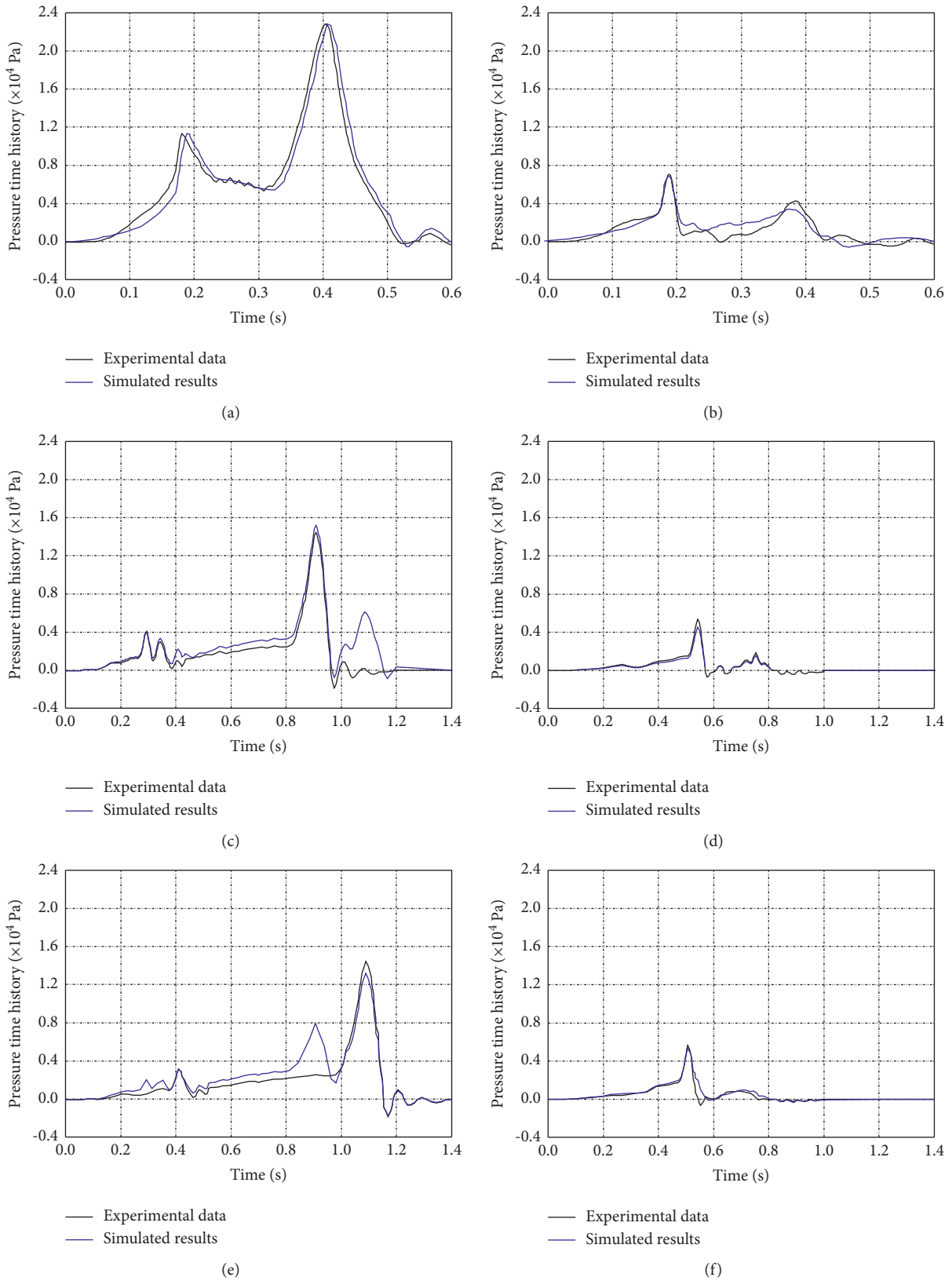


FIGURE 3: Pressure time histories from experimental data and simulated results. (a) Chamber I with a 2.7 m<sup>2</sup> vent (Hydrogen): IP1 (b) Chamber II with a 5.4 m<sup>2</sup> vent (Hydrogen): IP2. (c) Chamber I with a 2.7 m<sup>2</sup> vent (Methane): IP1 (d) Chamber II with a 5.4 m<sup>2</sup> vent (Methane): IP2. (e) Chamber I with a 2.7 m<sup>2</sup> vent (Propane): IP1 (f) Chamber II with a 5.4 m<sup>2</sup> vent (Propane): IP2.



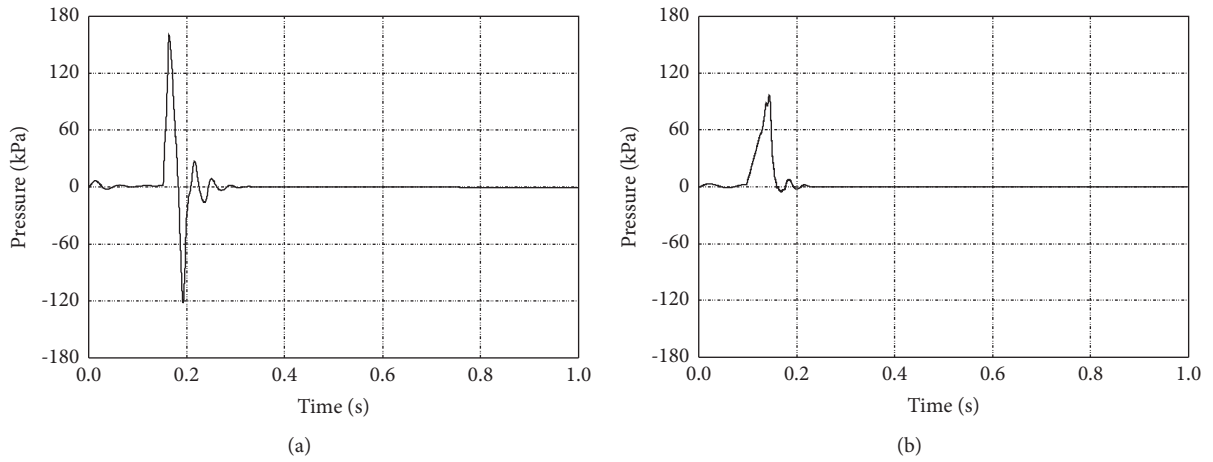


FIGURE 4: Pressure time history of the blast shock wave. (a) Scheme 1. (b) Scheme 2

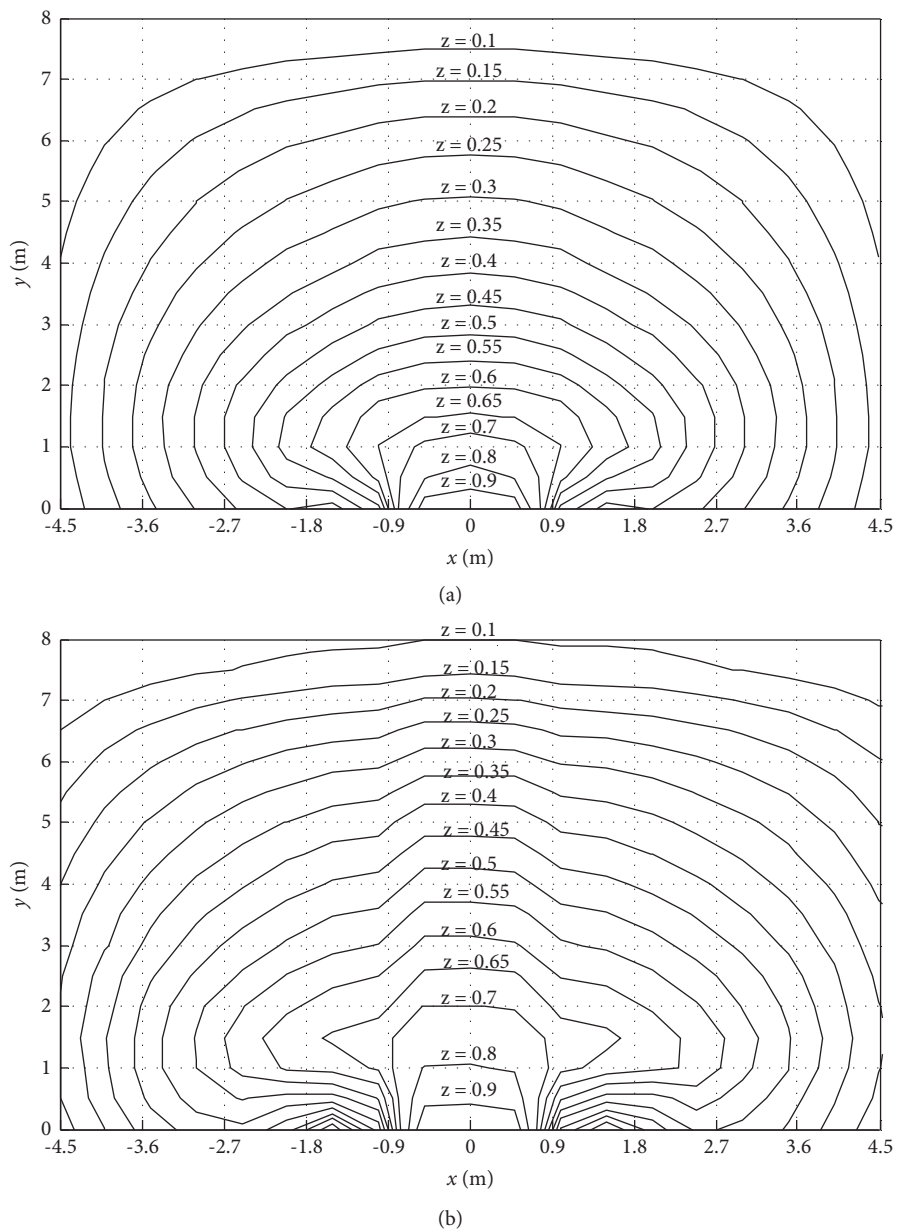


FIGURE 5: Peak pressure space distributions of Schemes 1 and 2. (a) Scheme 1. (b) Scheme 2

## 5. Parametric studies

Different from explosive charge explosion, the shock wave of gas explosion is easily affected by the surrounding environment, such as initial conditions (initial temperature [34, 35] and gas volume concentration [34–36]) and kitchen parameters (width, length, height, opening, and buffer) [37, 38]. Therefore, it is necessary to have a deep understanding of these interfering factors.

**5.1. Initial condition.** In the section, a series of finite element analyses are conducted on the premixed methane/air mixture explosion in the kitchen to investigate the influence of the initial temperature and gas volume concentration on the peak pressure.

**5.1.1. Initial temperature.** Figure 6 illustrates the relation between  $p_{ic}$  and  $T$  under different initial gas volume concentration environments, where  $p_{ic}$  is the peak pressure considering the initial condition and  $T$  is the initial temperature.

According to the basic theory of combustion, the higher the initial temperature is, the higher the gas combustion reaction rate becomes. However, the gas is expelled from the kitchen with the increase in the initial temperature, and the corresponding total mass of the gas in the kitchen is smaller at higher initial temperature. It can be observed from figure 6 that the peak pressure is mainly determined by the latter. Therefore, the peak pressure decreases gradually as the initial temperature increases.

**5.1.2. Initial gas volume concentration.** Figure 7 describes the relation between  $p_{ic}$  and  $C$  under different initial temperature environments, where  $p_{ic}$  is the peak pressure in consideration of the initial condition and  $C$  is the initial gas volume concentration.

The gas complete combustion occurs at the lower initial gas volume concentration, and directly determines the peak pressure. Nevertheless, the gas incomplete combustion occurs at higher initial gas volume concentration. The main reason for this is the limited oxygen volume concentration, which governs the peak pressure in such case. Hence, with the increase in the initial gas volume concentration, the peak pressure first increases and reaches a maximum, then decreases gradually. Additionally, the initial gas volume concentration corresponding to the highest pressure is close to the stoichiometric volume concentration [39] which is about 10%.

Figure 8 depicts the relation among  $\gamma_{ic}$ ,  $T$  and  $C$ , where  $\gamma_{ic}$  is the influence coefficient of the initial condition,  $T$  is the initial temperature and  $C$  is the initial gas volume concentration. The initial temperature has an important influence on the gas detonation parameters [40]. The upper explosion limit of the gas increases but the lower explosion limit of the gas decreases as the initial temperature increases. Consequently, there is a significant influence on the peak pressure by the coupled interaction between the initial

temperature and the initial gas volume concentration, especially at the upper and lower explosion limits of the gas [41].

In view of the relevant researches and the results from finite element analyses of this study, an empirical relation among  $\gamma_{ic}$ ,  $T$  and  $C$  can be obtained through the nonlinear regression and expressed as equation (10). It can be seen from Figures 6–8 that the results predicted by (10) coincide very well with the numerical simulation results.

The influence coefficient of the initial condition can be gained by dividing  $p_{ic}$  by  $p_{Op}$ . Thus, the difference in the kitchen design layout is eliminated. The corresponding suggested equation can be expressed as follows:

$$\begin{aligned} \gamma_{ic} &= \frac{p_{ic}}{p_{Op}} \\ &= (3.56 \times 10^{-5}T - 0.0356) \\ &\quad \cdot [10000C^2 - 1980C + 4.44 \times 10^{-2}T + 84.52] + 0.57. \end{aligned} \quad (10)$$

**5.2. Kitchen parameter.** In order to explore the influence of the kitchen on the peak pressure, a range of numerical simulation analyses are conducted on the kitchens of different sizes, openings, and buffers. All the parameters under consideration are illustrated as follow: kitchen width  $w$  from 1.20 to 4.80 m; kitchen length  $l_1$  from 1.20 to 4.80 m; kitchen height  $h$  from 2.40 to 6.00 m; wall hole ratio  $\lambda$  from 0.00 to 0.60; and buffer length  $l_2$  from 1.20 to 4.80 m. The relation between  $p_k$  and kitchen parameters is displayed in figure 9, where  $p_k$  is the peak pressure with taking into account the kitchen.

**5.2.1. Width, length, and height.** It can be observed from Figures 9(a)–9(c) that the peak pressure increases slowly but linearly with the increase in the width, length, and height. Furthermore, the width, length, and height of kitchen enhance the peak pressure in different extents [42]. Because of the gravity effect, the height show slightly significant effect than other parameters.

**5.2.2. Opening.** Once there is a gas explosion in the kitchen, the glasses in the window is easy to be destroyed. The window opening just plays the role of pressure relief and releases a large amount of explosive energy quickly, greatly reducing the peak pressure [43]. It can be seen from Figure 9(d) that the peak pressure decreases significantly with increase in the hole ratio of the wall.

**5.2.3. Buffer.** If a gas explosion occurs in the kitchen, first of all, the blast shock wave first gets into the buffer zone, and then it continues to propagate in a building. Consequently, the buffer zone plays the buffer role and reduces the peak pressure [44]. It can be found from Figure 9(e) that the longer the length of the buffer is, the smaller the peak pressure becomes.

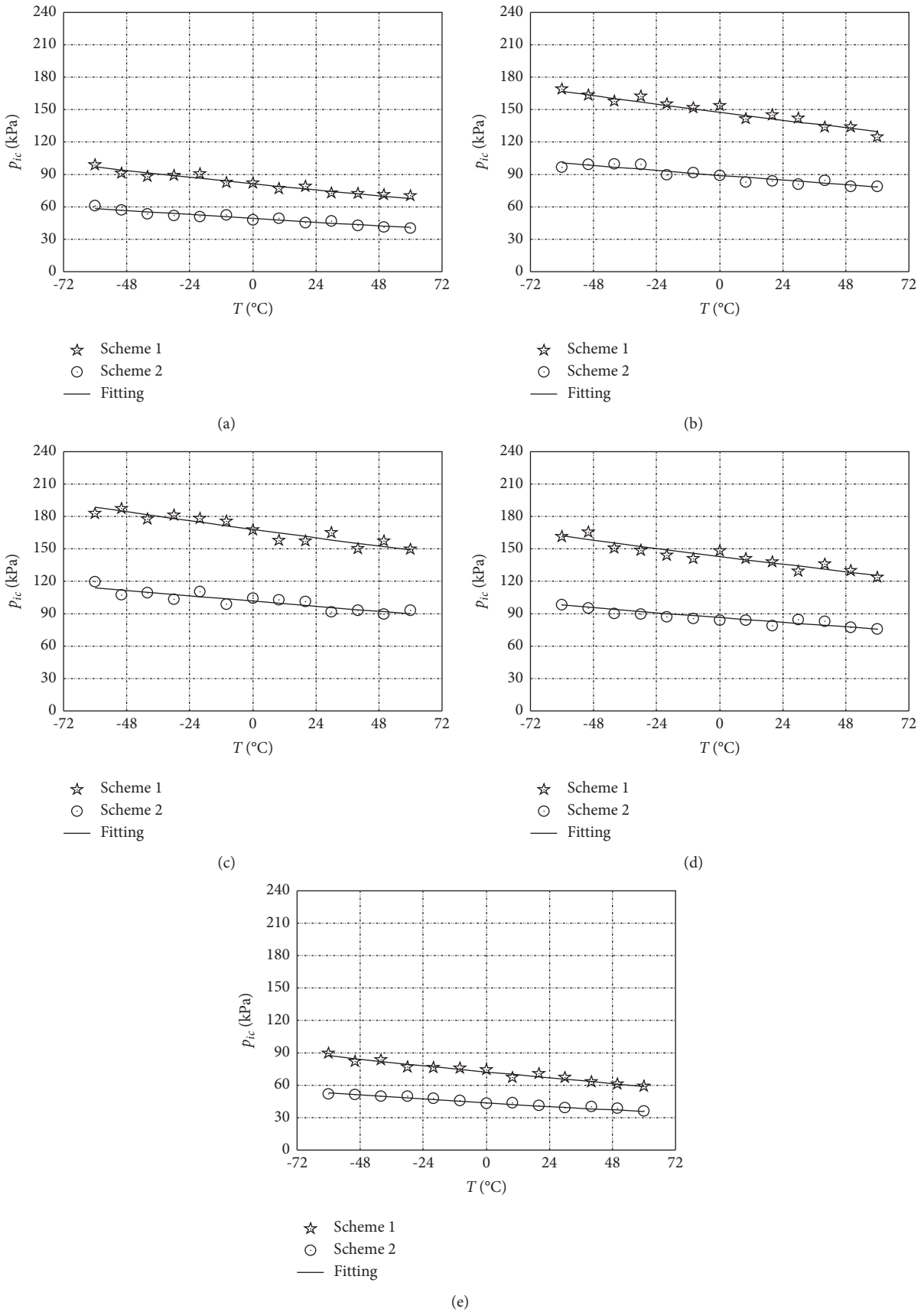


FIGURE 6: Relation between  $(p)_{ic}$  and  $(T)$  under different initial gas volume concentration environments. (a)  $(C) = 6\%$  (b)  $(C) = 8\%$ . (c)  $(C) = 10\%$  (d)  $(C) = 12\%$ . (e)  $(C) = 14\%$ .

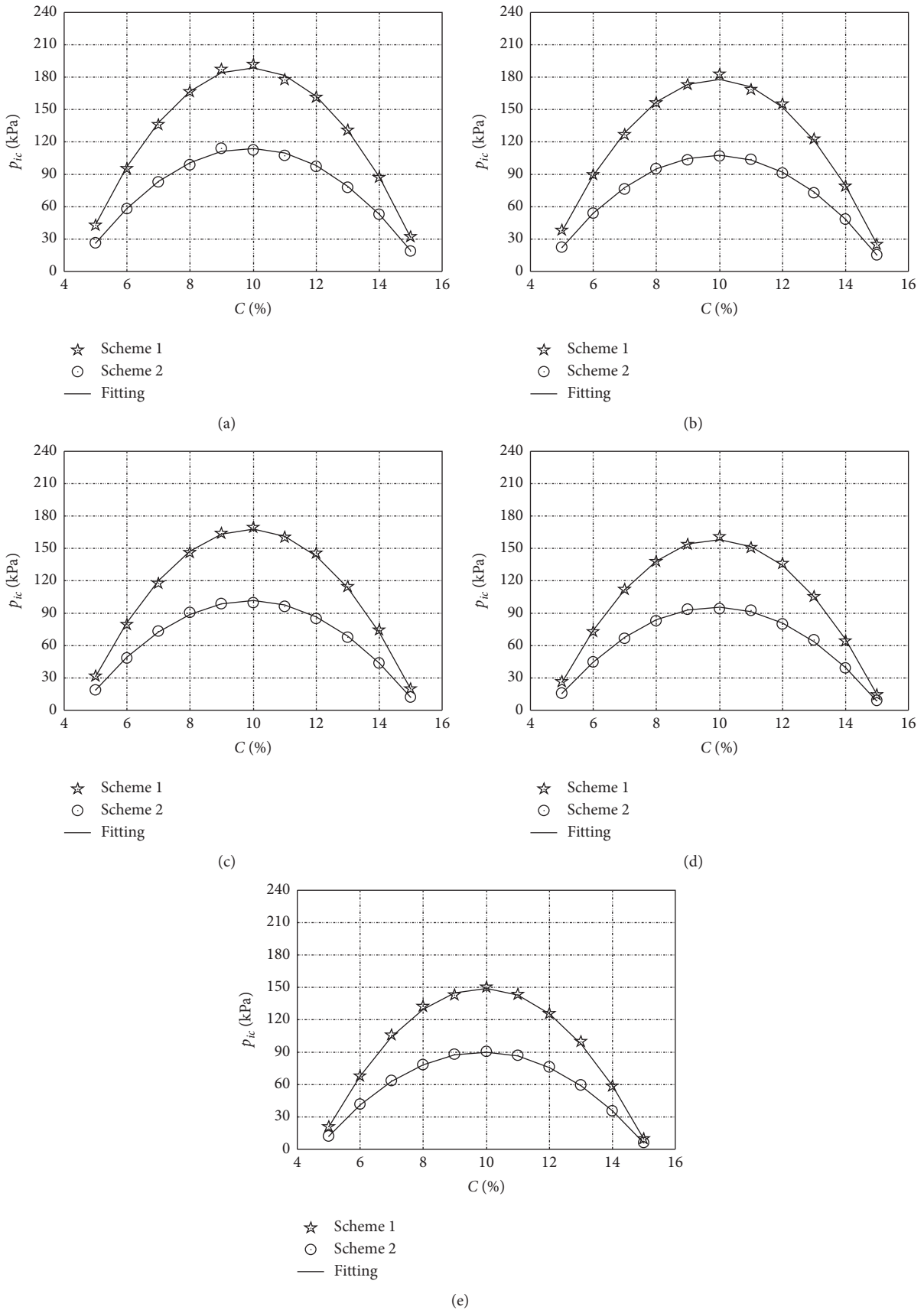


FIGURE 7: Relation between  $(p)_{ic}$  and  $(C)$  under different initial temperature environments. (a)  $(T) = -60^\circ\text{C}$  (b)  $(T) = -30^\circ\text{C}$ . (c)  $(T) = +0^\circ\text{C}$  (d)  $(T) = +30^\circ\text{C}$ . (e)  $(T) = +60^\circ\text{C}$ .

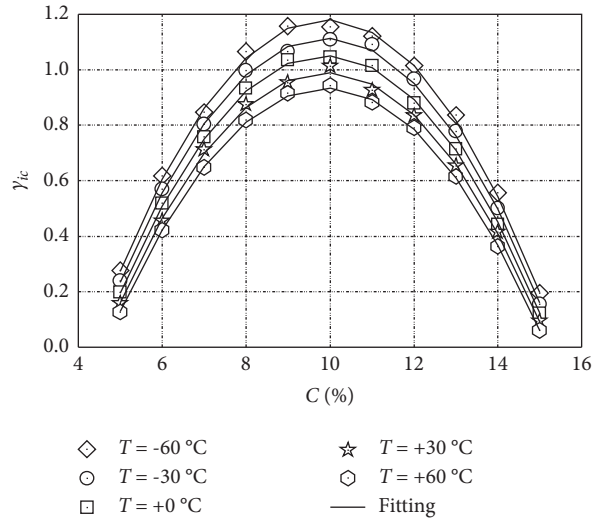


FIGURE 8: Relation among  $\gamma_{ic}$  (T) and (C).

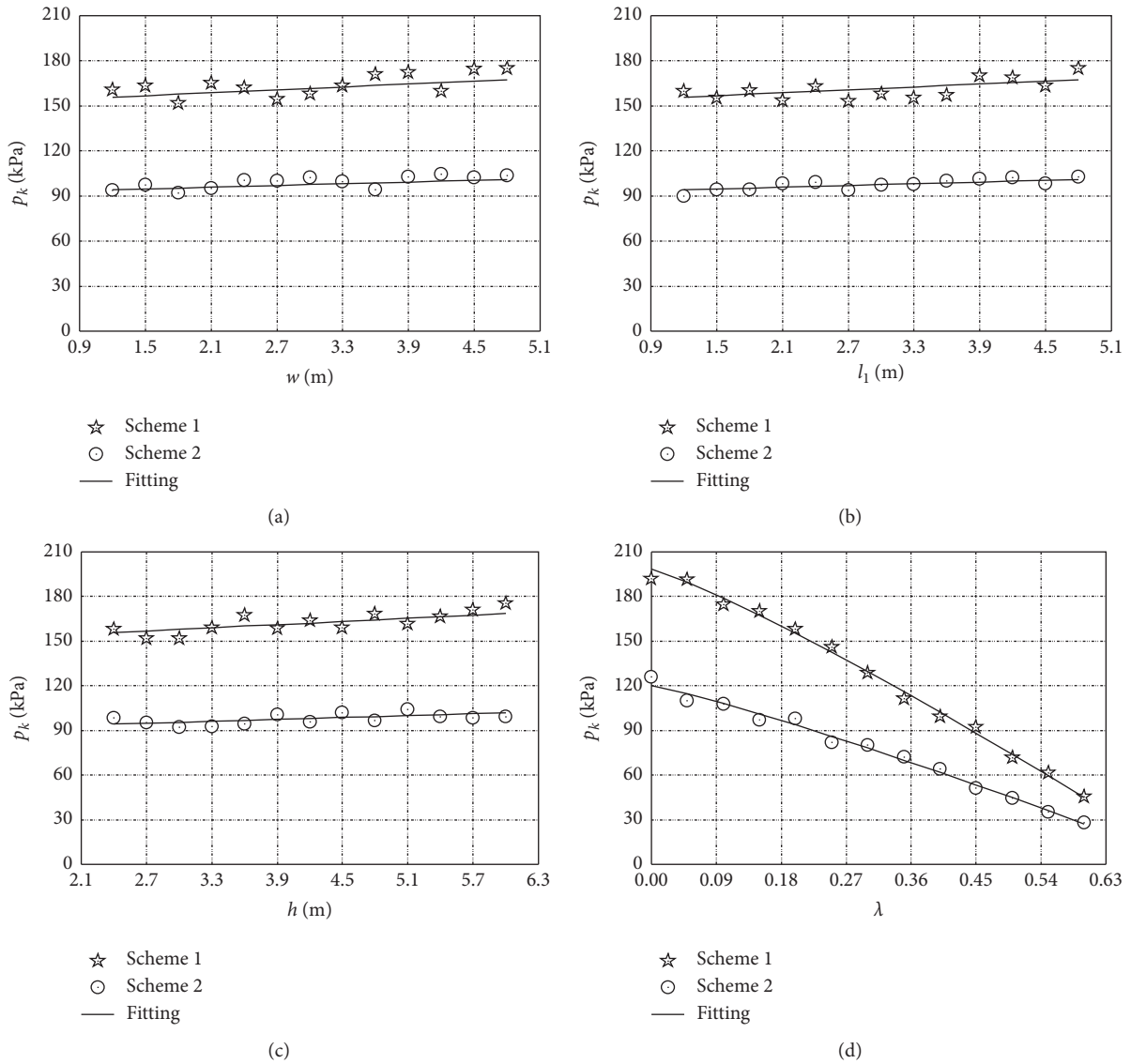


FIGURE 9: Continued.

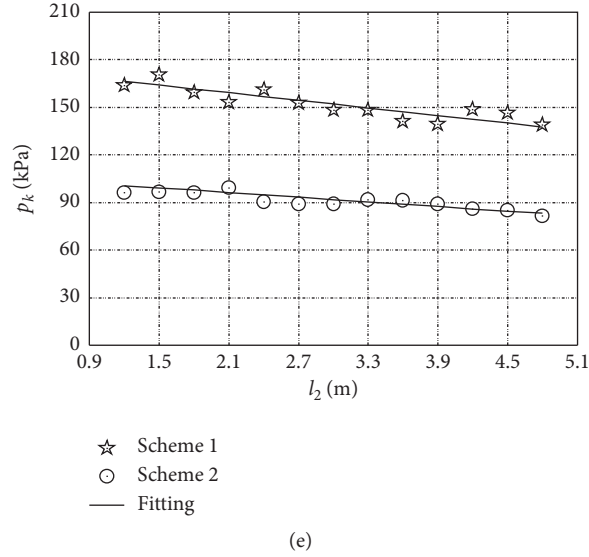


FIGURE 9: Relation between  $(p)_k$  and kitchen parameters. (a) Width. (b) Length. (c) Height. (d) Opening. (e) Buffer.

To sum up, the peak pressure varies significantly with the opening and the buffer. However, it has little relation with the width, length, and height of kitchen.

From the associated documents and the numerical simulation results in the present study, an empirical relation between  $\gamma_k$  and kitchen parameters can be gained through the nonlinear fitting by using the ordinary least square method and expressed as (11). It can be seen from Figure 9 that the fitting results are in good accordance with the simulated results, regardless of any kitchen parameter.

The influence coefficient of the kitchen can be gained by dividing  $p_k$  by  $p_{Op}$ . Thus, the difference in the kitchen design layout is eliminated. It can be given by:

$$\gamma_k = \frac{p_k}{p_{Op}} = 0.05 \left( \frac{w}{w_k} + \frac{l_1}{l_k} \right) + 0.08 \frac{h}{h_k} - 0.24 \left( \frac{\lambda}{\lambda_k} \right)^{1.15} - 0.10 \frac{l_2}{l_b} + 1.16. \quad (11)$$

## 6. Proposed method to predict the properties of the blast shock wave

**6.1. Basic step of the proposed method.** Through the analysis and the research on the gas explosion inside the building, a new method is proposed herein to predict the peak pressure of the blast shock wave. The flow chart is depicted in Figure 10 below, and its basic steps are as follows:

- (1) Give the basic information that needed in this study, such as gas type, initial conditions (initial temperature and gas volume concentration) and kitchen parameters (width, length, height, opening, and buffer). If not the methane gas, the equivalent mass can be calculated according to equation (12), and the corresponding initial gas volume concentration is also obtained. Repeat steps (2) through (4).

The equivalent mass of other gas can be defined as follows:

$$m_{Eq} = \frac{E_{Other}}{E_{Methane}} m_{Other}, \quad (12)$$

where  $E_{Methane}$  and  $E_{Other}$  are the initial internal energy of methane and other gas, respectively;  $m_{Other}$  is the mass of other gas.

- (2) The two influence coefficients  $\gamma_{ic}$  and  $\gamma_k$  can be obtained according to equations (10) and (11), respectively. Thus, the maximum pressure considering the initial conditions and the kitchen parameters is  $\gamma_{ic}\gamma_k p_{Op}$ .
- (3) The peak pressure of the explosion shock wave is not uniformly distributed in the building, and it is needed to calculate the peak pressure at any position. Calculate it based on Figures 5(a) and (b).
- (4) If the blast shock wave spreads to the wall, the pressure increases immediately and generates a reflective high-pressure zone near the blast side. Use equation (13). Henrych [45] derived an empirical relation between the peak pressures of the reflected and incident wave. It can be expressed as follows:

$$\frac{p_r}{p_i} = \frac{8p_i + 14}{p_i + 7.2}, \quad p_i \leq 4 \text{ MPa}, \quad (13)$$

where  $p_r$  and  $p_i$  are the peak pressures of the reflected and incident wave, respectively.

- (5) Draw the peak pressure nephogram under different working conditions.

The calculation formulas used in the proposed method are based on the previous researches and the numerical

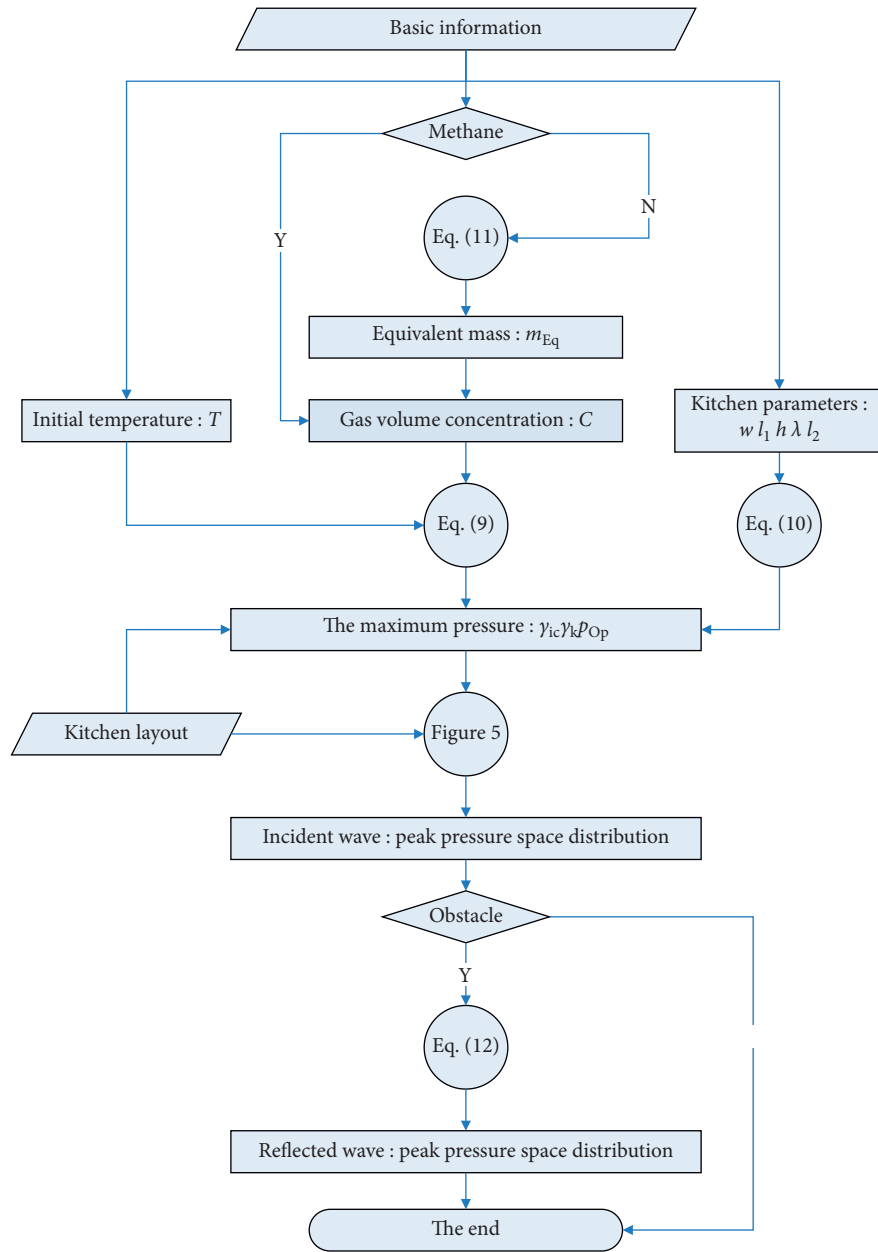


FIGURE 10: Flow chart of the proposed method.

simulation results. The analysis procedure is comprehensive whilst the results are reliable. Furthermore, it indicates that the proposed method can accurately and effectively predict the peak pressure of the blast shock wave inside the building.

**6.2. Example study.** In order to estimate the killing power of the explosion shock wave accurately, it is urgent to present some quantitative killing criterions, such as the pressure, the impulse and the combination of the above two. The U.S. military standard [7] specifies the pressure criterion of 45.7 kPa for eardrum rupture with a probability of 10% and 103.4 kPa in the duration of 50 ms for lung damage. Using the above two kitchens as the

examples, the propagation processes of the gas explosion are simulated using the CFD analysis software OpenFOAM to analyze the space distribution of the blast shock wave.

The peak pressure nephograms under different working conditions: Schemes 1 and 2 are illustrated Figures 11 and 12, respectively. The lower the initial temperature is, the higher the peak pressure is. The peak pressure first increases and then decreases gradually with the increase in the initial gas volume concentration. Additionally, the kitchen design layout seriously affects the peak pressure.

In terms of the peak pressure space distribution of the explosion shock wave, the peak pressure is much higher than the threshold of the killing pressure which is unsafe for the humans in the building.

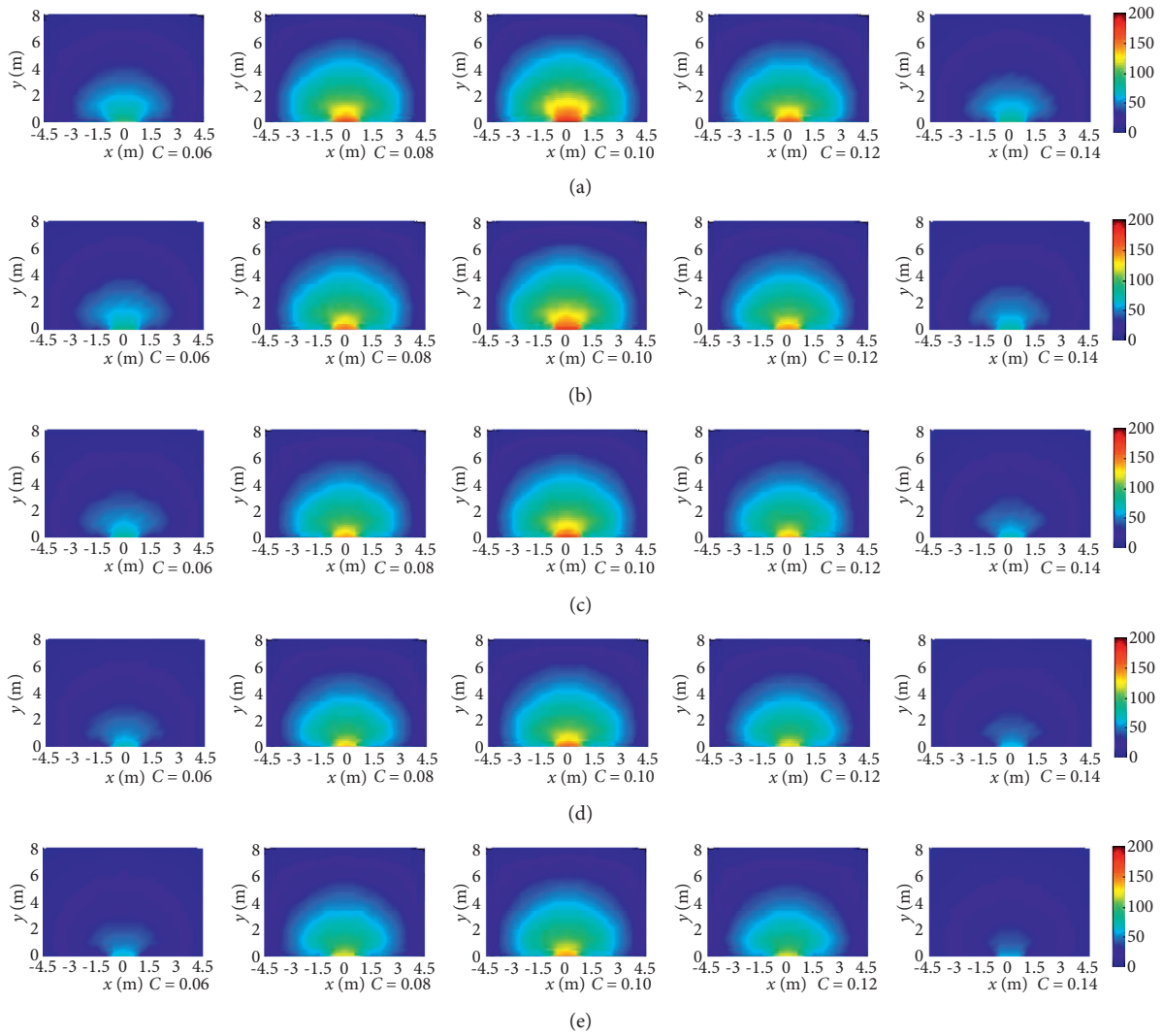


FIGURE 11: Peak pressure nephograms under different working conditions: Scheme 1 (kPa). (a)  $(T) = -60^\circ\text{C}$ . (b)  $(T) = -30^\circ\text{C}$ . (c)  $(T) = +0^\circ\text{C}$ . (d)  $(T) = +30^\circ\text{C}$ . (e)  $(T) = +60^\circ\text{C}$ .

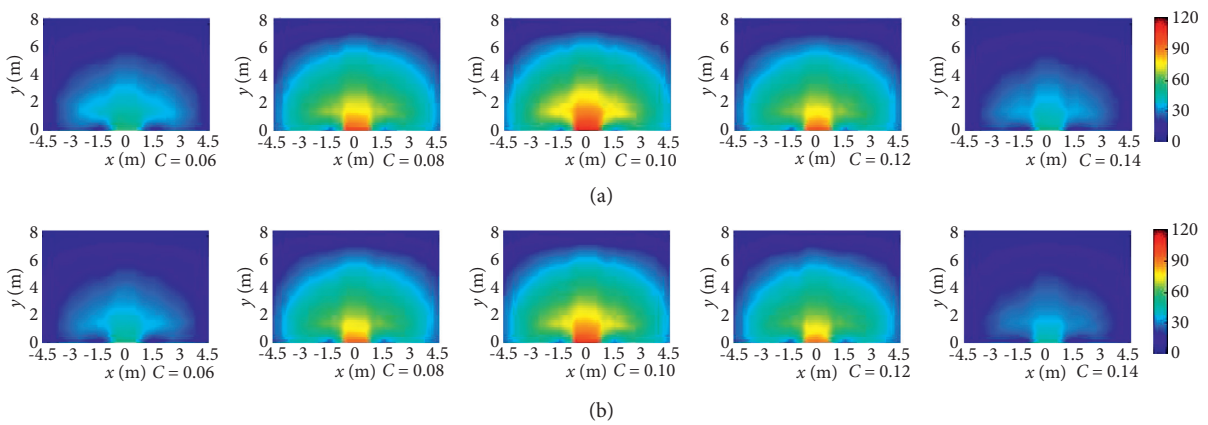


FIGURE 12: Continued.



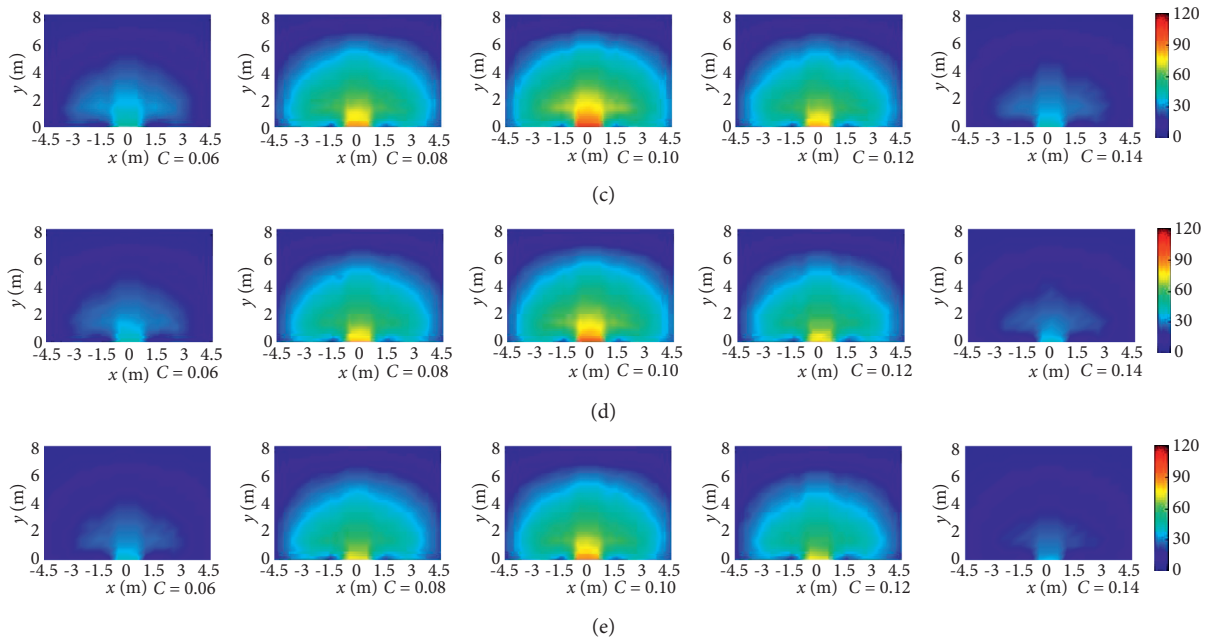


FIGURE 12: Peak pressure nephograms under different working conditions: Scheme 2 (kPa). (a)  $(T) = -60\text{ }^{\circ}\text{C}$ . (b)  $(T) = -30\text{ }^{\circ}\text{C}$ . (c)  $(T) = +0\text{ }^{\circ}\text{C}$ . (d)  $(T) = +30\text{ }^{\circ}\text{C}$ . (e)  $(T) = +60\text{ }^{\circ}\text{C}$ .

## 7. Conclusion

In this research, a new method has been developed herein to predict the peak pressure of the blast shock wave of a gas explosion inside a building. A series of numerical simulation analyses are conducted on this problem. From the research results of this present study, the main conclusions are drawn as follows:

- (1) The pressure time history and the peak pressure space distribution are greatly influenced by the kitchen design layout. There is a significant influence on the peak pressure by the coupled interaction between the initial temperature and the initial gas volume concentration, especially at the upper and lower explosion limits of the gas.
- (2) The peak pressure varies significantly with the opening and the buffer. However, it has little relation with the width, length, and height of the kitchen. The proposed method can accurately and effectively predict the peak pressure of the blast shock wave inside the building.
- (3) In terms of the peak pressure space distribution of the explosion shock wave, the peak pressure is much higher than the threshold of the killing pressure, which is unsafe for the humans in the building.

## Data Availability

The simulation data used to support the findings of this study are included within the article.

## Conflicts of Interest

The authors declare that they have no conflicts of interest.

## Acknowledgments

The authors would like to gratefully acknowledge the financial support provided by the Key Research and Development (R&D) Program of Tangshan [No. 19150232E], National Natural Science Foundation of China [NO. 51908085], Natural Science Foundation of Chongqing [cstc2020jcyj-msxmX0010], Fundamental Research Funds for the Central Universities [2020CDJ-LHZZ-013], The Youth Innovation Team of Shaanxi Universities [21JIP138] and Key Research and Development Program of Shaanxi [2021SF-521].

## References

- [1] J. Pospíšil, P. Charvát, O. Arsenyeva, L. Klimeš, M. Špiláček, and J. J. Klemeš, "Energy demand of liquefaction and regasification of natural gas and the potential of LNG for operative thermal energy storage," *Renewable and Sustainable Energy Reviews*, vol. 99, pp. 1–15, 2019.
- [2] E. Strantzali, K. Aravossis, G. A. Livanos, and C. Nikoloudis, "A decision support approach for evaluating liquefied natural gas supply options: implementation on Greek case study," *Journal of Cleaner Production*, vol. 222, pp. 414–423, 2019.
- [3] J. Weerheijm, J. Verreault, and M. M. Van Der Voort, "Quantitative risk analysis of gas explosions in tunnels," *Fire Safety Journal*, vol. 97, pp. 146–158, 2018.
- [4] X. Meng, Q. Liu, X. Luo, and X. Zhou, "Risk assessment of the unsafe behaviours of humans in fatal gas explosion accidents in China's underground coal mines," *Journal of Cleaner Production*, vol. 210, pp. 970–976, 2019.
- [5] T. Chyzy and M. Mackiewicz, "Simplified function of indoor gas explosion in residential buildings," *Fire Safety Journal*, vol. 87, pp. 1–9, 2017.

- [6] AASTP-1, *Manual of NATO Safety Principles for the Storage of Military Ammunition and Explosives*, North Atlantic Treaty Organization, Brussels, Belgium, 2006.
- [7] DoD 6055.9-STD, *DoD Ammunition and Explosive Safety Standards*, Departments of Defense, Arlington, VA, USA, 2008.
- [8] J. Henrych, *The Dynamics of Explosion and its Use*, Elsevier Scientific Publishing Company, Amsterdam, Netherlands, 1979.
- [9] ОРЛЕНКО ЛШ. физика взрыва. ФИЗМАТЛИТ, Moscow, Russia, 2002.
- [10] O. Penner, M. William-Louis, and A. Langlet, "Numerical and reduced-scale experimental investigation of blast wave shape in underground transportation infrastructure," *Process Safety and Environmental Protection*, vol. 94, pp. 96–104, 2015.
- [11] T. Ma, X. Xu, and J. Ning, "Research on propagation laws of explosion shock wave inside metro station," *Journal of Loss Prevention in the Process Industries*, vol. 46, pp. 54–68, 2017.
- [12] I. E. Edri, V. R. Feldgun, Y. S. Karinski, and D. Z. Yankelevsky, "The blast load acting on a structure in an internal explosion scenario," *Blast, Impact Loading, and Response; and Research and Education*, ASCE Structures Congress, Reston, VA, USA, pp. 362–375, 2018.
- [13] T. Ji, X. Qian, M. Yuan et al., "Case study of a natural gas explosion in Beijing, China," *Journal of Loss Prevention in the Process Industries*, vol. 49, pp. 401–410, 2017.
- [14] D. Wang, X. Qian, M. Yuan, T. Ji, W. Xu, and S. Liu, "Numerical simulation analysis of explosion process and destructive effect by gas explosion accident in buildings," *Journal of Loss Prevention in the Process Industries*, vol. 49, pp. 215–227, 2017.
- [15] K. Wang, T. Shi, Y. He, M. Li, and X. Qian, "Case analysis and CFD numerical study on gas explosion and damage processing caused by aging urban subsurface pipeline failures," *Engineering Failure Analysis*, vol. 97, pp. 201–219, 2019.
- [16] J. Li and H. Hao, "Internal and external pressure prediction of vented gas explosion in large rooms by using analytical and CFD methods," *Journal of Loss Prevention in the Process Industries*, vol. 49, pp. 367–381, 2017.
- [17] S. Kundu, J. Zanganeh, and B. Moghtaderi, "A review on understanding explosions from methane-air mixture," *Journal of Loss Prevention in the Process Industries*, vol. 40, pp. 507–523, 2016.
- [18] S. Shi, B. Jiang, and X. Meng, "Assessment of gas and dust explosion in coal mines by means of fuzzy fault tree analysis," *International Journal of Mining Science and Technology*, vol. 28, no. 6, pp. 991–998, 2018.
- [19] M. Nyström, "Kitchen design: energy and health in the eyes of the beholder," *Energy for Sustainable Development*, vol. 7, no. 3, pp. 8–29, 2003.
- [20] O. Han, A. Li, and R. Kosonen, "Hood performance and capture efficiency of kitchens: a review," *Building and Environment*, vol. 161, Article ID 106221, 2019.
- [21] C.-M. Chiang, C.-M. Lai, P.-C. Chou, and Y.-Y. Li, "The influence of an architectural design alternative (transoms) on indoor air environment in conventional kitchens in Taiwan," *Building and Environment*, vol. 35, no. 7, pp. 579–585, 2000.
- [22] V. J. L. Gan, H. K. Wong, K. T. Tse, J. C. P. Cheng, I. M. C. Lo, and C. M. Chan, "Simulation-based evolutionary optimization for energy-efficient layout plan design of high-rise residential buildings," *Journal of Cleaner Production*, vol. 231, pp. 1375–1388, 2019.
- [23] V. Bychkov, M. Modestov, and C. K. Law, "Combustion phenomena in modern physics: I. Inertial confinement fusion," *Progress in Energy and Combustion Science*, vol. 47, pp. 32–59, 2015.
- [24] ANSYS, *ANSYS Help*, ANSYS Corporation, Canonsburg, PA, USA, 2019.
- [25] T. Poinso and D. Veynante, *Theoretical and Numerical Combustion*, R T Edwards, Inc., Philadelphia, PA, USA, 2001.
- [26] B. E. Launder and D. B. Spalding, "The numerical computation of turbulent flows," *Computer Methods in Applied Mechanics and Engineering*, vol. 3, no. 2, pp. 269–289, 1974.
- [27] R. D. Cowan and W. Fickett, "Calculation of the detonation properties of solid explosives with the kistiakowsky-wilson equation of state," *The Journal of Chemical Physics*, vol. 24, no. 5, pp. 932–939, 1956.
- [28] ANSYS, *AUTODYN Theory Manual*, ANSYS Corporation, Canonsburg, PA, USA, 2019.
- [29] R. I. Issa, "Solution of the implicitly discretised fluid flow equations by operator-splitting," *Journal of Computational Physics*, vol. 62, pp. 40–65, 1985.
- [30] OpenFOAM, *OpenFOAM User's Guide*, CFD Direct & The OpenFOAM Foundation, London, UK, 2020.
- [31] C. R. Bauwens, J. Chaffee, and S. B. Dorofeev, "Vented explosion overpressures from combustion of hydrogen and hydrocarbon mixtures," *International Journal of Hydrogen Energy*, vol. 36, no. 3, pp. 2329–2336, 2011.
- [32] O. Ram, E. Nof, and O. Sadot, "Dependence of the blast load penetrating into a structure on initial conditions and internal geometry," *Experimental Thermal and Fluid Science*, vol. 78, pp. 65–74, 2016.
- [33] T. A. Rose and P. D. Smith, "Influence of the principal geometrical parameters of straight city streets on positive and negative phase blast wave impulses," *International Journal of Impact Engineering*, vol. 27, no. 4, pp. 359–376, 2002.
- [34] A. M. Remennikov and T. A. Rose, "Modelling blast loads on buildings in complex city geometries," *Computers & Structures*, vol. 83, no. 27, pp. 2197–2205, 2005.
- [35] Y. Z. Li, H. T. Su, H. J. Ji, and W. Y. Cheng, "Numerical simulation to determine the gas explosion risk in longwall goaf areas: a case study of Xutuan Colliery," *International Journal of Mining Science and Technology*, vol. 1, pp. 1–8, 2020.
- [36] C. Guo, H. Shao, S. Jiang, Y. Wang, K. Wang, and Z. Wu, "Effect of low-concentration coal dust on gas explosion propagation law," *Powder Technology*, vol. 367, pp. 243–252, 2020.
- [37] Q. Zhang, L. Pang, and H. M. Liang, "Effect of scale on the explosion of methane in air and its shockwave," *Journal of Loss Prevention in the Process Industries*, vol. 24, no. 1, pp. 43–48, 2011.
- [38] M. Mitu, M. Prodan, V. Giurcan, D. Razus, and D. Oancea, "Influence of inert gas addition on propagation indices of methane-air deflagrations," *Process Safety and Environmental Protection*, vol. 102, pp. 513–522, 2016.
- [39] B. Vanderstraeten, D. Tuerlinckx, J. Berghmans, S. Vliegen, E. Van't Oost, and B. Smit, "Experimental study of the pressure and temperature dependence on the upper flammability limit of methane/air mixtures," *Journal of Hazardous Materials*, vol. 56, no. 3, pp. 237–246, 1997.
- [40] M. Gieras, R. Klemens, G. Rarata, and P. Wolański, "Determination of explosion parameters of methane-air mixtures in the chamber of 40dm<sup>3</sup> at normal and elevated temperature," *Journal of Loss Prevention in the Process Industries*, vol. 19, no. 2-3, pp. 263–270, 2006.

- [41] F. Gharagheizi, "Quantitative structure–property relationship for prediction of the lower flammability limit of pure compounds," *Energy & Fuels*, vol. 22, no. 5, pp. 3037–3039, 2008.
- [42] E. Salzano, F. S. Marra, G. Russo, and J. H. S. Lee, "Numerical simulation of turbulent gas flames in tubes," *Journal of Hazardous Materials*, vol. 95, no. 3, pp. 233–247, 2002.
- [43] E. S. Oran, V. N. Gamezo, and R. K. Zipf, "Large-scale experiments and absolute detonability of methane/air mixtures," *Combustion Science and Technology*, vol. 187, no. 1-2, pp. 324–341, 2015.
- [44] V. Di Sarli, A. Di Benedetto, and G. Russo, "Using large eddy simulation for understanding vented gas explosions in the presence of obstacles," *Journal of Hazardous Materials*, vol. 169, no. 1-3, pp. 435–442, 2009.
- [45] C. Wu and H. Hao, "Modeling of simultaneous ground shock and airblast pressure on nearby structures from surface explosions," *International Journal of Impact Engineering*, vol. 31, no. 6, pp. 699–717, 2005.

## Research Article

# Seismic Behavior Experimental Study on the Joint of Circular Tubed Steel-Reinforced Concrete Columns

Yan Dai <sup>1</sup>, Shaofeng Nie,<sup>2</sup> Tianhua Zhou,<sup>2</sup> Chengfeng Xue,<sup>1</sup> and Jingrong Peng<sup>1</sup>

<sup>1</sup>Shaanxi Key Laboratory of Safety and Durability of Concrete Structures, Xijing University, Xi'an 710123, China

<sup>2</sup>School of Civil Engineering, Chang'an University, Xi'an 710061, China

Correspondence should be addressed to Yan Dai; daiyan@xijing.edu.cn

Received 29 July 2021; Revised 24 August 2021; Accepted 11 September 2021; Published 29 September 2021

Academic Editor: Kang Shao-Bo

Copyright © 2021 Yan Dai et al. This is an open access article distributed under the Creative Commons Attribution License, which permits unrestricted use, distribution, and reproduction in any medium, provided the original work is properly cited.

A new type joint of Circular Tubed Steel-Reinforced Concrete (CTSRC) columns was designed in this paper. The structural characteristics, manufacturing process, and mechanical properties of raw materials of the new joint were introduced. In order to simulate the earthquake action, two joint specimens were subjected to low-cycle cyclic loading at the end of the column. Based on the in-depth study of the failure characteristics, load-displacement hysteretic curve, skeleton curve, ductility index, load-strain hysteretic curve in the core area of the joint, energy dissipation performance, strength and stiffness degradation performance, and shear deformation in the core area of the joint during the whole loading process, the seismic behavior of this new type of joint was investigated. The results show that the new joint has reasonable failure characteristics, high bearing capacity, good ductility, excellent seismic energy dissipation performance, and strong resistance to strength and stiffness degradation, which meets the seismic design principle of "strong joint and weak component" and is suitable for the results with special requirements for seismic performance. In addition, preliminary design recommendations were put forward. The research results of this paper can provide a theoretical basis for the application of this kind of new structure.

## 1. Introduction

At present, steel-concrete composite structure has been widely used in the field of civil engineering construction. Concrete-filled steel tubular column and steel-reinforced concrete column are two main forms of steel-concrete composite structure. The concrete-filled steel tubular column makes the concrete in the tube in a three-dimensional compressive stress state through the circumferential restraint effect of the outer steel tube on the concrete in the tube, so as to improve the concrete strength and the bearing capacity of the structural column [1–3]. Steel-reinforced concrete column refers to the column concrete, equipped with steel, and with a certain stress and structural reinforcement, steel-reinforced concrete column through the synergistic effect of steel and concrete gives full play to the performance of the two materials and at the same time has excellent seismic performance and good economy. At present, it is widely used in high-rise and superhigh-rise buildings [4].

But the shortcomings of the two are also very obvious. The axial load shared by the steel tube and concrete is easy to cause the buckling of steel tube plate, leading to the decline of seismic performance of columns. Steel-reinforced concrete column is not convenient for concrete pouring because of setting steel skeleton and section steel at the same time, and the steel skeleton has insufficient constraints on concrete, which leads to low axial compression ratio limit and cannot make full use of material properties.

Therefore, on the basis of long-term engineering practice, experience accumulation, and previous research results, a new type of composite structure column has emerged: Circular Tubed Steel-Reinforced Concrete (CTSRC) column. Its outer steel tube is disconnected at the beam-column joint and does not pass through the core area of the joint. Therefore, its steel tube does not directly bear the longitudinal load but only restrains the core concrete, as shown in Figure 1. Research by relevant scholars shows that [5–7] the CTSRC column has high compression and shear bearing

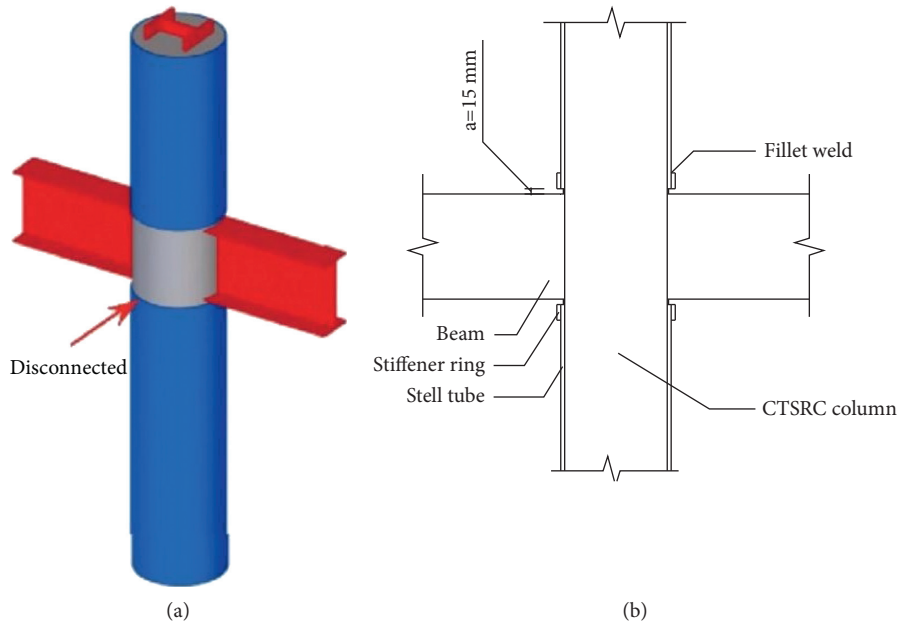


FIGURE 1: Structural diagram of the circular steel tube-confined H-SRC column steel beam joint. (a) Diagram. (b) Slotted structure of the steel pipe at the column end.

capacity, superior seismic performance, strong interlayer deformation capacity, good fire resistance, and convenient construction and can make full use of high-strength material performance.

In recent years, people have carried out extensive research on the mechanical properties of this structure. Takamasa Yamamoto made three kinds of square and circular steel tube-confined concrete short columns with different cross-section sizes and carried out an axial compression test to study the restraint effect of circular steel tube and square steel tube on concrete [8]. Fam made five specimens to compare the axial bearing capacity of concrete-filled steel tubular columns and confined concrete-filled steel tubular columns. The results show that the axial bearing capacity of confined concrete-filled steel tubular columns is significantly higher [9]. Chen et al. carried out axial compression, eccentric compression, and seismic performance tests on two kinds of partially through CFST column RC beam joints with different strengthening methods [10–12]. Nie et al. studied the axial compression and seismic behavior of a kind of steel tube-confined concrete column RC beam joint with transverse multiple hoops. The results show that this kind of strengthening form can make up for the deficiency caused by the disconnection of steel tube [13, 14]. Han et al. conducted a comparative experimental study on the hysteretic behavior of steel tubular confined concrete column RC beam joints and steel tubular concrete column RC ring beam joints. The results show that the seismic performance of steel tubular confined concrete column RC beam joints is better than that of steel tubular concrete column RC ring beam joints [15]. Zhang et al. have carried out an experimental study on the seismic behavior of a kind of connection form of concrete-filled steel tubular column and RC beam outer

steel tubular unconnected ring beam joint [16]. Gan et al. designed a ring reinforced steel tube-confined RC column joint and studied its axial compression and hysteretic behavior [17]. On the basis of collecting the shear failure results of steel tube-confined reinforced concrete columns with various sections, Gan et al. compared and verified the existing calculation methods and formulas of shear capacity, improved the existing calculation methods, and proposed the calculation formulas of shear capacity for square steel tubes and circular steel tubes, respectively [18]. Duan et al. designed a new type of square steel tube-confined concrete column joint, carried out two-stage tests to investigate the overall axial compressive behavior of the specimen and the influence of joint geometry size, concrete strength, and mesh volume on its bearing capacity, and proposed the bearing capacity expression of this new type of joint [19]. Lin et al. analyzed the shear mechanism and shear capacity of framework joints of steel-reinforced concrete-filled circular steel tube (SRCFCST), and the calculation method of composite shear capacity in the core area of joints is proposed, which can provide a reference for nonlinear analysis and engineering design of similar joints [20]. Yu et al. designed a new type of joint, in which the concrete in the core area is restrained by the steel tube in the core area, and the outer part is restrained by the ring stirrup. The nonlinear finite element analysis of the axial compression bearing capacity test was carried out, the influence of the steel tube and stirrup in the core area on the bearing capacity is discussed, and the calculation formula of the ultimate bearing capacity is proposed [21–23]. Peng et al. designed four specimens of concrete-filled square steel tubular frame joints with unequal beam heights, carried out low-cycle cyclic loading tests, discussed their seismic performance, and analyzed their shear capacity [24].

Literature review shows that the mechanical properties of the CTSRC column are superior, and it has a wide application prospect, but there are two main deficiencies in its research.

Firstly, at present, the research of CTSRC structures mainly focuses on the axial compression performance of columns and joints, and the research on seismic performance of joints is less. If the joints are damaged, the whole structure will be destroyed no matter how strong the beam-column members are. Therefore, it is necessary to study the seismic performance on joints of the CTSRC column.

Secondly, the existing research on seismic performance on joints of CTSRC column is carried out by a small-scale model. There is a big difference between the test and the actual situation, and the representativeness is not strong.

As a consequence, it is necessary to study the seismic performance on joints of the CTSRC column, especially the way to strengthen the weakened joint area, the impact of the strengthened joint area on the seismic performance of such joints, and the way to make it meet the design principles of strong column, weak beam, and stronger joint. It is the key problem to be solved in steel tube-confined steel-reinforced concrete structure. Therefore, a new type joint is designed in this paper. The concrete ring beam is used to strengthen the weakened joint area, as shown in Figure 2. The specimen is designed with the size of 1:1. Through the pseudostatic test method, the displacement and strain data of each part of the specimen are collected, and the seismic mechanical properties are further studied. It provides a theoretical basis for the popularization and application of this kind of new structure.

## 2. Test Plan

**2.1. Specimen Design and Manufacturing.** In this paper, two full-scale frame joints are designed, the height is 4375 mm, the outer diameter of the cylinder is 400 mm, the wall thickness of the circular steel tube is 5 mm, and the width is 3370 mm. In order to ensure that the circular steel tube does not bear the longitudinal load, the circular steel tube is disconnected in the joint area, and a 15 mm ring opening is reserved from the upper and lower edges of the concrete ring beam. The other structures and dimensions are shown in Figure 3 (taking SH-1 specimen as an example), and the parameters of the specimen are shown in Table 1.

In this paper, the specimen processing is divided into four stages: first, steel structure processing and component assembly; second, sticking strain gauges; third, formwork and concrete pouring; finally, curing and specimen painting antirust.

**2.2. Mechanical Properties of Materials.** The measured average cube compressive strength of the test reserved concrete block is 57.58 MPa, and the material properties of steel and reinforcement are shown in Table 2.

**2.3. Test Device.** The joint specimen is loaded by reaction wall and reaction frame. The horizontal loading device adopts MTS electrohydraulic servo program-controlled

structure testing machine. The maximum load of the actuator applying horizontal reciprocating load is 500 kN, and the travel range is  $\pm 250$  mm. The maximum load of the jack used in the vertical loading test is 2000 kN. The loading schematic diagram and loading panoramic photo are shown in Figures 4 and 5.

**2.4. Loading System.** There are two loading methods for seismic performance test of joints: one is beam end loading and the other is column end loading. Because the column end loading can simulate the second-order gravity effect ( $P-\Delta$  effect) of buildings under earthquake, the column end loading method is adopted in this paper, as shown in Figure 4, and the beam end is supported by a chain bar. The vertical displacement, rotation angle, and horizontal displacement can be realized at the top of the column. This loading method can truly reflect the deformation and mechanical performance of beam-column joints under earthquake.

On the basis of referring to relevant specifications [25] and relevant research [26, 27], the specific loading system is determined. Displacement loading mode is adopted in the whole loading process of column top. First, apply the axial load on the column top, and then apply the horizontal load, which is loaded to the yield displacement by 2-3 single cycles. After yielding, the load is carried out according to the multiple of the yield displacement value of the column top. Each cycle is repeated three times (as shown in Figure 6). The cycle does not stop until the specimen is damaged or the horizontal load of the column top drops below 85% of its peak load [16, 25]. In the loading system, the yield displacement of the column top of the joint specimen is the estimated value of the horizontal displacement of the column top when the stress of the flange edge of the section at the junction of the steel beam and the concrete ring beam reaches " $f_y$ ." In the test, the loading steps are determined or adjusted in combination with the relevant instrument values. At the same time, the yield point of the specimen is judged from the change of the load-displacement hysteretic curve, and the hysteretic curve is analyzed after the test. The actual yield point of the specimen is determined [25-27].

**2.5. Measuring the Content.** The test includes displacement measurement and strain measurement. The deformation of the specimen is measured by displacement meter and dial indicator, the strain of circular steel tube, section steel in column, steel beam, and concrete ring beam, reinforcement is measured by strain gauge or strain rosette, the data measured by strain gauge is collected by TDS-602 static strain measurement system and input into a computer, the load-displacement hysteretic curve of column top is automatically collected by MTS servo actuator, and the concrete cracks are measured by crack observation instrument.

## 3. Test Results

**3.1. Analysis of Failure Characteristics of Specimens.** Because the design parameters of the two specimens are basically similar, the failure modes of the two specimens are

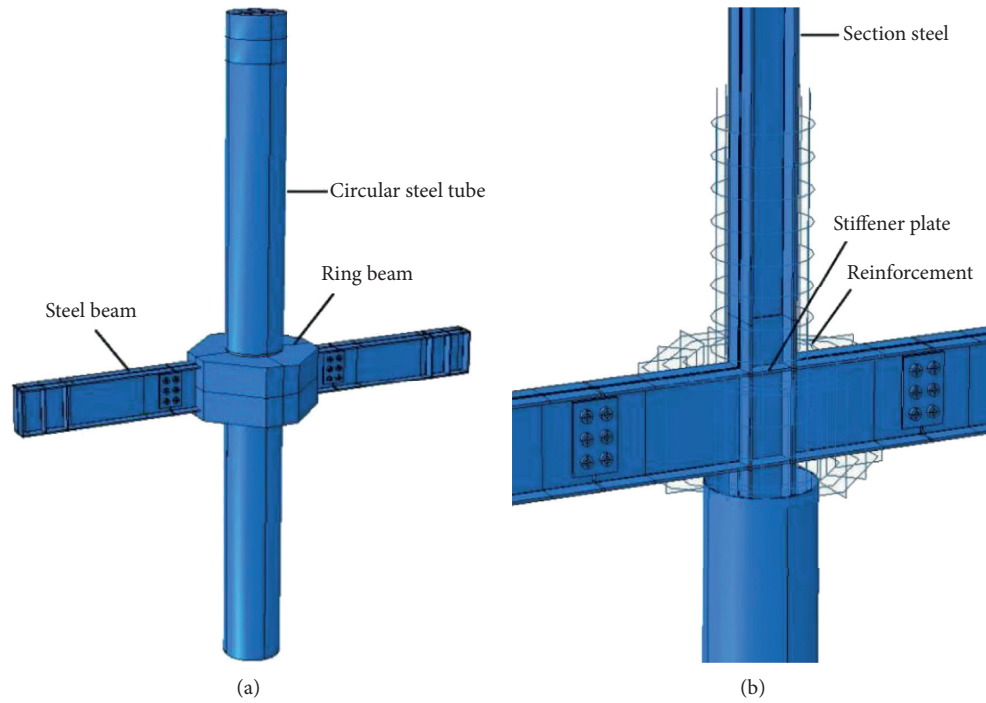


FIGURE 2: Schematic diagram of the specimen structure. (a) Overall structure of the specimen. (b) Internal structure of the joint area.

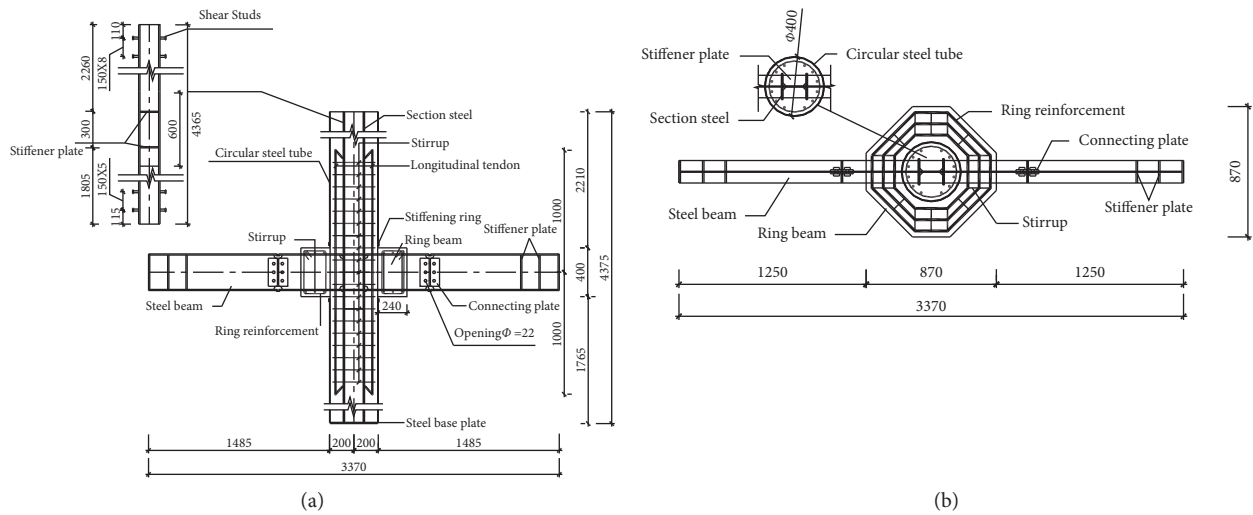


FIGURE 3: Structural diagram of specimen (SH-1). (a) Elevation (mm). (b) Plan (mm).

TABLE 1: Parameters of the specimen.

Specimen number	Steel ratio (%)	Thickness of the circular tube steel pipe (mm)	Form of the ring beam	Reinforcement ratio of the ring beam (%)
SH-1	4.19	5	Octagon	3.55
SH-2			circular	2.05

obviously similar, the failure starts from the concrete cracking at the junction of the steel beam and the ring beam, and with the continuous increase of the horizontal displacement at the top of the column, the flange at the junction of the steel beam and the ring beam first enters into yield.

Finally, the two specimens are in full section shape at the end of the steel beam about 5 cm away from the edge of the ring beam. Plastic hinge is formed (because of the quality problem of the lower flange weld of the steel beam on the west side of the SH-1 specimen, the lower flange of the steel

TABLE 2: Steel material data.

Location of the material test piece	Yield strength ( $f_y$ ) (MPa)	Ultimate strength ( $f_u$ ) (MPa)	Elastic modulus ( $E$ ) (MPa)	Elongation after fracture (%)
Flange (section steel in column)	284.19	437.38	212404	37.2
Web (section steel in column)	309.35	453.02	217199	30.0
Flange (steel beam)	308.26	463.54	212867	23.9
Web (steel beam)	337.52	483.25	213321	27.7
Circular steel tube	355.62	488.81	194907	27.2
Reinforcement (20 mm)	486.85	691.60	195426	20.2
Reinforcement (10 mm)	389.39	553.28	210564	23.0

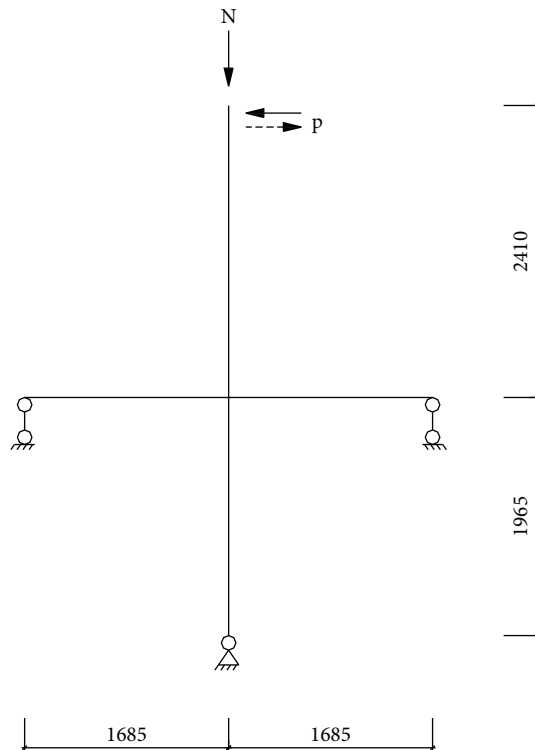


FIGURE 4: Loading schematic diagram.

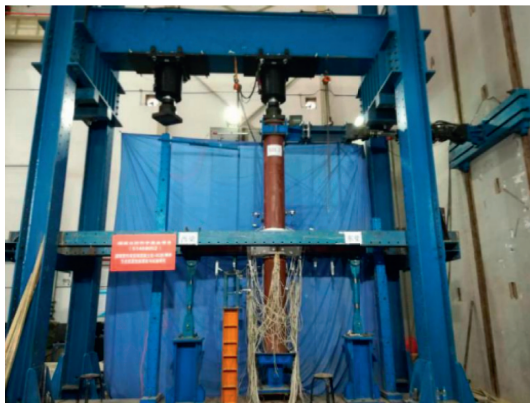


FIGURE 5: Loading panoramic photo.

beam on the west side of the SH-1 specimen is fractured when the SH-1 specimen is finally destroyed), and the concrete at the junction of the ring beam and the steel beam cracks and partially falls off. In the whole test process, except

for the beam end, there is no obvious failure sign in the joint core area of the two specimens. Figures 7 and 8 show the final failure state of SH-1 and SH-2 specimens.

On account of the difference in the volume reinforcement ratio of the ring beam between the two specimens, the concrete shedding degree of the ring beam is quite different when the two specimens are damaged. Due to the high reinforcement ratio of SH-1 specimen, especially the stirrups are arranged near the two sides of the steel beam at the junction of the steel beam and the ring beam, and the concrete of the ring beam of the specimen will not fall off a lot after being broken, but it is still connected to the damaged ring beam. Due to the small stirrup ratio of the SH-2 specimen, the stirrups on both sides of the junction between the steel beam and the ring beam are far away from the steel beam, resulting in a large amount of concrete falling off near the steel beam after fragmentation.

**3.2. Load-Displacement Hysteretic Curve at the Top of the Column.** The load-displacement hysteretic curves of the two specimens are shown in Figure 9. It can be seen from the hysteretic curves of the above two specimens that, at the initial stage of cyclic loading, the hysteretic curves are parallelogram. With the continuous cyclic loading, the hysteretic curves gradually change from parallelogram to rectangle. At the same time, the fullness of the hysteretic curves of the two specimens is much higher than that of the corresponding steel frame joints and concrete frame joints, showing a very good energy dissipation performance.

At the same time, the curves of the two specimens show different characteristics: first, due to the poor manufacturing quality of specimen SH-1, when loading to the second cycle of 180 mm, the west side of the weld is completely broken, resulting in a sharp drop in the curve. Second, the hysteretic curve of the specimen SH-1 has a more obvious difference about the horizontal coordinate axis; the results show that the peak value of the positive horizontal force (thrust) at the top of the column is significantly greater than the negative horizontal force (tension) at the top of the column under each displacement amplitude loading cycle.

**3.3. Skeleton Curve.** The skeleton curve can be obtained by connecting the peak points of each loading point in the same direction on the load-displacement hysteretic curve. The skeleton curve cannot only reflect the load and displacement of each characteristic point in the loading process but also



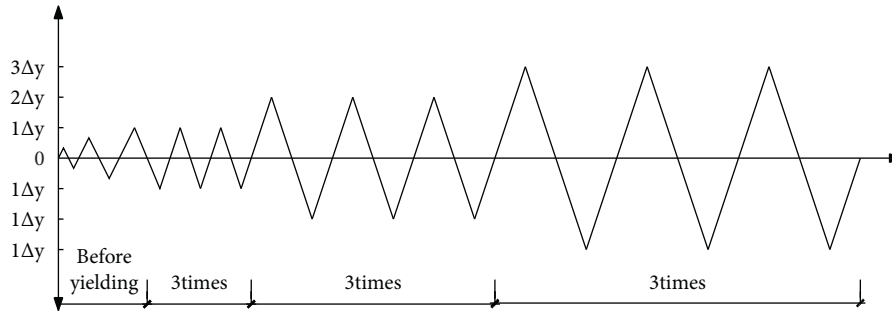
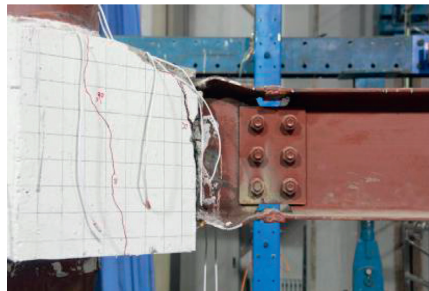


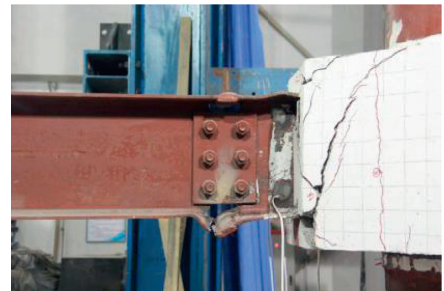
FIGURE 6: Loading system of the test.



(a)



(b)



(c)

FIGURE 7: Failure of the specimen (SH-1). (a) Overall situation after failure. (b) Failure of the east steel beam and ring beam. (c) Failure of the west steel beam and ring beam.



(a)



(b)

FIGURE 8: Failure of the specimen (SH-2). (a) Overall situation after failure. (b) Failure of the east steel beam and ring beam.

reflect the energy absorption, ductility, strength, stiffness, and degradation of the structure or component under repeated loading. Figure 10 shows the skeleton curve of each specimen.

From the skeleton curves of each specimen, it can be seen that the skeleton curves of the two specimens show obvious S-shape, and they have experienced three stages of elasticity, elastoplasticity, and failure. During the loading process, the positive and negative directions of the specimens are not

completely symmetrical; especially, the SH-1 specimen is obvious; the influence of ring beam shape and ring beam reinforcement ratio on the bearing capacity and deformation capacity of the joint is not significant; the two specimens are not symmetrical. After the specimens enter the plastic state, with the continuous increase of the displacement at the top of the column, the load does not immediately decrease, indicating that both specimens have good ductility; the

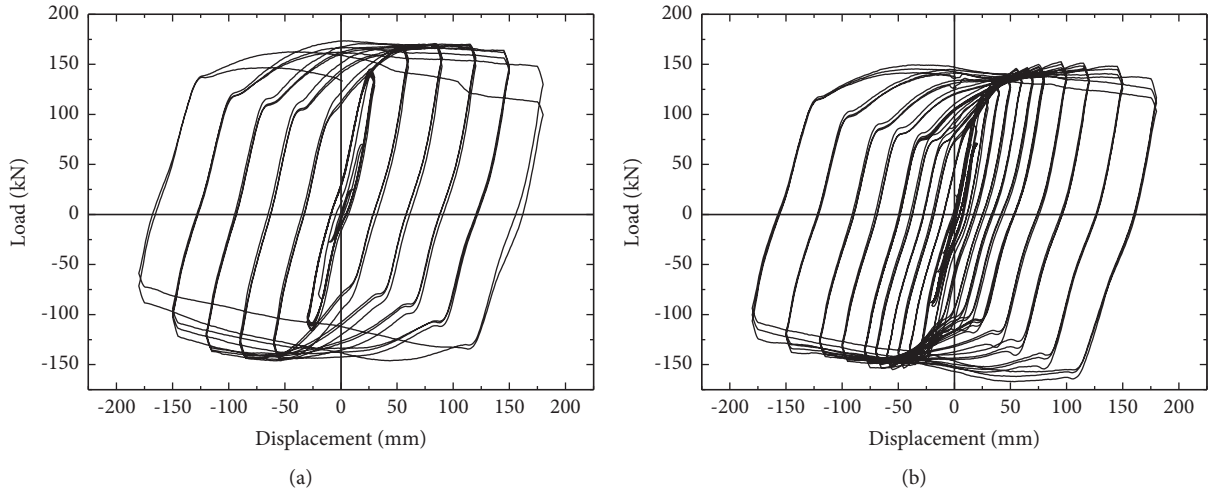


FIGURE 9: Load-displacement hysteretic curve of specimen column top. (a) SH-1. (b) SH-2.

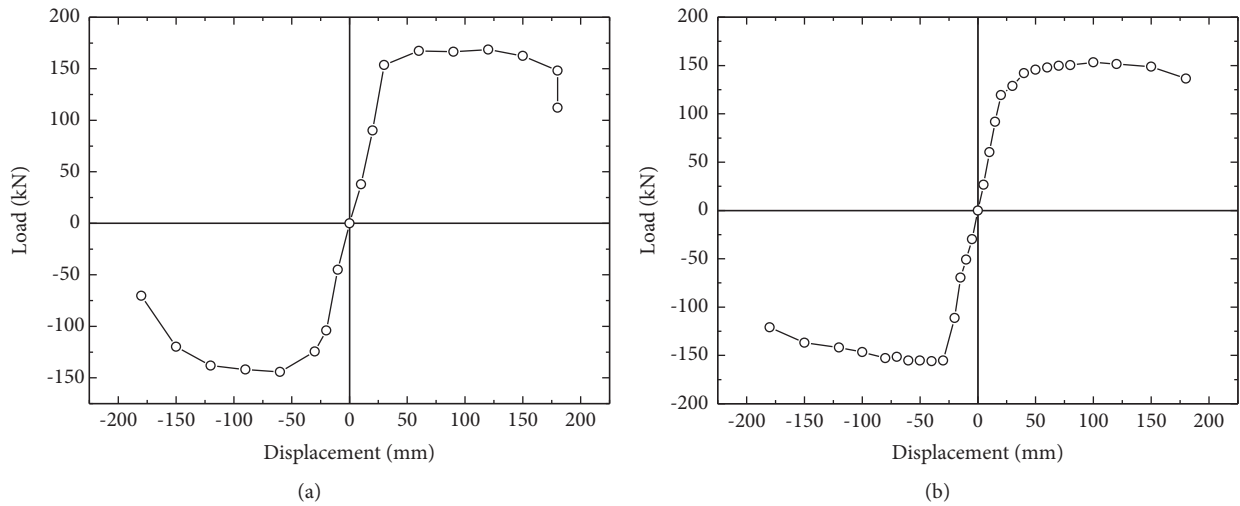


FIGURE 10: Load-displacement skeleton curve of the specimen column top. (a) SH-1. (b) SH-2.

skeleton curves of both specimens have no obvious yield point; and after the peak load, the curve and the stiffness gradually decrease.

**3.4. Characteristic Point Load and Ductility Index of Specimens.** It can be seen from the skeleton curve of the two specimens that there is no obvious yield point on the skeleton curve. Therefore, this paper adopts the “general yield moment method” to determine the displacement and load value of the characteristic points (yield, ultimate, and failure) in the loading process of the two specimens. The determination method is shown in Figure 11.  $P_y$ ,  $\Delta_y$ ,  $P_{max}$ ,  $\Delta_{max}$ ,  $P_u$ , and  $\Delta_u$  determined by the above method are shown in Table 3.

It can be seen from the above table, skeleton curve, and hysteretic curve that the positive and reverse force performance of specimen SH-1 is quite different. However, this situation does not appear in the test of specimen SH-2, which may be caused by the deviation of the east and west

steel beams of SH-1 in the process of processing and test installation.

The displacement ductility coefficient ( $\mu$ ) [28] is an index reflecting the plastic deformation capacity of the structure under earthquake action. The larger the displacement ductility coefficient is, the better the ductility of the structure or component is. The calculation of the displacement ductility coefficient is shown in

$$\mu = \frac{\Delta_u}{\Delta_y}, \quad (1)$$

where “ $\Delta_u$ ” is the horizontal displacement at the top of the column when the joint specimen fails and “ $\Delta_y$ ” is the horizontal displacement at the top of the column when the joint specimen yields. The calculation is shown in Table 3.

The interlaminar deformation angle ( $\varphi$ ) of each joint specimen can be obtained according to the geometric relationship. The calculation of ductility coefficient of interlaminar deformation angle is shown in

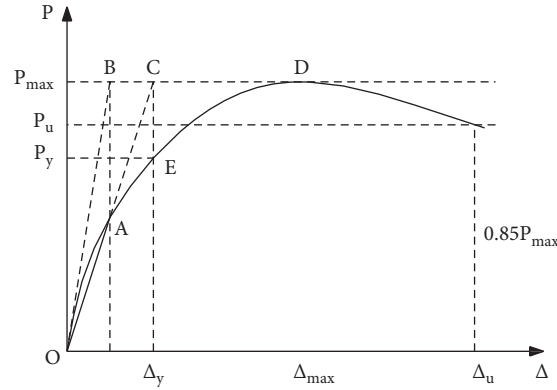


FIGURE 11: Determination method of the characteristic point load.

TABLE 3: Load and displacement of the characteristic point.

Specimen		Yield state		Ultimate load state		Failure state	
		$P_y$ (kN)	$\Delta_y$ (mm)	$P_{max}$ (kN)	$\Delta_{max}$ (mm)	$P_u$ (kN)	$\Delta_u$ (mm)
SH-1	Positive	155.80	41.67	168.44	60.01	143.17	178.51
	Reverse	127.65	32.35	144.29	60.04	122.65	154.20
SH-2	Positive	131.25	31.25	151.46	80.01	128.74	180.02
	Reverse	120.74	30.29	155.31	60.03	132.01	157.54

$$\mu_\varphi = \frac{\varphi_u}{\varphi_y}, \quad (2)$$

where “ $\varphi_u$ ” is the interlaminar deformation angle when the joint specimen fails and “ $\varphi_y$ ” is the interlaminar deformation angle when the joint specimen yields. The calculation is shown in Table 4.

It can be seen from Table 3 and the skeleton curves of the two specimens that the maximum displacement ductility coefficient and interlaminar deformation angle ductility coefficient of the two specimens are 5.76 and the minimum is 4.28. The results show that the interlaminar deformation angle ranges from 0.00658 to 0.00905 at yield and from 0.0335 to 0.0391 at failure. The relevant index is far more than the general reinforced concrete structure, which has very good ductility and deformation performance.

**3.5. Strain Analysis of the Specimen.** According to the failure characteristics of the specimen in Section 3.1, the ultimate failure of the two specimens occurs at the junction of the steel beam and the ring beam, where the plastic hinge is formed in the whole section of the steel beam, and the concrete cracks and falls off. The following takes the SH-1 specimen as an example to illustrate the characteristics of the data of each strain measurement point of the specimen.

From the load-strain hysteretic curves of flange, web, and ring beam concrete at the junction of steel beam and ring beam, it can be seen that the flange at the junction of steel beam and ring beam first enters into yield state and then slightly warps compared with the web. When the final specimen fails, plastic hinge is formed at the junction of the east and west steel beams and the ring beam. During the whole loading process, the maximum strain of each

measuring point of flange reaches  $40000 \mu\epsilon$  (as shown in Figure 12(a)). The web in yield state lags behind the flange (as shown in Figure 12(b)). At the initial stage of loading, the ring beam concrete is not cracked, the load-strain curve is linear, and there is almost no residual strain. However, with the cracking of the concrete, the strain value of each measuring point increases rapidly, and most of the deformation cannot be recovered, which indicates that, after the crack appears, with the continuous loading, the crack can hardly be closed, and the residual deformation is very large (as shown in Figure 12(c)).

From the reading of strain measuring points arranged in the rest parts of the specimen, it can be seen that the strain values of the rest parts remain elastic throughout the loading process, except that the central part of the section steel web in the column enters the yield state in the later stage of loading, which fully indicates that the existence of concrete ring beam makes the failure part move out, which plays a good role in protecting the core area of the joint.

**3.6. Energy Dissipation Performance of Specimens.** Energy dissipation performance is another important index to investigate the seismic performance of a certain structure. The equivalent viscous damping coefficient ( $h_e$ ) is often used to judge the energy dissipation capacity of the structure, and “ $h_e$ ” is calculated according to the envelope diagram of the load-displacement hysteretic curve of the specimen (as shown in Figure 13). According to formula (3), the equivalent viscous damping coefficients of the hysteresis loops of the two specimens under each displacement amplitude are calculated, and the curves are drawn as shown in Figure 14:

TABLE 4: Ductility index of specimens.

Specimen		Displacement ductility coefficient	Interlaminar deformation angle and ductility coefficient		
			$\varphi_y$ (rad)	$\varphi_u$ (rad)	$\mu_\varphi = \varphi_u/\varphi_y$
SH-1	Positive	4.28	0.00905	0.0388	4.29
	Reverse	4.77	0.00703	0.0335	4.77
SH-2	Positive	5.76	0.00679	0.0391	5.76
	Reverse	5.20	0.00658	0.0342	5.20

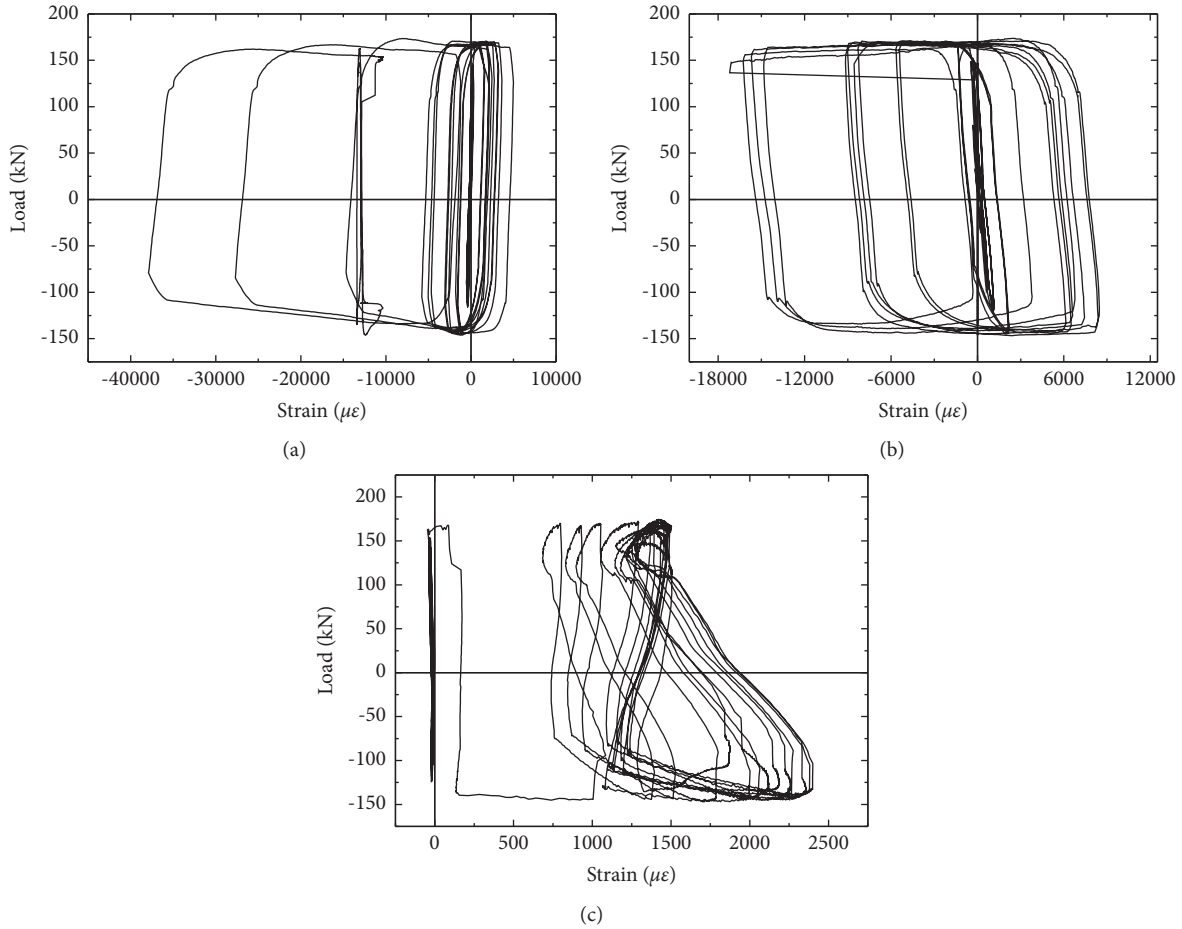


FIGURE 12: Load-strain hysteretic curves. (a) Flange. (b) Web. (c) Ring beam concrete.

$$h_e = \frac{1}{2\pi} \frac{\text{area of hysteresis curve (FBE + FDE)}}{\text{area of triangle (AOB + COD)}}. \quad (3)$$

From the equivalent viscous damping coefficient curves of the above two specimens, the following conclusions can be obtained:

- (1) The ultimate equivalent viscous damping coefficients ( $h_e$ ) of the two specimens are 0.535 (SH-1) and 0.615 (SH-2). Relevant studies have shown that the “ $h_e$ ” of reinforced concrete joints is 0.1 and that of steel-reinforced concrete joints is about 0.3. “ $h_e$ ” values of the two new joints are 5.35 times and 6.15 times of reinforced concrete joints and 1.78 times and 2.05 times of steel-reinforced concrete joints. The joint

specimen has superior energy dissipation performance.

- (2) In the initial elastic stage, the equivalent viscous damping coefficients of the two specimens are relatively small, and the energy dissipation capacity increases rapidly with the increase of cyclic loading displacement; after entering the yield stage, the plastic hinge is formed at the end of the steel beam, and the concrete at the junction of the steel beam and the ring beam cracks and gradually falls off, but the energy dissipation capacity of the two specimens continues to improve. With the continuous loading, the beam end is completely cut off. The bearing capacity of the two specimens remains at a high level,

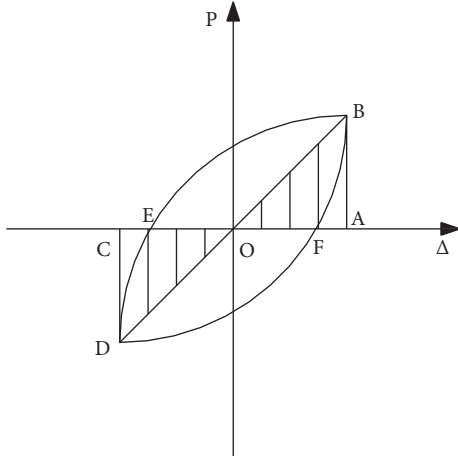


FIGURE 13: Envelope diagram.

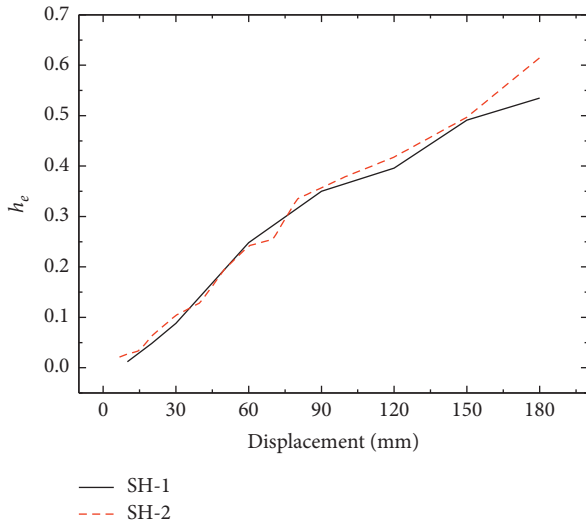


FIGURE 14: Equivalent viscous damping coefficient curve.

and the energy dissipation capacity is still in a rising state until the end of the failure loading. It fully shows that the energy dissipation capacity of the two specimens increases with the continuous low-cycle cyclic loading.

- (3) From the initial stage of loading to the near failure of the specimen, the energy dissipation index curves of the two joint specimens have little difference, showing the phenomenon of alternating rise, while the end of the curve shows bifurcation. This is due to the sharp drop of the hysteretic curve caused by the fracture of the lower flange weld of the steel beam on the west side of the specimen SH-1, which makes the energy dissipation indexes of the final specimen SH-1 smaller than that of SH-2.

**3.7. Strength Degradation of Specimens.** Strength degradation refers to the characteristic that the bearing capacity of the specimen decreases with the increase of the number of reciprocating loading processes under the condition of

constant displacement amplitude. The strength degradation of joint specimens under repeated loading has an important impact on its seismic performance. In this paper, the same level bearing capacity reduction coefficient ( $\lambda_i$ ) and the overall bearing capacity reduction coefficient ( $\lambda_j$ ) are used to reflect the strength degradation characteristics of joint specimens in the test.

The same level bearing capacity reduction coefficient is as follows:

$$\lambda_i = \frac{P_j^i \min}{P_j^1 \max}, \quad (4)$$

where  $P_j^i \min$  is the minimum value of the peak load in the same loading cycle when the displacement is  $j$  and  $P_j^1 \max$  is the peak point load of the first loading cycle when the displacement is  $j$ .

The overall bearing capacity reduction coefficient is as follows:

$$\lambda_j = \frac{P_j}{P_{\max}}, \quad (5)$$

where  $P_j$  is the minimum value of the load at the peak point of the  $j$ -th loading cycle and  $P_{\max}$  is the ultimate value of the bearing capacity of the specimen during the whole loading process.

According to the above calculation method, the bearing capacity reduction coefficient of SH-1 and SH-2 under different displacement loads can be obtained in the process of positive (push) and reverse (pull) loading, and the bearing capacity reduction coefficient curve of SH-1 and SH-2 is drawn, as shown in Figure 15.

The following conclusions can be drawn from the bearing capacity reduction coefficient curves of the above two specimens:

- (1) At the initial stage of loading, with the increase of displacement amplitude, the values of  $\lambda_i$  and  $\lambda_j$  of the two specimens increase rapidly. With the continuous loading, the two values remain stable and fluctuate in a certain range. With further increase of displacement amplitude, the values of  $\lambda_i$  and  $\lambda_j$  decrease slowly, and the decrease is obvious until the last displacement.
- (2) From the initial stage of loading to the near failure of the specimen, the  $\lambda_i$  values of the two specimens are kept at a high level (except for the corresponding value of  $\lambda_i$  of SH-2 specimen when the displacement is 20 mm in the positive direction), and the fluctuation range is between 0.933 and 0.977; this shows that both specimens have strong resistance to strength degradation. When the loading reaches 180 mm displacement amplitude, the  $\lambda_i$  value of the two specimens decreases obviously. The curve of the SH-1 specimen decreases more than that of the SH-2 specimen, because the lower flange of the west steel beam breaks during the second 180 mm cycle of the SH-1 specimen,

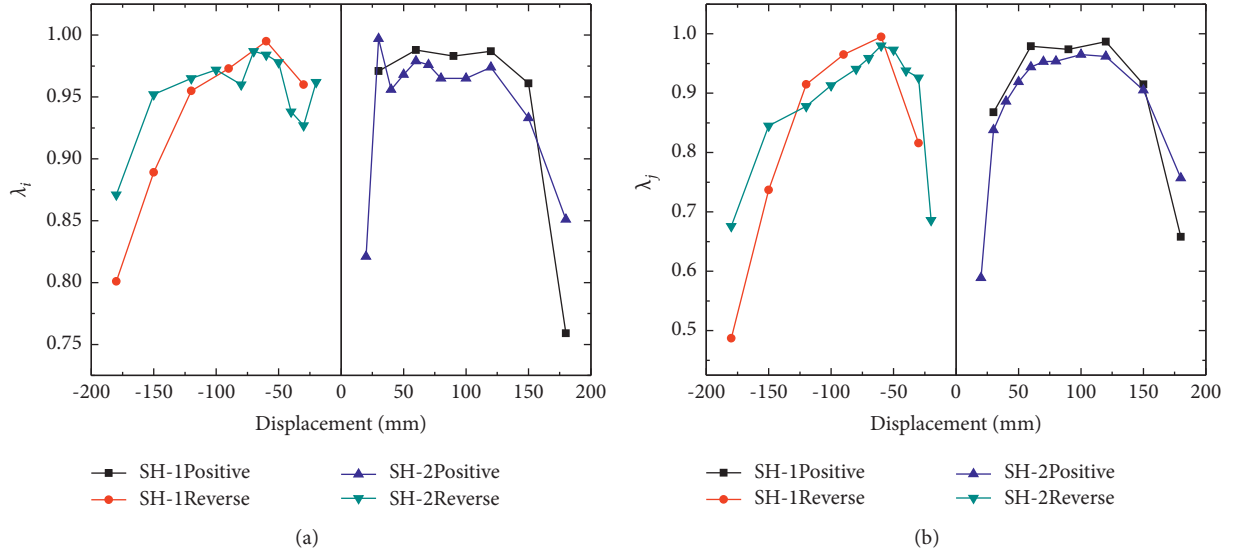


FIGURE 15: Bearing capacity reduction coefficient curve. (a) The same level bearing capacity reduction coefficient curve. (b) Overall bearing capacity reduction coefficient curve.

resulting in a sharp drop in load, which leads to a larger drop in  $\lambda_i$  value. Comparing Figures 15(a) with 15(b), it can be seen that the same level strength degradation law of the two specimens is similar to the overall strength degradation law. Although the strength degradation curve values of the two specimens are different, the trend of the curve is basically the same, which also shows that the strength degradation performance of the specimens mainly depends on the performance of the steel beam end rather than the ring beam reinforcement.

**3.8. Stiffness Degradation of Specimens.** Stiffness degradation is a characteristic that the stiffness of specimen decreases with the increase of repeated loading times under the condition of constant displacement amplitude, which is mainly caused by steel yield and concrete cracking and falling off. The stiffness degradation is represented by loop stiffness [28].

The loop stiffness is as follows:

$$K_i = \frac{\sum_{j=1}^n P_j^i}{\sum_{j=1}^n \Delta_j^i}, \quad (6)$$

where  $K_i$  is the loop stiffness,  $P_j^i$  is the peak point load value of the  $i$ -th cycle when the displacement is  $j$ ,  $\Delta_j^i$  is the peak point deformation value of the  $i$ -th cycle when the displacement is  $j$ , and  $n$  is the number of cycles under the same displacement.

From the above calculation method, the loop stiffness of the two joint specimens at all levels of displacement can be obtained, and the stiffness degradation curve of the two joint specimens is drawn, as shown in Figure 16.

The following conclusions can be drawn from the stiffness degradation curves of two specimens:

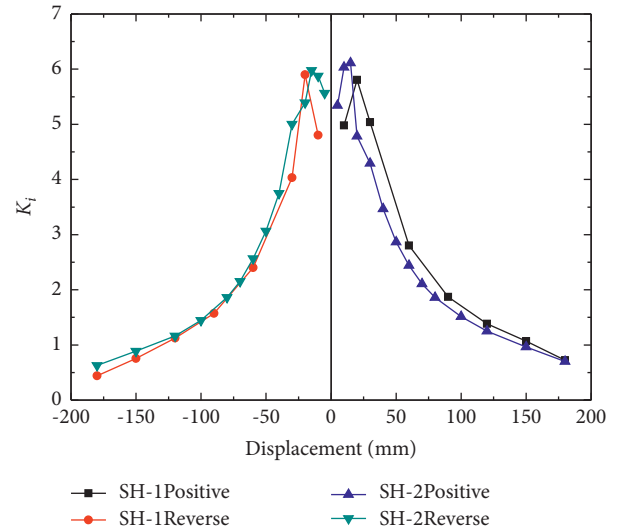


FIGURE 16: Stiffness degradation curve.

- (1) In the initial stage of loading, the loop stiffness value of the two specimens increases slightly. When the two specimens reach their yield displacement and enter the cyclic loading stage, the  $K_i$  value reaches the maximum and then decreases with the continuous loading. In the middle and late stages of loading, the reduction rate of  $K_i$  value gradually decreases, which is reflected in the gradual decrease of the slope of the stiffness degradation curve and the gradual slowing of the curve. This shows that the ability to resist stiffness degradation is superior.
- (2) In the early stage of loading, the  $K_i$  value of SH-2 is slightly higher than that of SH-1. In the middle and late stage of loading and until failure, the positive stiffness degradation curve of SH-1 is always higher than that of SH-2; that is, the  $K_i$  value of SH-1 is

greater than that of SH-2 at the same positive displacement, while the negative stiffness degradation curve of SH-1 and SH-2 has little difference in the process of test loading. From the test results, it can be seen that there is a great difference between the positive and reverse mechanical properties of SH-1 specimen during the loading process, and the difference between the positive and reverse load values of the three characteristic points is 16.73%–22.05%, which leads to the fact that the value of the negative stiffness degradation curve is smaller than that of the positive.

**3.9. Deformation Analysis of the Joint Area.** The joint area refers to the joint area of beam and column. Under the action of beam end reaction and column end horizontal thrust, the joints will expand, bend, and shear. Due to the steel beam constraints, the expansion and bending deformation of the joint region can be ignored. This paper focuses on the shear deformation of the joint region.

Due to the existence of a concrete ring beam, it is not convenient to arrange dial indicator in the diagonal direction outside the joint area for measurement. Therefore, the method in [29] is adopted in this test, and strain gauges are pasted in the core area of the joint to measure the deformation of the steel web along the diagonal direction in the core area of the joint during loading (as shown in Figure 17). In order to compare the data of different specimens when analyzing the data, the data measured by the strain gauge when the axial pressure of the specimen has been applied and the horizontal load on the top of the column has not been applied is taken as the datum point data (zero points), the difference between the real strain test data and the datum point when the horizontal displacement on the top of the column is the maximum is taken as the standard strain data, and then the average value of two diagonal strains is taken, respectively. It should be noted that, in the process of specimen test on SH-2, due to the limitation of acquisition instrument, when the load is applied to 80 mm cycle, the data acquisition of all strain measuring points stops, so the strain data of node domain of SH-2 specimen is only collected at 80 mm cycle.

It can be seen from Table 5 that the strain measuring points of nos. 13, 14, 15, 16, and 17 steel are compressive strain at the maximum horizontal displacement at the top of the column, and the strain measuring points of nos. 18, 19, and 20 steel are tensile strain at the maximum horizontal displacement at the top of the column; that is, one diagonal of the joint area is compressive deformation and the other diagonal is tensile deformation. Moreover, when the horizontal displacement of the top of the column reaches the maximum, the average strain does not reach the yield strain of the steel and remains in the elastic state.

Using the average value of the maximum strain in the diagonal direction of the node area in Table 5 and using the geometric relationship shown in Figure 18 and formulas (7) and (8), the actual deformation value and relevant parameters in the diagonal direction of the node core area can be calculated by Hooke's law, as shown in Table 6.

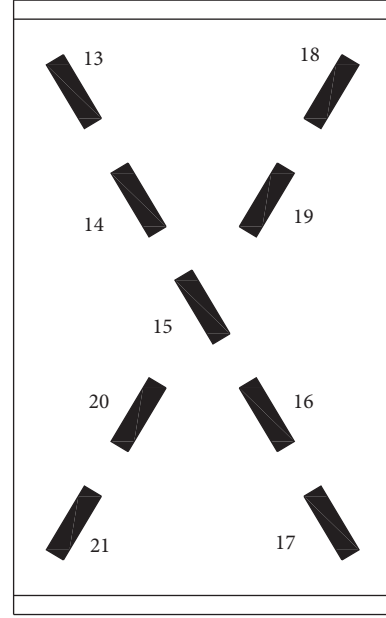


FIGURE 17: Strain gauges in the joint area.

The average deformation in a diagonal direction is as follows:

$$\bar{X} = \frac{|\Delta_1 + \Delta_2| + |\Delta_3 + \Delta_4|}{2}. \quad (7)$$

Because  $\sin \theta = b/\sqrt{a^2 + b^2}$ ,  $\cos \theta = a/\sqrt{a^2 + b^2}$ ,  $\alpha_1 = \bar{X} \sin \theta/a$ , and  $\alpha_2 = \bar{X} \cos \theta/b$ . The shear angle is

$$\gamma = \alpha_1 + \alpha_2 = \frac{\sqrt{a^2 + b^2}}{ab} \bar{X}. \quad (8)$$

It can be seen from Table 6 that when the horizontal displacement of the top of the column reaches 180 mm, the maximum shear angle deformation of the specimen SH-1 is 9.85% of the relative ultimate angle of the beam-column. When the horizontal displacement of the top of the column reaches 80 mm and the specimen is adjacent to the failure, the maximum shear angle deformation of the specimen SH-2 is only 5.58% of the relative ultimate angle of the beam-column. It can be seen that the shear strength and stiffness of the joint region of this kind of joint specimen are very large, which meets the requirements of “strong joints and weak members” of the structure, and the shear deformation of the joint region has a negligible effect on the deformation of the structure.

## 4. Preliminary Design Recommendation

**4.1. Structural Design Recommendation.** It can be seen from Section 3 that the new joint proposed in this paper has excellent seismic performance. Therefore, on the basis of meeting the requirements of seismic and bearing capacity, it is necessary to strive for simple structure and convenient construction. Combined with some current codes and research results, the following structural design suggestions are put forward for this kind of joint:

TABLE 5: Strain standard data of joint area.

Specimen	Steel strain gauge number and strain measurement value ( $\mu\epsilon$ )										
	13	14	15	16	17	Average	18	19	20	21	Average
SH-1	-2658	Invalid	-421	Invalid	-41	-1040	Invalid	Invalid	320	489	405
SH-2	-326	-573	-308	-100	-1164	-494	51	757	1045	Invalid	618

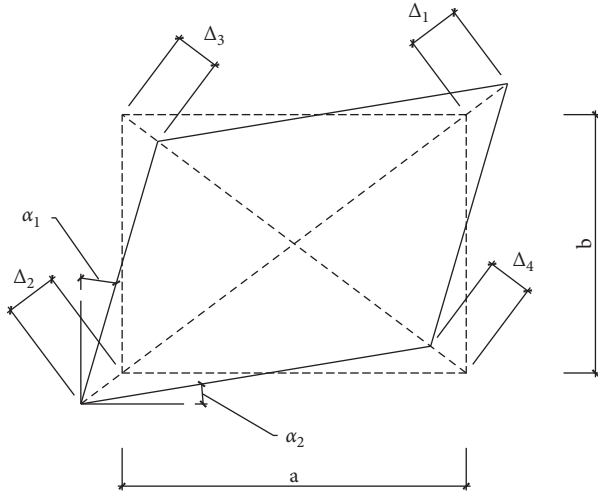


FIGURE 18: Geometric relationship of shear deformation.

TABLE 6: Shear deformation in the joint area.

Specimen	$\bar{X}$ (mm)	$\gamma$	$\theta$	$\gamma/\theta$
SH-1	0.2319	1.724°	17.5°	0.0985
SH-2	0.1785	1.327°	23.8°	0.0558

- (1) In order to ensure that the circular steel tube does not bear the longitudinal load, the circular steel tube is disconnected in the joint area, and a 15 mm ring opening is reserved from the upper and lower edges of the concrete ring beam. At the same time, a reinforcing steel ring can be welded at the end of the steel pipe to prevent the tearing of the steel pipe weld caused by concrete expansion. The thickness of the reinforcing ring shall not be less than the wall

thickness of the steel pipe, and the height shall not be less than 6 times the thickness of the steel pipe.

- (2) When the shear bearing capacity of the core area of the joint is insufficient, the steel plate can be used to reinforce the section steel web in the column in the joint area. The thickness and reinforcement range of the steel plate shall be implemented according to the relevant provisions in [30].
- (3) In order to ensure the overall mechanical properties of the column, a certain number of shear studs shall be set on the section steel flange in the column outside the reinforcement skeleton in the joint area, and the specification and spacing of shear studs shall be implemented according to the relevant provisions in [31, 32].
- (4) In order to avoid holes in the corner of the horizontal stiffener in the node area when pouring concrete, it is necessary to set an exhaust hole in this part, and the opening form shall be implemented according to the relevant provisions in [33].
- (5) In the design of the joint, the number of main reinforcements in the column passing through the flange of the steel beam shall be minimized. When it is inevitable, appropriate reinforcement measures shall be taken. At the same time, when the column stirrup through hole is reserved on the web of the steel beam, the section loss rate of the web shall not exceed 25% [34].

4.2. Calculation Formula of Shear Capacity. Based on the experimental study of seismic performance of joints, the calculation formula of shear capacity of such joints is proposed [35]:

$$V = V_f + V_h + V_{sv} + V_{hl} + V_{lf}$$

$$= 0.96\phi_j\eta_j f_t (D_{hl} - D_z) [b_0 + 0.5(D_{hl} + D_z)] + (0.037n_0 + 0.172)f_c b_j h_j + f_{yv} A_{sv} \frac{h_0 - a}{s} + 0.58(t_w h_w f_y + t_{lw} h_{lw} f_{lw}), \quad (9)$$

where  $V_f$  is the shear capacity of the section steel web in the column,  $V_h$  is the shear capacity of the column concrete in the core area of the joint,  $V_{sv}$  is the shear capacity of the stirrup in the

joint area,  $V_{HL}$  is the shear capacity of the concrete ring beam, and  $V_{LF}$  is the shear capacity of the web of the cantilever short steel beam and the meaning of other symbols can be seen in [35].



It can be seen from the formula that the shear capacity of such joints consists of five parts. Compared with the results of the test and finite element numerical analysis [35], the formula is reasonable, which can provide a basis for the engineering design of such joints.

## 5. Conclusion

A new type joint of CTSRC column is designed. Through the pseudostatic test, the mechanical properties of this kind of new joints under earthquake action are investigated.

The main conclusions include the following:

- (1) The failure modes of the two specimens are basically the same, and the existence of the concrete ring beam effectively protects the core area of the joint, which makes the failure move outward.
- (2) The results show that the load-displacement hysteretic curves of the two specimens are very full, and the energy dissipation performance is excellent. The displacement ductility coefficient, interlayer deformation angle, and ductility coefficient of the two specimens are far greater than those of the traditional joints.
- (3) The results show that the ultimate equivalent viscous damping coefficients ( $h_e$ ) of specimens are much larger than those of traditional joints. The specimens show strong resistance to strength degradation and stiffness degradation. The shear deformation in the joint area is very small and the stiffness is very large.
- (4) The preliminary design recommendation is put forward, which can provide a basis for the engineering design of this new type of joint.

## Data Availability

The data used to support the findings of this study are available from the corresponding author upon request.

## Conflicts of Interest

The authors declare that there are no conflicts of interest with respect to the research, authorship, and/or publication of this paper.

## Acknowledgments

This research was supported by the National Natural Science Foundation of China (no. 51408052), the Youth Science and Technology Star Project of Shaanxi Province (no. 2016KJXX-51), Key Research and Development Plan of Shaanxi Province (no. 2018SF-354), and the Special Fund for Basic Scientific Research in Central Universities of Chang'an University (no. 300102289205).

## References

- [1] A. H. Varma, J. M. Ricles, R. Sause, and L.-W. Lu, "Seismic behavior and design of high-strength square concrete-filled steel tube beam columns," *Journal of Structural Engineering*, vol. 130, no. 2, pp. 169–179, 2004.
- [2] A. Varma, J. Ricles, R. Sause, and L. Lu, "Seismic behavior of high-strength square CFT beam- columns," in *Proceeding of 6th ASCCS Conference Los Angeles.confer.On Composit and Hybrid Structures*, vol. 1, pp. 547–556, Los Angeles, Ca, USA, March 2002.
- [3] A. Elremaily and A. Azizinamini, "Behavior and strength of circular concrete-filled tubu columns," *Journal of Constructional Steel Research*, vol. 58, no. 12, pp. 1567–1591, 2002.
- [4] N. E. Shanmugam and B. Lakshmi, "State of the art report on steel-concrete composite columns," *Journal of Constructional Steel Research*, vol. 57, no. 10, pp. 1041–1080, 2001.
- [5] X. Zhou, J. Liu, and S. Zhang, "Experimental study on seismic behavior of square steel tube confined steel reinforced concrete short columns," *Journal of Building Structures*, vol. 31, no. 7, pp. 49–55, 2010.
- [6] J. Liu, X. Zhang, and S. Zhang, "Axial compression behavior of circular steel tube confined steel reinforced high strength concrete short columns," *Journal of Building Structures*, vol. 30, pp. 242–248, 2009.
- [7] X. Zhou and J. Liu, "Seismic behavior and strength of tubed steel reinforced- concrete(SRC) short columns," *Journal of Constructional Steel Research*, vol. 66, no. 1, pp. 28–36, 2010.
- [8] T. Yamamoto, J. Kawaguchi, and S. Morino, "Experimental study of scale effects on the compressive behavior of short concrete-filled steel tube Columns," in *Proceedings of the Composite Construction in Steel and Concrete IV Proceedings of the Fourth International Conference on Composite Construction in Steel and Concrete*, pp. 879–890, Slovakia, June 1994.
- [9] A. Fam, F. Qie, and S. Rizkalla, "Concrete-filled steel tubes subjected to axial compression and later alcylic loads," *Journal of Struetural Engineering*, vol. 130, no. 4, pp. 631–640, 2004.
- [10] Q. Chen, J. Cai, and Y. Lin, "New concrete filled steel tubular(CFST) column-beam joint with discontinuous column tube(I)-Behavior at joint zone strengthened by horizontal mesh reinforcement under axial loading," *Journal of South China University of Technology*, vol. 30, no. 9, pp. 91–95, 2002.
- [11] Q. Chen, J. Cai, Y. Lin, J. Liang, and Z. Tang, "New concrete filled steel tubular(CFST) column-beam joint with discontinuous column tube(II)-Behavior at joint zone strengthened by reinforcing ring bars under axial loading," *Journal of South China University of Technology*, vol. 30, no. 12, pp. 58–61, 2002.
- [12] J. Liang, J. Cai, D. Yao, and Q. Chen, "Experimental research on a new type of concrete filled steel tubular column-beam joint:column tube discontinued in the joint zone," *Journal of South China University of Technology*, vol. 30, no. 10, pp. 79–83, 2002.
- [13] J. Nie, Y. Bai, and C. Cai, "New connection system for confined concrete columns and beams I: experimental study," *Journal of Structural Engineering*, vol. 134, no. 12, pp. 1787–1799, 2008.
- [14] Y. Bai, J. Nie, and C. Cai, "New connection system for confined concrete columns and beams. II: theoretical modeling," *Journal of Structural Engineering*, vol. 134, no. 12, pp. 1787–1799, 2008.
- [15] L. Han, H. Qu, Z. Tao, and Z. Wang, "Experimental behaviour of thin-walled steel tube confined concrete column to RC beam joints under cyclic loading," *Thin-Walled Structures*, vol. 47, no. 8-9, pp. 847–857, 2009.

- [16] Y. F. Zhang, J. H. Zhao, and C. S. Cai, "Seismic behavior of ring beam joints between concrete-filled twin steel tubes columns and reinforced concrete beams," *Engineering Structures*, vol. 39, pp. 1–10, 2012.
- [17] D. Gan, X. Zhou, B. Yan, F. Han, and J. Liu, "Experimental study on mechanical behavior of circular steel tube confined RC columns with ring stiffened joints," *Journal of Building Structures*, vol. 39, no. 4, pp. 91–101, 2018.
- [18] D. Gan, X. Zhou, J. Liu, and B. Yan, "Calculation of shear capacity of steel tube confined reinforced concrete columns," *Journal of Building structure*, vol. 39, no. 9, pp. 96–103 +111, 2018.
- [19] W. Duan, J. Cai, X.-L. Tang, Q.-J. Chen, C. Yang, and A. He, "Axial compressive behaviour of square through-beam joints between CFST columns and RC beams with multi-layers of steel meshes," *Materials*, vol. 13, no. 11, p. 2482, 2020.
- [20] Y. Lin, K. Liu, T. Xiao, C. Zhou, and F. Lusquiños, "Shear bearing capacity of framework joints of steel-reinforced concrete-filled circular steel tube," *Advances in Materials Science and Engineering*, vol. 2020, Article ID 7324865, 15 pages, 2020.
- [21] F. Yu, Y. C. Guan, Q. Q. Liu, S. L. Wang, and Y. Fang, "Compressive behavior of joint core confined with core steel tube for connection of polyvinyl chloride-carbon fiber reinforced polymer –confined concrete column and reinforced concrete beam," *Advances in Structural Engineering*, vol. 23, no. 12, pp. 2570–2586, 2020.
- [22] F. Yu, S. Bu, D. Li, C. Feng, and Y. Fang, "Experimental investigation and theoretical study on bearing capacity of strong PVC-FRP confined concrete column-weak joint strengthened with core steel tube under axial loading," *Construction and Building Materials*, vol. 271, Article ID 121880, 2021.
- [23] F. Yu, C. Feng, D. Li, and Y. Fang, "Finite element analysis on weak PVC-frp confined concrete column and strong joint strengthened with core CFST under axial compression," *Iranian Journal of Science and Technology, Transactions of Civil Engineering*, vol. 51, 2020.
- [24] S. Peng, Z. Xiong, C. Xu, J. Fei, and X. Chen, "Research on shear strength of CFSST column and H-section with beam composite joint of unequal depth," *Journal of Constructional Steel Research*, vol. 180, Article ID 106575, 2021.
- [25] China Construction Industry Press, *Code For Seismic Test Methods of Buildings*, China Construction Industry Press, Beijing, China, 2015.
- [26] T. Zhou, *Study on Seismic Behavior and Load-Carrying Capacity of Concrete-filled Square Tubular Column to Steel Beam Connection*, Xi'an University of architecture and technology, Xi'an, China, 2004.
- [27] C. Fang, Y. Ping, and Y. Chen, "Loading protocols for experimental seismic qualification of members in conventional and emerging steel frames," *Earthquake Engineering and Structural Dynamics*, vol. 49, no. 2, pp. 155–174, 2020.
- [28] J. Fan, M. Tao, J. Nie, T. Li, and N. Zhao, "Experimental study on seismic behavior of steel reinforced concrete column steel truss composite joints," *Journal of Building Structures*, vol. 31, no. 2, pp. 1–10, 2010.
- [29] J. Yuan, *Analysis of Testing Method and Boundary Condition of Beam-To-Column Joint Behaviour in Frame*, Shantou University, Shantou, China, 2004.
- [30] China Construction Industry Press, *Code For Design of Steel Structures*, China Construction Industry Press, Beijing, China, 2017.
- [31] Standards Press of China, *Cheese Head Studs for Arc Stud Welding*, Standards Press of China, Beijing, China, 2002.
- [32] China Construction Industry Press, *Technical Specification for Steel Structure of Tall Buildings*, China Construction Industry Press, Beijing, China, 2015.
- [33] China Construction Industry Press, *Code For Design of Composite Structures*, China Construction Industry Press, Beijing, China, 2016.
- [34] China communication press, *Beam To Column Frame Connections of Tall Building Composite Structures Analysis And Design*, China communication press, Beijing, China, 2006.
- [35] Y. Dai, S. Nie, and T. Zhou, "Shear capacity of circular steel tube confined H-SRC concrete column steel beam joint with ring beam," *Journal of Jilin University (Engineering and Technology Edition)*, vol. 51, no. 3, pp. 977–988, 2021.

## Research Article

# Restoring Force Model Research on Joint of Circular Tubed Steel-Reinforced Concrete Column

Yan Dai <sup>1</sup>, Shaofeng Nie,<sup>2</sup> Tianhua Zhou,<sup>2</sup> Yichun Xu,<sup>3</sup> and Jingrong Peng<sup>1</sup>

<sup>1</sup>Shaanxi Key Laboratory of Safety and Durability of Concrete Structures, Xijing University, Xi'an 710123, China

<sup>2</sup>School of Civil Engineering, Chang'an University, Xi'an 710061, China

<sup>3</sup>Ping an Construction Group Co., Ltd, Hangzhou 310000, China

Correspondence should be addressed to Yan Dai; daiyan@xijing.edu.cn

Received 29 July 2021; Accepted 28 August 2021; Published 17 September 2021

Academic Editor: Jingxuan Wang

Copyright © 2021 Yan Dai et al. This is an open access article distributed under the Creative Commons Attribution License, which permits unrestricted use, distribution, and reproduction in any medium, provided the original work is properly cited.

In this paper, two joints of circular tubed steel-reinforced concrete (CTSRC) column were designed. The load-displacement hysteretic curve and skeleton curve of this new type of joint are obtained by the pseudostatic test under low cycle cyclic load on the top of the column. The results show that this new type of joint has good seismic energy dissipation performance. On the basis of the test, a three-fold skeleton curve model considering three characteristic points of yield, limit, and failure is proposed, and the expression of skeleton curve model is given. The load and unload stiffness degradation law of specimens under reciprocating load is studied, and the expression of stiffness degradation law is given. The hysteresis law of the new type joint specimens is described in detail. The validity of the model is verified by comparing the experimental curve with the model curve. The model can be used in the elastic-plastic seismic time-history analysis on the joint of circular tubed steel-reinforced concrete (CTSRC) column.

## 1. Introduction

The restoring force model is used to explain the relationship between the load and displacement of the structure under repeated load, which can reflect the ability of the structure to recover the original deformation after unloading. In the study of the seismic performance of the structure, the restoring force model is the basis of the seismic stress analysis, which mainly reflects the performance of the structure, such as energy consumption, ductility, strength, and stiffness. Since 1940s, seismic engineering has carried out extensive research on structural restoring force curve modeling. Researchers have proposed the following models: the Ramberg–Osgood model [1, 2] proposed by Jennings is shown in Figure 1(a). The model is mainly used to describe the restoring force characteristics of metal materials and also used in soil and reinforced concrete flexural structures; as shown in Figure 1(b), Clough [3] proposed a relatively early model considering the degradation of loading and unloading stiffness, which is mainly proposed as the restoring force characteristic model of reinforced concrete flexural members. Takeda et al. [4] proposed a three-fold line stiffness degradation

model, as shown in Figure 1(c). The model is obtained through the low cycle reciprocating loading test of reinforced concrete columns and based on the test results. Because it has one more crack point than the two-fold line model, it can more truly reflect the mechanical characteristics of steel reinforced concrete structures.

In recent years, a series of research studies have been carried out on the load displacement relationship models of various new structures under repeated loads. Yan et al. established the hysteretic model of the joints between steel reinforced ultrahigh strength concrete columns and steel reinforced concrete beams and put forward the quantitative method of seismic damage and attenuation coefficient [5]. Zhang and Han proposed a prediction model for cyclic lateral load deformation response of RC columns subjected to axial compression and cyclic shear; comparison between the predicted cyclic response and experimental results indicates that the proposed model can predict the observed hysteretic response of flexure-shear critical RC columns well [6]. Yuka and Hideki proposed a hysteretic model of H-beam considering

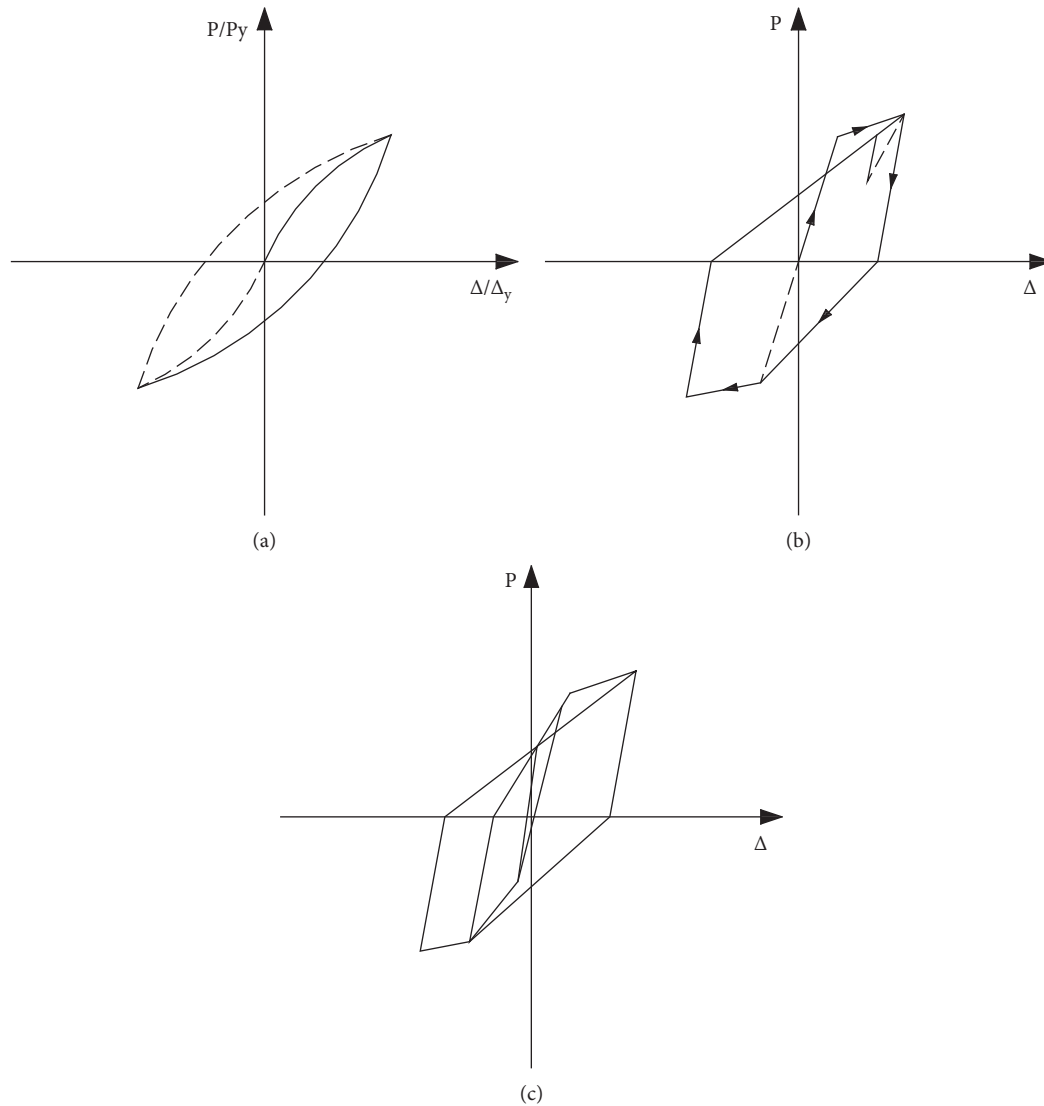


FIGURE 1: Common restoring force models. (a) Ramberg–Osgood model. (b) Clough degenerate bilinear model. (c) Takeda three-fold line stiffness degradation model.

slenderness ratio and also proposed a hysteretic model suitable for uniform moment and antisymmetric moment [7]. Zhang et al. studied the hysteretic behavior of six glass bead insulation concrete frame columns (GIC columns) and one ordinary concrete frame column; the results can provide theoretical basis for elastic-plastic analysis of GIC column under earthquake action [8]. Hao et al. proposed an effective method to calculate the monotone curve and hysteretic curve of H-beam under bending moment. The accuracy of predicting the hysteretic behavior of H-beam is verified by comparing with the numerical results [9]. Wang et al. carried out nonlinear time-history analysis on a new type of energy dissipation joint of bamboo steel hybrid frame and proposed the joint restoring force model with the best performance [10]. Li et al. proposed an innovative method to consider the influence of dynamic effects and degradation on seismic performance analysis of

reinforced concrete frame structures [11]. Xie et al. carried out quasistatic tests on three 1/10 scale pier specimens and established the hysteretic model of prefabricated pier, which was in good agreement with the test results [12]. Wu et al. studied the restoring force model of h-steel-reinforced concrete column composite joints (hereinafter referred to as MPSC joints), which has high accuracy and can be used for the design of MPSC joints [13]. Song et al. designed ten PVC-CFRP confined concrete column-ring beam interior joints (PCCC-RBIJs) and one PVC confined concrete column-ring beam interior joint (control interior joint) and studied their restoring force models [14]. Ni et al. conducted in-depth experimental research on the seismic performance of high-strength reinforced concrete shear walls and proposed a restoring force model of high-strength reinforced concrete shear walls composed of skeleton curves and a group of empirical hysteretic laws [15].

The CTSRC column is a new type of composite structure. The relative research [16–18] shows that it has high compressive and shear capacity and superior seismic performance and can make full use of the performance of high-strength materials. On this basis, the authors put forward a new type joint of CTSRC column [19–21]. By applying low-cycle reciprocating load on the top of the column, the load displacement relationship under reciprocating load is studied.

There are mainly two methods to analyze and study the restoring force model: one is based on the basic research of the steel bar, steel tube, and concrete and the bond relationship between steel bar and concrete, steel tube and concrete, to obtain the idealized material constitutive model and structural strain model and to obtain the hysteretic curve of the restoring force relationship by the iterative method; the second is to simulate the test results directly [22, 23]. In this paper, the second method is used to study the restoring force characteristics of the new type joint based on the quasistatic test and the measured hysteretic curves. The restoring force model suitable for the new type joint is established, which provides the basis for the future elastic-plastic time-history analysis of structures.

## 2. Test Preparation and Results

**2.1. Specimen Design and Loading Scheme.** In this paper, two full-scale joints in frame structure were designed. The specimen numbers are SH-1 and SH-2. The main differences between the two specimens are the reinforcement ratio of ring beam and the form of ring beam. The specimen numbers and parameters are shown in Table 1.

The height and width of the two specimens are 4375.0 mm and 3370.0 mm, respectively. The outer diameter of circular steel tube is 400.0 mm. In order to ensure that the circular steel tube does not bear the longitudinal load, the circular steel tube was disconnected in the joint area and a 15.0 mm ring opening is reserved from the upper and lower edges of the concrete ring beam. The other structures and dimensions are shown in Figure 2 (taking SH-1 specimen as an example).

The quasistatic test is generally divided into column end loading and beam end loading. Because the second-order effect of gravity can be considered in the column end loading [24], the column-end-loading mode was adopted in this paper: First, the vertical load is gradually applied to 1500 kN by the jack at the top of the column in three stages and the load lasts for several minutes; second, the MTS servoactuator is used to apply the low-cycle reciprocating load on the top of the column, and the load control is used before yielding. After yielding, the load is carried out according to the multiple of the yield displacement of the top of the column, and each cycle is carried out three times until the specimen is damaged or the horizontal load of the top of the column drops below 85% of its peak load. The test device diagram and loading diagram are shown in Figure 3.

**2.2. Test Result.** The load-displacement hysteretic curves of the two specimens are shown in Figure 4. It can be seen from the figure that the hysteretic curves of the two specimens are full, showing a very good seismic energy dissipation performance.

## 3. Establishment of the Restoring Force Model

The restoring force model for nonlinear analysis consists of three parts: skeleton curve, stiffness degradation law, and hysteretic characteristics. The results show that a reasonable restoring force model can reflect the hysteretic stress characteristics of actual structure or component and be simple and practical within the acceptable limit, so as to facilitate the effective elastic-plastic response analysis.

**3.1. Skeleton Curve Model.** The skeleton curve determines the characteristic points of the restoring force model, which is the connecting line of the characteristic points in the 1/4 hysteretic curve. In this test, the characteristic point loads and displacements of the two joint specimens are different. In order to facilitate the comparison, the skeleton curves of the two specimens are first treated as dimensionless. The formula is as follows:

$$\frac{\pm P}{|\pm P_{\max}|}, \quad \frac{\pm \Delta}{|\pm \Delta_{\max}|} \quad (1)$$

where  $\pm \Delta P_{\max}$  is the maximum positive and reverse load on the top of the column and  $\pm \Delta_{\max}$  is the displacement corresponding to the maximum positive and reverse load. The results are shown in Table 2, and the dimensionless skeleton curves of specimens are obtained, as shown in Figure 5.

It can be seen from the above figure that the skeleton curves of the two specimens after dimensionless treatment still show their own regular characteristics. By analyzing the hysteretic curves and dimensionless skeleton curves of specimens, it can be seen that the skeleton curves of the two specimens can be approximately fitted with a broken line. Therefore, the skeleton curve in this paper adopts the form of three broken lines considering yield load, ultimate load, and stiffness degradation and is simulated by the connecting line of three characteristic points. The three characteristic points are yield point, ultimate load point, and failure point (when the bearing capacity decreases to 0.85 times of the ultimate load point).

According to the dimensionless values of the characteristic points of the specimens in Table 2, the coordinates of the characteristic points corresponding to the specimens SH-1 and SH-2 are given as follows:  $(-\Delta_u/|\Delta_{\max}|, -P_u/|-P_{\max}|)$ ,  $(1, 1)$ ,  $(-\Delta_y/|\Delta_{\max}|, -P_y/|-P_{\max}|)$ ,  $(0, 0)$ ,  $(+\Delta_y/+\Delta_{\max}, +P_y/+P_{\max})$ ,  $(1, 1)$ , and  $(+\Delta_u/+\Delta_{\max}, +P_u/+P_{\max})$ .

Taking these coordinate points as the control points of regression analysis and connecting the characteristic points, the three-fold line skeleton curve model of two specimens can be drawn, as shown in Figure 6.

TABLE 1: Test piece number and parameter table.

Specimen number	Steel ratio (%)	Thickness of circular tube steel pipe (mm)	Form of ring beam	Reinforcement ratio of ring beam (%)
SH-1	4.19	5.0	Octagon	3.55
SH-2	4.19	5.0	Circular	2.05

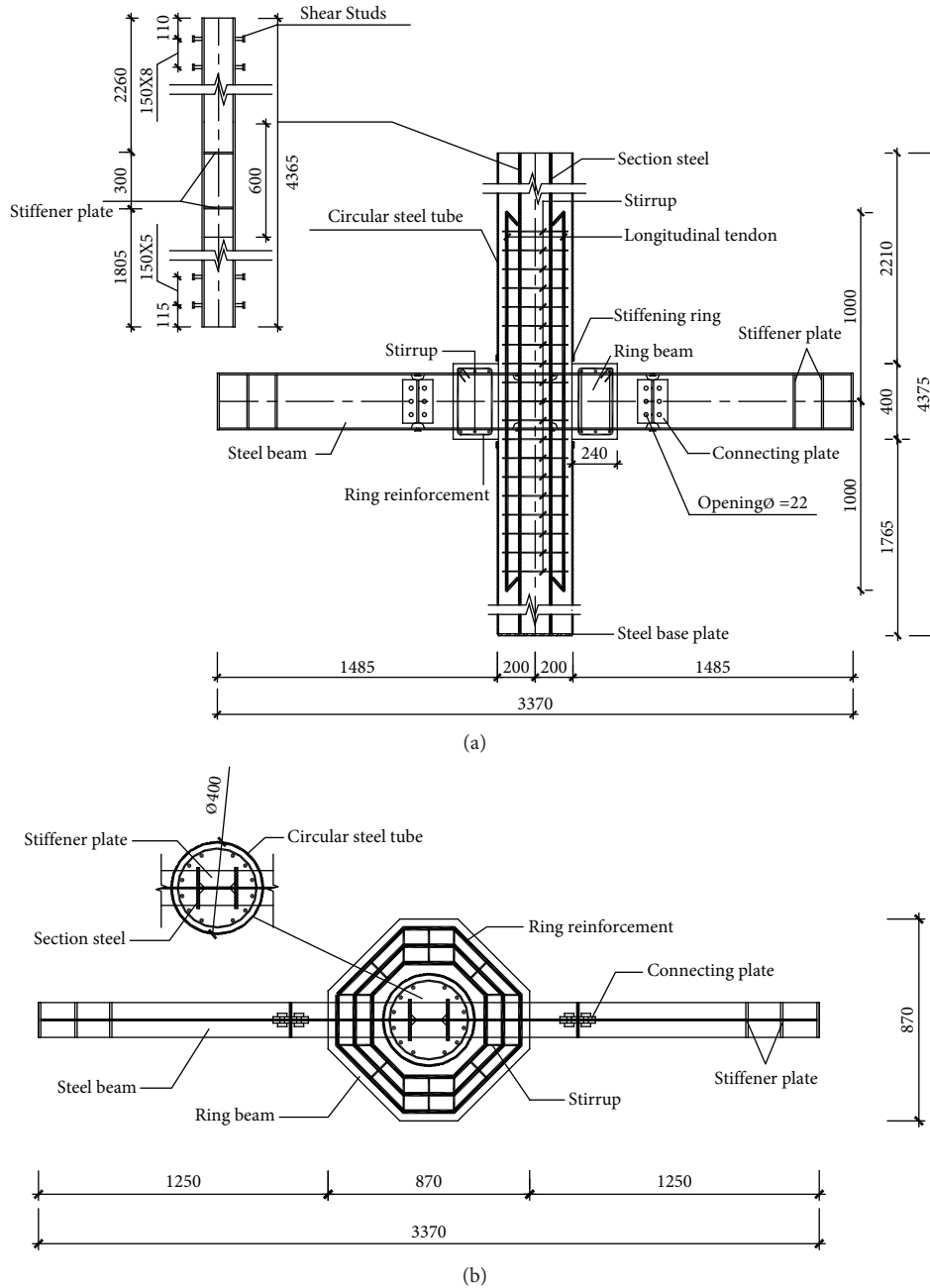


FIGURE 2: Structural diagram of the specimen (mm). (a) Elevation. (b) Plan.

In Figure 6, the control points A and A' are the positive and reverse yield points, B and B' are the positive and reverse ultimate load points, and C and C' are the positive and reverse failure points. According to the control points on the skeleton curve, the three-fold line skeleton curve expression of the two specimens can be obtained, as shown in Table 3.

3.2. *Stiffness Degradation Law.* According to the hysteretic curve and skeleton curve, the loading and unloading stiffness of the specimen has a certain degree of degradation. The following is the degradation law of loading and unloading stiffness of the specimen under repeated loading [25]. As shown in Figure 7, K1 is the positive unloading stiffness, K2



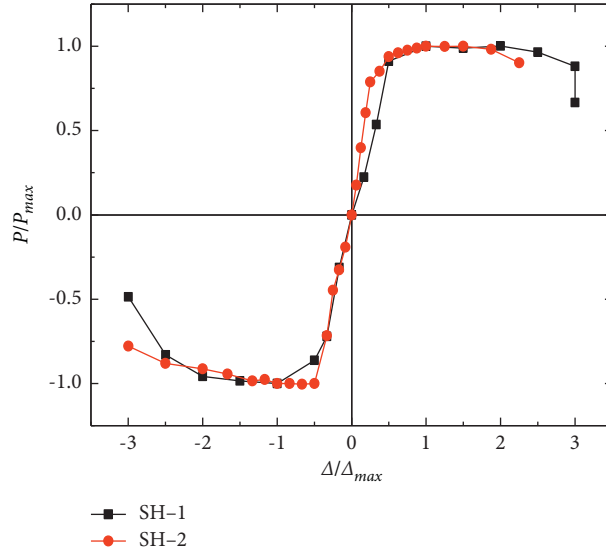


FIGURE 5: Dimensionless skeleton curves of specimens.

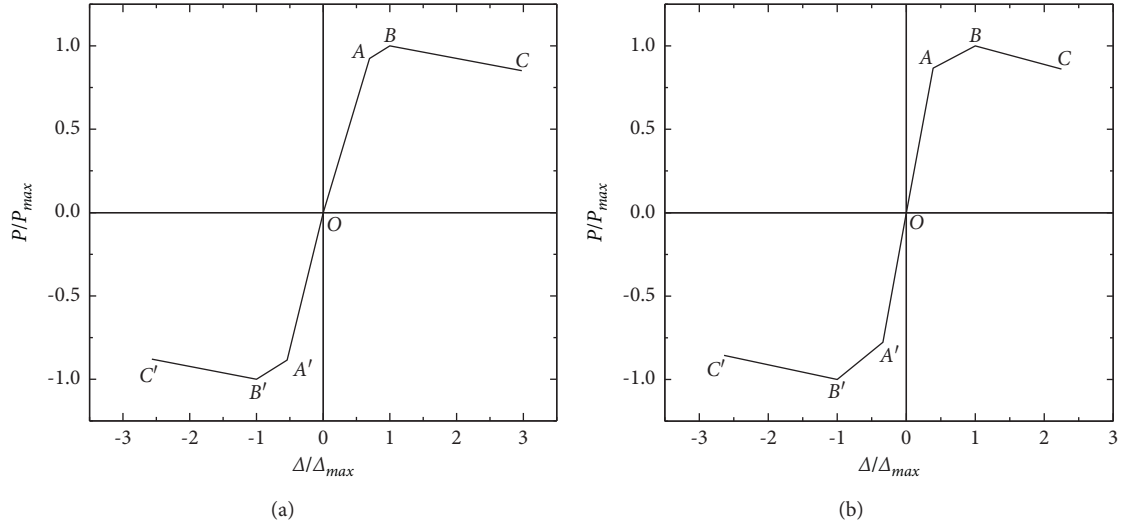


FIGURE 6: Curve model of three-fold line skeleton of test piece. (a) SH-1. (b) SH-2.

TABLE 3: Three-fold line skeleton curve expression.

Line segment	SH-1	SH-2
OA	$P/+P_{\max} = 1.3329(\Delta/+\Delta_{\max})$	$P/+P_{\max} = 2.2174(\Delta/+\Delta_{\max})$
AB	$P/+P_{\max} = 0.2451(\Delta/+\Delta_{\max}) + 0.7549$	$P/+P_{\max} = 0.2184(\Delta/+\Delta_{\max}) + 0.7816$
BC	$P/+P_{\max} = -0.0754(\Delta/+\Delta_{\max}) + 1.0754$	$P/+P_{\max} = -0.1112(\Delta/+\Delta_{\max}) + 1.1112$
OA'	$P/ -P_{\max}  = 1.6419(\Delta/ \Delta_{\max} )$	$P/ -P_{\max}  = 2.2988(\Delta/ \Delta_{\max} )$
A'B'	$P/ -P_{\max}  = 0.2495(\Delta/ \Delta_{\max} ) - 0.7505$	$P/ -P_{\max}  = 0.3369(\Delta/ \Delta_{\max} ) - 0.6631$
B'C'	$P/ -P_{\max}  = -0.0772(\Delta/ \Delta_{\max} ) - 1.0772$	$P/ -P_{\max}  = -0.0893(\Delta/ \Delta_{\max} ) - 1.0893$

is the reverse loading stiffness,  $K_3$  is the reverse unloading stiffness,  $K_4$  is the positive loading stiffness,  $a$  is the positive unloading point,  $b$  is the reverse loading point,  $c$  is the reverse unloading point,  $d$  is the positive loading point,  $\Delta_1$  is the displacement corresponding to the positive unloading point  $a$ ,  $\Delta_2$  is the residual deformation when positive unloading to zero,  $\Delta_3$  is the displacement corresponding to

the reverse unloading point  $c$ , and  $\Delta_4$  is the residual deformation when reverse unloading to zero, and the meanings of other symbols are the same as above.

**3.2.1. Degradation Law of Specimen Stiffness under Positive Unloading ( $K_1$ ).** As shown in Figure 7, the slope of line  $ab$  is the positive unloading stiffness  $K_1$ . By sorting out the



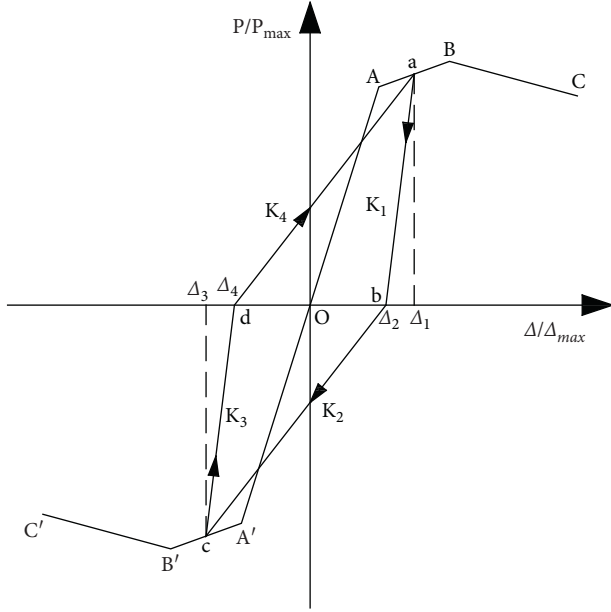


FIGURE 7: Stiffness degradation law.

hysteretic curve data of two specimens, the slope value of line  $ab$  under different displacement amplitudes of each specimen can be obtained, and it can be dimensionless. The abscissa is  $\Delta_1/\Delta_{\max+}$ , and the ordinate is  $K_1/K_{0+}$ . The scatter diagram of the degradation law of positive unloading stiffness ( $K_1$ ) of each specimen can be obtained, where  $\Delta_{\max+}$  represents the displacement corresponding to the peak point when the joint specimen is under positive loading.  $K_{0+}$  represents the initial elastic stiffness of the joint under positive loading. After removing the obvious singular points, using the method of nonlinear data fitting, the degradation law curve and its regression formulas of the positive unloading stiffness  $K_1$  of each specimen can be obtained, as shown in Figure 8 and equations (2) and (3).

The regression formulas of  $K_1$  are as follows:

$$\frac{K_1}{K_0^+} = 1.221e^{(0.20164/(\Delta_1/\Delta_{\max}^+)+0.16819)}, \quad (2)$$

$$\frac{K_1}{K_0^+} = 1.11917e^{-((\Delta_1/\Delta_{\max}^+)/0.31645)} + 1.23644. \quad (3)$$

**3.2.2. Degradation Law of Specimen Stiffness under Reverse Loading ( $K_2$ ).** As shown in Figure 7, the slope of line  $bc$  is the reverse loading stiffness  $K_2$ . Using the same method as in Section 3.2.1, the degradation law curve and its regression formulas of the reverse loading stiffness  $K_2$  of each specimen can be obtained, as shown in Figure 9 and equations (4) and (5).

The regression formulas of  $K_2$  are as follows:

$$\frac{K_2}{K_0} = e^{-1.4838(\Delta_2/\Delta_{\max}^+)}, \quad (4)$$

$$\frac{K_2}{K_0} = e^{0.10061-2.83541(\Delta_2/\Delta_{\max}^+)+0.8073(\Delta_2/\Delta_{\max}^+)^2}. \quad (5)$$

**3.2.3. Degradation Law of Specimen Stiffness under Reverse Unloading ( $K_3$ ).** As shown in Figure 7, the slope of line  $cd$  is the reverse unloading stiffness  $K_3$ . Using the same method as in Section 3.2.1, the degradation law curve and its regression formulas of the reverse unloading stiffness  $K_3$  of each specimen can be obtained, as shown in Figure 10 and equations (6) and (7).

The regression formulas of  $K_3$  are as follows:

$$\frac{K_3}{K_0} = e^{0.57368-0.32551(\Delta_3/\Delta_{\max}^-)+0.07056(\Delta_3/\Delta_{\max}^-)^2}, \quad (6)$$

$$\frac{K_3}{K_0} = e^{0.61056-0.49113(\Delta_3/\Delta_{\max}^-)+0.14038(\Delta_3/\Delta_{\max}^-)^2}. \quad (7)$$

**3.2.4. Degradation Law of Specimen Stiffness under Positive Loading ( $K_4$ ).** As shown in Figure 7, the slope of line  $da$  is the positive loading stiffness  $K_4$ . Using the same method as in Section 3.2.1, the degradation law curve and its regression formulas of the positive loading stiffness  $K_4$  of each specimen can be obtained, as shown in Figure 11 and equations (8) and (9).

The regression formulas of  $K_4$  are as follows:

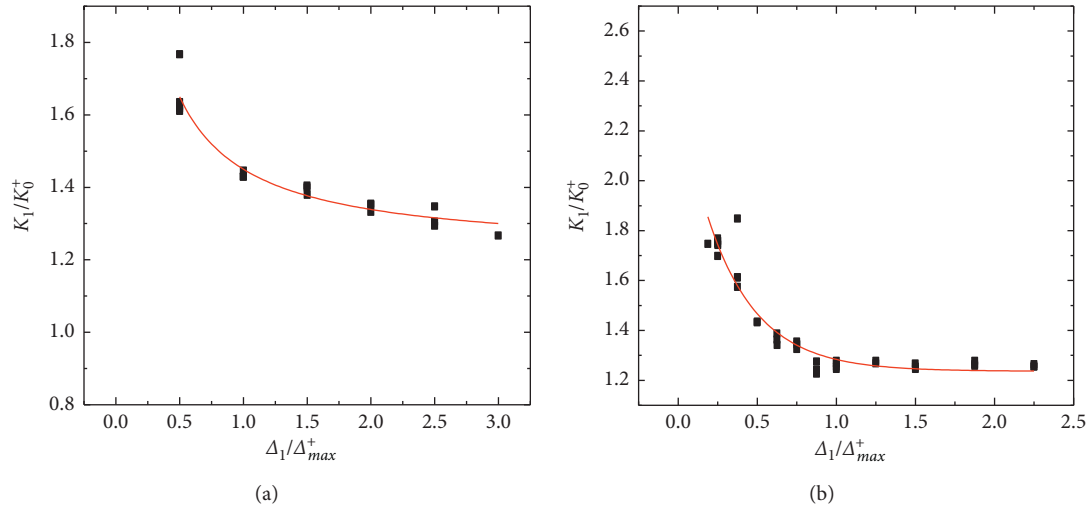
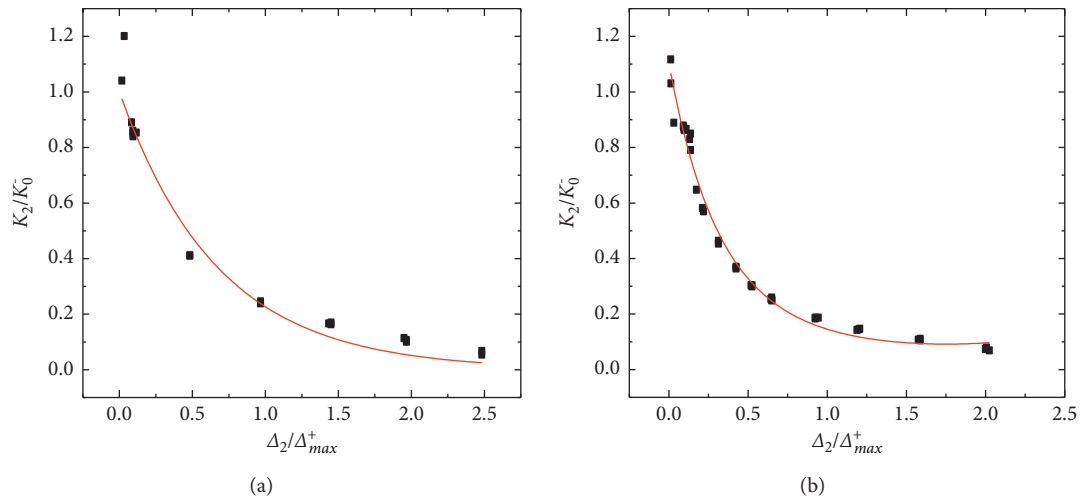
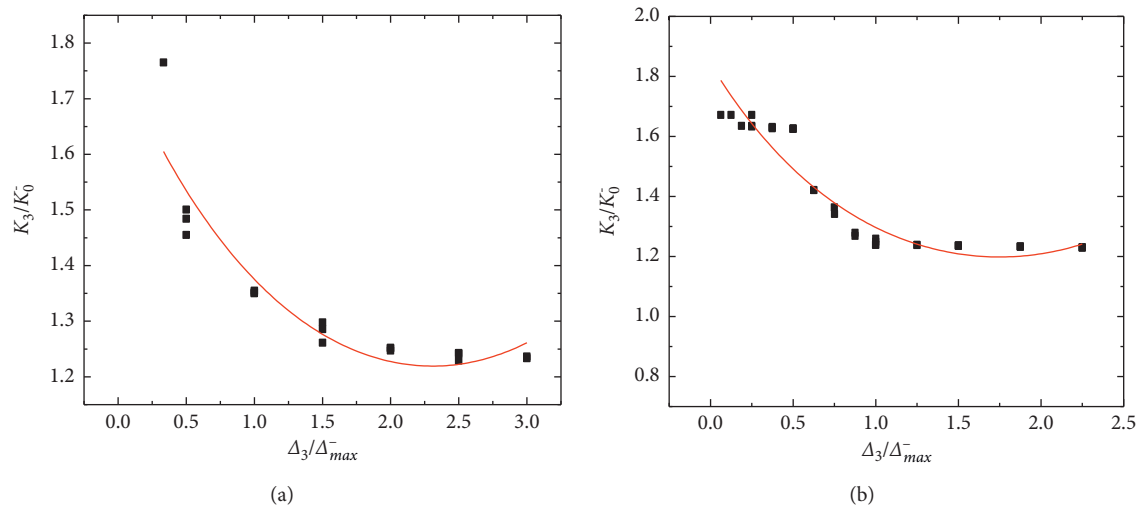
$$\frac{K_4}{K_0^+} = e^{0.30267-1.95449(\Delta_4/\Delta_{\max}^-)+0.40772(\Delta_4/\Delta_{\max}^-)^2}, \quad (8)$$

$$\frac{K_4}{K_0^+} = e^{0.28584-1.57987(\Delta_4/\Delta_{\max}^-)+0.03819(\Delta_4/\Delta_{\max}^-)^2}. \quad (9)$$

**3.3. Description of Hysteresis Rule.** The actual restoring force curve on the joint of CTSRC column is hard to describe, so it is necessary to establish a simplified model which can reflect the actual restoring force characteristics. According to the skeleton curve model and stiffness degradation law, combined with the hysteretic curve, the restoring force model of the specimens was established, as shown in Figure 12.

The hysteresis rule is described as follows:

- (1) When the specimen is under positive loading, the relationship between load and displacement develops along the skeleton curve  $OABC$ . If the specimen is unloading in the  $OA$  section (the positive loading does not yield), the positive loading stiffness does not degenerate and the relationship between load and displacement returns along the  $AO$  section (the unloading line is  $AO$ ). If the specimen is unloading in the  $AB$  section (the positive loading yields), the positive loading stiffness begins to degenerate and the relationship between load and displacement returns along the  $ab$  line (the unloading line is  $ab$ ). If the specimen is unloading in the  $BC$  section (the load has passed the peak point), the relationship between load and displacement returns along  $eb$  section (the unloading line is  $eb$ ).

FIGURE 8: Regression curve fitting ( $K_1$ ). (a) SH-1. (b) SH-2.FIGURE 9: Regression curve fitting ( $K_2$ ). (a) SH-1. (b) SH-2.FIGURE 10: Regression curve fitting ( $K_3$ ). (a) SH-1. (b) SH-2.

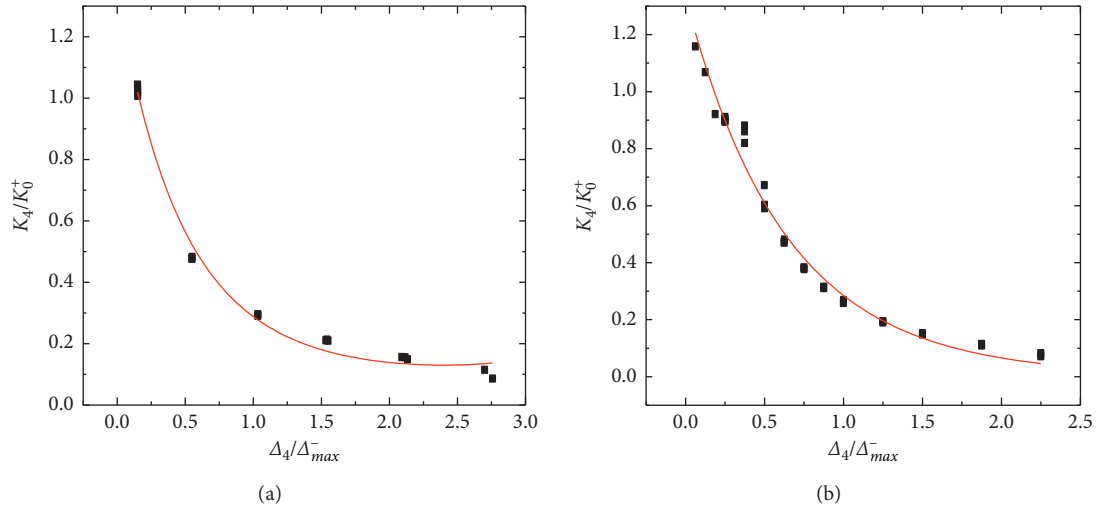


FIGURE 11: Regression curve fitting ( $K_4$ ). (a) SH-1. (b) SH-2.

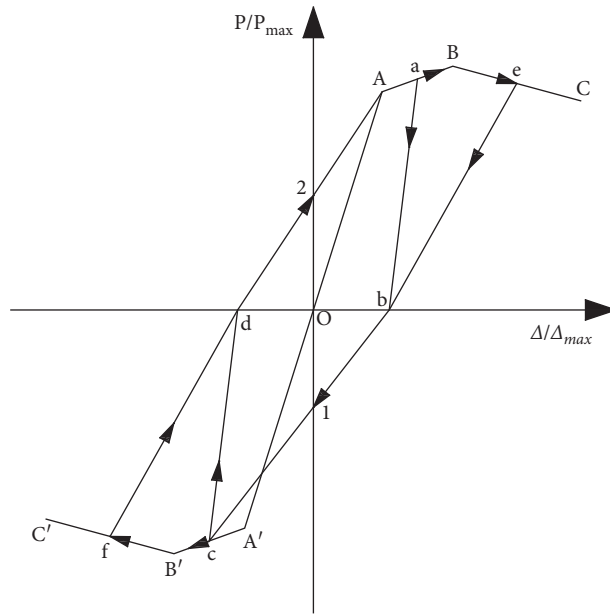


FIGURE 12: Restoring force model.

(2) When the specimen is unloading to  $b$  point and then loading reversely, the relationship between load and displacement develops along  $blA'B'C'$ . If the specimen is unloading at  $1A'$  section (the reverse loading does not yield), the reverse loading stiffness does not degenerate and the relationship between load and displacement returns along  $A'O$  line section (the unloading line is  $A'O$ ). If the specimen is unloading at  $A'B'$  section (the reverse loading yields), the reverse loading stiffness will degenerate and the relationship between load and displacement returns along section  $cd$  (the unloading line is  $cd$ ). If the specimen is unloading at  $B'C'$  section (the reverse loading has passed the peak point), the relationship between load and displacement returns along  $fd$  section (the unloading line is  $fd$ ).

(3) When the specimen is unloading to  $d$  point and then loading again, the relationship between load and displacement develops along  $d2ABC$ , and the subsequent loading and unloading is the same as the first loading.

#### 4. Verification of Resilience Model

4.1. Verification of Skeleton Curve. The skeleton curve model can be obtained by connecting the feature points in front, and the skeleton curve model is compared with the measured skeleton curve, as shown in Figure 13. It can be seen that the skeleton curve model can better reflect the load displacement variation law of two joint specimens.

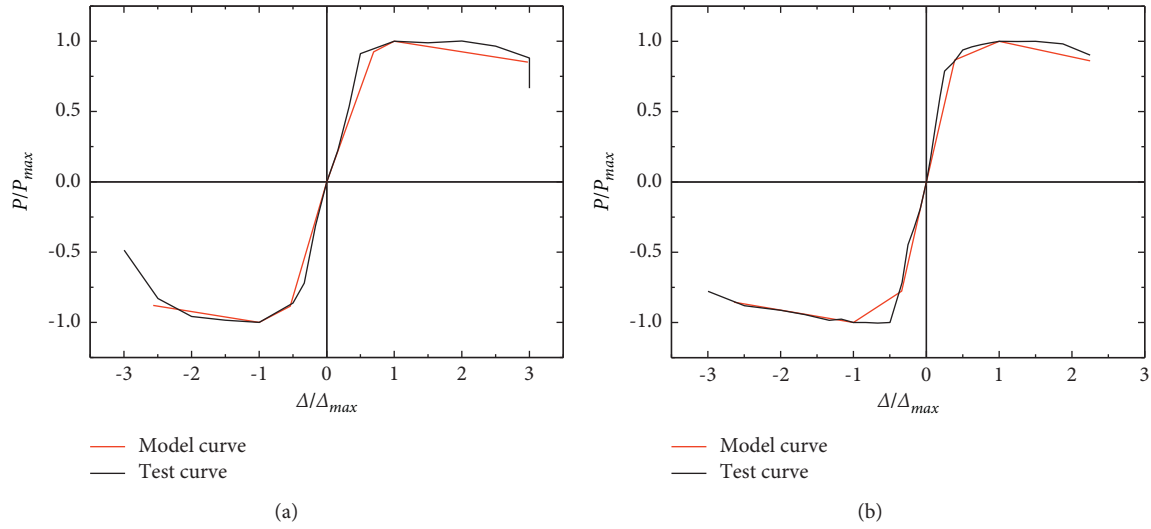


FIGURE 13: Comparison between the model curve and test curve. (a) SH-1. (b) SH-2.

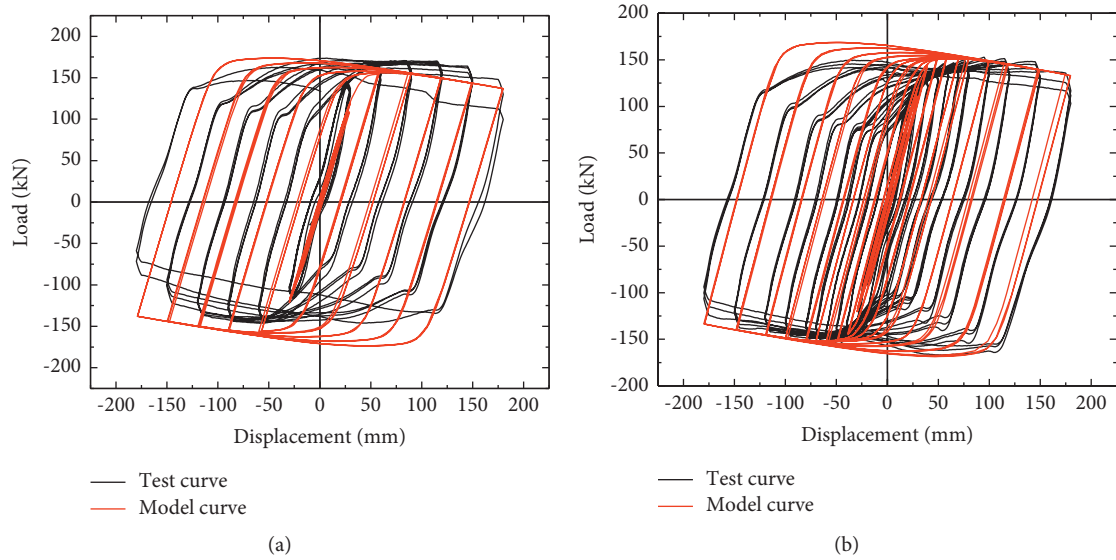


FIGURE 14: Comparison between the model curve and test curve. (a) SH-1. (b) SH-2.

4.2. *Verification of Hysteresis Curve.* The hysteresis curve drawn by the above hysteresis rule is compared with the experimental hysteresis curve, as shown in Figure 14, and the results show that they are consistent.

## 5. Conclusions

Based on the load-displacement hysteretic curve and skeleton curve obtained from the test, we establish a restoring force model suitable for the new type joints. This model mainly consists of three parts: the three-fold line skeleton model obtained from the test data, the specific calculation formula of stiffness degradation, and the mathematical description of hysteretic rules.

From the above results, it can be seen that the restoring force model on the joint of CTSRC column has the following characteristics:

- (1) Under low cycle cyclic loading, the positive and reverse loading and unloading stiffness of the new type joint is equal to the initial stiffness of the joint in the elastic stage
- (2) When the specimen enters the yield stage, the initial stiffness of positive and reverse loading and unloading gradually degenerates, and the degradation in the early stage is more obvious than that in the later stage
- (3) Compared with the positive unloading stiffness and reverse unloading stiffness of the specimen, the stiffness degradation of positive loading stiffness and reverse loading stiffness is more obvious

The restoring force model can reflect the hysteretic behavior of the new type joint and can be used for

elastoplastic seismic time-history analysis on the joint of CTSRC column.

## Data Availability

The data used to support the findings of this study are available from the corresponding author upon request.

## Disclosure

This is an open access article distributed under the Creative Commons Attribution License, which permits unrestricted use, distribution, and reproduction in any medium, provided the original work is properly cited.

## Conflicts of Interest

The authors declare no potential conflicts of interest with respect to the research, authorship, and/or publication of this article.

## Acknowledgments

This research was supported by the National Natural Science Foundation of China (No. 51408052), Youth Science and Technology Star Project of Shaanxi Province (No. 2016KJXX-51), Key Research and Development Plan of Shaanxi Province (No. 2018SF-354), and special fund for basic scientific research in Central Universities of Chang'an University (No. 300102289205).

## References

- [1] W. Ramberg and W. Osgood, "Description of steel stain curve by three parameters," National Advisory Committee for Aeronautics, Moffett Field, CA, USA, Technical Notes No: 902, 1943.
- [2] P. Jennings, "Periodic response of a general yielding structure," *Journal of Engineering Mechanical Division*, vol. 90, no. 20, pp. 131–165, 1964.
- [3] R. Clough and S. Johnston, "Effect of stiffness degradation on earthquake ductility requirements," in *Proceedings of the 2nd Japan National Conference on Earthquake Engineering*, pp. 227–232, Tokyo, Japan, September 1966.
- [4] T. Takeda, M. A. Sozen, and N. N. Nielsen, "Reinforced concrete response to simulated earthquakes," *Journal of the Structural Division*, vol. 96, no. 12, pp. 2557–2572, 1970.
- [5] C. Yan, D. Yang, Z. Ma, and J. Jia, "Hysteretic model of SRUHSC column and SRC beam joints considering damage effects," *Materials and Structures*, vol. 50, no. 1, 2017.
- [6] Y. Zhang and S. Han, "Hysteretic model for flexure-shear critical reinforced concrete columns," *Journal of Earthquake Engineering*, vol. 22, no. 9, pp. 1639–1661, 2018.
- [7] O. Yuka and I. Hideki, "Smooth hysteretic model of H-shaped steel beams," *Ce/Papers*, vol. 3, no. 3-4, pp. 145–150, 2019.
- [8] Y. Zhang, G. Ma, S. Du, Y. Liu, Z. Li, and Y. F. Chen, "Hysteretic behavior and restoring force model of reinforced glazed hollow bead insulation concrete (GIC) columns," *KSCE Journal of Civil Engineering*, vol. 23, no. 7, pp. 3049–3065, 2019.
- [9] Q. Hao, T. Motohide, T. Naoki, and S. Yu, "Monotonic and hysteretic model for H-shaped beams incorporating deterioration behavior owing to the local buckling," *Thin-Walled Structures*, vol. 157, Article ID 107016, 2020.
- [10] Y. Wang, Y. Feng, D. Huang, Z. Huang, and Z. Chen, "Restoring force model of an energy-dissipation joint and non-linear dynamic analysis of a hybrid frame," *Journal of Building Engineering*, vol. 32, Article ID 101762, 2020.
- [11] H. Li, R. Li, C. Li, and D. Wang, "Development of hysteretic model with dynamic effect and deterioration for seismic-performance analysis of reinforced concrete structures," *Journal of Structural Engineering*, vol. 146, no. 10, 2020.
- [12] Q. Xie, X. Zhao, X. Yao, W. Hao, and F. Hu, "Seismic behaviors of precast assembled bridge columns connected with prestressed threaded steel bar: experimental test and hysteretic model," *Advances in Structural Engineering*, vol. 23, no. 9, pp. 1975–1988, 2020.
- [13] C. Wu, X. Liu, W. Pan, and B. Mou, "Restoring force model for modular prefabricated steel-reinforced concrete column to H-shaped steel beam composite joints," *Journal of Building Engineering*, vol. 42, 2021.
- [14] Z. Song, F. Yu, N. Zhang, and Y. Fang, "A model for predicting load-displacement hysteretic behavior of PVC-CFRP confined concrete column-ring beam interior joints under low cyclic loading," *Composite Structures*, vol. 265, 2021.
- [15] X. Ni, S. Cao, and Y. Hou, "Hysteretic model of shear walls built with high-strength reinforcement," *Structural Concrete*, vol. 22, no. 3, pp. 1378–1395, 2021.
- [16] X. Zhou, J. Liu, and S. Zhang, "Experimental study on seismic behavior of square steel tube confined steel reinforced concrete short columns," *Journal of Building Structures*, vol. 31, no. 7, pp. 49–55, 2010.
- [17] J. Liu, X. Zhang, and S. Zhang, "Axial compression behavior of circular steel tube confined steel reinforced high strength concrete short columns," *Journal of Building Structures*, vol. 30, no. 2, pp. 242–248, 2009.
- [18] X. Zhou and J. Liu, "Seismic behavior and strength of tubed steel reinforced-concrete (SRC) short columns," *Journal of Constructional Steel Research*, vol. 66, no. 1, pp. 28–36, 2010.
- [19] Y. Dai, S. Nie, and T. Zhou, "Finite element analysis of hysteretic behavior of Square steel tube confined steel reinforced concrete column steel frame ring beam joint," *Journal of Jilin University (Engineering and Technology Edition)*, vol. 48, no. 5, pp. 1426–1435, 2018.
- [20] Y. Dai, S. Nie, and T. Zhou, "Seismic behavior of Circular steel tube confined H steel reinforced concrete column steel frame ring beam joint," *Journal of South China University of Technology*, vol. 47, no. 5, pp. 110–122, 2019.
- [21] Y. Dai, S. Nie, and T. Zhou, "Shear capacity of circular steel tube confined H-SRC concrete column steel beam joint with ring beam," *Journal of Jilin University (Engineering and Technology Edition)*, vol. 51, no. 3, pp. 977–988, 2021.
- [22] Z. Guo and X. Lv, "Experimental study on the hysteretic model of RC columns with high axial compressive ratio," *China Civil Engineering Journal*, vol. 37, no. 5, pp. 32–38, 2004.
- [23] G. Zhang, X. Lv, and B. Liu, "Study on resilience models of high-strength concrete frame columns," *Engineering Mechanics*, vol. 24, no. 3, pp. 83–90, 2004.
- [24] China Construction Industry Press, *Code for Seismic Test Methods of Buildings*, China Construction Industry Press, Beijing, China, 2015.
- [25] L. Zeng, *Research on Seismic Behaviors and Design Method of Steel Reinforced High Strength and High Performance Concrete Frame Joints*, Xi'an University of Architecture and Technology, Xi'an, China, 2008.

## Research Article

# Analysis for Shear Behavior of SRC Deep Beams Based on Tests, Digital Image Correlation Technique, and Finite Elemental Simulation

Buqing Chen <sup>1</sup>, Jun Wu <sup>1,2</sup>, Changjun Liu,<sup>1</sup> Yanhua Liu,<sup>1</sup> Wenmei Zhou,<sup>1</sup> and Yunfeng Xiao<sup>3</sup>

<sup>1</sup>School of Urban Construction, Yangtze University, Jingzhou 434023, China

<sup>2</sup>Beijing Building Materials Academy of Sciences Research, Beijing 100043, China

<sup>3</sup>School of Civil and Hydraulic Engineering, Huazhong University of Science and Technology, Wuhan 430074, China

Correspondence should be addressed to Jun Wu; [wujun737@yangtzeu.edu.cn](mailto:wujun737@yangtzeu.edu.cn)

Received 22 July 2021; Revised 26 August 2021; Accepted 30 August 2021; Published 11 September 2021

Academic Editor: Jingxuan Wang

Copyright © 2021 Buqing Chen et al. This is an open access article distributed under the Creative Commons Attribution License, which permits unrestricted use, distribution, and reproduction in any medium, provided the original work is properly cited.

Seven steel-reinforced concrete (SRC) deep beams were tested to investigate the shear performance, including peak loads, failure modes, mid-span deflections, and cracking patterns. The parameters include the shear span-to-depth ratio and the dimensions of the steel skeleton. The digital image correlation (DIC) technique was utilized for real-time recording of the in-plane strain and deformation. The experiment results show that the failure modes of specimens could be concluded as two forms: diagonal compression failure and shear failure. The DIC technique was proved to be efficient for tracking the development of crack patterns and recording the failure modes. The corresponding numerical analyses based on experiments were carried out and demonstrated to be a reliable method to simulate the shear response. Furthermore, the most significant parameters and their interactions were identified by finite element models parameter analysis. The steel skeleton height and shear span-to-depth ratio were the main parameters affecting shear capacity. A design formula based on the strength superposition method was presented. The calculated results were basically in agreement with the test results, where the mean and coefficient of variation were 1.04 and 0.09, respectively.

## 1. Introduction

The steel-reinforced concrete (SRC) deep beam is a composite member formed by built-in steel sections. Due to good seismic performance, high shear capacity, and ductility, SRC deep beams have been widely used in housing construction, bridges, and underground engineering [1–4], especially the gigantic transition beams of complicated high-rise building structures [5–8].

Few codes give a clear definition of the SRC deep beams. Generally, the definition of the reinforced concrete (RC) deep beams is used to define the SRC deep beams. ACI 318-19 defines deep beams as beams whose shear span-to-depth ratio does not exceed 2 [9]. Previous studies [10, 11] have shown that the mechanical properties of SRC deep beams are quite different from those of slender beams. Due to the small

span-depth ratio, its bearing capacity is controlled by shear stress instead of bending stress. The section of SRC deep beam under concentrated load causes bending normal stress, shear stress, and compressive stress simultaneously, resulting in a complex and nonlinear strain distribution.

A suitable calculation model is a basis for understanding the shear transfer mechanism and predicting the bearing capacity. According to the recommendations of the design code including ACI 318-19 [9] and EC-2 [12], the Strut-and-Tie Model (STM) is applied to calculate the shear capacity of deep beams. To optimize and enhance the accuracy of the model, many scholars have proposed various modified STMs. Hwang SJ and Lee [13] proposed a softened STM to predict the destructive strength of discontinuous areas in diagonal compression of concrete. Lu [10] calculated the shear capacity based on softening STM and considering the

combined action of the internal steel skeleton and concrete. Chen et al. [11] considered the depth of the steel skeleton as a major influence parameter and derived an SST-SRC model to predict the shear capacity of SRC deep beams. However, the STM model is based on the theory of lower plastic limit values, with various forms. It is very important whether the established model can truly reflect the real force. At the same time, establishing an effective STM is a hard problem. Additionally, for SRC structural members, the concept of strength superposition is recommended by many design codes including the AIJ Standard [14] and the JGJ 138-2016 [15]. Weng and Wang [16] studied the influence of shear studs and stirrups on the shear behavior of SRC deep beams. The shear capacity of SRC members is divided into the RC part and the steel skeleton part. Based on the strength superposition method, the shear capacity is affected by many parameters of the component, such as the concrete tensile strength, web and flange of steel skeleton, shear span-to-depth ratio, longitudinal reinforcement ratio, and stirrups. However, the above research including the modified Strut-and-Tie Models predicted the shear capacity by describing the load transfer path, whereas many influence parameters were not discussed. Furthermore, the strength superposition method was mostly used to analyze slender beams; only a few influence parameters of deep beams were analyzed. Existing studies cannot fully consider the changing trend of shear capacity. Therefore, studying the factors of the effect of the shear capacity of SRC deep beams and establishing an accurate method for predicting shear capacity were urgently important issues.

The traditional measuring tools were used in many structural tests, such as strain gauges, displacement transducer, and extensometer. But the disadvantage of these tools is that they can only measure the strain in a certain area. The strain gauge will fail once the concrete cracks and cannot record the full-field strain of the surface of the beams. Due to the complex stress state of SRC deep beams, it is difficult for traditional measuring tools to capture the variation law of concrete surface strain. Thus, in order to continuously and accurately observe the shear response and cracking pattern of SRC deep beams, the digital image correlation (DIC) technology was applied to this experiment. This technology is a noncontact modern optical measurement technology, which has the merits of a simple measuring device, strong environmental adaptability, and a wide measurement range. Thus, it has been widely used in civil engineering, mechanical, materials science, and other scientific or engineering fields [17]. Its basic principle is to get the displacement by tracking the position of the same pixel in the two speckle images before and after the surface deformation, thereby obtaining the whole field displacement and strain of the surface. This technology overcomes the shortcomings of traditional strain gauge measurement and naked eye identification of cracks, which can continuously observe the development of crack and surface strain [18]. Therefore, the DIC technique was used to study the shear cracking response, crack pattern, initial crack load, and location and track the crack development of SRC deep beams.

In this paper, seven SRC deep beams were tested to study the shear performance using the DIC technique. The influence of the shear span-to-depth ratio and the size of the steel skeleton on the shear response were investigated. Furthermore, the finite element models were established and verified with good agreement. Besides, the effect of reinforcement ratio, stirrup spacing, and concrete strength on shear capacity was further studied by a series of parameter analyses. According to the strength superposition theory, the calculation formula of shear bearing capacity was proposed. The results can provide a reference for predicting the shear performance of SRC deep beams.

## 2. Test Program

*2.1. Test Specimen Design and Material Properties.* All specimen sizes were designed according to the facilities of the laboratory. Half-scale specimens were selected for this paper because deep beams of this size were large enough to capture essential response phenomena experienced by full-scale deep beams, while they were small enough to keep the overall project costs within budget. The reinforcements were arranged based on the permissible range of ACI 318-19. The dimensions of the steel skeleton and reinforcement drawings are shown in Figure 1. All SRC deep beams have the same cross-sectional dimension of 180 mm × 320 mm. Two 18 mm diameter longitudinal bars are arranged at the top of the beam section while four are arranged at the bottom. The stirrups consisted of  $\phi 6@100$  mm steel bars. The H-shaped steel skeleton was embedded inside the beams. Table 1 shows the main parameters of specimens. The main research parameters are the height of the steel skeleton, the shear span-to-depth ratio  $\lambda$ , and the width of the steel skeleton flange. The specimens are designed in three lengths, including 860 mm, 1020 mm, and 1200 mm, respectively. A total of five different dimensions of steel skeleton were studied. RDB-1, RDB-2, and RDB-3 had the same properties, except  $\lambda$  varied from 1.1 to 1.7.

All the specimens were cast-in-place. The concrete used in the study was provided by a local supplier, with a maximum aggregate size of 20 mm. The target compressive strength is C40. On the day of testing, three sizes of 150 mm(length) × 150 mm(width) × 300 mm(height) prisms and three cubes with 150 mm edges were reserved for each test beam. Three prisms were used to measure the compressive and three cubes are used to measure splitting tensile strengths. According to the Chinese standard GB/T 50081 [19], the average concrete compressive strength  $f_c$  was 25.2 MPa and the average tensile strength  $f_t$  was 2.14 MPa; besides, the elastic modulus was  $3.31 \times 10^4$  MPa. The longitudinal reinforcements and the stirrups are in grade HRB335 and HPB300 hot rolled reinforced bars, respectively. The steel skeleton is hot rolled H-shaped steel with grade Q235. Table 2 shows the properties of reinforcements and steel.

*2.2. Test Setup.* Figure 2 shows the schematic diagram of the test. A three-point bending monotonic static load test method is applied to the specimen. The YHD-50 displacement sensor was fixed at the bottom of the beam to record the central displacement. Two dial gauges were installed near

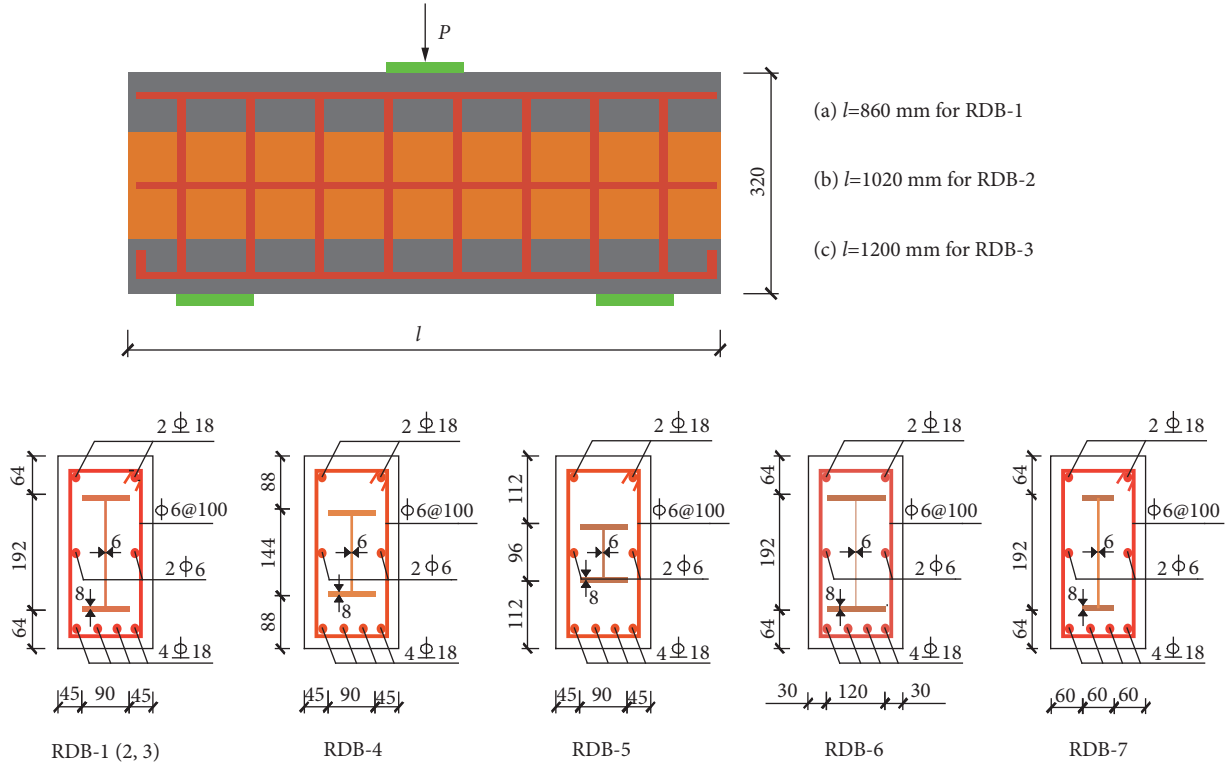


FIGURE 1: Dimensions and reinforcements of specimens.

TABLE 1: Main parameters of SRC beams.

Specimens	Length (mm)	$\lambda$	Width ratio	Height ratio	Cross section of H-shaped steel (mm)
RDB-1	860	1.1	0.5	0.6	192 × 90 × 6 × 8
RDB-2	1020	1.4	0.5	0.6	192 × 90 × 6 × 8
RDB-3	1200	1.7	0.5	0.6	192 × 90 × 6 × 8
RDB-4	860	1.1	0.5	0.45	144 × 90 × 6 × 8
RDB-5	860	1.1	0.5	0.3	96 × 90 × 6 × 8
RDB-6	860	1.1	0.67	0.6	192 × 120 × 6 × 8
RDB-7	860	1.1	0.33	0.6	192 × 60 × 6 × 8

TABLE 2: Measured material characteristics of steels.

Steel grade	Diameter/thickness (mm)	Yield strength $f_u$ (MPa)	Ultimate strength $f_u$ (MPa)	Young's modulus $E_s$ (MPa)
HPB300	6	313	534	$2.1 \times 10^5$
HRB335	18	440	515	$2.1 \times 10^5$
Q235	6	272	406	$2.0 \times 10^5$
	8	315	430	$2.0 \times 10^5$

the supports to observe the angle of rotation. The strain gauges were attached to the longitudinal reinforcement, stirrups, and steel skeleton to measure strains, as shown in Figures 2(a) and 2(b).

A 2D digital image correlation (DIC) method was applied to monitor surface full-field strain of concrete, displacement, and the crack pattern of specimens. The system consists of a single camera and a light source as shown in Figures 2(c) and 2(d). The surface of the observation area is kept parallel to the image plane of the camera throughout the measurement process. The system was able to measure an

approximately 430–600 mm wide area from the center to the end of the beams, corresponding to the moment-shear area. The speckle spots of the specimen are drawn manually, and the white light source was used to ensure that a clear picture of the experiment was captured. The experimental device is tested in conjunction with DIC digital camera, and the images were captured every 10 kN. The analysis is completed using a subset size of 41 pixels, a step size of 5 pixels.

The electrohydraulic servo actuator is employed to apply load by means of the displacement controlled method. When the applied load on the specimens dropped below 85%



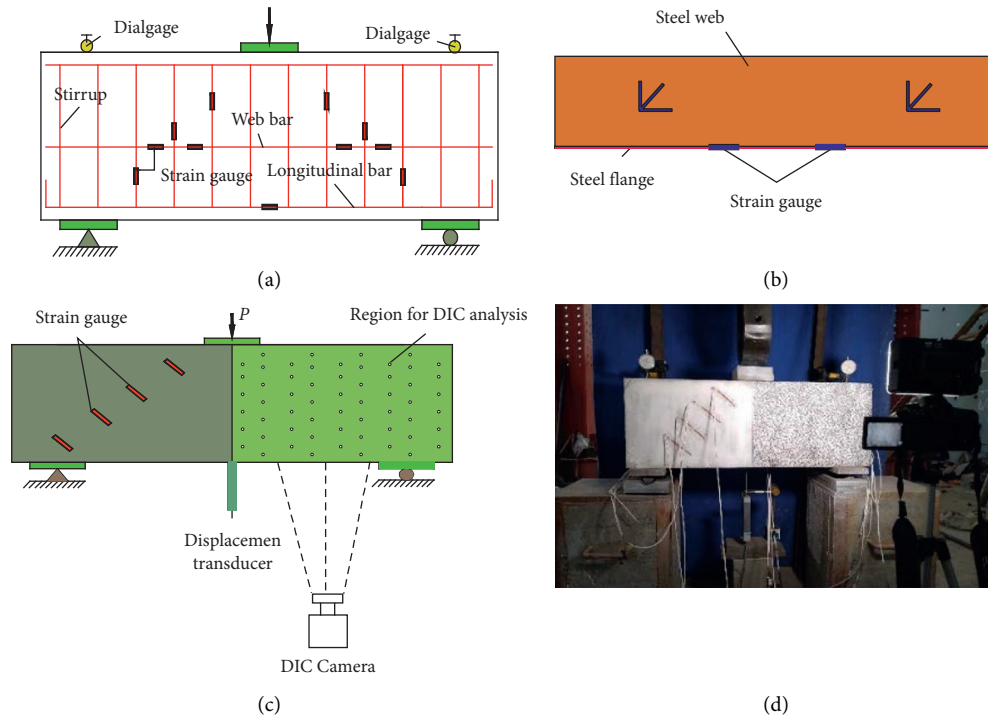


FIGURE 2: The schematic diagram of the test setup. (a) Typical instrumentation of the beam. (b) Strain position of steel shape. (c) Schematic of the DIC test loading system. (d) Test method system.

of the peak load or obvious failure occurred, the tests were stopped. All data of strain gauges, load, and displacement transducer were registered corresponding to DIC images using a data acquisition system. In the process of testing, the initial shear and flexural cracking load and crack patterns at each stage were recorded.

**2.3. Test Results.** Figures 3 and 9 show the failure modes and the load-deflection curves of specimens. The DIC technique was used to record the crack patterns and study the cracking process during the test. Under concentrated load, the failure modes of seven test specimens were concluded as two forms: (a) diagonal compression failure and (b) shear failure. The test results including cracking loads, peak loads, mid-span deflections, and failure modes are listed in Table 3.

The diagonal compression failure occurred in the specimens RDB-1 and RDB-4~RDB-7. These beams mainly failed by the crushing of concrete from the loading point to the support. The  $\lambda$  ( $\lambda=1.1$ ) of these specimens are smaller than the others. Failure usually occurs along one of the main diagonal cracks. For a clear description of the diagonal compression, specimen RDB-1 is taken as an example; its failure mode and the measured load-deflection curve are shown in Figures 3(a) and 9(a). Before cracking, the load-deflections response of the beam was completely dominated by the bending stiffness. As the load increased, the cracks appeared gradually, which led to the decrease of stiffness and the large deformation. All test specimens exhibited vertical cracks prior to the diagonal cracking. The vertical concrete cracks in the beam RDB-1 commenced under the load of 90 kN at the bottom of the mid-span surface. But unlike

RDB-2 and RDB-3, the vertical cracks did not develop further. The diagonal cracks occurred soon after the vertical cracks appeared. Because  $\lambda$  ( $\lambda=1.1$ ) of such beams was relatively small, the bending moment effect at the mid-span was not obvious. The concrete diagonal compressive strut from the loading point to the support was subjected to a larger load.

The primary diagonal crack initiated approximately at the middle of the beam section at a load of 110 kN. Then, as the load increased, it extended to the support and the loading point. The same crack propagated to the diagonal compression zone up to peak load ( $F_p=788$  kN). When the peak load was reached, the specimen failed suddenly without warning and exhibited a brittle failure mode. At this time, a serious diagonal crack emerged on the concrete failure surface, and the bearing capacity of the specimen decreased rapidly. At ultimate load ( $F_u=680$  kN), the displacement in the beam mid-span of beam reached 8.6 mm and the width of the diagonal cracks further increased. The strains of stirrups close to diagonal cracks reached their yielding value and were bigger than those stirrups which were far from the cracks. Similarly, the strains of steel skeleton web embedded in the beam had also reached their yielding value. But, no longitudinal reinforcement yielded during the test procedure. The cracks at the bottom of the specimen were only slightly developed. Probably, the bending moment in the beam mid-span was small, resulting in the fact that the longitudinal reinforcement at the bottom was subject to tensile force slightly.

The specimens RDB-2 and RDB-3 with large  $\lambda$  ( $\lambda=1.4$  and 1.7) had experienced shear failure. Figures 3(c) and 3(d)

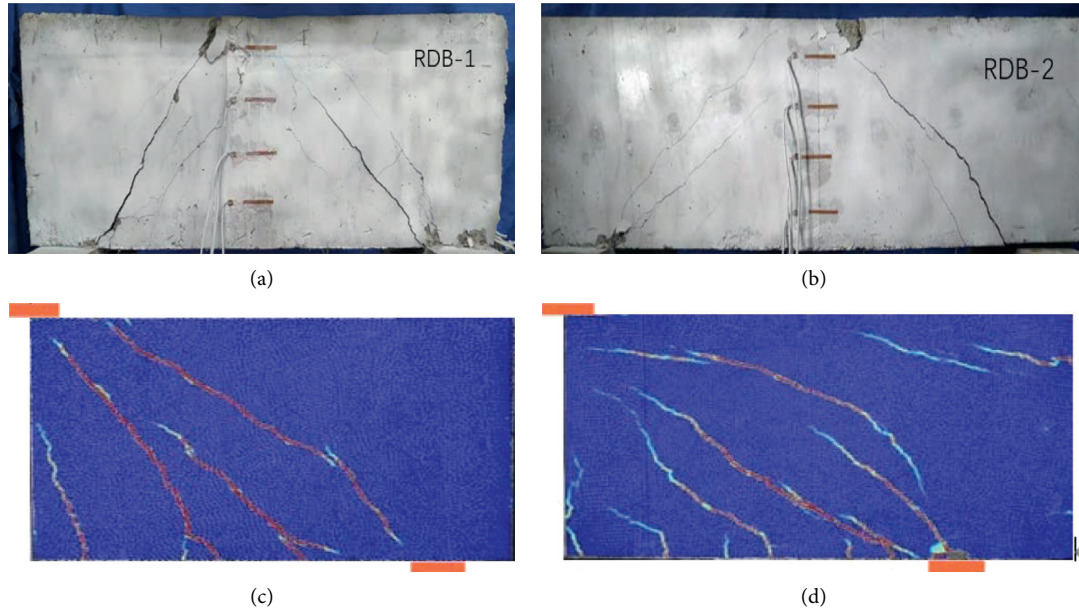


FIGURE 3: Failure modes and crack pattern. (a) Diagonal compression failure. (b) Shear failure. (c) Crack patterns of RDB-1 recorded by DIC. (d) Crack patterns of RDB-2 recorded by DIC.

TABLE 3: The test results of seven SRC deep beams.

Specimens	Shear cracking load (kN)	Peak load (kN)	Deflections (mm)	Failure modes
RDB-1	110	788	8.6	Diagonal compression
RDB-2	100	682	9.1	Shear
RDB-3	130	548	9.5	Shear
RDB-4	120	734	7.6	Diagonal compression
RDB-5	130	645	8.9	Diagonal compression
RDB-6	160	816	9.8	Diagonal compression
RDB-7	100	698	8.1	Diagonal compression

show the failure mode and crack pattern of RDB-2. It can be clearly seen that there are many cracks distributed on the shear span area of the beams. These beams mainly failed by the crushing of concrete at the shear span area. The cracks that ultimately lead to beam failure are diagonal shearing cracks rather than bending cracks. Hence, the failure mode of beams RDB-2 and RDB-3 is defined as shear failure.

The vertical cracks in the mid-span surface of beam RDB-2 were initiated under 60 kN load and they propagated up to load 100 kN until diagonal cracks occurred. As expected, these vertical cracks gradually extended up to about two-thirds of the beam section height by increasing load. A large number of cracks occurred densely in the shear span area. From Figure 3, a smaller spacing between the diagonal cracks can be seen for beams with larger  $\lambda$ . As the load increased further and enhanced the bending moment, the mid-span displacement expanded. At the ultimate load ( $F_u = 590$  kN), the displacement reached 9.1 mm. Similarly, in beam RDB-3, at ultimate load ( $F_u = 460$  kN), the displacement reached 9.5 mm. Both RDB-2 and RDB-3 failed in larger displacement and the better ductile mode is shown. The experimental data showed that the strains of longitudinal reinforcement at the bottom reached a yielding value.

As with other beams, strain measurements indicated that the stirrups and steel skeleton webs at the diagonal cracks of the beams all reached the yielding value. From Table 3, it can be shown that the shear capacity decreases with the increase of  $\lambda$ . When  $\lambda$  varied from 1.1 to 1.7, the shear capacity decreased by 31%. In addition, the steel skeleton flange and web also have a positive influence on the shear capacity. When the web height ratio increased from 0.3 to 0.6, the shear capacity increased by 22%. When the flange width ratio increased from 0.33 to 0.67, the shear capacity increased by 17%.

### 3. Finite Element Analysis

Three-dimensional finite element models (FEMs) have been developed to simulate the nonlinear shear response of the SRC deep beams based on the ABAQUS software. The simulation results were compared with those of experimental results. The relevant parameters affecting the shear response were further studied by FEM. Then, the relationship between the research parameters and the shear capacity of SRC deep beams was established by the finite element analysis.

**3.1. General Details.** Figure 4 shows the typical FEM of the SRC deep beam. Except for the reinforcement bars, all parts are simulated using solid elements (C3D8R). This element only contains an integral point in the center of the element, and the shear self-locking is difficult to occur under the bending load. Moreover, the analytical accuracy of the C3D8R element could not be greatly affected when the mesh is distorted, and it solves the displacement problem more accurately. The reinforcement bars are simulated using two-node truss elements (T3D2). All bars are merged into a whole. Since no bonding failure of the internal reinforcement bars, steel skeleton, and surrounding concrete was observed in the test, it is assumed that they are perfectly bonded. Therefore, the longitudinal bars, stirrups, and steel skeleton are “embedded” in the concrete. Reinforcement bars and steel skeleton were meshed with elements of 25 mm in length. The size of the concrete element is 25 mm at the analysis position and 50 mm at the edge of beams. The rigid steel was modeled using solid elements C3D8R to avoid stress concentration at concrete loading points and supports. “Tie” command was applied for the contact between supports and concrete. The material properties of rigid steel are elastic modulus of  $2.1 \times 10^{12}$  Pa and the Poisson ratio of 0.3. Furthermore, in the ABAQUS standard procedure, the parameter NLGEOM was activated to consider the large displacement.

**3.2. Material Modeling of Steel.** The material behaviors of steel reinforcement and steel skeleton were assumed as a nonlinear elastic-plastic. The nonlinear stress ( $\sigma$ )-strain ( $\varepsilon$ ) model proposed by Chinese code GB 50010-2010 [20] for steel material is shown in Figure 5. The classical metal plasticity model was used in plasticity analysis. In ABAQUS, the classic metal plasticity models use the standard Mises yield surface and associated plastic flow to achieve the isotropic yield, while also providing the definition of perfect plasticity and isotropic hardening. Because the experimentally measured data is nominal stress-strain data, equations (2) and (3) need to be converted into true stress and logarithmic strain data before inputting into ABAQUS. where  $\sigma_s$  is the stress of steel skeleton and reinforcing bars;  $E_s$  is Young’s modulus;  $\varepsilon_s$  is the strain of steel skeleton and reinforcing bars;  $k$  is the slope of the hardening section of steel;  $f_y$  is the yield strength;  $\varepsilon_y$  is the strain at the yield strength;  $f_{st}$  is the ultimate strength of steel; and  $\varepsilon_u$  is the strain at the ultimate strength.

$$\sigma_s = \begin{cases} E_s \varepsilon_s, & \varepsilon_s \leq \varepsilon_y, \\ f_y + k(\varepsilon_s - \varepsilon_y), & \varepsilon_y < \varepsilon_s \leq \varepsilon_u, \end{cases} \quad (1)$$

$$\sigma_{\text{ture}} = \sigma_{\text{nom}} (1 + \varepsilon_{\text{nom}}), \quad (2)$$

$$\varepsilon_{\text{ln}}^{\text{pl}} = \ln(1 + \varepsilon_{\text{nom}}) - \frac{\sigma_{\text{ture}}}{E}, \quad (3)$$

where  $\sigma_{\text{ture}}$  is the true stress;  $\sigma_{\text{nom}}$  is the nominal stress;  $\varepsilon_{\text{ln}}^{\text{pl}}$  is the logarithmic strain; and  $\varepsilon_{\text{nom}}$  is the nominal strain.

**3.3. Material Modeling of Concrete.** The nonlinear response of concrete in the test beam was simulated by using the CDP model. The damage and stiffness degradation of concrete has been considered by the CDP model that was proposed according to the research of Lubliner et al. [21] and the revision of Lee and Fenves [22]. In ABAQUS, not merely concrete materials but also some quasi-brittle materials can be simulated with the CDP model in all different types of structures including solid elements.

The five main parameters need to be determined in the CDP model. The default flow potential eccentricity  $\epsilon = 1$ . The dilation angle ( $\psi$ ) is an important parameter to defined nonassociated potential plastic flow. Its value usually ranges from  $0^\circ$  to  $56^\circ$  [23]. In this study, based on conducting a sensitivity analysis, the value  $35^\circ$  was used. The default value parameter  $f_{bo}/f_{c0}$  is 1.16. The parameter  $K_c$  must meet the conditions  $0.5 < K_c \leq 1.0$ . This paper takes the default value  $2/3$ . Usually, the viscoelastic regularization of the small value of the viscosity coefficient  $\mu$  helps to increase the convergence rate of the model during the softening stage without affecting the results. Thus, a value of 0.005 was taken.

The concrete stress-strain response in tension and compression was simulated using the relationship provided in the code GB 50010-2010 [20]. Figure 6 presents the stress-strain curve of concrete. The concrete stress-strain response in compression can be used by the following relation: where  $E_c$  is elastic modulus;  $\alpha_c$  is the parameter value of the descending section;  $\varepsilon_{cr}$  is the peak compressive strain of concrete;  $f_{cr}$  is the uniaxial compression strength of concrete; and  $d_c$  is the damage parameter of concrete.

$$\begin{aligned} \sigma &= (1 - d_c) E_c \varepsilon, \\ d_c &= \begin{cases} 1 - \frac{\rho_c n}{n - 1 + x^n}, & x \leq 1, \\ 1 - \frac{\rho_c}{\alpha_c (x - 1)^2 + x}, & x > 1, \end{cases} \\ \rho_c &= \frac{f_{cr}}{E_c \varepsilon_{cr}}, \\ n &= \frac{E_c \varepsilon_{cr}}{E_c \varepsilon_{cr} - f_{cr}}, \\ x &= \frac{\varepsilon}{\varepsilon_{cr}}. \end{aligned} \quad (4)$$

The concrete stress-strain response in tension can be used by the following relation:

$$\begin{aligned} \sigma &= (1 - d_t) E_c \varepsilon, \\ d_t &= \begin{cases} 1 - \rho_t [1.2 - 0.2x^5], & x \leq 1, \\ 1 - \frac{\rho_t}{\alpha_t (x - 1)^{1.7} + x}, & x > 1, \end{cases} \\ x &= \frac{\varepsilon}{\varepsilon_{tr}}, \\ \rho_t &= \frac{f_{tr}}{E_c \varepsilon_{tr}}, \end{aligned} \quad (5)$$

where  $\alpha_t$  is the parameter value of the descending section;  $\varepsilon_{tr}$  is the peak tension strain of concrete;  $f_{tr}$  is the uniaxial tension strength of concrete; and  $d_t$  is the damage parameter of concrete.

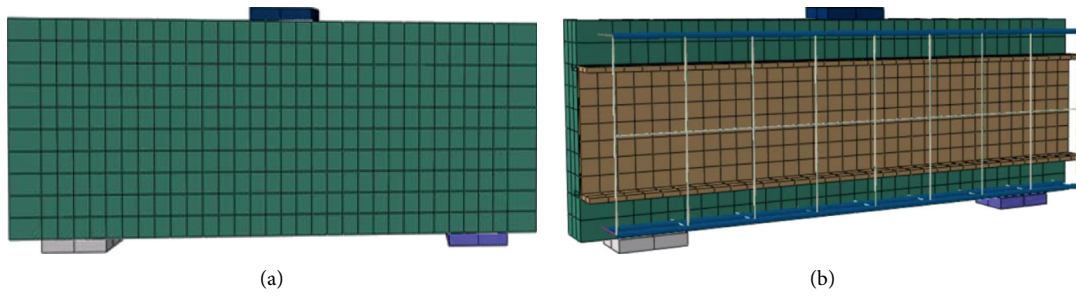


FIGURE 4: Typical FEM meshing of the SRC deep beam. (a) FEM meshing of concrete. (b) FEM meshing of reinforcement bars and steel skeleton.

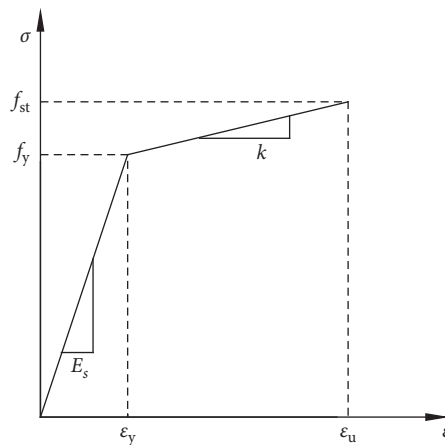


FIGURE 5: The stress-strain curve of steel.

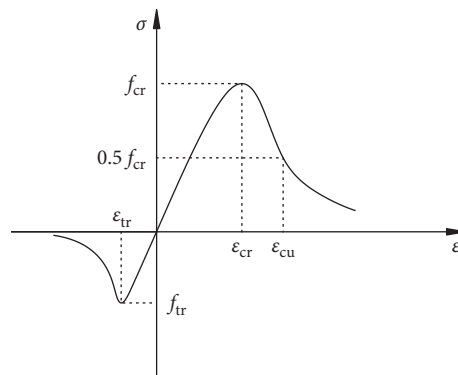


FIGURE 6: The stress-strain curve of concrete.

**3.4. FEM Validation.** In ABAQUS, the CDP model cannot clearly output the cracks at the material integration point. However, the concept of effective crack direction can be introduced to acquire the graphical visualization of crack patterns in concrete structures. The vector direction perpendicular to the crack plane is assumed to be parallel to the direction of the maximum principal plastic strain. At the same time, the concept of equivalent plastic strain (PEEQ) is introduced in ABAQUS. When the PEEQ is greater than 0, the material has yielded. It is the cumulative result of plastic deformation during the whole deformation process.

According to the above methods for determining the crack patterns, the maximum principal plastic strain and

PEEQ contour plots are reported in this study. The comparison between crack patterns from FEM and those recorded by DIC is shown in Figure 7. Figure 8 presents the comparison between failure mode from the test and the PEEQ of FEM. It can be clearly noticed that experimental and finite element models have similar failure modes. The shear diagonal cracks extended between the loading point and the support. The pattern and development process of cracks obtained by numerical simulation are consistent with the experimental specimen. The FEM can precisely capture and simulate the failure modes of SRC deep beams.

Figure 9 shows the load-deflection curves of the test and FEM in the mid-span of all specimens. At each stage of

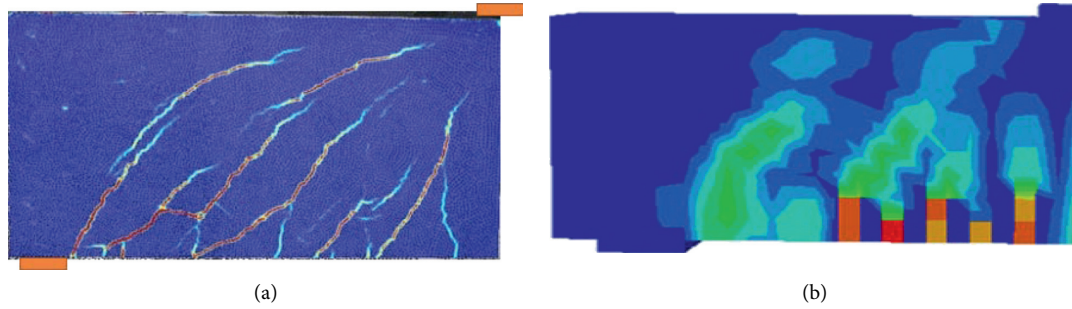


FIGURE 7: Comparison of crack pattern from FEM and recorded by DIC of RDB-3.

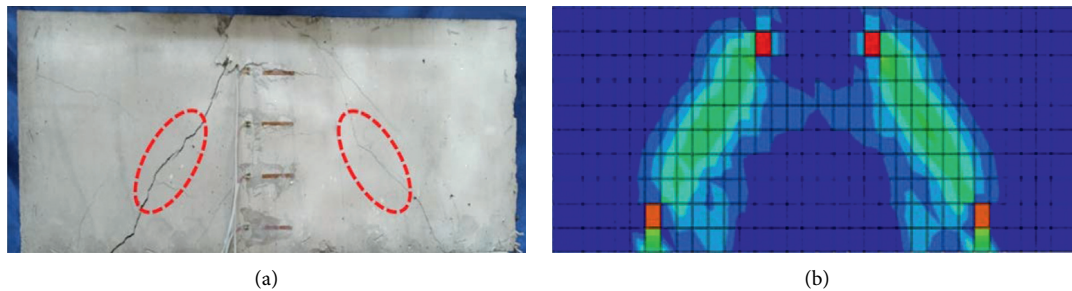


FIGURE 8: Comparison of failure modes between experimental and FEM of RDB-5.

loading, the results of predicted FEM load and deflection agree well with the test data. All curves are almost linear at the beginning of the load, before the crack forms. Subsequently, the curves are converted nonlinearly due to the stiffness degradation caused by the cracking of the specimen. The shear diagonal cracks developed with increased loading until the specimen was destroyed. After reaching the peak load, the bearing capacity of the specimen begins to decrease. By analyzing the results of FEM and the experimental, the accuracy of the FEM in simulating the nonlinear response of the experimental beam was further verified.

Furthermore, the FEM simulated the shear capacity with accuracy. The average simulated-to-test ratio of shear capacity was 1.05, and the coefficient of variation (COV) was 0.04. The shear capacity of the test results agrees well with the numerical simulation. The FEM has been proved as a reliable numerical method to simulate the shear response of specimens. Therefore, the FEM can be applied to the parametric design-oriented study and also can be researched for the effects of main parameters on the shear behavior.

#### 4. Parameter Analysis

Table 4 shows the finite element simulation results. In this study, a total of 21 finite element models of SRC deep beams are established. According to the validated finite element models, a parametric analysis was executed to study the influence of stirrup spacing, concrete tensile strength  $f_t$ , shear span-to-depth ratio  $\lambda$ , the longitudinal reinforcement ratio  $\rho$ , flange width of the steel skeleton, and steel skeleton height on the shear capacity. The effects of different parameters on the shear strength of the specimens are discussed hereinafter.

**4.1. Influence of Concrete Tensile Strength  $f_t$ .** Five finite element models were established to research the influence of  $f_t$  on the shear capacity of specimens. According to the code GB 50010-2010 [20], the tensile strength of five beams is 2.01, 2.39, 2.64, 2.85, and 2.99 MPa corresponding to C30, C40, C50, C60, and C70 grade concrete, respectively. It can be clear from Table 4 that  $f_t$  has a large influence on the shear capacity. When  $f_t$  increased from 2.01 to 2.39 MPa, the shear capacity increased by 10%. As the concrete tensile strength varied from 2.85 to 2.99 MPa, the shear capacity increased by 2.7%. The shear capacities of specimens increase with  $f_t$ . But, as  $f_t$  further increases, the shear capacity of the specimen changes slowly.

**4.2. Influence of Shear Span-to-Depth Ratio  $\lambda$ .** The influence of  $\lambda$  on the shear capacity was studied on four FEM specimens with various  $\lambda$  of 1.1, 1.4, 1.7, and 2, respectively, as shown in Table 4. When  $\lambda$  increases from 1.1 to 2, the shear capacity decreases from 421 kN to 292 kN. This shows that  $\lambda$  is mainly a factor affecting the shear capacity. On the other hand, the failure mode of the specimen also varies with  $\lambda$ . When  $\lambda$  is less than 1.4, the specimen suffers from diagonal compression failure. And when  $\lambda$  is between 1.4 and 2, the shear failure occurred.

**4.3. Influence of Flange Width of Steel Skeleton.** Table 4 provides the results of the shear capacity of the simulated SRC deep beams with five ratios of steel skeleton flange width to the beams section width equal to 0.33, 0.42, 0.5, 0.58, and 0.67. It clearly shows that the increase of the width ratio slightly enhanced the shear capacity. The shear

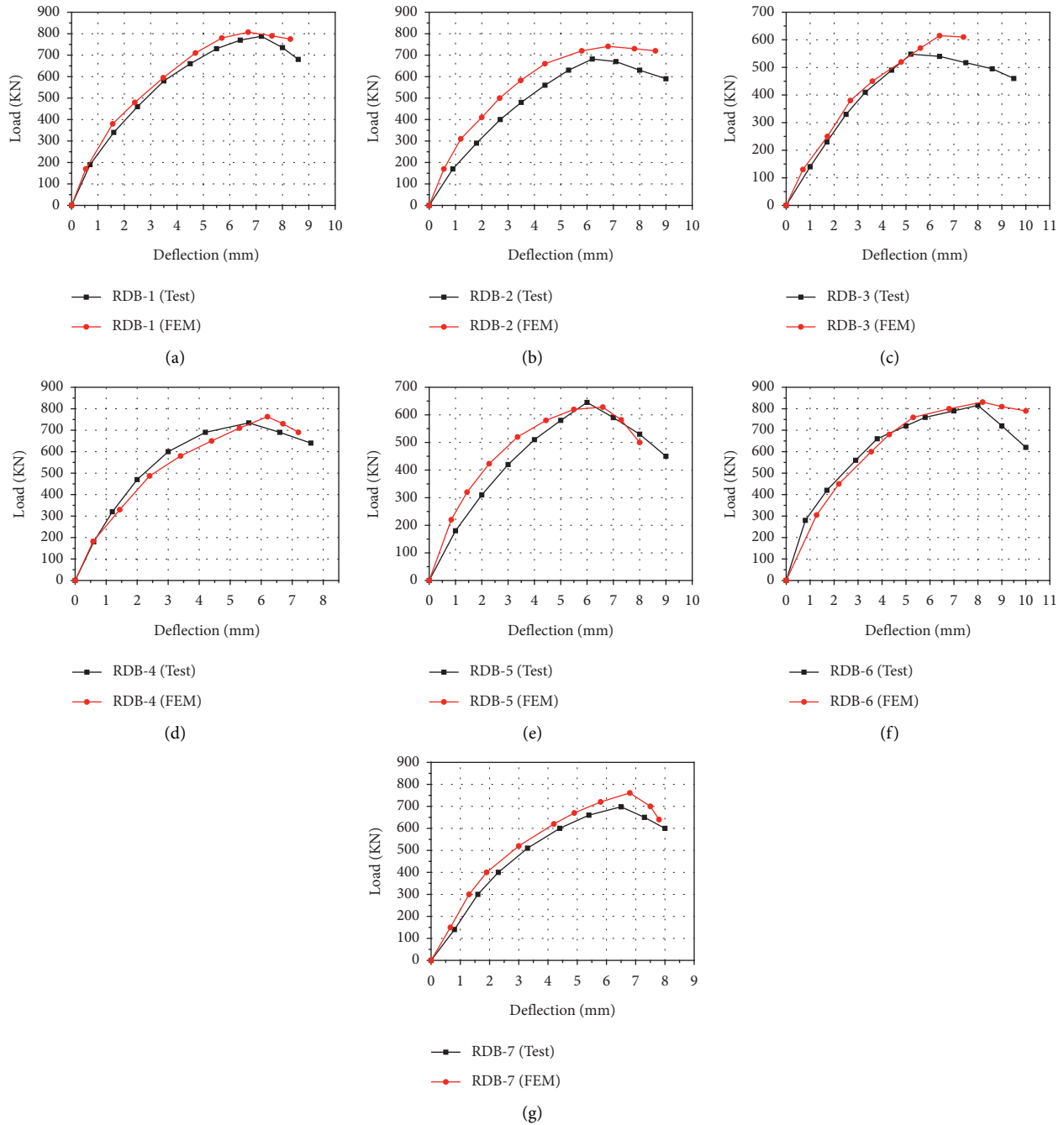


FIGURE 9: The load-deflection curves are compared between experimental and the FEM. (a) RDB-1. (b) RDB-2. (c) RDB-3. (d) RDB-4. (e) RDB-5. (f) RDB-6. (g) RDB-7.

capacity increased by 5.7% when the width ratio varied from 0.33 to 0.5. But with the increase of the width ratio from 0.5 to 0.67, the shear capacity increased by 2.8% only. With the further increase of flange width of the steel skeleton, there is no noticeable increase in the shear capacity. This may be because the steel skeleton flange is arranged at the bottom of the beams, which is mainly subjected to tensile stress and has little contribution to the shear resistance of the specimens.

**4.4. Influence of Steel Skeleton Height.** Four FEMs were implemented to research the steel skeleton height on the shear capacity of SRC beams. Table 4 shows that the steel skeleton height had a noticeable effect on the shear capacity. There are a total of four different ratios of steel skeleton height to beam section height of 0.3, 0.45, 0.6, and 0.75, respectively. When the height ratio increases from 0.3 to 0.75, the shear capacity of the specimens increases from 284 kN to 474 kN. With an average 36% increase in steel

skeleton height, the shear capacity increased by 18.8% on average. Thus, the steel skeleton web provides a great contribution to shear capacity and shows an important shear behavior in SRC deep beams.

**4.5. Influence of Longitudinal Reinforcement Ratio  $\rho$ .** The change of the shear capacity under different longitudinal reinforcement ratios  $\rho$  is shown in Table 4. It clearly shows that  $\rho$  between 1% and 2% has no obvious influence. But, when  $\rho$  increased from 0.5% to 1%, the shear capacity increased by 14.1%. Low-reinforced SRC deep beams are prone to bending damage. With the increase of  $\rho$ , from low-reinforced to overreinforced, the specimens change from flexural failure to shear failure. However, when  $\rho$  increased by more than 1%, further increasing  $\rho$  has no obvious influence on the specimens. At this point, the longitudinal reinforcement and the steel skeleton flange seem to have the same influence on the shear performance.

**4.6. Influence of Stirrup Spacing.** The influence of stirrup spacing on the shear capacity of SRC beams was investigated by four finite element models. Table 4 presents the results of the finite element predicted. There are a total of four different values of stirrup spacing of 50 mm, 75 mm, 100 mm, and 125 mm, respectively. It clearly shows that shear capacity decreases with the increase of stirrup spacing. Increasing stirrup spacing from 50 mm to 75 mm decreased the shear capacity by 1%. As the stirrup spacing changed from 75 to 100 mm, the shear capacity of the specimens reduced by 0.5%. And when the stirrup spacing varied from 100 to 125 mm, the shear capacity decreased by 1.3%. Thus, compared with other parameters, the stirrup spacing has a minimal influence.

## 5. Proposed Method and Verification

**5.1. Proposed Method.** For SRC structures, the strength superposition theory usually assumes that the shear strength is the sum of the steel skeleton web and the reinforced concrete portion. Furthermore, the strength superposition theory is widely applied to many codes to calculate the SRC slender beams only, not deep beams. There are many factors to consider when using this theory to make theoretical predictions. According to the experiment and finite element analysis in this paper, concrete tensile strength, flange width of the steel skeleton, shear span-to-depth ratio, and steel skeleton height have a relatively large influence on the shear capacity. The stirrup spacing has a slight influence on shear capacity. To ensure the comprehensiveness and accuracy of the calculation results, all of the above influencing parameters have been considered. In this paper, the shear capacity  $V_{cal}$  can be assumed to consist of four parts:  $V_c$  is the shear capacity contributed by concrete,  $V_s$  is the shear capacity contributed by the stirrup,  $V_{sw}$  is the shear capacity contributed by steel skeleton web, and  $V_f$  is the shear capacity contributed by steel skeleton flange.

It can be observed that  $V_c$  decreases with the increase of  $\lambda$  and increases with the increase of  $f_t$ . The shear capacity

contributed by the concrete portion  $V_c$  can be estimated as follows:

$$V_c = \frac{\beta f_t}{\alpha \lambda} b h, \quad (6)$$

where  $h$  is the specimen height,  $b$  is the specimen width, and  $\beta$  and  $\alpha$  are the impact coefficients of  $f_t$  and  $\lambda$ , respectively.

According to the experiment and FEM analysis results, the relation of impact coefficient  $\beta$  and  $\alpha$  can be estimated as

$$\frac{\beta}{\alpha} = 1.92. \quad (7)$$

It is clearly shown from Table 4 that the shear capacity decreases with the increase of stirrup spacing, but not much impact. Thus, the shear capacity contributed by stirrup  $V_s$  can be defined as

$$V_s = 0.11 f_{yv} \frac{A_{sw}}{s} h, \quad (8)$$

where  $f_{yv}$  is the yield strength of stirrups,  $A_{sw}$  is the area of the stirrups, and  $s$  is the stirrup spacing.

The data obtained in the previous section showed that the steel skeleton web had a noticeable effect on the shear capacity. By studying the law of change and linear fitting, the shear capacity contributed by steel skeleton web  $V_{sw}$  can be estimated as follows:

$$V_{sw} = 0.43 t_w f_w h_w, \quad (9)$$

where  $t_w$  is the web thickness of steel skeleton,  $f_w$  is the yield strength of steel skeleton web, and  $h_w$  is the height of steel skeleton web.

Many scholars have only studied the shear behavior of the steel skeleton web, but not the shear behavior of the steel skeleton flange. According to the results of this study, as a part of the steel skeleton, the steel flange shows relatively good shear resistance. Therefore, shear capacity contributed by steel skeleton flange  $V_f$  cannot be ignored, and it can be estimated exactly as

$$V_f = 0.14 b_f t_f f_{fv}, \quad (10)$$

where  $b_f$  is the width of the steel skeleton flange,  $t_f$  is the thickness of the steel skeleton flange, and  $f_{fv}$  is the yield strength of the steel skeleton flange.

Thus, the shear capacity of SRC deep beams  $V_{cal}$  is expressed as follows:

$$V_{cal} = 1.92 \frac{f_t}{\lambda} b h + 0.11 f_{yv} \frac{A_{sw}}{s} h + 0.43 t_w f_w h_w + 0.14 b_f t_f f_{fv}. \quad (11)$$

**5.2. Verification of the Proposed Method.** The test results of 24 specimens are used to verify the accuracy of the prediction method. These test results are from Chen et al. [11], Deng et al. [24], Wang [25], and Liang [26], respectively. All the specimens are simply supported. Their failure modes are a shear failure and diagonal

TABLE 4: The shear capacity obtained by FEM.

Specimens	Specimen length (mm)	$\lambda$	Width ratio	Height ratio	$f_t$ (MPa)	$\rho$ (%)	Stirrup spacing (mm)	Shear capacity (kN)
SDB-1	860	1.1	0.5	0.6	2.39	1.5	100	421 kN
SDB-2	1020	1.4	0.5	0.6	2.39	1.5	100	387 kN
SDB-3	1200	1.7	0.5	0.6	2.39	1.5	100	346 kN
SDB-4	1350	2	0.5	0.6	2.39	1.5	100	292 kN
SDB-5	1020	1.4	0.33	0.6	2.39	1.5	100	365 kN
SDB-6	1020	1.4	0.42	0.6	2.39	1.5	100	374 kN
SDB-7	1020	1.4	0.58	0.6	2.39	1.5	100	393 kN
SDB-8	1020	1.4	0.67	0.6	2.39	1.5	100	398 kN
SDB-9	1020	1.4	0.5	0.3	2.39	1.5	100	284 kN
SDB-10	1020	1.4	0.5	0.45	2.39	1.5	100	353 kN
SDB-11	1020	1.4	0.5	0.75	2.39	1.5	100	474 kN
SDB-12	1020	1.4	0.5	0.6	2.01	1.5	100	352 kN
SDB-13	1020	1.4	0.5	0.6	2.64	1.5	100	414 kN
SDB-14	1020	1.4	0.5	0.6	2.85	1.5	100	438 kN
SDB-15	1020	1.4	0.5	0.6	2.99	1.5	100	456 kN
SDB-16	1020	1.4	0.5	0.6	2.39	0.5	100	333 kN
SDB-17	1020	1.4	0.5	0.6	2.39	1	100	380 kN
SDB-18	1020	1.4	0.5	0.6	2.39	2	100	390 kN
SDB-19	1020	1.4	0.5	0.6	2.39	1.5	50	393 kN
SDB-20	1020	1.4	0.5	0.6	2.39	1.5	75	389 kN
SDB-21	1020	1.4	0.5	0.6	2.39	1.5	125	382 kN

TABLE 5: Experimental verification.

Data sources	Beam	$\lambda$	$V_{test}$ (kN)	$V_{cal}$ (kN)	$V_{test}/V_{cal}$
This paper	RDB-1	1.1	394	366	1.08
	RDB-2	1.4	341	322	1.06
	RDB-3	1.7	274	294	0.93
	RDB-4	1.1	367	332	1.11
	RDB-5	1.1	313	298	1.05
	RDB-6	1.1	408	376	1.09
	RDB-7	1.1	349	355	0.98
Chen et al. [11]	B-H1	1.04	2423	1998	1.21
	B-H2	1.08	2399	1958	1.23
	BW-H2A	1.11	2281	2134	1.07
	BW-H2B	1.09	2605	2369	1.1
	B-H3	1.11	2109	1890	1.12
Deng et al. [24]	B-H4	1.15	1766	1760	1
	C-1	1	650	578	1.12
	C-1.5	1.5	473	426	1.11
Wang [25]	C-2	2	355	350	1.01
	SBI-1	1	400	358	1.12
	SBI-2	1.5	260	292	0.89
Liang [26]	SBI-3	2	240	259	0.92
	SRC-18	1	475	469	1.01
	SRC-19	1.5	310	356	0.87
	SRC-21	1.5	350	370	0.95
	SRC-22	1.5	345	391	0.88
AVG	SRC-23	1.5	350	336	1.04
	COV				1.04
					0.09

compression failure. The section height of the test piece is 200 mm–550 mm, and there are no shear studs.  $\lambda$  varied from 1 to 2.

Table 5 and Figure 10 compare the tested shear capacity  $V_{test}$  with the calculated shear capacity  $V_{cal}$  of the suggested

method. It can be shown that the calculated results are basically consistent with the experimental. The mean and coefficient of variation are 1.08 and 0.07, respectively. The suggested method can reasonably calculate the shear capacity of SRC deep beams.



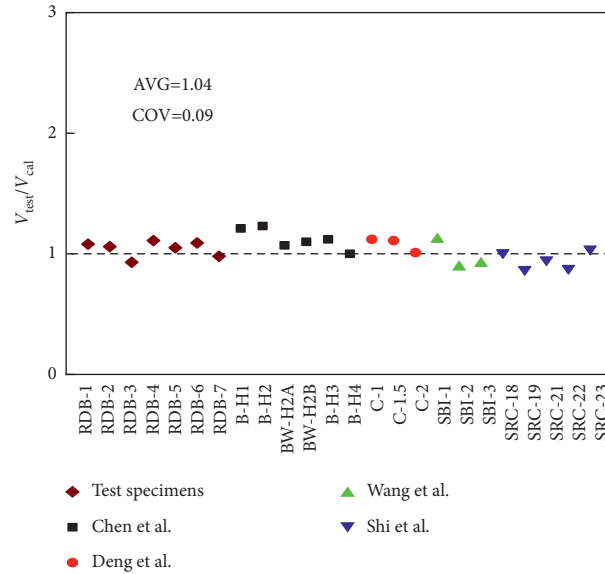


FIGURE 10: Comparison of test values with calculated values.

## 6. Conclusions

The shear behavior and failure modes of SRC deep beams have been studied by experiment and finite element analysis. The DIC technique was used to record the shear cracking response, initial crack load and location, crack pattern, and track the crack development. Furthermore, the FEM was used to research the influence parameters including the concrete tensile strength  $f_b$ , shear span-to-depth ratio  $\lambda$ , stirrup spacing, the longitudinal reinforcement ratio  $\rho$ , flange width of the steel skeleton, and steel skeleton height on the shear capacity. In addition, based on the strength superposition theory, the calculation method was recommended for calculating the shear capacity of SRC deep beams.

When the effects of each investigated parameter on failure modes and the shear capacity of SRC deep beams are evaluated in terms of test results and finite element analysis perspective, the following conclusions are deduced:

- (1) The failure modes of SRC deep beam under concentrated load can be concluded as two forms: hear failure and diagonal compression failure. When  $\lambda$  is less than 1.4, the specimen suffers from diagonal compression failure. When  $\lambda$  is between 1.4 and 2, shear failure occurred
- (2) The DIC technology is proved to be a reliable tool for recording the load at the first crack and track the cracks continuously. Using DIC technology can better understand the shear cracking response and the crack pattern of specimens
- (3) The finite element model analysis can accurately simulate the shear response of SRC deep beams. The shear capacity simulated by the finite element models is consistent with the test results. Excellent similarity in load-displacement curves and the failure mode is recorded between finite element analysis and experiment

- (4) The shear capacity of SRC deep beams is mainly affected by  $\lambda$  and the height of the steel skeleton web. The shear capacity increases with the increase of the height of the steel skeleton web and decreases with the increase of  $\lambda$ . With an average 36% increase in web height, the shear capacity increased by 18.8% on average. Therefore, under the premise of satisfying the specification, increasing the height of the section web can improve the shear capacity of the SRC deep beams
- (5) The proposed calculation method can predict accurate shear strengths of SRC deep beams. A compiled database, which consisted of the 24 SRC deep beams, is used to validate the proposed calculation method. The mean ratio of predicted to tested shear strength and its coefficient of variation is 1.04 and 0.09, respectively.

## Data Availability

The data used to support the findings of this study are available from the corresponding author upon request.

## Conflicts of Interest

The authors declare that there are no conflicts of interest with respect to the research, authorship, and/or publication of this article.

## Acknowledgments

This work was supported by the National Natural Science Foundation of China (No. 51978078) and State Key laboratory of Solid Waste Reuse for Building Materials (Subject No. SWR-2021-010).

## References

- [1] H. Chen, W.-J. Yi, and H.-J. Hwang, "Cracking strut-and-tie model for shear strength evaluation of reinforced concrete deep beams," *Engineering Structures*, vol. 163, pp. 396–408, 2018.
- [2] A. N. Hanoon, M. S. Jaafar, S. R. Al Zaidee, F. Hejazi, and F. N. A. A. Aziz, "Effectiveness factor of the strut-and-tie model for reinforced concrete deep beams strengthened with CFRP sheet," *Journal of Building Engineering*, vol. 12, pp. 8–16, 2017.
- [3] L. Zhou and S. Yi-sheng, "Experimental study on seismic behavior of SRC deep beam-to-CFST column frames," *Journal of Constructional Steel Research*, vol. 155, pp. 157–175, 2019.
- [4] L. Zeng, Y. Xiao, J. Chen, and Y. Chen, "Quasi-static cyclic test on a concrete-encased frame-reinforced concrete tube building model," *Shock and Vibration*, vol. 2018, Article ID 5643872, 14 pages, 2018.
- [5] Y. Xu, H. Zheng, and J. Ma, "Experimental and analytical research on the hysteretic behavior of steel plate deep beams infill steel frame," *Journal of Constructional Steel Research*, vol. 127, pp. 66–76, 2016.
- [6] J. Mo and L. Zeng, "Experimental study on damping properties of rubber powder modified styrene-acrylic emulsion concrete beam," *Journal of Structural Engineering*, vol. 32, Article ID 101728, 2020.
- [7] L. Tong, S. Xiao, L. He, Y. Zhang, and X.-L. Zhao, "Fatigue behavior of steel reinforced concrete (SRC) beams with different shear span-to-depth ratios," *Engineering Structures*, vol. 166, pp. 339–353, 2018.
- [8] L. Zeng, W. Ren, Z. Zou, Y. Chen, W. Xie, and X. Li, "Experimental study on seismic behavior of frame structures composed of concrete encased columns with L-shaped steel section and steel beams," *Earthquakes and structures*, vol. 16, no. 1, pp. 97–107, 2019.
- [9] ACI (American Concrete Institute), "ACI 318-19 & ACI 318R-19: building code requirements for structural concrete and commentary," American Concrete Institute, Farmington Hills, Michigan, USA, 2019.
- [10] W.-Y. Lu, "Shear strength prediction for steel reinforced concrete deep beams," *Journal of Constructional Steel Research*, vol. 62, no. 10, pp. 933–942, 2006.
- [11] C.-C. Chen, K.-T. Lin, and Y.-J. Chen, "Behavior and shear strength of steel Shape reinforced concrete deep beams," *Engineering Structures*, vol. 175, pp. 425–435, 2018.
- [12] British Standards Institution, *Eurocode 2: Design of Concrete Structures: Part 1-1: General Rules and Rules for Buildings*, British Standards Institution, London, UK, 2004.
- [13] S. J. Hwang and H. J. Lee, "Strength prediction for discontinuity regions failing in diagonal compressions by softened strut-and-tie model," *Journal of Structural Engineering*, vol. 128, no. 1519, p. 12, 2002.
- [14] Architectural Institute of Japan, *AIJ Standard for Structural Calculation of Steel Reinforced Concrete Structures*, Architectural Institute of Japan, Tokyo, Japan, 2001.
- [15] JGJ 138-2016, *Code for Design of Composite Structures*, China Architecture and Building press, Beijing, China, 2016.
- [16] C. C. Weng and H. S. Wang, "Shear strength of steel reinforced concrete (SRC) deep beams," *Journal of the Chinese Institute of Civil and Hydraulic Engineering*, vol. 16, no. 3, pp. 403–414, 2004, in Chinese.
- [17] B. V. Mai, C. H. Pham, G. J. Hancock, and G. D. Nguyen, "Block shear strength and behaviour of cold-reduced G450 steel bolted connections using DIC," *Journal of Constructional Steel Research*, vol. 157, pp. 151–160, 2019.
- [18] Z. Huang, Y. Tu, S. Meng, C. Sabau, C. Popescu, and G. Sas, "Experimental study on shear deformation of reinforced concrete beams using digital image correlation," *Engineering Structures*, vol. 181, pp. 670–698, 2019.
- [19] Gb/T 50081, *Standard for Test Methods of concrete Physical and Mechanical Properties*, China Architecture and Building Press, Beijing, China, 2019.
- [20] GB 50010-2010, *Code for Design of concrete Structures*, China Architecture and Building press, Beijing, China, 2015.
- [21] J. Lubliner, J. Oliver, S. Oller, and E. Oñate, "A plastic-damage model for concrete," *International Journal of Solids and Structures*, vol. 25, no. 3, pp. 299–326, 1989.
- [22] J. Lee and G. L. Fenves, "Plastic-damage model for cyclic loading of concrete structures," *Journal of Engineering Mechanics*, vol. 124, no. 8, pp. 892–900, 1998.
- [23] Z. Tao, Z.-B. Wang, and Q. Yu, "Finite element modelling of concrete-filled steel stub columns under axial compression," *Journal of Constructional Steel Research*, vol. 89, pp. 121–131, 2013.
- [24] M. Deng, F. Ma, B. Li, and X. Liang, "Analysis on shear capacity of SRC deep beams based on modified strut-and-tie model," *Engineering Mechanics*, vol. 34, no. 12, pp. 95–103, 2017, in Chinese.
- [25] Z. Wang, *Study on Cracks and Deflections of Steel Reinforced concrete Beams*, Xi'an University of Architecture and Technology, Xi'an, China, 2006, in Chinese.
- [26] S. Liang, *Experimental Study and Theory Analysis on Stiffness and Crack of Steel Reinforced High Strength-High Performance concrete Beams*, Xi'an University of Architecture and Technology, Xi'an, China, 2007, in Chinese.

## Research Article

# Seismic Performance of CFST Frame-Steel Plate Shear Walls Connected to Beams Only

Qin Rong,<sup>1</sup> Zhonghui Zhao,<sup>1</sup> Lanhui Guo,<sup>2</sup> Xiaomeng Hou ,<sup>2</sup> Li Lin ,<sup>1</sup> and Hongtao Bi<sup>1</sup>

<sup>1</sup>School of Architecture and Civil Engineering, Harbin University of Science and Technology, Harbin 150080, China

<sup>2</sup>Key Lab of Structures Dynamic Behavior and Control of the Ministry of Education, Harbin Institute of Technology, Harbin 150090, China

Correspondence should be addressed to Xiaomeng Hou; [houxiaomeng@gmail.com](mailto:houxiaomeng@gmail.com) and Li Lin; [13766899951@163.com](mailto:13766899951@163.com)

Received 12 May 2021; Accepted 4 August 2021; Published 14 August 2021

Academic Editor: Trupti Ranjan Lenka

Copyright © 2021 Qin Rong et al. This is an open access article distributed under the Creative Commons Attribution License, which permits unrestricted use, distribution, and reproduction in any medium, provided the original work is properly cited.

The safety and cost of structures composed of concrete-filled steel tube (CFST) frame-steel plate shear walls (SPSWs) with two-side connections are governed by the seismic performance. The response modification factor  $R$  and displacement amplification factor  $C_d$  are important seismic performance factors. In this paper, nonlinear seismic responses of 10-story, 15-story, and 20-story CFST frame-SPSWs (CFST-SPSWs) are studied. A nonlinear finite element model which includes both material and geometric nonlinearities is developed using the finite element software OpenSees for this study. The accuracy of model was validated by comparing with experimental results. Nonlinear seismic analysis shows that CFST-SPSWs, in high seismic region, behave in a stable and ductile manner. Also,  $R$  and  $C_d$  of CFST-SPSWs were evaluated for the structure models using incremental dynamic analysis (IDA), and the average values of 3.17 and 3.05 are recommended, respectively. The recommended  $R$  value is greater than the value (2.8) in the “Chinese Code for seismic design of buildings” for composite structures, indicating the code is conservative. The structural periods provided by current code are generally lower than the periods calculated by finite element analysis. Research results show that  $R$  and  $C_d$  increase with increasing story number, span number, and structural period. Ductility reduction factor  $R_\mu$  increases with increasing span number and decreasing story number. Overstrength factor  $R_s$  increases with increasing story number and decreasing span number.

## 1. Introduction

Increasing material strength and deformation properties and using composite structures are two effective methods of improving the seismic performance of building structures [1]. Steel plate shear walls with composite columns and infill plates connected only to beams are important types of composite structures with high seismic performance. Current seismic design methods are primarily based on load-carrying capacity. Currently, in order to ensure structures into inelastic phase, seismic action (horizontal base shear) in design is determined by reducing the elastic seismic force using the response modification factor  $R$  for structural seismic acceleration (“moderate earthquake” in Chinese seismic fortification intensity). The  $R$  is governed by structural overstrength performance, ductility, and energy

dissipation. The structural inelastic degree depends directly on a reduced seismic force, and reduction factor values are concerned with seismic action in design. In the performance-based seismic design method, the inelastic response spectrum is widely applied in the displacement-based design method. In this method, the inelastic response spectrum is obtained by using response modification factor to reduce the elastic response spectrum. Therefore, the structural response modification factor is one of the most crucial parameters in structural seismic design.

The structural response modification factor values from various seismic codes around the world are different. In Chinese code, the “General rule for performance-based seismic design of buildings” (CES160:2004) [2] (following shorted form is “General rule”) lists some of the structural response modification factors within a structural system;

however, the “Code for seismic design of buildings” (GB50011-2010) [3] uses information frequently collected during earthquakes to calculate seismic action. The connotative structural response modification factor is 2.8, which neglects the difference between seismic performance and plastic deformation capacity within the system. Structural response modification factor values in American code were studied and compared with Japanese code by Uang [4] and Whittaker et al. [5]. The reinforced concrete structure designed according to EC8 (Eurocode 8: Design of structures for earthquake resistance) was evaluated in terms of behavior coefficient by Elnashai and Broderick [6], who found that the structural behavior coefficient of European code is conservative. The behavior factor of steel frame structure was analyzed by Kim and Choi [7]. The response modification factors of 20 buckling restrained braced frames (BRBFs) and 30 concentric braced frames (CBFs) were evaluated using Pushover analysis [8]. The response modification factors for CBFs were lower than the BRBF values. The response modification factors for CBFs ranged from 4.10 to 6.10 and ranged from 7 to 22 for BRBFs. The response modification factors of BRBFs with type *V*, inverted *V*, diagonal, and split *X* restrained bracing configurations were calculated using OpenSees software [9]. The response modification factors for BRBFs ranged from 7 to 9.4. The response modification factors of steel moment-resisting frames were calculated using different pushover analysis methods [10]. The response modification factors for steel moment-resisting frames ranged from 3.3 to 3.8, and the maximum difference for response modification factors calculated by adaptive pushover analysis (APA) method and conventional pushover analysis (CPA) method was 16%. The response modification factors of *X*-braced steel frames with different boundary conditions were calculated using pushover analysis methods using Sap2000 software [11]. The response modification factors for *X*-braced steel frames ranged from 4.3 to 11. The response modification factors varied with different boundary conditions. The response modification and overstrength factors in moment-resisting steel frames (MRSFs) with added triangular-plate damping and stiffness devices (TADAS) were evaluated using OpenSees software [12]. The response modification factors for MRSFs with TADAS were 15.9, and the factors for MRSFs with TADAS were greater than the MRSFs values. The response modification of steel slit panel-frames was evaluated using pushover analysis and nonlinear incremental dynamic analysis (NIDA) [13]. The response modification factors for steel slit panel-frames ranged from 6.14 to 8.11. The response modification factors calculated using pushover analysis are smaller than those derived from NIDA.

Apart from the steel structures [14, 15], the response modification factors of reinforced concrete structures were also investigated [16–19]. The response modification of reinforced concrete frames was evaluated using incremental dynamic analysis (IDA) [20]. The response modification factors  $R=6$  satisfied the expected safety level-against earthquake-induced collapse. The  $R=3$  value in current Chinese codes [2] is conservative for RC frames. The seismic behavior and failure mechanism of elevated concrete tanks

with shaft and frame staging were evaluated using finite element (FE) modeling [21]. The response modification factors for elevated concrete tanks were 1.5–3, less than the recommended value of 3 by ACI 371R-08 [22]. The values of structural response modification factors for a reinforced concrete frame structure were evaluated based on Indian code by Mondal et al. [23]. The value in Indian code was greater than the actual value, meaning that the code was not safe.

Cyclic loading tests on four steel frames assembled with concrete-filled steel tubular (CFST)-bordered composite walls were conducted by Cao et al. [24]. Test results showed that the seismic performance of steel frame was improved by CFST-bordered composite wall. As compared with steel frame, the displacement ductility factor of steel frame CFST-bordered composite wall was reduced from 2.6–3.4 to 1.3–1.8. This is mainly because with the increase in steel ratio, the increase in the damage displacement is lower than that of yield displacement. Five steel-concrete-steel composite shear walls with J hook connectors (SCSSWJ) and boundary CFST columns under cyclic loading were conducted by Yan et al. [25]. Test results showed that the failure mode of SCSSWJs was flexure, which indicated the SCSSWJs exhibit good seismic performance.

Recently, our research group conducted seismic behavior tests on steel plate shear walls (SPSWs) and concrete filled steel tube (CFST) columns [26, 27]. The SPSWs exhibited acceptable hysteretic responses under cyclic loading. Literature review shows that the structural response modification factors of reinforced concrete and steel frame structure were studied. However, the research regarding the CFST frame-SPSW response modification factor was limited [28, 29]. To answer this question, the seismic performance of CFST frame-SPSWs is evaluated using the IDA method in this paper. Evaluating structural response modification factor systematically in a composite structural system of CFST frame-SPSWs will improve the seismic design and economy of engineering structures. The influence of story number, span number, and structural period on structural response modification factor  $R$ , ductility reduction factor  $R_{\mu}$ , overstrength factor  $R_s$ , and displacement amplification factor  $C_d$  is analyzed. The reasonable values are presented for the CFST frame-SPSWs to provide a base value for the corresponding code.

## 2. CFST Frame-SPSWs Modeling

In order to evaluate the response modification factor  $R$ , ductility reduction factor  $R_{\mu}$ , overstrength factor  $R_s$ , and displacement amplification factor  $C_d$ , CFST frame-SPSWs models were built using OpenSees.

*2.1. Definition of Structural Response Modification Factor  $R$ .*  $R$  is the ratio of the minimum strength to designed strength required to keep a structure fully elastic during a moderate earthquake. This coefficient is concerned with ductility and energy dissipation capacity, and it is an important coefficient for structural seismic design.  $C_d$  is the ratio between the

maximum elastic-plastic deformation and displacement calculated by elastic analysis according to the reduced seismic effect at the same intensity level during a moderate earthquake. Using the displacement amplification factor, the largest inelastic displacement of the structure can be estimated by determining the elastic displacement generated by seismic action.

The elastic-plastic deformation of a structure during an earthquake is shown in Figure 1. The nonlinear curve is simplified using a bilinear elastic-plastic curve. The structural response modification factor  $R$  and displacement amplification factor  $C_d$  are calculated as follows:

$$\begin{aligned} R &= \frac{V_e}{V_d} \\ &= \frac{V_e}{V_y} \frac{V_y}{V_d} \\ &= R_\mu R_s, \\ C_d &= \frac{\Delta_{\max}}{\Delta_d}. \end{aligned} \quad (1)$$

In formula (1),  $V_e$  is the maximum base shear when the structure remains completely elastic under moderate earthquake;  $V_y$  is the base shear when the structure yields;  $V_d$  is the designed base shear;  $\Delta_d$  is the top horizontal displacement related to the designed base shear;  $\Delta_y$  is the top horizontal displacement when the structure yields;  $\Delta_{\max}$  is the maximum top horizontal displacement of the structure during a moderate earthquake;  $R_\mu$  is the structural ductility reduction factor; and  $R_s$  is structural overstrength factor.

**2.2. Structural Response Modification Factor Modeling Process.** The process for calculating the structural response modification factor  $R$  and displacement amplification factor  $C_d$  of the CFST frame-SPSWs using IDA is as follows:

- (1) The structural analysis model was designed, and the corresponding design-based shear  $V_d$  is solved according to the current domestic design code. The base shear method was used to analyze structures less than 40 m in height, and the mode decomposition method is used to analyze structures greater than 40 m in height.
- (2) The CFST frame-SPSWs analysis model was built by using the finite software OpenSees based on the equivalent bars model of steel plate shear walls. Using the IDA method, the seismic response of real structures under the action of one artificial wave and multiple natural ground shocks was analyzed. The maximum base shear, top displacement, and inter-story drift of the structure under different seismic levels were obtained by constantly adjusting the acceleration amplitude to analyze IDA. The curve of maximum base shear and top displacement under varying seismic was drawn and analyzed.

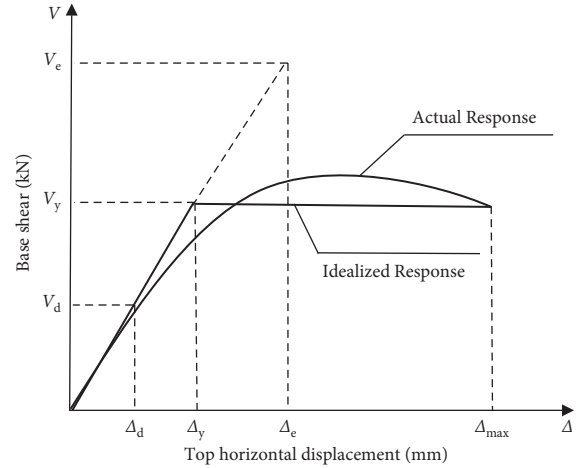


FIGURE 1: General structural response.

- (3) Adjusting seismic peak acceleration of earthquake waves to the peak seismic acceleration under fortification seismic and conducting the time-history analysis of elastic structures, the maximum base shear  $V_e$  of elastic structures under fortification seismic was calculated. Then, structural response modification factor  $R$  was calculated according to the ratio of maximum base shear  $V_e$  to designed base shear  $V_d$ .
- (4) Adjusting seismic peak acceleration to seismic fortification peak acceleration can get the maximum top displacement of the structure. According to the ratio of  $\Delta_{\max}$  to the design top displacement  $\Delta_d$  of the elastic structure, the displacement amplification factor  $C_d$  could be calculated during various amounts of ground shaking. The average value of  $C_d$  is used as the analysis result.

### 3. Modeling and Validation of CFST Frame-SPSWs Using the Equivalent Bars Model

To simplify the CFST frame-SPSWs model, the steel plate shear walls can be considered as the equivalent bars model. Steel plate shear walls and equivalent bars provide the same shear force capacity and same horizontal stiffness. The SPSWs with two-side connections are regarded as bidirectional crossbar. The specifics of the methods can be found in [28]. The analytical model of the CFST frame-SPSWs composite structure with two-side connections was developed using the finite element software OpenSees. The core concrete [29, 30] was simulated using the Concrete02 model based on Kent–Scott–Park provided in OpenSees. The stress-strain relationship was confirmed using a concrete constitutive model under axial compression and bending. Steel tubes and beams were modeled using the Steel02 model based on Giuffrè–Menegotto–Pinto in OpenSees [31]. The Bauschinger effect can also be considered using the Steel02 model. The softening rate from elastic to plastic phase in this model is  $R_0=18$ ,  $a_1=0.925$ , and  $a_2=0.15$ , respectively. Compressive and tensional yield stresses were considered

equal to steel yield stress. The nonlinear beam-column element and fiber sections were used to simulate the CFST columns and steel beams. This element considers some characteristics like plastic, stress strengthening, large strain, and large deformation. Steel02 material with 2% strain-hardening is used for these fibers.

The nonlinear beam-column element was used to simulate the CFST columns and steel beams. This element considers some characteristics like plastic, stress strengthening, large strain, and large deformation. The simplified bar model was adopted to simulate SPSWs with two-side connections, which allowed for the use of a shell element. The disadvantages of large amount of calculation and difficult in convergence can be avoided. This model uses two crossed steel bars to simulate the performance of SPSWs with two-side connections, and the two crossed steel bars have the same SPSWs hysteretic model under the tensile and compressive load. The two crossed steel bars were simulated using the Truss element in OpenSees, and the *hysteretic uniaxial* material is used to define the tension and compressive properties of simplified bars. The crossed steel bars hysteretic model was determined using SPSWs hysteretic curves with characteristic points on corresponding skeleton curves and damage factors. The damage parameters “*damage1*” and “*damage2*” represent the damage of the material in every consecutive cycle in terms of ductility and energy, respectively. These parameters are considered as 0.005 and 0.01. The hysteretic uniaxial material also requires inputting the pinching parameters ‘*pinchx*’ and ‘*pinchy*,’ which was defined as follows [29]:

$$\begin{aligned} \text{pinchy} &= 0.07 \ln\left(\frac{L}{H}\right) - 0.11 \ln(\lambda) + 0.8, \\ \text{pinchx} &= 1.20\left(\frac{\lambda}{100}\right)^{0.44} - 0.17\left(\frac{\lambda}{100}\right) - 0.98, \end{aligned} \quad (2)$$

where  $L$  is the length of SPSW,  $H$  is the height of SPSW, and  $\lambda$  is the height-to-thickness ratio of SPSW.

The hysteretic performance tests of CFST frame-SPSW (specimens F2SW) and CFST frame (specimen CFST) conducted in Ref [26] were selected to validate the numerical model. The dimensions of specimens are shown in Table 1. The thickness and width,  $t$  and  $L_1$ , of SPSW are 3 mm and 1100 mm, respectively. The measured yield strength and tensile strength of steel are 290 MPa and 421 MPa, respectively. By conducting the same loading as experiment as in the model, the calculated shear force at the F2SW and CFST base columns can be obtained. The comparison of hysteretic curves for F2SW and CFST obtained from the experiment by Guo et al. [26] and the simulations from this study are shown in Figure 2. The stiffness of loading and unloading in the hysteretic curve seems credible as the calculated curves and test curves are consistent. The measured peak load is slightly greater than the calculated peak load. In order to enhance the connection of steel beams and shear walls, each steel plate was attached to beams of the boundary frame through 6 mm thick fishplates. Length of each fishplate was the same as that of the infill plate. In the finite element model, the contribution of the fishtail plate is difficult to simulate. Hence, the

load-carrying capacity in the experiment is slightly greater. To summarize, the finite element model can analyze the hysteretic performance under cyclic load of the CFST frame-SPSWs.

#### 4. Evaluating Structural Seismic Performance Using the IDA Method

In this study, the numerical model developed in Section 2 was used to evaluate the structural seismic performance of CFST frame-SPSWs. Six planar structural models were designed with 10, 15, and 20 stories, respectively, and the influence of story number, span number, and structural period on the structural response modification factor  $R$  is studied. These buildings are located in 9 seismic precautionary intensity zone, and designed basis seismic acceleration is 0.4g. In addition, using Chinese code [2], these buildings’ site classifications were selected as class 2, and their earthquake classification was selected as group one. Each model’s height and span are 3.6 m and 6m, with the span numbers of 3 and 5, respectively. In addition, SPSWs were designed with the span-to-depth ratio of 1.0 and were settled at the midspan of the frame. The steel of the SPSW is Q235, and the steel of the frame beams and CFSTs is Q345. Q235 and Q345 mean that the standard yield strength of steel is 235 MPa and 345 MPa, respectively, as per the Standard for design of steel structures (GB 50017-2017). The core concrete grade in the steel-tube columns is C50 (compressive strength design value of 23.1 MPa). The floors are east-in-place reinforced concrete with a thickness of 100 mm and concrete grade of C30 (compressive strength design value of 14.3 MPa). C50 and C30 mean that the standard cube compressive strength of concrete is 30 MPa and 50 MPa, respectively, as per the Code for design of concrete structures (GB50010-2010).

The dead load of floor and roof is 4.2 kN/m<sup>2</sup> and 4.6 kN/m<sup>2</sup>, respectively. The live load is 2 kN/m<sup>2</sup>. The dead load and live load are calculated according to load code for the design of building structures (GB50009-2012). The frames were designed according to the “Code for seismic design of buildings,” and the cross section dimensions are listed in Table 2.

By comparing the acceleration response spectrum in seismic records with Chinese code, 8 seismic records including 7 ground motion records and 1 artificial seismic wave were selected from the 22 available long field ground motion records, which are recommended in FEMA P695. According to the spectrum characteristics, amplitude, and duration of seismic records, the selected seismic records are similar to the site design spectrum, and the 8 seismic records are selected. The 8 seismic records (as listed in Table 3) were used in CFST frame-SPSWs seismic response evaluation using the IDA method. The peak accelerations of seismic records are amplified or reduced in proportion to ensure that the adjusted peak accelerations of seismic records satisfy the requirements of the highest value of acceleration time-history curves under the corresponding seismic levels in Chinese code. Using this method, only the highest value in the seismic response spectrum is changed but the spectral characteristics remain the same.

TABLE 1: Dimension of specimens.

$H$ (mm)	$L$ (mm)	$L_1$ (mm)	$t$ (mm)	$D \times t$ (mm)	Middle beam (mm)	Top and bottom beam (mm)
1500	2000	1100	3	$219 \times 4$	$H194 \times 150 \times 6 \times 9$	$H300 \times 150 \times 6 \times 9$

Note. The Chinese designation of  $H$  shapes corresponds to the United States designation of  $W$  shapes and reflects member depth, width, web thickness, and flange thickness (unit in mm), respectively. The columns were CFSTs, the steel tube with a diameter of  $D$  and depth of  $t$  (unit in mm).

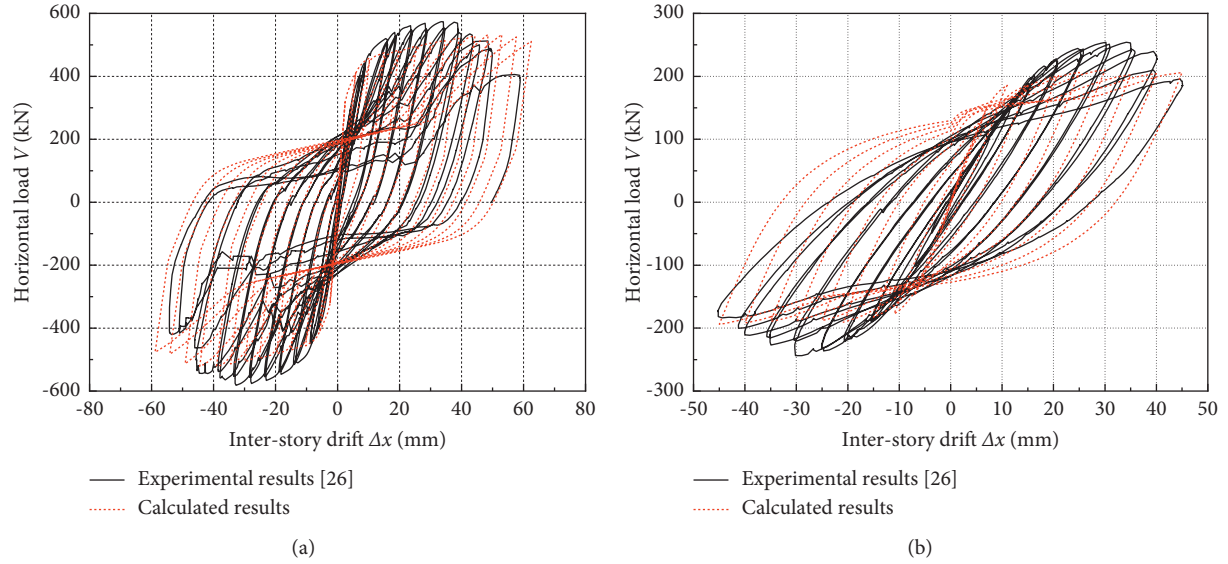


FIGURE 2: Comparison of experimental and calculated results: (a) specimen F2SW; (b) specimen CFST.

TABLE 2: Model dimensions.

Model number	Floor number	Column $D \times t$ (mm)	Beam (mm)	Steel plate depth (mm)
M-10-3	1-3	$450 \times 10$	$H500 \times 300 \times 11 \times 15$	8
M-10-5	4-6	$400 \times 9$	$H600 \times 300 \times 12 \times 20$ (HBE)	6
	7-10	$350 \times 8$		6
M-15-3	1-5	$500 \times 12$	$H500 \times 300 \times 11 \times 15$	10
M-15-5	5-10	$450 \times 10$	$H600 \times 300 \times 12 \times 20$ (HBE)	8
	11-15	$400 \times 9$		6
M-20-3	1-5	$600 \times 16$	$H500 \times 300 \times 11 \times 15$	12
	6-10	$550 \times 15$		10
M-20-5	11-15	$500 \times 12$	$H600 \times 300 \times 12 \times 20$ (HBE)	8
	16-20	$450 \times 10$		6

Note. Six planar structural models were designed with 10, 15, and 20 stories. The M-10-3 means the model has 10 stories and 3 spans. The HBE is horizontal boundary elements connected to shear walls. The beams were  $H$ -shaped steels and reflect member depth, width, web thickness, and flange thickness (unit in mm), respectively. The columns were CFSTs, and the steel tubes reflect diameter of  $D$  and depth of  $t$  (unit in mm).

TABLE 3: Information from the selected earthquake records.

Number	Level	Year	Name	Recording station
GM1	6.5	1979	Imperial Valley	Delta
GM2	6.5	1979	Imperial Valley	EI Centro Array #11
GM3	6.9	1989	Loma Prieta	Capitola
GM4	6.9	1989	Loma Prieta	Gilroy Array #3
GM5	7.4	1990	Manjil, Iran	Abbar
GM6	7.0	1992	Cape Mendocino	Rio Dell Overpass
GM7	6.6	1971	San Fernando	LA-Hollywood Stor Lot,090
GM8			Artificial waves	

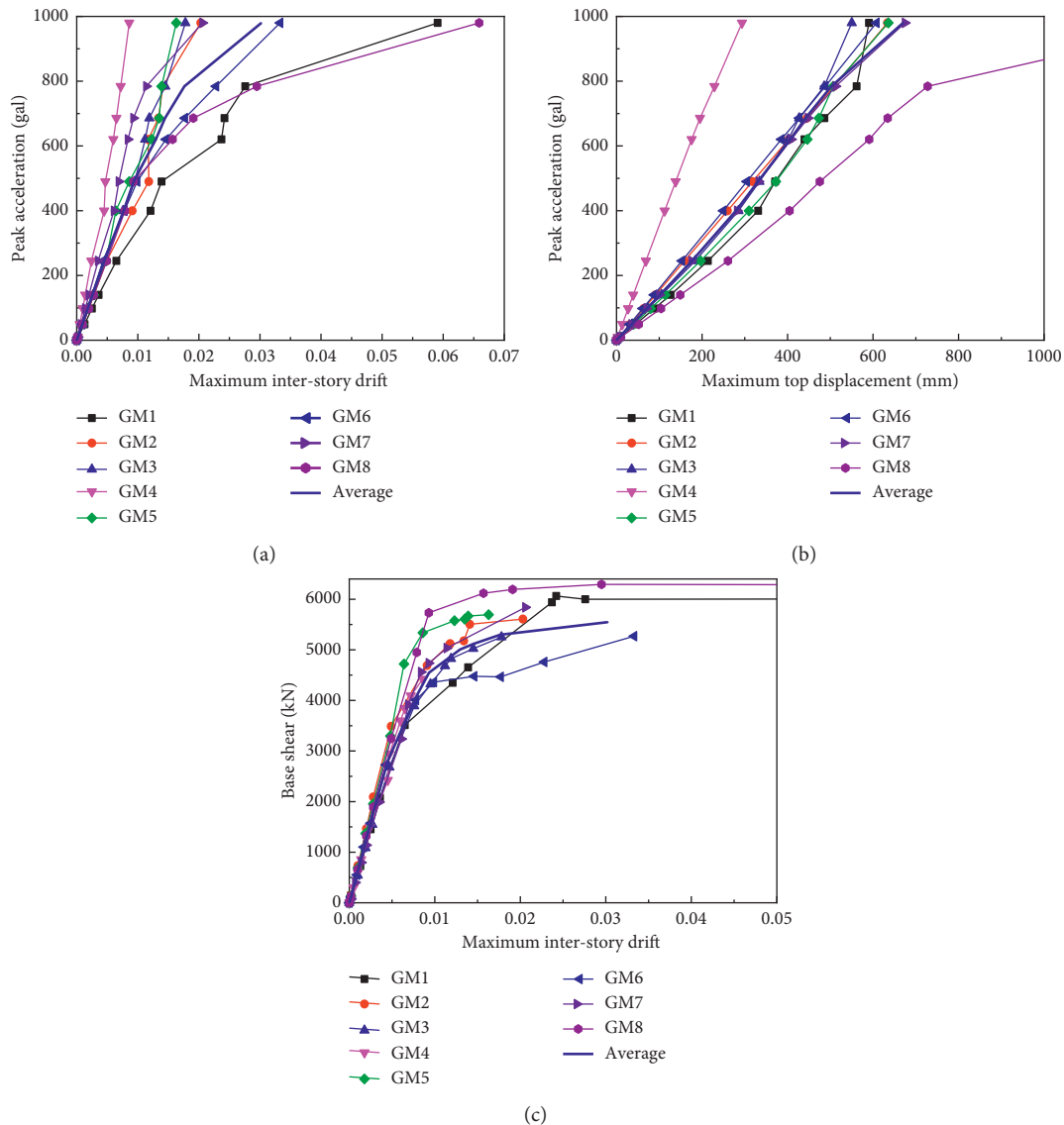


FIGURE 3: Capacity envelopes of structure: (a) maximum interstory drift; (b) maximum top displacement; (c) base shear-maximum interstory drift curves.

**4.1. Capacity Curves of Model M-20-5.** In the 8 selected seismic records, peak acceleration increased to 1.0 g, and the capacity curves of model M-20-5 were analyzed using the IDA method in OpenSees. The capacity curves of M-20-5 under different ground motions are shown in Figure 3. The structural response increases gradually with increasing peak acceleration. Even when the acceleration is greater than the corresponding acceleration in the number 9 seismic fortification zone (the design basic acceleration is 0.4 g), the structure maintains good seismic performance.

Peak acceleration reaches 0.8 g under the artificial seismic curve and GM1, and story displacement angle increases rapidly, indicating the structure will collapse. Under other seismic curves, when the peak acceleration reaches approximately 1000 gal, the structure maintains good seismic performance; hence, the anticollapse capacity of M-20-5 is 800 gal.

**4.2. Distribution of Interstory Drift.** The envelope of inter-story drift of M-20-5 under frequently occurring, moderate, and rare earthquakes is shown in Figure 4. The change of structural maximum interstory drift under frequently occurring earthquakes for varying height of structure is small (maximum interstory drift is less than 4/1000). The average value in this situation is 0.26%, and the average value of maximum interstory drift during a moderate earthquake is 0.77%. The average value of maximum interstory drift during a rare earthquake is 1.3%. The model maximum interstory drift under frequently occurring and rare earthquakes can satisfy deformation requirement for elastic and elastic-plastic in the “Code for seismic design of buildings,” which is less than 1/300 and 1/50, respectively. It also satisfies the requirement for moderate earthquake fortification standards (0.004  $h$ –0.008  $h$ ) ( $h$  is story height) in the “General rule.”



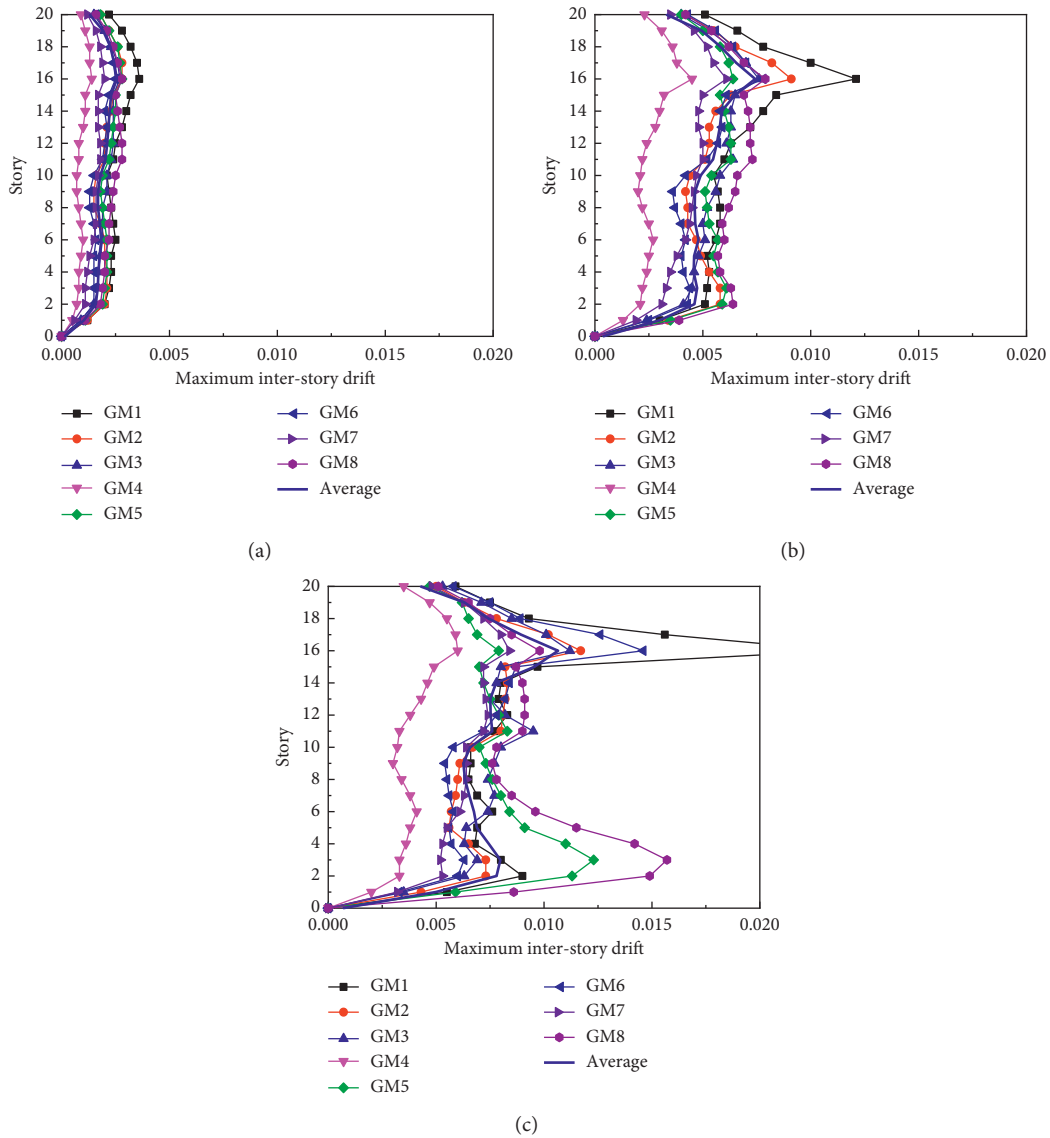


FIGURE 4: The maximum interstory drift with height of the structure under different seismic waves: (a) frequently occurring earthquake; (b) moderate earthquake; (c) rare earthquake.

Furthermore, the structural maximum interstory drift under frequently occurring and moderate earthquakes changes inconspicuously with height; however, these changes are significant in the bottom and middle-upper sections during rare earthquakes. The maximum interstory drift occurs at the 16th floor primarily because the structural members dimension as well as the stiffness is reduced at this floor. Under frequently occurring earthquakes, the structure is completely elastic, and under moderate earthquakes, the steel plates, acting as energy dissipation elements, yielded first and become plastic hinges to consume energy. In addition, the steel plates also absorb earthquake energy and prevent structural failure. Under rare earthquakes, numerous SPSWs and frame beams yielded to form plastic hinges; however, the structure does not collapse. After yielding, the maximum interstory drift decreased with increasing peak acceleration

primarily because the location and order of structural plastic hinge change after the peak acceleration, resulting in internal force redistribution and changing the structure force transfer paths (Figure 4(a)). All of these research results show that CFST frame-SPSWs exhibit good seismic capacity.

4.3. *Analysis of Structural Capacity Curve.* The 8 capacity curves of maximum interstory drift-base shear for different models under ground motion are shown in Figure 5. The structural seismic response on elastic phase under different ground motions is close to each other (Figure 5). Shear force increases with increasing peak acceleration until the structure yielded into the elastic-plastic phase. Then, the difference in structural response under different ground motions is larger, and the average values from the seismic

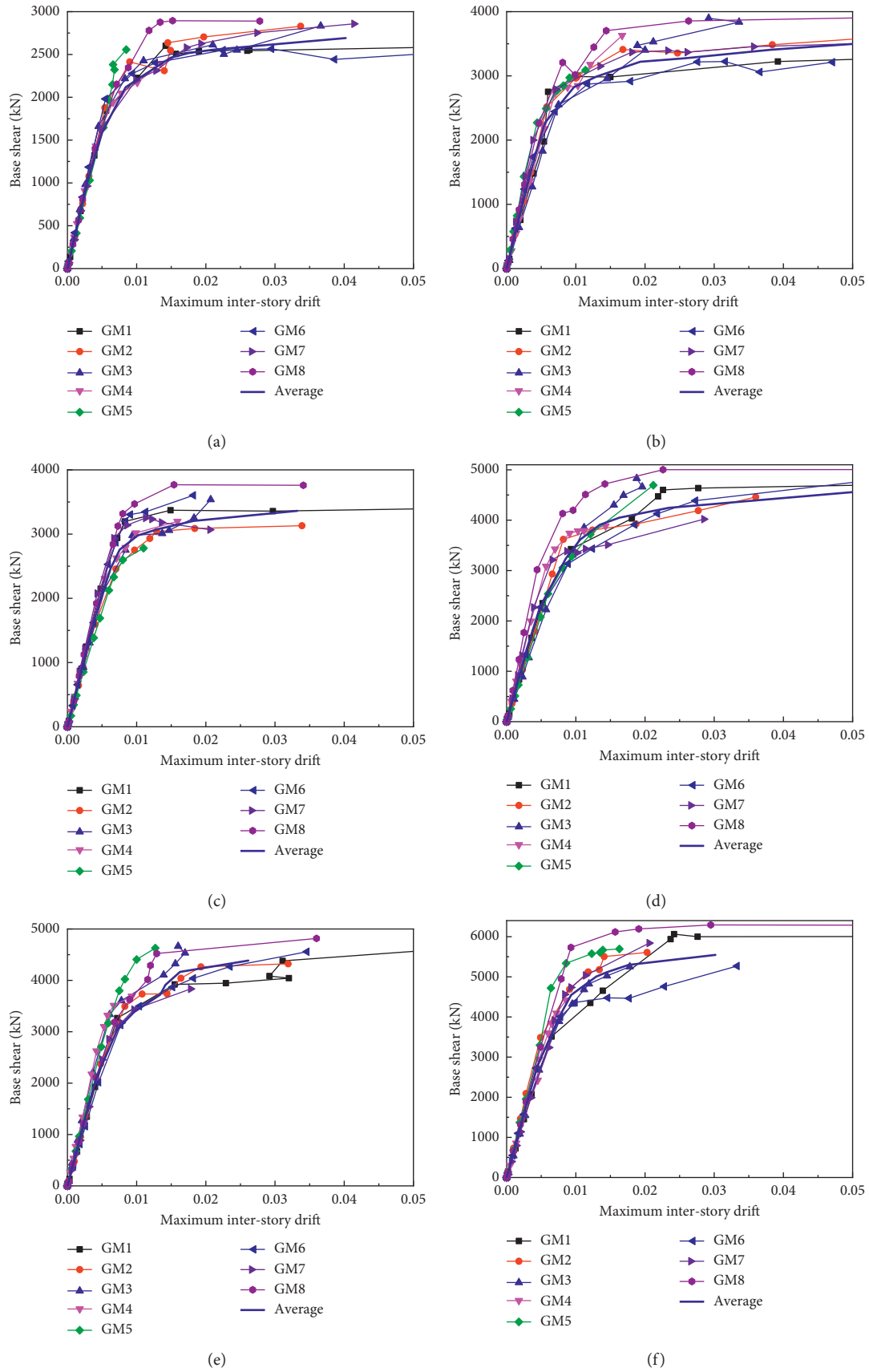
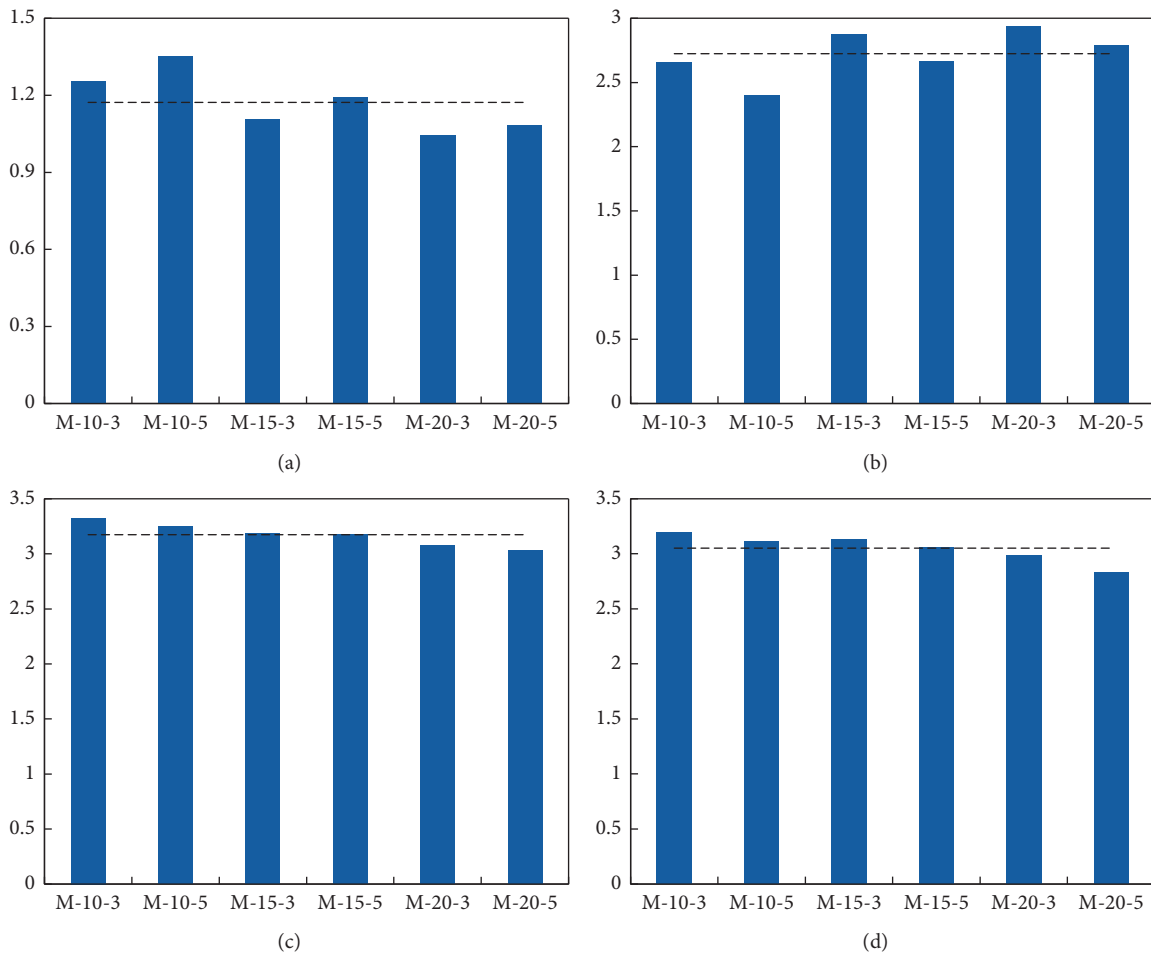


FIGURE 5: Capacity envelopes of structures for a 9 seismic intensity: (a) Model M-10-3; (b) Model M-10-5; (c) Model M-15-3; (d) Model M-15-5; (e) Model M-20-3; (f) Model M-20-5.

TABLE 4: Structural performance factors.

Model number	Structural basis period T/s	Structural ductility reduction factor $R_\mu$	Structural overstrength factor $R_s$	Structural response modification factor $R$	Displacement amplification factor $C_d$
M-10-3	1.06	1.254	2.660	3.326	3.194
M-10-5	1.25	1.352	2.402	3.248	3.117
M-15-3	1.57	1.106	2.881	3.187	3.129
M-15-5	1.79	1.192	2.669	3.180	3.056
M-20-3	1.99	1.046	2.938	3.073	2.988
M-20-5	2.19	1.084	2.794	3.029	2.826
Average		1.172	2.724	3.174	3.052
Standard deviation		0.106	0.176	0.098	0.119
Variation coefficient		0.090	0.065	0.031	0.039

FIGURE 6: Structural performance factors: (a) structural ductility reduction factor  $R_\mu$ ; (b) structural overstrength factor  $R_s$ ; (c) structural response modification factor  $R$ ; (d) displacement amplification factor  $C_d$ .

records are adopted to reveal the structural performance. Although the seismic peak acceleration increased to 1.0 g, the structural maximum interstory drift is still less than 2% under the partial ground motions. Results show that CFST frame-SPSWs exhibit good seismic performance, and the structural seismic response is relatively large under the artificial seismic waves. When the peak acceleration increases to 0.8 g, interstory drift increases rapidly, and the

structural anticollapse capacity reaches approximately 800 gal.

## 5. Analysis of Structural Performance Coefficient

For each model, the calculated results  $R$ ,  $R_\mu$ ,  $R_s$ , and  $C_d$  are listed in Table 4. The comparison of structural performance

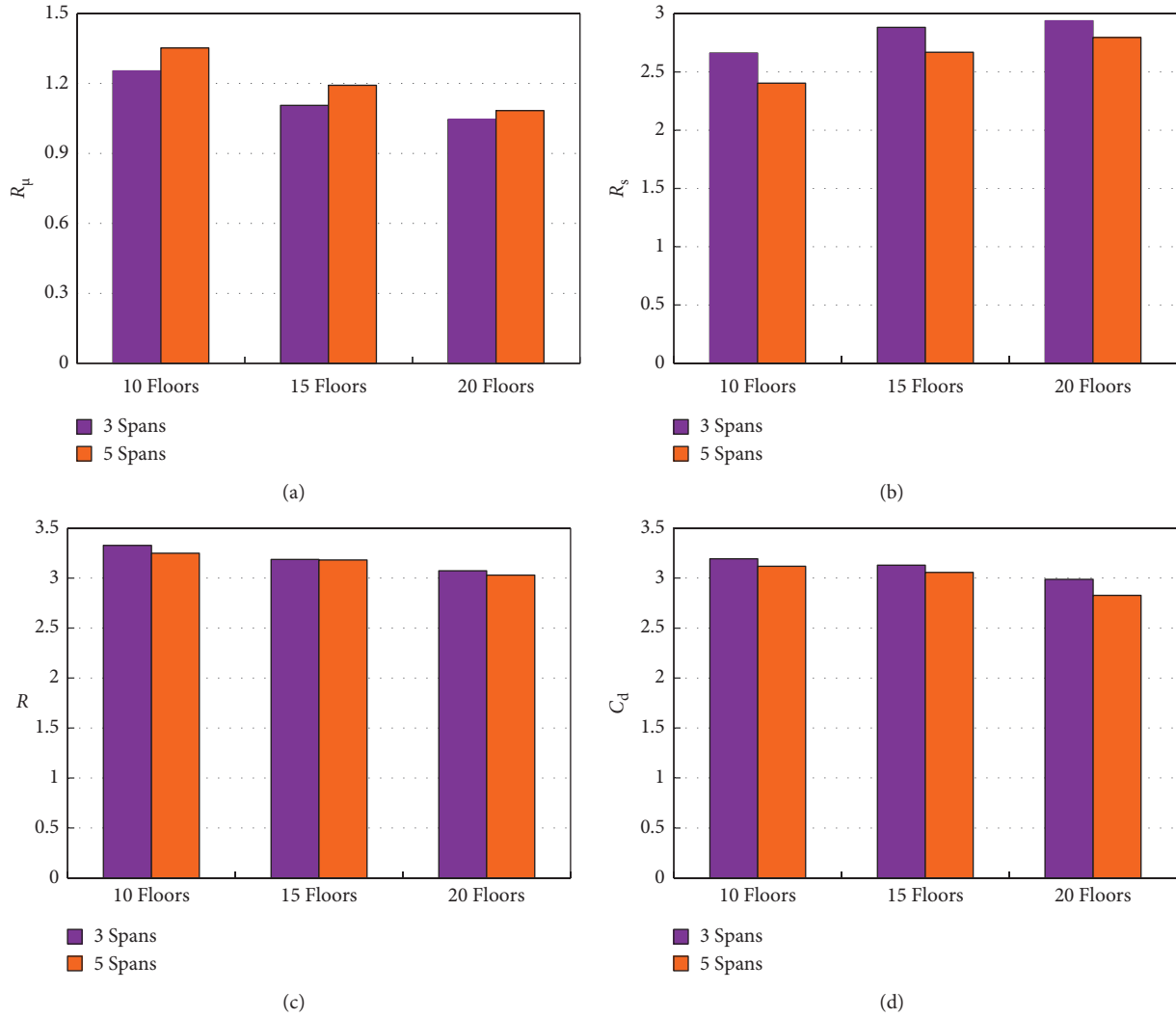


FIGURE 7: Influence of span number on structural performance factors: (a) structural ductility reduction factor  $R_{\mu}$ ; (b) structural over-strength factor  $R_s$ ; (c) structural response modification factor  $R$ ; (d) displacement amplification factor  $C_d$ .

coefficients and their corresponding calculated average values is shown in Figure 6.

The structural performance coefficient changes with changing story number, span number, and structural period (Figure 6). For the models in this contribution, the average values of  $R$ ,  $R_{\mu}$ ,  $R_s$ , and  $C_d$  are 3.194, 1.172, 2.274, and 3.052, respectively. The Chinese “Code for seismic design of buildings” implies that the structural response modification factor is 2.81. The structural response modification factor and displacement amplification factor of CFST frame-SPSW are regulated the same as concrete frame in the “General rule,” and their values are 2.63 and 2.2, respectively. The CFST frames-SPSWs have a good seismic performance, and the structural performance coefficient currently used in Chinese code is conservative. This contribution can offer some reasonable suggestions regarding the design and research on some performance coefficients and structural response modification factors. If this result,  $R$  is 3.194, is adopted, the designed seismic action will decrease 12%

compared with the “Code for seismic design of buildings.” Compared with the “General rule,” the designed action will decrease 17.7%.

**5.1. Influence of Period.** The influence of structural period on structural ductility reduction factor  $R_{\mu}$ , structural over-strength factor  $R_s$ , structural response modification factor  $R$ , and displacement amplification factor  $C_d$  is shown in Figure 6. As the number of spans and floors of the structure increases, the period of the structure keeps increasing, but for  $R_{\mu}$  and  $R_s$ , this phenomenon is not significant (Table 4). In addition,  $R$  and  $C_d$  decrease slightly with increasing structural period.

**5.2. Influence of Span Number.** The influence of span number on  $R_{\mu}$ ,  $R_s$ ,  $R$ , and  $C_d$  is shown in Figure 7.  $R_{\mu}$  increases with increasing span number, but the extent decreases gradually with increasing structural height.  $R_s$  decreases with

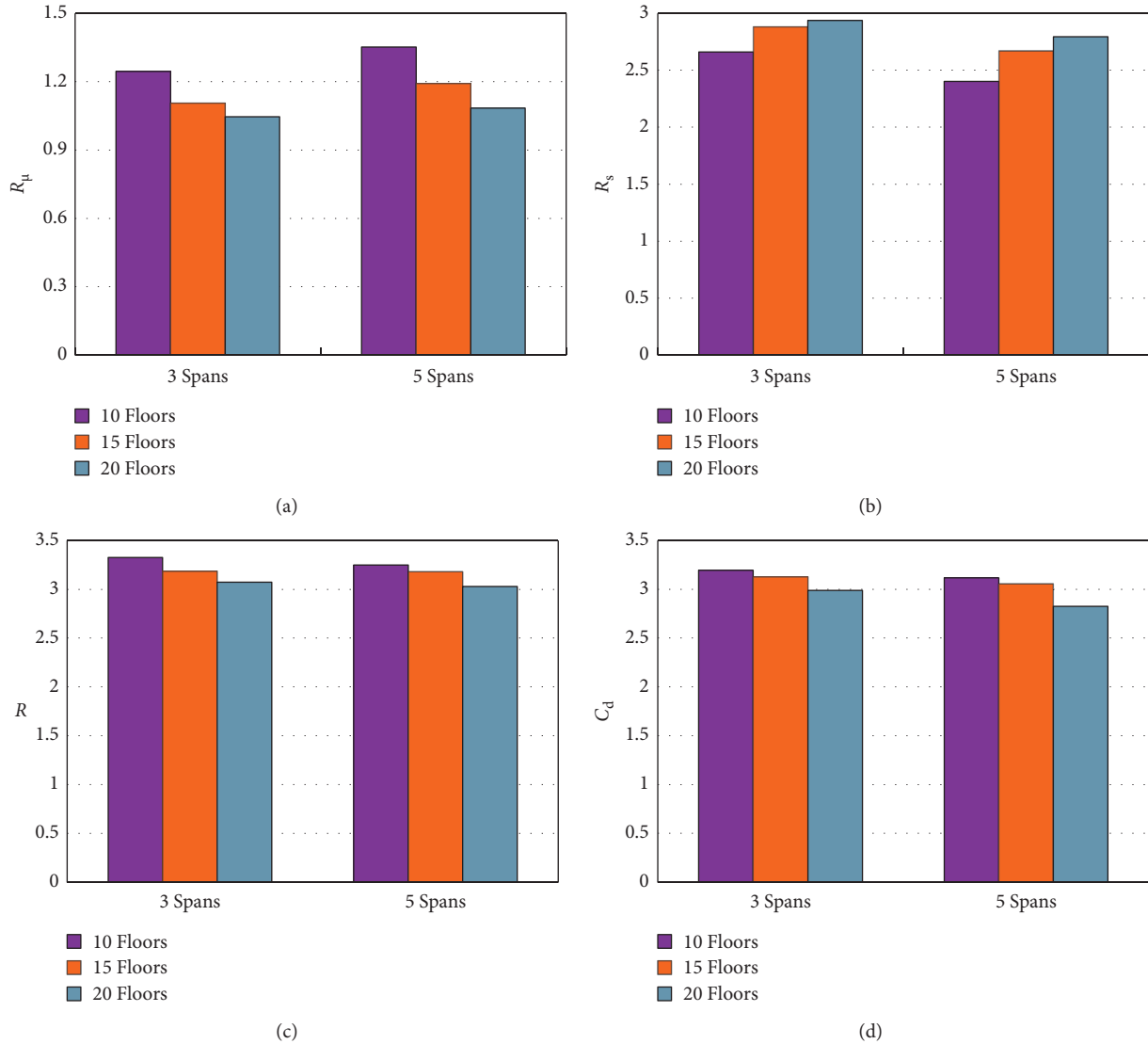


FIGURE 8: Influence of story number on structural performance factors: (a) structural ductility reduction factor  $R_\mu$ ; (b) structural over-strength factor  $R_s$ ; (c) structural response modification factor  $R$ ; (d) displacement amplification factor  $C_d$ .

increasing span number, but this trend still decreases with increasing structural height. Both  $R$  and  $R_s$  decrease with increasing span number, and the maximum variable magnitude is 5%, indicating that there is a minor influence between span number and structural performance coefficients within a given period.

**5.3. Influence of Story Number.** The influence of story number on  $R_\mu$ ,  $R_s$ ,  $R$ , and  $C_d$  is shown in Figure 8.  $R_\mu$ ,  $R$ , and  $C_d$  decrease with increasing story number, and  $R_s$  increases with increasing story number. This trend decreases gradually with increasing structural height for all 4 of these coefficients.

## 6. Conclusions

The nonlinear finite element software OpenSees is adopted to develop the model for CFST frame-SPSWs connected with beams only. These models evaluate structural seismic

performance using the IDA method and analyze governing factors, such as  $R$  and  $C_d$ . The following conclusions can be drawn:

- (1) The SPSWs as energy dissipation elements yielded firstly to form plastic hinges under moderate earthquakes. In addition, most SPSWs and frame beams yielded under rare earthquakes, but the structure is not collapse.
- (2)  $R$  and  $C_d$  decrease gradually with increasing story number, span number, and structural period.  $R_\mu$  increases with increasing span number but decreases with increasing story number.  $R_s$  decreases with increasing span number but increases with increasing story number.
- (3) The obtained overstrength factor  $R_s$  and structural ductility reduction factor  $R_\mu$  of CFST frame-SPSWs are 2.72 and 1.17, respectively.

- (4) The recommended value of response modification factor and displacement amplification factor for CFST frame-SPSWs is 3.17 and 3.05, respectively. The recommended  $R$  is greater than the value (2.8) in the “Chinese Code for seismic design of buildings” for composite structures, which indicates the code is conservative.

## Nomenclature

$C_d$ :	Displacement amplification factor
$R$ :	Response modification factor
$R_\mu$ :	Ductility reduction factor
$R_s$ :	Overstrength factor
$T$ :	Structural basis period
$V_d$ :	Designed base shear
$V_e$ :	Maximum base shear when the structure remains completely elastic under moderate earthquake
$V_y$ :	Base shear when the structure yields
$\Delta_{\max}$ :	Maximum top horizontal displacement of the structure during a moderate earthquake
$\Delta_d$ :	Top horizontal displacement related to the designed base shear
$\Delta_y$ :	Top horizontal displacement when the structure yields.

## Data Availability

The data used to support this study are available upon request to the corresponding author (e-mail: houxiaomeng@gmail.com).

## Conflicts of Interest

The authors declare that there are no conflicts of interest.

## Authors' Contributions

Qin Rong investigated the study, developed the methodology, provided software, performed formal analysis, wrote original draft, and reviewed and edited the manuscript. Zhonghui Zhao investigated the study and reviewed and edited the manuscript. Lanhui Guo investigated the study and reviewed and edited the manuscript. Xiaomeng Hou developed the methodology, performed formal analysis, reviewed and edited the manuscript, and was responsible for funding acquisition. Li Lin reviewed and edited the manuscript. Hongtao Bi investigated the study and reviewed and edited the manuscript.

## Acknowledgments

This contribution was supported by the National Natural Science Foundation of China (No. 52078169), Excellent Youth Foundation of Heilongjiang Province (No. YQ2019E028), Outstanding Young Talents Project of Harbin University of Science and Technology (No. LGYC2018JQ018), and University Nursing Program for Young Scholars with Creative Talents in Heilongjiang Province (No. 8607-324018601).

## References

- [1] Q. Rong, X. M. Hou, and C. Ge, “Quantifying curing and composition effects on compressive and tensile strength of 160–250 MPa RPC,” *Construction and Building Materials*, vol. 241, Article ID 117987, 2020.
- [2] Association Standard of Engineering Construction Standardization of China, *CECS 160:2004 General Rule for Performance-Based Seismic Design of Buildings*, China Planning Press, Beijing, China, 2004.
- [3] National Standard of the People’s Republic of China, *GB50011-2010 Code for Seismic Design of Buildings*, China Architecture and Building Press, Beijing, China, 2010.
- [4] C. M. Uang, “Establishing  $R$  (or  $r_w$ ) and  $C_d$  factors for building seismic provisions,” *Journal of Structural Engineering*, vol. 117, no. 1, pp. 19–28, 1991.
- [5] A. Whittaker, G. Hart, and C. Rojahn, “Seismic response modification factors,” *Journal of Structural Engineering*, vol. 125, no. 4, pp. 438–444, 1999.
- [6] A. S. Elnashai and B. M. Broderick, “Seismic response of composite frames-II. Calculation of behaviour factors,” *Engineering Structures*, vol. 18, no. 9, pp. 707–723, 1996.
- [7] J. Kim and H. Choi, “Response modification factors of chevron-braced frames,” *Engineering Structures*, vol. 27, no. 2, pp. 285–300, 2005.
- [8] M. Mahmoudi and M. Zaree, “Evaluating response modification factors of concentrically braced steel frames,” *Journal of Constructional Steel Research*, vol. 66, no. 10, pp. 1196–1204, 2010.
- [9] B. Asgarian and H. R. Shokrgozar, “BRBF response modification factor,” *Journal of Constructional Steel Research*, vol. 65, no. 2, pp. 290–298, 2009.
- [10] M. Izadinia, M. A. Rahgozar, and O. Mohammadrezaei, “Response modification factor for steel moment-resisting frames by different pushover analysis methods,” *Journal of Constructional Steel Research*, vol. 79, pp. 83–90, 2012.
- [11] W. A. Attia and M. M. M. Irheem, “Boundary condition effect on response modification factor of X-braced steel frames,” *HBRC Journal*, vol. 14, no. 1, pp. 104–121, 2018.
- [12] M. Mahmoudi and M. G. Abdi, “Evaluating response modification factors of TADAS frames,” *Journal of Constructional Steel Research*, vol. 71, pp. 162–170, 2012.
- [13] F. Aliakbari and H. Shariatmadar, “Seismic response modification factor for steel slit panel-frames,” *Engineering Structures*, vol. 181, pp. 427–436, 2019.
- [14] Q. Gu, Y.-K. Shen, and C. Li, “The seismic response modification factors of steel structures,” *Journal of Suzhou University of Science and Technology (Engineering and Technology)*, vol. 24, no. 4, pp. 18–24, 2011.
- [15] H. G. Jouneghani and A. Haghollahi, “Assessing the seismic behavior of steel moment frames equipped by elliptical brace through incremental dynamic analysis (IDA),” *Earthquake Engineering and Engineering Vibration*, vol. 19, no. 2, pp. 435–449, 2020.
- [16] S. Arthi and K. Jaya, “Seismic performance of precast shear wall-slab connection under cyclic loading: experimental test vs. Numerical analysis,” *Earthquake Engineering and Engineering Vibration*, vol. 19, no. 3, pp. 739–757, 2020.
- [17] Y. Zhang, P. Pan, R. Gong, T. Wang, and W. Xue, “Substructure hybrid testing of reinforced concrete shear wall structure using a domain overlapping technique,” *Earthquake Engineering and Engineering Vibration*, vol. 16, no. 4, pp. 761–772, 2017.

- [18] C. H. Zhai, *Research of the Severest Designed Ground Motions and Strength Reduction Coefficients*, pp. 55–125, Harbin Institute of Technology, Harbin, China, 2004.
- [19] S. S. Cui, D. G. Lu, and P. Y. Song, “Effects of infill walls and casting slabs on global overstrength of RC frames,” *Journal of Building Structures*, vol. 35, no. 8, pp. 30–36, 2014.
- [20] S. Cui, Y. Chen, and D. Lu, “Probability assessment of structural response modification factor of RC frames by the demand-capacity-factor method,” *Structure*, vol. 30, pp. 628–637, 2021.
- [21] M. Masoudi, S. Eshghi, and M. Ghafory-Ashtiany, “Evaluation of response modification factor (R) of elevated concrete tanks,” *Engineering Structures*, vol. 39, pp. 199–209, 2012.
- [22] Aci Committee, *ACI 371R-08. Guide for the Analysis, Design, and Construction of Elevated concrete and Composite Steel-concrete Water Storage Tanks*, American Concrete Institute, Farmington Hills, MI, USA, 2008.
- [23] A. Mondal, S. Ghosh, and G. R. Reddy, “Performance-based evaluation of the response reduction factor for ductile RC frames,” *Engineering Structures*, vol. 56, no. 6, pp. 1808–1819, 2013.
- [24] W. L. Cao, R. W. Wang, F. Yin, and H. Y. Dong, “Seismic performance of a steel frame assembled with a CFST-bordered composite wall structure,” *Engineering Structures*, vol. 219, Article ID 110853, 2020.
- [25] J. B. Yan, Y. Y. Yan, and T. Wang, “Cyclic tests on novel steel-concrete-steel sandwich shear walls with boundary CFST columns,” *Journal of Constructional Steel Research*, vol. 164, Article ID 105760, 2020.
- [26] L. Guo, Q. Rong, B. Qu, and J. Liu, “Testing of steel plate shear walls with composite columns and infill plates connected to beams only,” *Engineering Structures*, vol. 136, pp. 165–179, 2017.
- [27] Q. Rong, Y. H. Zeng, L. H. Guo, X. M. Hou, and W. Z. Zheng, “Response of RPC-filled circular steel tube columns under monotonic and cyclic axial loading,” *Shock and Vibration*, vol. 2019, Article ID 9141592, 16 pages, 2019.
- [28] Q. Rong, J. Hou, L. H. Guo, and S. M. Zhang, “Structural response modification factor analysis of CFST frame-composite steel plate shear walls with two side connections,” *China Civil Engineering Journal*, vol. 49, no. S2, pp. 45–50, 2016.
- [29] Q. Rong, *Research of CFST Frame -SPSWs with Two Sides Connections for Seismic Performance*, pp. 133–155, Harbin Institute of Technology, Harbin, China, 2013.
- [30] S. Mazzoni, F. McKenna, M. H. Scott et al., *Open System for Earthquake Engineering Simulation User Command- Language Manual*, pp. 145–170, University of California Berkeley, Berkeley, CA, USA, 2004.
- [31] M. H. Scott, *Software Frameworks for the Computational Simulation of Structural Systems*, pp. 65–79, University of California, Berkeley, CA, USA, 2004.

## Research Article

# Simulation of Delamination Evolution of Slab Ballastless Track under Vertical Impact

Yu Liu <sup>1,2</sup>, Qianqi Xu <sup>1</sup>, Xiaodan Sun <sup>1</sup>, Guotao Yang <sup>3</sup>, and Guotang Zhao <sup>3</sup>

<sup>1</sup>School of Civil Engineering, Southwest Jiaotong University, Chengdu 610031, China

<sup>2</sup>Key Laboratory of High-Speed Railway Engineering, Ministry of Education, Southwest Jiaotong University, Chengdu 610031, China

<sup>3</sup>Department of Science, Technology and Information Technology, China Railway, Beijing 100844, China

Correspondence should be addressed to Yu Liu; liuyu@swjtu.edu.cn

Received 2 May 2021; Accepted 9 June 2021; Published 29 June 2021

Academic Editor: Feng Fu

Copyright © 2021 Yu Liu et al. This is an open access article distributed under the Creative Commons Attribution License, which permits unrestricted use, distribution, and reproduction in any medium, provided the original work is properly cited.

During the running of a high-speed train, the wheel may bounce on the rail due to the track irregularity. The wheel bounce could generate a vertical impact, leading to the initiation and expansion of delamination between layers of the track structure. In this paper, the evolution of the interfacial damage and delamination subjected to the vertical impact is simulated using finite element analysis (FEA). In the FEA, a bilinear cohesive zone model (CZM) is adopted to simulate the interface between the track slab and the CA mortar layer. For different levels of impact energy, the contact force, vertical deformation, absorbed energy, area of interfacial damage, and area of delamination are calculated and compared. The effects of the tangential and normal stiffness of the interface on the distribution of interfacial damage and delamination are investigated. The results show that the contact force, vertical deformation, absorbed energy, area of interfacial damage, and area of delamination increase with the increase of the impact energy. The area of interfacial damage in the compression stage is closely related to the tangential stiffness, whereas the area of delamination depends on the normal stiffness. The normal stiffness that gives the largest area of delamination is recommended to be taken as the lower bound of the normal stiffness for both controlling the delamination and preventing an exceedance of the track irregularity limit.

## 1. Introduction

The slab ballastless track structure of China Railway Track System type II (CRTS II SBTS) is a longitudinal continuous layered structure that consists of the track slab, the cement asphalt (CA) mortar layer, and the concrete base, as illustrated in Figure 1. It is specially used for high-speed railway (HSR) because it can provide high rail smoothness and ensure high comfort, stability, and safety of high-speed train. CRTS II SBTS is widely used in northern and eastern China. It was firstly applied in the Beijing-Tianjin HSR in 2008 and then utilized in the Beijing-Shanghai HSR in 2011. Up to now, the total mileage of CRTS II SBT application is over 9,000 km, about 26% of the total mileage of China HSR.

Delamination of CRTS II SBTS refers to the phenomenon that the track slab separates from the CA mortar layer or the CA mortar layer separates from the concrete base. It

can cause the buckling of CRTS II SBTS at the joint of two track slabs and endanger the operation safety of high-speed train [1, 2]. A large amount of delamination has been found in the Beijing-Shanghai HSR, many of which exceed the height limit of 15 mm required by the “Maintenance Rules for Ballastless Track of High Speed Railway” in China [3]. For instance, Figure 2 shows one delamination observed in the Beijing-Shanghai HSR in 2018, approximately 2000 mm long, 560 mm wide, and 2 mm high. Delamination may occur in different stages of the construction and operation of CRTS II SBTS. In the construction stage, delamination may occur between the track slab and the CA mortar layer when the temperature difference between the top and bottom surface of the track slab is larger than 20°C and will grow under the combined action of the overall temperature rise of the top surface of track slab and the vertical temperature difference within the track structure [4–6]. In the operation



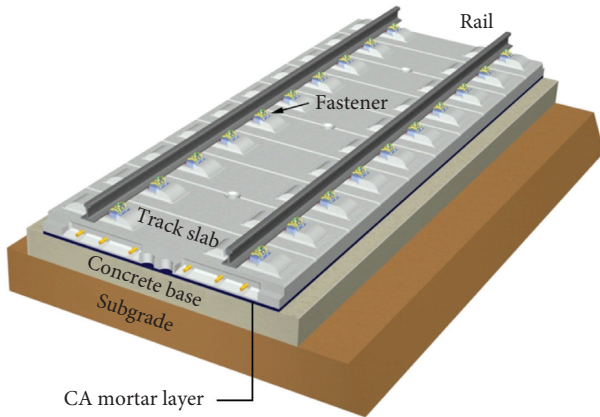


FIGURE 1: Sketch of CRTS II SBTS.



FIGURE 2: Example of delamination of CRTS II SBTS from the on-site survey of the Beijing-Shanghai HSR.

stage with trains running on the rail, delamination may expand rapidly under the additional impact load from train passage [6, 7].

During the running of a high-speed train, the wheel may roll, slide, or bounce on the rail. The bounce of the wheel happens when the wheel passes the top of an irregularity region at a high speed, as illustrated in Figure 3. At the moment when the wheel falls on the rail, the wheel will generate a vertical impact force on the rail which is instantly transmitted into the substructure via the track. This impact load is very different from the load in terms of track irregularity spectrum that is commonly used in the dynamic response analysis of the vehicle-track system [8, 9]. However, the track irregularity spectrum is rather correlated to the high-frequency vibration of the rail which has a limited effect on the substructure. The interfacial damage may be more closely correlated to the vertical impact on the track slab directly from the wheel bounce than to the track irregularity spectrum. There is very little research addressing the impact force caused by wheel bounce and even less on the response and damage of the track slab under the impact force. The impact-induced damage is more concerned in the field of aerospace composite materials [10–13] and explosion mechanics [14, 15]. In the existing studies of the impact-induced damage, the damage is usually evaluated from the energy point of view, by studying the mutual transmission of

potential and kinetic energy. Similarly, the impact energy caused by the wheel vertical impact consists of kinetic energy related to the falling speed and potential energy due to the height difference between the wheel and the track. Although the impact velocity of the wheel is much slower than that in the field of aerospace and explosion, it is still worth interpreting the input load from the energy point of view to investigate the generation and evolution of delamination. The wheel impact energy and the energy transmitted into the track slab, however, cannot be evaluated by the commonly used track irregularity spectrum.

On the other hand, CRTS II SBTS is a composite “sandwich” structure that contains steel bar, CA mortar, and concrete which is composed of aggregate, cement, and mineral powder. Therefore, the study of the delamination of CRTS II SBTS under the wheel impact is essentially a problem of the interfacial damage within composite material under vertical impact. In the field of railway track, there are very few studies addressing the damage from the vertical wheel impact and on determining a reasonable range of the impact energy for the wheel bounce. Kaewunruen et al. consider that the vertical loading from the wheel impact with a speed of 1.94 m/s can be equivalent to that caused by a 600-kg-weight mass dropping from a height of 0.2 m [16]. Wu et al. investigate the relationship between the damage of a concrete slab and the explosion load by changing the magnitude of explosion, the explosion location, and the thickness of the concrete slab [17]. Yilmaz et al. investigate the damage of a concrete slab caused by a hammer dropping from different heights [18]. They found that the greater the impact energy, the greater the maximum acceleration, maximum displacement, and area of interfacial damage. In the field of aerospace, the damage under impact is usually analyzed using a three-dimensional progressive damage analysis method that considers damage evolution and stiffness degradation [19–21]. In the method, the interface of composites is generally simulated using cohesive elements [22, 23], and the generation and development of the damage are described by the variation of the total stiffness of the cohesive elements. In this paper, the 3D progressive damage analysis method is adopted to simulate the damage evolution of CRTS II SBTS. The interface of CRTS II SBTS is simulated by cohesive elements with the parameters obtained from scale model push plate tests. The effects of the impact energy and interfacial bond property on the simulated interfacial damage and delamination are analyzed.

## 2. Analysis Model of CRTS II SBTS under Vertical Impact

The response of CRTS II SBTS under the vertical impact is simulated using ABAQUS. Considering that the delamination of CRTS II SBTS under the wheel impact is essentially the interfacial damage within composite material under the vertical impact, the finite element model includes three parts: a layered model of CRTS II SBTS, a cohesive zone model (CZM) that simulates the interface, and a puncher that carries all the impact energy from the vehicle. The impact energy applied on the layered model is estimated

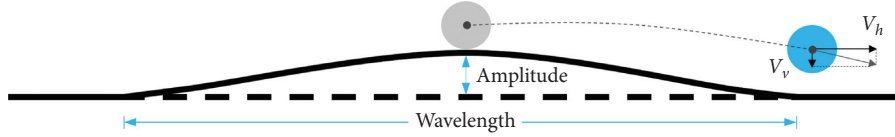


FIGURE 3: Diagram for the wheel running through the irregularity region.

based on the mass, velocity, and initial height of the puncher. Figure 4 shows the puncher and the layered model of the CRTS II SBTS inserted with a layer of cohesive elements.

**2.1. Layered Model of CRTS II SBTS and Puncher.** The geometrical and mechanic parameters of the layered model of CRTS II SBTS are listed in Table 1 according to [6]. The length, width, and thickness of the layered model are set to be the same as a real unit track slab. A layer of cohesive elements with a thickness of  $10^{-3}$  m is set between the CA mortar layer and the track slab since the delamination is most likely to occur on the upper surface of the CA mortar layer [8]. The track slab, CA mortar layer, and concrete base are built using solid elements. For all nodes at the bottom and longitudinal boundary of the layered model, the constraint is applied to all six degrees of freedom. The contact between the puncher and the track slab as well as the contact between the track slab and the CA mortar is set to be hard contact in the normal direction and friction in the tangential direction with the penalty friction coefficient of 0.3. The other contacts are set to be tie.

As illustrated in Figure 3, the ratio of the vertical velocity to the horizontal velocity can be assumed to be equal to the ratio of the amplitude to the half of the wavelength of the irregularity. Therefore, the impact energy that the puncher carries includes two parts: the potential energy related to the amplitude of the irregularity and the kinetic energy related to the initial vertical velocity. For the train CRH380A, the weight on one wheel is 6400 kg including the weight of the car body, two bogies, and four wheelsets. According to the level I management value in “Maintenance Rules for Ballastless Track of High Speed Railway” [3], the amplitude of irregularity is taken to be 4 mm and the wavelength is 30 m [24]. With a speed of 300 km/h, the total energy of the wheel at the instant of bounce will be 257.5 J. Therefore, the upper limit of the impact energy in the finite element analysis (FEA) is set to be 300 J. Another six levels of impact energy, 20 J, 50 J, 100 J, 150 J, 200 J, and 250 J, are also considered in the FEA to evaluate the effect of the impact energy. The variation of the impact energy is achieved by changing the initial vertical velocity of the puncher which is a 1000-kg-weight ball with a diameter of 0.1 m that drops from a fixed height.

**2.2. Cohesive Zone Model (CZM).** A bilinear CZM is employed to characterize the force-displacement relationship during the process from interfacial damage initiation to delamination, as shown in Figure 5.

Assuming that  $\sigma_n$ ,  $\sigma_t$ , and  $\sigma_s$  are the interfacial stresses in normal and two tangential directions, respectively,  $\sigma_n^0$ ,  $\sigma_t^0$ ,

and  $\sigma_s^0$  are the corresponding interfacial strength. For a tangentially isotropic interface,  $\sigma_t = \sigma_s$  and  $\sigma_t^0 = \sigma_s^0$ . According to the bilinear CZM, the force-displacement curve increases linearly during loading, with the slope of the stiffness  $E_n$  and  $E_s$  for normal and tangential direction, respectively. When the force-displacement curve reaches the peak, the interfacial damage initiates, which can be quantitatively judged by the Quads criterion:

$$\left(\frac{\sigma_n}{\sigma_n^0}\right)^2 + \left(\frac{\sigma_t}{\sigma_t^0}\right)^2 + \left(\frac{\sigma_s}{\sigma_s^0}\right)^2 \geq 1, \quad (1)$$

where  $\sigma_n = (\sigma_n + |\sigma_n|)/2$ . The stress for the damage initiation is the interfacial strength,  $\sigma_n^0$  and  $\sigma_s^0$ , for the normal and tangential direction, respectively, while the corresponding displacement is  $\delta_n^0$  and  $\delta_s^0$ , respectively. Therefore,  $E_n = \sigma_n^0/\delta_n^0$  and  $E_s = \sigma_s^0/\delta_s^0$ .

According to the bilinear CZM, the softening evolution after damage initiation is also linear. Thus the stress after damage occurs can be given by

$$\begin{cases} \sigma_n = (1 - D)E_n\delta_n, \\ \sigma_s = (1 - D)E_s\delta_s, \end{cases} \quad (2)$$

where  $\delta_n$  and  $\delta_s$  are the displacements and  $D$  represents the overall damage in the CZM, which is zero initially and then gradually evolves from 0 to 1 upon further loading:

$$D = \frac{\delta_m^f(\delta_m - \delta_m^0)}{\delta_m(\delta_m^f - \delta_m^0)}, \quad (3)$$

where  $m = n$  for the normal direction and  $m = t$  or  $m = s$  for the longitudinal or transverse tangential direction. When  $D$  equals 1, delamination occurs. Assuming  $\delta_n^f, \delta_s^f$  are the normal and tangential displacement for the moment of delamination occurrence, respectively, the corresponding fracture toughness,  $G_{IC}$  and  $G_{IIC}$ , can be measured by the triangle area in Figure 5,  $G_{IC} = 1/2\sigma_n^0\delta_n^f$  or  $G_{IIC} = 1/2\sigma_s^0\delta_s^f$ . The delamination initiation can be evaluated by fracture toughness. It can be judged that the delamination occurs if the fracture toughness follows the equation below:

$$\left(\frac{G_I}{G_{IC}}\right)^2 + \left(\frac{G_{II}}{G_{IIC}}\right)^2 + \left(\frac{G_{III}}{G_{IIC}}\right)^2 = 1. \quad (4)$$

The parameters of the CZM are determined by model tests in which normal cohesive parameters are determined from the vertical push plate test, and tangential cohesive parameters are determined from the horizontal push plate test. The specimen of the CRTS II SBTS has the length, width, and height of 60 cm  $\times$  20 cm  $\times$  20 cm, bonded on the base via the CA mortar layer with the height of 3 cm. The

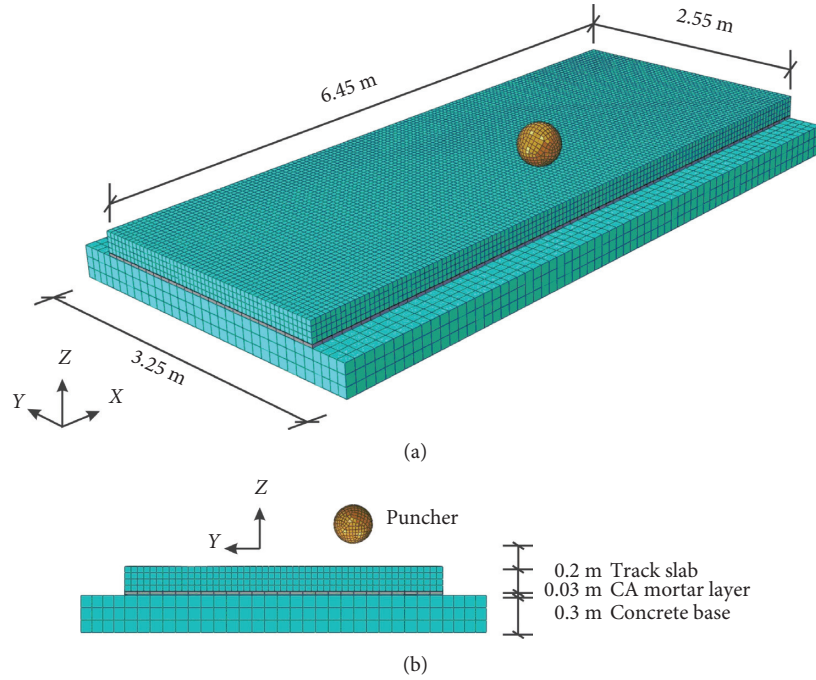


FIGURE 4: Dimension of the analysis model (a) and the thickness for each layer (b).

TABLE 1: Geometrical and mechanic parameters of the layered model of CRTS II SBTS.

Layers	Density ( $\text{kg/m}^3$ )	$E$ (MPa)	Length (m)	Width (m)	Thickness (m)
Track slab	2500	36000	6.45	2.55	0.2
CA mortar layer	1950	10000	6.45	2.55	0.03
Concrete base	2400	22000	6.45	3.25	0.3

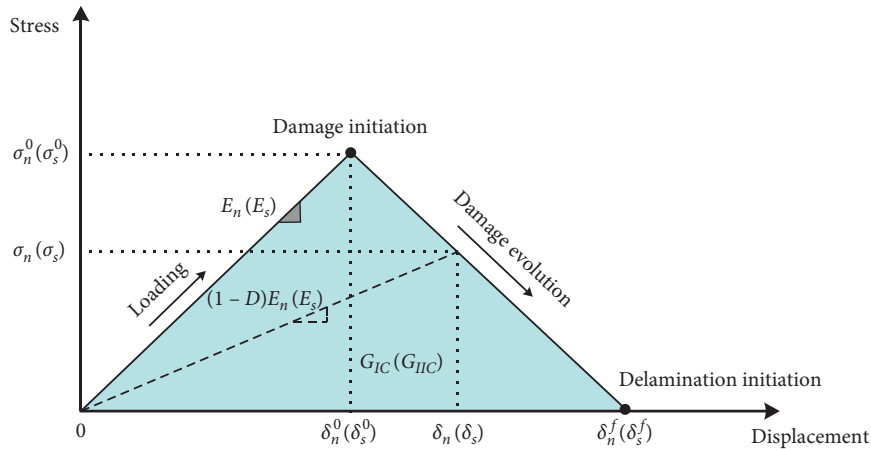


FIGURE 5: The bilinear stress-displacement relationship for the CZM.

mechanic parameters of the concrete for the track slab and base are the same as listed in Table 1. The specimens were tested 28 days after the CA grouted. The setup of the vertical push plate test is shown in Figure 6. The track slab is lifted vertically with the load applied at the midpoint of the track slab. Two dial gauges are placed 20 cm away from the midpoint at each side. The setup of the horizontal push plate

test is shown in Figure 7. In the test, the load is horizontally applied at the center of one end cross-section, and two dial gauges are arranged horizontally at both of the two ends of the specimen. The relative displacement between the track slab and the base was tested using a linear variable differential transformer (LVDT). The jacks work synchronously by an automation control system to provide a constant-rate



FIGURE 6: Setup of the scale central-loading vertical push plate test.

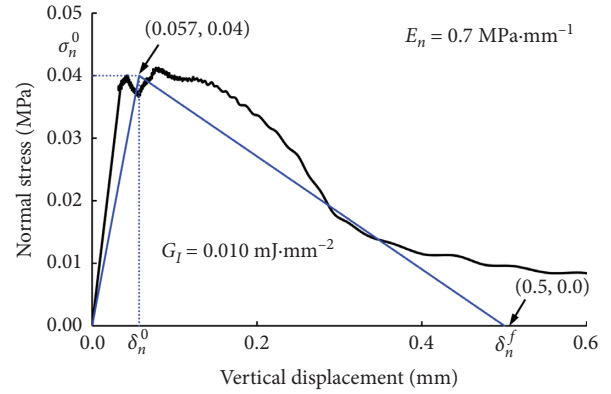


FIGURE 8: Force-displacement curve of the vertical push plate test.



FIGURE 7: Setup of the scale horizontal push plate test.

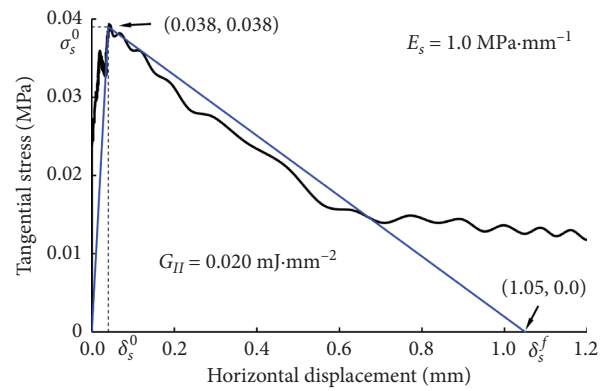


FIGURE 9: Force-displacement curve of the horizontal push plate test.

increased load. The force-displacement curves obtained from the vertical and horizontal push plate test are plotted in Figures 8 and 9, respectively.  $\sigma_n^0$  and  $\sigma_s^0$  can be determined by the peak stress of the vertical and horizontal force-displacement curve, respectively.  $\delta_n^0$  and  $\delta_s^0$  are then identified corresponding to  $\sigma_n^0$  and  $\sigma_s^0$ , respectively. Afterward,  $E_n$  and  $E_s$  can be calculated using  $E_n = \sigma_n^0/\delta_n^0$  and  $E_s = \sigma_s^0/\delta_s^0$ .  $\delta_n^f$  and  $\delta_s^f$  are visually picked as the displacement after which the fluctuation in the force-displacement curve is slight. Based on  $\delta_n^f$  and  $\delta_s^f$ ,  $G_{IC}$  and  $G_{IIC}$  can be calculated using  $G_{IC} = 1/2\sigma_n^0\delta_n^f$  or  $G_{IIC} = 1/2\sigma_s^0\delta_s^f$ . The determined cohesive parameters are indicated in Figures 8 and 9 and listed in Table 2.

### 3. Simulation Results

**3.1. Contact Force.** The contact force for different impact energies is shown in Figure 10. For each curve in Figure 10, the ascending part represents the compression stage in which the puncher presses down the track slab, whereas the descending part describes the rebound stage in which the puncher begins to rebound. The contact force reaches the peak value at approximately  $2 \times 10^{-3}$  s regardless of the impact energy. The maximum contact force versus the impact energy and the contact time versus the impact energy

are shown in Figure 11. As seen from Figure 11, the maximum contact force varies linearly with the impact energy. The contact time for the impact energy of 20 J is slightly larger than that for other impact energies. After the impact energy exceeds 150 J, the contact time is not sensitive to the level of the impact energy.

**3.2. Vertical deformation of the Track Slab.** As shown in Figure 4, one of the two long sides of the track slab, which is closer to the puncher, is chosen for the illustration of the vertical deformation. Figure 12 shows the vertical deformation of the selected side for the moment when the impact point achieves the maximum deformation in the compression stage. As seen from Figure 12, most of the slab shows a downward compression deformation. When the impact energy is larger than 50 J, there will be an upward deformation at both sides of the track slab due to the constraint applied at the end of the track slab. The maximum vertical deformation at the impact point increases with the impact energy, from 0.2 mm for the impact energy of 20 J to 0.65 mm for the impact energy of 300 J. Figure 13 shows the vertical deformation of the selected side of the track slab at the moment when the impact point achieves the maximum deformation in the rebound stage. As seen from Figure 13, most of the slab shows an upward tensile deformation.

TABLE 2: Parameters of the cohesive zone model.

Value	$\sigma^0$ (MPa)	$\delta^0$ (mm)	$E$ (MPa·mm <sup>-1</sup> )	$G$ (mJ·mm <sup>-2</sup> )	$\delta^f$ (mm)
Normal direction	0.040	0.057	0.7	0.010	0.5
Tangential direction	0.038	0.038	1.0	0.020	1.05

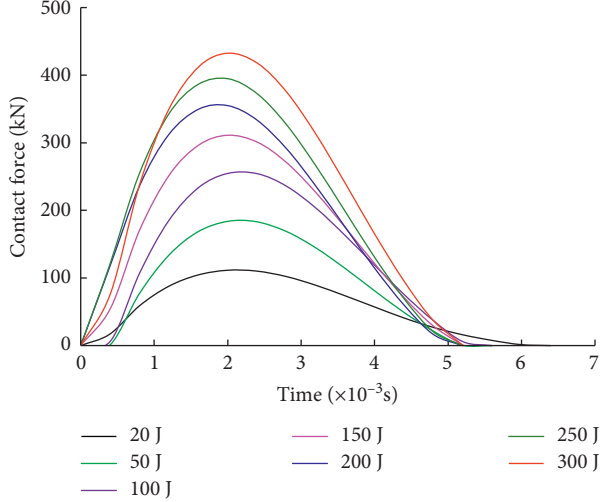


FIGURE 10: Time histories of the contact force for different impact energies.

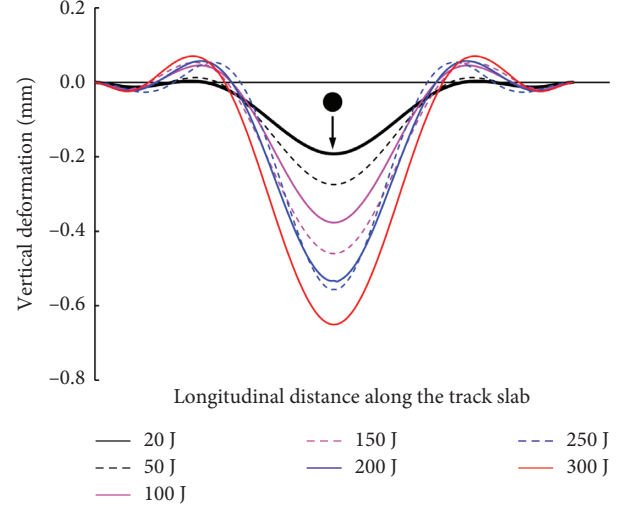


FIGURE 12: The maximum compression deformation for the selected side of the track slab for different impact energies.

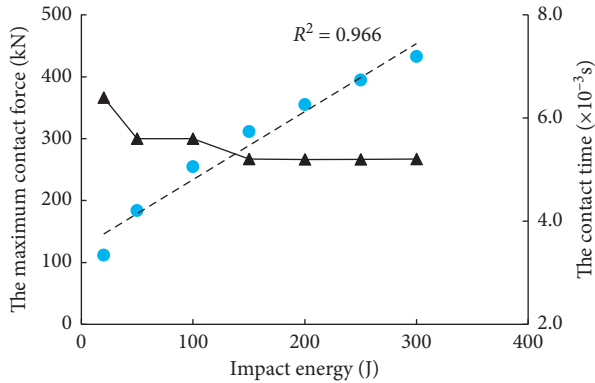


FIGURE 11: The maximum contact force (blue dot) and contact time (black triangle) vs. impact energy.

When the impact energy is lower than 100 J, there will be a downward deformation at both sides of the track slab due to the constrain applied at the end of the track slab. The maximum vertical deformation at the impact point increases with the impact energy, from 0.1 mm for the impact energy of 20 J to 1.1 mm for the impact energy of 300 J.

The ratio of the maximum rebound deformation (crest in Figure 13) and the maximum compression deformation (trough in Figure 12) for different impact energies are calculated, as shown in Figure 14. As seen from Figure 14, the ratio of the deformation increases as the impact energy increases. When the impact energy is less than approximately 130 J, the maximum rebound deformation is smaller

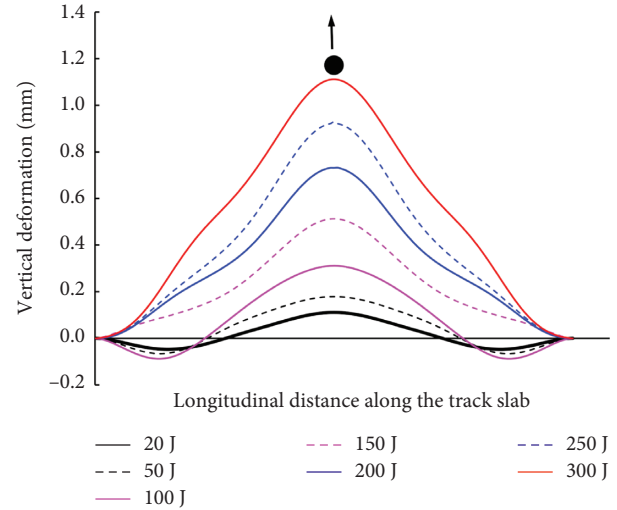


FIGURE 13: The maximum rebound deformation for the selected side of the track slab for different impact energies.

than the maximum compression deformation. For the impact energy of 300 J, the maximum rebound deformation is almost 1.7 times the maximum compression deformation of 0.65 mm. For the impact energy of 20 J, the maximum rebound deformation is 0.11 mm which exceeds  $\delta_n^0$  of 0.057 mm in Table 2. It indicates that the interfacial damage will initiate even if the impact energy is 20 J. The maximum rebound deformation for the impact energy of 150 J is 0.51 mm, which exceeds  $\delta_n^f$  of 0.5 mm in Table 2. This

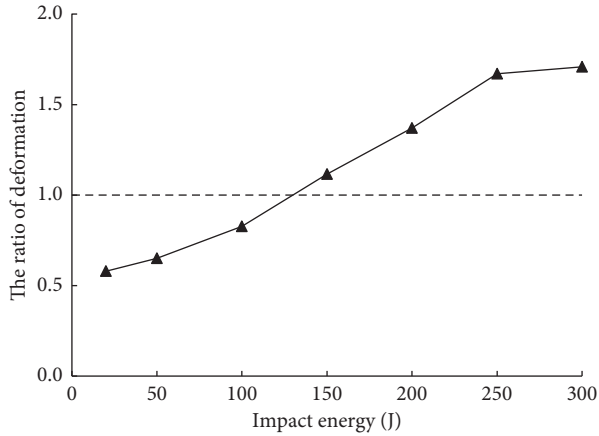


FIGURE 14: The ratio of the maximum rebound deformation and the maximum compression deformation versus impact energy.

indicates that delamination will occur for the impact energy of 150 J.

**3.3. Conversion of Energy.** The conversion of the energy in the system that consists of the puncher and the layered model is investigated. Right before the puncher touches the track slab, the energy of the whole system equals the kinetic energy of the puncher. After the puncher impacts the track slab, a portion of the kinetic energy convert into the internal energy of the layered track structure. There will also be a portion of the energy that is absorbed due to the interfacial damage and delamination.

Figure 15 shows the conversion between the kinetic energy, internal energy, and absorbed energy for the impact energy of 250 J. As seen from Figure 15, the kinetic energy and the internal energy have an inverse trend of variation. With greater kinetic energy comes smaller internal energy. The total energy of the whole system attenuates as time grows, whereas the absorbed energy increases. To interpret the whole progress of the impact, five moments are selected and plotted in Figure 15 to divide the whole impact process into several stages. Line I represents the moment when the puncher touches the track slab; Line II represents the moment when the track slab reaches the maximum compression deformation; Line III represents the moment when the track slab rebounds back to the equilibrium position; Line IV represents the moment when the track slab reaches the maximum tensile deformation; Line V represents the moment when the track slab moves back to the equilibrium position from the maximum tensile deformation. As seen from Figure 15, the internal energy rapidly increases to the maxima in the stage between moment I and II and then decreases to the trough in the stage between moment II and III. Before moment III, the absorbed energy slightly increases due to the small area and the low amplitude of the interfacial shear damage. After moment III, if the rebound displacement exceeds  $\delta_n^0$ , the tensile damage will occur. When the rebound displacement exceeds  $\delta_n^f$ , delamination will initiate. The corresponding

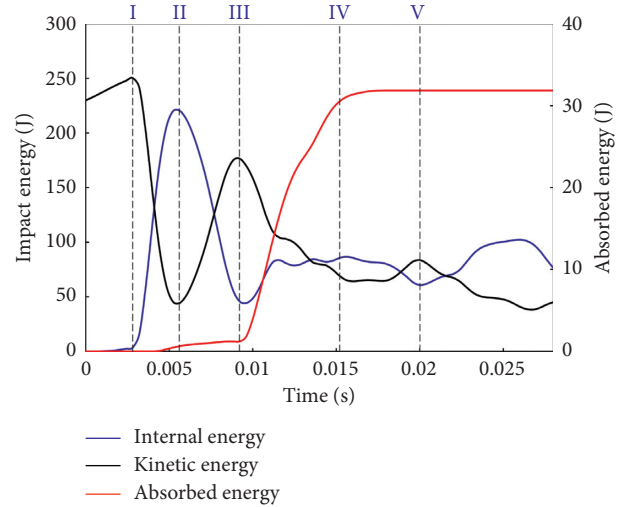


FIGURE 15: Conversion between the kinetic energy, internal energy, and absorbed energy for the impact energy of 250 J.

absorbed energy increases significantly due to the rapid expansion of the damage and delamination.

Figure 16 shows the distribution of the interfacial damage and delamination at selected moments in terms of SDEG calculated using equation (3). Figure 16(a) represents moment II when damage occurs on the interface. The damage is mainly induced by the interfacial shear stress in the compression stage. Figure 16(b) shows moment III when the interfacial shear damage extends to the edge of the track slab. Figure 16(c) shows the moment when the tensile damage occurs in the rebound stage. Figure 16(d) illustrates the moment IV when the delamination area reaches the maxima.

**3.4. Interfacial damage and Delamination for Different Impact Energies.** The area of the interfacial damage and the area of the delamination for different impact energies are shown in Figure 17. As seen from Figure 17, the two areas increase with the increase of the impact energy. For the impact energy of 300 J, the area of the interfacial damage is approximately  $8 \text{ m}^2$ , accounting for about 48.6% of the area of the track slab. For the impact energy of 300 J, the area of the delamination is approximately  $2 \text{ m}^2$ , accounting for about 12% of the area of the track slab. Figure 17 also indicates that 150 J is the critical impact energy for the delamination initiation. For a train running at a speed of 300 km/h, impact energy of 150 J can be achieved if the dynamic irregularity height of the rail is 2 mm. Therefore, in regular maintenance, more attention should be paid to the railway line with the height of dynamic irregularity greater than 2 mm. Figure 18 shows the relationship between the impact energy and the maximum absorbed energy, which corresponds to the value of the platform of the absorbed energy in Figure 15. Figure 18 shows an apparent increase of the absorbed energy with the increase of the impact energy. For the impact energy of 300 J, the energy absorbed reaches about 40 J.

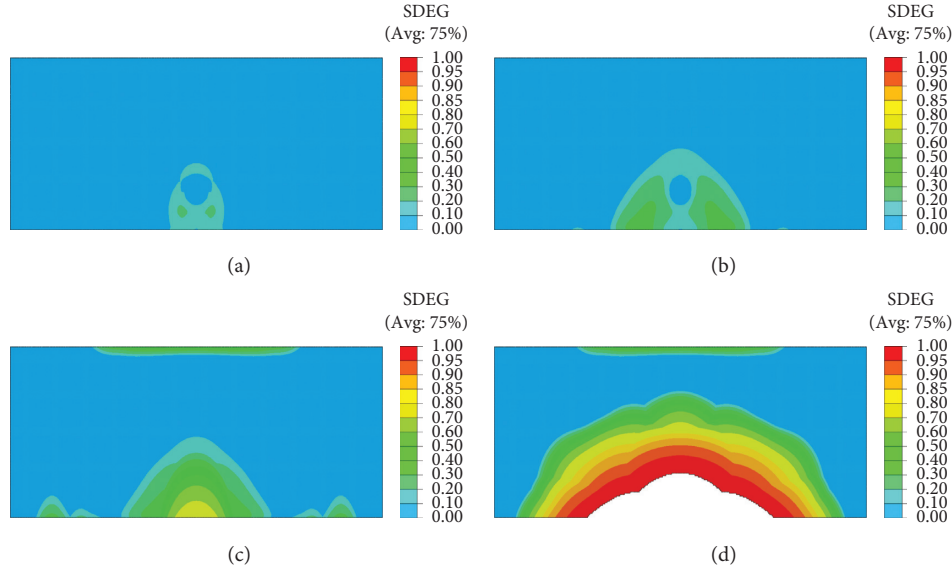


FIGURE 16: The evolution of the interfacial damage and delamination for selected moments. (a) Moment II. (b) Moment III. (c) The moment for the initiation of the interfacial tensile damage. (d) Moment IV.

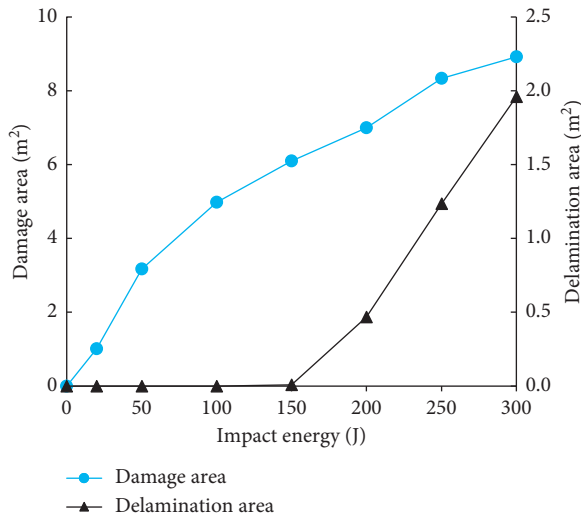


FIGURE 17: Damage area and delamination area vs. impact energy.

### 3.5. Effect of Interfacial Stiffness on Interfacial Damage.

The effect of the interfacial stiffness on the interfacial damage is investigated. We first vary  $E_s$  from 1.0 MPa/mm to 2.0 MPa/mm for the fixed  $E_n$  of 0.7 MPa/mm and  $E_t$  of 0.7 MPa/mm under the impact energy of 300 J. Figure 19 shows the distribution of the interfacial damage for  $E_s$  of 1.0 MPa/mm and 2.0 MPa/mm. In Figure 19, the upper and bottom two panels indicate the distribution of the interfacial damage when the maximum vertical deformation is achieved in the compression and rebound stages, respectively. As seen from Figure 19, in the compression stage, the greater  $E_s$  leads to the larger area of the interfacial damage. The damage is asymmetric due to the boundary effect along the transverse direction. The

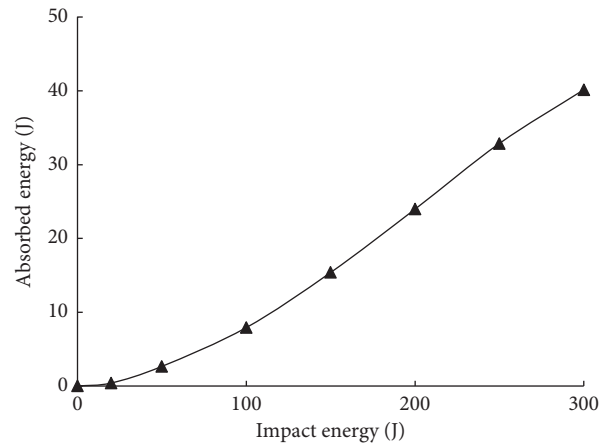


FIGURE 18: The relationship of the absorbed energy and the impact energy.

effect of  $E_s$  on the delamination area (the blank area in the figure) is slight.

We then vary  $E_t$  from 1.0 MPa/mm to 3.0 MPa/mm for the fixed  $E_n$  of 0.7 MPa/mm and  $E_s$  of 0.7 MPa/mm under the impact energy of 300 J. Figure 20 shows the distribution of the interfacial damage for the  $E_t$  of 1.0 MPa/mm, 1.5 MPa/mm, and 3.0 MPa/mm, respectively. As seen from Figure 20, the damage is symmetrically distributed along the longitudinal direction of the track slab. The greater  $E_t$  leads to the larger area of interfacial damage in the compression stage. The effect of  $E_t$  on the delamination area is slight.

Figure 21 shows the variation of the maximum area of delamination with the tangential stiffness for various normal stiffness under the impact energy of 300 J. As seen from Figure 21, the maximum area of delamination is not sensitive to the tangential stiffness when the normal stiffness is larger

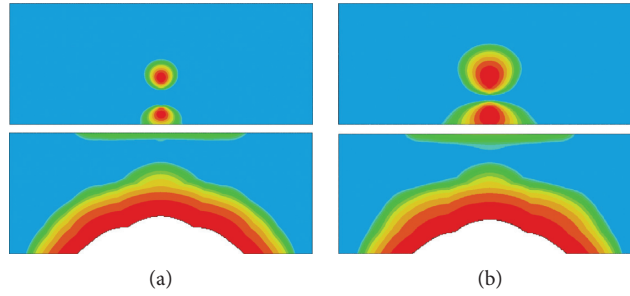


FIGURE 19: Distribution of the interfacial damage for the moment when the maximum vertical deformation is achieved for different  $E_s$ . The upper and bottom two panels are for the compression stage and the rebound stage, respectively. (a)  $E_s = 1.0$  MPa/mm. (b)  $E_s = 2.0$  MPa/mm.

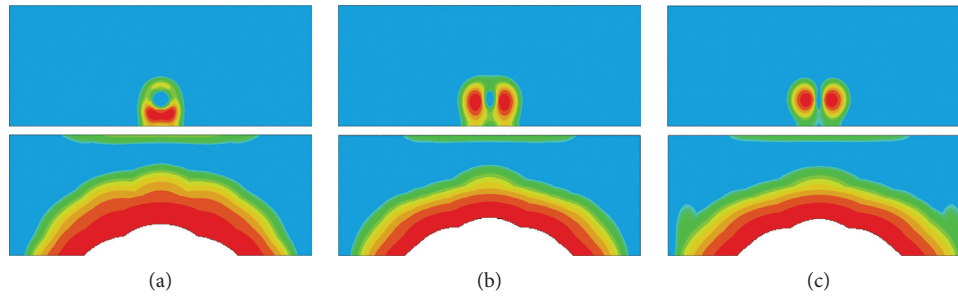


FIGURE 20: Distribution of the interfacial damage for the moment when the maximum vertical deformation is achieved for different  $E_t$ . The upper and bottom two panels are for the compression stage and the rebound stage, respectively. (a)  $E_t = 1.0$  MPa/mm. (b)  $E_t = 1.5$  MPa/mm. (c)  $E_t = 3.0$  MPa/mm.

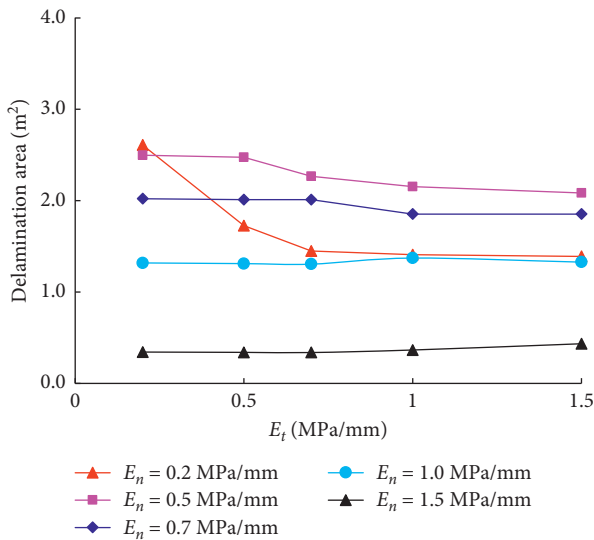


FIGURE 21: The delamination area versus  $E_t$  for various  $E_n$  under the impact energy of 300 J.

than 0.5 MPa/mm. The area of delamination becomes the largest when both the normal stiffness and tangential stiffness are the smallest (0.2 MPa/mm). As the tangential stiffness increases from 0.2 MPa/mm to 0.7 MPa/mm, the bond behavior of the interface enhances, and thus, the area of delamination reduces rapidly. Figure 22 compares the relationship between the maximum area of delamination and  $E_t$  for the impact energies of 200 J, 250 J, and 300 J,

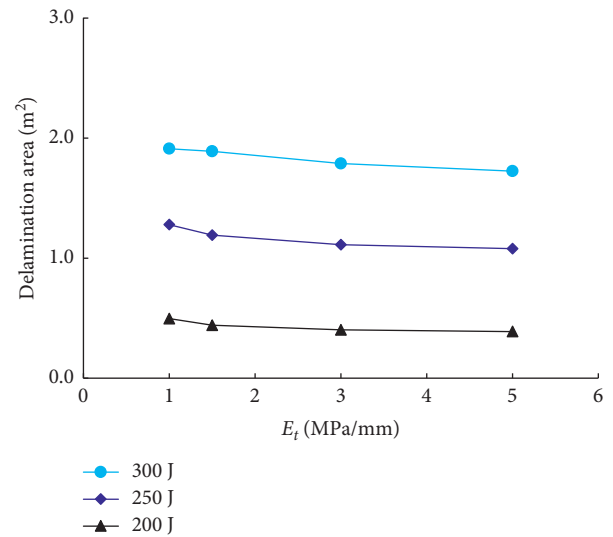


FIGURE 22: The delamination area versus  $E_t$  for various impact energies.

respectively. Figure 22 shows that, for given impact energy, the maximum area of delamination is not sensitive to the longitudinal tangential stiffness.

Figure 23 shows the distribution of the interfacial damage when the maximum compression deformation is achieved in the compression stage and the distribution of the delamination when the maximum tensile deformation is achieved in the rebound stage for selected  $E_n$  under the impact energy of 300 J. As seen from Figure 23, the distribution of the interfacial



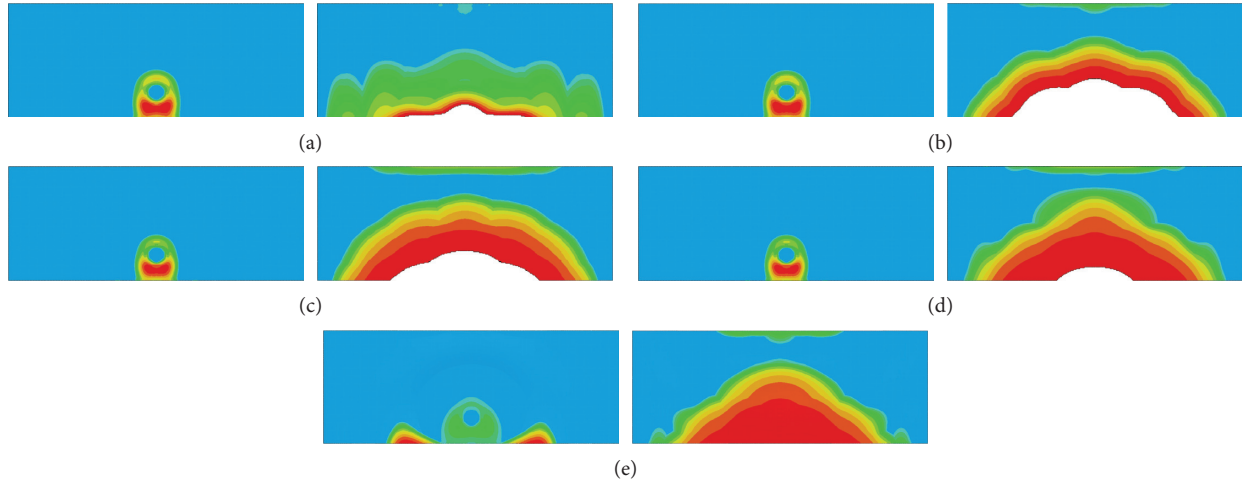


FIGURE 23: Distribution of the interfacial damage when the maximum vertical deformation is achieved for different  $E_n$ . The left and right five panels are for the compression stage and the rebound stage, respectively. (a)  $E_n = 0.2$  MPa/mm. (b)  $E_n = 0.5$  MPa/mm. (c)  $E_n = 1.0$  MPa/mm. (d)  $E_n = 1.5$  MPa/mm. (e)  $E_n = 2.0$  MPa/mm.

damage in the compression stage is almost the same for all cases except for  $E_n$  of 2.0 MPa/mm, which indicates a very slight effect of the normal stiffness on the interfacial damage in the compression stage. As the normal stiffness increases, the maximum area of delamination shows a trend of increasing first and then decreasing. This trend is more obvious in Figure 24 which shows the variation of the maximum area of delamination with the normal stiffness for various tangential stiffnesses under the impact energy of 300 J.

As seen from Figure 24, for almost all tangential stiffnesses, the delamination area achieves the maxima when the normal stiffness is 0.5 MPa/mm. Only when the tangential stiffness is 0.2 MPa/mm, the maximum area of delamination will be achieved at a smaller normal stiffness. Figure 25 compares the maximum area of delamination versus the normal stiffness for the impact energies of 200 J, 250 J, and 300 J, respectively. Figure 25 indicates that, for given impact energy, the delamination area achieves the maxima when the normal stiffness is 0.5 MPa/mm.

Figures 26 and 27 show the maximum compression and rebound deformation of the selected side of the track slab for various normal stiffnesses under the impact energy of 300 J. In the compression stage, the interface of the track structure follows the continuity and uniformity assumptions of the laminated plate theory. The greater the normal stiffness of the interface, the stronger the ability of deformation compatibility, and hence the smaller the maximum vertical deformation, as shown in Figure 26. In the rebound stage, it can also be observed that a greater normal stiffness gives a smaller maximum vertical deformation except for  $E_n$  of 0.2 MPa/mm. The unexpected small vertical deformation for the normal stiffness of 0.2 MPa/mm may be explained in terms of the energy since the continuity and uniformity

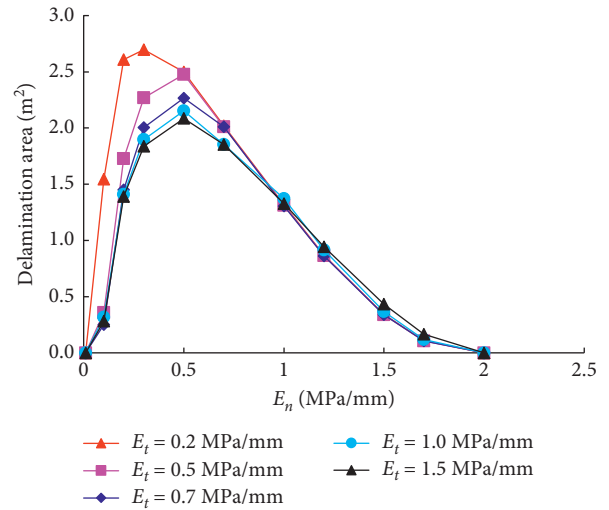


FIGURE 24: The delamination area versus  $E_n$  for selected  $E_t$  under the impact energy of 300 J.

assumptions are not valid due to the existence of the delamination. As seen from Figure 26, the normal stiffness of 0.2 MPa/mm leads to a remarkably larger vertical deformation than other normal stiffness. This larger deformation will cause a larger consumption of the impact energy, which hence leads to a smaller energy left for the puncher to rebound. This is the reason why 0.2 MPa/mm gives a lower rebound deformation and a smaller area of delamination than 0.5 MPa/mm. However, it cannot be concluded that 0.2 MPa/mm is more recommended than 0.5 MPa/mm because the larger compression deformation for 0.2 MPa/mm will be a big challenge to the track irregularity limit.

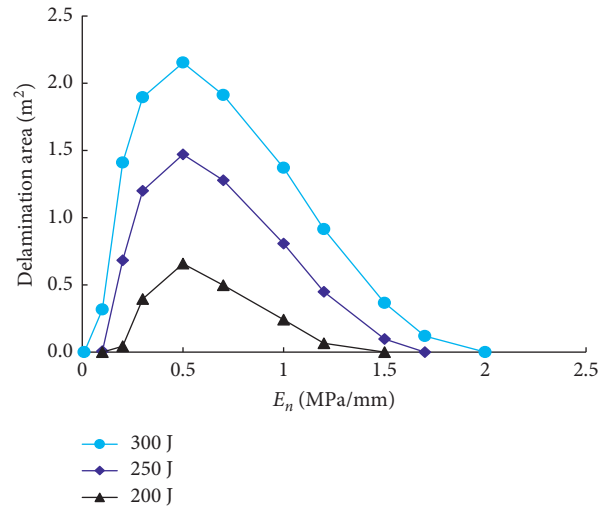


FIGURE 25: The delamination area versus  $E_n$  for selected impact energies.

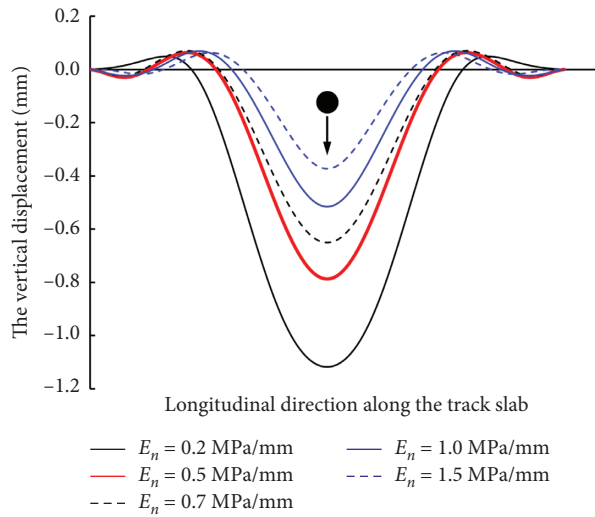


FIGURE 26: Maximum compression deformation of the selected side for various  $E_n$ .

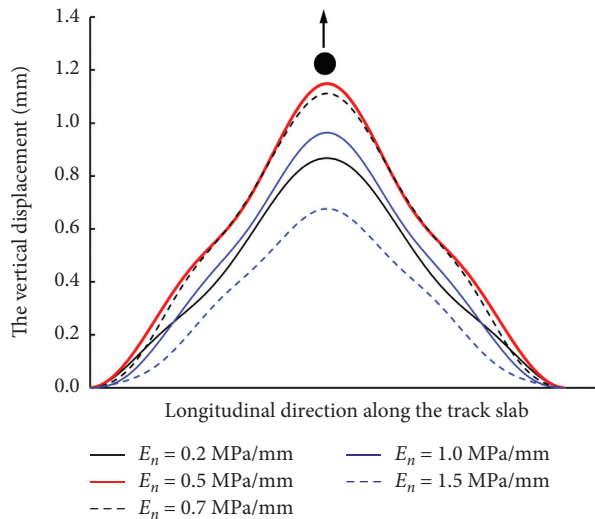


FIGURE 27: Maximum rebound deformation of the selected side for various  $E_n$ .

Therefore, it is reasonable to take 0.5 MPa/mm as the lower bound of the normal stiffness to meet the requirement of both the delamination control and track irregularity limit.

#### 4. Conclusions

The evolution of the interfacial damage and delamination of CRTS II SBTS under the vertical wheel impact are simulated. Based on the simulation, the conversion of the energy during the entire impact process, the variation of the impact force, the vertical deformation of the track slab, the distribution of the interfacial damage, and the distribution of the delamination for different impact energies are analyzed. The effects of the normal and tangential stiffness on interfacial damage and delamination are discussed.

The main conclusions include

- (1) The maximum contact force between the puncher and the track slab varies linearly with the impact energy, whereas the contact time is not sensitive to the level of the impact energy. The ratio of the rebound deformation over compression deformation also increases as the impact energy increases. The impact energy of 20 J and 150 J corresponds to the energy for the interfacial damage initiation and the delamination initiation, respectively. Therefore, for a train running at a speed of 300 km/h, the dynamic irregularity height of 2 mm that leads to the impact energy of 150 J should be more concerned.
- (2) During the entire impact process, the kinetic energy and the internal energy have an inverse trend of variation. With greater kinetic energy comes smaller internal energy. The absorbed energy increases rapidly along with the expansion of the damage and delamination. The greater the impact energy, the larger the energy absorbed.
- (3) The interfacial damage in the compression stage is more correlated to the tangential stiffness than the normal stiffness, whereas the maximum area of delamination is controlled by the normal stiffness. The greater the longitudinal tangential stiffness, the greater the area and amplitude of the interfacial damage in the compression stage. As the normal stiffness increases, the maximum area of delamination shows a trend of increasing first and then decreasing. There is always a critical normal stiffness that gives the largest area of delamination. This critical value depends on the geometrical and material properties of the track structure. It is suggested to find this critical normal stiffness for both controlling the delamination and preventing an exceedance of the track irregularity limit.

This is the first trial to investigate the interfacial damage and delamination by considering the wheel-rail contact as a vertical impact. The relationship between the impact response and the impact energy is consistent with that of the research for composite material [25]. It is a preliminary attempt to interpret the generation of delamination of the

track structure from the energy point of view. This paper concentrates on a single time of impact to exhibit the energy conversion and the evolution of the interfacial damage and delamination. Future analysis could be conducted on the cumulative damage of the interface under the cyclic wheel impact. Field test would be a powerful tool to validate the simulated result in this paper. However, due to the limits of the experimental facilities and cost, there is still a lack of the full-scale test regarding the interfacial damage of CRTS II SBTS caused by the vertical wheel impact. There once was a wheel-drop test of CRTS II SBTS, in which, however, only the acceleration of the track slab was recorded [26]. The development of the interfacial damage was not observed due to technical difficulty. Future work could also be conducted on the full-scale or scale model test of CRTS II SBTS under wheel impact so that the simulated result in this study could be validated.

#### Data Availability

The data used to support the findings of this study are available from the corresponding author upon request.

#### Conflicts of Interest

The authors declare no potential conflicts of interest with respect to the research, authorship, and/or publication of this article.

#### Acknowledgments

This research was financially supported by the National Natural Science Foundation of China (Grants nos. 51708459 and 51878578), the Project of Science and Technology Research Development of China Railway Co., Ltd. (Grant no. K2020G007), and the Open Foundation of Undergraduate-Oriented Engineering Practice Project of Key Laboratory of Southwest Jiaotong University (ZD2020010035).

#### References

- [1] G. T. Zhao, L. Gao, L. Zhao, and Y. Zhong, "Analysis of dynamic effect of gap under CRTS II track slab and operation evaluation," *Journal of the China Railway Society*, vol. 39, no. 1, pp. 1–10, 2017.
- [2] X. Cai, B. Luo, Y. Zhong, Y. Zhang, and B. Hou, "Arching mechanism of the slab joints in CRTSII slab track under high temperature conditions," *Engineering Failure Analysis*, vol. 98, pp. 95–108, 2019.
- [3] China Railway Publishing House, *Maintenance Rules for Ballastless Track of High Speed Railway (Trial)*, China Railway Publishing House, Beijing, China, 2012.
- [4] Y. Liu and G. Zhao, "Analysis of early gap between layers of CRTS II slab ballastless track structure," *China Railway Science*, vol. 34, no. 4, pp. 1–7, 2013.
- [5] Y. Li, J. Chen, J. Wang, X. Shi, and L. Chen, "Study on the interface damage of CRTS II slab track under temperature load," *Structures*, vol. 26, pp. 224–236, 2020.
- [6] G. Zhao and Y. Liu, "Mechanism analysis of delamination of CRTSII slab ballastless track structure," *Journal of the China Railway Society*, vol. 42, no. 7, pp. 117–126, 2020.

- [7] S. Zhu, J. Luo, M. Wang, and C. Cai, "Mechanical characteristic variation of ballastless track in high-speed railway: effect of train-track interaction and environment loads," *Railway Engineering Science*, vol. 28, no. 4, pp. 408–423, 2020.
- [8] S. Zhu and C. Cai, "Interface damage and its effect on vibrations of slab track under temperature and vehicle dynamic loads," *International Journal of Non-linear Mechanics*, vol. 58, pp. 222–232, 2014.
- [9] X. Lei, S. Wu, and B. Zhang, "Dynamic analysis of the high speed train and slab track nonlinear coupling system with the cross iteration algorithm," *Journal of Nonlinear Dynamics*, vol. 2016, Article ID 8356160, 17 pages, 2016.
- [10] P. Robinson and G. Davies, "Impactor mass and specimen geometry effects in low velocity impact of laminated composites," *International Journal of Impact Engineering*, vol. 12, no. 2, pp. 189–207, 1992.
- [11] F. Yang and W. Cantwell, "Impact damage initiation in composite materials," *Composites Science and Technology*, vol. 70, no. 2, pp. 336–342, 2010.
- [12] Z. Wu, L. Zhang, Z. Ying, J. Ke, and X. Hu, "Low-velocity impact performance of hybrid 3D carbon/glass woven orthogonal composite: experiment and simulation," *Composites Part B*, vol. 196, Article ID 108098, 2020.
- [13] J. Zhou, B. Liao, Y. Shi, L. Ning, Y. Zuo, and L. Jia, "Experimental investigation of the double impact position effect on the mechanical behavior of low-velocity impact in CFRP laminates," *Composites Part B*, vol. 193, Article ID 108020, 2020.
- [14] Y. Tai, T. Chu, H. Hu, and J. Wu, "Dynamic response of a reinforced concrete slab subjected to air blast load," *Theoretical and Applied Fracture Mechanics*, vol. 56, no. 3, pp. 140–147, 2011.
- [15] Z. Leng, W. Lu, M. Chen et al., "Explosion energy transmission under side initiation and its effect on rock fragmentation," *International Journal of Rock Mechanics and Mining Sciences*, vol. 86, pp. 245–254, 2016.
- [16] S. Kaewunruen, C. Ngamkhanong, and C. Lim, "Damage and failure modes of railway prestressed concrete sleepers with holes/web openings subject to impact loading conditions," *Engineering Structures*, vol. 176, pp. 840–848, 2018.
- [17] J. Wu, Y. Zhou, R. Zhang, C. Liu, and Z. Zhang, "Numerical simulation of reinforced concrete slab subjected to blast loading and the structural damage assessment," *Engineering Failure Analysis*, vol. 118, Article ID 104926, 2020.
- [18] T. Yilmaz, N. Kıraca, Ö. Anil et al., "Experimental investigation of impact behaviour of RC slab with different reinforcement ratios," *Structural Engineering*, vol. 24, no. 1, pp. 1–14, 2019.
- [19] R. Talreja and C. Singh, *Damage and Failure of Composite Materials*, Cambridge University Press, New York, NY, USA, 2012.
- [20] H. Tuo, Z. Lu, X. Ma, C. Zhang, and S. Chen, "An experimental and numerical investigation on low-velocity impact damage and compression-after-impact behavior of composite laminates," *Composites Part B: Engineering*, vol. 167, pp. 329–341, 2019.
- [21] M. Donadon, L. Iannucci, B. Falzon, J. Hodgkinson, and S. De Almeida, "A progressive failure model for composite laminates subjected to low velocity impact damage," *Computers & Structures*, vol. 86, no. 11–12, pp. 1232–1252, 2008.
- [22] J. Zhou, P. Wen, and S. Wang, "Finite element analysis of a modified progressive damage model for composite laminates under low-velocity impact," *Composite Structures*, vol. 225, Article ID 111113, 2019.
- [23] A. Riccio, A. De Luca, G. Di Felice, and F. Caputo, "Modelling the simulation of impact induced damage onset and evolution in composites," *Composites Part B: Engineering*, vol. 66, pp. 340–347, 2014.
- [24] L. Luo, G. Zhang, W. Wu et al., *Control of Track Smoothness of Wheel-Rail System*, China Railway Publishing House, Beijing, China, 2006.
- [25] T. Pärnänen, M. Kanerva, E. Sarlin, and O. Saarela, "Debonding and impact damage in stainless steel fibre metal laminates prior to metal fracture," *Composite Structures*, vol. 119, pp. 777–786, 2015.
- [26] W. Zhai, K. Wang, Z. Chen, S. Zhu, C. Cai, and G. Liu, "Full-scale multi-functional test platform for investigating mechanical performance of track-subgrade systems of high-speed railways," *Railway Engineering Science*, vol. 28, no. 3, pp. 213–231, 2020.